Bulletin 48
(Part 2 of 4 Parts)

THE SHOCK AND VIBRATION BULLETIN

Part 2
Isolation and Damping, Impact, Blast

SEPTEMBER 1978

A Publication of
THE SHOCK AND VIBRATION
INFORMATION CENTER
Naval Research Laboratory, Washington, D.C.

Office of
The Director of Defense
Research and Engineering

SYMPOSIUM MANAGEMENT

THE SHOCK AND VIBRATION INFORMATION CENTER

Henry C. Pusey, Director
Rudolph H. Volin
J. Gordan Showalter
Barbara Szymanski
Carol Healey

Bulletin Production

Graphic Arts Branch, Technical Information Division,
Naval Research Laboratory

Bulletin 48
(Part 2 of 4 Parts)

THE SHOCK AND VIBRATION BULLETIN

September 1978

A Publication of
THE SHOCK AND VIBRATION
INFORMATION CENTER
Naval Research Laboratory, Washington, D.C.

The 48th Symposium on Shock and Vibration was held at the Von Braun Civic Center, Huntsville, Alabama on October 18–20, 1977. The U.S. Army Missile Research and Development Command, Redstone Arsenal, Huntsville, Alabama was the host.

Office of
The Director of Defense
Research and Engineering

CONTENTS

PAPERS APPEARING IN PART 2

Partial contents: Isolation and Damping

PAPERS APPEARING IN PART 1

Keynote Address

Invited Papers

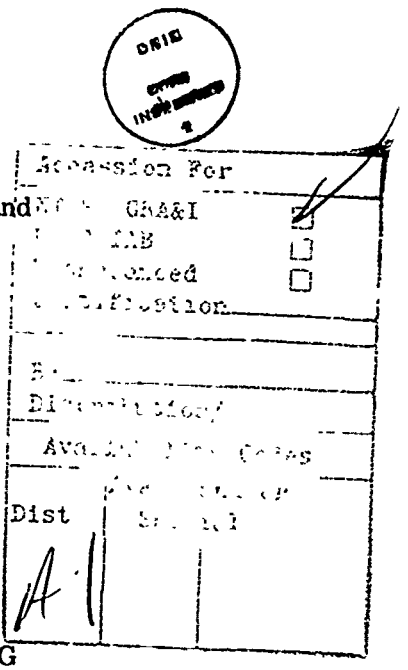

Panel Sessions

Modal Test and Analysis

PAPERS APPEARING IN PART 3

Structural Analysis

Instrumentation

Loads and Environments

Tracked Vehicles

PAPERS APPEARING IN THE SUPPLEMENT

ISOLATION AND DAMPING

SPECIFICATION OF DAMPING MATERIAL PERFORMANCE

D.I.G. Jones and J.P. Henderson
Air Force Materials Laboratory
Wright Patterson AFB, Ohio 45433

In this paper a simple reduced - temperature nomogram is applied to developing a specification for controlling damping material performance, and the resonant beam test technique is discussed as a possible standard method for measuring complex dynamic moduli of damping materials

INTRODUCTION

Now that damping materials are becoming extremely widely used for industrial and aerospace vibration and noise control applications, the problems of specifying damping properties of materials for specific environments and of establishing, by measurement, that materials supplied by vendors meet these specifications have become extremely acute. First, the user is burdened with the task of evaluating and selecting the proper materials, from innumerable sources and often without sufficient knowledge of their damping properties, and of verifying that the vendor has met requirements. And, secondly, the vendor has problems of quality control and of proving, again by measurement, that each batch of material supplied actually meets the agreed-upon definitions of performance. The result is, as might be expected, chaos! The legal and technical problems involved are well known, and a solution is urgently needed.

In this paper, we propose a possible approach toward the problem. It involves (i) the establishment of an appropriate and adequate method for measuring the data needed, namely a particular form of the well known resonant beam technique, and (ii) the specification of the required material properties in terms of a complex modulus-reduced temperature nomogram with allowable limits superimposed. It is shown that reliable data can be obtained by this technique, and that batches of damping material can be easily and quickly shown to meet, or fail to meet, the selected criteria.

2. SPECIFICATION OF MEASUREMENT TECHNIQUE

2.1. Need for a standard technique

Many techniques have been proposed and used for measuring damping properties of elastomeric or other energy dissipating materials [1-7]. Some examples of commercially available measurement systems are the Rheovibron [1], the Viscoelasticimetre [2], the Bruel and Kjaer Complex Modulus Apparatus (a resonant beam technique) [3], Fitzgerald's Rheometer [4] or the duPont DMA system. These techniques can give reliable data when used properly, with due attention being paid to sources of error. However there is considerable evidence to lead one to believe that such care is not taken often enough. We shall not attempt to evaluate such techniques in general, in this paper, but will confine attention to one particular technique which we have used for many years, namely the vibrating beam technique.

While most measurement techniques, when properly used, lead to useful data, the resonant composite beam technique [3] is one of the most successfully and widely used. For example, it forms the basis of a German standard for measuring dynamic moduli of relatively stiff elastomeric materials, used for free layer damping treatments [6]. Furthermore, the technique can be used, in conjunction with appropriate beam geometries, to measure the dynamic moduli of soft elastomeric materials, such as those used in constrained layer damping treatments. Therefore, depending on the range of values of the dynamic modulus of the specific damping material being evaluated, one should select a suitable specimen geometry, and apply appropriate criteria to each test measurement in order to confirm the validity or otherwise of that measurement.

2.2 Resonant Beam Measurement Techniques

The types of specimen used in the vibrating beam tests are illustrated in Figure 1. A typical block diagram is shown in Figure 2. In the tests, the beams are often excited by means of a magnetic transducer and the response picked up by a miniature accelerometer, although any methods of excitation and pickup are usable provided that the modes are strongly excited. Response spectra comprising graphs of transverse acceleration versus frequency are plotted using the recorder and the resonant frequencies, f_m, and half power bandwidth, Δf_m, noted for many temperatures. For reliable results with commercial versions of this system, it is often necessary to use beams made of a relatively low modulus metallic material with machined roots as indicated in Figure 3 for reduced root damping. The beam is often made of aluminum or steel and is usually not more than about 0.080 inches thick (2.0 mm) nor shorter than about 7 inches (178 mm). The root must be clamped in a fixture which does not move significantly. This is usually accomplished by using a relatively heavy fixture with no resonances of its own in the frequency range of interest.

An advantage of the method is that it is reasonably simple to use, errors can be estimated and kept within limits and a wide band of frequencies and temperatures can be covered with a single specimen. A disadvantage is that only low-strain-level data are obtainable.

By means of the vibrating beam test, one can determine the complex Young's modulus $E_D(1+i\eta_D)$ of the applied layer or the shear modulus $G_D(1+i\eta'_D)$ for the damping material in the core of the sandwhich beam. The values of G_D and η'_D or E_D and η_D are calculated from the measured resonant frequencies and modal damping (half-power bandwidth) at each selected temperature. While the procedure described seems simple, great care should be taken in measurement because it is easy to introduce small errors in the measured quantities, and this can lead to very large errors in the calculated values of G_D and η'_D or E_D and η_D, as will be discussed presently.

The homogenous beam type specimen is used for stiff materials, such as epoxies and plastics, which are self supporting at ordinary temperatures i.e., have Young's moduli greater than 10^6psi

$$|E_D| \geq 10^6 \text{lb/in}^2 \text{ or } 6.89 \times 10^9 \text{ N/m}^2$$

If $|E_D|$ is between 10^4 lb/in^2 (6.89×10^7 N/m^2) and 10^6 lb/in^2 (6.89×10^9 N/m^2), then the "Oberst" (non-symmetric) or "modified Oberst" (symmetric beams are usable with required h_D/h increasing as E_D falls toward the lower limit.

If $|E_D|$ is between 5 lb/in^2 (3.45×10^4 N/m^2 and 5×10^5 lb/in^2 (3.45×10^9 N/m^2), the symmetric sandwich beam is useful, since it relies on shear of the damping material between the two supporting beams and requires far lower dynamic muduli to have an appreciable effect on system response. It will be noted that some overlap does exist between the useful ranges of each type of beam specimen.

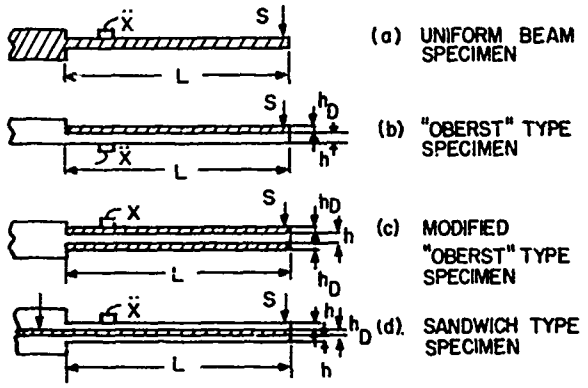

Figure 1. Vibrating beam test specimens

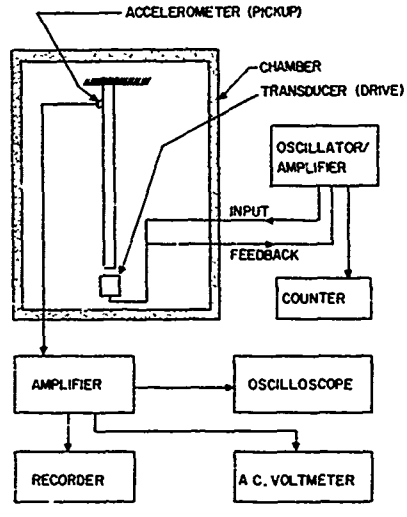

Figure 2. Block diagram of test system

2.3 EXTERNALLY COATED BEAMS

2.3.1 Equations and Criteria

For the beam with the damping material coated on one side only, the complex Young's modulus is derived from formulae due orginally to Oberst [7], these are:

$$Z^2=\left[\frac{1+\rho_D h_D}{\rho h}\right]\left[\frac{f_m}{f_{om}}\right]^2=\frac{1+2ne(2+3n+2n^2)+e^2n^4}{1+ne} \qquad (1)$$

$$\frac{\eta_m}{\eta_D}=\frac{en}{1+en}\left[\frac{3+6n+4n^2+2en^3+e^2n^4}{1+2en(2+3n+2n^2)+e^2n^4}\right] \qquad (2)$$

where $e=E_D/E$ and $n=h_D/h$. In these formulae, Z^2 is calculated from the measured resonance frequencies, f_m, of the mth mode of the damped beam and the measured frequencies, f_{om}, of the undamped beam and e is then deduced from equation (1). η_D is then calculated from equation (2), this value of e, and the measured value of the modal damping η_m. In fact, after some algebraic manipulation, the following equation for e in terms of Z^2 and n can be derived

$$e=[-(4+6n+4n^2-Z^2)n+\sqrt{n^2(4+6n+4n^2-Z^2)^2+4n^2(Z^2-1)}]/2n^4 \qquad (3)$$

In order to obtain satisfactory test results by this method, the beam length L should not be less than 7 inches (178 mm) and the thickness should not be less than about 0.05 inches (1.27 mm) because of machining difficulties. For ambient temperature tests (below 300°F/149°C) aluminum beams would normally be used, while for high temperature tests (up to 2000°F, 1093°C) steel or superalloy beams would normally be used. On the other hand, for the sandwich beam test, steel or aluminum beams could be used, as will be discussed presently.

For the beam with the damping material coated symmetrically on both sides, the complex Young's modulus is derived from the simpler formulae [8]:

$$E_D=E(Z^2-1)/[8n^3+12n^2+6n], \qquad (4)$$

$$\eta_D=\eta_m Z^2/(Z^2-1), \qquad (5)$$

where $Z^2=(1+2\rho_D n/\rho)(f_m/f_{om})^2$ and η_D and n are defined as before. In these formulae Z^2 and η_m are determined as before.

2.3.2 Sources of Errors for externally coated beams

For the vibrating beam tests, as for any other measurement technique, errors in the measured complex moduli of the material being evaluated can arise from several possible sources, including

(a) specimen perparation e.g. poor adhesion, voids, slipping in fixture grips non-uniform thickness, etc.

(b) temperature control - the specimen temperature may not be that indicated by the thermocouple, there may be thermal lag (insufficient time for thermal equilibrium to be reached) or there may be non-uniformity of temperature distribution within the specimen.

(c) Errors in measuring resonant frequencies - these can arise because of too high a frequency sweep rate, nonlinear response (especially of the undamped beam) and distortion of measured signals (hence the need to always monitor "input" and "output" signals for proper wave form).

(d) Errors in measuring modal damping arising from closely spaced modes, extraneous sources of damping (e.g. damping in grips), and erroneous interpretation of non-linear response in terms of apparently increased damping.

(e) Error magnification - the effect of unstable regions in the equation being used to derive the complex moduli from the measured quantities. As an example, in the "Oberst" equations (1) and (2), or the "modified""Oberst" equations (4) and (5), the term $(Z^2-1)^{-1}$ acts to magnify errors in η_m or f_m and as $Z^2 \rightarrow 1$, this factor becomes infinite!!

One must therefore be constantly aware of these and other possible sources of erroneous data and apply every possible precaution both in obtaining the data and in interpreting and utilizing it. Figure 3 shows the typical variation of error magnification with Z^2 for a speci-

fic value of n for a non-symmetric externally coated beam, based on equation 3 (see reference 8 for symmetric beam).

(f) Long term changes in humidity can be a factor for some cases; materials should be stored in a constant humidity environment until ready for evaluation. Once a sandwich beam is assembled, typically the humidity effects are insignificant. However, this may not be the case for externally coated beams.

(g) Positioning of pickup and excitation points - at some temperatures, certain modes may not be well conditioned for accurate observation. Moving the points can help improve the signal to noise ratio.

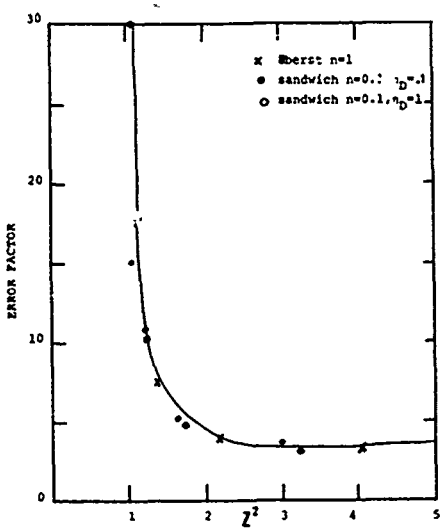

Figure 3. Errors as function of Z^2

2.4. SANDWICH BEAM TEST METHOD

2.4.1. Equations

The sandwich beam test is appropriate for measurements on elastomeric materials in the range 5 lb/in^2 (3.45 x 10^5 N/m^2) $\leq E_D \leq$ 5 x 10^5 lb/in^2 (3.45 x 10^9 N/m^2) and $0.01 \leq \eta_D \leq 2.0$, provided that care is taken in regard to choice of specimen demensions and specimen preparation.

For the symmetric sandwich beam (Figure 1), the approach is based on a set of equations due to Kerwin and others, reduced to an uncoupled form. The shear modulus, G_D, and loss factor, η'_D, of the viscoelastic material may then be derived from the equations. The now classical equation of Ross, Kerwin and Ungar are, for the symmetric sandwich beam in the current notation [9]:

$$(EI)^*_e = \frac{Eh^3}{6} + Eh(h+h_D)^2 \frac{g^*}{1+2g^*} \qquad (6)$$

when $(EI)^*_e$ is the equivalent complex flexural rigidity of the three layer sandwich [$\equiv (EI)_e(1+i\eta_m)$] and g^* is the shear parameter given by:

$$g^* = \frac{G^*_D L^2}{Ehh_D \xi_m^2} \qquad (7)$$

Equation (6) and (7) may be solved to give simple algebraic equations for G_D and η'_D, namely:

$$G_D = \frac{[A-B)-2(A-B)^2-2(A\eta_m)^2][Ehh_D\xi_m/L^2]}{(1-2A+2B)^2+4(A\eta_m)^2} \qquad (8)$$

$$\eta'_D = A\eta_m/[A-B-2(A-B)^2-2(A\eta_m)^2] \qquad (9)$$

where

$$A=(f_m/f_{om})^2(2+\rho_D h_D/\rho h)(B/2)=BZ^2 \qquad (10)$$

and

$$Z^2=(1+\rho_D h_D/2\rho h)(f_m/f_{om})^2 \qquad (11)$$

$$B=1/6(1+h_D/h)^2 \qquad (12)$$

It should be noted that bending of the viscoelastic core is neglected in equation (5). However, for most cases where the core is not too stiff or thick, these terms are not significant. The eigenvalues ξ_m define the relationship between the resonant frequencies of the uncoated individual beams, and the modulus E, by the classical relationship

$$\rho h \omega^2_{om} L^4/(Eh^3/12)=\xi_m^4 \qquad (13)$$

The first six eigenvalues of the cantilever beam system are:

$$\xi_1^2 = 3.515$$
$$\xi_2^2 = 22.0345$$
$$\xi_3^2 = 61.6970$$
$$\xi_4^2 = 120.902$$
$$\xi_5^2 = 199.866$$
$$\xi_6^2 = 298.56$$

Finally, it should be noted that for most elastomeric materials, $E_D = 3G_D$ and

$\eta_D \approx \eta_D'$ [10], so that results from sandwich and externally coated beams can be compared.

2.4.2. Source of errors for sandwich beams

The sources of error are precisely the same as delineated for the externally coated beams, although the magnitudes may be somewhat different. For example, Figure 3 shows the effect of errors in the frequency parameter Z^2 on the G_D, as a function of Z^2. It is seen that, in this case, errors are magnified for values of Z^2 near 1.0.

Furthermore the combination of experimental errors and approximations in the derivation of equation (6) usually result in unacceptable errors in data obtained from the first bending mode. Therefore, this mode should normally be omitted when testing sandwich beams.

2.4.3. Tolerances and recommended dimensions

In conducting tests with the sandwich technique, it is vital that each metal beam be matched, i.e., that dimensions are matched extremely closely and that the resonant frequencies f_{0m} of the individual beams be well matched also (within 1%). Beam thicknesses less than 0.05 inches (1.27 mm) should be avoided, again mainly because of machining difficulties. The thickness h_D of the damping material being evaluated should not be less than 0.005 inches (0.127 mm), and preferably much more, because of difficulties in controlling the dimensions of the composite specimen.

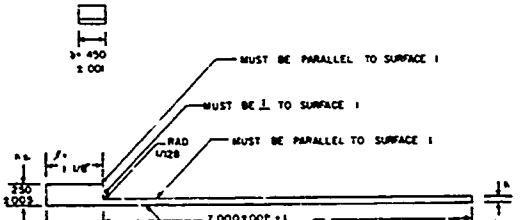

Figure 4. Sandwich beam specimen

Recommended specimen dimensions for sandwich beams (figure 4) are:

L=7 ins ±0.002 ins (177.8mm±0.05mm)
ℓ=1.125 ins ±1/64 in (28.58mm±0.40mm)
$h_{s1}=h_{s2}$=0.25 ins ±0.005 in (6.35mm±0.12mm)
n=0.07 ins ±0.0005 in (1.778mm±0.018mm)
h_D=0.005 ins to 0.05 in ± 0.001 in (0.127mm to 1.27mm±0.025mm)
b=0.45 ins ±0.001 in (11.43mm ±0.03mm)

For the thickness h the tolerances are especially important, since the two aluminum beams must form a matched pair, having very close resonant frequencies when tested individually. For example, if h_1=0.070"+0.0005 and h_2+0.070"-0.0005, the n^{th} resonant frequency of each beam will differ by the ratio

$$\frac{0.070+0.0005}{0.070-0.0005} = \frac{0.0705}{0.0695} = 1.0144$$

which represents a difference of over 1.4%. If f_m=1000 Hz nominally, the difference could be as high as 14 Hz in this case, which is significant. What this part of the specification means, therefore, is that the tolerances of each pair of beams, while lying within the above limits, at all points along the beam, must do so as a pair i.e., if h_1 is oversize, so must h_2 be by an equal amount. this means that, as beams are made, they must be matched in pairs. A vibration test is needed to verify this matching.

Each metal beam must be vibration tested at several temperatures to determine the first four or more resonant frequencies (f_{01}, f_{02}, f_{03}, f_{04} . . .) which must be within 1.0% of each other at all temperatures of concern.

2.4.4. Surface preparation and fabrication for sandwich specimens

The matched pair of metal beams must be cleaned and degreased. The surface should be primed, where appropriate. The thickness of the primer should not exceed 0.0005 inches (0.0127mm) under any circumstances. The damping material, in a thickness from 0.005 ins. (0.127mm) to 0.05 inches (1.27mm), is then clamped between the two beams in an appropriate fixture and bonded directly in place with heat and modest pressure, as needed (see Figure 5). The spacer, equal in thickness to the damping material, should be glued in place at the same time as the damping material is set in place. A thin layer of good adhesive will be used. For example a cyano-acrylate adhesive can be used up to about 200°F (100°C). If an epoxy adhesive is needed for any particular case e.g. at higher temperature, its cured thickness should not exceed 0.002 inches (0.051mm), and care should be taken to insure this, and h_D should not be less than 0.01 ins (0.254 mm).

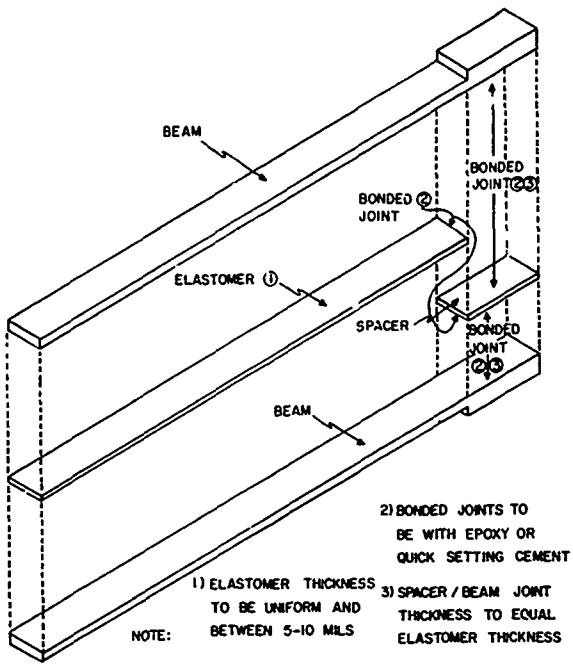

Figure 5. Composite beam assembly

2.5. TEST AND DATA ANALYSIS PROCEDURES

2.5.1. Undamped beam

Each beam should be set in the Brüel and Kjaer complex modulus apparatus (or equivalent system) and excited through a magnetic transducer or shaker. The pick-up should be by means of an accelerometer or another transducer. A small soft iron disc ($\leq$0.1 gm weight) should be glued on the beam under the transducer so as to provide the appropriate magnetic interactions. A microminiature accelerometer (e.g. Endevco type 22) with lightweight cable should generally be used for pick-up except at very high temperatures. The accelerometer must weigh less than 0.25 grams. An accelerometer is generally more sensitive than another magnetic transducer for pickup, and avoids the problems of cross-coupling of the driving and pickup signals.

The vibration test system must produce plots of amplitude (velocity or acceleration) versus frequency. From these, one can identify the first four (or more) resonant frequencies f_{01}, f_{02}, f_{03}, f_{04}. The modal damping of the individual beam, defined as $(f_{om}^{+}-f_{om}^{-})/f_{om}$, must be less than 0.002 for every mode. Here f_{om}^{+} and f_{om}^{-} are the frequencies at which the amplitude is 0.707 times the maximum amplitude at the frequency f_{om} (3 db below). From this data, one can select the matched beams, having all relevent values of f_{om} within ±1.0%.

These tests should be conducted at several temperatures, so that the Young's modulus E of the beam material can be calculated from equation (13), for each point, and inserted in Table I (see later).

2.5.2. Testing of Composite Beam

The tests are conducted in exactly the same way as for the individual aluminum beams. Typical spectra obtained using an accelerometer for pickup are shown in Figure 6.

At temperatures far removed from the temperature of peak damping of the composite beam, sharp peaks should be observed as in Figure 6, whereas, near the optimum damping temperature, the peaks are far less pronounced.

For good results each peak should be distinct and rise above the "background" by 10 db or more. If the peak is less than 10 db above the background the data in a given mode may be difficult to obtain in a satisfactory manner, especially if the peak is highly "unsymmetrical". If such "bad" points are obtained one can attempt the following remedies before rejecting the test data outright.

a. Carefully check the system for loose clamps, bad transducers or cables, or malfunctioning electronics.

b. Integrate the acceleration signal electronically. This has the effect of looking at "velocity" instead of "acceleration".

c. Try another pickup position on the beam.

d. Try another (usually lower) thickness of damping material.

e. Try filtering the output signal - but this must be done very carefully in order not to obscure a problem!

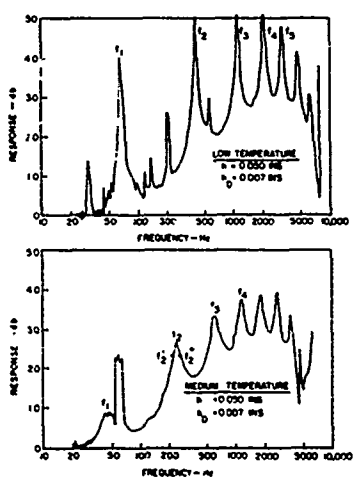

Figure 6. Typical response spectra

Other methods of measuring the modal damping η_n are also usable. For example, one could plot a graph of the real part of the response versus the imaginary part (Nyquist diagram) and estimate η_n from the circular arc trace near each resonant frequency. Equally, the signals to the driver, and from the accelerometer, can be treated as analoy voltage or they may be handled digitally. The end results, provided that the signals are adequate, should be identical. However, it is not the purpose of this paper to discuss test techniques in detail.

2.5.3. Data Acquisition

For each "good" point, obtained as described already, the resonant frequency f_m is measured for each mode (m=2,3,4) and temperature. Also measured are the frequencies f_m^+ and f_m^- for which the amplitude of the voltmeter signal is 3db (0.707 times) lower than the maximum amplitude at f_m. Note the results in Table 1. The frequencies should be read on the frequency counter. The precision of measurement should be ±0.1 Hz, and at least one repeat cycle of the counter should be observed before writing down the figure.

--The waveforms should be noted on the oscilloscope. If a non-sinsuosoidal shape is noted on the oscilloscope, reject the point and check the system.

--For each temperature, a response spectrum such as in Figure 6 should be obtained to verify that the peaks are "good" as described above, and to avoid spurious peaks caused by the line picking up stray voltages (usually multiples of 60 Hz) or fixture resonances. Some such peaks can be seen in Figure 6. They must be watched out for!

2.5.4. Data Reduction

No matter which beam type of specimen is used, each test "point" consists of a set of simultanously measured values of temperature, mode number, resonant frequency and modal damping. Along with the corresponding figures for the undamped beams, the complete set of data points can be tabulated as in Table I. The last two columns represent the calculated values of (E_D and η_D) or G_D and η'_D, obtained from the appropriate equations and beam and treatment dimensions. The set of values of temperature, damped resonant frequency, G_D or E_D and η'_D comprise the raw test data for the damping material being evaluated.

When digital data reduction techniques are used, it is possible to automate the entire process and obtain the nomograms directly. For example, it is possible to display the data directly on a cathode ray screen, as discussed in reference [11].

An important step in evaluating the validity of the data being generated by the test is the plot of η_m, f_m and f_{om} against temperature. Figure 7 shows such a plot, generated from the test data for a specific damping material given in Table 2. Ideally, of course, one would wish to generate such graphs automatically as testing proceeds, but in any event the subjective evaluation of the "raw" test data in this way is a most important step. The appearance of "bad" data at this point should be used as an indicator of the need to pinpoint problems in the test system before too much effort is invested.

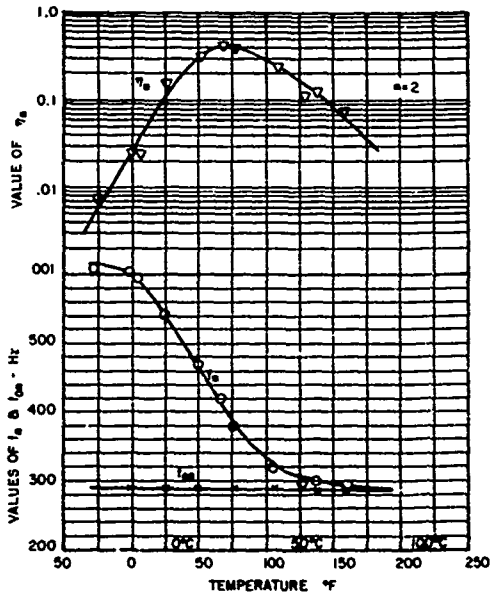

Figure 7. Typical graphs of η_m, f_m & f_{om} versus temperature

2.5.5. Test temperatures

The tests should be conducted in an ordered sequence of selected temperatures. For example 75°F, 50°F, 25°F, 0°F, repeat 0°F, 25°F, 50°F, 75°F, 100°F, repeat 100°F, 75°F (11 points total) might be used for a room temperature damping material. A 15 minute soak should be allowed after thermal equilibrium has been reached, i.e., after two successive readings of temperature at 1 minute intervals are within about ±2°F (1°C) of each other. Temperature should be measured by a thermocouple embedded in the specimen at the root. An initial check-out of the oven should verify that temperatures are uniform (±2°F) at

all points along the beam, at all temperature settings.

3. SPECIFICATION OF MATERIAL PROPERTIES

The final product of the test program, if successful, is a matrix of values of G_D and η'_D or E_D and η_D at several discrete temperatures and frequencies. It is not the purpose of this paper to describe all the available approaches toward analyzing this data. For purposes of verifying whether a candidate material meets the specific requirements, however, one must compare the data with that already known from prior batches of the material.

In seeking to rationally collapse this data into a useful form, one would first generate a graph of E_D (or G_D) and η_D versus a reduced frequency $f\alpha_T$ where α_T is a "shift factor" depending on temperature [12]. This somewhat tedious task can be circumvented by utilizing a "reduced temperature" nomogram, as described in reference [13]. In this nomogram, one has superimposed a series of diagonal lines with non-uniform spacing, each line representing a fixed temperature. The development of this nomogram is described in reference [13], but its use is extremely simple. For each measurement point (simultaneous values of temperature, frequency, E_D and η_D) one simply looks along the lower horizontal axis to choose a diagonal line representing the temperature, then along the diagonal line until the horizontal frequency line is cut, as in Figure 8. From this intersection point X one then moves vertically up or down to plot the measured values of E_D and η_D. One selects the temperature scale arbitrarily, but only one temperature scale will collapse the data properly, so some judgement is needed just as in drawing a "reduced frequency" curve. Figure 8 shows a plot for 3M-467 adhesive, based on test data given in Table 2.

Data obtained by the sandwich beam method agrees well with that obtained by other methods [12].

The graph shows the test data directly as a function of frequency and temperature. The scatter between test points is available, one can then draw upper and lower limit lines for E_D and for η_D. Sometimes an upper limit is not desired for η_D, but the range and limits depend entirely on the sensitivity of the application. What is important is the fact that users and suppliers of damping materials have a tool for directly specifying the damping performance they wish to duplicate in future batches of material (based on tests of an initial batch) and a means for determining directly whether or not measured test data does or does not lie within this specification. Clearly, wisdom and judgement is needed to use such a specification, but that problem has always existed so far as specifications are concerned.

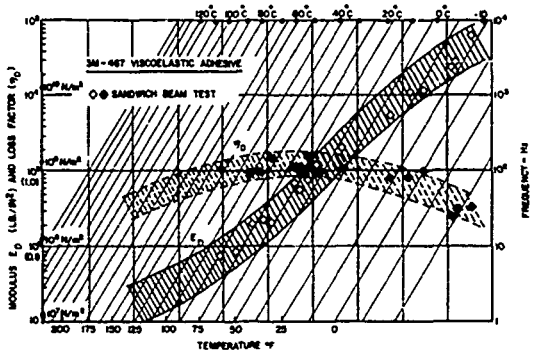

Figure 8. Reduced temperature nomogram for material with hypothetical acceptance limits added

SUMMARY AND CONCLUSIONS

Details of the utilization of a resonant beam technique, particularly with a sandwich configuration, have been presented of soft viscoelastic materials. Recommended specimen geometries and testing procedures have been described.

Finally use has been made of a newly developed "reduced temperature" nomogram to create a simple process for specifying the required damping properties of a material, based on resonant beam tests for an initial or reference "batch" or "sample". Such a specification allows one to set rational goals in regard to quality and batch control, but must be used with the same care as all specifications, since over-or-under specification is always a potential source of unexpected problems.

ACKNOWLEDGEMENTS

Thanks are due to A. D. Nashif, president, Anatrol Corporation , Cincinnati, D. Caldwell, 3M Company, Minneapolis, Minnesota, M.C. Parin, University of Dayton and Dr. L. C. Rogers, Air Force Flight Dynamics Laboratory, for useful technical discussions about the development of standards for damping materials. Thanks are also due to Judy Owens for typing the manuscript.

REFERENCES

1. Anon., Product information on "Model DDV II Rheovibron", Imass Inc., PO Box 134, Accord (Hingham), Mass. 02018.

2. Anon., Product information on "Viscoelasticimeter", Metravib, 24 bis chemin des Mouilles, 69130 Ecully, France.

3. Anon., Product information on "Complex modulus apparatus", Bruel and Kjaer Inc., Cleveland, Ohio.

4. E. Fitzgerald and J. Ferry, "Method for determining the dynamic mechanical behavior of gels and solids at audio frequencies; comparison of mechanical and electrical properties", J. Colloid Sci., 8, 1-34, 1953.

5. Anon., "Thermal Analysis Review: dynamic mechanical analysis", DuPont Inst., Wilmington, Delaware.

6. Anon., DIN 53440, "Bending vibration test for plastic and damped laminated systems", German Standard for Damping Material Evaluation.

7. H. Oberst, "Uber die Dampfung Biegeschwingungen Dunner Bleche Durch fest Haftende Belage", Acustica (Akustische Beihefte) 4, 181-194, 1952.

8. A.D. Nashif, "A new method for determining the damping properties of viscoelastic materials", Shock and Vibration Bulletin 36, 37-47, 1967.

9. D. Ross, E.E. Ungar and E.M. Kerwin, Jr., "Damping of plate flexural vibrations by means of viscoelastic laminae", Structural Damping, ed. J.E. Ruzicka, Proc. ASME Colloq., 1959.

NOMENCLATURE

A,B	non-dimensional parameters
b	breadth of beam
D	suffix denoting damping material
e	E_D/E - modulus ratio
E	Young's modulus of metal beam material
E_D	real part of complex Young's modulus of damping material
f	frequency (Hertz)
f_{om}	mth natural frequency of undamped beam
f_m	mth resonant frequency of damped beam
G_D	real part of complex shear modulus of damping material
h	thickness of beam
h_s	thickness of root
l	length of root
L	Length of beam
m	mode number
n	thickness ratio h_D/h
T	temperature
T_o	reference temperature
Z^2	non-dimensional parameter
α_T	temperature shift factor
η_D'	shear loss factor of damping material
η_m	loss factor of beam specimen in mth mode
η_D	extensional loss factor of damping material
λ_m	wavelength of mth mode
ξ_m	mth eigenvalue for beam
ρ_l	density of metal beam
ρ_D	density of damping material
ω	circular frequency
ω_m	mth circular frequency of damped beam
ω_{om}	mth circular frequency of undamped beam

TABLE 1 - SUGGESTED DATA COLLECTION SYSTEM

Material: _____

Beam Dimension: h_D= h= L= b=

Material Data: ρ= ρ_D= Test Conducted by

Date	Temp	Mode No.(n)	ζ_n	Undamped Resonant freq. f_{on}	E	Damped Resonant freq. f_n Hz	f_n^+ Hz	f_n^- Hz	$\eta_n = \frac{f_n^+ - f_n^-}{f_n}$	G_D Eq(1)	η'_D Eq(2)

TABLE 2 - SANDWICH TEST SYSTEM DATA

h =0.070 ins.(1·78mm), h_D =0.008 ins.(0·20mm), L=7.0 in.(178mm)

Temp. °F	Temp. °C	Mode No.m	f_o Hz	f_m Hz	η_m	G_D psi	G_D N/m²	η'_D	α_T (T_o=150°F,66°C)
0	-18	2	290.0	597	0.027	10140	6.99E7	0.334	1.0×10^5
		3	798	1609	0.039	18012	1.24E8	0.339	
		4	1566	3043	0.058	21245	1.47	0.343	
25	- 4	2	288.6	537	0.164	2009	1.39E7	0.807	6×10^3
		3	795	1397	0.208	3623	2.50	0.828	
		4	1559	2521	0.285	4149	2.86	0.994	
50	10	2	287.5	462	0.311	711	4.90E6	1.113	500
75	24	2	286.6	374	0.394	240	1.65E6	1.469	90
104	40	2	285.9	313	0.244	72.5	5.00E5	1.599	15
		3	787.5	854	0.154	189	1.30E6	1.021	
		4	1544	1629	0.119	251	1.73	1.065	
		5	2527	2645	0.091	357	2.46	0.906	
133	56	2	285.1	299	0.137	41.5	2.86E5	1.361	2.0
		3	785.3	814	0.082	91.1	6.28	0.970	
		4	1540	1572	0.062	118	8.10	1.063	
		5	2520	2583	0.050	219	1.51E6	0.756	
153	67	2	284.5	293	0.078	28.5	1.96E5	1.061	0.9
		3	783.6	798	0.049	55.3	3.87	0.899	
		4	1537	1550	0.034	70.9	4.89	0.927	
		5	2515	2550	0.028	149	1.03E6	0.597	
66	19	2	286.9	414	0.410	374	2.58E6	1.499	200
		3	790.4	1042	0.279	802	5.53	0.904	
125	52	2	285.3	296	0.116	33.6	2.32E5	1.378	3.5
		3	785.9	804	0.077	63.9	4.40	1.247	
		4	1541	1548	0.050	55.5	3.83	1.728	
2	-17	2	289.5	588	0.026	7881	5.43E7	0.250	8×10^4
-25	-32	2	290.5	600	0.008	12031	7.79E7	0.105	2×10^6
		3	800.2	1649	0.007	30600	2.13E8	0.088	
		4	1569	3194	0.017	45342	3.13E8	0.169	

DISCUSSION

Mr. Wada,(Jet Propulsion Laboratory): In relation to the first resonant frequency in the calculation of damping, physically why do you throw out the first mode of a cantiliever beam?

Mr. Henderson: For years we did that because the data never looked good. More recently I have been given another explanation which I am still in the process of checking out through usually reliable sources. Looking back to what Ross, Ungar and Kirwin[1] did in their initial equations, they expanded the mode shapes in terms of sinusoidal functions for a pin-pin beam and they made certain approximations in their equations as a result of this. I think that really the reason is the first mode shape in a cantilever beam is not accurately described by this kind of expansion. You run into a mathematical problem of using the simplifications that Ross, Ungar and Kirwin applied to a cantilever beam as opposed to a pin-pin beam.

Mr. Wada: So its not really in the data it is in the mathematical representation.

Mr. Henderson: That is what I am hearing now and I tend to believe it but I have to go back and check that myself.

(1) D. Ross, E.E. Ungar and E.M. Kerwin, J.R. 1959, Structural Damping, American Society of Mechanical Engineers 49-87.

A REDUCED-TEMPERATURE NOMOGRAM FOR CHARACTERIZATION OF DAMPING MATERIAL BEHAVIOR

David I.G. Jones
Air Force Materials Laboratory
Wright-Patterson Air Force Base, Ohio 45433

An adaptation of the well known "reduced-frequency" concept for linear damping materials is made, so as to produce a "reduced-temperature" nomogram. This simple nomogram has the advantage of allowing one to directly read off the complex modulus properties of damping materials at any given temperature and frequency, without the need for intermediate calculations

1. INTRODUCTION

It has been known for many years that most, if not all, elastomeric type materials used for vibration control and isolation have dynamic properties which depend strongly on temperature and frequency. It is also well accepted that the temperature and frequency variables can be combined into a single variable, called the reduced frequency $f\alpha_T$, so that the shear modulus G_D (or Young's Modulus E_D) and the loss factor η_D depend only on $f\alpha_T$. Such "universal curves" are constructed. using experimental data for each material at many discrete temperatures and frequencies, by empirically choosing α_T for each temperature T in such a way as to give the "best fit" of the data.

The graphs of E_D and η_D versus $f\alpha_T$ and of α_T versus temperature T contain all the information necessary to characterize a given material at any selected frequency and temperature. However, it has always been tedious to construct such curves from the test data and just as tedious to use the curves for interpolation of data to perform calculations or for generating materials specifications or for any other applications. What is needed, and has been needed for a very long time, is a useful "reduced temperature" concept in place of the important but difficult to use "reduced frequency" concept.

The aim of this paper is to show how, once the master "reduced frequency" plot has been drawn, it is a very simple task to go the one step more that is necessary in order to create a "reduced temperature" plot. This is done by superimposing oblique coordinates on the master curve to represent the temperature variations. The resulting nomogram is a simple multiple scale graph containing all data in a form directly readable from the axes representing temperature and frequency. The nomogram is extremely useful for data extrapolation, data reduction or material specification. Examples are given illustrating the development and use of typical nomograms.

2. MODELIZATION OF LINEAR RHEOLOGICAL BEHAVIOR

2.1 Characterization of Linear Behavior (Complex Moduli)

For many rubberlike or linear rheological materials, the hysteresis loop of the stress-strain relationship is not thin but is close to being an ellipse. The shape of the loop does not change greatly with amplitude, within a certain range, and the area enclosed by the loop is nearly proportional to the square of the strain amplitude, other things being equal. In this case, although the shape of the stress-strain curve does not appear to support such a point of view, the damping may be regarded as linear, and a very convenient and simple representation of the stress-strain behavior is possible, namely the complex modulus representation (1-5), which we shall now briefly summarize.

Consider a hypothetical elliptical hysteresis loop as in Figure 1. The approximate equation of this ellipse is:

$$\sigma = \sigma_0 \left\{ \varepsilon/\varepsilon_0 \pm \eta_D \sqrt{1-(\varepsilon/\varepsilon_0)^2} \right\} \qquad (1)$$

where σ_0, ε_0 and η_D are defined in Figure 1, η_D being at this point only a measure of the thickness of the hysteresis loop. In this equation, the + sign relates to the loading part of the cycle and the - sign relates to the unloading part of the cycle. The positive square root is implied in equation (1), of course.

Now if $\varepsilon = \varepsilon_0 \sin\omega t$, where ω is the frequency, equation (1) becomes:

$$\begin{aligned} \sigma &= \sigma_0 \{\sin \omega t \pm \eta_D |\cos \omega t|\} \\ &= \sigma_0 \{\sin \omega t + \eta_D \cos \omega t\} \end{aligned} \qquad (2)$$

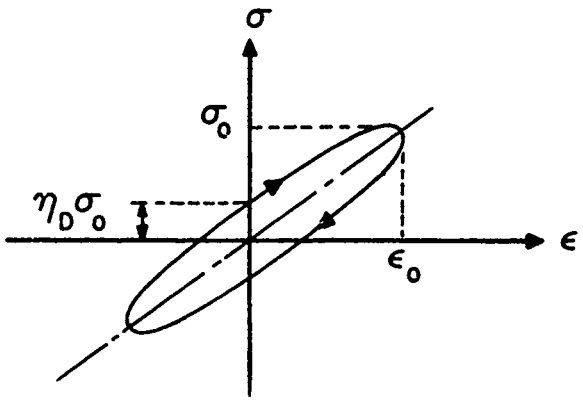

Fig. 1. Hysteresis loop for linear rheological material.

$\cos \omega t$ is +, $\omega t = -90^{o}$ to $+90^{o}$, corresponding to the loading part of the cycle (+ sign), and $\cos \omega t$ is negative from $\omega t = +90^{o}$ to $+270^{o}$, corresponding to the unloading part of the cycle (- sign). Since we know the first derivative of $\sin \omega t$, equation (2) gives:

$$\sigma_e = E_D\{\varepsilon + i\omega(\eta_D/|\omega|)\dot{\varepsilon}\} = E_D(1+i\eta_D)\varepsilon \qquad (4)$$

This is the well known complex modulus representation of linear rheological material behavior under harmonic excitation. η_D is a measure of the damping and is called the loss factor. Note that $\eta_D \cdot E_D$ is sometimes known as the loss modulus. In practical cases, both E_D and η_D are functions of frequency, temperature and strain level, but the concept is still useful in a wide variety of problems, even those involving non-sinusoidal excitation.

Similar considerations apply to deformations in shear, so that the relationship between the shear stress σ_s and the shear strain ϕ is:

$$\sigma_s = G_D(1+i\eta_D')\phi \qquad (5)$$

where G_D is the real part of the shear modulus and η_D' is the shear loss factor, usually considered to be equal to η_D.

2.2 Effects of Temperature and Frequency

One of the ways in which the large number of available linear rheological materials differ from each other is by the variation of E_D and η_D with frequency, temperature, strain amplitude and pre-stress. Temperature is by far the most important factor since E_D can vary by as much as four orders of magnitude over a narrow temperature range in some cases. The variation of Young's modulus E_D (or shear modulus G_D) and loss factor η_D with temperature at fixed frequency and cyclic strain amplitude are typically of the form shown in Figure 2. Three distinct temperature regions are observed, namely the glassy region, the transition region and the rubbery region. In the glassy region E_D is high and η_D is low; in the transition region E_D varies more slowly with temperature and η_D is high; and in the rubbery region E_D varies more slowly with temperature and η_D is lower than in the transition region, although not as low as in the glassy region. At the very highest temperatures, irreversible thermal decomposition of the material occurs. Although the variation of complex modulus properties with frequency is less drastic than with temperature, it is often important. For a typical material, graphs of E_D and η_D versus temperature for a number of frequencies might look as sketched in Figure 3.

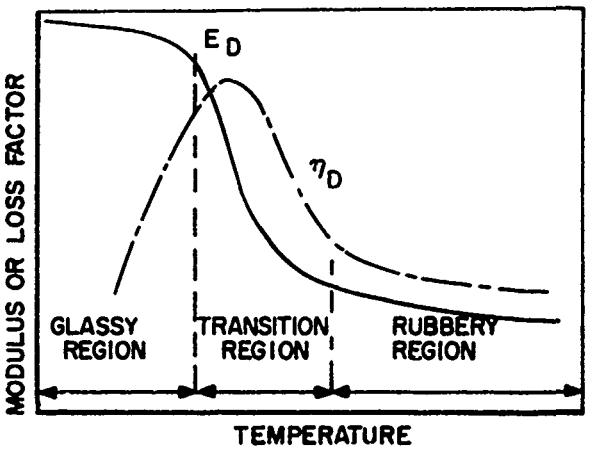

Figure 2. Complex modulus dependence on temperature.

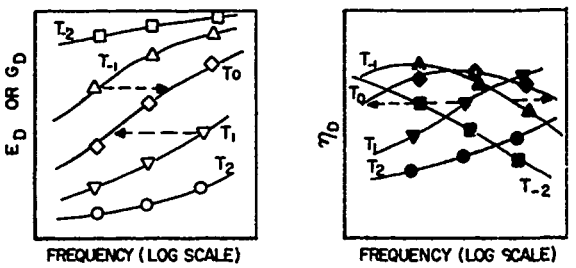

Figure 3. Dependence of complex modulus on frequency.

2.3 Temperature-Frequency Equivalence

If the effects of frequency on damping material behavior are taken into account, one of the most useful techniques for presenting the experimental data is by means of the

temperature-frequency equivalence (reduced frequency) for linear rheological materials (6-8). In this approach, both $(T\rho_0/T\rho) \times E_D$ and η_D are plotted against the so-called reduced frequency parameter $f.\alpha_T$, where f is the actual frequency, α_T is a function of the absolute temperature T, and T_o is a reference temperature, again on the absolute scale. Frequently T_o/T and the density ratio ρ_0/ρ are taken to be 1.0 over a wide temperature range and are ignored with little significant errors. The preparation of "master curves" of E_D and η_D against $f.\alpha_T$ is extremely useful for extrapolating test results obtained at discrete frequencies and temperatures. For example, in a test series one may have data over the frequency range 100 to 1000 Hz and a temperature range from 0°C. to 100°C. and wish to estimate the properties at 50°C. and 2 Hz. In order to achieve this, one first uses the available data to produce a best fitting set of master curves. The process is most satisfactorarily accomplished empirically by judging the factor α_T on the basis of the shift needed to make the curve of log E_D versus log (frequency) as in Figure 3, at temperature T_i (i = ±1,2,. . .), match as closely as possible the curve of E_D versus frequency at temperature T_o, while at the same time matching the curves of η_D versus frequency at temperatures T and T_o, to produce curves like those shown in Figure 4. In this way, the limitations of the measuring techniques can be at least partly compensated for. Typically, α_T will vary with temperature in the manner illustrated in Figure 5.

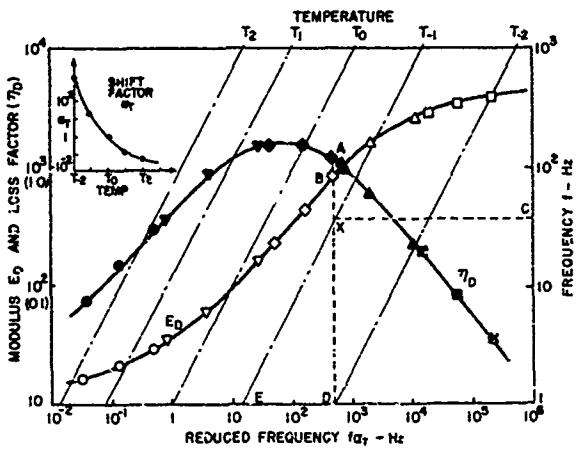

Figure 4. Reduced variables.

3. TEST RESULTS

A number of materials have already been evaluated for damping behavior, using resonance and resonant beam tests (8), including an acrylic adhesive (9), a filled silicone elastomer (10), a silicone potting compound (11) and a vitreous enamel (12), as well as several other materials. Some of the test data is summarized in Tables 1 through 4. The reference temperature T_o and the shift factor α_T at each temperature T were selected so as to give a "best fit" of the experimental data in the "reduced frequency" plot. Figure 5 shows the graph of α_T versus temperature difference $T-T_o$, when T_o is chosen suitably for each material so as to generate a "universal curve" of α_T versus $T-T_o$, in the usual manner. Figure 6 to 9 show graphs of E_D and η_D versus reduced frequency $f\alpha_T$ for the four materials considered here.

The graph of α_T versus $T-T_o$ can be represented by the following empirical equation, based on the WLF equation (7,13):

$$\log_{10}\alpha_T = \frac{-12(T-T_o)}{525+T-T_o}$$

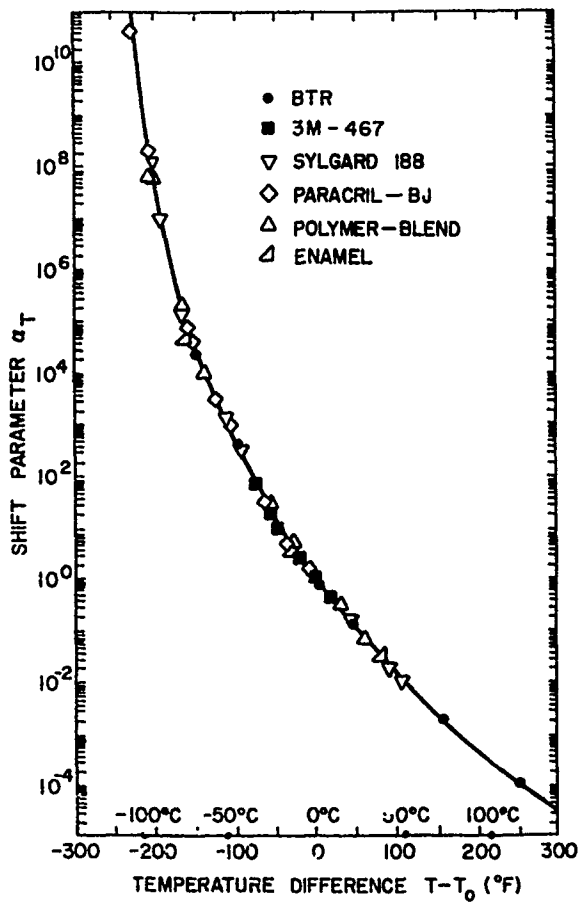

Figure 5. Graph of α_T versus temperature difference.

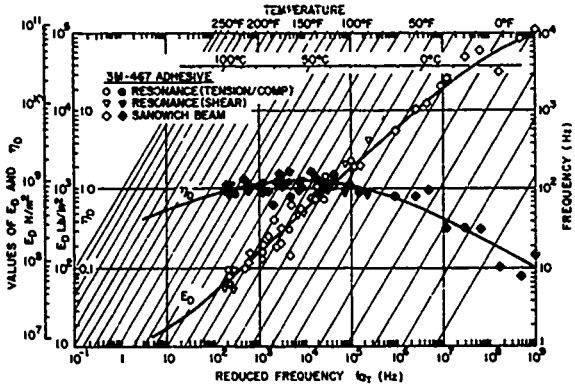

Figure 6. Reduced variables applied to acrylic adhesive.

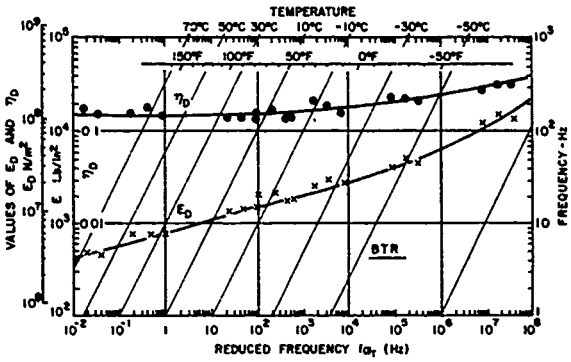

Figure 7. Reduced variables applied to silicone elastomer.

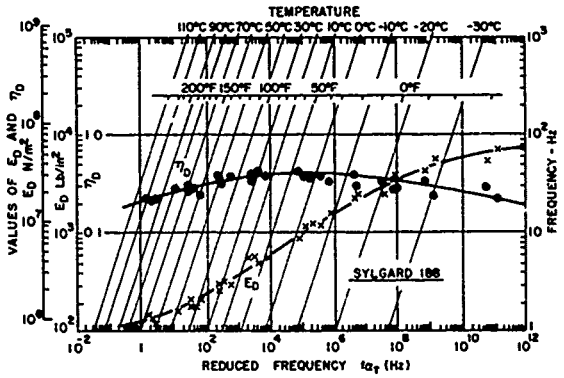

Figure 8. Reduced variables applied to silicone potting compound.

4. THE REDUCED TEMPERATURE NOMOGRAM

The graph of E_D and η_D versus frequency $f\alpha_T$ represents a fundamental relationship between the various parameters and variables; however, the calculation of E_D and η_D as a function of frequency at a constant temperature, say T_i, can be considerable simplified by defining an auxiliary function $f_j\alpha_{T_i}$, where α_{T_i} is the value of α_T at temperature T_i (see Fig. 5) and f_j is the frequency in hertz. $f_j\alpha_{T_i}$ is plotted as a function of f_j using the same absissca as for the plots of E_D and η_D versus $f\alpha_T$, and an auxiliary frequency scale given as the ordinate on the right side of the figure. (See Fig. 4). Each point of each oblique line $f_j\alpha_{T_i}$ defines a reduced frequency $(f\alpha_T)_{T_i,f_j}$ at T_i frequency f_j from which E_D and η_D at temperature T_i and frequency f_j can be determined using the plots of E_D and η_D versus $f\alpha_T$. To illustrate, let us calculate the values of E_D and η_D at temperature T_{-1} and frequency f. The intersection of the horizontal line f = constant (Line CX) with $f_j\alpha_{T_{-1}}$ (Line EX) defines a value $(f\alpha_T)_{f_j,T_i}$ (point D) of approximately 4×10^2 Hz. for this value of $f\alpha_T$, it follows from the plots of E_D and η_D versus $f\alpha_T$ that $E_D = 10^3$ N/m^2, and $\eta_D = 1.2$ Another equally important use for such a nomogram is to reduce the data in the first place. For if one selects the proper position for T_o and the interval (ΔT) between T_o and T_1, T_2, etc. then the grid of lines can be used to place the test data in position - in effect, by calculating $f\alpha_T$ according to the assumed T_o and ΔT. Only one combination of values of T_o and ΔT will give an adequate reduction of the data just as in the original reduced-frequency approach the values of α_T are dictated by the test data. Figure 6 shows the application of the nomogram for plotting the test data given in Table 1. The collapse of the data is easily achieved once the temperature scale is properly selected. This is clearly a matter of judgment, but not any more than in the use of any other type of scale. Figure 7 shows the nomogram applied to the silicone potting compound. Even if one computerizes this data handling process, judgment is still needed to validate the best fit obtained by a "least-squares" or other scheme.

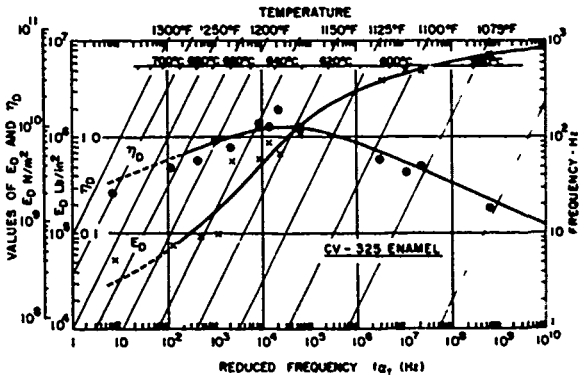

Figure 9. Reduced variables applied to enamel.

Figure 10 shows a basic nomogram in which proper choice of temperature and other scales allows one to treat the process of data reduction in

a graphical manner.

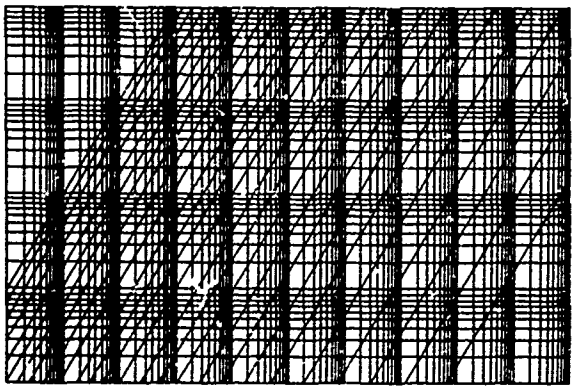

Figure 10. Nomogram.

5. CONCLUSIONS

A new "reduced-temperature" nomogram has been developed which greatly simplifies the task of collapsing test data into the form of universal "reduced frequency" master curves and also allows one to read the materials properties directly off the graph as a function of both frequency and temperature. This represents a major advance in handling complex modulus data of damping materials.

ACKNOWLEDGMENTS

Thanks are due to L.C. Rogers, Air Force Flight Dynamics Laboratory, WPAFB, Ohio; A.D. Nashif, Anatrol Corporation, Cincinnati, Ohio; and J. Martinat, Soc. Metravib, Ecully, France for encouraging the author to seek a simple "reduced-temperature" concept as an adjunct to, or even replacement for, the well known but difficult to use "reduced frequency" concept. Thanks are due to Barbara McDermott for typing the manuscript and tables, and Mr. de Marey for preparation of the figures. Finally, thanks are due to the SVIC reviewer for his useful suggestion for improving Section 4.

REFERENCES

1. B.J. Lazan, Damping of Materials and Members in Structural Mechanics, Pergamon Press, Oxford, 1968.

2. J.P. Henderson, "Energy Dissipation in a Vibration Damper Utilizing a Viscoelastic Suspension", Shock and Vibration Bulletin 35, 213-229, 1966.

3. H. Oberst and K. Frankenfeld, "Uber die Dampfung dunner bleche durch Festhaftende belage", Acustica, Vol. 2, leaflet 4, 181-194, Part I, 1959 and Part 2, 1954.

4. P. Grootenhuis, "Vibration Control with Viscoelastic Materials", Environmental Engineering, Proc. S.E.E., No. 38, May 1969.

5. H. Oberst, "Reduction of Noise by the Use of Damping Materials", Trans. Roy. Soc. A 263, 1968, 441.

6. J.E. Ferry, Viscoelastic Properties of Polymers, John Wiley and Sons Inc., New York, 1961.

7. J.D. Ferry, E.R. Fitzgerald, L.D. Grandine, Jr., and M.L. Williams, "Temperature Dependence of Dynamic Properties of Elastomers: Relaxation Distributions". Industrial and Engineering Chemistry, 44, 703-706, 1952.

8. D.I.G. Jones, "Temperature Frequency Dependence of Dynamic Properties of Damping Materials", Journal of Sound and Vibration, 33(4), 451-470, 1974.

9. 3M-467 - "An Acrylic Adhesive", Minnesota Mining and Mfg. Co., Minneapolis, Minnesota, U.S.A.

10. "BTR - A Broad Temperature Range Filled Silicone Elastomer, Lord Mfg. Co., Erie, PA, U.S.A.

11. "Sylgard 188 - A Two Part Silicone Potting Compound", Dow Corning Corporation, Midland, Michigan, U.S.A.

12. "CV-17214 Enamel", Chicago Vitreous Corporation (CV-325),

13. L.C. Rogers, AFFDL/FBG, WPAFB, OH, private communication.

14. R.L. Adkins, "Design Considerations and Analysis of a Complex Modulus Apparatus", Experimental Mechanics, July 1966.

15. J.L. Edwards and D.R. Hicks , "Useful Range of a Mechanical Impedance Technique for Measurement of Dynamic Properties of Materials", J. Acoust. Soc. Am., 52, pp. 1053-1056, 1972.

16. D.I.G. Jones and M.L. Parin, "Technique for Measuring Damping Properties of Thin Viscoelastic Materials", J. Sound. Vib., 24, pp. 201-210, 1972.

17. C.M. Cannon, A.D. Nashif, and D.I.G. Jones, "Damping Measurements on Soft Viscoelastic Materials Using a Tuned Damper Technique", Shock and Vibration Bulletin 38, pp. 151-163, 1968.

18. A.D. Nashif, "A New Method for Determining Damping Properties of Viscoelastic Materials", Shock and Vibration Bulletin 36, pp. 37-47, 1967.

19. D. Ross, E.E. Ungar and E.M. Kerwin, Jr., "Damping of Plate Vibrations by Means of Viscoelastic Laminae", Structural Damping, (ASME), pp. 69-87, 1959.

20. A.D. Nashif, "Materials for Vibration Control in Engineering", Shock and Vibration Bulletin 48, pp. 145-151, 1973.

21. J.C. Snowdon, Vibration and Shock in Damped Mechanical Systems, John Wiley and Sons, Inc., New York, 1968.

APPENDIX I - MEASUREMENT TECHNIQUES

A great variety of test techniques have been developed for measuring the complex modulus properties of materials (8,14,20). Some of the techniques are difficult to use and require complex electronic instrumentation. The techniques used to obtain the data evaluated in this paper are relatively simple and include the classical resonance technique (17) and the vibrating cantilever beam technique with the damping material applied as a single external coating (8,18), a symmetric external coating (18) or the inner layer of a three layer sandwich beam (19,20).

RESONANCE TESTS

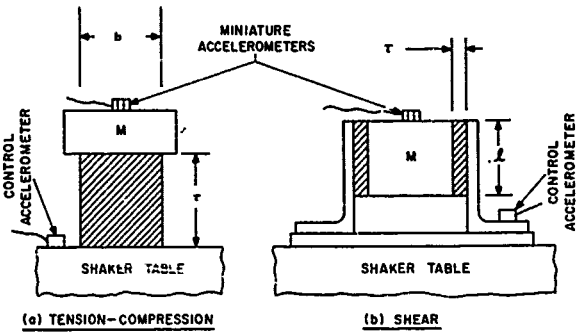

Figure 11. Resonance test specimen.

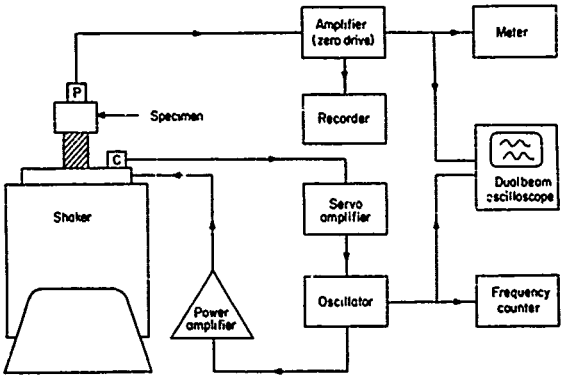

Figure 12. Resonance test system.

The types of specimen used in the resonance tests are illustrated in Figure 11. A typical test setup block diagram is shown in Figure 12. In the tests, the specimens are excited harmonically with constant acceleration level at the shaker table, and the response of the mass, M, is measured by means of an accelerometer. The input acceleration, $\ddot{X}$, the output acceleration $\ddot{Y}$, the resonance frequency, f_1, and the temperature, T, are measured for several values of the mass, M. From these measured quantitites, the real part of the Young's modulus, E_D, and the loss factor, η_D, are derived (8) from the relationships:

$$\eta_D = (A^2-1)^{-\frac{1}{2}} \qquad (6)$$

$$E_D = 4\pi^2 f_1^2 \tau (M+m/3)/S(1+\beta S^2/S_1^2) \qquad (7)$$

Alternatively, for the shear specimen (9),

$$G_D = 4\pi^2 f_1^2 \tau (M+m/3)\{1+\tau^2/6R^2\}/S \qquad (8)$$

By varying the input level, the material properties can be measured over a wide range of peak strain levels but, in the present tests, levels were kept low enough to remain within the range of linear behavior. The primary advantages of the resonance test are simplicity, both in testing and analysis, and the capability of assessing the effects of strain amplitude. Disadvantages are the necessity of changing mass to vary frequency and the difficulty of changing frequency and pre-load independently. The use of several specimens of varying geometry is a useful way of ensuring that data obtained are reliable and cover the appropriate range of parameters. Specimens should be simple and not have too low a height to diameter ratio to avoid errors resulting from highly non-uniform strains in the specimen. At very high frequencies, care should be taken to avoid standing waves in the specimens, which will render the above equations invalid.

VIBRATING BEAM TESTS

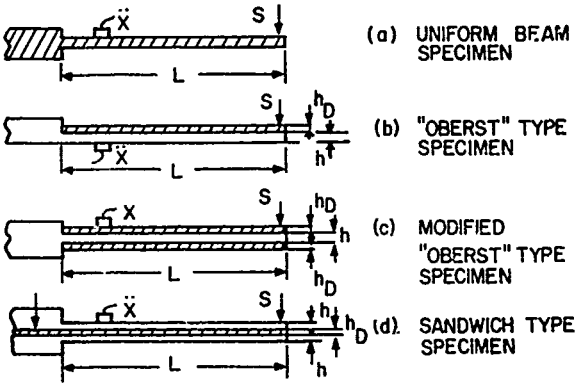

Figure 13. Vibrating beam test specimen.

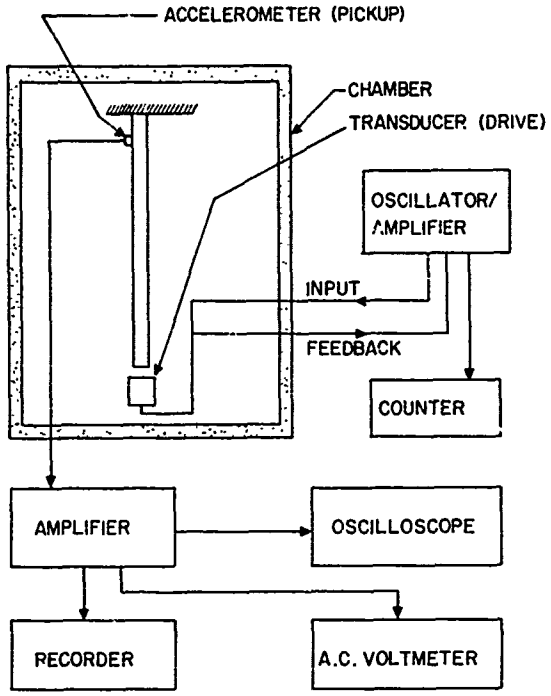

Figure 14. Vibrating beam test system.

The types of specimen used in the vibrating beam tests are illustrated in Fig. 13. A typical block diagram is shown in Figure 14. In the tests, the beams were generally excited by means of a magnetic transducer at the free end and the response picked up by another magnetic transducer near the root. By using the graphic level recorder, response spectra comprising graphs of transverse peak velocity versus frequency were plotted and the resonant frequencies, f_m, and half-power bandwidth, Δf_m, noted for many temperatures. For the high-temperature tests, however, for which suitable transducers were not available, the beam was instead excited by a shaker through an impedance head and a pillar made of Hastelloy-x. In this case, the force transmitted back to the transducer from the beam was measured, with the force due to the pillar inertia cancelled electronically, and the same quantities, f_m and Δf_m, measured. For reliable results with commercial versions of this method. it is usually necessary to use beams made of a relatively low modulus material, such as aluminum, with machined roots as indicated in Fig. 13 for reduced root damping, not more than about 0.05 inches thick nor shorter than about 7 inches. However, for the enamels it was necessary to use another material because of the high temperatures involved and this made testing more difficult. The advantage of the method is that it is reasonably simple to use, errors can be assessed and kept within limits (18) and a wide band of frequencies and temperatures can be covered with a single specimen. The disadvantage is that only low-strain-level data are obtainable, within the linear range for the damping material. This, however, is not usually a problem since one would use another method if such data were needed.

"Oberst beam" tests

For the beam with the damping material coated on one side only, the complex Young's modulus is derived from formulae (3,8) due originally to Oberst. These are:

$$Z^2 = \frac{1+2en(2+3n+2n^2)+e^2n^4}{1+ne} \qquad (9)$$

$$\frac{\eta_m}{\eta_D} = \frac{en}{(1+en)} \cdot \frac{3+6n+4n^2+2en^3+e^2n^4}{1+2ne(2+3n+2n^2)+e^2n^4} \qquad (10)$$

where $Z^2=(1+\rho_D n/\rho)(f_m/f_{om})^2$, $e=E_D/E$, $n = h_D/h$. In these formulae, Z^2 is calculated from the measured resonance frequency, f_m, of the mth mode of the damped beam and the measured frequency, f_{om}, of the undamped beam and e is then deduced from an inversion of equation (9). η_D is then calculated from equation (10), using this value of e and the measured value of $\eta_m = \Delta f_m/f_m$. These equations give reasonably accurate results provided that $Z^2-1 \geq 0.1$ or so.

Modified "Oberst beam" tests

For the beam with the damping material coated symmetrically on both sides, the complex Young's modulus is derived (18) from the formulae

$$E_D = E(Z^2-1)/(8n^3+12n^2+6n) \qquad (11)$$

$$\eta_D = \eta_m Z^2/(Z^2-1) \qquad (12)$$

where $Z^2 = (1+2\rho_D n/\rho)(f_m/f_{om})^2$ and e and n are defined as before. In these formulae Z^2 and η_m are determined as before. Again, the equation gives reasonably accurate results whenever $Z^2-1 \geq 0.1$ or so. These formulae are also applicable directly to the high temperature specimens provided that the beam is coated symmetrically. A similar technique is also applicable for beams with multiple constrained layers added (16).

Sandwich beam tests

Finally, for the symmetric sandwich beam, the approach is based on a set of equations due to Kerwin and others (19), reduced to an uncoupled form. The shear modulus, G_D, and loss factor, η_D, of the viscoelastic material may then be derived from the equations

$$G_D = \frac{[(A-B)-2(A-B)^2-2(A\eta_m)^2]\,Ehh_D\xi_m^2/L^2}{(1-2A+2B)^2+4(A\eta_m)^2} \qquad (13)$$

$$\eta'_D = A\eta_m / \{A-B-2(A-B)^2-2(A\eta_m)^2\} \quad (14)$$

where

$$A = (\omega_m/\omega_{0m})^2 (2+\rho_D h_D/\rho h)(B/2) \quad (15)$$

and

$$B = 1/6(1+h_D/h)^2 \quad (16)$$

For most elastomeric materials in the rubbery and transition regions, $E_D \sim 3G_D$ and $\eta_D \sim \eta'_D$ (21). These equations are derived from the classical equations of Ross, Kerwin and Ungar (RKU equations) (19) by neglecting the bending term for the viscoelastic core and algebraically inverting the equations. In these equations:

$\xi_1^2 = 3.515$ $\quad$ $\xi_4^2 = 120.902$

$\xi_2^2 = 22.035$ $\quad$ $\xi_5^2 = 199.860$

$\xi_3^2 = 61.697$ $\quad$ $\xi_6^2 = 298.556$

NOMENCLATURE

A	amplification factor $\lvert\ddot{Y}/\ddot{X}\rvert$ for resonance specimen; also a non-dimensional parameter
b	breadth of cylindrical specimen
B	non-dimensional parameter
D	suffic denoting damping material
e	E_D/E: the modulus ratio
E	Young's modulus of beam material
E_D	real part of complex Young's modulus of damping material
f	frequency (Hertz)
f_{om}	mth natural frequency of undamped beam
f_m	mth resonant frequency of damped beam
G_D	real part of complex shear modulus of damping material
h	thickness of beam
h_D	thickness of damping material
ℓ	length of viscoelastic material in shear resonance specimen
L	length of beam
m	mode number
m_o	mass of viscoelastic material
M	added mass on resonance test specimen
n	thickness ratio: (h_D/h)
R	radius of gyration of shear specimen about horizontal axis ($R=\ell/\sqrt{12}$ for rectangular specimen)
S	load carrying area of damping material in resonance specimens
S_1	non-load carrying (free) area of damping material in resonance specimens
T	temperature
T_o	reference temperature
$\ddot{X}$	input acceleration for resonance specimen
$\ddot{Y}$	output acceleration for resonance specimen
Z^2	non-dimensional parameter
a_T	temperature shift factor
β	shape factor for cylindrical resonance test specimen; $\beta \approx 2{\cdot}0$ for unfilled elastomers and $\approx 1{\cdot}5$ for filled elastomers
ϵ	strain
η'_D	shear loss factor
η_m	loss factor of beam specimen in mth mode
η_D	extensional loss factor of damping material
λ_m	wavelength of mth beam mode
ξ_m	mth eigenvalue for beam
ρ	density of beam; also density in general
ρ_D	density of damping material where specific identification is necessary
ρ_O	density at reference temperature
σ	stress
ω	circular frequency
ω_m	th circular frequency of damped beam
ω_{om}	mth circular frequency of undamped beam

TABLE 1A
Resonance Tests on 3M-467 Adhesive (Tension-Compression)

S=0.25 in², b=0.5 in, t=0.5 in, m_s=2.0 gm, ρ_D=0.038 lb/in³

m gm	Temp °F	Temp °C	X g's	Y g's	f_c Hz	f_1 Hz	η_D	E_D psi	E_D N/m²	η_T (T_0=150°F,66°C)
12.9	75	24	0.2 2.0 20.0	0.265 2.64 22.80	490 474 479	849 833 824	1.15 1.16 1.25	981 936 [illegible]	6.74E6 6.43 6.47	90
	95	35	0.2 2.0 10.0 20.0	0.25? 2.58 12.4 45.5	272 250 239 234	478 451 449 437	1.24 1.23 1.36 1.37	303 256 235 234	2.08E6 1.76 1.62 1.61	20
	133	56	0.2 2.0 20.0	0.310 3.38 31.0	153 141 137	217 206 203	0.85 0.85 0.85	96 82 77	6.69E5 5.63 5.29	2.0
65.7	68	20	0.5 5.0 10.0	0.67 6.70 13.0	43 233 229	—	1.24 1.14 1.20	1430 1320 1080	9.82E6 9.07 7.42	200
	97	36	0.5 5.0 10.0	6.66 6.35 12.6	92 88 82	—	1.27 1.26 1.26	175 161 140	1.20E6 1.11 9.62E5	20
	125	52	0.5 5.0	0.715 7.30	69 63	—	0.90 0.95	94 79	6.46E5 5.43	1.0
	50	10	0.5 5.0 10.0	0.68 6.70 13.1	35? 33? 346	—	1.08 1.22 1.18	2440 2260 2360	1.68E7 1.55 1.62	500
3.2	85	29	0.5 5.0 20.0	0.69 6.75 27.8	885 847 834	--	1.05 1.04 1.03	740 722 700	5.08E6 4.96 4.81	40
	122	50	0.5 1.0	0.68 1.35	370 370	697 706	1.10 1.10	337 337	9.41E5 9.41	4.0

TABLE 1B
Resonance Tests on 3M-467 Adhesive (Shear)

t=0.079 ins.(2.01mm), L=1.25 ins. (31.8mm)
b=1.0 ins. (25.4mm) ρ_D=0.038 lb/in³(1052 Kg/m³)

m gm	Temp °F	Temp °C	X g's	Y g's	f_c Hz	η_D	G_D psi	G_D N/m²	η_T (T_0=150°F 66°C)
68.2	70	21	0.5 5.0 20	0.77 7.5 35.0	1067 1063 1072	0.86 0.89 0.89	750 750 760	5.15E6 5.15 5.22	100
	91	33	0.5 5.0 20.0	0.62 6.25 25.2	514 483 469	1.34 1.34 1.32	175 155 148	1.20E6 1.06 9.62E5	30
	140	60	0.50 5.0 10.0	0.67 7.20 14.0	104 109 100	1.12 1.00 1.02	22.5 23.8 21.5	1.55E5 1.64 1.48	1.6
232	75	24	0.5 5.0 20.0	0.66 6.6 26.6	507 489 485	1.10 1.16 1.15	326 304 299	2.24E6 2.09 2.05	90
	137	58	0.5 5.0 10.0	0.76 7.6 [illegible]	117 123 110	0.89 0.88 0.87	17.6 19.1 17.6	1.20E5 1.31 1.21	3.0
239	50	10	0.5 5.0 10.0	[illegible] 8.05 16.3	822 843 844	0.80 0.82 0.78	1560 1640 1640	1.07E7 1.13 1.13	500
	83	28	0.5 5.0 10.0	0.64 6.45 12.6	272 252 242	1.25 1.22 1.3?	171 146 136	1.17E6 1.00 9.36E5	40
	133	56	0.5 5.0 10.0	0.75 7.65 15.?	[illegible] 92 87	0.91 0.87 0.87	20.5 19.1 17.5	1.41E5 1.31 1.20	2.0

TABLE 1C
Sandwich Beam Tests on 3M-467 Adhesive

h =0.070 ins.(1.78mm), h_s =0.008 ins.(0.20mm), L=7.0 in.(178mm)

Temp. °F	Temp. °C	Mode No. n	f_s Hz	f_n Hz	η_n	G_D psi	G_D N/m²	η'_D	η_T (T_0=155°F,68°C)
0	-18	2 3 4	290.0 798 1566	597 1609 3043	0.027 0.039 0.058	10140 18012 21245	6.99E7 1.24E8 1.47	0.334 0.339 0.343	1.0x10³
25	-4	2 3 4	288.6 795 1559	537 1397 2521	0.164 0.238 0.285	2609 3623 4149	1.39E7 2.52 2.86	0.837 0.828 0.994	6x10³
50	10	2	287.5	462	0.311	711	4.90E6	1.113	500
75	24	2	286.6	374	0.394	240	1.65E6	1.469	90
104	40	2 3 4 5	285.9 787.5 1546 2527	313 854 1629 2645	0.244 0.154 0.119 0.091	72.5 189 251 357	5.00E5 1.30E6 1.73 2.46	1.599 1.021 1.065 0.906	25
133	56	2 3 4 5	285.1 785.3 1540 2520	299 814 1572 2583	0.137 0.082 0.062 0.050	41.5 91.1 118 219	2.86E5 6.28 8.10 1.51E6	1.361 0.970 1.063 0.756	2.0
153	67	2 3 4 5	284.5 783.6 1537 2515	293 798 1550 2550	0.076 0.049 0.034 0.020	28.5 55.3 79.9 149	1.96E5 3.87 4.89 1.03E6	1.041 0.899 0.927 0.597	0.9
66	19	2 3	286.9 790.4	414 1342	0.410 0.279	374 802	2.58E6 5.53	1.499 0.904	200
125	52	2 3 4	285.3 785.9 1541	296 804 1548	0.116 0.077 0.050	33.6 63.9 55.5	2.32E5 4.40 3.83	1.378 1.247 1.728	3.5
2	-17	2	289.?	580	0.026	7881	5.43E7	0.250	8x10⁴
-25	-32	2 3 4	290.5 800.2 1569	600 1649 3194	0.008 0.007 0.017	12031 30600 45342	7.79E7 2.13E8 3.13E8	0.105 0.088 0.169	2x10⁵

TABLE 2
Resonance Tests on BRT Silicone (Tension-Compression)

t=0.86 in (21.8mm) b=0.50 in (12.7mm)
ρ_D=0.048 lb/in³ (1329 Kg/m³)

TEMPERATURE °F	TEMPERATURE °C	M gm	X g's	Y g's	f_r Hz	E_D lb/in²	E_D N/m²	η_D	η_T (T_0=45°F,7°C)
-103 -103 -105	-75 -75 -73	103.7 25.2 4.7	0.10 0.10 0.10	0.366 0.340 0.329	338 750 1487	8874 11120 10276	6.10E7 7.64 7.06	0.284 0.384 0.319	3.00 x 10⁶ 3.00 x 10⁶ 3.00 x 10⁶
-49 -55 -51	-45 -48 -46	103.7 25.2 4.7	0.10 0.10 0.10	0.452 0.472 0.494	204 445 880	3232 3985 3599	2.22E7 2.74 2.47	0.227 0.217 0.202	3.00 x 10² 5.00 x 10² 3.00 x 10²
0 0 0	-18 -18 -19	103.7 25.2 4.7	0.10 0.10 0.10	0.485 0.551 0.670	173 367 729	2325 2663 2479	1.60E7 1.83 1.70	0.202 0.185 0.154	[illegible] 1.00 x 10¹ 1.00 x 10¹
51 43 51	11 6 11	137.0 25.2 4.7	0.10 0.30 0.10	0.596 1.740 0.735	142 324 637	2062 2075 1886	1.42E7 1.43 1.30	0.167 0.173 0.137	8.00 x 10⁻¹ 1.30 x 10⁰ 8.00 x 10⁻¹
90 90 85	32 32 29	64.1 15.5 2.1	0.20 0.10 0.10	1.520 0.730 0.730	178 363 763	1520 1620 1585	1.04E7 1.11 1.09	0.133 0.139 0.139	1.30 x 10⁻¹ 1.30 x 10⁻¹ 1.50 x 10⁻¹
201 201 201	94 94 94	137.0 25.2 4.7	0.10 0.10 0.10	0.624 0.548 0.672	99 222 461	1002 974 988	6.88E6 6.69 6.79	0.161 0.182 0.150	2.00 x 10⁻³ 2.00 x 10⁻³ 2.00 x 10⁻³
295 295 297	146 146 147	137.0 25.2 4.7	0.10 0.10 0.10	0.667 0.587 0.669	81 192 382	671 729 678	4.61E6 5.01 4.66	0.150 0.173 0.150	1.00 x 10⁻⁴ 1.00 x 10⁻⁴ 1.00 x 10⁻⁴

TABLE 3
Resonance Tests on Sylgard 188 Potting Compound (Tension-Compression)

h_{max} = 0.50 in. (12.7mm), h_{min} = 0.45 in.(11.4mm)
T=1.00 in. (25.4mm), ρ_D=0.038 lb/in³ (1012 Kg/m³)

TEMPERATURE °F	TEMPERATURE °C	M gm	X g's	Y g's	f_r Hz	E_D lb/in²	E_D N/m²	η_D	η_T T_0=160°F,71°C
-38 -41 -29 -26	-39 -41 -34 -32	2.17 14.00 65.23 114.00	0.20 0.20 0.2? 0.20	0.92 0.78 0.38 0.65	2174 485 243 159	4685 3528 3836 28?4	3.23E7 2.43 2.63 1.97	0.22 0.27 0.23 0.32	[illegible] 1.80 x 10⁶ 1.00 x 10⁷ 4.00 x 10⁶
2 -2 0 13 10	-17 -19 -18 -11 -12	2.17 6.16 14.00 65.13 114.00	0.20 0.20 0.20 0.20 0.20	0.79 0.77 0.63 0.72 [illegible]	893 616 349 169 119	2670 2780 1825 1850 1583	1.83E7 1.91 1.25 1.27 1.09	0.27 0.27 0.33 0.29 0.37	9.0 x 10⁴ 1.30 x 10⁵ 1.00 x 10⁵ 3.20 x 10⁴ 3.50 x 10⁴
50 69 48 42 54	10 21 9 6 12	2.17 6.16 14.00 65.13 114.00	0.20 0.20 0.20 0.20 0.20	0.67 0.57 0.56 0.61 0.53	610 348 255 127 79	1260 875 975 .020 709	8.68E6 6.03 6.72 7.03 4.87	0.32 0.37 0.38 0.35 0.41	1.20 x 10³ 3.9 x 10² 1.50 x 10³ 2.50 x 10³ 1.09 x 10³
104 112 100 98 118	40 44 38 37 48	2.17 6.16 14.00 65.23 114.00	0.20 0.20 0.20 0.20 0.20	0.58 0.55 0.51 0.60 0.57	393 239 173 87 57	525 501 448 491 285	3.61E6 3.44 3.08 3.37 1.96	0.37 0.39 0.43 0.35 0.37	2.60 x 10¹ 1.20 x 10¹ 2.80 x 10¹ 3.00 x 10¹ 1.90 x 10¹
159 156 150 166 151	71 69 66 74 66	2.17 6.16 14.00 65.13 114.99	0.20 0.20 0.20 0.20 0.20	0.62 0.57 0.55 0.74 0.85	307 191 136 53 42	[illegible] 268 277 182 98	2.21E6 1.84 1.93 1.25 1.37	0.34 0.37 0.39 0.28 0.24	1.00 x 10⁰ 1.40 x 10⁰ 1.80 x 10⁰ 8.00 x 10⁻¹ 1.60 x 10⁰
202 215 198	94 102 92	2.17 6.16 14.00	0.20 0.20 0.20	0.74 0.75 0.71	253 158 112	217 182 [illegible]	1.49E6 1.25 [illegible]	0.28 0.28 [illegible]	1.46 x 10⁻² 7.09 x 10⁻² 1.75 x 10⁻¹
265 258 250	129 126 121	2.17 6.16 14.00	0.20 0.20 0.20	0.88 0.94 0.94	229 150 98	178 165 144	1.22E6 1.13 9.89E5	0.23 0.22 0.22	1.00 x 10⁻³ 1.40 x 10⁻³ 1.80 x 10⁻³

TABLE 4
Coated Beam Tests (Modified Oberst) for CV-325 (CV-17214) Enamel

SPEC A, h_s=0.0165 in.(0.42mm), h=0.030 in (0.76mm), L=1.75 in.
SPEC B, h_s=0.0045 in (0.11mm), h=0.07 in (1.78mm), L=3.00 in.
ρ_D=0.09 lb/in³ (2491 Kg/m³), ρ=0.283 lb/in³ (7916 Kg/m³)

Spec #	Temperature °F	Temperature °C	f_o Hz	f_s Hz	η_s	r²	E(lb/in² x 10⁶)	η_D	E_D(lb/in²)	η_T (T_0=1250°F,677°C)
A	75 440 563 840 900 955 1005 1050 1095 1175 1225 1260 1265 1330	24 227 295 449 482 513 541 566 591 635 663 682 685 721	326 318 315 309 306 305 304 302 301 299 299 298 298 297	536 579 522 527 526 465 450 439 433 285 259 250 57 55	0.001 [illegible] 0.002 0.004 0.006 0.013 0.035 0.116 0.323 0.190 0.036 0.023 0.015 0.004	3.752 [illegible] 3.812 3.811 3.795 3.226 3.150 2.932 2.072 1.761 1.041 1.040 1.032 1.023	2.83 2.69 2.64 2.54 2.50 2.48 2.46 2.43 2.42 2.38 2.38 2.37 2.37 2.35	0.061 0.023 0.003 0.065 0.080 0.219 0.051 0.47? 0.496 1.923 0.914 0.590 0.404 0.267	7.60 x 10⁴ 7.62 x 10⁴ 7.32 x 10⁴ 7.84 x 10⁴ 6.89 x 10⁴ 5.46 x 10⁴ 5.22 x 10⁴ 4.53 x 10⁴ 4.45 x 10⁴ 4.13 x 10⁴ 9.62 x 10³ 9.35 x 10³ 7.49 x 10³ 5.33 x 10³	— — — — — — [illegible] 6.0 x 10¹ 5.0 x 10¹ 8.0 x 10⁰ 4.0 x 10⁰ 1.0 x 10⁰ 5.0 x 10⁻¹ 3.0 x 10⁻²
B	75 800 950 1060 1065 1095 1110 1155 1175 1185 1210	24 427 510 571 574 591 599 624 635 641 654	239 224 221 219 218 217 216 216 215 215 214	252 238 236 [illegible] 227 222 220 214 213 212 [illegible]	0.004 0.005 0.004 0.009 0.021 0.036 0.038 0.027 0.020 0.016 0.009	1.157 1.275 1.167 1.150 1.120 1.009 1.070 1.021 1.026 1.012 1.012	2.65 2.33 2.27 2.23 2.21 2.19 2.19 2.17 2.15 2.15 2.13	0.030 0.034 0.042 0.066 0.184 0.440 0.585 1.295 1.240 1.884 0.792	9.49 x 10⁴ 9.30 x 10⁴ 8.64 x 10⁴ 8.44 x 10⁴ 6.40 x 10⁴ 4.66 x 10⁴ 7.48 x 10³ 4.66 x 10³ 9.65 x 10³ 5.76 x 10³ 5.68 x 10³	— — — 1.0 x 10⁻² 3.9 x 10⁴ 5.0 x 10⁴ [illegible] 1.0 x 10² 7.0 x 10¹ 4.0 x 10¹ 1.0 x 10¹

DISCUSSION

Mr. Coch, (Sound Coat Company): In the plot of α_T versus temperature, is it truly not a linear curve?

Dr. Jones: Yes, it has a curve in it; at a higher temperatures it has a lower slope than at low temperatures. The reason is that toward the left hand side where the slope is getting greater and greater approaching the T_G or Transition Temperature where the material eventually becomes glass-like; at that point presumeably your α_T is infinite. Its got to asymptote toward infinity on the left hand side at a finer temperature for any given material. By choosing to you shove all the curves around to the same line.

Voice: I thought using a temperature time super position that there was a correction factor we had to use in sliding those elements up.

Dr. Jones: That is the way that J.D. Ferry presented it in one of his papers. But, he is not plotting modulus and loss factor but complex compliances. He is doing much the same thing but because he is operating on different measured quantities he is sliding it in both directions, which mystified me for quite a while. If you read some of the other reports that Ferry has done or if you read John Snowdon's book for example you find other intrepretations of the same data. So what I am plotting here is really not new except for the actual nomogram itself. It is essentially a fairly well established technology for a class of materials with limitations.

Voice: Did you find when using different methods or tests say that resonant mass of sheer versus a beam test that the results agree?

Dr. Jones: Yes, provided we took great care in controlling our specimens and making them. You must watch out for all the possible sources of error such as making sure you take samples from the same batch, sometimes that is necessary. We found in fact in one of the graphs we've got a resonance test in shear another in tension compression and a sandwich being tested all superimposed on the same curve and they agree pretty well within perhaps plus or minus 20 percent and this is pretty good. You can always run into trouble; it is a constant step by step process. The next material you do, because of ill-conditioned beam specimens, for example, you could fall flat on your face and have to start again with different beams, so you have got to be alert.

Voice: Do you have to be most careful about controlling the temperatures?

Dr. Jones: Extremely, within plus or minus 1 or at most approximate 2 degrees fahrenheit. If you were ever off more than that you just couldn't make the data collapse properly.

COMPUTERIZED PROCESSING AND EMPIRICAL REPRESENTATION OF VISCOELASTIC MATERIAL PROPERTY DATA AND PRELIMINARY CONSTRAINED LAYER DAMPING TREATMENT DESIGN

Lynn C. Rogers, Ph.D.
Air Force Flight Dynamics Laboratory
Wright-Patterson AFB, Ohio

and

Ahid D. Nashif
Anatrol Corporation
Cincinnati, Ohio

Technology advancements in the state-of-the-art of processing and representing modulus and loss factor data as a function of temperature and frequency are presented; further, a new method for performing preliminary constrained layer damping treatment design covering the complete range of interest of practical engineering parameters is outlined. This is given in the context of historical development, current practice, and other recent developments.

INTRODUCTION

Damping treatments have been recently applied to structures to increase their resonant fatigue life and/or reduce their structure-borne noise. However, the successful application of such materials depends a great deal on three important factors. These are: knowledge of how the properties of the damping materials vary with the environment to which they are subjected, a good understanding of the dynamics of the structure to which the damping material is to be applied, and finally, how to design a material in a damping treatment configuration for the desired performance.

In this paper, a description will be made of the characterization of the damping properties of materials. A discussion of how the characterized properties of materials can be used to study the performance of various damping treatments will also be presented. The curve fitted analytical expressions of the modulus and loss factor were used to predict how much damping can be achieved when a constrained layer treatment is applied to a vibrating structure. The predicted results were compared with measured ones and the agreement was found to be excellent over a wide temperature and frequency range.

CHARACTERIZATION OF MATERIAL PROPERTIES

Efficient, systematic and standarized procedures must be established to process, store, retrieve, and transmit viscoelastic damping material property characterization to enable widespread utilization of damping technology to control vibration, noise, and resonant fatigue. Such procedures should accommodate any level of sophistication in a particular organization from manual data processing to completely automated and should be compatible to information interchange with the industry in general.

The approach taken here basically is to develop equations with parameters which are to be chosen to best fit the experimental data. The form of the equations and the effect of incremental changes in the parameter values are relatively unimportant when using computers to least squares fit the data. However, if the approach is trial and error selection of parameter values, the process is greatly facilitated if the effects of the parameters are uncoupled. The Jones (2) coordinate system is used for data interchange with organizations which do not have some type of machine plotting or computers.

Thus, the specific equation with values of parameters to best fit experimental data becomes the basis for data processing, storage, retrieval, and transmittal.

Empirical Equation for Modulus

The general character of the log modulus versus log reduced frequency curve is that it has a horizontal asymptote at a low reduced frequency and has a higher value horizontal asymptote at high reduced frequency. It is sigmoidal in shape, monotonic, and more or less an odd function about offsets. Consider the equation

$$y = L + \frac{H-L}{1+e^{-\left(\frac{X-X_0}{c}\right)}} \qquad (1)$$

which has the properties outlined above. Obviously, the denominator is unity for X much greater than X_0, and very large for X much less than X_0; further, the value for c dictates the rapidity with which the transition occurs. When X is replaced by the log of reduced frequency, F_R, the term in the denominator becomes

$$e^{-\frac{X-X_0}{c}} = e^{-\frac{\log f_R + \log f_{RO}}{c}} = \left(\frac{F_{RO}}{F_R}\right)^N \qquad (2)$$

where the properties of logarithms and exponents have been used and where the exponent N is defined implicitly. Equation (1) then becomes

$$y = L + \frac{H-L}{1+\left(\frac{F_{ROG}}{F_R}\right)^N} \qquad (3)$$

which is seen to be closely related to that employed by Kelley and Williams (1). Replacing y by the log of the modulus, G_0, yields

$$y_{G_0} = \log G_0 = \log G_L + \frac{\log G_H - \log G_L}{1+\left(\frac{F_{ROG}}{F_R}\right)^N} \qquad (4)$$

Referring to Figure 1 it may happen that the experimental modulus data defines a straight line segment, and little or nothing else. For convenience, a parameter G_{FROG} is defined by

$$\log G_{FROG} = \frac{\log G_L + \log G_H}{2} \qquad (5)$$

and Equation (4) becomes

$$y_{G_0} = \log G_0 = \log G_L + \frac{2 \log \frac{G_{FROG}}{G_L}}{1+\left(\frac{F_{ROG}}{F_R}\right)^N} \qquad (6)$$

This equation is asymptotic to G_L, passes through G_{FROG} at FROG with slope governed by N and is asymptotic to G_H. It is an odd function about (F_{ROG}, G_{FROG}) in log-log coordinates.

The effects of parameter variations about nominal values are illustrated in Figure 1.

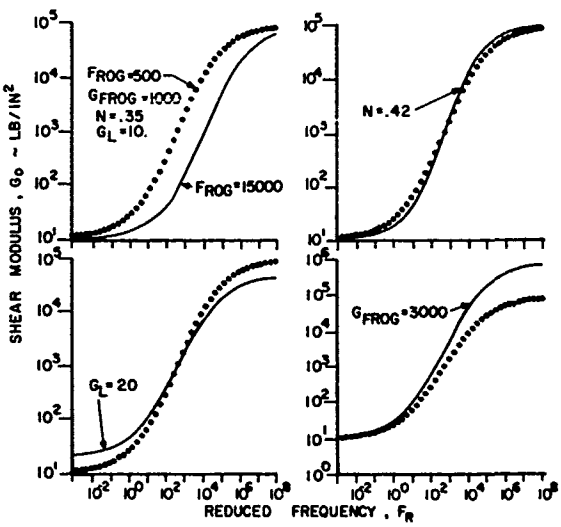

Figure 1: Modulus Empirical Equation

The above Equation (6) for the shear modulus, G_0, is valid at temperature T_0 and is related to G, the modulus at temperature T, by

$$G_0 = \frac{T_0+459.7}{T+459.7} G \qquad (7)$$

from which

$$\log G = \log G_0 - \log \frac{T_0+459.7}{T+459.7} \qquad (8)$$

or

$$\log G = \log G_L + \frac{2 \log \frac{G_{FROG}}{G_L}}{1+\left(\frac{F_{ROG}}{F_R}\right)^N} - \log \frac{T_0+459.7}{T+459.7} \qquad (9)$$

Equation (7) is used to adjust experimental data for plotting and the curve from Equation (6) is used to illustrate the fit achieved. Equation (9) is used to calculate the modulus G as a function of temperature T and frequency F.

Empirical Equation for Loss Factor

For a class of materials, the log of a loss factor versus log of reduced frequency curve is hyperbola. The general equation for an offset symmetric hyperbola is

$$\frac{y-k}{u} = \pm\sqrt{1+\left(\frac{X-h}{v}\right)^2} \qquad (10)$$

and when a straight line is added to this expression to make it more general, the hyperbola of interest may be written

$$y_{LF} + Y_0 + \frac{c}{2}(S_L+S_H)\left(\frac{X-X_0}{c}\right) + (S_L-S_H)\left[1-\sqrt{1+\left(\frac{X-X_0}{c}\right)^2}\right] \qquad (11)$$

Replacing X by the log of F_R and y by the log of loss factor η respectively gives

$$y_{LF} = \log\eta = \log\eta_{FROL} + \frac{c}{2}\left[(S_L+S_H)\frac{1}{c}\log\frac{f_R}{f_{ROL}} + (S_L-S_H)\left[1-\sqrt{1+\left(\frac{1}{c}\log\frac{f_R}{f_{ROL}}\right)^2}\right]\right] \qquad (12)$$

The effects of variations in parameters about nominal values are illustrated in Figure 2. The parameter η_{FROL} shifts the curve up and down, F_{ROL} shifts it right or left, c stretches or contracts the horizontal axis, S_L is the slope at very low values of reduced frequency, and S_H is the slope at high values. These latter two cause coupled effects which complicate the trial and error fitting of data.

The Temperature Shift Parameter

In the typical explanation of frequency-temperature equivalence(2), a temperature shift parameter curve is constructed by finding a number as a function of temperature which simultaneously shifts shear modulus and loss factor data to define curves and to minimize scatter about those curves. In practice, after comparing the results for many materials, a universal curve is defined and new data is processed by using the universal curve and selecting a reference temperature T_0 which minimizes scatter. There are two universal or master temperature shift parameter curves in use. They are shown in Figure 3 together with equations which approximate them.

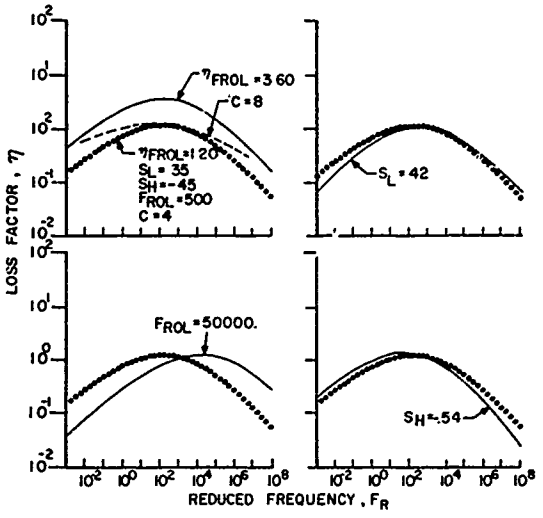

Figure 2: Loss Factor Empirical Equation

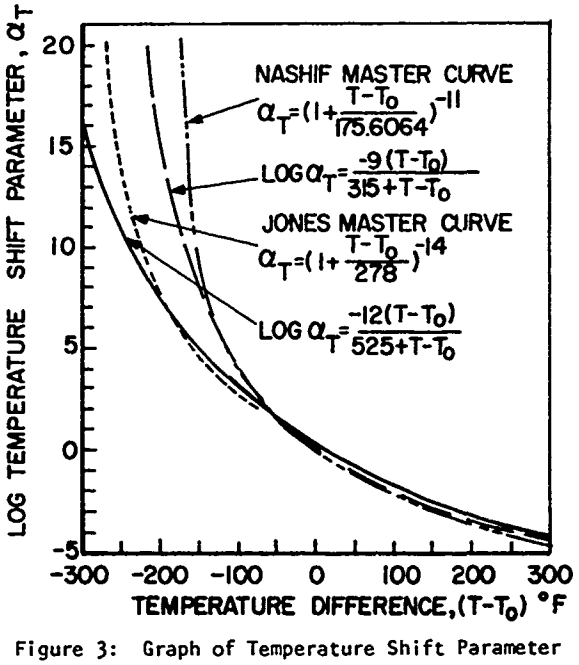

Figure 3: Graph of Temperature Shift Parameter Versus Temperature Difference

In Figure 3, the exponential expressions were developed to approximate the master curves and in fact came to define the master curves. For elastomers, the temperature range of interest is within 100° of T_0 and it is seen that the WLF equations(3) of the form

$$\log \alpha_T = \frac{-C_1(T-T_0)}{C_2+(T-T_0)}$$

approximate the exponentials closely over that range as may be seen in Figure 3 and Table I. In fact, the WLF equations serve equally well to define the master curves. Since there exists a theoretical rationalization for the form of the WLF equation(3), the WLF equation is the preferred definition of the master curves.

It happens that for elastomers, either master curve serves equally well to process data. Assume that a T_0 has been found with the Nashif master curve, and imagine that α_T has been plotted versus temperature for the range of experimental temperatures. The Jones master curve could be shifted horizontally and vertically such that some portion of it matches very closely that portion of the Nashif curve in use. The horizontal shift has the effect of using a different T_0, and the vertical shift causes the reduced frequency to be multiplied by a constant factor, which is an alternative of equal merit.

In work with enamels(2), not treated here, it has been found that a greater temperature range is of engineering interest and therefore the temperature shift curve must accommodate the greater range. With enamels, the Nashif curve does not have an adequate range, whereas the Jones curve was developed for both elastomers and enamels.

Based on this rationale, the universal or master temperature shift parameter curve is established

$$\log \alpha_T = \frac{-12(T-T_0)}{525+(T-T_0)} \qquad (13)$$

and is the WLF representation of the Jones master curve. The reduced frequency

$$F_R = F\alpha_T \qquad (14)$$

is computed in the customary way and may be expressed

$$F_R = F \cdot 10^{**}(-12\Delta T/(525+\Delta T)) \qquad (15)$$

where

$$\Delta T = T - T_0 \qquad (16)$$

Processing Data for Unobtainium

In order to illustrate some of the features of data processing under ideal conditions, a set of simulated data was generated and is presented in the last four columns of Table II. The hypothetical material is called Unobtainium. Equations (6) and (12) were used to obtain G_0 and n for values of reduced frequency chosen at equal increments on the log scale and for a set of assumed parameter values. The reduced frequency Equation (15) was solved for the frequency F, and evaluated

TABLE I TEMPERATURE SHIFT PARAMETER

	JONES				NASHIF			
	EXPONENTIAL		WLF		EXPONENTIAL		WLF	
DEL T	ALPH T	LOG ALPH T	ALPH T	LOG ALPH T	ALPH T	LOG ALPH T	ALPH T	LOG ALPH T
300.	.3545E-04	-.4458E 01	.4329E-04	-.4364E 01	.1739E-04	-.4760E 01	.4872E-04	-.4398E 01
275.	.6584E-04	-.4182E 01	.7499E-04	-.4125E 01	.3149E-04	-.4502E 01	.6384E-04	-.4195E 01
250.	.1258E-03	-.3900E 01	.1346E-03	-.3871E 01	.5908E-04	-.4229E 01	.1042E-03	-.3982E 01
225.	.2481E-03	-.3605E 01	.2512E-03	-.3600E 01	.1148E-03	-.3948E 01	.1778E-03	-.3750E 01
200.	.5366E-03	-.3295E 01	.4894E-03	-.3310E 01	.2333E-03	-.3632E 01	.3198E-03	-.3495E 01
175.	.1075E-02	-.2969E 01	.1000E-02	-.3288E 01	.4977E-03	-.3303E 01	.6105E-03	-.3214E 01
150.	.2379E-02	-.2624E 01	.2154E-02	-.2667E 01	.1123E-02	-.2958E 01	.1258E-02	-.2903E 01
125.	.5525E-02	-.2258E 01	.4924E-02	-.2328E 01	.2704E-02	-.2568E 01	.2774E-02	-.2557E 01
100.	.1354E-01	-.1868E 01	.1222E-01	-.1928E 01	.7827E-02	-.2153E 01	.6781E-02	-.2169E 01
75.	.3538E-01	-.1452E 01	.3162E-01	-.1588E 01	.2888E-01	-.1699E 01	.1859E-01	-.1731E 01
50.	.9872E-01	-.1006E 01	.9047E-01	-.1043E 01	.6354E-01	-.1197E 01	.5858E-01	-.1233E 01
25.	.2995E 00	-.5236E 00	.2848E 00	-.5455E 00	.2313E 00	-.6358E 00	.2179E 00	-.6618E 00
.	.1000E 01	.0000E 00	.1000E 01	.0000E 00	.1000E 01	.0000E 00	.1000E 01	.0000E 00
25.	.3741E 01	.5720E 00	.3981E 01	.6000E 00	.5416E 01	.7337E 00	.5968E 01	.7750E 00
50.	.1605E 02	.1205E 01	.1833E 02	.1263E 01	.3989E 02	.1601E 01	.4998E 02	.1698E 01
75.	.8158E 02	.1912E 01	.1000E 03	.2000E 01	.4582E 03	.2661E 01	.6494E 03	.2812E 01
100.	.5137E 03	.2711E 01	.6661E 03	.2824E 01	.1861E 05	.4826E 01	.1535E 05	.4186E 01
125.	.4275E 04	.3631E 01	.5623E 04	.3750E 01	.8784E 06	.5944E 01	.8338E 06	.5921E 01
150.	.5196E 05	.4716E 01	.6310E 05	.4800E 01	.1578E 10	.9198E 01	.1528E 09	.8182E 01
175.	.1889E 07	.6037E 01	.1000E 07	.6000E 01			.1778E 12	.1125E 02
200.	.5337E 08	.7727E 01	.2424E 08	.7385E 01			.4489E 16	.1565E 02
225.	.1193E 11	.1008E 02	.1000E 10	.9000E 01			.3162E 23	.2250E 02
250.	.9845E 14	.1396E 02	.8111E 11	.1091E 02				
275.	.3443E 28	.2754E 02	.1585E 14	.1320E 02				
300.			.1000E 17	.1600E 02				

for ΔT increments of 50 degrees. Simulated data points were selected which had frequencies between 50 and 5000 Hz. A reference temperature, T_C of 100°F was assumed and the simulated experimental temperature T was obtained from T_0 and ΔT. Then the simulated experimental shear modulus G was obtained by using Equation (7). It should be noted that the simulated temperatures extend to 500°, too high for many common materials.

With the simulated data in hand, the problem becomes one of selecting a T_0 to best define curves and minimize scatter for loss factor and shear modulus simultaneously. The first approach is to plot the data for various values of T_0 and examine the plots. Values of -50°F, 0, 50, 100, 150, 200, and 250 were used for T_0. With a trial T_0, Equations (7) and (15) are used to calculate G_0 and F_R respectively. Since the range of reduced frequency varies by several orders of magnitude as T_0 is changed, the effect makes the interpretation of scatter difficult; and a normalized log scale, X_{PLOT}, is used to minimize the effect of horizontal scale on apparent scatter. These parameters are listed in Table IIA for T_0 = 100°F and in Table IIB for T_0 = 250°F.

The simulated data is plotted for T_0 = 100°F in Figure 4. The data is plotted for various other values of T_0 in Figure 5. In Figure 5F, note the shingle effect which occurs in both the modulus and the loss factor curves; it is not so apparent at lower values of reduced frequency, but actually does exist in this simulated data. Also note the water wheel bucket effect in Figure 5C, again present in both curves and not so obvious at low values of reduced frequency. The shingle or bucket effects are present in actual data when T_0 is significantly different from its optimum value. Groups of data corresponding to the lower temperature in Figure 5C and 5F are labeled according to the temperature. It may be seen how the segments coalesce and define a curve with no scatter as the optimum value for T_0 is approached.

TABLE II UNOBTAINIUM DATA (A) T_0 = 100

TO = 100.0

FR	LOG FR	XPLOT	LOG GO	LOG ETA	DEL G	GO		ETA	T	F
.1000E+02	=3.000	.9000	1.048	=.8210	71,56	19,96	18,81	.1510	500.0	184,8
.1779E+02	=2,750	.2274	1.049	=.7520	71,56	11,19	19,28	.1769	500.0	275.8
.3163E+02	=2,500	.4546	1.060	=.6850	71,56	11,47	19,68	.2070	500.0	489,8
.3162E+02	=2,500	.4545	1.060	=.6858	62,61	11,48	18,66	.2070	450.0	199,5
.5626E+02	=2,250	.6528	1.073	=.6198	62,61	11,83	19,23	.2410	450.0	355,8
.1000E+01	=2,000	.9091	1.089	=.5548	62,61	12,26	19,94	.2798	450.0	631.8
.9999E+02	=2,000	.9090	1.089	=.5540	53,67	12,27	18,85	.2798	400.0	231,8
.1779E+01	=1,750	1.137	1.105	=.4920	53,67	12,82	19,78	.3230	400.0	411.8
.3164E+01	=1,500	1.364	1.131	=.4310	53,67	13,54	20,89	.3710	400.0	731,8
.3163E+01	=1,500	1.364	1.131	=.4310	44,72	13,53	19,58	.3710	350.0	235.8
.5626E+01	=1,250	1.591	1.150	=.3720	44,72	14,44	20,98	.4258	350.0	418.8
.1000	=1,000	1.818	1.194	=.3158	44,72	15,62	22,69	.4840	350.0	743.8
.9984E+01	=1,001	1.818	1.194	=.3158	35,78	15,61	21,28	.4840	300.0	284.8
.1776	=.7504	2.045	1.235	=.2618	33,78	17,16	23,38	.5488	300.0	363.8
.3161	=.5001	2.273	1.282	=.2108	35,78	19,15	26,08	.6170	300.0	646.8
.3163	=.4999	2.273	1.282	=.2108	26,83	19,16	24,38	.6170	250.0	146.8
.5627	=.2500	2.500	1.339	=.1612	26,83	21,84	27,78	.6988	250.0	261.8
.9997	=.1487E+03	2.727	1.489	=.1168	26,83	25,62	32,58	.7668	250.0	464.8
1.777	.2498	2.954	1.488	=.7448E+01	26,83	30,75	39,08	.8438	250.0	825.8
1.778	.2500	2.954	1.488	=.7448E+01	17,89	30,79	36,30	.8438	200.0	147.9
3.162	.5000	3.182	1.581	=.3670E+01	17,89	38,09	44,98	.9190	200.0	263.8
5.627	.7502	3.409	1.688	=.3198E+01	17,89	48,77	57,58	.9930	200.0	468.8
10.00	1.000	3.636	1.811	.2588E+01	17,89	64,72	76,30	1.061	200.0	832.8
9.997	.9999	3.636	1.811	.2588E+01	8,945	64,71	78,58	1.061	150.0	118.5
17.79	1.250	3.864	1.949	.4994E+01	8,945	88,94	96,98	1.122	150.0	196.8
31.67	1.501	4.091	2.102	.6888E+01	8,945	126,6	137,9	1.172	150.0	350.8
56.27	1.750	4.318	2.270	.8228E+01	8,945	186,3	203,8	1.285	150.0	622.8
99.97	2,000	4.545	2.451	.8998E+01	8,945	282,7	308,8	1.238	150.0	1105.
100.0	2,000	4.545	2.452	.8998E+01	,0000	283,8	283,8	1.238	100.0	100.0
177.8	2,250	4.773	2.642	.9160E+01	,0000	439,8	439,8	1.235	100.0	177.8
316.8	2,500	5.000	2.848	.8720E+01	,0000	692,8	692,8	1.222	100.0	316.8
562.8	2,750	5.227	3.041	.7650E+01	,0000	1099,	1099,	1.193	100.0	562.8
1000,	3,000	5,455	3.241	.5960E+01	,0000	1743,	1743,	1.147	100.0	1000,
1778,	3,250	5,682	3.438	.3650E+01	,0000	2748,	2748,	1.088	100.0	1778,
1778,	3,250	5,682	3.437	.3650E+01	=8,945	2735,	2498,	1.088	50,00	97,00
3162,	3,500	5,909	3,624	.7360E+02	=8,945	4286,	3830,	1,017	50,00	172,5
5627,	3,750	6,137	3,800	=.2778E+01	=8,945	6384,	5748,	,9380	50,00	387,8
.1001E 05	4,000	6,364	3,962	=.6840E+01	=8,945	9159,	8348,	,8548	50,00	546,8
.1778E 05	4,250	6,591	4,189	=.1144	=8,945	.1286E 05	.1171E 05	,7688	50,00	970,8
.3162E 05	4,500	6,818	4,241	=.1656	=8,945	.1742E 05	.1586E 05	,6838	50,00	1725,
.5627E 05	4,750	7,046	4,397	=.2218	=8,945	.2273E 05	.2078E 05	,6010	50,00	3070,
.5622E 05	4,750	7,045	4,397	=.2218	=17,89	.2275E 05	.1869E 05	,6010	,0000	84,48
.9998E 05	5,000	7,273	4,459	=.2828	=17,89	.2874E 05	.2360E 05	,5238	,0000	150,1
.1778E 06	5,250	7,500	4,546	=.3468	=17,89	.3528E 05	.2898E 05	,4510	,0000	267,0
.3164E 06	5,500	7,727	4,621	=.4148	=17,89	.4177E 05	.3430E 05	,3858	,0000	475,0
.5622E 06	5,750	7,954	4,684	=.4869	=17,89	.4835E 05	.3970E 05	,3270	,0000	844,0
.9998E 06	6,000	8,182	4,739	=.5600	=17,89	.5488E 05	.4508E 05	,2750	,0000	1501,
.1778E 07	6,250	8,409	4,784	=.6388	=17,89	.6877E 05	.4998E 05	,2308	,0000	2670,
.3164E 07	6,500	8,637	4,821	=.7188	=17,89	.6625E 05	.5440E 05	,1914	,0000	4750,
.3161E 07	6,500	8,636	4,821	=.7188	=26,83	.6629E 05	.4859E 05	,1914	=50,00	50,18
.5622E 07	6,750	8,863	4,853	=.8018	=26,83	.7121E 05	.5218E 05	,1583	=50,00	89,18
.1000E 08	7,000	9,091	4,879	=.8858	=26,83	.7572E 05	.5548E 05	,1302	=50,00	158,8
.1778E 08	7,250	9,318	4,901	=.9728	=26,83	.7954E 05	.5828E 05	,1067	=50,00	282,8
.3161E 08	7,500	9,545	4,918	=1,068	=26,83	.8282E 05	.6068E 05	.8708E=01	=50,00	501,8
.5622E 08	7,750	9,773	4,933	=1,151	=26,83	.8570E 05	.6278E 05	.7078E=01	=50,00	891,8
.1000E 09	8,000	10,00	4,945	=1,242	=26,83	.8816E 05	.6458E 05	.5736E=01	=50,00	1585,

TABLE II CONT'D UNOBTAINIUM DATA (B) T_0 = 250

TO = 250.0

FR	LOG FR	XPLOT	LOG GO	LOG ETA	DEL G	GO	G	ETA	T	P
.2881G-01	-1.682	.0000	1.143	-.8218	35.26	13.91	18.81	.1510	500.0	194.6
.3781G-01	-1.432	.1198	1.152	-.7528	35.26	14.19	19.28	.1769	500.0	276.0
.6582G-01	-1.182	.2395	1.1[illegible]	-.6858	35.26	14.55	19.68	.2070	500.0	489.0
.9763G-01	-1.010	.3215	1.1[illegible]	-.6858	28.21	14.55	18.66	.2070	450.0	199.5
.1737	-.7631	.4414	1.176	-.6198	28.21	15.08	19.23	.2410	450.0	385.0
.3088	-.5103	.5610	1.192	-.5548	28.21	15.55	19.94	.2798	450.0	631.0
.4977	-.3331	.6602	1.192	-.5548	21.16	15.56	18.65	.2798	400.0	231.0
.8855	-.5282G-01	.7881	1.211	-.4928	21.16	16.26	19.78	.3238	400.0	411.0
1.575	.1973	.8998	1.235	-.4313	21.16	17.17	20.88	.3718	400.0	731.0
2.825	.4511	1.021	1.235	-.4316	14.19	17.16	19.58	.3718	350.0	235.0
5.025	.7012	1.141	1.263	-.3728	14.19	18.32	20.98	.4298	350.0	410.0
8.933	.9518	1.261	1.297	-.3158	14.19	19.81	22.68	.4848	350.0	743.0
18.46	1.266	1.412	1.297	-.3158	7.852	19.80	21.28	.4848	300.0	294.0
32.84	1.516	1.532	1.338	-.2618	7.852	21.77	23.38	.5488	300.0	363.0
58.45	1.767	1.651	1.385	-.2188	7.852	24.29	26.88	.6178	300.0	646.0
146.8	2.167	1.843	1.386	-.2188	.0000	24.38	24.38	.6178	250.0	146.8
261.8	2.417	1.963	1.442	-.1612	.0000	27.78	27.78	.6988	250.0	261.8
464.8	2.667	2.082	1.512	-.1168	.0000	32.58	32.58	.7660	250.0	464.8
825.8	2.916	2.202	1.591	-.7448G-01	.0000	39.98	39.98	.8438	250.0	825.8
2711.	3.433	2.449	1.592	-.7448G-01	-7.852	39.85	36.38	.8438	200.0	147.9
4921.	3.683	2.569	1.684	-.3678G-01	-7.852	48.31	44.96	.9198	200.0	263.0
8578.	3.933	2.689	1.791	-.3198G-01	-7.852	61.86	57.98	.9938	200.0	458.8
.1525G 05	4.183	2.809	1.914	.2588G-01	-7.852	82.89	78.38	1.061	200.0	832.8
.7388G 05	4.867	3.136	1.914	.2588G-01	-14.18	82.88	78.58	1.061	150.0	110.5
.1318G 06	5.117	3.256	2.052	.4998G-01	-14.18	112.8	96.98	1.122	150.0	196.6
.2331G 06	5.368	3.376	2.286	.6888G-01	-14.18	168.5	137.9	1.172	150.0	350.8
.4143G 06	5.617	3.495	2.374	.8228G-01	-14.18	236.3	283.8	1.208	150.0	622.8
.7368G 06	5.867	3.615	2.555	.8998G-01	-14.18	358.8	388.8	1.238	150.0	1188.
.6313G 07	6.800	4.862	2.555	.8998G-01	-21.16	358.9	283.8	1.238	100.0	188.8
.1122G 08	7.050	4.181	2.746	.9168G-01	-21.16	556.8	439.8	1.235	100.0	177.8
.1994G 08	7.300	4.301	2.943	.8728G-01	-21.16	877.7	692.8	1.222	100.0	316.8
.3546G 08	7.550	4.421	3.144	.7658G-01	-21.16	1394.	1099.	1.193	100.0	562.8
.6318G 08	7.800	4.541	3.345	.5968G-01	-21.16	2211.	1743.	1.147	100.0	1000.
.1122G 09	8.050	4.660	3.541	.3658G-01	-21.16	3475.	2748.	1.088	100.0	1778.
.2352G 10	9.371	5.293	3.540	.3658G-01	-28.21	3466.	2498.	1.080	50.00	97.08
.4182G 10	9.621	5.413	3.727	.7368G-02	-28.21	5335.	3838.	1.017	50.00	172.8
.7443G 10	9.872	5.533	3.903	-.2773G-01	-28.21	7995.	5748.	.9388	50.00	307.8
.1324G 11	10.12	5.653	4.065	-.6848G-01	-28.21	.1162G 05	8348.	.8548	50.00	546.8
.2352G 11	10.37	5.772	4.212	-.1144	-28.21	.1631G 05	.1171G 05	.7688	50.00	970.8
.4182G 11	10.62	5.892	4.344	-.1656	-28.21	.2289G 05	.1586G 05	.6838	50.00	1725.
.7443G 11	10.87	6.012	4.468	-.2218	-28.21	.2883G 05	.2078G 05	.5918	50.00	3070.
.6846G 13	12.84	6.952	4.468	-.2218	-35.26	.2887G 05	.1869G 05	.6618	.0000	84.48
.1218G 14	13.09	7.072	4.562	-.2828	-35.26	.3645G 05	.2368G 05	.5238	.0000	159.1
.2166G 14	13.34	7.192	4.658	-.3468	-35.26	.4484G 05	.2898G 05	.4518	.0000	267.8
.3853G 14	13.59	7.311	4.724	-.4148	-35.26	.5298G 05	.3438G 05	.3868	.0000	475.8
.6846G 14	13.84	7.431	4.788	-.4868	-35.26	.6132G 05	.3978G 05	.3278	.0000	844.8
.1218G 15	14.09	7.551	4.842	-.5608	-35.26	.6951G 05	.4508G 05	.2758	.0000	1501.
.2166G 15	14.34	7.672	4.887	-.6388	-35.26	.7788G 05	.4998G 05	.2388	.0000	2670.
.3853G 15	14.59	7.790	4.924	-.7188	-35.26	.8483G 05	.5448G 05	.1914	.0000	4750.
.5818G 18	17.78	9.282	4.925	-.7188	-42.31	.8487G 05	.4858G 05	.1914	-50.00	58.18
.8918G 18	17.95	9.481	4.956	-.8818	-42.31	.9832G 05	.5218G 05	.1583	-50.00	89.18
.1585G 19	18.28	9.521	4.982	-.8858	-42.31	.9684G 05	.5548G 05	.1382	-50.00	158.5
.2828G 19	18.45	9.641	5.084	-.9728	-42.31	.1089G 06	.5828G 05	.1867	-50.00	282.8
.5018G 19	18.78	9.768	5.021	-1.060	-42.31	.1058G 06	.6068G 05	.8788G-01	-50.00	501.8
.8918G 19	18.95	9.888	5.036	-1.151	-42.31	.1087G 06	.6278G 05	.7878G-01	-50.00	891.8
.1585G 20	19.28	10.08	5.048	-1.242	-42.31	.1118G 06	.6458G 05	.5738G-01	-50.00	1585.

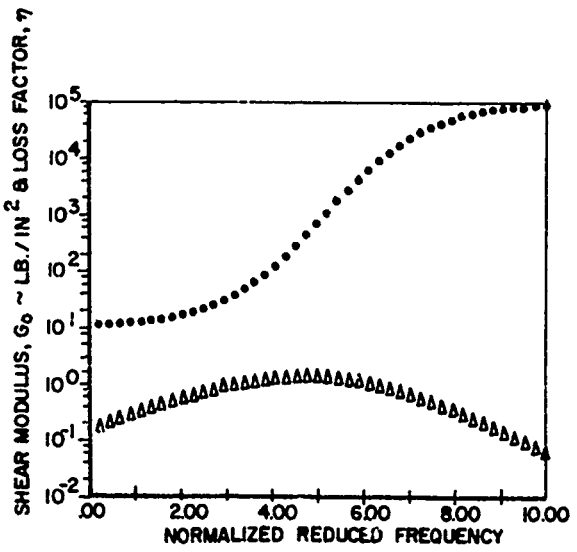

Figure 4: Unobtainium Properties at To = 100

Another possible approach for selecting T_0 is to least squares fit the data at various values of T_0 and select the T_0 which minimizes the residuals. The results of this type of study for the G_0 and η of Unobtainium are listed in Table III. The least squares fitting was performed on log η and log G to give the same weight to each data point. The residual of each attain a minimum at T_0 = 100 as expected. The parameters and residuals appear to be smooth functions of T_0 except for the parameters for η at T_0 = 175. It probably happens that the residual is insensitive to a locus of parameter values, although there is confidence in the value for the residual.

The modulus data for Unobtainium were also processed multiplying by the temperature ratio, Equation (7), and these results are also presented in Table III. It appears that the residual is minimized for T_0 about 85°F. The two values for the experimental modulus G and that at the reference temperature G_0 are compared in Tables IIA and B where the percent difference DEL G is given. It is seen that G

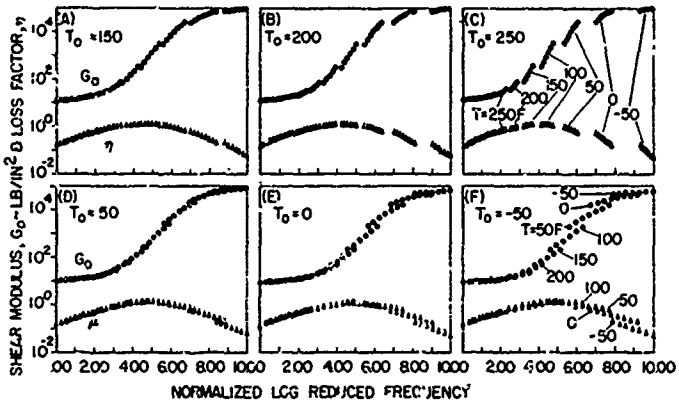

Figure 5: Reference Temperature Effects on Scatter of Unobtainium Data

TABLE III LEAST SQUARES FIT FOR SIMULATED DATA

	η						G_0					G				
T_0	η_{FROL}	S_L	S_H	F_{ROL}	C	ϵ_{ETA}	f_{ROG}	G_{FROG}	N	G_L	ϵ_{GO}	f_{ROG}	G_{FROG}	N	G_L	ϵ_G
UNOBTAINIUM																
25°F	1.18	.355	-.555	23.3	2.41	.0390	15.2	902.	.448	8.87	.0559	16.6	1110	.486	17.0	.0441
50	1.18	.366	-.536	63.6	3.00	.0256	44.2	938.	.414	9.27	.0365	46.7	1100	.450	17.0	.0274
75	1.18	.359	-.497	184.	3.49	.0125	141.	970.	.381	9.65	.0179	157.	1090	.415	16.9	.0150
100	1.20	.350	-.450	500.	4.00	.0002	500.	1000.	.350	10.0	.0005	564.	1070	.381	16.8	.0172
125	1.22	.337	-.395	1240.	4.49	.0120	2000.	1030.	.320	10.3	.0172	2300.	1060	.348	16.7	.0300
150	1.23	.321	-.337	2850.	4.94	.0232	9240.	1050.	.290	10.6	.0336	10800.	1040	.316	16.5	.0444
175	1.19	.362	-.309	2590.	6.51	.0342	50200.	1070.	.262	10.9	.0493	60200.	1020	.285	16.3	.0587
UNOBTAINIUM-N																
25°F	.0221	.732	-2.72	19100	5.36	.0994	10.2	927	.599	7.51	.191					
50	.336	.479	-1.47	19800	3.89	.0853	32.7	1020	.535	7.73	.159					
75	1.15	.235	- .511	160	1.34	.0665	115.	1120	.478	7.95	.128					
100	1.12	.225	- .510	816	1.64	.0524	452.	1210	.426	8.12	.0984					
125	1.09	.215	- .502	4960	2.00	.0385	1990	1270	.380	8.28	.0709					
150	1.06	.206	- .486	36500	2.47	.0252	10100	1320	.339	8.45	.0467					
175	1.01	.203	- .473	356000	3.17	.0147	59300	1340	.302	8.61	.0304					

and G_0 differ by up to 25% in the range of temperatures of engineering interest. Regardless, the experimental values are very closely recovered for the range of temperature and frequencies of engineering interest whether G or G_0 is used. This may be explained by noting that F_R is strongly dependent on temperature; the difference between G and G_0 is therefore easily accounted for in curve fitting. The only effect is some increased scatter (as indicated by the residuals in Table III) and this scatter is not noticeable when working with actual data. Obviously, if the frequency temperature equivalence principle were relied on to extrapolate the curves, then the effect must be accounted for.

Also covered in Table III is processing of Unobtainium-N data which were generated in exactly the same way as Unobtainium except the Nashif WLF equation with T_0 = 100 was used to select the temperature and frequency data. As indicated by the residuals, the T_0 for best fit is probably about 200°F. This example serves as an illustration that the Jones and Nashif temperature shift parameter curves both work for these temperature ranges.

More sophisticated fitting was considered but rejected due to insensitivity of results and convergence difficulties with methods utilized.

TABLE IV LEAST SQUARES FIT FOR ACTUAL DATA

	η						G_0				
T_0	η_{FROL}	S_L	S_H	F_{ROL}	C	ϵ_η	F_{ROG}	G_{FROG}	N	G_L	ϵ_{GO}
MATERIAL N467											
25°F	.931	.1	-.551	359.	1.05	.153	162.	735.	.254	1.04	.0996
50	1.03	.1	-.405	505.	.979	.152	499.	726.	.233	1.	.101
75	.995	.608	-.887	2140.	5.54	.147	2380.	874.	.211	1.14	.107
100	1.03	.1	-.443	23800.	1.19	.138	8060.	794.	.191	1.	.114
125	.998	.546	-.792	66600.	6.74	.137	67400.	1050.	.164	1.	.125
150	1.08	.839	-1.01	212000.	11.4	.133	171000.	722.	.159	1.	.133
175	1.2	7.19	-7.17	88700.	111.	.128	1320000.	758.	.140	1.	.144
MATERIAL J467											
25°F	1.21	.450	-.301	6.0	2.00	.0241	63.4	460.	.420	5.37	.105
50	1.29	.134	-.120	48.3	.247	.0226	189.	450.	.404	5.75	.0965
75	1.28	.151	-.101	108.	.356	.0226	650.	454.	.382	6.01	.0883
100	1.22	.265	-.143	192.	1.32	.0237	2470.	449.	.364	6.48	.0805
125	1.29	.142	-.1	1720.	.479	.0228	11000.	449.	.337	6.55	.0733
150	-	-	-	-	-	-	-	-	-	-	-
175	1.24	.183	-.1	24100.	1.32	.0236	345000.	430.	.291	7.01	.0621

Processing Actual Data

Results from processing two sets of actual data designated N467 and J467 are summarized in Table IV and Figures 6 through 10. The loss factor values versus temperature (without regard to frequency) for all N467 data points are plotted in Figure 6 together with a quadratic fit. The dependence on temperature is dominant compared to frequency and the peak may tentatively serve as a guide to the T_0 selection. The temperature and frequency at whichthe N467 data points were taken are shown in Figure 7, which serves to display the range of applicability of the data without extrapolation and to indicate the data quality by how smoothly the modal frequencies vary with temperature.

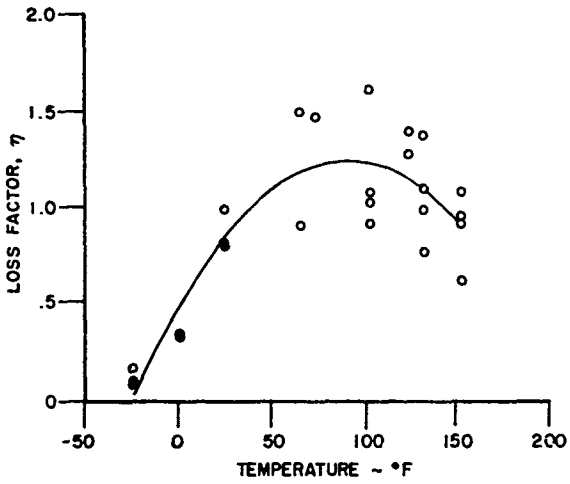

Figure 6: N467 Data Loss Factor Versus Temperature

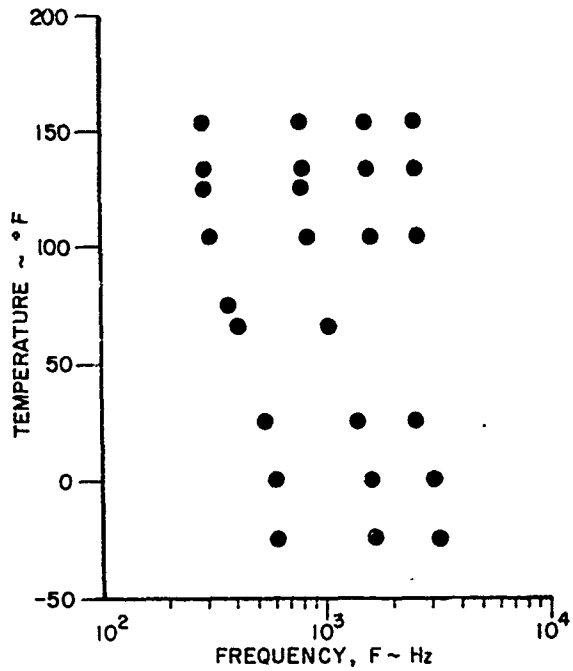

Figure 7: N467 Temperature and Frequency of Data Points

A general purpose, interactive, least squares program was used to determine parameter values for Equations (6) and (12). Data points and the curve were displayed simultaneously. Parameters could be held constant or constrained within specified ranges. Figure 8 presents a fit for modulus which was obtained without regard to constraints or care in initial parameter values. The fit is obviously

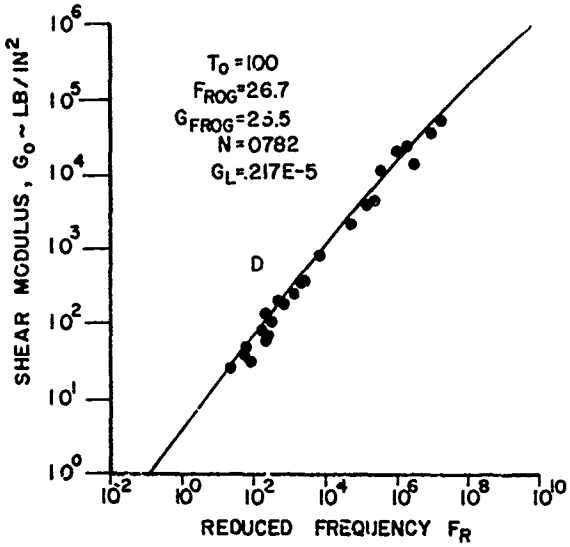

Figure 8: N467 Modulus Fit at To = 100

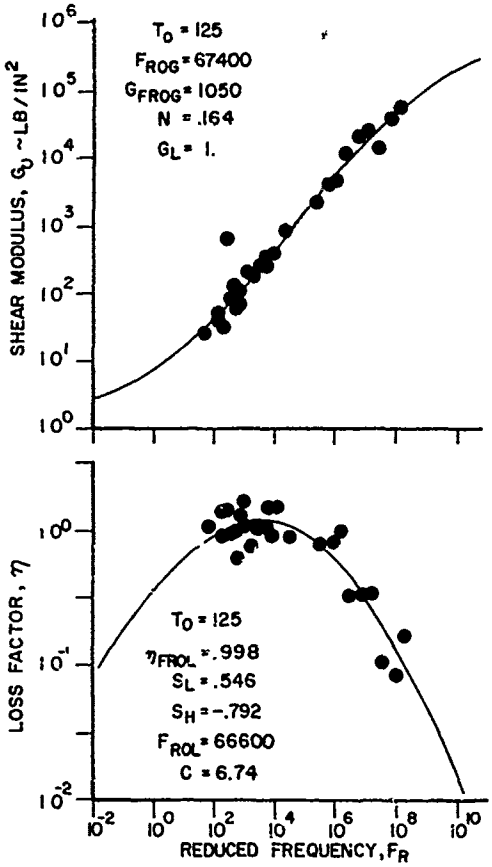

Figure 9: N467 Data Fit

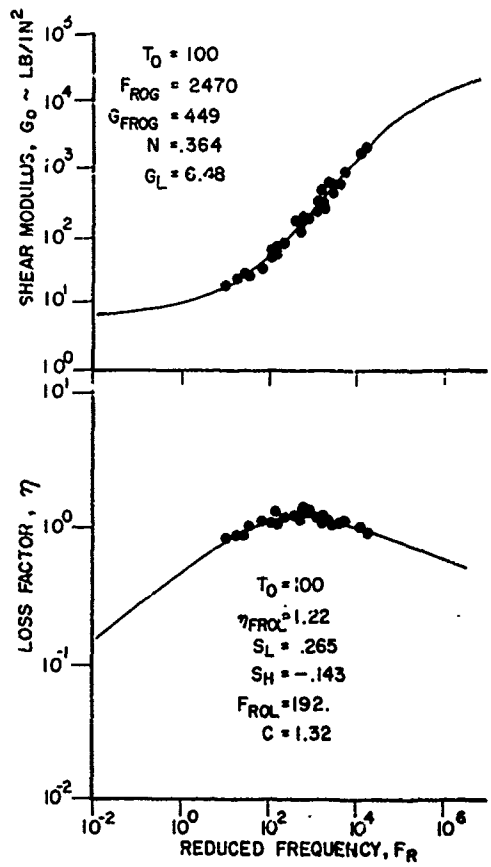

Figure 10: J467 Data Fit

valid over the range of data, but the value of .215E-5 for G_L, which is the lower asymptote, is physically impossible, and makes any significant extrapolation suspect. Convergence of these parameter values is caused in part by the minimum range of reduced frequency covered by

Based on findings of preliminary convergence attempts, the following constraints were imposed:

$$\begin{aligned} \eta_{FROL} &\geq .5 \\ S_L &\geq .1 \\ S_H &\leq -.1 \\ f_{ROL} &\geq .01 \\ 100 &\leq G_{FROG} \leq 10000 \\ G_L &\geq 1. \end{aligned} \qquad (17)$$

In addition, care was taken in selecting initial values. Furthermore, η_{FROL}, S_L, and S_H were held fixed and the computer program used to find corresponding values for F_{ROL} and c. Then this set of values was used as initial

values for another least square fit. Similarly, G_{FROG} and G_L were sometimes held constant. The interactive feature (or at least an interative procedure) seems to be essential for proper covergence.

Sample fits are shown in Figures 9 and 10 for N467 and J467 respectively. These fits may be used to represent the material properties with a reasonable amount of extrapolation. From Table IV it is seen that a simultaneous minimum in the residuals for loss factor and modulus does not occur for either material.

USE OF CHARACTERIZED PROPERTIES IN PREDICTION TECHNIQUES

Constrained layer damping treatments have been receiving considerable attention recently because of their effectiveness in reducing vibratory levels and high damping efficiency as compared with other types of treatments. This applies to both the single- and multiple-layer configurations. However, the drawback is in the rather difficult design procedure for such treatments.

An effective damping treatment must be specifically tailored for each application. In particular, the temperature at which damage occurs in service and the problem mode(s) must be known. This is because the modal damping is highly dependent on environmental temperature and on the shear strains induced in the viscoelastic layer by vibration of the structure in the problem mode(s).

The design process is typically an iterative experimental one in which the modal damping of a candidate design is measured on a suitable specimen under controlled temperature. If the modal damping is high enough over the service temperature range, the design is satisfactory, and if not, the candidate design must be modified to improve damping and temperature range. Analysis is used to guide initial and modified candidate selection.

The analysis approximates the actual structure as an idealized, simply-supported beam or plate whose size is determined by the node line spacing of the problem mode(s). Candidate viscoelastic damping layer and constraining layer materials and thicknesses are selected and analyses used to obtain corresponding modal damping versus temperature characteristics.

The analysis used for this investigation was based on that developed by Ross, Kerwin, and Ungar(5) for a three-layer system. This analysis can be modified to handle both single- and multiple-layer configurations. However, only single constrained layer configurations will be discussed here.

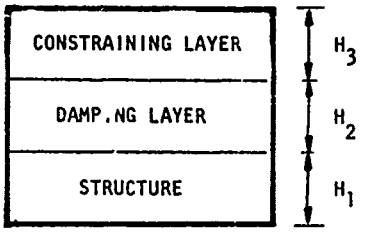

Figure 11: Sketch of Constrained-Layer Damping Treatment

The flexural rigidity EI of the three-layer system of Figure 11 is

$$EI = E_1 \frac{H_1^3}{12} + E_2 \frac{H_2^3}{12} + E_3 \frac{H_3^3}{12} - E_2 \frac{H_2^2}{12} \frac{H_{31}-D}{1+g}$$

$$+ E_1 H_1 D^2 + E_2 H_2 (H_{21}-D)^2 + E_3 H_3 (H_{31}-D)^2$$

$$- \left[\frac{E_2 H_2}{2} (H_{21}-D) + E_3 H_3 (H_{31}-D) \right] \frac{H_{31}-D}{1+g} \qquad (18)$$

where

$$D = \frac{E_2 H_2 (H_{21} - \frac{H_{31}}{2}) + g(E_2 H_2 H_{21} + E_3 H_3 H_{31})}{E_1 H_1 + \frac{E_2 H_2}{2} + g(E_1 H_1 + E_2 H_2 + E_3 H_3)} \qquad (19)$$

$$H_{31} = \frac{H_1 + H_3}{2} + H_2 \qquad (20)$$

$$H_{21} = \frac{H_1 + H_2}{2} \qquad (21)$$

$$g = \frac{G_2}{E_3 H_3 H_2 D^2} \qquad (22)$$

E is the Young's modulus of elasticity.

G is the shear modulus.

I is the second moment of area.

H is the thickness.

p^2 is the wave number.

Subscript 1 refers to the base structure.

Subscript 2 refers to the damping layer.

Subscript 3 refers to the constraining layer.

No subscript refers to the composite system.

The above analysis applies to either simply supported beams or plates.

To include the damping terms into Equation (18), it will be necessary to replace each modulus term by a complex modulus term. For example, in the general case, it will be necessary to have

$$g \rightarrow g(1 + i\eta_2) \tag{23}$$

$$E_2 \rightarrow E_2(1 + i\eta_2) \tag{24}$$

$$E_3 \rightarrow E_3(1 + i\eta_3) \tag{25}$$

$$E_1 \rightarrow E_1(1 + i\eta_1) \tag{26}$$

$$E \rightarrow E(1 + i\eta) \tag{27}$$

where η is the loss factor and also it is assumed to be the same for viscoelastic material subjected to either extensional or shear deformation.

To solve Equation (18), it will be necessary to substitute the expressions given in Equations (23) through (27) in Equation (18) and then equate the real and imaginary parts of the Equation to arrive at the expressions for η and EI.

The above analysis was used in conjunction with the characterized material properties of Figure 4 and Equations (9) and (12) to describe the performance of various configurations of constrained layer damping treatments on an

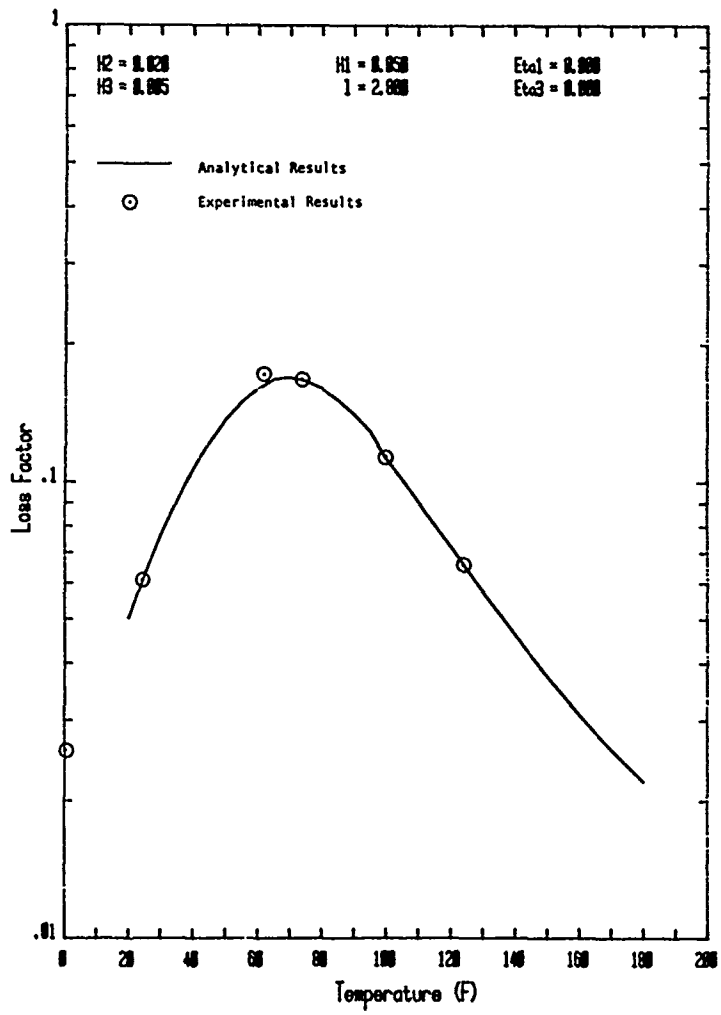

Figure 12: Comparison Between the Measured and Predicted Results

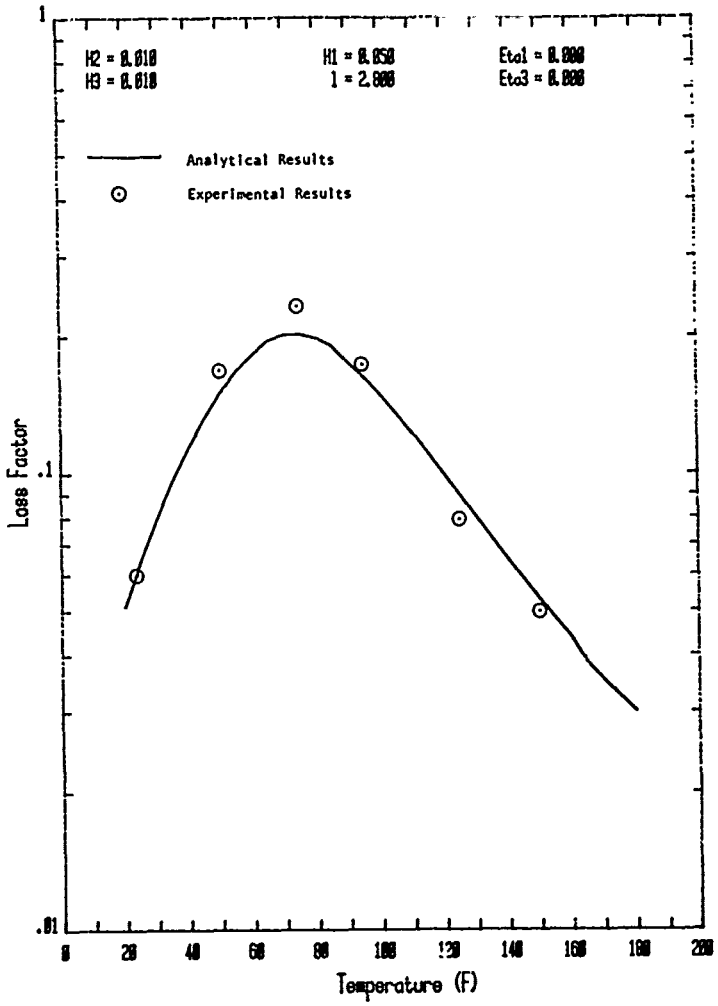

Figure 13: Comparison Between the Measured and Predicted Results

aluminum cantilever beam. The beam thickness was 0.05 in. while its length was 7.0 in. Constraining layers of the aluminum type were considered. All the data is presented for the third mode of vibration of the beam which corresponds to a semi-wavelength of vibration of 2.8 in.

Two typical results generated by the computer of the above analysis are shown in Figures 12 and 13, which present modal loss factor as a function of temperature. Experimental data are also superimposed in these two Figures for comparison purposes. It can be seen here that the agreement between the predicted and measured results is excellent. Several other cases were also investigated and found to be similar in agreement, which establishes confidence in this approach.

Having established the confidence in this analytical approach to predict the performance of damping treatments, it now becomes possible to generate design charts that can be used to select a damping configuration having the desired performance. This is illustrated in Figure 14. In this Figure, the practical ranges of viscoelastic thickness and of constraining layer thickness are covered systematically. For each configuration, the peak damping and the temperature of peak damping are determined, for example, from the peak of Figure 12. Figure 14 shows these points plotted for viscoelastic layer thicknesses of .001, .005, .010, and .020, each with constraining layer thicknesses of .001, .005, .010, and .020; the points are connected, forming a "carpet plot." Such a plot is extremely useful in quickly recognizing at what

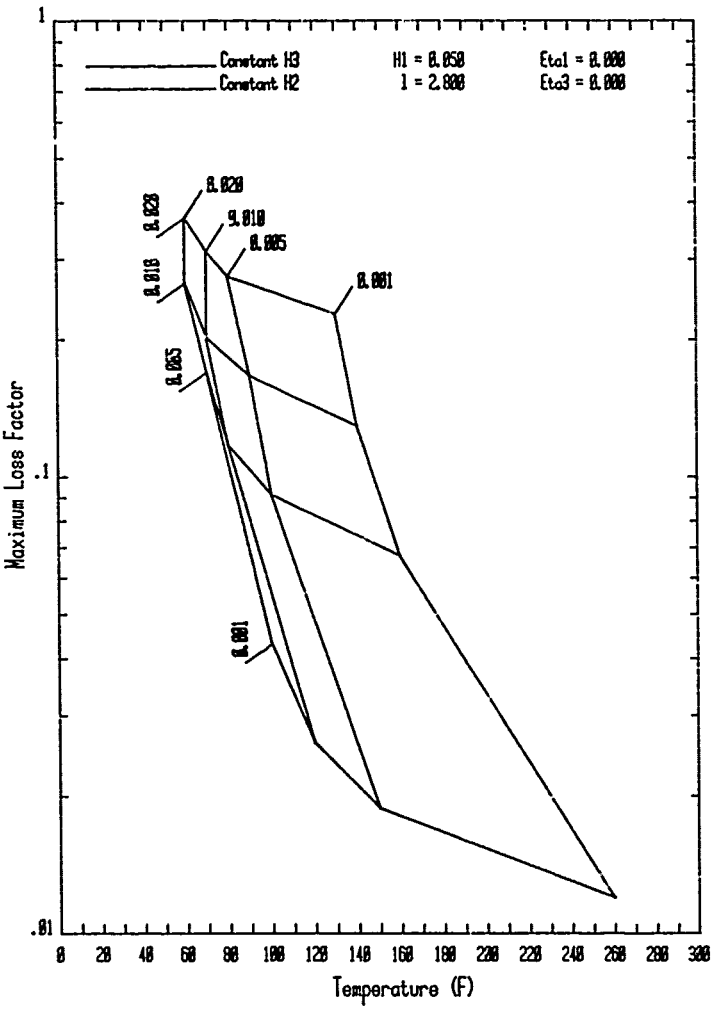

Figure 14: Typical Carpet Plot for the Maximum Loss Factor with Temperature

temperatures and how much damping can be achieved from the various configurations. After deciding on a desired configuration, then it will be possible to study its performance with temperature more closely as illustrated in Figures 12 and 13.

Sensitivity Studies

To gain some insight into the relative importance of fitting the loss factor or modulus data, some sensitivity studies were performed. The need for this is shown by studying the N467 residuals for loss factor and modulus as a function of reference temperature. It is seen that, in the range of T_o covered, the trends for the two are opposite.

The sensitivity study was performed by increasing the modulus by 20% and repeating a carpet plot. Similarily, the loss factor was decreased by 20% and the carpet plot again repeated. These results are presented in Figure 15. The somewhat irregular effect is caused by performing the analysis at 10 degree increments.

As expected, it can be seen that the 20% increase in the modulus results in a slight shift to higher temperature for the maximum composite loss factor values. The effects of reducing the material loss factor by 20% results in almost comparable reductions for the composite loss factor values. This illustrates that even large errors of up to 20% curve fitting the data has only a small effect on the predicted composite loss factor.

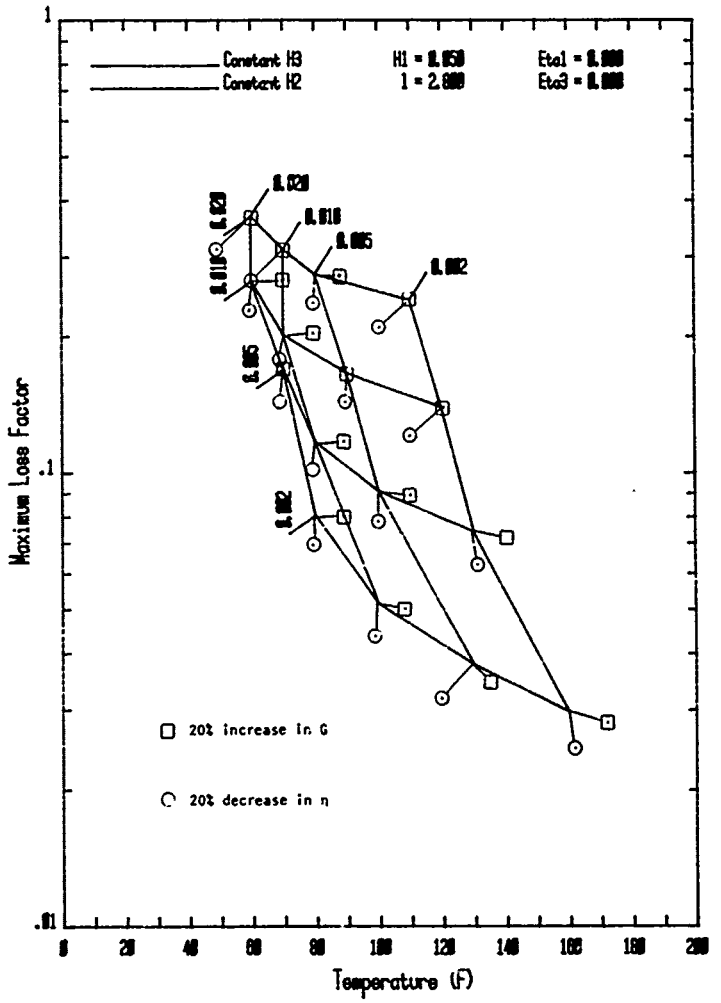

Figure 15: Sensitivity Study Results

CONCLUSIONS AND RECOMMENDATIONS

The equations presented to represent the properties of viscoelastic damping materials have been found convenient and accurate. Values of parameters for best fit may be chosen by computer or by trial and error. They are useful for processing, storing, retrieving, and communicating material data. Temtatively, the T_o selection should be made by taking hte peak of the loss factor as a function of temperature and rounding to the nearest 25 degrees. To facilitate convergence by defining the material properties over a greater range of temperature than is customary at present. One hundred degrees on each side of peak damping should be adequate.

The carpet plot has proven to be a very useful tool. It shows at a glance the peak damping and corresponding temperature for the practical engineering ranges of viscoelastic material and constraining layer thicknesses. Therefore, it may be used to make an initial selection of a damping treatment for experimental study. It also may by used to modify a design to change damping level or temperature coverage.

ACKNOWLEGEMENTS

This work was performed while Mr. Nashif was under a self-employed, visiting scientist contract with the Air Force Flight Dynamics Laboratory, which was partially funded by the Air Force Materials Laboratory. Mrs. Karen S. Hall and Sgt. S. A. Zastrow assisted with programming and data processing. Mr. Tom Rowland and Dr. Phil Poirier of the ASD

Computer Center provided computer programming consultations. Drs. J. P. Henderson and David I. G. Jones of the Air Force Materials Laboratory, and Messrs. C. Cannon, M. Drake, and M. Parin of the University of Dayton Research Institute provided stimulating discussion and technical assistance.

REFERENCES

1. Kelley, F.N. and Williams, M.L., "The Engineering of Polymers for Mechanical Behavior", Rubber Chemistry and Technology, Vol 42, N4, September 1969, pp. 1175-1185.

2. Jones, D.I.G., "Temperature-Frequency Dependence of Dynamic Properties of Damping Materials", Journal of Sound and Vibration, Vol 22, N4, 1974, pp. 451-470.

3. Aklonis, J.J, MacKnight, W.J., and Sher, M. eds. "Introduction to Polymer Viscoelasticity", Wiley-Interscience, 1972, p.52.

4. Jones, D.I.G., "A Reduced-Temperature Nomogram for Characterization of Damping Material Behavior", 48th Shock and Vibration Symposium, October 1977.

5. Ross, Kerwin, and Ungar, "Damping of Plate Flexural Vibrations by Means of Viscoelastic Laminae", in Ruzicka (ed.) Structural Damping, Section 3, The American Society of Mechanical Engineers, 1959.

NEW STRUCTURAL DAMPING TECHNIQUE FOR VIBRATION CONTROL

B. M. Patel
Lord Kinematics
Erie, Pennsylvania

G. E. Warnaka
Corporate Research and Development
Lord Corporation
Erie, Pennsylvania

D. J. Mead
Department of Aeronautics and Astronautics
The University
Southampton, United Kingdom

A new structural damping configuration is presented which makes efficient use of damping materials by subjecting them to both shear and extensional deformations. The configuration consists, in one form, of a series of rows of vertically oriented platelets with damping material sandwiched between them. Adjacent rows of platelets may overlap each other to enhance the deformation of the damping material. A theoretical analysis of the configuration is summarized and shown to compare extremely well with experimental results which are given for a variety of varying configurations. The new structural damping configuration is shown to apply to very rigid structures where it can control flexural vibrations and sound radiation with low added weight. The new structural damping design optimization study is made and a numerical example is included.

INTRODUCTION

Structural damping has been employed for many years to reduce vibration, noise and fatigue. Some of the application areas of structural damping are in commercial and military aircraft, surface ships, submarines, missiles, buildings, domestic appliances and office machinery.

The unconstrained damping layer and the constrained damping layer methods, as shown in Figure 1, are two distinct structural damping methods to damp flexural vibrations. The unconstrained damping layer method involves application of a visco-elastic layer on the base plate. The damping effect is obtained due to the internal losses in the visco-elastic layer resulting from alternating extensional and compressional strains. The constrained damping layer method makes use of a soft, highly damped material bonded between two plates or beams of rigid structural material. When this composite structure is flexed, the damping material is sheared and this gives rise to damping of the structure. The design and performance details of these configurations are well-known in the literature and need no repetition here. Countless variations of these basic techniques have also been developed.

It is the purpose of this paper to describe a new structural damping configuration. The effectiveness of

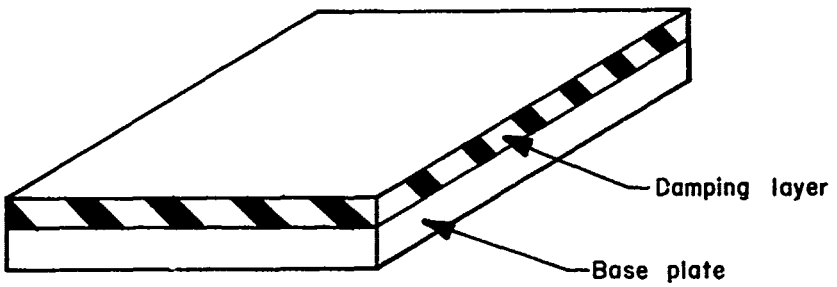

Unconstrained damping layer method

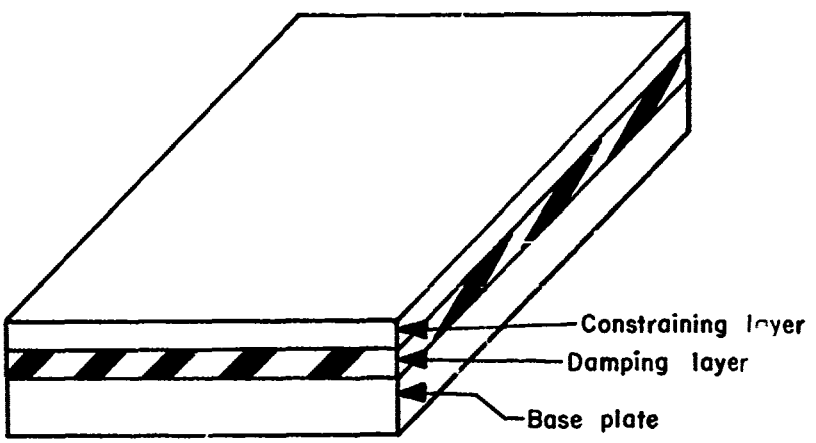

Constrained damping layer method

Figure 1 Structural damping layer methods

damping material can be increased substantially by using new structural damping configurations and this new configuration is extremely efficient as compared to the previously mentioned treatments. Because of its high effectiveness, the new treatment is suitable for damping large and very rigid structures. It is also suitable for damping more flexible conventional structures where it offers the advantage of providing the same level of damping as previous treatments but with much less added weight. The treatment is extremely rugged and can employ a wide variety of materials for maximum environmental resistance. It can be attached to vibrating structures by a wide variety of mechanical means such as bolting, riveting, welding and adhesive bonding.

This method was patented in 1965, but there was no product developed. Recently there has been a significant interest in damping methods and devices, and hence research and development work is done.

Structural Damping

There are two well-known methods for damping flexural vibrations. The simplest treatment is the unconstrained damping layer treatment. A layer of stiff, highly damped material, usually a polymer, is adhered to the structure to be damped. When the structure is flexed, the damping is achieved due to the extension and compression of the damping material. The unconstrained damping layer treatment has the advantages of being simple, relatively inexpensive and frequency insensitive, within the limits of the adhesive to couple the damping material. A limitation of this technique is represented in the requirement that the material be simultaneously very stiff and highly damped. The requirement for high stiffness arises from the necessity for the damping material to be well coupled to the flexural vibrations of the structure and to contribute to the composite rigidity. When the damping material is deformed, some of the energy of deformation is transformed into heat and damping results. Under the most favorable conditions, the loss factor of the composite structure will only be about half that of the damping material. Furthermore, the requirement for high stiffness, Young's modulus > 3.45 GPa (500,000 psi), and a high loss factor, $\eta > 0.5$, can only be easily achieved with a certain few polymers. Even in these cases, the temperature bandwidth over which high stiffness and high damping can be obtained simultaneously is not great, being not more than 38°C (100°F).

The other well-known damping treatment is the constrained damping layer treatment. Here a soft, highly damped material is sandwiched between two layers of stiff structural material. When this composite is flexed, the core is sheared and the damping of the composite results from this deformation. The constrained damping layer treatment has the advantage of being relatively thin and light weight. The composite loss factor can approach that of the material itself with proper design and it offers good environmental protection to the damping material. Furthermore, the constrained damping layer treatment can make use of a wide variety of relatively soft, highly damped polymers. However, the constrained damping layer treatment is also frequency sensitive. That is, good damping is achieved in a specific frequency range. At frequencies outside this range the damping may be very low.

New Structural Damping Configuration

A new structural damping configuration has been devised which is more efficient than previously mentioned configurations [1-7]*. The new configuration combines some of the characteristics of both the unconstrained and constrained damping treatments making use of both shear and bending deformations of the material. A higher amount of damping of the overall composite can be achieved using this combination. The configuration has very good design flexibility so that damping materials of any stiffness can be utilized to maximum efficiency. Because of the efficiency and stiffness that can be achieved with the new configuration, it is suitable for damping extremely rigid structures that were previously impossible to damp effectively. The configuration can also be effectively designed for light weight structures so that structural vibration may be suppressed with a treatment weight much lower than that of an unconstrained treatment.

In one of its basic forms the new structural damping configuration is made up of continuous strips of damping material attached to the structure to be damped by means of overlapping vertical platelets. This arrangement is

*Numbers in brackets designate References at end of paper.

shown in Figure 2. When the composite structure is flexed, adjacent vertical platelets in a given row tend to separate during one half cycle and close together during the next half cycle. This results in shearing of the damping material relative to the platelets in the next row. Also, the damping layer is bent around the radius of curvature of the overall structure. This deformation is shown in Figure 3.

Mathematical Model

To understand more fully the definition and capability of the new structural damping configuration refer again to Figure 2. A generalized mathematical model may now be constructed; however, the mathematical theory is more complex than that of the constrained layer configuration. As a result, only a simplified version will be presented here. The general theory allows for:

1. Shear flexibility of the damping layer,
2. extensional flexibility of the damping layer, and
3. extensional flexibility of the platelets.

For the sake of simplicity, the case is considered where the platelets have an infinite shear stiffness. The damping layers are sheared as the beam bends during beam vibration and the platelet crests stretch under the action of direct stresses set up when the damping layer is sheared.

It can be shown that the contribution of one platelet and damping layer element to the extensional stiffness of the array is given by:

$$(EA)^*_{eff} = E_2'A_2\,(1+i\eta)\left(1+\frac{2}{s}\right)\times$$

$$\left[1+\frac{2\tanh\frac{\lambda_2 d}{4}}{s\frac{\lambda_2 d}{4}\left(\frac{\lambda_2}{\lambda_1}\tanh\frac{\lambda_1 d}{4}\tanh\frac{\lambda_2 d}{4}+1\right)}\right]^{-1}, \qquad (1)$$

where

$$s = \frac{E_2A_2}{E_1A_1}$$

Substituting the value of $E_2 = E_2'+iE_2''$ in the expression for s and simplifying gives:

$$s = \frac{1+i\eta}{E_{12}} \quad \text{where} \quad E_{12} = \frac{E_1A_1}{E_2'A_2}$$

also

$$\lambda_1 = \frac{1}{t_d}\sqrt{\frac{1}{(1+\nu)k_d}}\sqrt{s},$$

$$\lambda_2 = \frac{1}{t_d}\sqrt{\frac{1}{(1+\nu)K_d}}\sqrt{s+2}.$$

For n rows of damping layers across the whole array, the total extensional stiffness will be n times the extensional stiffness given by equation (1). Now suppose that the total flexural stiffness of the beam to be damped is $(EI)_b$, and its total extensional stiffness is $(EA)_b$.

Therefore, the flexural stiffness of the beam with an n-row platelet array is:

$$B^* = (EI)_b + \frac{(EA)_b\, n\, (EA)^*_{eff}\, h_2^2}{n\,(EA)^*_{eff} + (EA)_b}. \qquad (2)$$

Measures of Effectiveness

The effectiveness of the structural damping application can be identified by evaluating the loss factor of the composite, η_c, stiffness ratio, k, and harmonic displacement criteria, $k\eta_c$.

The general definition of a loss factor requires expression of B* in E(Real) + i E(Imaginary) form. Dividing equation (2) by the effective moment of inertia of the total system, I_{eff}, yields the effective Young's Modulus, E*, and is expressed as:

$$E^* = \frac{B^*}{I_{eff}} = \frac{(EI)_b}{I_{eff}} + \frac{(EA)_b\, n\, (EA)^*_{eff}\, h_2^2}{I_{eff}\{\, n\,(EA)^*_{eff} + (EA)_b\,\}},$$

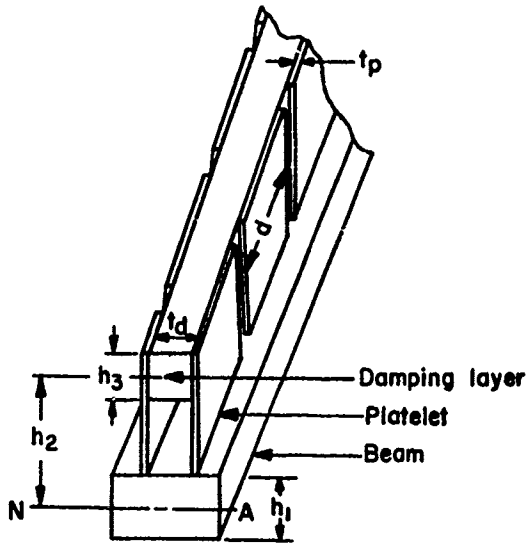

Figure 2 New structural damping configuration

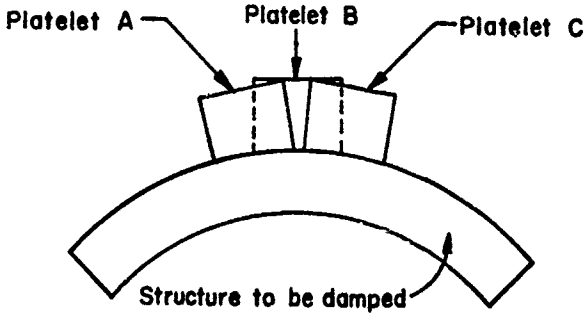

Figure 3 Motion of platelets due to deformation of the composite structure.

or

$$E^* = E(\text{Real}) + i\,E(\text{Imaginary}). \quad (3)$$

The composite loss factor, η_c, is defined as:

$$\eta_c = \frac{E(\text{Imaginary})}{E(\text{Real})}$$

$$= \frac{B(\text{Imaginary})}{B(\text{Real})} \quad . \quad (4)$$

The composite loss factor, η_c, gives a measure of the damping capability that is often useful in comparing various damping treatments. However, other criteria can also be developed.

The stiffness ratio, k, is defined as:

$$k = \frac{B(\text{Real})}{(EI)_b} \quad . \quad (5)$$

An harmonic displacement criterion, kn_c, is defined as:

$$kn_c = \frac{B(\text{Imaginary})}{(EI)_b} \quad . \quad (6)$$

The harmonic displacement criterion considers not only the effect of damping in reducing the flexural motion of the structure to be damped, but also the effect of the added stiffness of the damping treatment in limiting flexure. For damping treatments, like the one under consideration, that are capable of imparting considerable added stiffness, the harmonic displacement criterion gives a more appropriate measure of the treatment's effectiveness.

Numerical Example

A numerical example is presented here to familiarize one with the design parameters of the new structural damping design. A steel beam 101.6 cm (40") long, 7.6 cm (3") wide, 1 cm (3/8") thick is required to be damped. Four platelet rows and three damping layers are considered. The platelets are 0.05 cm (0.02") and 0.1 cm (0.04") thick for two specific designs. Platelet width to damping layer thickness ratio is varied over a practical range. The platelet height is 4.4 cm (1.75") and damping layer height is 1.3 cm (0.5"). These and other relevant dimensions are related to notations in Figure 2 and are expressed below.

Damping Layer:
Material: LD500
Complex Young's Modulus and the loss factor of LD500 are selected corresponding to 27°C (80°F) temperature.

$E_2' = 4.485$ GPa (650,000 psi).

$\eta = 0.64$

$h_3 = 1.3$ cm (0.50").

$A_2 = h_3\, t_d$.

Platelet:
Material: Steel

$E_1 = 207$ GPa (30×10^6 psi).

$h_2 = 4.3$ cm (1.69").

$$A_1 = \frac{h_3 t_p}{2} \quad , \text{ or}$$

$$= (h_2 + \frac{h_3}{2} - \frac{h_1}{2})\,\frac{t_p}{2} \quad .$$

$$\text{Select } A_1 = \frac{h_3 t_p}{2} \quad .$$

Beam:
Material: Steel

$E = 207$ GPa (30×10^6 psi).

$A = 7.3$ cm^2 (1.125 in.^{2}).

$I = 0.5$ cm^4 (0.01318 in.^{4}).

$(EA)_b = 15.3 \times 10^6$ kg (33.75×10^6 lb.).

$(EI)_b = 1.05 \times 10^6$ kg. cm^2 ($.39 \times 10^6$ lb. in.^{2}).

$n = 3$

$\nu = 0.50$

$k_d = 1.0$

Using above data and the computerized analysis, the values of η_c, k and kn_c were calculated for various values of d/t_d, t_d and t_p. The results are presented in graphical form. Figures 4 to

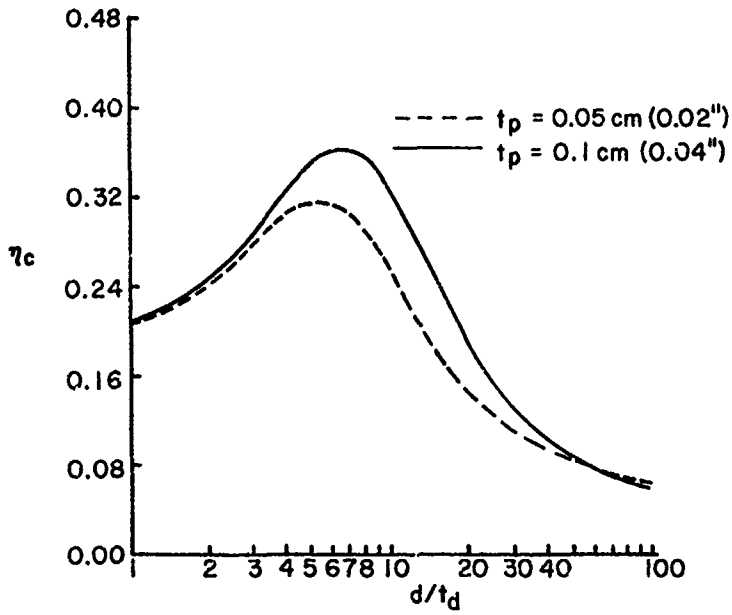

Figure 4 System loss factor with different platelet thicknesses, t_d = 0.16 cm (0.0625").

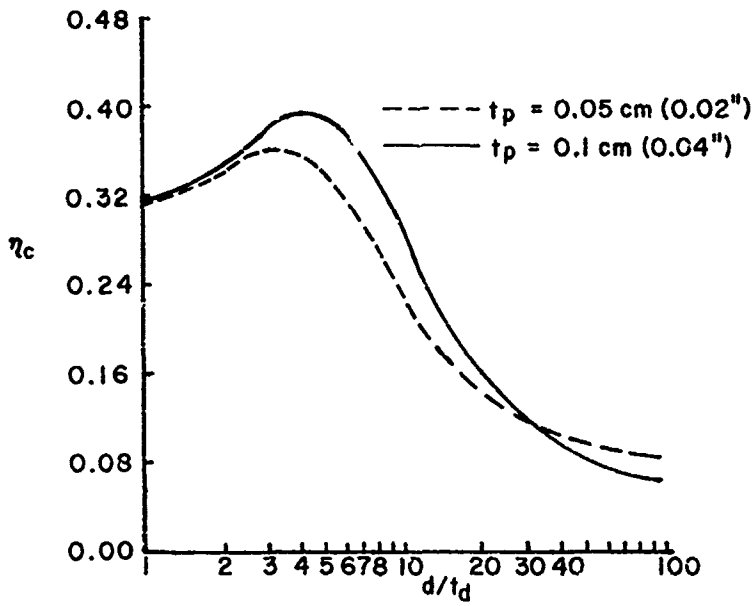

Figure 5 System loss factor with different platelet thicknesses, t_d = 0.3 cm (0.125").

7 represent the variation of η_c with d/t_d. Each figure contains two curves representing two different platelet thicknesses. It can be seen that the loss factor of the total system, η_c, is higher for platelet thickness, t_p = 0.1 cm (0.04") than for platelet with t_p = 0.05 cm (0.02") everywhere except at high values of d/t_d. At these high values of d/t_d, the two plots cross each other. The physical significance of this behavior is that stretching of the platelet crests reduces the deformation of the damping material, reducing overall damping.

Figures 4 to 7 are for a given damping layer thickness, t_d = 0.16 cm (0.06"), 0.3 cm (0.12"), 0.6 cm (0.25"), and 1.3 cm (0.5"). The platelet width, d, is allowed to vary. In Figures 8 and 9, the composite loss factor, η_c, is shown for four different damping layer thicknesses, t_d = 0.16 cm (0.06"), 0.3 cm (0.12"), 0.6 cm (0.25"), and 1.3 cm (0.5"). The platelet thickness is 0.05 cm (0.02") and 0.1 cm (0.04"). Figures 10 and 11 show the effects of the same parameters on the harmonic displacement criteria, $k\eta_c$. All of these curves illustrate that for a given damping material and platelet thickness, there is a range of platelet lengths that maximize the deformation of the damping material and the stiffening effects. The maximum loss factor and maximum reduction in flexural vibrations, as represented by the harmonic displacement criteria, do not occur at the same platelet width. Thus, it is important to decide, in advance, the criteria to be used to evaluate damping treatments based on the functioning of the final structure. Nevertheless, the new structural damping configuration is capable of achieving high values of loss factor and harmonic displacement criteria. The loss factor is important when vibration transmission and certain resonant conditions are of primary interest. Harmonic displacement criterion is important when evaluating stiff structures and for minimizing overall motion as in fatigue problems.

Experimentation

The theory was tested by experiments on several specimens. These specimens consisted of a steel base strip nominally 27.3 cm (10.75") long, 0.7 cm (0.3") wide, and 0.3 cm (0.125") thick. Rows of brass platelets and damping layers were bonded together to form the sample. The brass platelets were 0.04 cm (0.016") thick and the damping layers were 0.3 cm (0.125") thick.

The B&K complex modulus apparatus was used to excite bending resonances in the samples. The samples were clamped at one end and excited at frequencies throughout the range of interest by an electromagnetic force transducer located near the opposite end. A second transducer was positioned along the specimen, within 0.2 or 0.3 cm of the surface, and measured the vibratory motion of the adjacent surface. The resonant frequencies were determined from plots of the response as a function of frequency. The composite loss factor, η_c, of the samples was determined from the width of the frequency response curve in the resonant region. The loss factors of the samples were obtained from the relationship

$$\eta_c = \frac{\Delta f_n}{f_n} ,$$

where f_n = resonance frequency, and

Δf_n = bandwidth at frequency, f_n, defined by half-power (± 3 dB) points of the response curve.

The measured resonance frequencies and loss factor of several samples are given below. Refer to Figure 12 for sketches of the samples.

1. Undamped Sample: 27.3 cm (10.75") long x 0.8 cm (0.3") wide x 0.3 cm (0.125") thick.

Resonance Frequency in Hz	Loss Factor η_c
37.3	0.02
73.0	0.007
109.6	0.011

2. Structural Damping Configuration 1: 1.3 cm (0.5") x 1.3 cm (0.5") x 0.04 cm (0.016") brass plates, overlapping configuration, supporting a 0.6 cm (0.25") x 0.3 cm (0.125") layer of LD-400.

Resonance Frequency in Hz	Loss Factor η_c
433.0	0.302

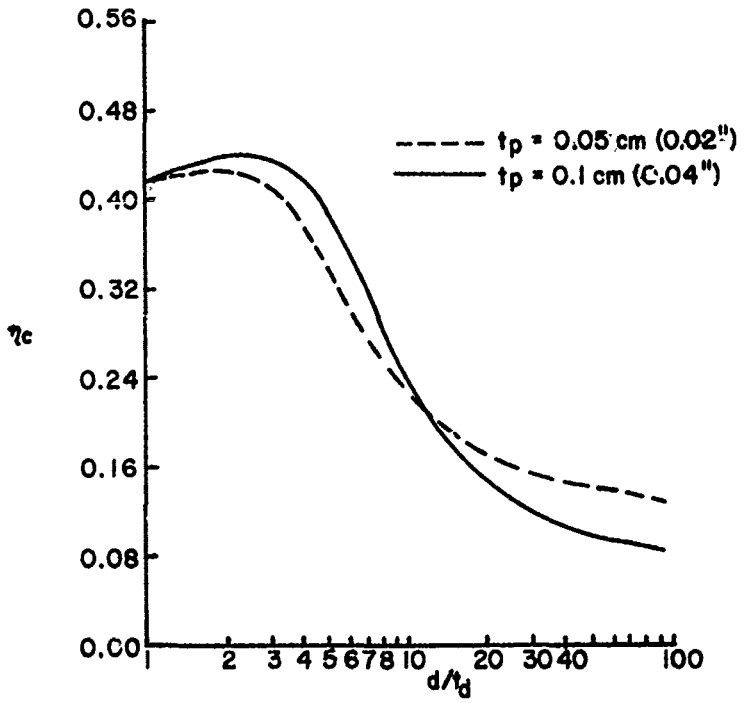

Figure 6 System loss factor with different platelet thicknesses, t_d = 0.6 cm (0.25").

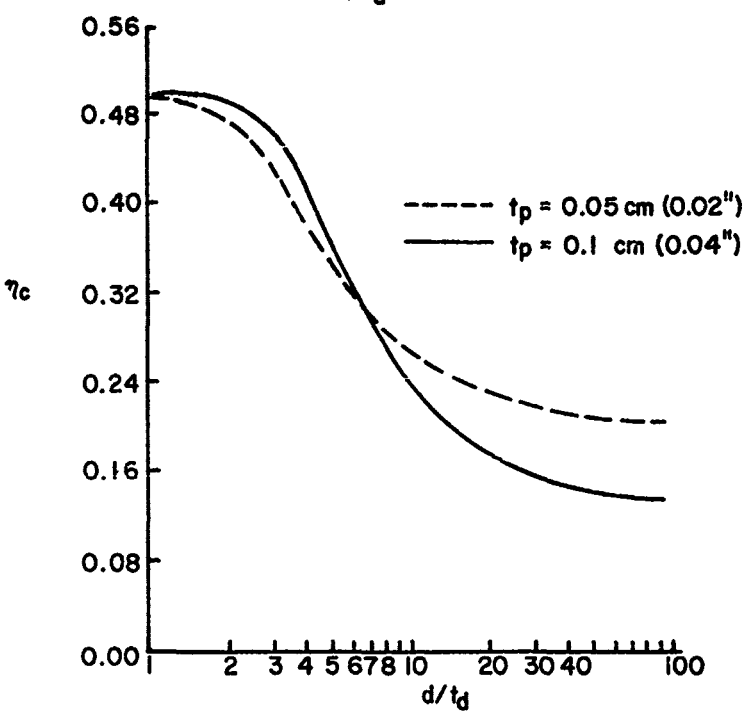

Figure 7 System loss factor with different platelet thicknesses, t_d = 1.3 cm (0.5").

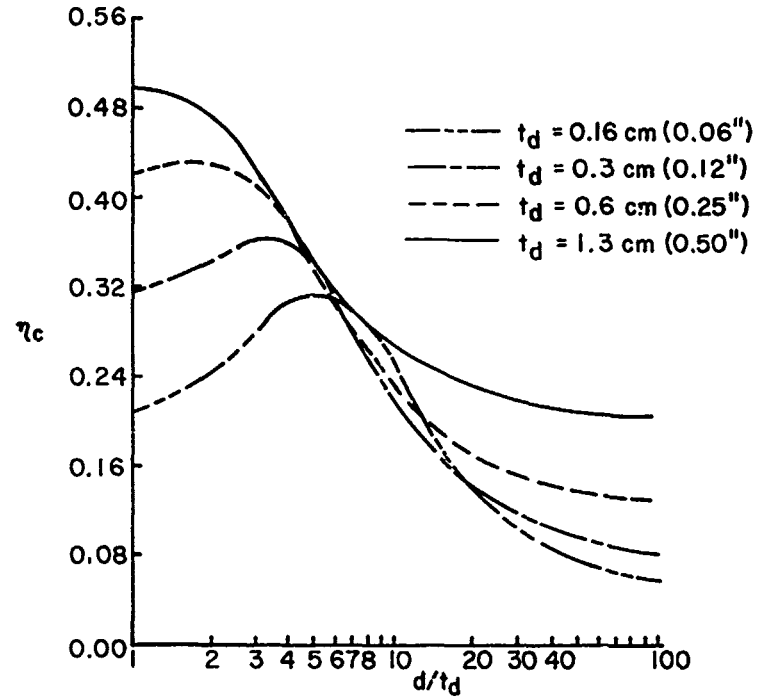

Figure 8 System loss factor with various damping layer thicknesses, t_p = 0.05 cm (0.02").

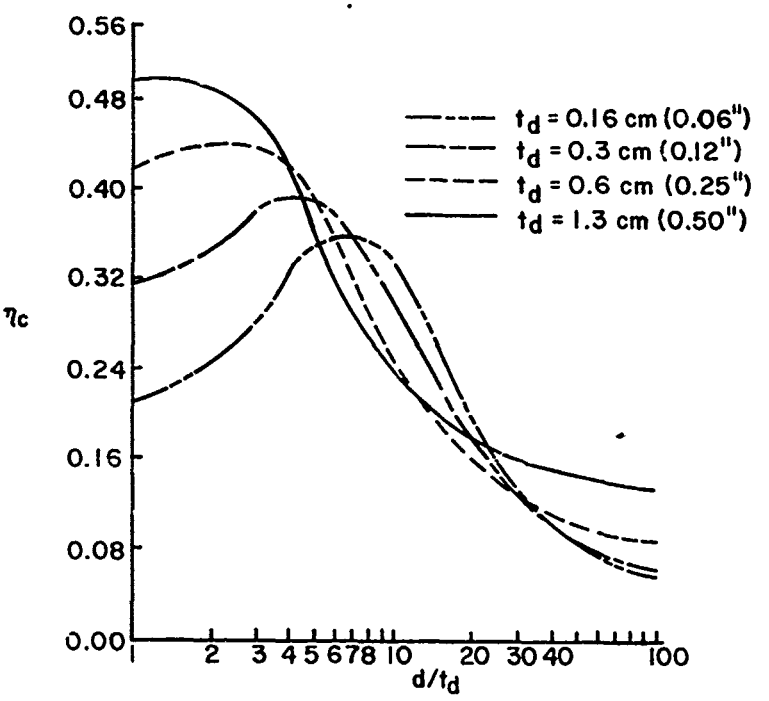

Figure 9 System loss factor with various damping layer thicknesses, t_p = 0.1 cm (0.04").

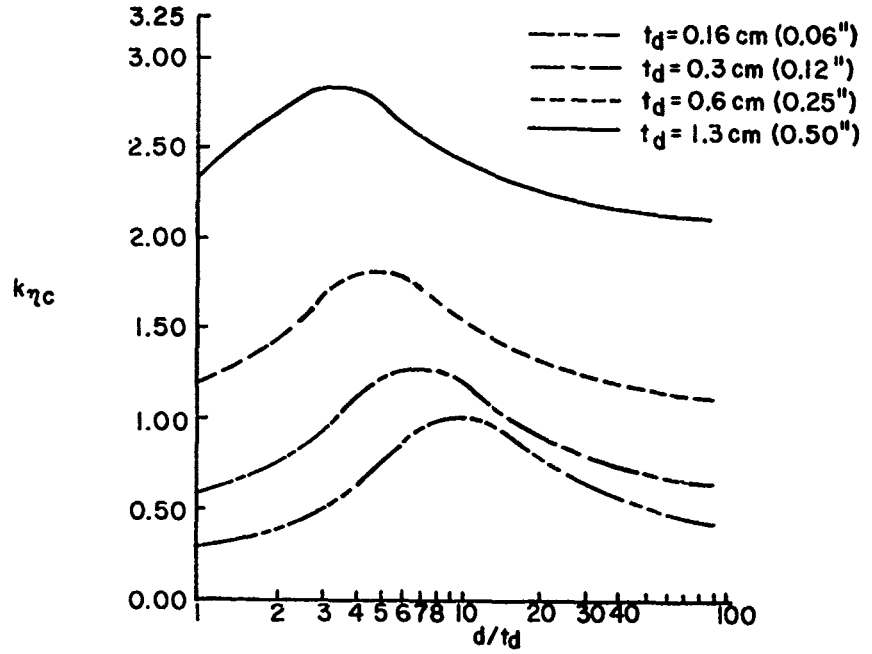

Figure 10 Harmonic displacement criteria different damping layer thicknesses, tp=0.05cm(0.02").

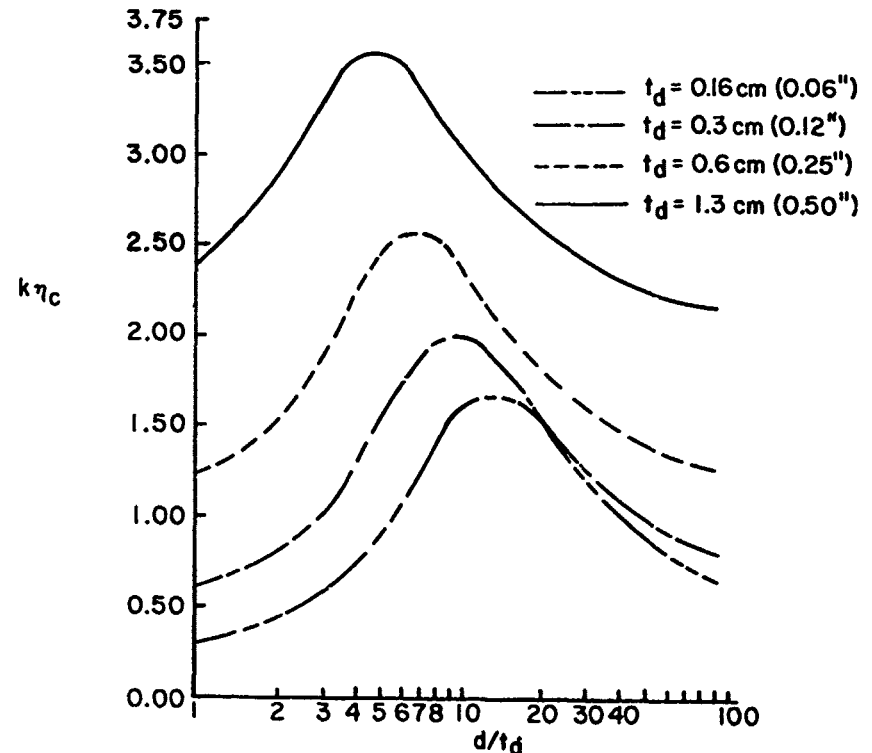

Figure 11 Harmonic displacement criteria with different damping layer thicknesses, tp=0.1cm (0.04").

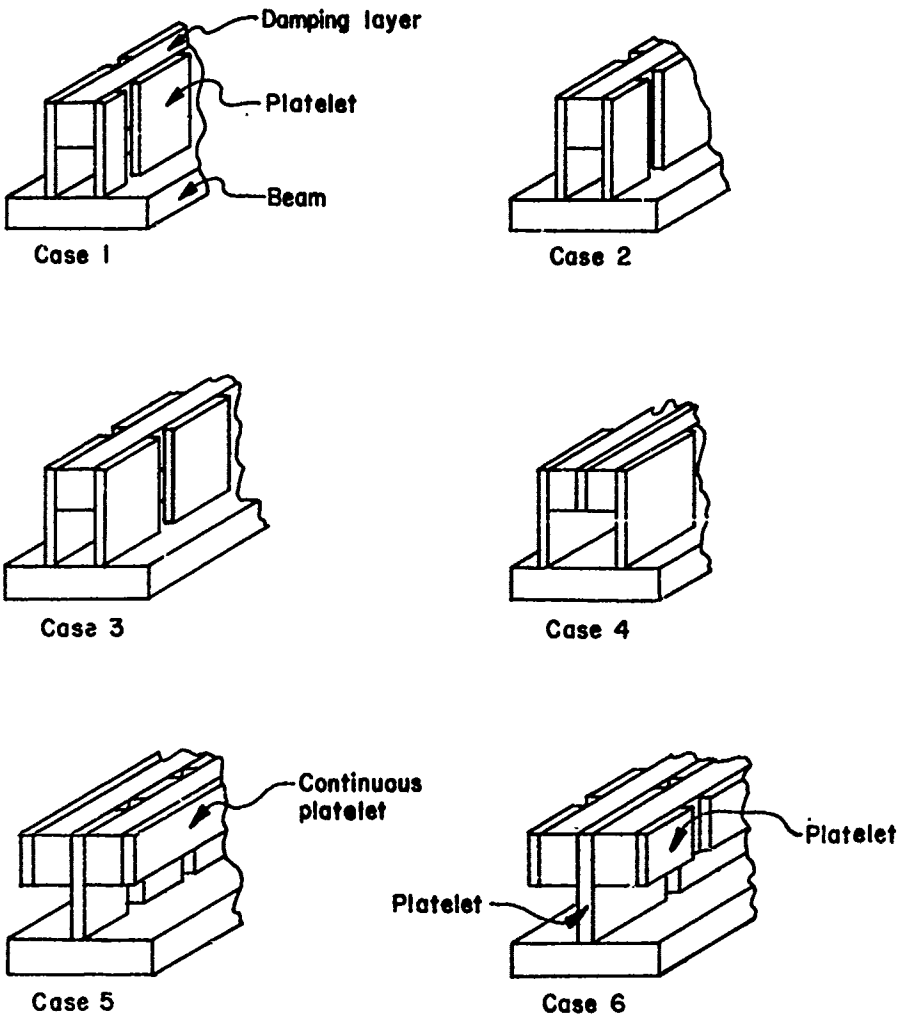

Figure 12 New structural damping experimental configurations.

3. Structural Damping Configuration 2: 1.3 cm (0.5") x 2.5 cm (1") x 0.04 cm (0.016") brass plates, overlapping configuration supporting a 0.6 cm (0.25") x 0.3 cm (0.125") layer of LD-400.

Resonance Frequency in Hz	Loss Factor η_c
481.7	0.341

4. Structural Damping Configuration 3: 1.3 cm (0.5") x 1.3 cm (0.5") x 0.04 cm (0.016") brass plates, not overlapping, supporting a 0.6 cm (0.25") x 0.3 cm (0.125") layer of LD-400.

Resonance Frequency in Hz	Loss Factor η_c
384.8	0.15

5. Structural Damping Configuration 4: Center brass strip 0.6 cm (0.25") x 0.04 cm (0.016") of continuous construction with layers of 0.6 cm (0.25") x 0.3 cm (0.125") LD-400 bonded to each side and with 1.3 cm (0.5") x 1.3 cm (0.5") x 0.04 cm (0.016") brass plates, not overlapping, supporting the sample.

Resonance Frequency in Hz	Loss Factor η_c
551.7	0.292

6. Structural Damping Configuration 5: See Figure 12.

Resonance Frequency in Hz	Loss Factor η_c
707.2	0.095

7. Structural Damping Configuration 6: See Figure 12.

Resonance Frequency in Hz	Loss Factor η_c
597.8	0.456

8. Unconstrained Damping Layer: 0.3 cm (0.125") thick LD-400 bonded directly to 0.3 cm (0.125") thick steel base strip.

Resonance Frequency in Hz	Loss Factor η_c
38.1	0.094
255.6	0.071
731.5	0.103
1460.6	0.095

Results for the unconstrained damping layer treatment are shown for comparison. It is interesting to note that, for the new structural damping configurations, the combination of increased damping and increased stiffness was so great that only one mode could be measured. All other resonances were so highly suppressed that no other measurements were possible.

The sample of configuration 2 was analyzed using the computer program. The composite loss factor obtained analytically is 0.326. Based on the experimentally obtained loss factor of 0.302, the error is about 8%. Thus, analytical and experimental results are in good agreement.

CONCLUSION

This paper has discussed the analysis and presented corroborating test results for a new structural damping configuration. The new configuration is capable of controlling the flexural vibrations of very rigid structures. It may also be used on light weight structures where a minimum of added weight is required. The new configuration has a great deal of design flexibility and may be used with both soft and rigid damping materials. Various configurations and patterns can be devised to control vibration and sound radiation for structures of two-dimensional extent.

In order that a damping treatment really represents the best loss factor and cost compromise, new structural damping design optimization is essential.

ACKNOWLEDGEMENTS

The assistance of Lord Kinematics, Lord Corporation in typing this paper and drawing figures is greatly appreciated.

Note:

The new structural damping designs presented in this paper, as well as others, are the subject of patents to Lord Corporation.

NOMENCLATURE

E_1 = Young's Modulus of the Platelet material

A_1 = effective cross-sectional are of the semi-platelet of thickness, $t_p/2$

t_p = platelet thickness

d = platelet width

E_2 = $E_2'+iE_2''$ = Complex Young's Modulus of the damping layer

A_2 = cross-sectional area of damping layer

η = E_2''/E_2' = loss factor of damping material

t_d = thickness of damping layer

n = number of damping layers

ν = Poisson's Ratio for damping material

k_d = steric factor for damping layer extensional stiffness

h_1 = height of the beam

h_2 = distance between the neutral axes of the basic beam and damping layer

h_3 = depth of damping layer

E = Young's Modulus of the beam material

I = moment of inertia of the beam about its neutral axis

A = cross-sectional area of the beam

k = stiffness ratio

η_c = composite loss factor

$k\eta_c$ = harmonic displacement criteria

LIST OF REFERENCES

1. Mead, D. J., "The Vertical Fish-scale Damping Configuration", Lord Kinematics Report, October, 1965.

2. Mead, D. J., "Criteria for Comparing the Effectiveness of Damping Treatments", Noise Control, Vol. 7, May/June, 1961, pp. 27-38.

3. Patel, B. M., "Vibration and Noise Reduction of Beams Using Structural Damping", Project Proposal No. P166, January, 1977.

4. Patel, B. M., Warnaka, G. E., "Damping Measurements on New Structural Damping Configuration", March 24, 1977.

5. Warnaka, G. E., Miller, H. T., and Zalas, J. M., "Structural Damping as a Technique for Industrial Noise Control", American Industrial Hygiene Association Journal, January, 1972.

6. Warnaka, G. E., Harris, A. J., and Campbell, B. W., "A Simplified Approach to Structural Damping Design", Shock and Vibration Bulletin, No. 35, Part 7, pp. 239-251, April, 1966.

7. Warnaka, G. E., U. S. Patent No. 3,262,521, Structural Damping, July 26, 1966.

DISCUSSION

Mr. Henderson, (Air Force Materials Lab.): Your study is a very interesting study and I am particularly interested in the design optimization aspects. I wonder if you have considered what variations in temperatures would do. For instance I noticed at least for some of your calculations you were using LD 400. Presumeably the complex modulus of the material were picked at a particular temperature. Have you done any studies to determine what variations in temperature would do to your design optimization.

Mr. Patel: No I have not done that study, but we want to look a little bit glorious; what we do is come out with a high estimate of loss factor at some temperature such as room temperature and around that we calculate all these loss factors. As I showed you in that equation there are a great many parameters involved. What we have tried to do right now is work with the geometry and material properties; we haven't touched the temperature and frequency so far.

VIBRATIONS OF A COMPRESSOR BLADE WITH SLIP AT THE ROOT

David I.G. Jones
Air Force Materials Laboratory
Wright-Patterson AFB, Ohio, USA

and

Agnieszka Muszyńska
Institute of Fundamental Technological Research
Polish Academy of Sciences
Warsaw, Poland

A simple analytical model is developed to represent the vibrational behavior of a jet engine compressor blade in its fundamental mode, allowing for slip at the root. The analysis is compared with experimental data and is shown to accurately modelize the important phenomena involved. Implications for design of compressor and turbine blades to optimize slip damping levels are briefly discussed.

1. INTRODUCTION

Vibration problems in fan, compressor and turbine blades of jet engines occur more frequently as the performance increases. This is especially true for the newer high thrust-to-weight-ratio engines, and will be especially severe for blades with variable geometry. Efforts to design around resonant vibration problems to the maximum extent possible are always necessary, but in the absence of a rational method for predicting the damping in the various modes of vibration, it will always be difficult to completely succeed. Hence, changes in design which are perfectly satisfactory in themselves for reducing stresses can be completely cancelled out by unpredictable reductions in modal damping caused by the very same changes. Furthermore, the random variation of modal damping from blade to blade in a single disc is so great (a factor of five or more), that even highly significant changes of stress resulting from design changes can be completely negated. This means that research into the sources of damping of blades, as well as into means of increasing that damping, is currently attracting considerable attention.

One damping mechanism is the sliding friction between mating surfaces on adjacent blades, or between the disc and the blades. The phenomena involved are highly non-linear, and most available analytical techniques are not easy to use. Significant prior work in this area has been accomplished already. Goodman and Klumpp[1] discuss slip between press-fitted beams. Hanson, Meyer and Manson[2] have shown experimentally how the modal damping in various types of blade vary with root geometry and centrifugal load or rotational speed. For most blade root geometries, the observed damping reaches negligible levels by the time the speed reaches normal operating conditions. Williams and Earles[3] have examined analytically and experimentally the effect of slip on the response of a simple cantilevered beam with integral "clappers". Some other relevant work is described in references 4 to 9.

In this paper, an effort is made to clarify some results of these prior investigations through the achievement of two main objectives, namely, (i) to develop a simple two-mass analytical model of a blade, based on modal concepts, allowing for slip at the blade-disc interface and (ii) to experimentally verify the analysis for a particular blade geometry.

2. VIBRATION TESTS OF BLADE

2.1 Test System

A twisted steel blade with a simple root geometry, as shown in Figure 1, was used in the tests. The blade was held in a heavy fixture having mating surfaces to match the contours of the blade root. The centrifugal load was represented by means of simple spring-loaded wires applied at the root in such a way as to minimize interference with the blade root motion during slip. This arrangement, shown in Figure 2, was not ideal insofar as it did not allow for the effect of centrifugal loads in untwisting the blade, but it did represent the root conditions far more adequately than, for instance, clamping the root by means of a bolt,

which would prevent slip and hence inhibit the very phenomenon being studied. The blade was excited by means of a magnetic transducer and the response was picked up by means of a small accelerometer as shown in Figure 3. In the tests to determine the mode shapes, a small shaker was used in conjunction with an impedance head to excite the blade and measure the exciting force. Mode shapes were obtained by moving the accelerometer to various points on the blade and measuring the transfer function (acceleration/force) at each point. For the mode shape measurements, as opposed to the measurements for slip, the blade root was clamped by means of a bolt so that slip did not occur. A Bruel and Kjaer Model 1014 Beat Frequency Oscillator was used to generate a harmonically varying voltage of magnitude 0 to 40 volts at any selected frequency from 20 to 2000 Hertz. As the frequency was varied, the current through the output terminals to the exciter was controlled by means of the "compressor", which is a feedback loop which measures the voltage across a fixed resistor in the output circuit and uses it to control the output current. The current output of the oscillator was fed directly to a magnetic transducer (Electro Model 3030-HIP). The impedance setting of the oscillator was set to best match the impedance of the transducer, thereby minimizing distortion of the output signal. The transducer consisted essentially of a magnetized iron rod with many coils of fine insulated wire surrounding it, through which the oscillating current flows as illustrated in Figure 4. This current produced an oscillating magnetic field which modulated the steady magnetic field of the rod, and hence produced an oscillating harmonic force on any iron object placed nearby. The magnitude of this force depended on the amplitude of the oscillating current and on the gap between the end of the magnetized rod and the object being excited. The waveform of the the input signal to the transducer was monitored on a dual-beam oscilloscope, and the frequency was measured by a digital frequency meter. The pickup system used a miniature accelerometer (Endevco Type 22) weighing about 0.2 grams. The acceleration amplitude of the blade at the point where the accelerometer was attached, with cyanoacrylate adhesive, was detected as a small voltage proportional to the acceleration across the crystal. The accelerometer, unlike the transducer, is an extremely high impedance device so that a special high input impedance amplifier had to be used to amplify the signal before it could be read off the voltmeter and monitored on the other channel of the dual beam oscilloscope. The purpose of the tests was to measure the response of the blade to an oscillating harmonic force applied at the tip leading edge in the fundamental mode of vibration. The force was applied by means of the magnetic transducer and the response acceleration was picked up by the miniature accelerometer.

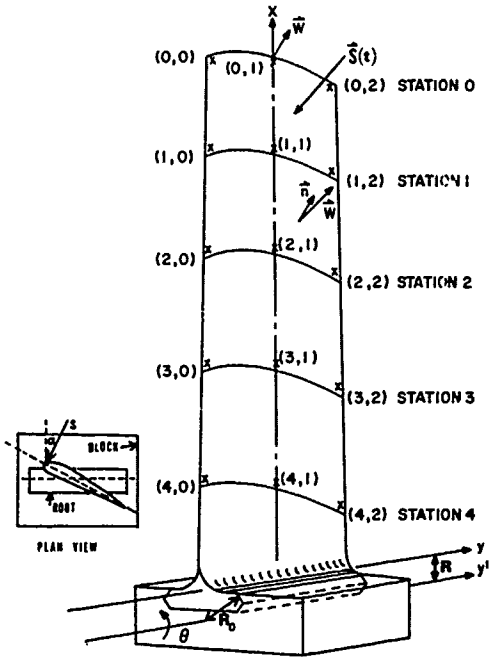

Figure 1 Blade Geometry

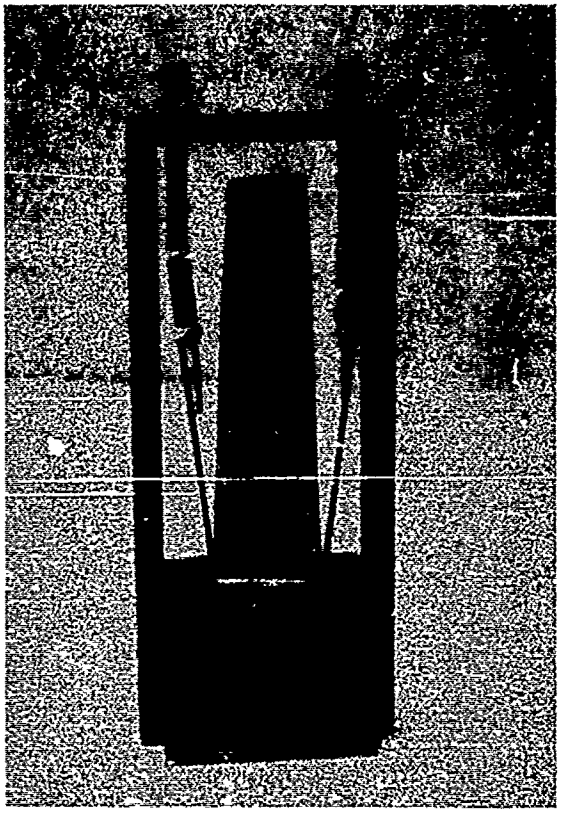

Figure 2 Photograph of Blade in Test Fixture

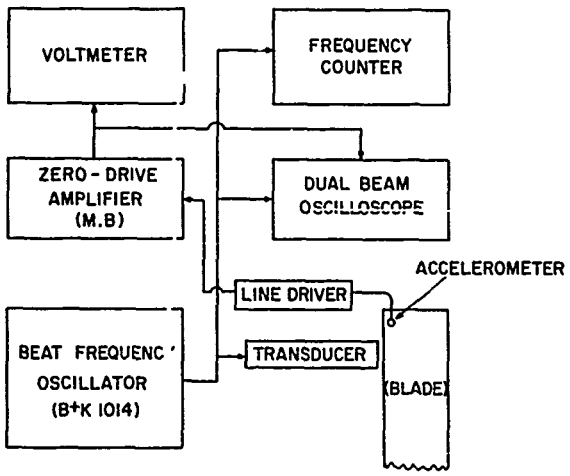

Figure 3 Test System

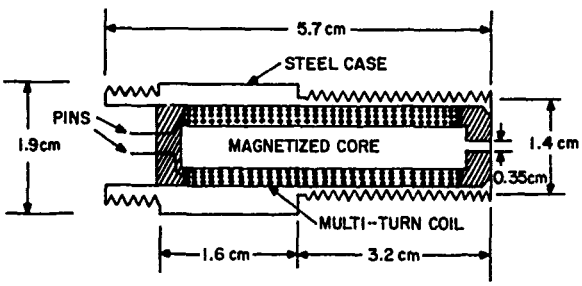

Figure 4 Typical Transducer Construction

2.2 Test Results

The tests with slip were conducted using the magnetic transducer for excitation, with a pre-selected gap, at several different force levels ranging from 0.0064 Newtons to 0.125 Newtons, the maximum that could be generated with the transducer available. The net normal force provided by the two springs to the wires at the root of the blade was varied from 10 Kg to 25 Kg. As the excitation frequency was increased slowly, at low force levels, the classical shape of the response curve (displacement versus frequency) was reproduced, but as the exciting force was increased the behavior became increasingly non-linear. The results obtained for tests with air and water as the working fluid around the blade root mating surface are shown in Figures 5 to 8, for the fundamental mode.

Several significant facts may be noted from these figures. One is that as S is decreased, a point is reached at which slip never occurs and the behavior is then linear. In that case, the only significant remaining source of damping is hysteresis of the blade-fixture system itself. The second is the fact that when water is substituted for air as the working fluid at the root by immersing the base in water, slip occurs far more readily. This is accounted for by the fact that the coefficient of friction is lower in these cases. "Inclined plane" sliding tests showed that the coefficient of friction between the blade root and the fixture is $\mu = 0.15$ for air and 0.10 for water between the sliding surfaces. The higher the value of μN (the maximum sliding force which can be sustained before slip of the blade root occurs) the higher the displacement needed to cause such slip, and hence the higher the values of S needed to produce such displacement. Hence it appears that $\mu N/S$ is an important parameter. Figures 9 and 10 show some of the acceleration waveforms observed on the oscilloscope screen for various conditions. The upper curves represent the blade acceleration, and the lower curves the force, all at the point of maximum amplitude. In air, one can see significant deviations from a true sinusoidal shape. In water, the lower threshold of slip seemed to allow high order harmonics to be present in the signal. The reason for this is not known.

Finally, for very low load levels, the residual damping is linear and apparently hysteretic in nature. For mode 1, $\eta_1 = 0.01$, and $\eta_2 = 0.006$ and $\eta_3 = 0.0015$ at 420 Hz and 920 Hz respectively. This variation of η_n with frequency is fairly consistent with published data for such damping.[10] Figure 11 shows a typical response spectrum, at low excitation levels, for the first several modes.

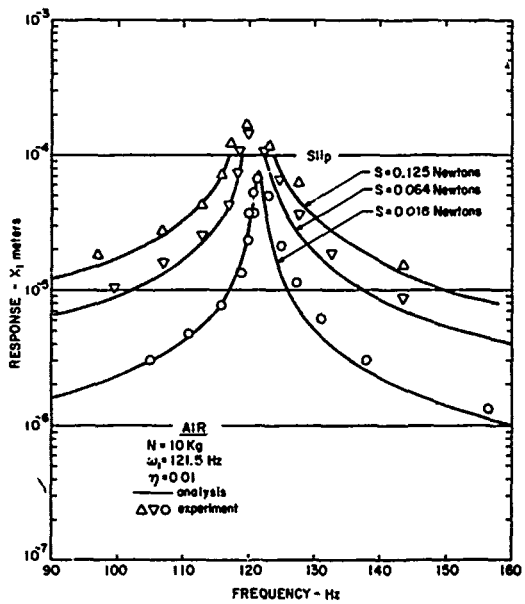

Figure 5 Response of Blade Tip (Air)

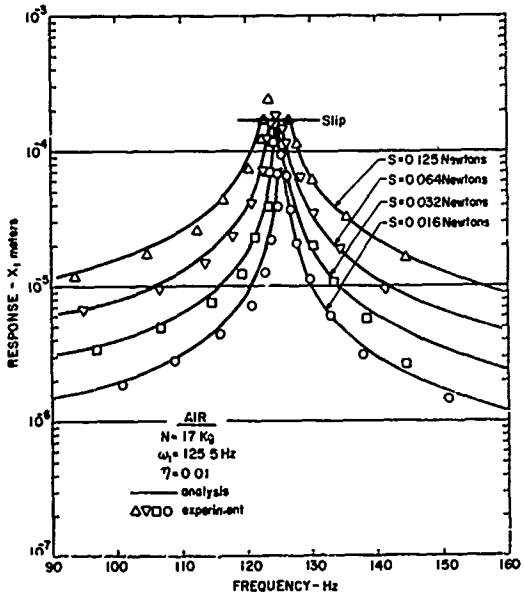

Figure 6 Response of Blade Tip (Air)

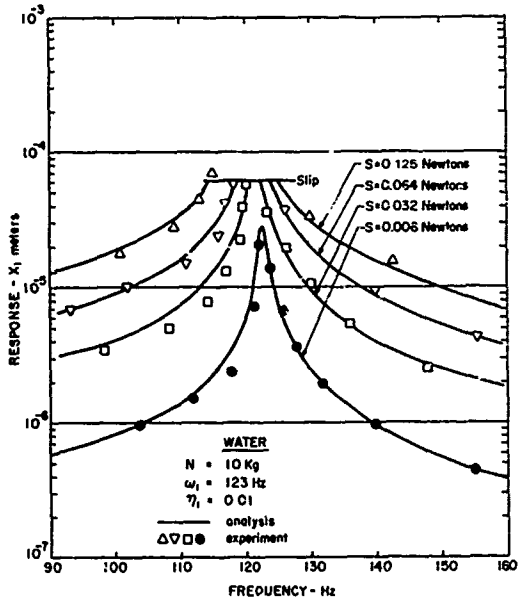

Figure 7 Response of Blade Tip (Water)

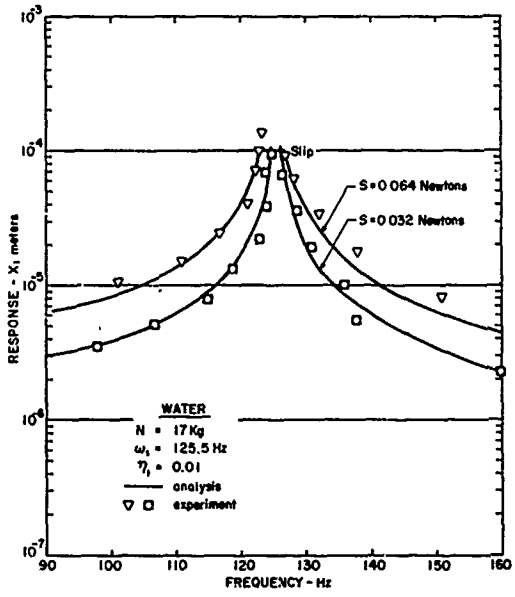

Figure 8 Response of Blade Tip (Water)

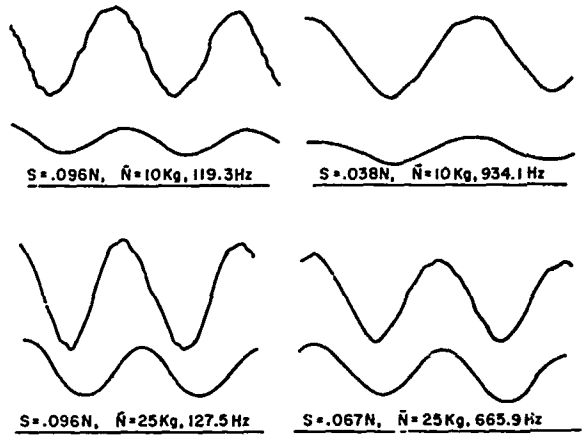

Figure 9 Waveforms (Air)

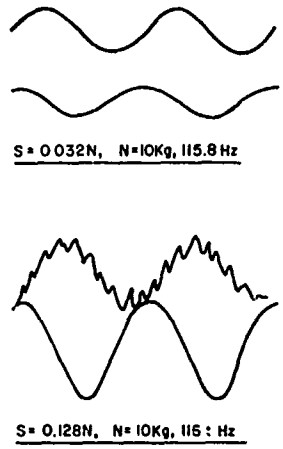

Figure 10 Waveforms (Water)

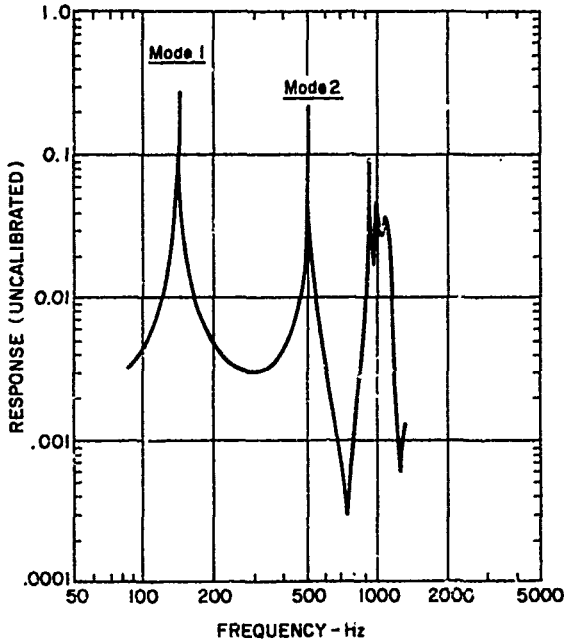

Figure 11 Typical Response Spectrum (No Slip)

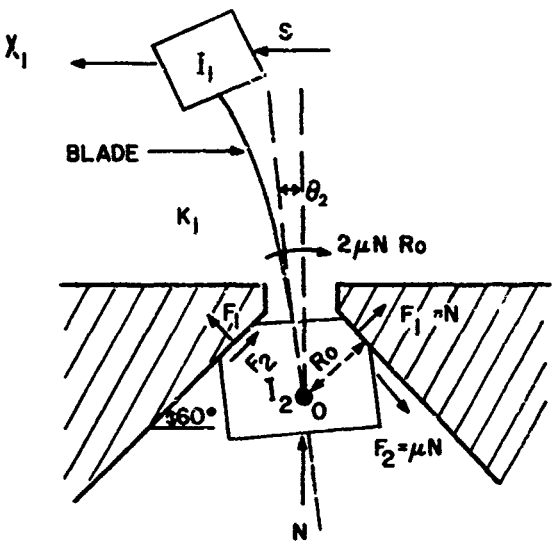

Figure 12 Two-Mass Model

3. ANALYSIS OF BLADE VIBRATIONS

3.1 Non-linear Equations of Motion With Slip

For the non-linear case where slip of the blade root takes place, the boundary condition seen by the vibrating blade changes from an essentially clamped-free condition to an essentially pinned-free condition. For the fundamental mode of the blade, the system can be represented with some degree of accuracy by the two mass model shown in Figure 12. The equations of motion of the system with slip are:

$$I_1\ddot{\theta}_1+K_1(1+i\eta_1)(\theta_1-\theta_2)=SLe^{i(\omega t-\gamma)}\cos\alpha \qquad (1)$$

$$I_2\ddot{\theta}_2+K_1(1+i\eta_1)(\theta_2-\theta_1)+(2\mu\bar{N}R_o)\,\mathrm{Sgn}\,\dot{\theta}_2=0 \qquad (2)$$

The term $2\mu\bar{N}R_o$ is the frictional moment opposing the motion. Figure 12 shows the geometrical factors involved in this derivation. α is the angle between the blade direction at the tip leading edge (where S is applied) and the root axis as illustrated in Figure 1 ($\cos\alpha = 0.724$). From vertical equilibrium in Figure 12:

$$2F_1 \sin 30^\circ = \bar{N} \text{ i.e. } F_1 = \bar{N}$$

$$F_2 = \mu F_1 = \mu\bar{N}$$

$$\text{Moment} = 2F_2R_o = 2\mu\bar{N}R_o \qquad (3)$$

Equation (1) and (2) can be rewritten in the form:

$$I_1(\ddot{\theta}_1/S)+K_1(1+i\eta_1)(\theta_1/S-\theta_2/S)=e^{i(\omega t-\gamma)}L\cos\alpha$$

$$I_2(\ddot{\theta}_2/S)+K_1(1+i\eta_1)(\theta_2/S-\theta_1/S)+(2\mu\bar{N}R_o/S).$$

$$\mathrm{Sgn}\,\dot{\theta}_2 = 0$$

This shows that the mobility θ_1/S depends on $\mu\bar{N}/S$, so that the analysis within its limits is valid for low or high values of S or of $\mu\bar{N}$; it is the ratio of these two quantities which is important.

3.2 Solution Without Slip

If $S/\mu\bar{N}$ is sufficiently small, slip cannot occur and the equations (1) and (2) reduce to:

$$I_1\ddot{\theta}_1+K_1(1+i\eta_1)(\theta_1) = Se^{i(\omega t-\gamma)}L\cos\alpha \qquad (4)$$

the solution of which is:

$$X_1=\theta_1 L=SL^2\cos\alpha\, e^{i(\omega t-\gamma)}/[-I_1\omega^2+K_1(1+i\eta_1)] \qquad (5)$$

The values of I_1, K_1 and η_1 needed to model the system are now determined by comparing the response X_1 with the measured response for low values of $S/\mu\bar{N}$ in Figures 5 to 8. The measured resonant frequency ω_1 gives one such relationship

$$I_1\omega_1^2 = K_1 \tag{6}$$

The measured response at resonance gives another:

$$\left|\frac{\ddot{X}_1}{S}\right| = \frac{\omega_1^2 L^2 \cos\alpha}{K_1\eta_1} = \frac{L^2\cos\alpha}{I_1\eta_1}$$

$$I_1 = L^2\cos\alpha/\eta_1|\ddot{X}_1|S \tag{7}$$

and the measured damping η_1 is given by:

$$\eta_1 = \frac{\Delta\omega_1}{\omega_1} \tag{8}$$

Where $\Delta\omega_1$ is the difference between the two frequencies at which the response is 3 db below the peak response (3.01 actually!). Table 1 gives the results of the calculations.

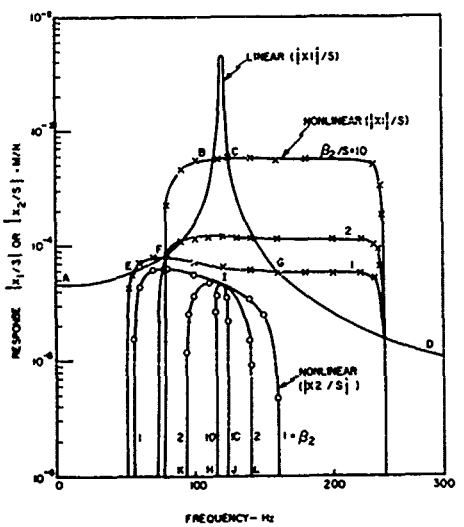

Figure 13 Analytical Solutions

Hence, the average values are:

$$I_1 = 1.04\times10^{-3}\ \text{Kg m}^2$$
$$K_1 = 635.1\ \text{Nm/radian}$$
$$\eta_1 = 0.010$$
$$\omega_1 = 124.2\ \text{Hz}$$

It will be noted that I_1, K_1 and η_1 have here been determined without measuring the mode shapes or any other properties of blade, but only from the response to point excitation at low levels. However, the values agree well with those determined from such measurements.[11] With these values of K_1, I_1 and η_1, the response X_1 without slip can be calculated for various values of S.

3.3 Solution with Slip

For simplicity, we let $\eta_1 = 0$ in equations (1) and (2); for the purposes of this part of the analysis it is sufficient. If we seek a steady state solution of these equations, then to the first order we assume that:

$$\theta_2 = \theta_2 \sin\omega t$$
$$\theta_1 = \theta_{11}\sin\omega t + \theta_{12}\cos\omega t \tag{9}$$
$$S = S_1\sin\omega t + S_2\cos\omega t$$

Furthermore, we consider only the first term in the expansion of Sgn $(\dot{\theta}_2)$.

{≡ Sgn (Cos ωt)} in ascending terms of Sin (nωt) and Cos (nωt), so that:

$$\text{Sgn}(\cos\omega t) = \frac{4}{\pi}\cos\omega t \tag{10}$$

Then, introducing these equations into (1) and (2), and comparing terms in Sin ωt and Cos ωt, we have the four algebraic equations for X_{11}, X_{12}, S_1 and S_2:

$$\begin{aligned}
(K_1 - I_1\omega^2)\theta_{11} - K_1\theta_2 &= S_1 L\cos\alpha \\
(K_1 - I_1\omega^2)\theta_{12} &= S_2 L\cos\alpha \\
(-I_2\omega^2 + K_1)\theta_2 - K_1\theta_{11} &= 0 \\
-K_1\theta_{12} &= 8\mu\bar{N}R_o/\pi
\end{aligned} \tag{11}$$

The solution of this equation is readily obtained. From the values of θ_{11}, θ_{12}, S_1, S_2 so determined, we then can write the solution for θ_1 and S in this form:

$$\theta_1 = \frac{-S_1(K_1 - I_2\omega^2)L\cos\alpha\sin\omega t}{\omega^2\{(I_1+I_2)K_1 - I_1I_2\omega^2\}} - \left(\frac{8\mu\bar{N}R_o}{\pi K_1}\right)\cos\omega t \tag{12}$$

$$SL\cos\alpha = S_1 L\cos\alpha\sin\omega t - (K_1 - I_1\omega^2)(8\mu\bar{N}R_o/\pi K_1)\cos\omega t \tag{13}$$

Clearly, we can eliminate S_1 in these two equations. This is most simply done for our present purposes by first calculating $|\theta_1|$ and $|S|$, since these are the quantities we would ordinarily measure. Then:

$$|\theta_1|^2 = \frac{S_1^2(K_1 - I_2\omega^2)^2 L^2\cos^2\alpha}{\omega^4\{(I_1+I_2)K_1 - I_1I_2\omega^2\}^2} + \left(\frac{8\mu\bar{N}R_o}{\pi K_1}\right)^2 \tag{14}$$

$$L^2\cos^2\alpha|S|^2 = S_1^2L^2\cos^2\alpha + (K_1 - I_1\omega^2)^2(8\mu\bar{N}R_o/\pi K_1)^2 \tag{15}$$

Eliminating S_1 and simplifying gives:

$$\left|\frac{X_1}{S}\right|^2 = \frac{L^4\cos^2\alpha[1-\beta^2(1-I_1\omega^2/K_1)^2]\left[1-\frac{I_2}{I_1}\left(\frac{I_1\omega^2}{K_1}\right)\right]^2}{K_1^2(I_1\omega^2/K_1)^2[(1+I_2/I_1)-(I_2/I_1)(I_1\omega^2/K_1)^2]^2}$$

$$+\frac{\beta^2}{K_1^2} \qquad (16)$$

$$\left|\frac{X_2}{S}\right|^2 = \frac{L^2\cos^2\alpha[1-\beta^2(1-I_1\omega^2/K_1)^2]}{K_1^2(I_1\omega^2/K_1)^2[1+I_2/I_1-(I_2/I_1)(I_1\omega^2/K_1)^2]^2} \qquad (17)$$

where

$$\beta = 8\mu\bar{N}R_o/\pi SL\ \text{Cos}\ \alpha = (4/\pi)\beta_2 \qquad (18)$$

If $\beta = 0$, as for a freely pinned blade or for S very large, then $|X_1|$ has an infinite amplitude at the frequency where:

$$\left(\frac{I_1\omega^2}{K_1}\right)^2 = (1+\frac{I_2}{I_1})\frac{I_1}{I_2} = \frac{I_1}{I_2}+1 \qquad (19)$$

This allows us to estimate I_2, since the pinned-free mode of the particular blade used was determined (in tests not described here) to be 260 Hz.

$$\therefore\ \frac{I_1}{I_2}+1 = \frac{(260)^2}{(124.2)^2} = 4.38$$

$$I_2 = 3.08\text{x}10^{-4}\ \text{Kg m}^2$$

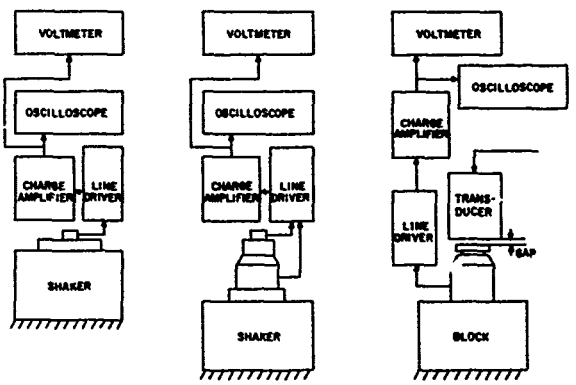

Figure 14 System for Calibrating Transducer

Figure 13 shows some analytical solutions for several values of $\beta_2 = 2\mu\bar{N}R_o/SL\ \text{Cos}\ \alpha$. It is seen that the range over which X_2/S exists is exactly equal to that over which the nonlinear solution for $|X_1/S|$ intersects the linear solution for $|X_1/S|$. This means that no ambiguity exists as to which solution is appropriate at any frequency and exciting force.

4. DISCUSSION AND CONCLUSIONS

The comparison between analysis and experiment in Figures 5 through 8 shows that it is possible to model the observed behavior of a blade, in terms of a simple two degree of freedom system with slip at one of the masses beyond a certain threshold level. In fact, in every case, the response curves follow the linear model until slip occurs whenever the response amplitude rises sufficiently, as resonance is approached, at which point a jump to a different solution (with slip $-X_2$ real) takes place if S is sufficiently large for such a solution to exist ($S\ \text{Cos}\ \alpha >> 8\mu\bar{N}R_o/\pi L$). Therefore, $S\ \text{Cos}\ \alpha \leq 8\mu\bar{N}R_o/\pi L$ is a necessary condition if drastic changes of blade motion are not to occur.

The modeling of the linear part of the response demands some variation of the assumed resonant frequency ω_1, as Figures 5 to 8 show. This variation is generally quite small, and apparently varies systematically with the value of $\bar{N}$, increasing as $\bar{N}$ increases. This is as one might expect. Perhaps the main value of this investigation lies in the fact that the analysis can be applied with only little further development to much more complex blade root configurations designed to provide for slip even at high rotational speeds. Some such investigations are in hand.[12, 13]

REFERENCES

1. L.E. Goodman and J.H. Klumpp, "Analysis of Slip Damping with Reference to Turbine-Blade Vibration", J. Appl. Mechanics, pp. 421-629, 1956.

2. M.P. Hanson, A.J. Meyer, S.S. Manson, "A Method of Evaluating Loose-Blade Mounting as a Means of Suppressing Turbine and Compressor Blade Vibration", Proc. S.E.S.A., Vol. 10, No. 2, p. 103, 1958.

3. E.J. Williams and S.W.E. Earles, "Optimization of the Response of Frictionally Damped Beam Type Structures with Reference to Gas Turbine Compressor Blading", J. Eng. for Industry, Trans. A.S.M.E., Paper No. 73-DET-108, 1973.

4. S.S. Manson, "Stress Investigation in Gas Turbine Discs and Blades", SAE Quarterly Trans., Vol. 3, No. 2, p. 229, 1969.

5. D.S. Whitehead, "Effect of Mistuning on the Vibration of Turbomachine Blades Induced by Wakes", J.Mech.Eng.Sci.,V.8, No. 1, 1966.

TABLE 1 - MODAL PARAMETERS

FLUID AT ROOT	$\bar{N}$ (Kg)	S (N)	$\ddot{X}_1$ (g's)	ω_1 (Hz)	η_1	I_1 (Kgm^2)	K_1 Nm/rad
AIR	17	0.016	5.96	125.8	6.36×10^{-3}	1.25×10^{-3}	778.5
	25	0.016	5.01	128.7	9.32×10^{-3}	1.01×10^{-3}	661.5
WATER	10	0.0064	1.216	122.5	1.39×10^{-2}	1.12×10^{-3}	662.2
	17	0.0064	2.114	126.6	1.11×10^{-2}	0.805×10^{-3}	509.5

6. R.C.F. Dye and T.A. Henry, "Vibration Amplitudes of Compressor Blades Resulting from Scatter in Blade Natural Frequencies", J. Eng. for Power, July 1969.

7. V.P. Ivanov, "Nekotorie voprosy kolebanyi lopatochnikh ventozov i drugikh uprugikh tel obladajushchikh ciklicheckoi simetriei (Vibration Problems of Blade Discs and Other Elastic Bodies Having Cyclic Symmetry)", Sbornik Statei No. 6, Moskva 1971.

8. V.O. Bauer, "Vlianie rastroiki chastot lopatok na resonansnyie kolebania (Influence of Mistuning of Blade Frequency on Resonant Vibrations)", Cbornik Statici, 6, Moskva, 1971.

9. P.O. Shimov, "Issledovanie vliania dinamicheskoi nieodnorodnosti koltzevoi reshotki na resonansnyie kolebania ieio profilei (Analysis of the Influence of Dynamic Inhomogeneity of the Ring Net on Resonant Vibration of its Profile)", Sbornik Statici, 6, 1971.

10. A.L. Eshleman, Jr., and J.D. Van Dyke, Jr., "A Rational Method of Analysis by Matrix Methods of Acoustically Loaded Structure for Prediction of Sonic Fatigue Strength", in Acoustical Fatigue in Aerospace Structures, p. 723, eds. W.J. Trapp and D.M. Forney, Jr., Syracuse University Press, New York, 1965.

11. D.I.G. Jones and A. Muszyńska, "Effect of Slip on Response of a Vibrating Compressor Blade", presented at ASME Gas Turbine Conference, Atlanta, GA, Nov. 1977 (ASME Paper No. 77-WA/GT-3).

12. D.I.G. Jones and A. Muszyńska, "Harmonic Response of a Damped Two-degree of Freedom System with Gaps", Nonlinear vibration problems - ZAGADNIENIA DRGAN NIELINIOWYCH, V 19, 1978, WARSZAWA.

13. A. Muszyńska and D.I.G. Jones, unpublished notes.

NOTATION

exp	exponential function
f	frequency (Hz)
F_1	normal force at root (see Fig. 12)
F_2	frictional force at root (see Fig. 12)
h	gap between transducer and blade
i	$\sqrt{-1}$
I_1, I_2	moments of inertia
K_1	modal stiffness in first mode
L	length of blade
M	moment
M_o	mass at moving element of impedance head
n	mode number
$\bar{N}$	static load on blade ("centrifugal")
R, R_o	root dimensions (see Fig. 1)
S(t)	applied force vector as function of time
S	amplitude of S in space variables
S_1, S_2	force amplitudes
t	time
V_s	voltage from impedance head
V	oscillator voltage
x, y	coordinates in plane of blade (Fig. 1)
x_1, y_1	point of application of S (t)
X_1	displacement of mass 1. ($=\theta_1 L$)
X_2	($\theta_2 L$)
$\ddot{X}$	acceleration
α	twist of blade at station x
β	$8\mu\bar{N}R_o/\pi SL\cos\alpha$
β_2	$2\mu\bar{N}R_o/LS\cos\alpha$
γ	phase angle
ΔM	added mass on impedance head
η	loss factor
η_n	modal loss factor in n^{th} mode
θ_1	X_1/L
θ_2	rotation of blade root during slipping (Fig. 12)
μ	mass per unit area of blade (also coefficient of friction)
ω	frequency (radians/sec)
ω_n	n^{th} natural frequency (rad/sec)

APPENDIX - CALIBRATION OF TEST SYSTEM

Calibration of the Accelerometer

The accelerometer-Zero Drive-Charge Amplifier-Voltmeter measurement chain was calibrated by introducing a known harmonic acceleration at the accelerometer and observing the root mean square voltage registered at the voltmeter. The acceleration was generated by a small electro-

dynamic shaker, having a steel ball embedded in a hollow cavity in the shaker table, as illustrated in Figure 14 (step 1). At an acceleration of just 1 g at the table, the steel ball separated from the floor of the cavity and impacts occurred, easily noted as "hash" on the otherwise smooth sinusoidal trace on the oscilloscope screen. For the Endevco 22 accelerometer-Zero Drive-Amplifier-voltmeter system, this calibration was:

$$1 \text{ g} \equiv 1.91 \text{ volts}$$

For the Endevco Type 2226 accelerometer used in the calibration of the transducer, the appropriate calibration was:

$$7 \text{ g} \equiv 7.60 \text{ volts}$$

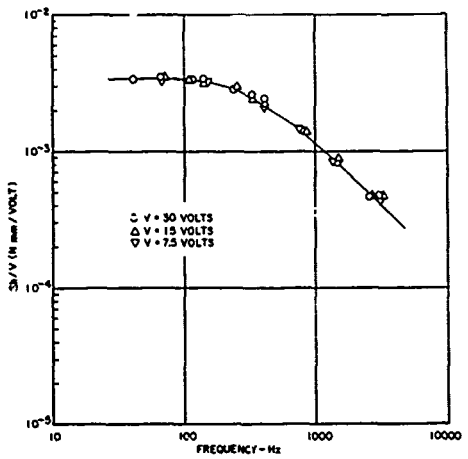

Figure 15 Transducer Calibration

Calibration of the Transducer

In order to calibrate the transducer, it was necessary to measure the force generated on a block of iron placed a distance h (the gap) from the active end of the transducer and having a certain oscillating voltage V at the output terminals, corresponding to a definite current in the circuit. A three-step process was necessary, since the force could not be measured directly. Figure 14 shows the three steps in this sequence. The first step was to calibrate the accelerometer, as discussed already.

The second step was to calibrate the impedance head, so that it in turn could be used to measure force. This was accomplished by applying a known acceleration, using the results of step 1, to a shaker table supporting the impedance head. The force experienced by the crystal of the impedance head is equal to $(M_o+\Delta M)\ddot{X}$, the d'Alembert force corresponding to the acceleration $\ddot{X}$ acting on the mass $M+\Delta M$ above the crystal. M_o is the built-in mass of the impedance head itself and ΔM is the added mass of the soft iron piece. Since M_o may not be known, one can vary the mass ΔM and measure the output voltage V_S of the force gage, registered at the voltmeter, for each case. With $\ddot{X}$ known from the corresponding accelerometer reading, one could then plot $V_S/\ddot{X}$ versus ΔM for the particular force gage used (Wilcoxon Z 602). The intersection of the line defined by the measured points with the negative ΔM axis corresponded to the mass M_o of the impedance head above the crystal. With M_o then known, any reading of $(M_o+\Delta M)\ddot{X}$ gives the force corresponding to the acceleration $\ddot{X}$ and the voltage output V_S from the force gage, via the charge amplifier, the zero drive and the cables. It was found that $M_o = 30$ grams. For $V_S = 13.5$ volts; for example, $\ddot{X}$ was observed to be 0.168 g's.

$$13.5 \text{ volts} \equiv \frac{(11.5+30)}{1000} \times 0.168 \times 9.81 \text{ Newtons}$$

$$\text{or } 1 \text{ volt} = 5.08 \times 10^{-3} \text{ Newtons}$$

This result was dimensioned properly by converting M_o and ΔM to kilograms and the acceleration (0.168 g's) to metres per second. The third step was to calibrate the transducer itself, using the force gage. The force gage was now placed on a rigid block and the transducer brought close to the iron block, with separation h as shown in Figure 14 (step 3). The voltage V, corresponding to a particular level of the oscillating current in the transducer coils, was set at a particular value, such as 30 volts. The gap was set at 0.043 inches (1.092 mm), by means of a feeler gage or a metal sheet of this thickness. The force gage was then connected, again through the same zero drive, charge amplifier and cables, to the voltmeter. From the force gage calibration, the force was calculated directly from the observed voltage. The same gap was used in all tests, so that gap variations were not important. The variation of Sh/V versus frequency is shown in Figure 15. One can therefore determine S for any given frequency, voltage and gap.

Calibration of Springs

The effective centrifugal load on the blade root was provided by two springs. This force was determined by measuring the change in length of the springs, and this in turn was calibrated very simply by applying known static loads to each spring and measuring the corresponding length.

ACKNOWLEDGEMENTS

This work was initiated while the authors were stationed at Institut National des Sciences Appliquées, Lyon, France, 1975-6. Thanks are due to Barbara McDermott, Jan Halldorson, and Sally Gardner for preparation of the typed document. Thanks are due to the reviewer for his useful comments.

RESPONSE OF A HELICAL SPRING CONSIDERING HYSTERETIC AND VISCOUS DAMPING

P. F. Mlakar and R. E. Walker
U. S. Army Engineer Waterways Experiment Station
Vicksburg, Mississippi

An analytical model of a helical spring is developed which includes distributed mass, viscous damping, and hysteretic damping. The limiting effects of both types of damping on the resonant response are discussed. The model is seen to compare reasonably with existing experimental data.

INTRODUCTION

Helical springs are widely used to isolate or control the motions of various mechanical systems. The shock-isolation mountings for sensitive electronic equipment, the recoil mechanisms of gun mounts, and the valve springs of internal combustion engines represent diverse examples of this usage. These systems are often designed under the simplifying assumption that the mass and the damping characteristics of the helical spring can be either neglected or combined with the characteristics of other elements in the system. However, the distributed mass of a helical spring has been studied and shown to cause the system to have natural frequencies which are not predicted under the massless spring assumption [1,2]. For a harmonic excitation whose frequency is near or equal to these natural frequencies, it is then expected that the damping present in the system will be the delimiting factor governing its response. The effect of both viscous and hysteretic damping on this response will be considered herein.

ANALYTICAL MODEL

Consider the helical spring system shown schematically in Figure 1. The spring is connected to a rigid mass, M, which might represent a fixture through which a force is applied to the spring or a component which is to be isolated by the spring. A viscous damper, C, acts in parallel with the spring and could model the energy dissipation of a specific mechanical damping device or the effects of other dissipative mechanisms within the system. A harmonic force $F_2e^{j\omega t}$ is applied to the rigid mass and the steady-state displacement of this mass is denoted by $Y_2e^{j\omega t}$. The force and displacement at the base of the spring and damper are $F_1e^{j\omega t}$ and $Y_1e^{j\omega t}$, respectively.

The equations of motion for this system imply:

$$F_1 + F_C + F_{K1} = 0 \tag{1}$$

$$F_2 - F_C - F_{K2} = -\omega^2 M Y_2 \tag{2}$$

in which the force in the viscous damper is

$$F_C = Cj\omega\,(Y_2 - Y_1) \tag{3}$$

and the forces at each end of the helical spring are F_{K1} and F_{K2}.

These end forces are shown on the helical spring in Figure 2. An analysis of this spring neglecting internal damping presented in Reference [2] indicates that the steady-state displacement, $Y(x)$, of the spring at position, x, must satisfy the differential equation of motion:

$$KL^2 \frac{d^2Y}{dx^2} + m\omega^2 Y = 0 \tag{4}$$

subject to the end conditions:

$$F_{K1} = KL \left.\frac{dY}{dx}\right| x = 0 \tag{5}$$

$$F_{K2} = KL \left.\frac{dY}{dx}\right| x = L \tag{6}$$

In these equations, m is the total mass of the spring which is assumed to be uniformly distributed throughout its free length L. The static stiffness of the helical spring is denoted by K, and this quantity is known to be proportional to the shear modulus of the spring material [1]. Now, the effect of damping within an elastic material can be examined by replacing the elastic moduli with complex quantities whose imaginary parts are measures of the energy dissipated [3]. It is thus

reasonable to account for internal damping within the helical spring by replacing its static stiffness in Equations 4 through 6 with the quantity $K(1 + j\eta)$ in which η is the shear modulus loss factor of the spring material. Since the actual damping mechanisms of spring metals are approximated by hysteretic models [4], η is assumed herein to be a constant which is independent of frequency.

From the solution of Equations 4 through 6 when modified as described above, it can be shown that the forces and displacements at the ends of a helical spring having hysteretic damping are related according to:

$$F_{K1}\, q(\Omega)$$

$$= K(1 + j\eta)(v\Omega + ju\Omega)(Y_2 - Y_1\, r(\Omega)) \qquad (7)$$

$$F_{K2}\, q(\Omega)$$

$$= K(1 + j\eta)(v\Omega + ju\Omega)(Y_2\, r(\Omega) - Y_1) \qquad (8)$$

in which the dimensionless frequency is defined by

$$\Omega \equiv \omega\sqrt{\frac{M}{K}} \qquad (9)$$

the mass ratio is given by

$$\mu \equiv \frac{M}{m} \qquad (10)$$

and

$$u \equiv \sqrt{\frac{\sqrt{1+\eta^2}+1}{2\mu\,(1+\eta^2)}} \qquad (11)$$

$$v \equiv \sqrt{\frac{\sqrt{1+\eta^2}-1}{2\mu\,(1+\eta^2)}} \qquad (12)$$

$$q(\Omega) \equiv \sinh v\Omega \cos u\Omega$$

$$+ j \cosh v\Omega \sin u\Omega \qquad (13)$$

$$r(\Omega) \equiv \cosh v\Omega \cos u\Omega$$

$$+ j \sinh v\Omega \sin u\Omega \qquad (14)$$

Substitution of Equations 3, 7, and 8 into the Equations of motion 1 and 2, leads to the transmission factor:

$$\tau(\Omega) = \frac{Y_2}{Y_1} \text{ for } F_2 = 0$$

$$= -\frac{F_1}{F_2} \text{ for } Y_1 = 0$$

$$= \frac{(1 + j\eta)(v + ju) + 2\beta j\, q(\Omega)}{(1 + j\eta)(v + ju)\, r(\Omega) - (\Omega + 2\beta j)\, q(\Omega)} \qquad (15)$$

wherein the viscous damping ratio is

$$\beta \equiv \frac{C}{2\sqrt{KM}} \qquad (16)$$

The magnitude and phase of this complex factor describe the transfer of motion and force in the helical spring system of Figure 1.

DISCUSSION

The effects of distributed mass and damping on the response of a helical spring can be seen through an examination of the transmission function obtained in Equation 15. First, consider a spring with no hysteretic or viscous damping for which $\eta = 0$ and $\beta = 0$. In this case, the transmission factor of Equation 15 reduces to

$$\tau(\Omega) = \frac{1}{\cos\frac{\Omega}{\sqrt{\mu}} - \sqrt{\mu}\,\Omega\,\sin\frac{\Omega}{\sqrt{\mu}}} \qquad (17)$$

Note from this equation that an undamped spring has an infinite transmission or resonance at the frequencies which satisfy

$$\cot\frac{\Omega}{\sqrt{\mu}} = \sqrt{\mu}\,\Omega \qquad (18)$$

in agreement with Reference [2]. The roots of this transcendental equation occur at the intersections of the cotangent and linear curves sketched in Figure 3. The root defined by the first intersection of these curves is the fundamental frequency of the rigid mass on the helical spring, and the other intersections are the surge frequencies of this system. It is clear in this figure that the higher dimensionless surge frequencies approach integral multiples of $\sqrt{\mu}\,\pi$. Observe also that, as the distributed mass of the helical spring increases, the fundamental and surge frequencies decrease. This decrease is illustrated in Figure 4 which is a plot of the amplitude of the transmission given in Equation 17 as a function of frequency for mass ratios of $\mu = 1$, 10, and 100. This figure also shows the transmission factor for a massless spring

$$\tau(\Omega) = \frac{1}{1 - \Omega^2} \qquad (19)$$

which can be found in Reference 3. The distributed mass is seen to be an important parameter in the response of helical spring systems.

Now, let the helical spring have viscous damping but no hysteretic damping. In this situation, Equation 15 becomes

$$\tau(\Omega) = \frac{\frac{1}{\sqrt{\mu}} + 2\beta j \sin\frac{\Omega}{\sqrt{\mu}}}{\frac{1}{\sqrt{\mu}}\cos\frac{\Omega}{\sqrt{\mu}} - (\Omega + 2\beta j)\sin\frac{\Omega}{\sqrt{\mu}}} \qquad (20)$$

which corresponds to the transmission function stated in Reference 2. To study the effect of viscous damping further, the amplitude of this factor is plotted for a mass ratio of $\mu = 10$ and for viscous damping ratios of $\beta = .01$, .10, and .25 in Figure 5. The resonant frequencies for which the transmission amplitude is a local maximum were found by a golden section search [5], and these frequencies are tabulated in this figure. Notice that the values of the resonant frequencies are only slightly affected by the amount of viscous damping considered. However, the viscous damping ratio does determine the amplitude of the resonant response, and this can be examined by evaluating the transmission factor of Equation 20 at the undamped natural frequencies given by Equation 18. The result is:

$$\tau(\Omega) = \frac{j\Omega}{2\beta \cos \frac{\Omega}{\sqrt{\mu}}} - 1 \qquad (21)$$

Now from Figure 3 for $\mu >> 1$

$$\left|\cos \frac{\Omega}{\sqrt{\mu}}\right| \doteq 1 \qquad (22)$$

so for $\left(\frac{\Omega}{2\beta}\right) >> 1$,

$$\left|\tau(\Omega)\right| \doteq \frac{\Omega}{2\beta} \qquad (23)$$

Thus, for large mass ratios and for small viscous damping ratios, the resonant transmission amplitude is approximately inversely proportional to the viscous damping ratio and directly proportional to the resonant frequency. Equation 23 is plotted in Figure 5 to indicate the accuracy of this approximation. Physically, the direct variation of transmission amplitude with frequency is due to the linear dependence on velocity of the force transmitted by the viscous damping mechanism.

On the other hand, the transmission factor of Equation 15 for a helical spring having hysteretic damping but no viscous damping is:

$$\tau(\Omega) = \frac{(1 + j\eta)(v + ju)}{(1 + j\eta)(v + ju)\, r(\Omega) - \Omega\, q(\Omega)} \qquad (24)$$

Figure 6 is a graph of the amplitude of this function for a mass ratio of $\mu = 10$ and for hysteretic loss factors of $\eta = .001$, .010, and .100 which encompass the loss factors typical of helical spring metals [4]. As in the case of viscous damping, the values of the resonant frequencies are seen to be only slightly affected by the amount of hysteretic damping considered. Hence, the effect of the hysteretic loss factor on the resonant transmission amplitude can be studied by substituting the undamped natural frequencies of Equation 18 into Equation 24. If Equation 22 is employed and the terms containing η^2 are neglected, then

$$\left|\tau(\Omega)\right| \doteq \frac{2}{\eta\,(1 + \Omega^2)} \qquad (25)$$

The accuracy of this result can be seen in Figure 6. Notice that the transmission amplitude at the fundamental frequency ($\Omega \doteq 1$) is approximately the inverse of the hysteretic loss factor. The transmission amplitudes at the surge frequencies are approximately inversely proportional to the hysteretic loss factor and to the square of the surge frequency. This indirect variation with the square of frequency is a contrast to the viscous damping model in Figure 5. It is interesting to note that in [6], the resonant transmission amplitudes for a beam having hysteretic damping are also inversely proportional to the square of natural frequency.

Finally, the combined effects of hysteretic and viscous damping are illustrated in Figure 7. In this figure, the transmission function of Equation 15 is plotted for $\mu = 10$ and for damping ratios of $\beta = .01$, .10, and $\eta = .001$, .010 . For these amounts of damping, the values of the resonant frequencies are observed to change insignificantly from the undamped values. Substituting the undamped natural frequencies of Equation 18 into Equation 15, using Equation 22, and neglecting the terms containing η^2 or $\eta.\beta$ leads to

$$\left|\tau(\Omega)\right| \doteq \frac{1}{\frac{\eta}{2}(1 + \Omega^2) + \frac{2\beta}{\Omega}} \qquad (26)$$

The validity of this approximation for the resonant transmission amplitude can be noted in Figure 7. Equation 26 implies that for $\mu >> 1$ $\beta << 1$ and $\eta << 1$, the fundamental transmission factor is influenced by both viscous and hysteretic damping. However, at the higher surge frequencies the importance of viscous damping is diminished and the response is dictated by the amount of hysteretic damping present. It is also worth observing from Equations 23, 25, and 26 that

$$\underset{\text{(Equation 26)}}{\frac{1}{\left|\tau_{\beta\&\eta}\right|}} = \underset{\text{(Equation 23)}}{\frac{1}{\left|\tau_{\beta}\right|}} + \underset{\text{(Equation 25)}}{\frac{1}{\left|\tau_{\eta}\right|}} \qquad (27)$$

or

$$\eta s_{\beta\&\eta} = \eta s_{\beta} + \eta s_{\eta} \qquad (28)$$

in which the reciprocal of the resonant transmission amplitude

$$\eta s \equiv \frac{1}{\left|\tau(\Omega \text{ resonant})\right|} \qquad (29)$$

is defined as the system loss factor. Thus, for a system having a large mass ratio, μ , and small amounts of damping, the loss factor for combined viscous and hysteretic damping is the sum of the system loss factors for each type of damping alone.

EXPERIMENTAL COMPARISON

Two previously published experimental results can be interpreted in light of the analytical model discussed in the preceding section. In [7], a laboratory experiment is described from which the transmission functions of four small helical springs were determined. One end of each specimen was fixed and the other end was driven by an electro-magnetic forcing device. The forces at both ends of the spring were measured with strain-gage load cells. One transmission function which was determined from these measurements is shown in Figure 8. For this particular specimen, it was reported that:

$$m = 93.4 \text{ gm } (.000533 \frac{\text{lb sec}^2}{\text{in.}})$$

$$\mu = .0794$$

$$K = 7.62 \times 10^3 \text{ N/m } (43.5 \text{ lb/in.})$$

The description of the experiment did not contain sufficient information to assign values independently for the viscous or hysteretic damping ratios in the system. However, the plot of Equation 15 in Figure 8 for $\mu = .0794$, $\beta = .05$, and $\eta = .02$ shows reasonable agreement with the experimental transmission function. These ratios do correspond to physically plausible amounts of viscous and hysteretic damping for the experiment.

Another comparison of the analytical model with experimental results is provided by the field evaluation of a large shock-isolated control platform [8]. This platform had a total mass of

$$M = 8.97 \times 10^4 \text{ kg } (512 \text{ lb sec}^2/\text{in.})$$

and was mounted on 18 damped helical spring isolators. From the design drawings of these isolators, the aggregate spring constant was calculated to be

$$K = 3.77 \times 10^6 \text{ N/m } (21500 \text{ lb/in.})$$

and the total moving mass of the springs was computed as

$$m = 3.73 \times 10^3 \text{ kg } (21.3 \text{ lb sec}^2/\text{in.})$$

which corresponds to a mass ratio of

$$\mu = 24.0$$

The results of the field tests are presented in Table 1. The field test value for the fundamental frequency was obtained from a free-vibration drop test of the platform. The corresponding tabulated transmission amplitude was computed by using the decay rate measured in this test in the equation of a single-degree-of-freedom system having viscous damping [3]. The first surge frequency was observed visually and measured with servo-accelerometers during a steady-state test in which the isolators were excited by an electro-hydraulic vibration machine. The field test natural frequency and transmission factor in the final line of Table 1 were measured in the same steady-state test. All the field test data were influenced by the many flexible modes of vibration of the platform itself, the lowest of which occurred at $\Omega = 2.87$. Nonetheless, these data show fair correspondence to the resonant frequencies and the transmission amplitudes calculated from Equation 15 for $\mu = 24.0$, $\beta = .15$, $\eta = .011$ which are credible ratios for this platform.

TABLE 1
Comparison of Field Test and Analytical Model

Field Test (Reference 7)		Analytical Model $\mu = 24$, $\beta = .15$, $\eta = .011$	
Ω	$\lvert\tau\rvert$	Ω	$\lvert\tau\rvert$
.956	3.35	.972	3.44
17.86	.74	15.45	.73
35.9	.08	30.8	.20

These two comparisons qualitatively corroborate the analytical model developed herein. A further experimental study in which the damping ratios and the resonant transmission factors are measured independently would quantitatively indicate the validity of this model.

CONCLUSIONS

Viscous damping is seen to limit the resonant response of a helical spring and the amplitudes of these responses are approximately proportional to the resonant frequencies. The effect of hysteretic damping is to cause these amplitudes to vary nearly inversely with the square of the resonant frequencies. Further, the system loss factor due to combined viscous and hysteretic damping is approximately the sum of the system loss factors for each type of damping alone.

ACKNOWLEDGMENT

This investigation was supported in part by the Defense Nuclear Agency and the U. S. Army Engineer Division, Huntsville.

NOMENCLATURE

C	Coefficient of viscous damping
F	Harmonic forces
j	$\sqrt{-1}$
K	Static stiffness of spring
L	Free length of spring
m	Mass of spring
M	Rigid mass
q	Dimensionless complex function defined in Equation 13
r	Dimensionless complex function defined in Equation 14
t	Time
u	Dimensionless sinusoidal characteristic defined in Equation 11
v	Dimensionless exponential characteristic defined in Equation 12
x	Position coordinate
Y	Steady state displacements
β	Viscous damping ratio $\equiv \frac{C}{2\sqrt{KM}}$
η	Hysteretic loss factor of spring material
η_s	System loss factor $\equiv 1/\lvert\tau(\Omega \text{ resonant})\rvert$
μ	Mass ratio $\equiv M/m$
τ	Transmission factor
ω	Angular frequency
Ω	Frequency ratio $\equiv \omega\sqrt{\frac{M}{K}}$

REFERENCES

1. A. M. Wahl, Mechanical Springs. McGraw-Hill, New York, 2d ed., 1963
2. B. L. Johnson and E. E. Stewart, "Transfer Functions for Helical Springs," Journal of Engineering for Industry, Vol. 91, pp. 1011-1016, Nov. 1969
3. R. E. D. Bishop and D. C. Johnson, The Mechanics of Vibration. Cambridge University Press, 1960
4. B. J. Lazan, Damping of Materials and Members in Structural Mechanics. Pergamon Press, London, 1968
5. R. L. Zahradnik, Theory and Techniques of Optimization for Practicing Engineers. Barnes and Noble, New York, 1971
6. J. C. Snowdon, Vibration and Shock in Damped Mechanical Systems. John Wiley and Sons, Inc., New York, 1968
7. E. E. Stewart, "The Transfer Function of a Helical Compression Spring," M.S. Thesis, Iowa State University, 1965
8. F. B. Safford and R. E. Walker, "Hardness Program, Non-EMP, In-Place Testing of Shock-Isolation Systems for SAFEGUARD TSE Ground Facilities," HNDSP-75-346-ED-R, March 1975, U. S. Army Engineer Division, Huntsville, AL

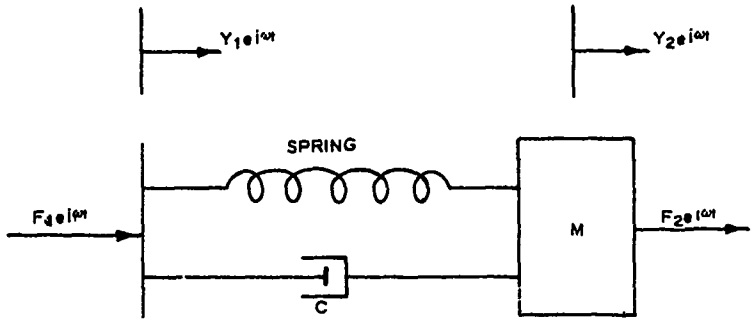

Figure 1. Helical spring, mass, and damper system.

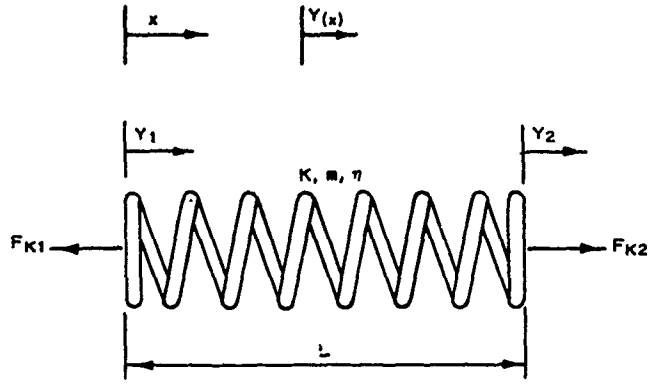

Figure 2. Helical spring with distributed mass and hysteretic damping.

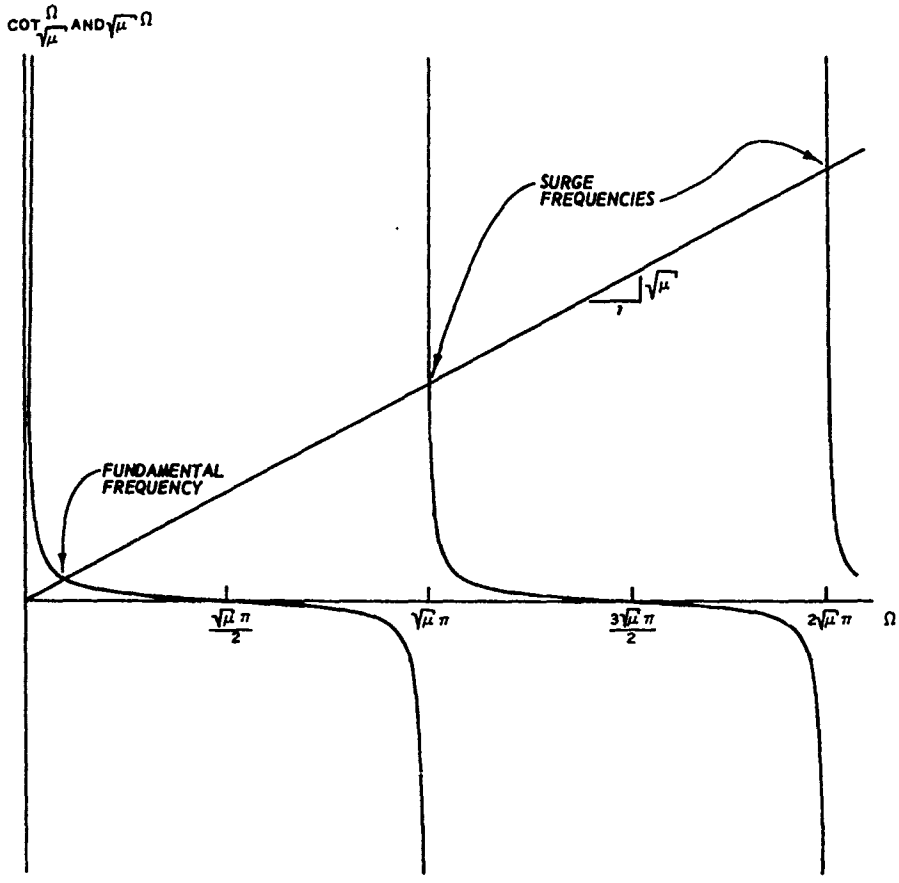

Figure 3. Resonant frequencies of undamped helical springs.

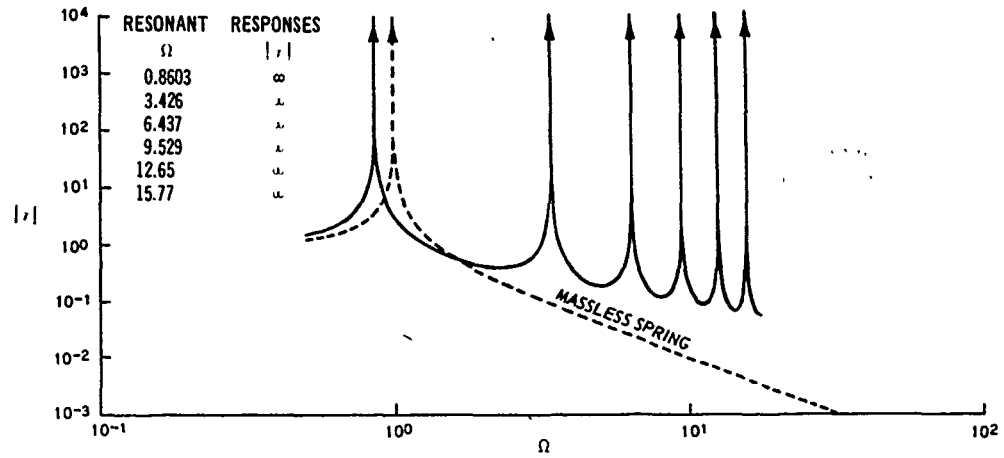

a. $\mu = 1$

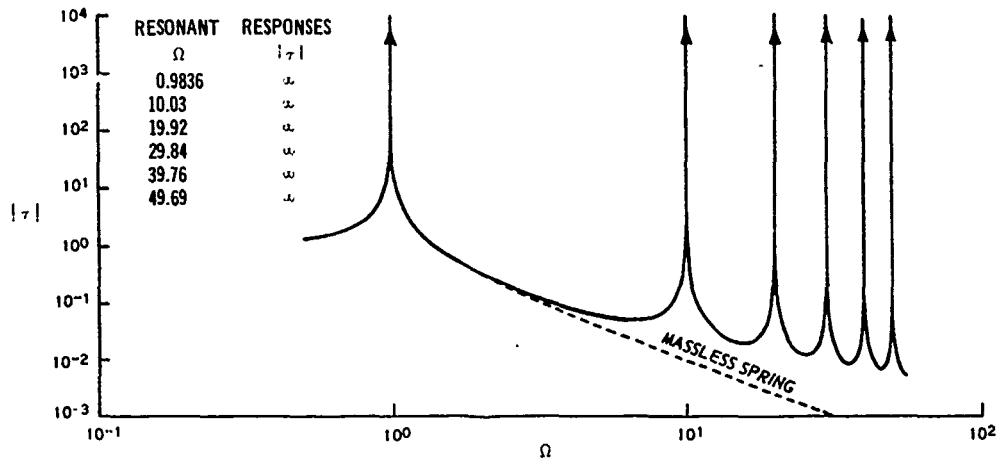

b. $\mu = 10$

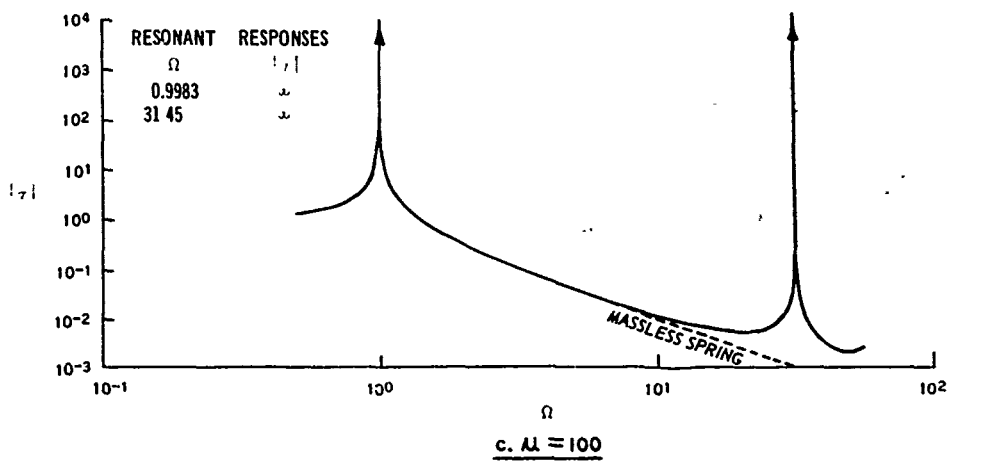

c. $\mu = 100$

Figure 4. Effect of distributed mass on transmission factor, $\beta = 0$ and $\eta = 0$.

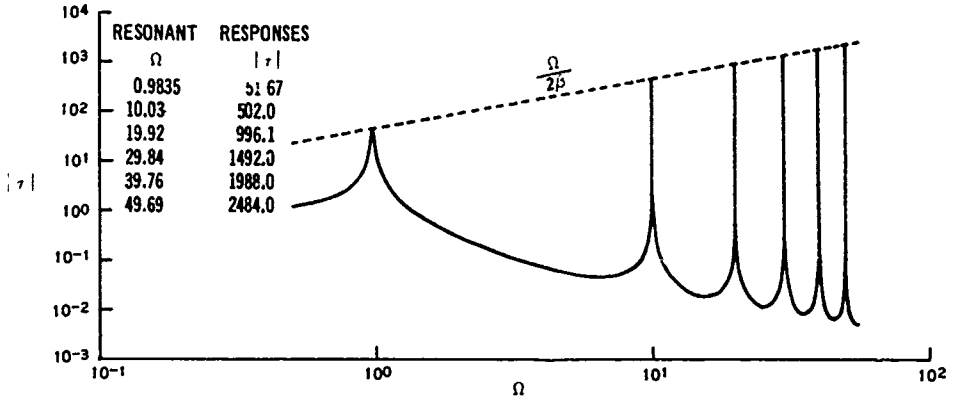

a β = 0.01

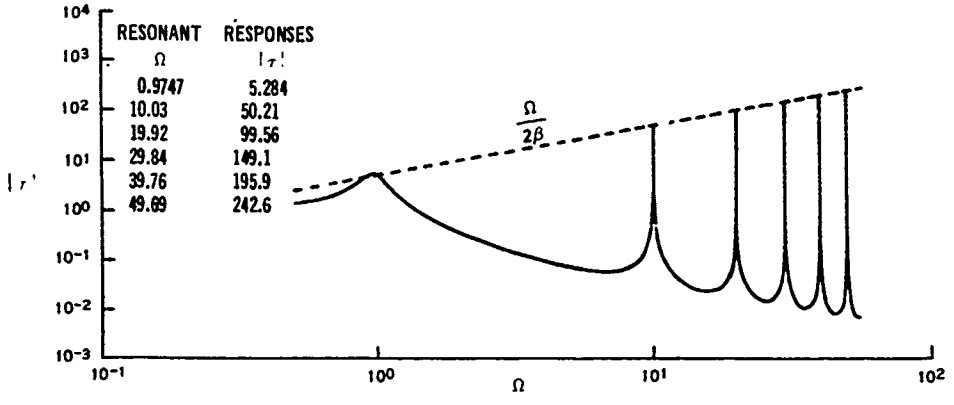

b β = 0.10

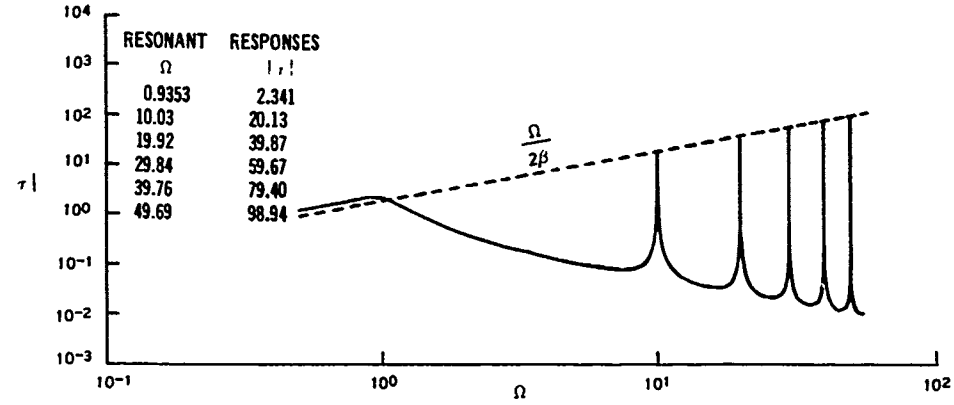

c. β = 0.25

Figure 5. Effect of viscous damping on transmission factor, $\mu = 10$ and $\eta = 0$.

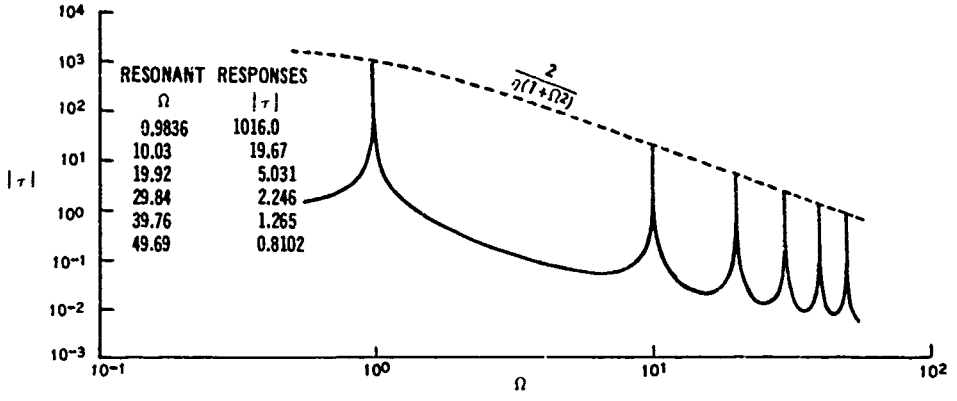

a. $\eta = 0.001$

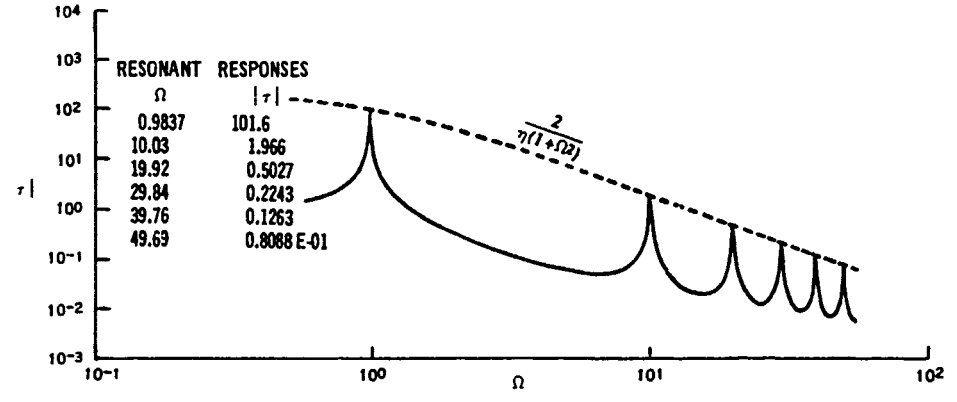

b. $\eta = 0.01$

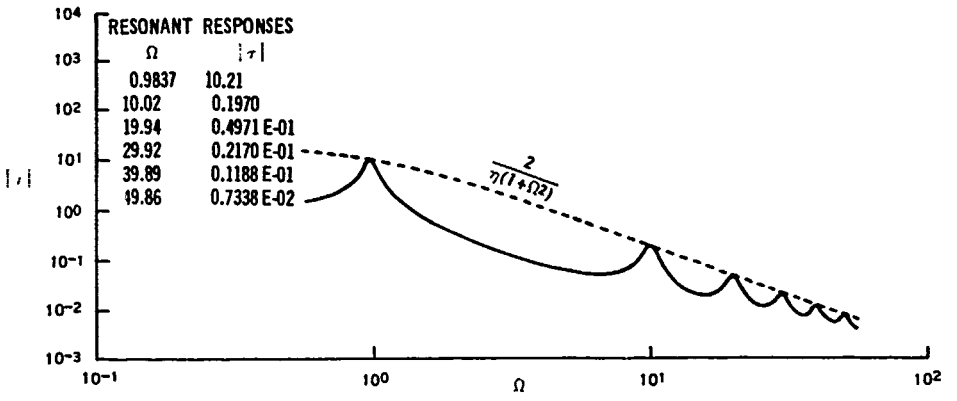

c. $\eta = 0.1$

Figure 6. Effect of hysteretic damping on transmission factor, $\mu = 10$ and $\beta = 0$.

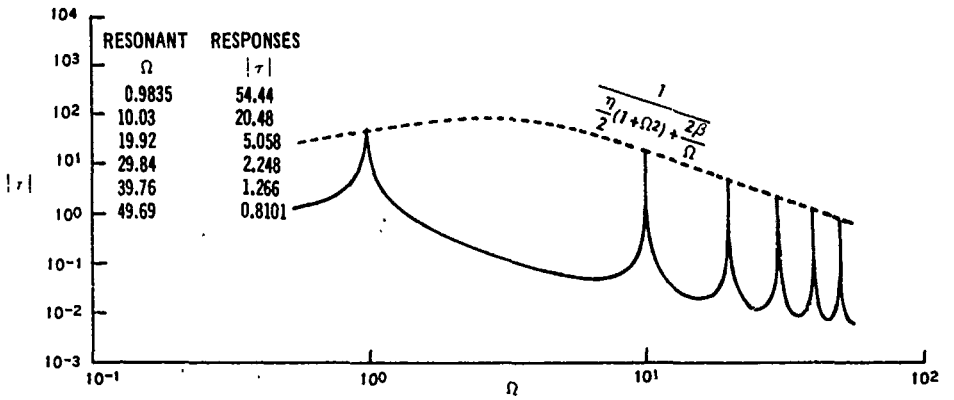

a. $\beta = 0.01$ AND $\eta = 0.001$

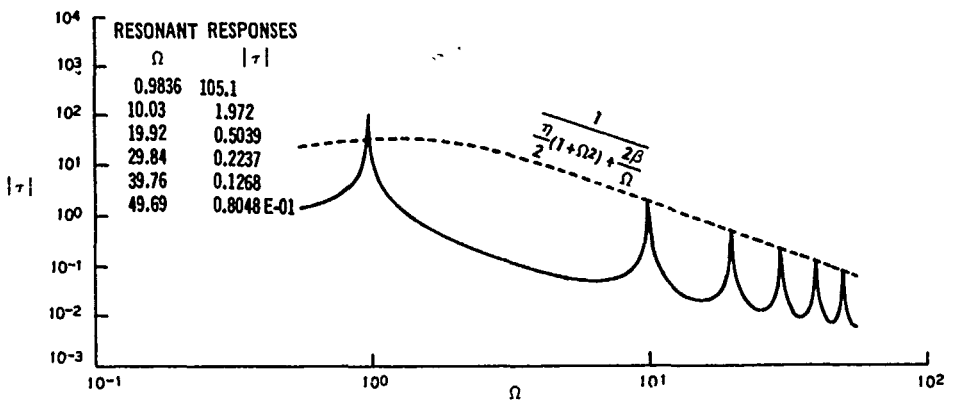

b. $\beta = 0.01$ AND $\eta = 0.01$

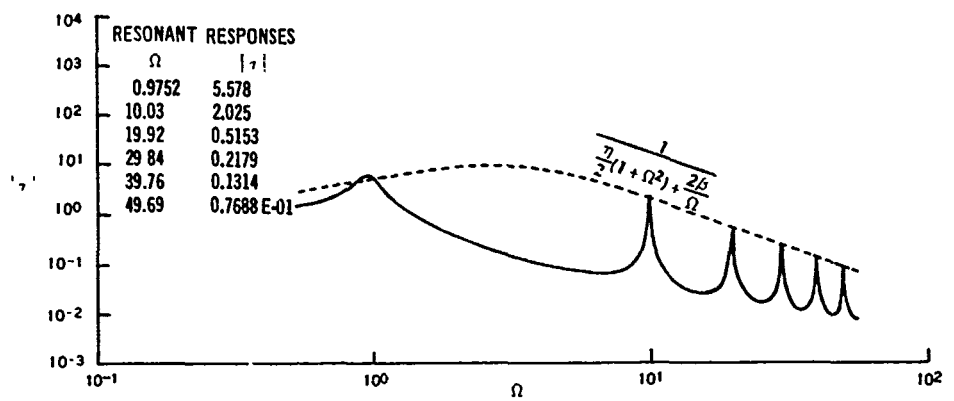

c. $\beta = 0.1$ AND $\eta = 0.01$

Figure 7. Effect of viscous and hysteretic damping on transmission factor, $\mu = 10$.

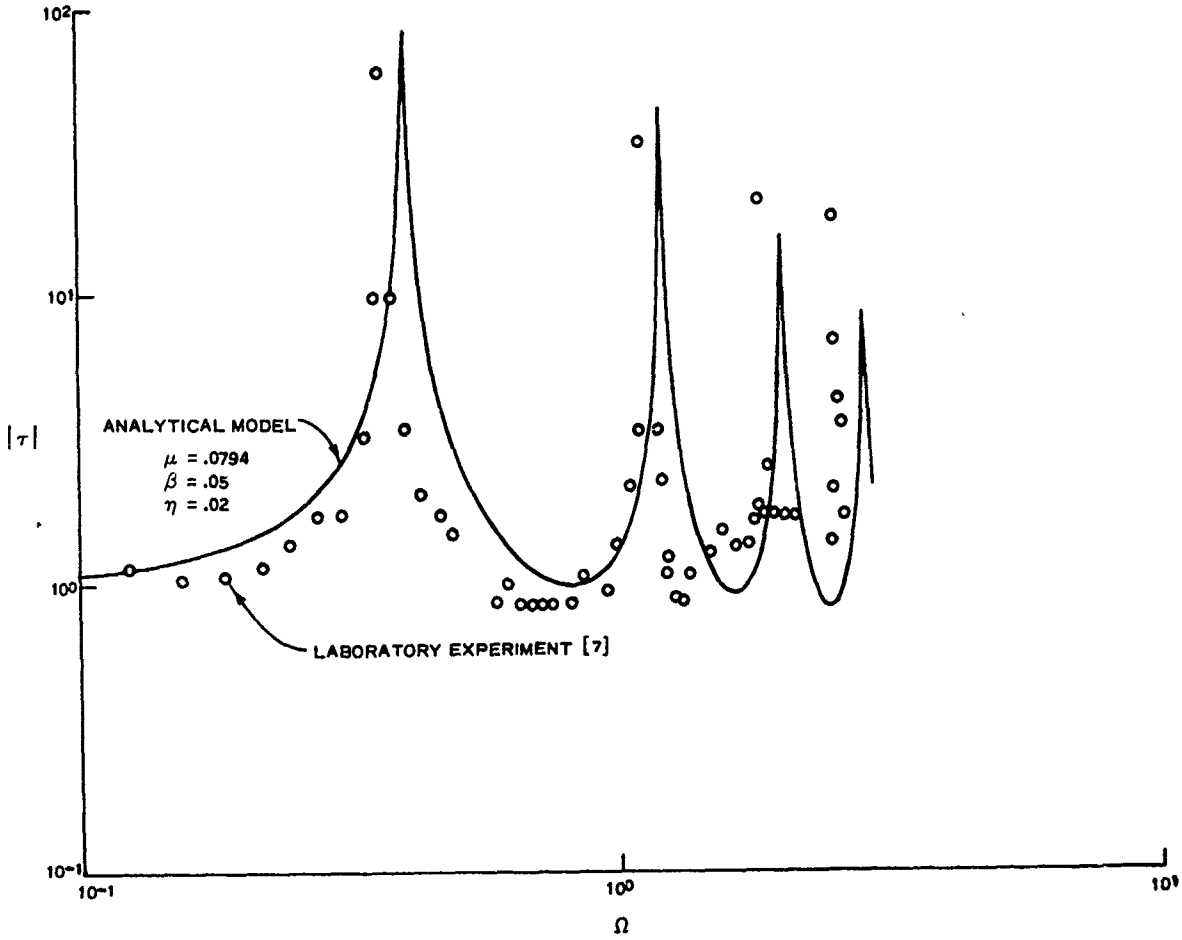

Figure 8. Comparison of laboratory experiment and analytical model.

DISCUSSION

Mr. Fox,(Rohr Marine:) When you look at that damping mechanism, that is really a nonlinear friction damper in there, it is not a viscous damper I believe. I worked at Barry Division when I designed that mount. They were originally supplied with a very nonlinear friction damper and you could see at your very high frequencies in your paper you didn't get any damping. It is because the friction damper is disengaged at zero mean displacement, so you might want to go back and review some of those things. I think it is interesting that you added the two, the hysteretic and viscous damping; I think that is a neat idea. I like it. But the actual big spring in the Safeguard system used friction damping it wasn't viscous, it was non linear too.

Mr. Mlakar: In a sense I guess what we are doing is fitting an equivalent viscous.

Mr. Fox: The specification was written as an equivalent viscous that is probably what fooled you. We had to meet an equivalent viscous and I think they were intending to use viscous but the friction damper did a better job and was cheaper. So you might get better correlation at the higher frequencies if you go back and look at that. I liked your paper it was interesting.

Mr. Mlakar: Thank you for your comment.

DAMPING OF AN ENGINE EXHAUST STACK

John J. DeFelice
Sikorsky Aircraft Division of United Technology Corporation
Stratford, Connecticut 06602

and

Ahid D. Nashif
Anatrol Corporation
Cincinnati, Ohio 45241

This paper describes a program whose objective was to introduce high damping into the helicopter engine exhaust extension in order to decrease its vibrational amplitude at resonance and thereby increase its fatigue life. A specialized high temperature damping material, in the form of vitreous enamel, was utilized to work effectively over the operational temperature range of the exhaust extension. The application of this high temperature damping material to the engine exhaust extension has significantly reduced the vibrational amplitudes at resonance and thereby increased component service life.

INTRODUCTION

Increasing the service life of engine exhaust extensions has been of great concern to both Sikorsky Aircraft and the United States Army because of fatigue failures that have occurred within a few hours of operation. Previous attempts to resolve this problem by introducing structural stiffness were not successful due primarily to the broadband excitation generated by the engines which resulted in small reduction in structural resonant response.

The most promising way of increasing the fatigue life of the exhaust extension is to reduce the vibrational amplitudes at resonance. This can be achieved successfully by additive damping. However, most damping materials being of the elastomeric type, will not survive the high temperatures associated with the subject tailpipe. The application of vitreous enamels has been used as a high temperature damping material on exhaust systems, and has successfully reduced their associated vibrational amplitudes and noise levels. The vibration failure problem on this component represented an opportunity for application of this material.

The major objectives of this effort were as follows:

1. An investigation to define the mode shapes and natural frequencies of the engine exhaust extension.

2. The selection of a proper damping treatment optimized at the operating temperature.

3. A thickness ratio to yield at least 10:1 increase in damping throughout the desired frequency range.

4. A 100 hour flight test program to evaluate the damping properties.

As will be further explained, each of these objectives were achieved.

DISCUSSION

Introducing damping into structures at high temperatures has been restricted in the past because most damping materials are of the elastomeric type and do not survive beyond 400°F. However, recent investigations[1,2] have shown that vitreous enamels are capable of providing extreme damping values at high temperatures if properly selected and designed. The main problem was in selecting the proper material that would maximize damping at the operational temperature of the tailpipe extension.

A flight test was performed to determine the operational temperature of the tailpipe extension. Four thermocouples were installed on the tailpipe flange, 90° apart at the four clock positions (12, 3, 6, 9). The test aircraft (CH-54; S/N 67-18417) maintained a stable hover condition for 30 minutes at a gross weight of 42,000 pounds and a neutral center of gravity. Temperature data was obtained at five minute intervals and is presented in Table 1. The critical temperature was obtained by finding the highest temperature of the exhaust extension during the hover survey. Since 742°F was the highest temperature value, it was decided to optimize the damping treatment at 800°F.

TABLE 1

FLIGHT TEST TEMPERATURE EVALUATION

Flight Condition - Hover - 100% N_R - Nose Into Wind

Engine Parameters - #1 Engine - 89% N_1 - Engine Speed
1900 lb./HR - Fuel Flow
1.75 Engine Pressure Ratio

#2 Engine - 91% N_1 - Engine Speed
1920 lb./HR - Fuel Flow
1.79 Engine Pressure Ratio
T_5 = Turbine Exhaust Temperature

5 Minute Hover - Nose Into Wind		10 Minute Hover - Nose Into Wind	
T_5 - 480°C (896°F)	T_5 - 460°C (860°F)	T_5 - 400°C	T_5 - 450°C
#1 Engine	#2 Engine	#1 Engine	#2 Engine
1 - 330°C(626°F)	5 - 300°C(572°F)	1 - 340°C(644°F)	5 - 300°C(527°F)
2 - 290°C(554°F)	6 - 220°C(428°F)	2 - 293°C(554°F)	6 - 250°C(482°F)
3 - 190°C(374°F)	7 - 250°C(482°F)	3 - 190°C(374°F)	7 - 260°C(500°F)
4 - 230°C(446°F)	8 - 300°C(572°F)	4 - 220°C(428°F)	8 - 310°C(590°F)

15 Minute Hover - Nose Into Wind		20 Minute Hover - Nose Into Wind	
T_5 - 495°C	T_5 - 490°C	T_5 - 490°C	T_5 - 460°C
#1 Engine	#2 Engine	#1 Engine	#2 Engine
1 - 340°C(644°F)	5 - 300°C(572°F)	1 - 333°C(626°F)	5 - 300°C(572°F)
2 - 295°C(563°F)	6 - 240°C(464°F)	2 - 270°C(618°F)	6 - 220°C(428°F)
3 - 190°C(374°F)	7 - 250°C(482°F)	3 - 180°C(356°F)	7 - 260°C(500°F)
4 - 210°C(410°F)	8 - 310°C(590°F)	4 - 190°C(374°F)	8 - 315°C(599°F)

25 Minute Hover - Nose Into Wind		30 Minute Hover - Nose Into Wind	
T_5 - 490°C	T_5 - 480°C	T_5 - 490°C	T_5 - 480°C
1 - 330°C(626°F)	5 - 300°C(572°F)	1 - 330°C(626°F)	5 - 310°C(590°F)
2 - 265°C(509°F)	6 - 230°C(446°F)	2 - 295°C(563°F)	6 - 220°C(428°F)
3 - 180°C(356°F)	7 - 240°C(464°F)	3 - 200°C(392°F)	7 - 260°C(500°F)
4 - 200°C(392°F)	8 - 310°C(590°F)	4 - 220°C(428°F)	8 - 310°C(590°F)

Right Side Into Wind		Left Side Into Wind	
T_5 - 490°C	T_5 - 480°C	T_5 - 490°C	T_5 - 490°C
#1 Engine	#2 Engine	#1 Engine	#2 Engine
1 - 350°C(662°F)	5 - 310°C(590°F)	1 - 350°C(662°F)	5 - 310°C(590°F)
2 - 395°C(742°F)	6 - 220°C(428°F)	2 - 320°C(608°F)	6 - 250°C(482°F)
3 - 200°C(392°F)	7 - 260°C(500°F)	3 - 200°C(392°F)	7 - 270°C(518°F)
4 - 220°C(428°F)	8 - 315°C(599°F)	4 - 235°C(455°F)	8 - 315°C(599°F)

After studying the driving point frequency response plot and the animated mode shapes of vibration, it was found that:

1. A large number of resonances occurred over a large frequency range.

2. Damping values at the various resonances were small. Typical loss factors (η) ranged between 0.001 and 0.01.

3. Deformation at resonance was associated with all surfaces of the engine exhaust extension over a wide frequency range.

4. Typical semi-length wavelengths of vibration ranged in value between five and fifteen inches for most observed modes.

The Transfer Function tests were performed to aid in determining the damping loss factors of the various modes of vibration. Transfer function plots were obtained by placing an impedance head between the shaker and the exhaust extension. Sinusoidal excitation was used to drive the structure. Both the input force and the output acceleration were measured by the impedance head and later used to obtain the compliance versus frequency plots. Data was generated at a number of locations close to the mounting holes in the flange in order to minimize mass loading effects. This data is presented in Figures 2 through 4. The half power bandwidth method was used to obtain the damping for the various modes. The sharpness of the peaks indicates that damping loss factor values are very low (between 0.001 and 0.01 for most modes).

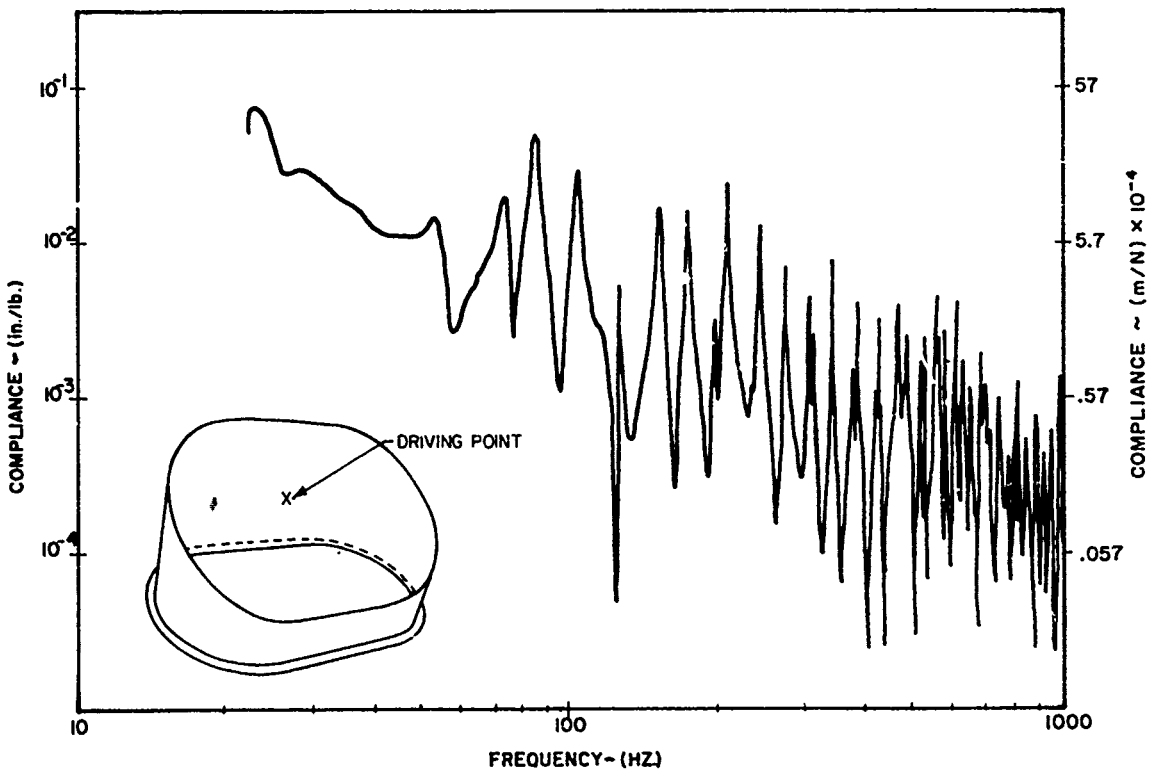

Figure 1 Driving Point Frequency Response of Undamped Exhaust Extension

Testing was then initiated to define the vibrational characteristics of the exhaust extension for proper optimization of the damping treatment. Both analog and digital techniques were used to generate the transfer function and mode shapes necessary for this investigation. These were the Transfer Function Alalyzer (TFA) and the Digital Fourier Analyzer (DFA) respectively. The engine exhaust stack was bolted through the existing mounting holes to a rigid plate which simulated actual boundary conditions.

The impulse technique was used to generate the data with the DFA setup. The input force impulse was applied to the exhaust extension and this signal was measured simultaneously with a load cell, while the output response was measured with an accelerometer at the same location. The input and output analog signals were then filtered, digitized, and Fourier transformed to yield magnitude and phase information in the frequency domain. The complex ratio of response to force was then computed and the resultant transfer function was plotted as compliance versus frequency. Typical driving point frequency response obtained by this technique is shown in Figure 1. Due to the large number of observed modes, only typical resonances were further investigated to determine their associated mode shape of vibration. These were 52.7, 84.0, 207.0 and 339.8 Hz. Animated mode shapes of vibration were obtained by the impulse technique by generating transfer function plots on 66 various locations on the engine exhaust extension. The animated mode shapes of vibration proved to be a successful aid in determining the general vibratory characteristics of the tailpipe extension.

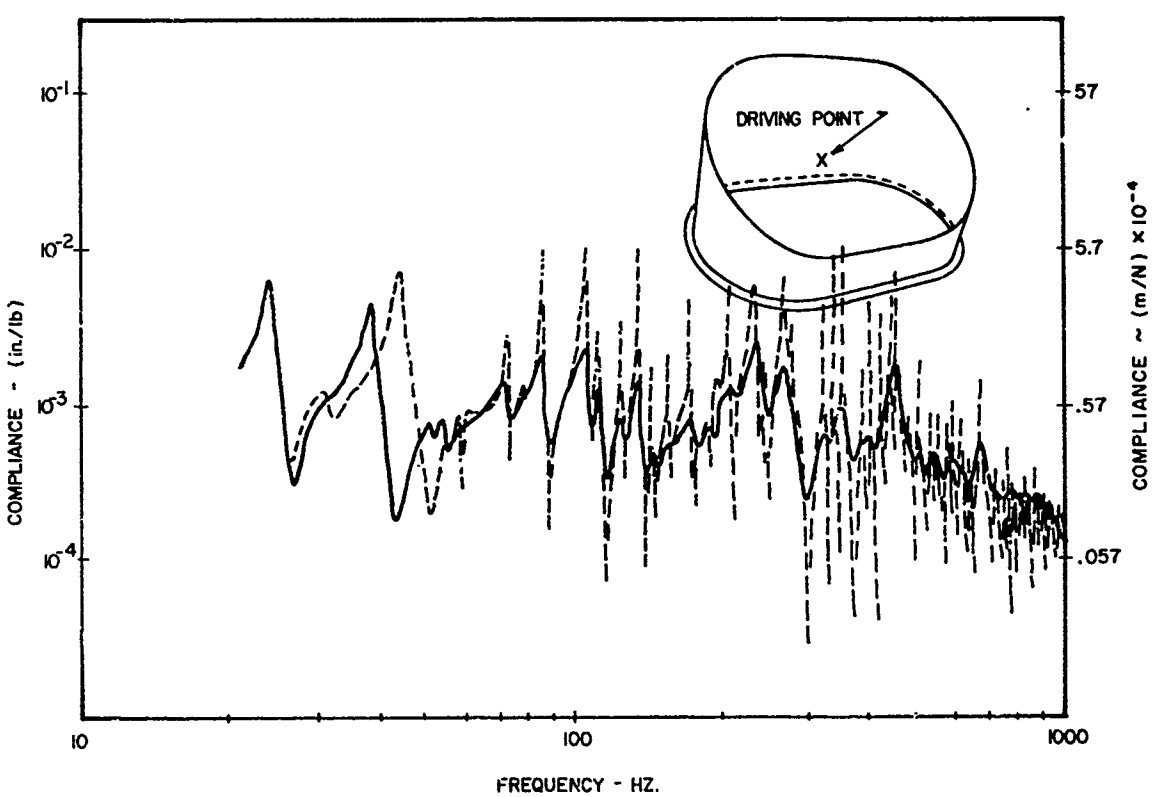

Figure 2 Driving Point Frequency Response Comparison of Damped and Undamped Exhaust Extension

A damping treatment, optimized for room temperature, was then applied to the exhaust extension for optimization studies. The room temperature treatment was selected to have damping properties equivalent to those of the high temperature damping treatment. In this manner, all optimization studies can be evaluated at room temperature and thereby avoid the usual problems associated with high temperature testing.

The room temperature treatment was a multiple layer damping tape configuration. Each layer of the tape considted of a damping adhesive of 0.002 inch (.0051 CM) thick and a constrained aluminum layer having a thickness of 0.002 inch (.0051 CM). The damping treatment[3] yields optimum damping capabilities at room temperature. The effective Young's modulus and loss factor of the room temperature damping treatment were computed[4], and this calculated information is presented in Figure 5 for typical semi-wavelengths of vibration.

The information presented in Figure 6 show the damping properties of the high temperature treatment. The loss factor and effective modulus are presented at two frequencies, 100 and 1000 Hertz. It can be seen from the data presented in Figures 5 and 6, that the room temperature treatment has properties equivalent to those of the selected high temperature vitreous enamel at the operational temperature of the exhaust extension. Therefore, any optimization for the room temperature damping treatment will be directly applicable to the vitreous enamel.

A number of layers of the room temperature damping treatment were applied until adequate reductions in the vibrational resonant amplitudes were achieved. This was accomplished with five layers (total thickness of 0.020 inch)(.051 CM) of the damping material. Testing was performed exactly as those performed on the untreated tailpipe extension. The results of the room temperature damping evaluation are shown in Figures 2 through 4. Comparing the results of the damped and undamped cases, it can be seen that the damping values have been increased by at least a factor of ten for most modes of vibration.

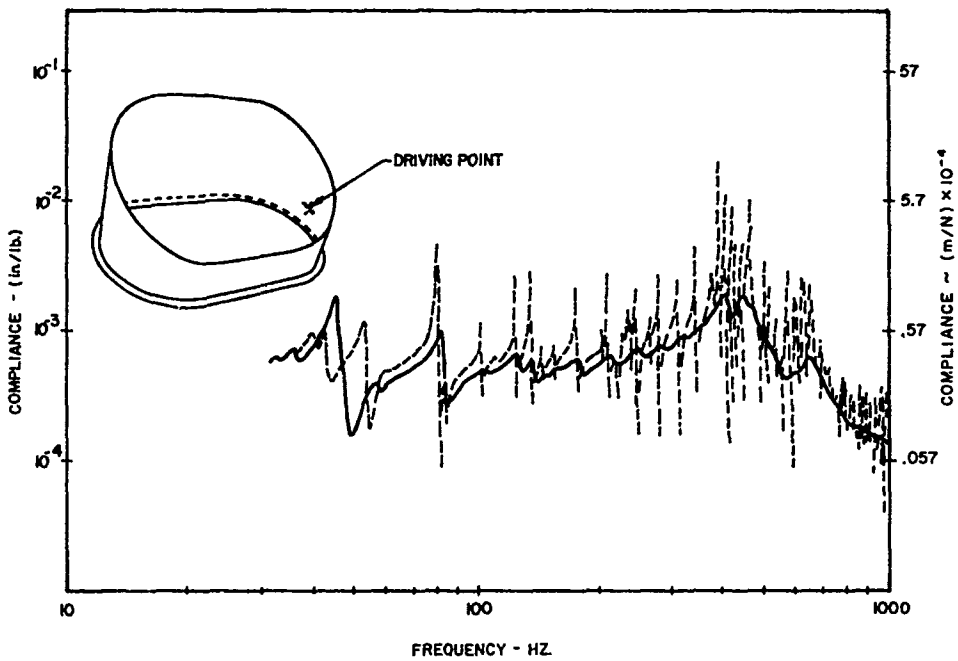

Figure 3 Driving Point Frequency Response Comparison of Damped and Undamped Exhaust Extension

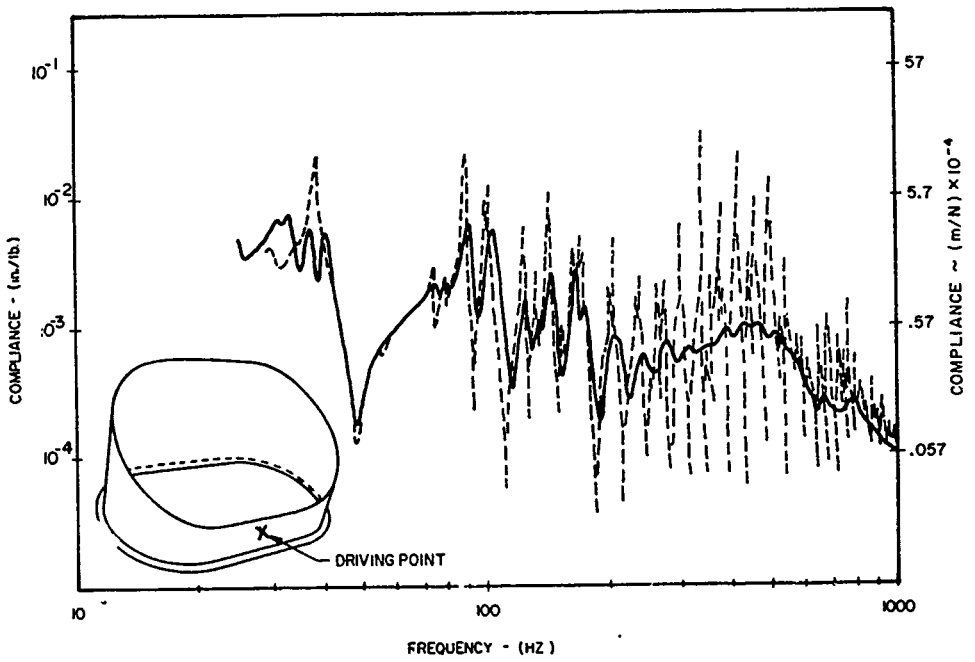

Figure 4 Driving Point Frequency Response Comparison of Damped and Undamped Exhaust Extension

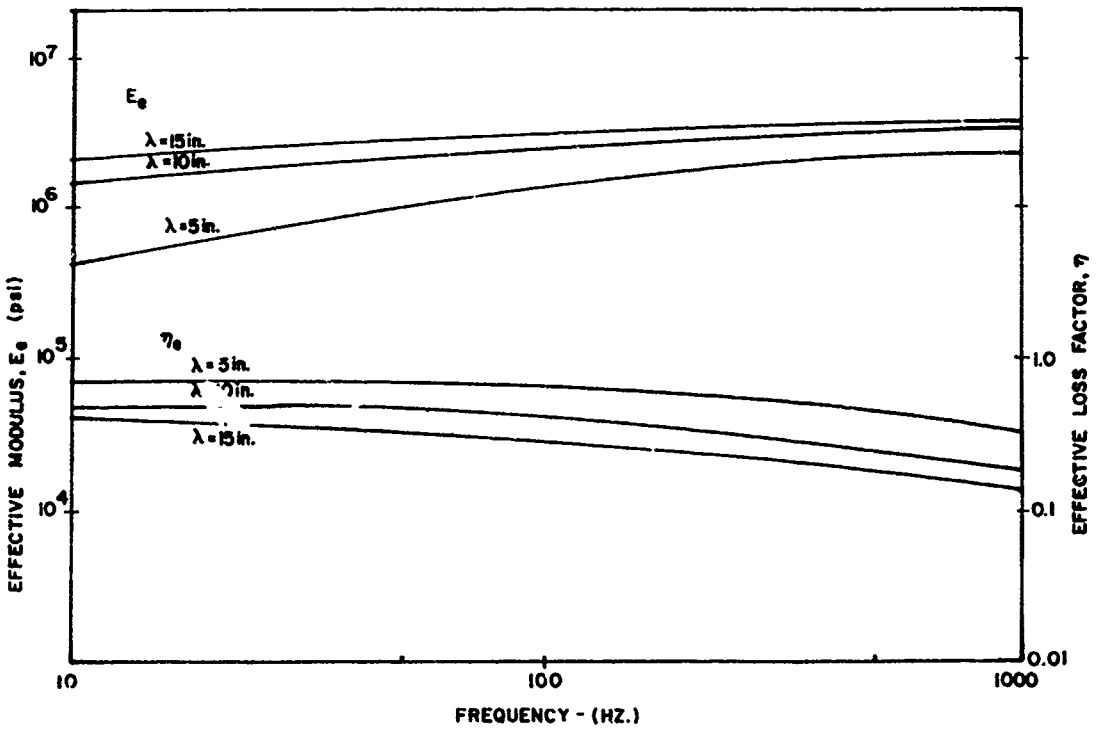

Figure 5 Equivalent Damping Properties of the Room Temperature Damping Treatment

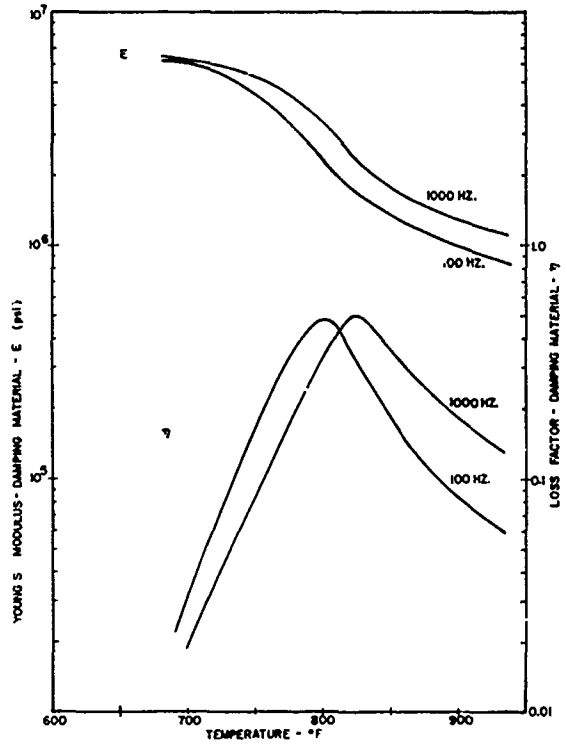

Figure 6 Damping Properties of Corning Glass No. 8363

Additional tests were performed which revealed that fifteen percent of the damping treatment could be removed with no significant change in spectrum shape. This is clearly shown in Figure 7. These tests were conducted to investigate the possibility that some of the damping treatment may chip during installation. The flaking problem which was encountered did not result in any damping degradation. Therefore, it was decided that for the high temperature enamel to be as effective as the room temperature treatment, and to completely alleviate any possible decrease in damping characteristics, the treatment should be applied to the entire surface in the same thickness (0.020 inch)(.051 CM).

Since the engine exhaust temperature ranged between 700°F (370°C) and 800°F (428°C), it was decided to select a damping material that exhibited optimum capabilities in that range. The enamel which conformed to these requirements was found to be Corning Glass No. 8363[5]. The damping properties of this enamel have been measured and were previously presented in Figure 6 in terms of temperature and frequency. It can be seen from the

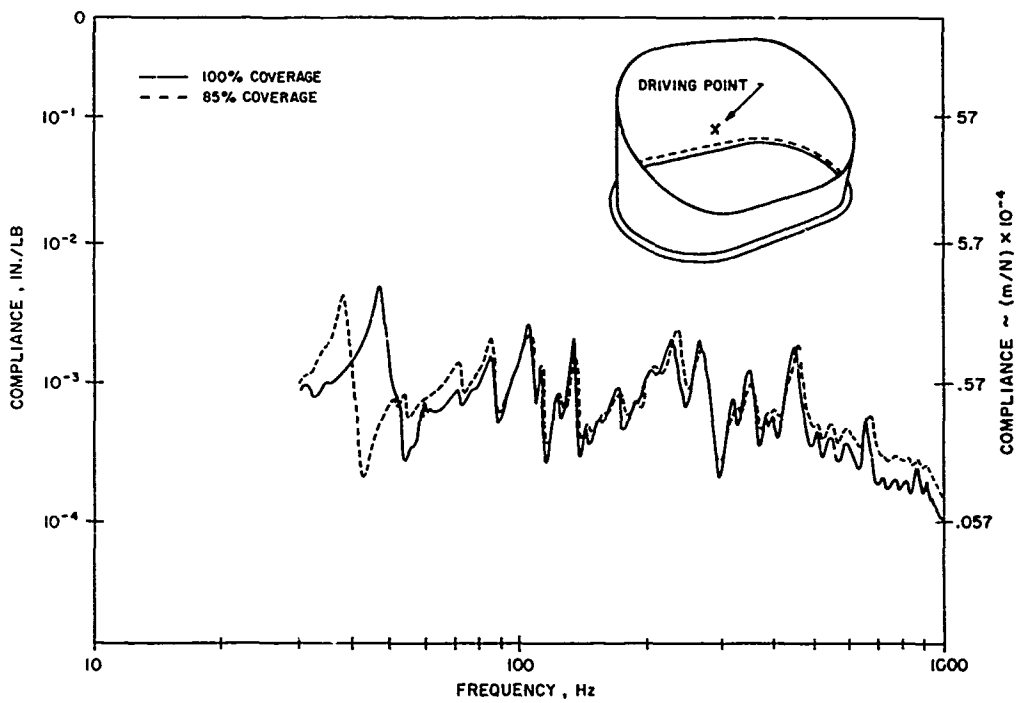

Figure 7 Driving Point Frequency Response of the Damped Exhaust Extension Showing 100% and 85% Coverage

data of Figure 6 that maximum damping for the enamel occurs at a somewhat lower temperature than that of the engine exhaust. This shift is in the appropriate direction since the outside surfaces of the exhaust extension were subjected to lower temperatures than those of the exhaust.

To verify the characterized high temperature damping properties shown in Figure 6, a 321 stainless steel cantilever beam was coated with the vitreous enamel on both sides. This beam having similar properties of the engine exhaust extension, was used to simplify further testing and verification of the high temperature damping treatment. The beam dimensions were 8.0 inches (20.32 CM) long, 0.75 inches (1.91 CM) wide, and 0.125 inches (.317 CM) thick. The coating thickness was 0.008 inches (.02 CM) on each side. The damping of the beam was measured in terms of frequency and temperature, and are presented in Figure 8 for the third mode of vibration. Superimposed on this data is the predicted performance of the beam using the characterized properties obtained from Figure 4. The predicted values were computed using standard equations[6] for symmetric free layer treatment. It can be seen from Figure 8 that there is good correlation between the two, and, therefore, the measured properties of the enamel can be used later for optimization purposes with confidence.

The thickness of the enamel coating for the tailpipe extension was chosen to be 0.020 inch (.051 CM) in order to achieve the same performance as that achieved with the room temperature damping tape. This selection was also confirmed by using the characterized material properties to predict the damping of the tailpipe extension for various thicknesses of enamel.[6] It was found that high damping could be achieved over the operational temperature range with a 0.010 inch (.025 CM) coating on each side of the structure. This is illustrated in Figures 9 and 10.

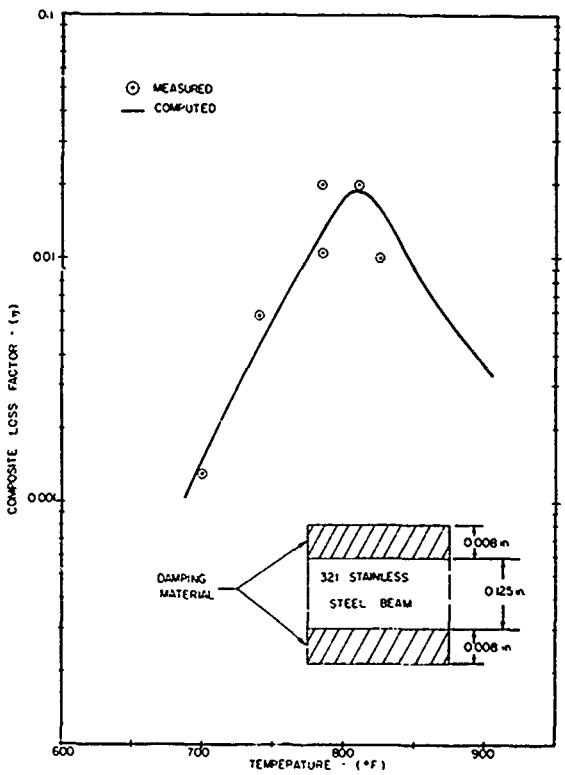

Figure 8 Comparison Between Computed and Measured Damping Values for a 321 Stainless Steel Beam

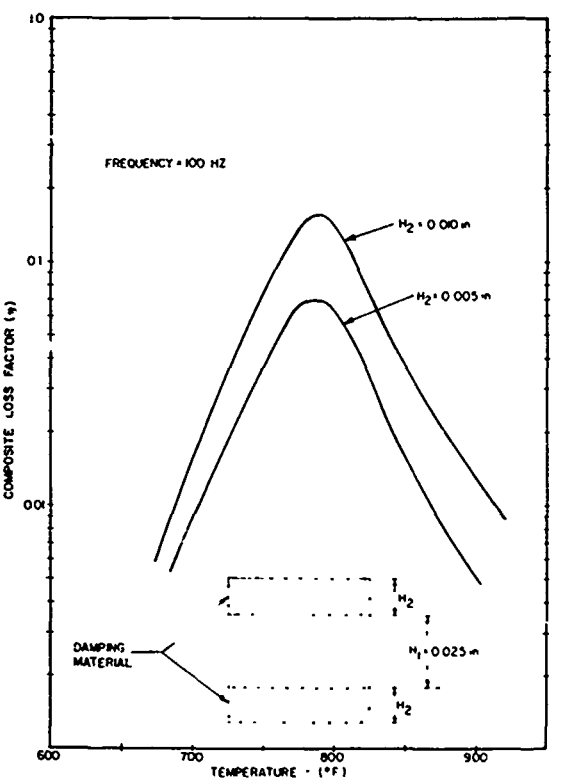

Figure 9 Composite Loss Factor of the Damped Exhaust Extension at 100 Hertz

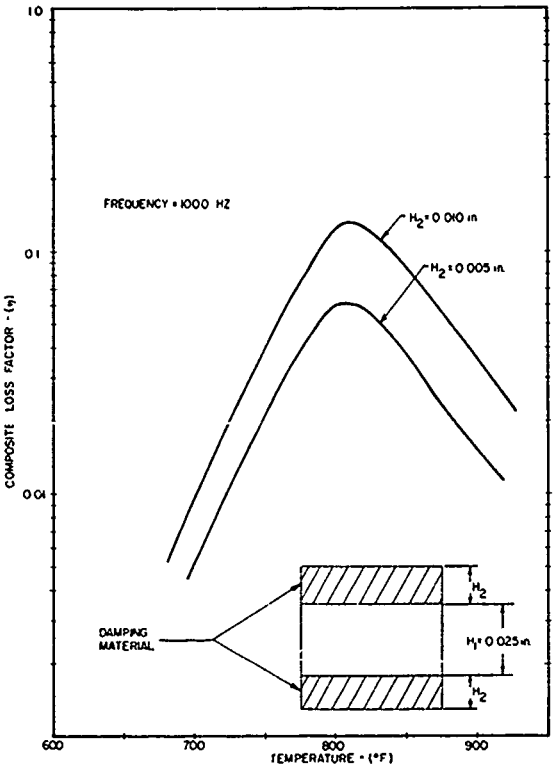

Figure 10 Composite Loss Factor of the Damped Exhaust Extension at 1000 Hertz

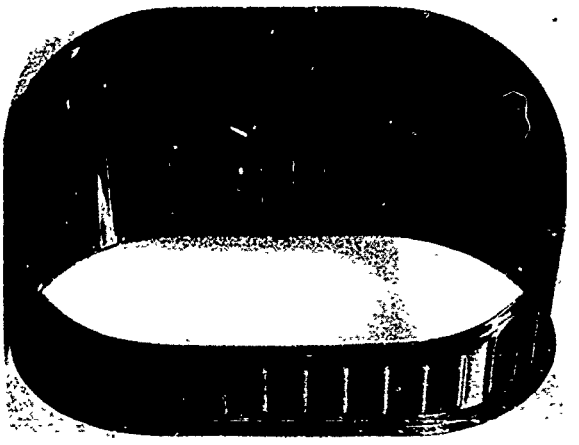

Figure 11 Damped Tailpipe Extension - Before Installation

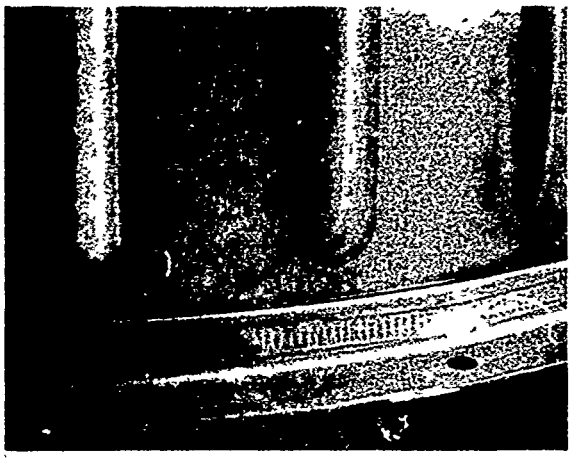

Figure 12 Damped Tailpipe Extension - Before Installation

Figures 11 and 12 show the tailpipe extension with the high temperature damping treatment applied. The entire tailpipe extension was coated, with the exception of the flange as is shown in Figure 12. The flange was not coated to alleviate any potential installation problems. The applied damping treatment resulted in a total tailpipe extension weight of 15.28 pounds (6.95 Kg) or an increase of 4.25 pounds (1.93 Kg).

The coated tailpipe was shipped to Ft. Eustis, Virginia where it was inspected and installed on a CH-54 Helicopter (A/C 18470). It was observed during the first thirty hours that some flaking of the damping material occurred on the inside section of the tailpipe. It was determined that the exhaust flow ablated the damping treatment from the inner tailpipe surface. Further investigations showed that the damping material could be applied to the outside surface only, maintaining the 10:1 increase in damping achieved previously. This would eliminate the flaking problem and tend to further increase the service life of the tailpipe extension.

Upon completion of the 100 hour flight test evaluation, the treated tailpipe extension was removed from the aircraft and shipped to Sikorsky Aircraft. A detailed inspection revealed no indications of metal fatigue. The flaking problem on the inner surface, discussed previously, can be clearly seen in Figure 13 and 14. This degradation has not significantly increased subsequent to its being discovered during the initial

30 hours. The outer surface of the extension show no evidence of flaking which substantiates the recommendation for applying the material to the outer surface only.

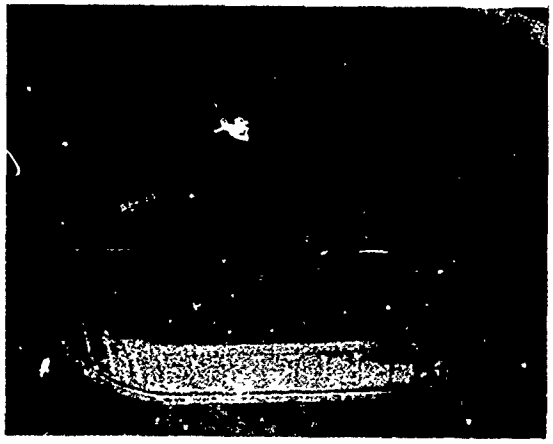

Figure 13 Damped Tailpipe Extension - 100 Hour Flight Evaluation

Figure 14 Damped Tailpipe Extension - 100 Hour Flight Evaluation

CONCLUSIONS

The testing performed under this program has successfully demonstrated the feasibility of applying high temperature damping treatment to an existing structure so as to significantly increase its fatigue life.

REFERENCES

1. Plunkett, R., "High Temperature Damping", Society of Automotive Engineers, Paper No. 720809 (1972)

2. Nashif, A. D., "Enamel Coating for High Temperature Damping Materials," American Ceramic Society Bulletin, Volume 53, No. 12 (1974)

3. ISD-112 produced by 3M Co., St. Paul, Minnesota 55101

4. Jones, D.I.G., Nashif, A.D., Parin, M.L., "Parametric Study of Multiple Layer Damping Treatments on Beams", Journal of Sound and Vibration No. 29, (1973)

5. Corning Glass No. 8363 produced by Corning Glass Works, Corning, New York 14830

6. Nashif, A. D., "A New Method for Determining the Damping Properties of Viscoelastic Materials", Shock and Vibration Bulletin 36, Part 4, (1967)

MULTI-VARIABLE OPTIMIZATION FOR VIBRATION ISOLATION OF ROAD VEHICLES

Ebrahim Esmailzadeh
Department of Mechanical Engineering
Arya Mehr University of Technology
Tehran, Iran

The transmission of road-generated vibrations into a vehicle body is treated as a source-path-receiver problem. The suspension system acts as the path, and improved isolation can be achieved by having a single compliant bushing at the connecting point of the shock absorber to the body with none at the other end. A mathematical model is derived for such a system and an expression for the absolute displacement transmissibility of the body and that of the wheel is derived. An optimization procedure is applied in order to evaluate the optimum values of the non-dimensional variables involved. This minimizes the maximum motion transmitted to the body from the road surface over a broad frequency range.

INTRODUCTION

The dynamical design of linear vibration isolators to provide a good ride quality and to protect the vehicle body from the sinusoidal motion generated from the road surface is an important engineering problem. The basic theory of vibration isolation is based on transfer response analysis of a mass supported by a parallel combination of a linear spring and a viscous damper [1]. This analysis is adequate for illustrating the fundamental principles of vibration isolation and resonance characteristics [2], but is an over simplification insofar as many practical problems are concerned. An alternative system for improving vibration isolation which eliminates the damping force at high frequencies, yet permits the damper to control motion at low frequencies has been discussed by Ruzicka and Cavanaugh [3], but only the case of single-degree-of-freedom has been considered. The vibration isolation for rigid and flexible equipment has been investigated by Ruzicka [4] and the effect of damping on the equipment has also been included. However, the case of a flexible supporting structure has not been studied.

Experimental study into the effect of foundation resilience on the isolation vibration has been discussed by Hamme [5], but he fails to give a method to obtain the optimum values of the parameters involved. A new technique was introduced to use a Hybrid computer to simulate the entire system [6]. This computer combines patchable logic circuitry to an analog computer and provides the means to obtain a self-optimizing damper. Vibration isolation of a compound system and dynamic vibration absorber has been studied in detail by Den Hartog [7] and an optimization method was developed for obtaining the optimum values of parameters.

The problem of multi-variable optimization may be studied, when investigating the dynamic properties of vehicle suspension systems [8]. An attempt is made here to apply a method of optimization to the dynamic characteristics of a vehicle suspension system in order to obtain optimum values of the parameters involved from which the maximum transmitted motion to the body would be minimum over a wide frequency range. Design data are presented non-dimensionally since this would facilitate the selection of the optimum values of the above-mentioned parameters in the design of road vehicle suspensions.

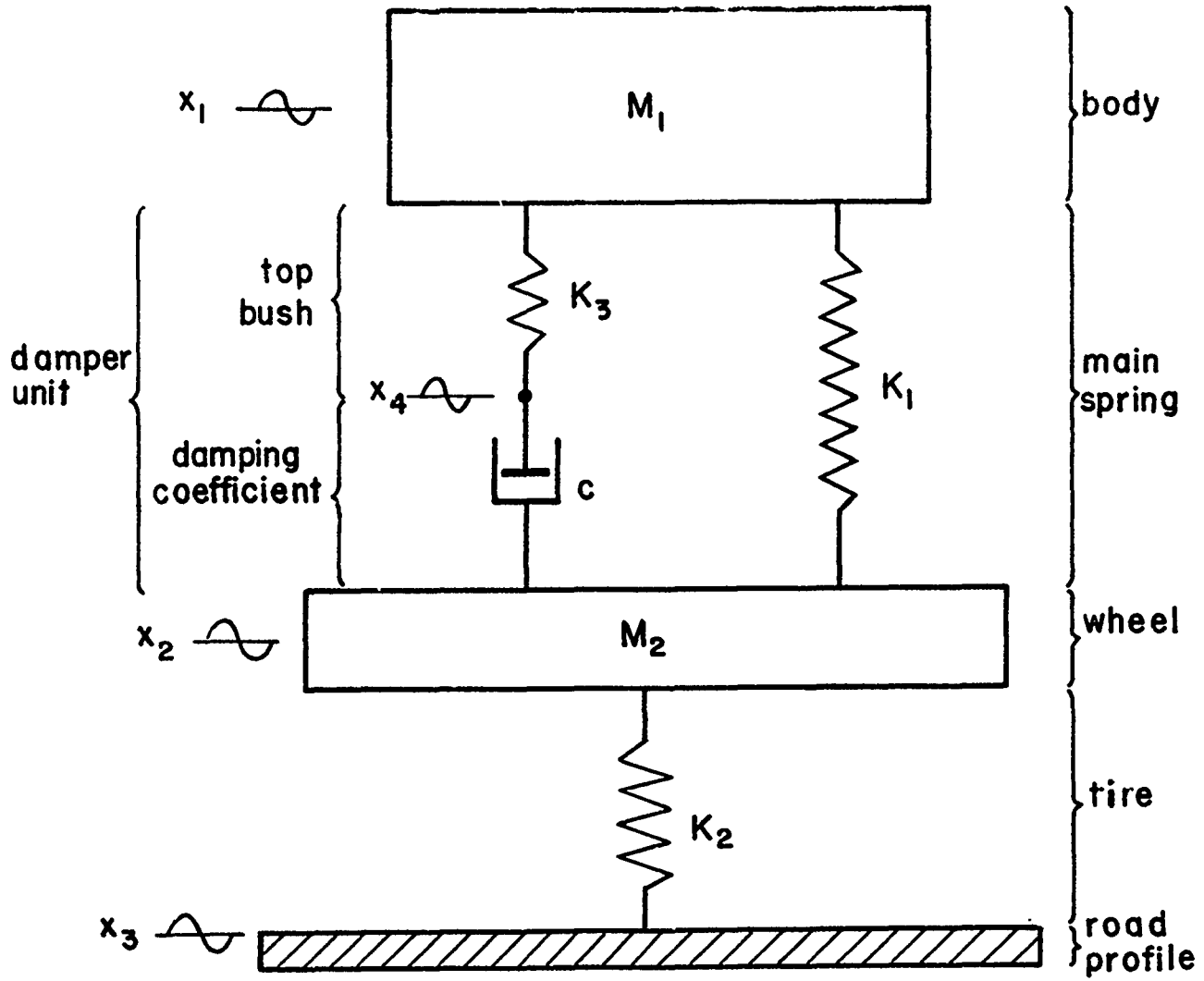

Fig. 1. Simplified Model of Vehicle Suspension System.

FORMULATION OF THE SUSPENSION SYSTEM

Conventional rigidly connected viscous damper can isolate motion successfully in a narrow range of frequencies. However, vibration environments are becoming more extreme as disturbing frequency increases and, in fact, damping is detrimental to the isolation effectiveness above resonance. Excessive damping also increases the transmitted force and, hence, results in an increase of severity of shock experienced by the body from wheel. Therefore, an elastically connected viscous damper is assumed in the mathematical model of the suspension system shown in Fig. 1. The elasticity of the viscous damping element is assumed to be a linear spring of stiffness K_3 in series with the shock absorber c. The equations of motion for the body and the wheel may be written as

$$M_1 D^2 X_1 = - K_e (X_1 - X_2) \qquad (1)$$

and

$$M_2 D^2 X_2 = K_e (X_1 - X_2) - K_2 (X_2 - X_3) \qquad (2)$$

where K_e is the equivalent spring stiffness of the vehicle suspension system; and is given by:

$$K_e = \frac{((c/K_1)D + Q/(1+Q)) \cdot (1+Q) \cdot K_1}{Q + (c/K_1)D} \qquad (3)$$

with Q = stiffness ratio, K_3/K_1;

and D = differential operator, d/dt.

For sustained sinusoidal motion of the vehicle suspension system of Fig. 1, the absolute displacement transmissibility of the body, $|T_{A1}|$, is given by

$$|T_{A1}| = \left|\frac{X_{01}}{X_{03}}\right| \qquad (4)$$

$$= \left[\frac{\mu^2 \gamma^4 \left(\frac{Q}{1+Q}\right)^2 + 4\xi^2 \mu^2 \gamma^4 (\omega/\omega_0)^2}{\left[\mu\gamma^2 \left(\frac{Q}{1+Q}\right) - (1+\mu)\left(\frac{Q}{1+Q}\right)(\omega/\omega_0)^2 - \mu\gamma^2 Q (\omega/\omega_0)^2 + \mu Q (\omega/\omega_0)^4\right]^2 + 4\xi^2 (\omega/\omega_0)^2 \left[\mu\gamma^2 + \mu(\omega/\omega_0)^4 - (1+\mu+\mu\gamma^2)(\omega/\omega_0)^2\right]^2} \right]^{1/2}$$

and the absolute displacement transmissibility of the wheel, $|T_{A2}|$, is given by

$$|T_{A2}| = \left|\frac{X_{02}}{X_{03}}\right| \qquad (5)$$

$$= \left[\frac{\mu^2 \gamma^4 Q^2 \left(\frac{1}{1+Q} - (\omega/\omega_0)^2\right)^2 + 4\xi^2 \mu^2 \gamma^4 (\omega/\omega_0)^2 \left(1 - \frac{\omega^2}{\omega_0^2}\right)^2}{\left[\mu\gamma^2 \left(\frac{Q}{1+Q}\right) - (1+\mu)\left(\frac{Q}{1+Q}\right)(\omega/\omega_0)^2 - \mu\gamma^2 Q (\omega/\omega_0)^2 + \mu Q (\omega/\omega_0)^4\right]^2 + 4\xi^2 (\omega/\omega_0)^2 \left[\mu\gamma^2 - (1+\mu+\mu\gamma^2)(\omega/\omega_0)^2 + \mu(\omega/\omega_0)^4\right]^2} \right]^{1/2}$$

where:

- X_0 = amplitude of the sustained sinusoidal motion;
- γ = resonant frequency ratio, $\sqrt{(K_2/M_2)}/\omega_0$;
- μ = mass ratio, M_2/M_1;
- ω = frequency of the input disturbance from road;
- ω_0 = reference frequency, $(K_1(1+Q)/M_1)^{1/2}$; and
- ξ = damping ratio, $c/(2K_1/\omega_0)$.

Typical variations of absolute transmissibility of the body and that of the wheel as a function of frequency ratio ω/ω_0 with arbitrary values for the variables damping ratio ξ, mass ratio μ, resonant frequency ratio γ, and stiffness ratio of damper unit Q are shown in Fig. 2 and Fig. 3.

MULTI-VARIABLE OPTIMIZATION OF SUSPENSION SYSTEM

The absolute transmissibility of the body, $|T_{A1}|$, given by equation (4) is function of four variables. The optimum values of ξ, μ, γ and Q are to be sought from which maximum value of transmissibility of the body would become minimum over the considered broad frequency range. Frequency response for absolute transmissibility of the body which is shown in Fig. 2 indicates that there are two maxima which are known as resonant transmissibilities of the body. Let these be denoted as X_1 and X_2, respectively, which, in turn, are functions of four variables.

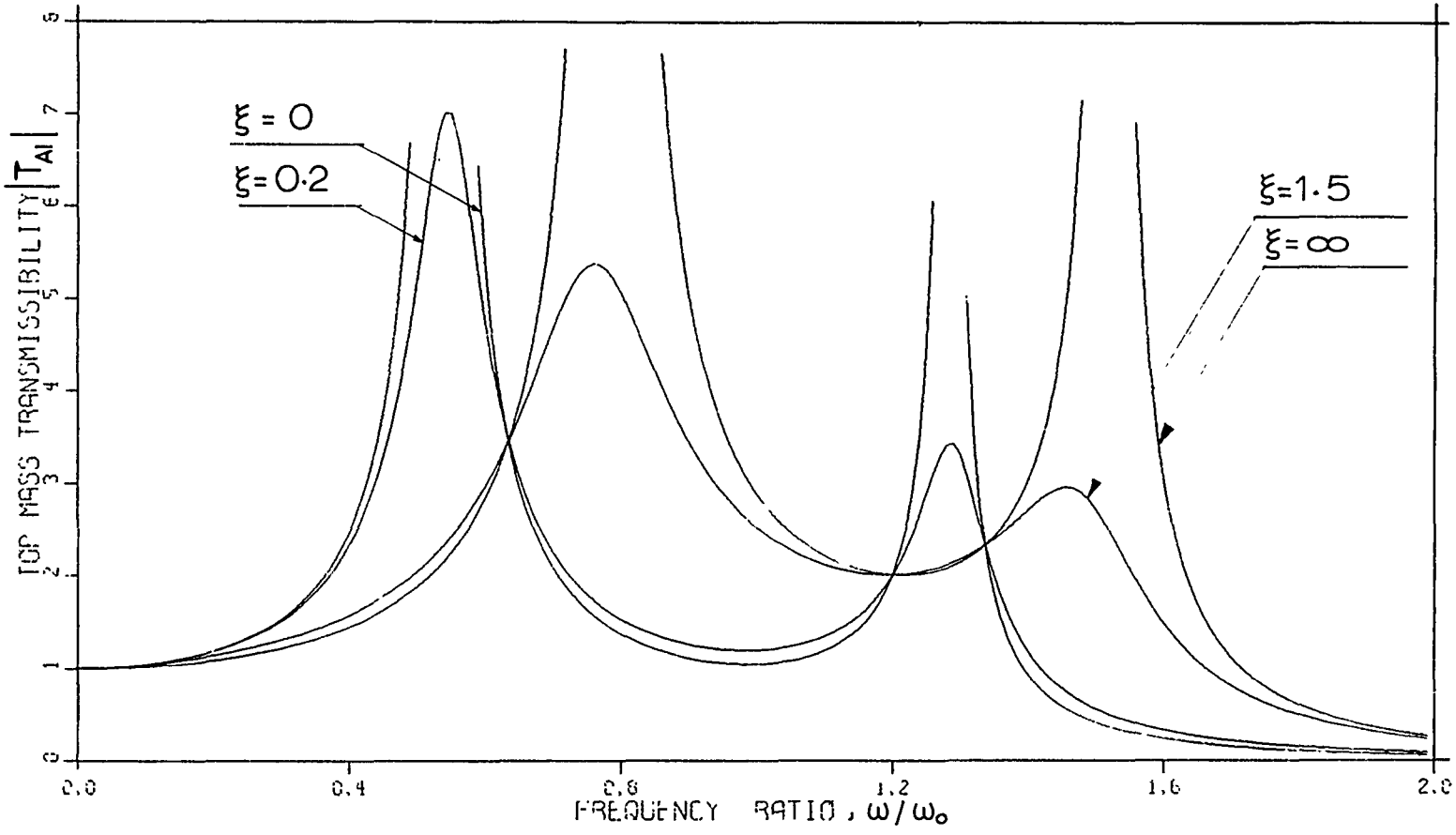

Fig. 2. Frequency Response of Body Transmissibility, $|T_{A1}|$, for Q = 2; μ = 2; γ = 1.2; ξ = 0.2 and 1.5.

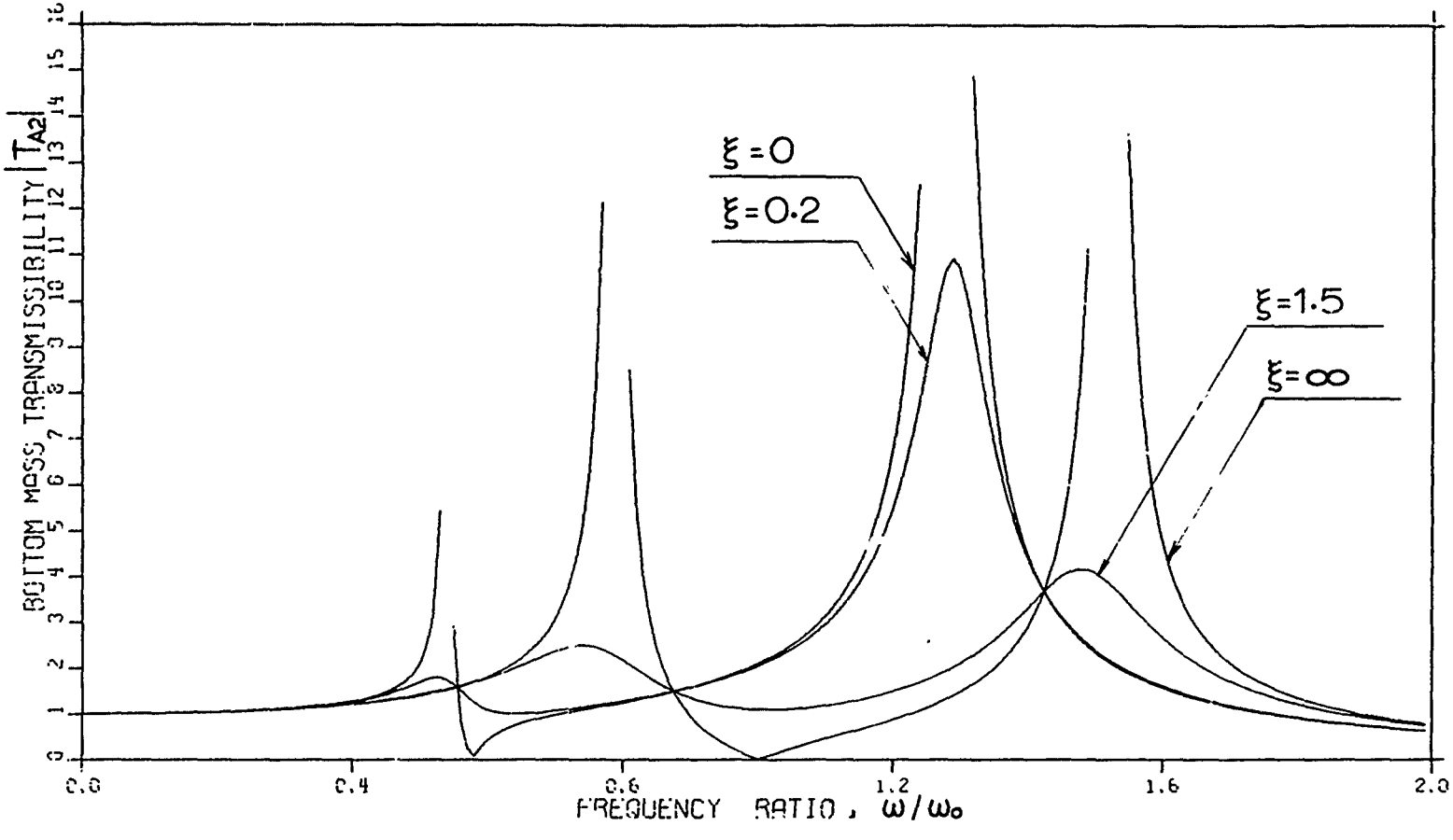

Fig. 3. Variation of Wheel Transmissibility with Frequency. $Q = 2$; $\mu = 2$; $\gamma = 1.2$; $\xi = 0.2$ and 1.5

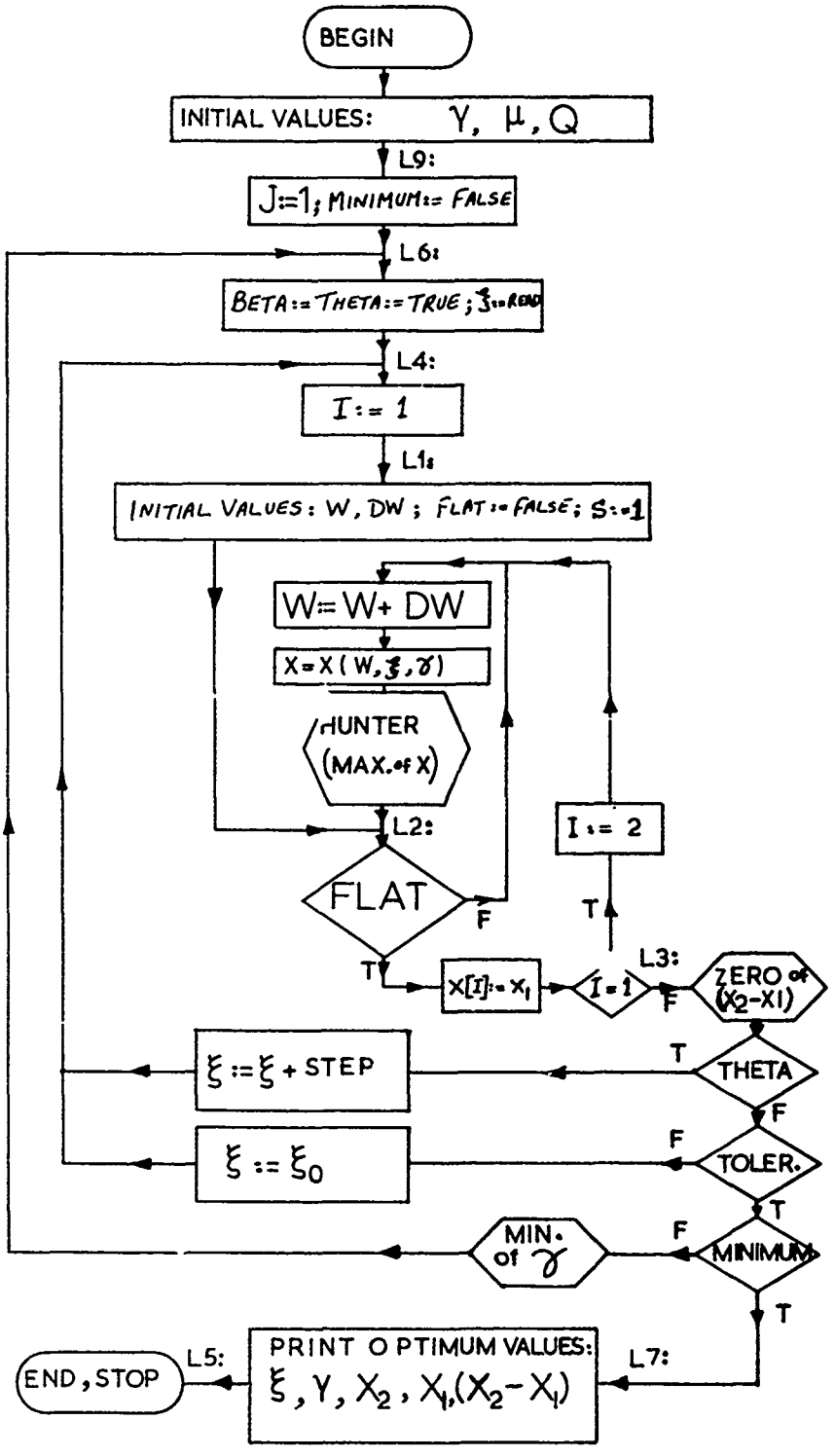

Fig. 4. Digital Computer Flow Chart for Optimization of Parameters

The digital computer flow diagram for the optimization of the variables ξ, γ, μ and Q is developed and shown in Fig. 4. Initially, arbitrary values for γ, μ and Q are assumed and optimum value of ξ is sought for which the two resonant transmissibilities, X_1 and X_2, become equal. The next step is to change value of γ for which a minimum value of the two maxima is obtained. This is the outer loop indicated by the label L6 in Fig. 4. The other two variables μ and Q are assumed to be constant in the program in order to save computing time. However, by selecting different values of μ and Q for every run of the program an optimum value of resonant transmissibility, $|T_{A1}|_{opt}$, can be obtained.

The optimum resonant transmissibility of the body, $|T_{A1}|_{opt}$, as a function of mass ratio, μ, and stiffness ratio of damper unit, Q, is shown in Fig. 5. The variation of μ is chosen to be between 0.1 and 10. However, for values of mass ratio of smaller than 0.1, the optimum transmissibility changes very slightly. It can be seen that the stiffness ratio of the damper unit, Q, and mass ratio, μ, do not have optimum values. However, for better isolation smaller values of mass ratio and larger values of Q are most desirable.

The variation of optimum resonant frequency ratio, γ_{opt}, as a function of mass ratio, μ, and Q for which minimum value of the resonant transmissibility occurs is shown in Fig. 6. The corresponding optimum values of damping ratio, ξ, as a function of μ and Q is shown in Fig. 7.

In designing an optimum suspension system the non-dimensional Figs.5,6 and 7 may be used as illustrated in the following example.

It has already been established that stiffness ratio of the damper unit, Q, and mass ratio, μ, do not have an optimum value . For this example Q is chosen to be 2 and the mass ratio, μ, is assumed to be an arbitrary value also of two. Fig. 5 indicates that the optimum resonant transmissibility of the body, $|T_{A1}|_{opt}$, for Q = 2 and μ = 2 must be 2.874. The corresponding optimum value of the resonant frequency ratio, γ_{opt}, which can be read off from Fig. 6 is 1.478 while the optimum value of the damping ratio, ξ_{opt}, equals.696 (from Fig. 7). Hence a complete set of optimum design parameters is determined. The frequency response of the absolute transmissibility of the body for these values of variables is shown in Fig. 8. It can be seen that the two maxima are equal and have a value of 2.874, which is already known from Fig. 5. Moreover, neither of the two resonant transmissibilities pass through the invariant points. The curves for extreme values of damping i.e. zero and infinity, are also included in Fig. 8.

CONCLUSIONS

The investigation into the vibration isolation of a vehicle suspension system with the conventional rigidly connected shock absorber indicates that damping is detrimental to the isolation effectiveness above resonance. Also excessive damping increases the transmitted force and, hence, leads to an increase of shock wave transmission to the body. A mathematical model of a vehicle suspension system with an elastically connected viscous damper, to represent the top rubber bush for the shock absorber, has been formulated and an expression for the absolute displacement transmissibility of the body is derived.

An optimization technique is developed in order to evaluate optimum values of the variables involved in the transmissibility expression from which the maximum transmitted motion to the body from the road surface would be minimum over the broad frequency range. It has been shown that the variation of optimum resonant transmissibility with mass ratio in the range 0.1 to 10 is of primary importance. For values of mass ratio less than 0.1 a slight change in the transmissibility values is noticed. Better isolation of vibration is achieved with smaller values of the mass ratio and larger values of stiffness ratio, Q. The variation of optimum values of variables which are presented non-dimensionally would facilitate the selection of optimum variables in the design of vehicle suspension system.

REFERENCES

1. C. M. Harris and C. E. Crede, Shock and Vibration Handbook, McGraw-Hill Book Co., Inc., New York, 1961.
2. J. E. Ruzicka, "Resonance Characteristics of Unidirectional Viscous and Coulomb-Damped Vibration Isolation Systems", Trans. of the ASME, Journal of Engineering for Industry, No. 3, pp. 729-740, 1967.
3. J. E. Ruzicka and R. D. Cavanaugh, "New Methods for Vibration Isolation", Machine Design, Vol. 30, pp. 114-121, 1958.
4. J. E. Ruzicka,"Vibration Control", Electro-Technology, Vol. 72, pp. 63-82, 1963.

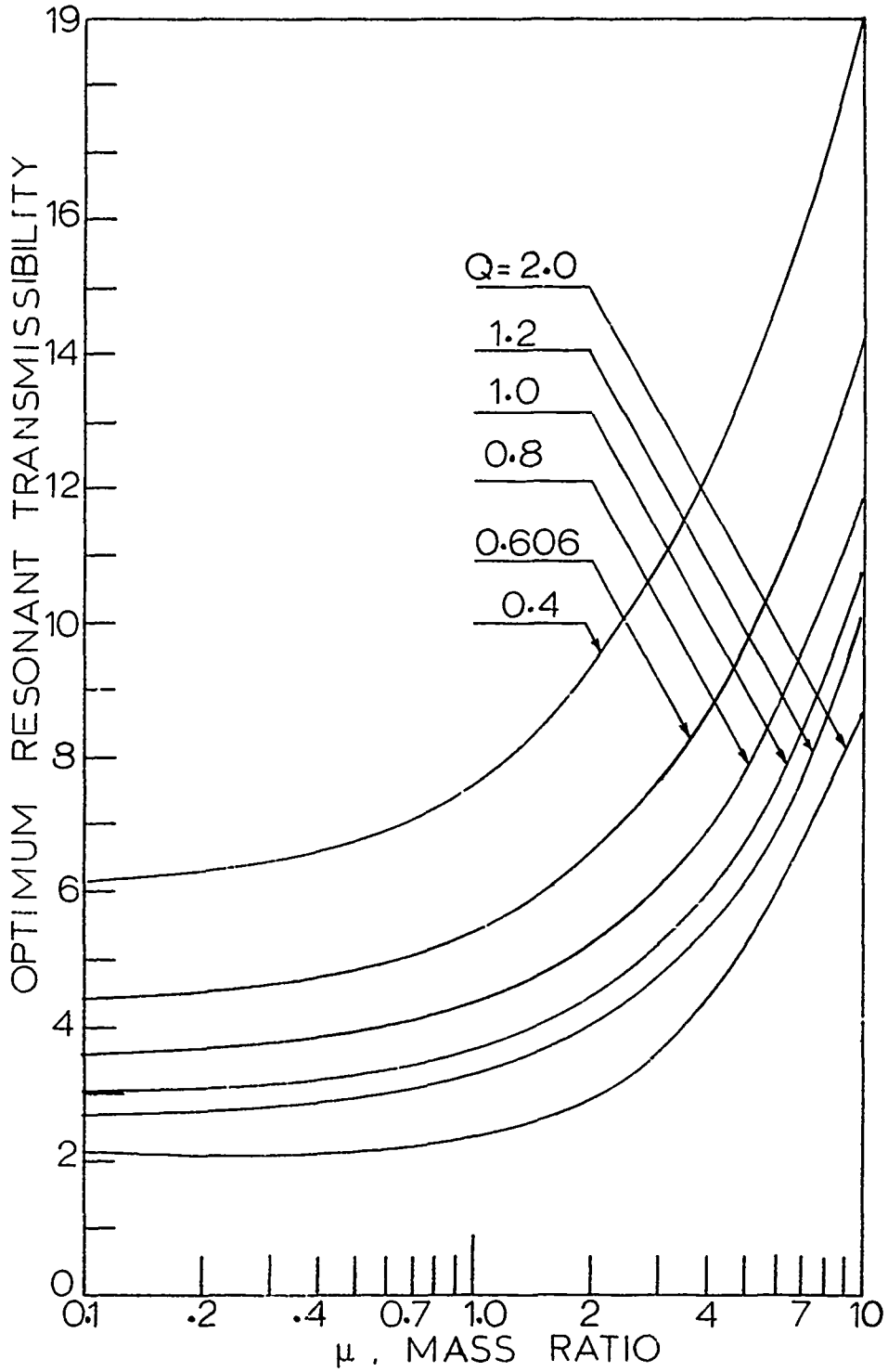

Fig. 5. Variation of Optimum Resonant Transmissibility as a Function of Mass Ratio, μ, and Damper Unit Stiffness Ratio, Q.

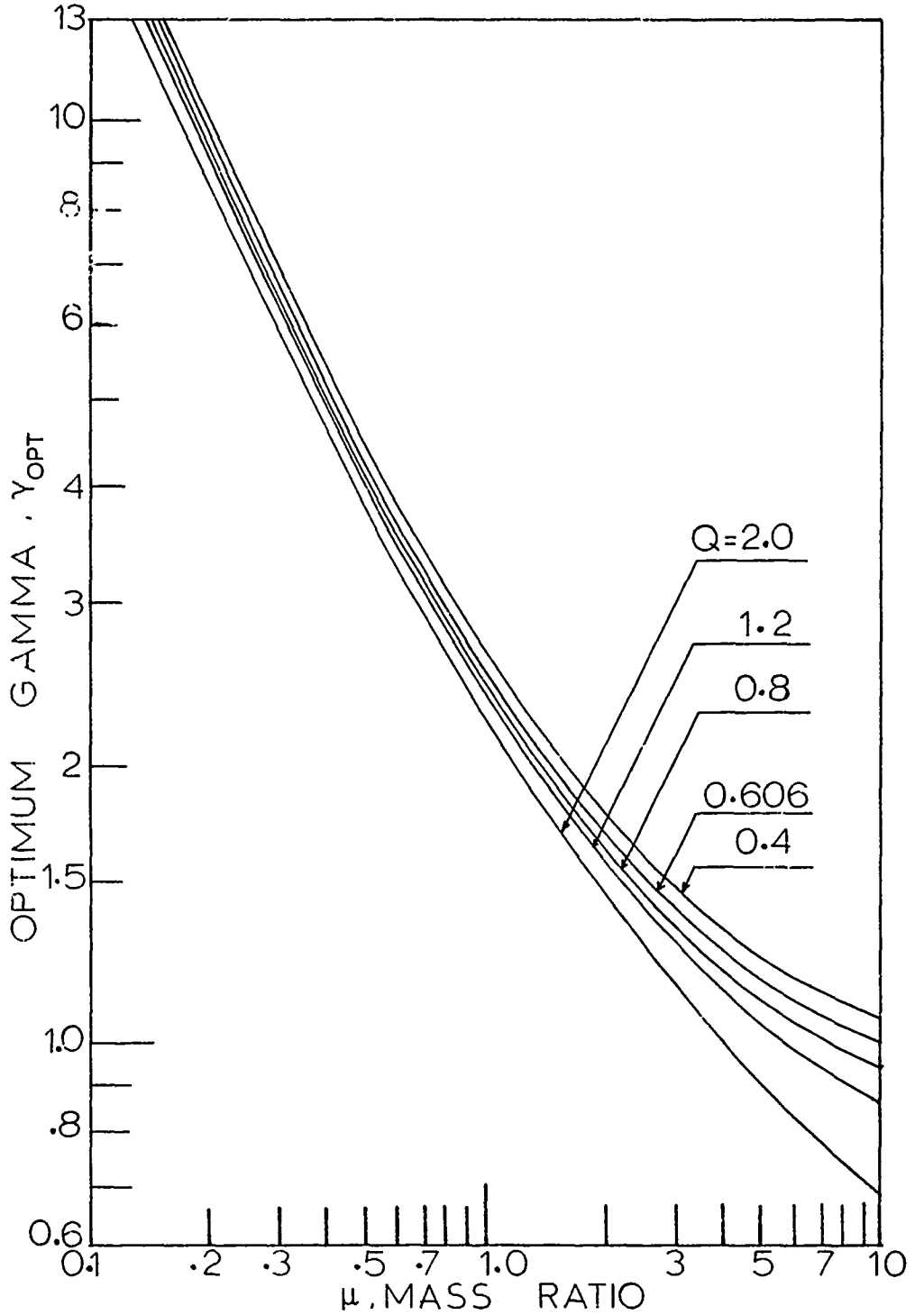

Fig. 6. Optimum Values of Resonant Frequency Ratio, γ_{opt} as a Function of μ and Q.

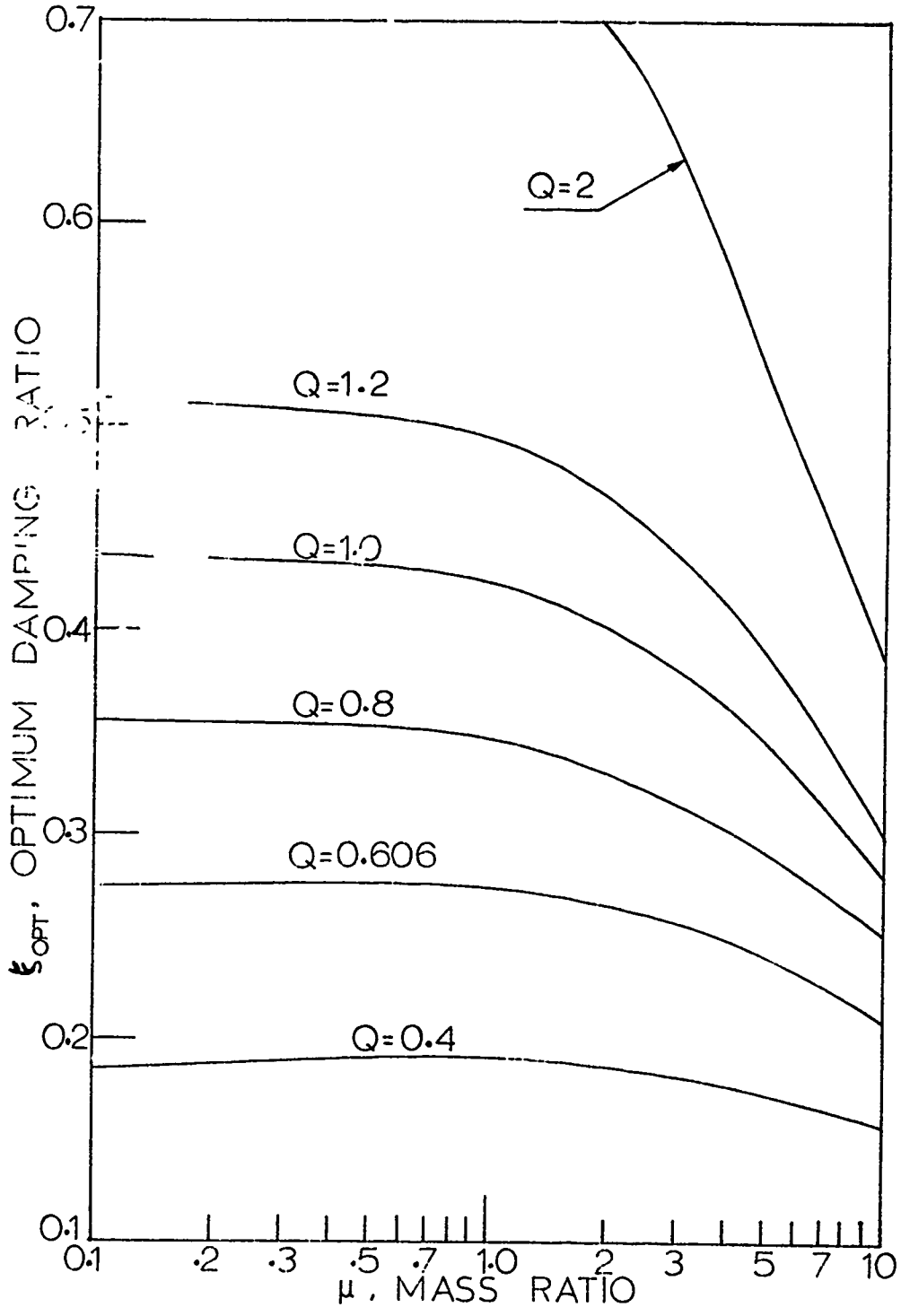

Fig. 7. Variation of Optimum Values of Damping Ratio, ξ_{opt} with μ and Q.

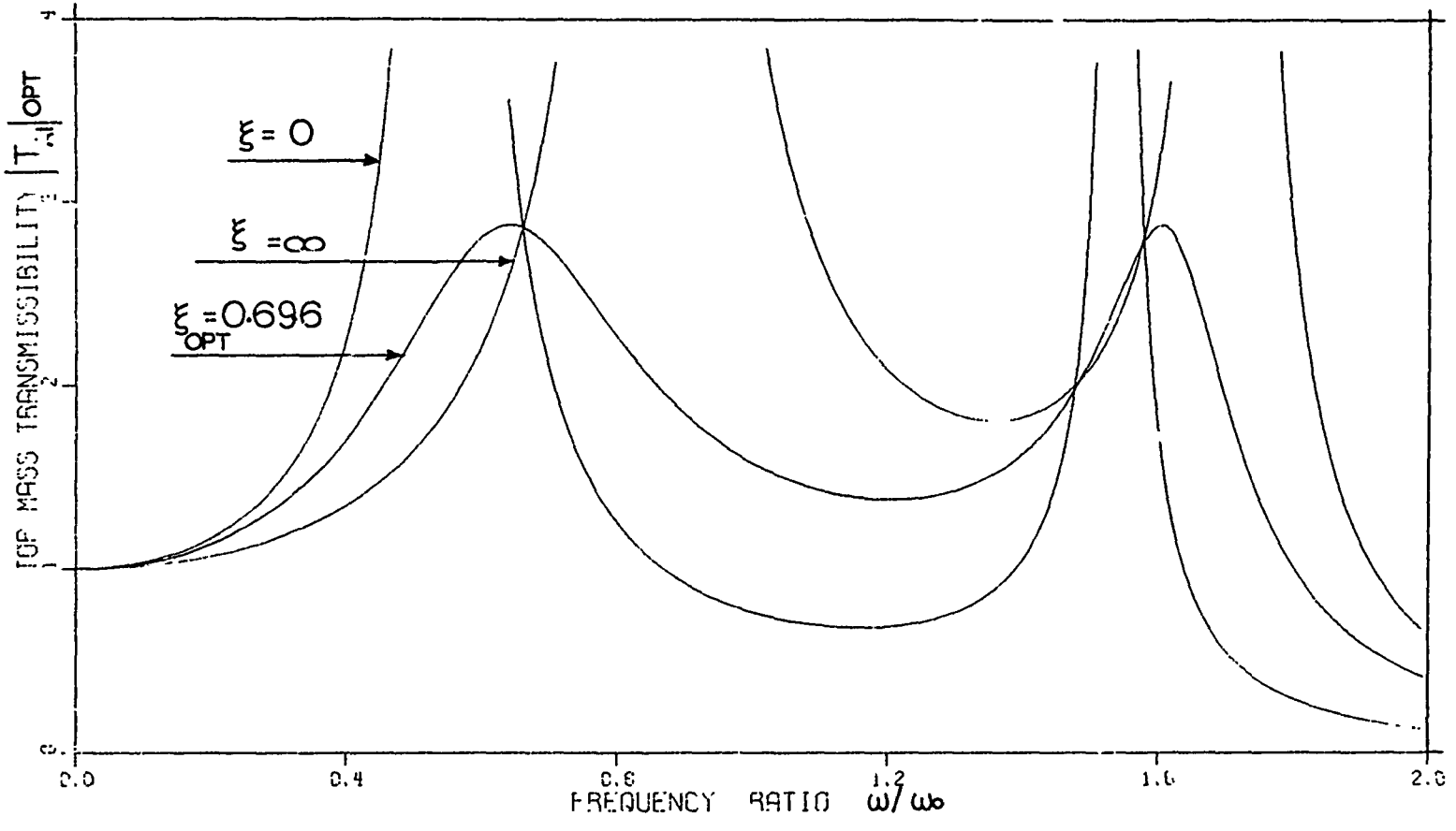

Fig. 8. Frequency Response of Body Tranamissibility for a Set of Optimum Variables: $\xi_{opt} = 0.696$; $\gamma_{opt} = 1.478$; $\mu = 2$; $Q = 2$.

5. R. N. Hamme, "Experimental Study of the Effects of Foundation Resilience on Vibration Isolation", ASME Shock and Vibration Instrumentation, pp. 41-54, 1956.
6. J. A. Bonesho and J. G. Bollinger, "Theory and Design of a Self-Optimizing Damper", 7th International M.T.D.R. Conference University of Birmingham, September 1966.
7. J. P. Den Hartog, Mechanical Vibrations, Fourth Edition, McGraw-Hill, New York, 1956.
8. J. R. Ellis, "An Introduction to the Dynamic Properties of Vehicle Suspensions", I. Mech. E. Proc.,Automobile Division, Vol. 179, Pt. 2A, No. 3, 1964.

DISCUSSION

Mr. Vatz, (Teledyne Brown): Did you look at ways of lowering the natural frequencies of both peaks and are they below the normal operating frequency of the vehicle suspension?

Mr. Esmailzadeh: In this presentation as you can see in fact it is in a nondimentional form, it is in a design form. But, for that particular case we have tried to change the stiffness ratio of the main body. We didn't have very much room to play there because it is already fixed. All we could do is put a rubber bushing on top of the shock absorber before it has been stuck to the main body. We couldn't play very much with that system because that has already been set up. However, in a passive system with pneumatic suspension which I am working on now, you can alter the characteristics of the system easily. We are negotiating with a European car manufacturer to implement a pneumatic system. It is just another air blow system because that is very well known and it has a better ride quality from the point of the softening spring system. But you have more leeway with the shock absorber type which replaces the viscous damper because the medium is compressible rather than incompressible, so we have a lot of room to play with the factors from the design point of view.

Mr. Silver, (Westinghouse): We have been doing a little work on trucks, exchanging steel springs for elastomeric type of springs and we have encountered similar things. We are making measurements as a function of a load and we are running the vehicles over roads and finding the response functions. As we load the body of the tractor trailer suspension from zero to 40,000 lbs on trucks we find the resonent frequency dropping and the damping getting less. I suppose because we have a sharper slightly lower frequency function. We are thinking we need to put in some sort of damping mechanism and the one you suggest sounds very interesting and we would like to look further into that. I have a question about this type of truck system which has a variable forcing function as a function of these parameters. What about the force generated going into the road bed; which is a very large cost factor to all of us I think? Is there any possibility that it would be a prudent thing to investigate the nature or degree of force contact into the road that might result from the suspension optimization?

Mr. Esmailzadeh: We as a team are looking at the different aspects of the roadway suspension interaction system and not only for sinusoidal input but also for random excitation and road-body interaction problem, both for the tracks and for the trucks and trailers and highways. We would be glad to give you some references.

Mr. Vatz: Speaking of the interaction of tires I was involved in a rather gross problem a number of years ago and we went to Waterways (USA Waterways Exp. Sta.) wheel. I think it was developed by our Corps of Engineers friends in Mississippi where there is a number of springs because your surface is not flat it has a lot of angles and you get into the modeling of the angles.

ISOLATION MOUNTS FOR THE HEAO-B X-RAY TELESCOPE*

H. L. Hain
Lord Kinematics
Erie, Pennsylvania

and

R. Miller
American Science and Engineering, Inc.
Cambridge, Massachusetts

This paper describes the orbiting HEAO-B X-ray Telescope experiment package and the isolation mounts which will be used to support and protect it. The design and testing phases of the isolation development program are fully described and data are presented.

THE HEAO-B OBSERVATORY

The High Energy Astronomy Observatory - Mission B is an earth orbiting satellite observatory for the purpose of performing a detailed X-ray survey of the celestial sphere. The observatory consists of the HEAO-B Spacecraft together with the X-ray Telescope. The primary viewing requirement is to provide final aspect solution and internal alignment information to correlate an observed X-ray image with the celestial sphere to within one-and-one-half arc seconds. Scientific requirements were established by a consortium consisting of Smithsonian Astrophysical Observatory, Massachusetts Institute of Technology, Columbia University, and NASA Goddard Space Flight Center. Dr. Riccardo Giaconni of SAO is the principal investigator. HEAO-B is a NASA program managed by the Marshall Space Flight Center. The HEAO-B Spacecraft prime contractor is TRW, Inc. The spacecraft provides the required attitude control and determination system, data telemetry system, space solar panels and power system, and interface with the Atlas-Centaur launch vehicle.

The HEAO-B X-ray Experiment configuration is shown in Figure 1. The high resolution mirror assembly is a grazing incidence optical system with 3.43 meter (135 inches) focal length. The focal plane crystal spectrometer, high resolution imaging detector, solid state spectrometer, and imaging proportional counter are X-ray detectors which can be positioned at the focal point of the mirror assembly. The optical bench provides precise positioning of the detectors relative to the optics. American Science and Engineering, Inc., is experiment integrator for the HEAO-B Telescope. The three thousand pound HEAO-B X-ray Telescope, shown in Figure 2, is currently undergoing X-ray calibration in preparation for integration with HEAO-B Spacecraft.

The primary interface between the HEAO-B Spacecraft and the X-ray Telescope is a set of four isolation mounts. The locations of the forward isolation mounts (two each) and aft isolation mounts (two each) are depicted in Figure 1. These isolation mounts, which are described herein,

*This work was supported under National Aeronautics and Space Administration Contract Number NAS8-30750.

HEAO-B EXPERIMENT CONFIGURATION

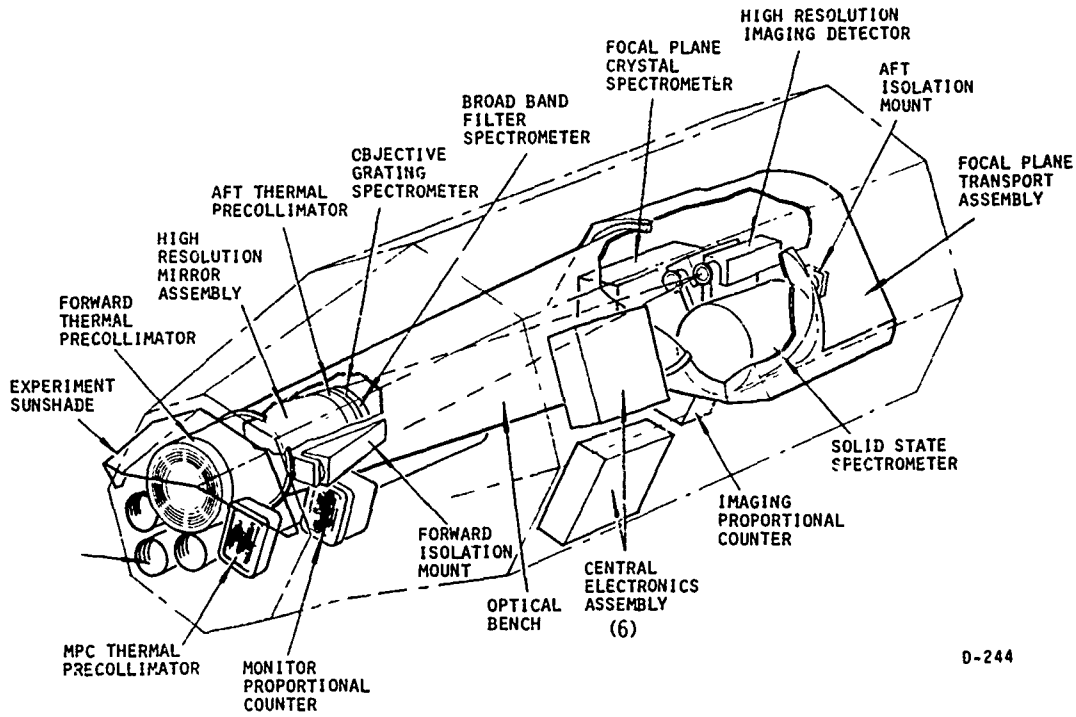

FIGURE 1

FIGURE 2 HEAO-B X-RAY TELESCOPE

were designed, fabricated, and tested by Lord Kinematics under contract to American Science and Engineering, Inc.

ISOLATOR DESIGN REQUIREMENTS

The function of the Isolation Mounts is threefold: to provide shock isolation during handling and shipping of the experiment, to produce controlled telescope-spacecraft dynamic characteristics during launch, and to minimize spacecraft induced thermal loads to the telescope during on-orbit operation. These functions are assured by proper specification of the isolator stiffness requirements as a function of load and frequency. The detailed HEAO-B isolator design requirements evolved from consideration of the launch load profile, telescope performance criteria, experiment operating environment, and state-of-the-art for elastomeric isolation mountings.

The primary launch events are outlined in Table I. A computer analysis of the static and dynamic loads was performed for the coupled Telescope-Spacecraft-Launch Vehicle. That analysis was based on isolation mount dynamic stiffness of 10,945 N/mm (62,500 lb/in) in both the axial and lateral directions.

As a result of the computer analysis, the MECO case was identified as producing the maximum dynamic loads, and the BECO case as producing the maximum static loads. Thus, the Isolation Mount dynamic stiffness requirement was established at the MECO loading condition. That is, at the predicted MECO loads and frequency the stiffness of 10,945 N/mm (62,500 lb/in) in each direction, was specified. Since stiffness less than the specified value would produce lower dynamic loads, a lower bound was also specified. The lower bound on stiffness was based on expected isolator design and manufacturing tolerances. The Isolation Mount stiffness requirements are given in Table II.

Table I - Primary HEAO-B Launch Events

Event	Acronym	Characteristics
Launcher Release	L. R.	Dynamic loading applied for a three second interval.
Maximum Aerodynamics	Max q	Dynamic loading during boost phase while at peak aerodynamic load.
Booster Firing	-	Steady state loading phase which includes Max q.
Booster Engine Cut-off	BECO	Steady state loading of maximum magnitude.
Booster Package Jettison	BPJ	Brief dynamic load during Atlas jettison.
Main Engine Firing	-	Steady state loading due to Centaur stage.
Main Engine Cut-off	MECO	Maximum dynamic load applied for one-half second at Centaur cut-off.

TABLE II - ISOLATION MOUNT STIFFNESS REQUIREMENTS

Con.	Dir.	Load x 10^{-3} (Newtons)	Load (Pounds)	Freq. (Hz)	Stiffness x 10^{-3} (Newtons/mm)	Stiffness (Lb./In.)
MECO	Axial	±13.57	±3050	25	10.94 to 8.50	62,500 to 48,400
	Lateral	±7.56	±1700	25	10.94 to 8.50	62,500 to 48,400
BECO	Axial	0 to ±23.57	0 to ±5300	Static	6.27 to 8.19	35,800 to 46,800
	Lateral	0 to ±5.89	0 to ±1300	Static	5.31 to 6.95	30,300 to 39,700
L.R.	Axial	±5.89	±1300	7 and 20	not a requirement	
	Lateral	±13.14 with 4.48 axial preload	±2900 with 1000 axial preload	7 and 20	not a requirement	

Predicted launcher release loads were specified for test purposes only. Stiffness values at these loads, given in Table II, were to be reported for reference only.

The Spacecraft-Telescope dynamic characteristics during launch are controlled by providing isolator stiffness in accordance with the Table II values. Shock isolation during handling and shipping is automatically provided by a highly damped elastomeric mount of this type. The control of spacecraft induced thermal loads to the telescope is assured by having a tested element of minimum static stiffness at the Spacecraft-Telescoper interface. A bonus in this regard is that for elastomers, the static stiffness is less than the dynamic stiffness (compare MECO and BECO in Table II). This ratio will be even greater for the small static loads encountered on-orbit.

A final design requirement is that of packaging. The Isolation Mount must be within the confines of a rather restrictive envelope (as discussed later) and have total mass less than 5.90 kg. (13.0 pounds) per mount.

DESIGN PROCESS: BACKGROUND

The design activity which took place for the HEAO-B isolation mountings was not typical of that for most vibration or shock isolators. In most cases, the isolator is specified as being required to respond with a given set of dynamic characteristics when subjected to a given vibration or shock input at the support structure side of the mounting. The function of the isolator is, then, to protect the supported equipment from this dynamic disturbance. Such was not the case with specifying the HEAO-B isolators.

Here, the dynamic disturbance was input at the launch vehicle and the response at the experiment location was studied. A computer model of the entire launcher-spacecraft-experiment complex provided the criteria for the isolator design. The isolators were simulated as linear springs and dampers. The determining factor on isolator characteristics was the magnitude of the loads transmitted to the X-ray Telescope, through the mountings, during various launch/flight events. The result of the study was the basic requirement that the spring rate of the isolator be 10,945 N/mm (62,500 lb/in) and that the isolator provide a certain amount of damping to the system. The isolator damping level was originally specified at 12.5% of critical damping.

Because of the inherent stiffness and damping properties of elastomers and the size economy of elastomeric isolators, it was decided that the mountings for the HEAO-B telescope would be elastomeric mountings. It was further decided that a silicone type elastomer would be used for reasons of its prior use and approval for space type applications due to low outgassing and stability over a broad temperature range. However, the stiffness properties of typical elastomers are not constant over a wide range of loading

conditions. This factor required a choice to be made for the actual design point of the isolator and, then, performance calculations to be made for other loading conditions of interest.

The design point chosen was the MECO (Main Engine Cut Off) event. This condition consisted of dynamic loading at 25 Hz at load magnitudes of:

$\pm$13,567 N ($\pm$3,050 lbs) axially
$\mp$7,562 N ($\pm$1,700 lbs) laterally

on each of the four mountings. At this loading condition the dynamic spring rate of the isolation mounting was to be in the range of 10,945 N/mm to 8,476 N/mm (62,500 lb/in to 48,400 lb/in). The task was then left to the designer to calculate the expected performance of the mountings at other specified loading conditions. It was quite important that the isolator performance be known over a wide range of loading conditions such that studies could be made to assure that the loads transmitted to the experiment were within allowable bounds. In order to provide such information, a thorough knowledge of the properties of the elastomer to be used was necessary.

ELASTOMER SELECTION

As was previously mentioned, the elastomer chosen for use in the HEAO-B isolators was a Broad Temperature Range (BTR^R) silicone material. The elastic and damping properties of this elastomer do vary with strain, frequency, and temperature. The strain and frequency sensitivity of this material, in particular, had to be critically examined during the design phase of the isolator development program.

Figure 3 is a plot of the dynamic modulus versus strain of two silicone base elastomers which were considered for use in the HEAO-B isolation mounts. These data were originally developed using a double shear type test sample very similar to the ASTM D-837 sample. As may be seen on the curves of Figure 3, these two elastomers exhibit the typical trend of viscoelastic materials, i.e., the dynamic modulus of the elastomer decreases with increasing strain. Since the dynamic spring rate of an elastomeric mounting is directly proportional to the dynamic modulus of the elastomer in it, this same trend of decreasing stiffness with increasing strain would be expected in the final mounting configuration. The data of Figure 3 were quite necessary to the eventual definition of mounting properties over a wide range of operating loads.

Note should be made of another significant point of consideration with elastomeric materials. That is, there is a difference not only between dynamic modulus values at different strain levels, but also between the dynamic modulus at any strain level and what we will call "static" modulus. The static properties of an elastomer are exhibited when the material is deflected very slowly (at less than 0.1 Hz). The static modulus of an elastomer is lower than the dynamic modulus in the strain region investigated for this program. Thus, the static stiffness of the final mounting will be less than the dynamic stiffness. This becomes significant in considering the performance of the isolators under conditions such as steady-state loading, e.g., accelerations. One flight event in this category is the Booster Engine Cut Off (BECO) event. Depending on the dynamic strain level at which the comparison is being made, the dynamic modulus of the elastomers considered here will be in the range of 5 to 1.2 times the static modulus.

Stiffness, both dynamic and static, was the primary specification requirement for these isolators. Secondary to this was the specification of the damping to be provided by the mountings. Figure 4 is a graph of the damping modulus (sometimes called loss modulus) of the two elastomers of interest. This modulus is that which is out of phase by 90 degrees to the previously described elastic modulus. The values of damping modulus are sensitive to frequency and strain as are those of elastic modulus. However, the trend of variability is different than for the elastic modulus. This may be seen by comparing Figures 3 and 4.

The damping value originally specified for the isolators was 12.5%. This was later found to be unnecessary since the original computerized system analysis had achieved acceptable results with the assumption of less than 1% damping. Figure 5 presents a plot of the percent damping of the BTR and BTR II elastomers which were under consideration. Percent damping may be related to the dynamic and damping moduli (G' and G") by

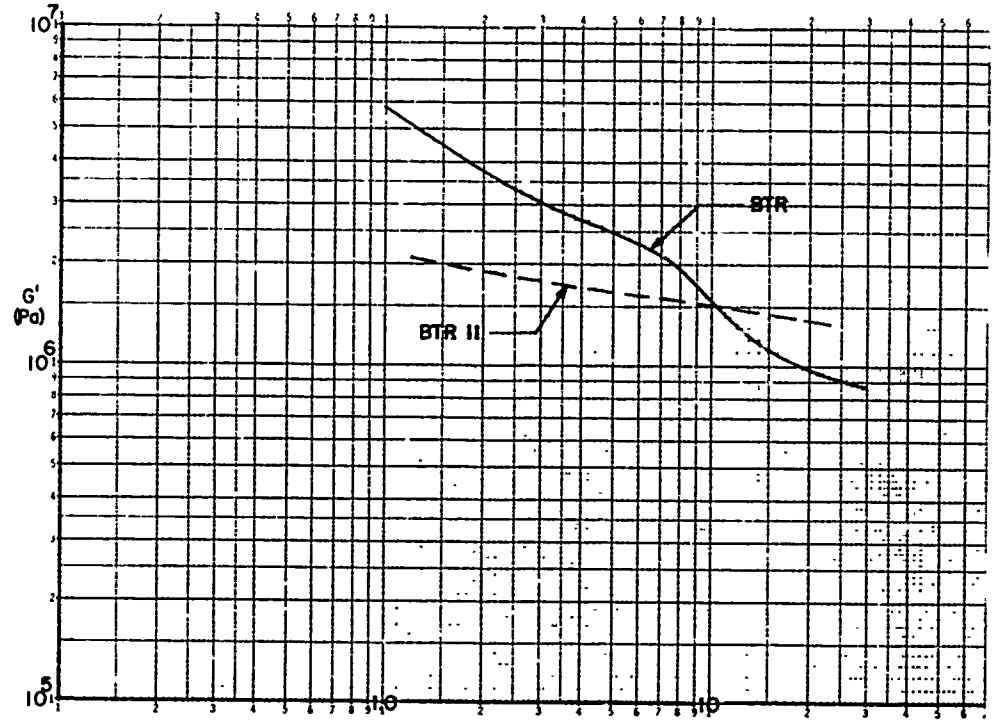

FIGURE 3
DYNAMIC MODULUS vs. STRAIN (%)

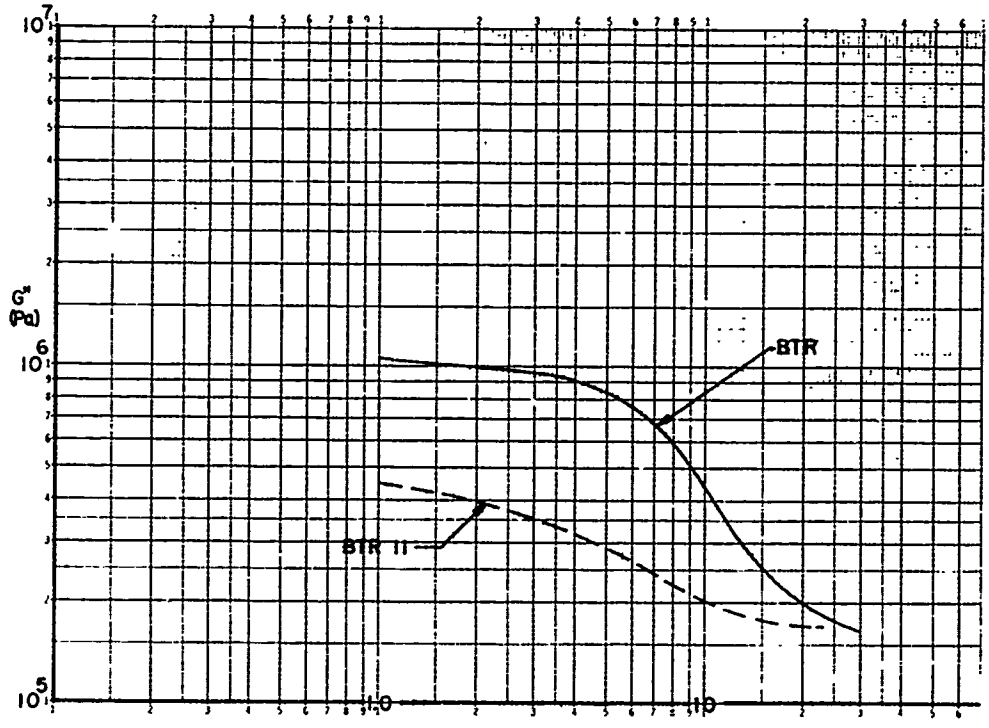

FIGURE 4
DAMPING MODULUS (G") vs. STRAIN (%)

$$\% \text{ Damping} = \frac{1}{2\ G'/G''} .$$

From Figure 5, it may be seen that either of the two elastomers would supply sufficient damping for this application.

The properties of the two elastomers shown on Figures 3, 4, and 5, were taken into account in the final selection for the HEAO-B isolators. The elastomer designated as "BTR II" was chosen on the basis of ability to meet the stiffness requirement, more linear performance over a wide range of loading conditions, acceptable amount of damping, better bondability, higher ultimate strength, better drift (creep) characteristics, and excellent stability over the specified temperature range of -10°C to +50°C (+14°F to +122°F).

ISOLATOR DESIGN AND CONFIGURATION

In order to achieve the desired mounting characteristics in the two different loading directions with the varied loading conditions, it was necessary to design an isolator with a combination of compression and shear in the elastomer. This is accomplished by locating the elastomer between nearly parallel conical metal surfaces. In order to economize space and weight and to provide a fail safe configuration, the total mounting was designed to consist of two halves, bolted together, back-to-back. Each of the two halves is made up of two metal components with the BTR II elastomer hot molded and bonded between them.

The angles of the conical metal faces are calculated to provide the right combination of shear and compression loading on the elastomer to result in the desired spring rates in the axial and lateral directions. The total size of the mounting was dictated by the maximum loads of 34,694 N (7,800 lbs) in the axial direction and 19,348 N (4,350 lbs) in the lateral direction which were specified as limit loads.

Figure 6 shows an external view of a HEAO-B isolator while Figure 7 shows a cutaway view of the interior of the mounting. This latter figure clearly depicts the conical section of elastomer sandwiched between metal components. Because of necessary strength in a minimally sized package, the top metal member and the 1/2 inch studs at the top of the isolator were 302 stainless steel. Weight considerations dictated that the remaining metal components be aluminum. In this case, 6061-T6 aluminim was used. The available space for the isolator was a box roughly 76.2 mm (3 inches) high and 209.6 mm (8.25 inches) square at the base.

CALCULATED PERFORMANCE

After considering the necessary tolerances for the design and manufacturing processes, the performance range of 10,945 N/mm to 8,476 N/mm (62,500 lb/in to 48,400 lb/in) was assigned as allowable at the MECO flight event. This was the design point for the HEAO-B isolation mounts.

At this point, acceptable operating stress and strain values for the BTR II elastomer were selected. These values set the thickness and amount of the elastomer to be used in the isolator. Once the design point was set, the data of Figures 3, 4, and 5 for the BTR II elastomer were employed to predict the performance of the mountings at conditions other than MECO. Two points of interest were the BECO and L.R. (Launcher Release) events. The loading conditions are indicated in Table II.

The BECO event, as previously described, results in a basically "static" loading on the isolators. Based on the MECO design point, the performance of the mounts at BECO was calculated to be within the bounds of 8,200 N/mm and 6,130 N/mm (46,800 lb/in and 35,000 lb/in) in the axial direction and between 6,950 N/mm and 5,300 N/mm (39,700 lb/in and 30,300 lb/in) in the lateral direction. Also, the isolator performance at L.R. was calculated as being between 11,155 N/mm and 7,775 N/mm (63,700 lb/in and 44,400 lb/in) in the axial direction and between 8,160 N/mm and 5,690 N/mm (46,600 lb/in and 32,500 lb/in) in the lateral direction.

In addition, it was desired that the performance of the isolators be known over a wide range of off-design conditions. Figures 8 and 9 are the calculated performance curves of the HEAO-B isolation mounts over the range of interest. Figure 8 is a presentation of isolator spring rate versus motion input while Figure 9 shows isolator spring rate versus load input. The manner of specification, study, and test of the HEAO-B isolators favored the presentation of Figure 9 and our

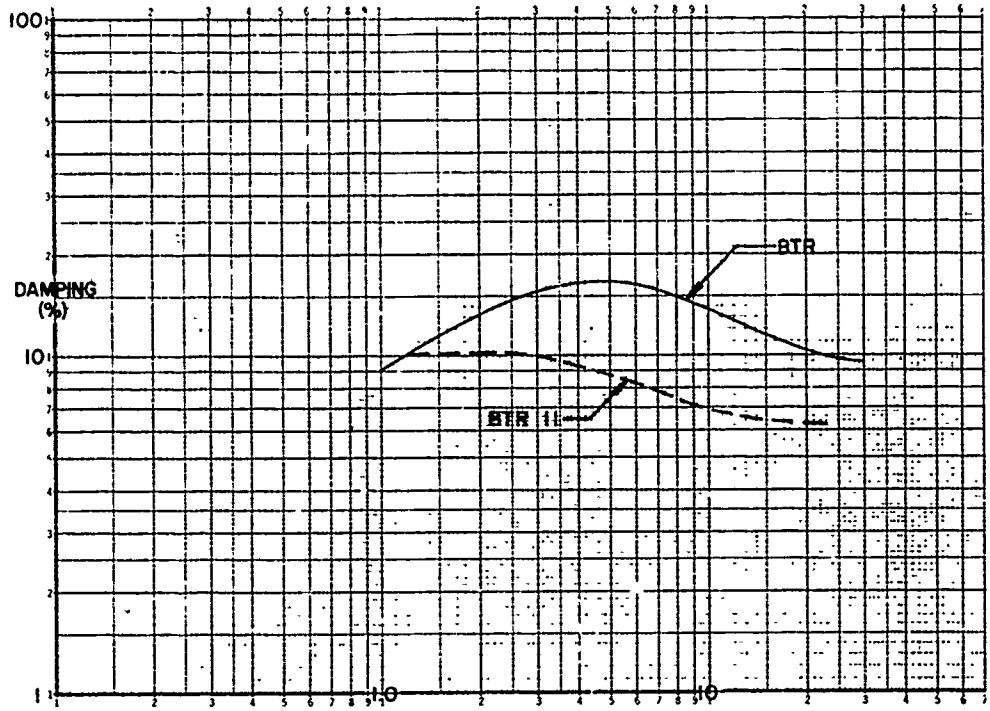

FIGURE 5
PER CENT DAMPING vs. STRAIN (%)

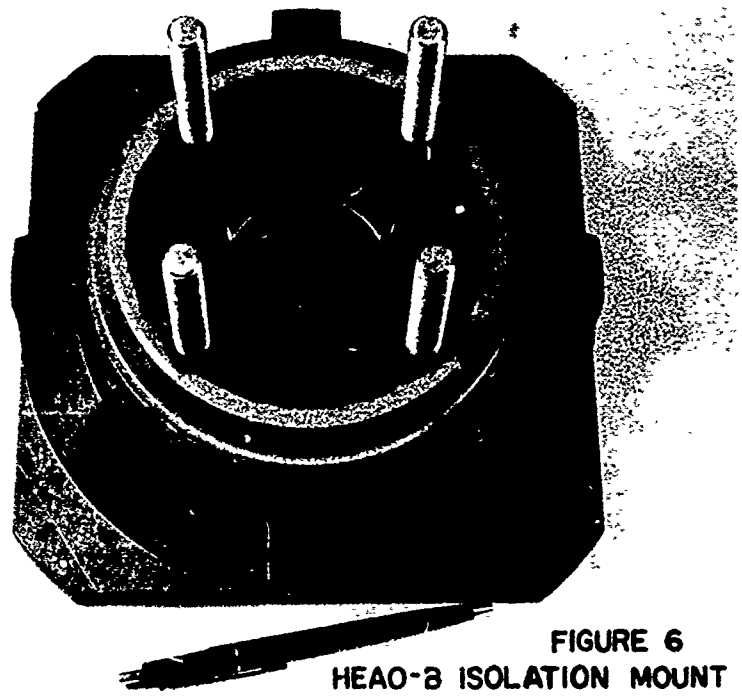

FIGURE 6
HEAO-B ISOLATION MOUNT

FIGURE 7
CUT-AWAY DRAWING HEAO-B ISOLATOR

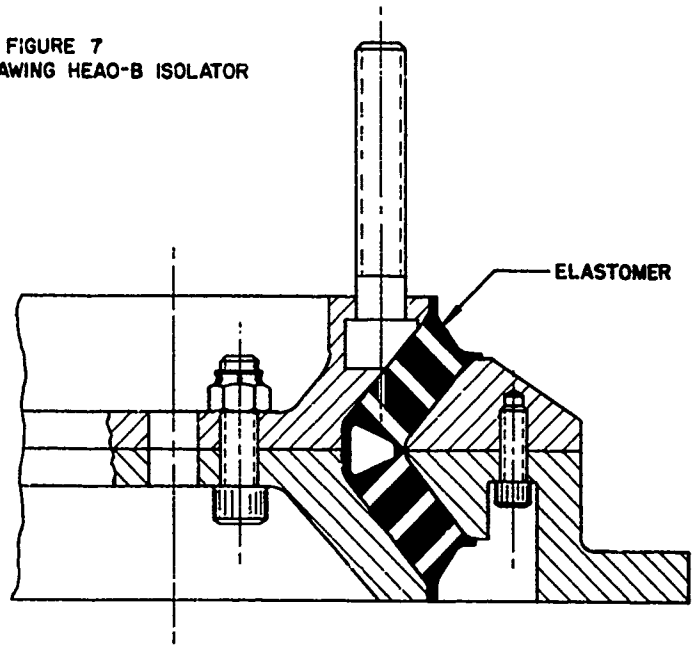

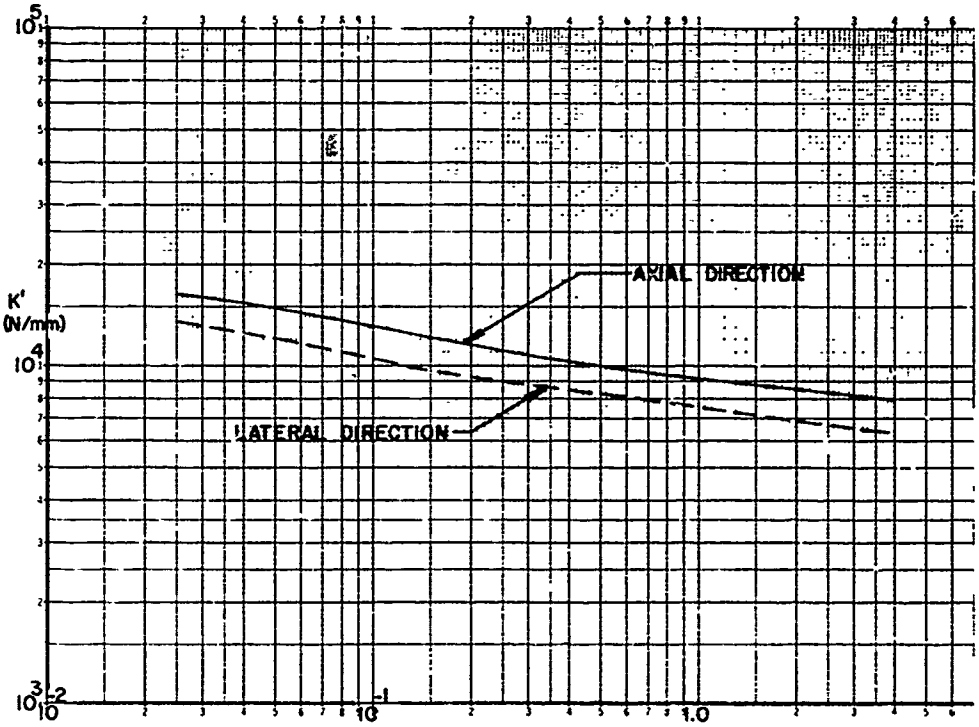

FIGURE 8
DYNAMIC SPRING RATE vs. MOTION (mm s. a.) CALCULATED BTR II

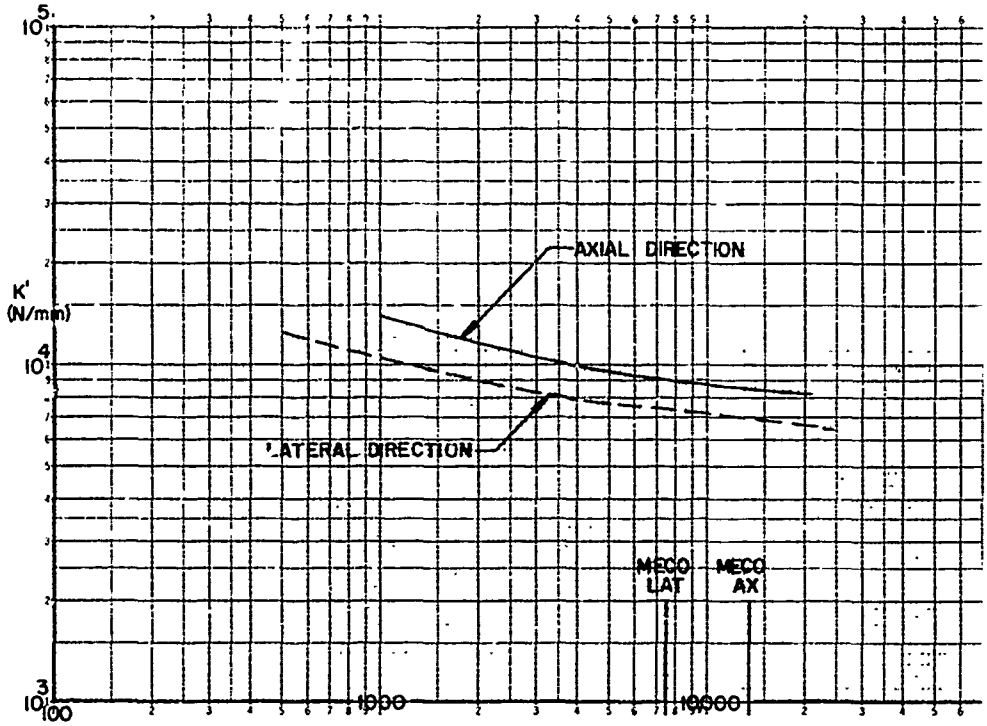

FIGURE 9
DYNAMIC SPRING RATE vs. LOAD (N) CALCULATED BTR II

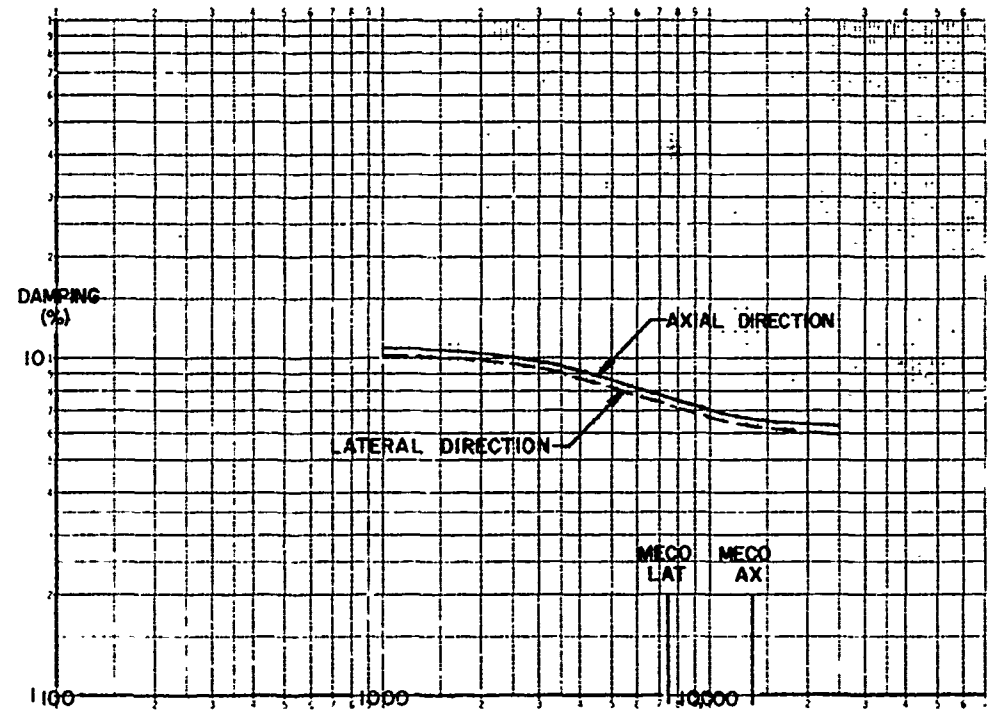

FIGURE 10
PER CENT DAMPING vs. LOAD (N) CALCULATED BTR II

further discussion will center on this calculated performance curve. For further interest and information, Figure 10 was plotted as an indication of the amount of damping to be expected from these elastomeric isolators over the range of loadings covered by Figure 9.

ISOLATOR TESTING

The HEAO-B isolation mounts are unique among vibration isolators in size, configuration, and application. Also, they are unique in the manner in which they are tested. Figure 11 shows a block diagram schematic of the test system used to determine the actual dynamic characteristics of the mountings.

The heart of this test system is the mini-computer/auto-controller segment which controls an hydraulic test machine, gathers response signals from the isolator on test, analyzes the data, and provides data output signals for a teletype printout. The control points for the HEAO-B isolator tests were the specified load conditions for the various flight events along with enough off-design load conditions to define actual performance curves over the load range of Figure 9. The specified load conditions at the given frequencies are programmed into the auto-controller and the test is conducted automatically except for the changing of the test samples in and out of the test machine.

At a preprogrammed point during the performance of a given test segment, the analyzer section of the mini-computer "reads" the output signals of deflection, elastic force, and damping force from the test sample along with a time reference at which each data point was collected. The analysis of these data points is based on a Fast Fourier Transform (FFT) method which is now being used over a wide spectrum of dynamic analyses. Reference 3 thoroughly describes the application of mini-computers and the FFT method to dynamic testing and data analysis. For purposes of this paper, suffice it to say that the basic equation involved in the FFT analysis is:

$$F_{Total}(t) = \frac{A_o}{2} + \sum_{n=1}^{N} F_{K(n)} \cos n\omega t + F_{C(n)} \sin n\omega t$$

Wherein the mini-computer is programmed to fit the actual data to the Fourier representation and to print out, by way of mathematical manipulation, the dynamic characteristics of the test sample. These characteristics may be calculated to any degree of nonlinearity desired as programmed into the analysis portion of the program.

In the case of the HEAO-B isolation mounts, only the first harmonic of the analysis equation was considered since it was known, from previous tests on similar products and from the known design point for these mountings, that the dynamic loadings would not deflect the mountings beyond their linear range of motion. The HEAO-B mountings were tested to the conditions noted in Table II and a typical data printout is shown in Figure 12. In addition to the conditions of Table II, two of the isolators were tested at a frequency of 20 Hz and at loads from ±890 N to ±4,450 N (±200 lbs to ±1,000 lbs) in order to more completely characterize the mountings.

Figures 13 and 14 are plots of the actual dynamic performance of the HEAO-B isolators against the calculated performance characteristics which were previously presented in Figures 9 and 10. Figures 15 and 16 show the actual "static" load versus deflection curves of the isolators in the axial and lateral directions of test at the BECO loading conditions. The static spring rates of the mountings were calculated as being the slope of the load deflection curve in the linear region. These spring rates are indicated on Figures 15 and 16. They were well within the allowable ranges for the static stiffnesses of the isolator specification.

One, final, long-term test of the HEAO-B isolation mounts is still in progress. That is the 60 day drift (creep) test in which the isolator is subjected to its 1g static load of 3,560 N (800 lbs) and its deflection is monitored over the entire test period. The reason for this test is to determine if the drift of the mountings will be such as to cause loss of calibration of the telescope during long-term loading prior to launch. The specification for the isolators allows a drift margin of 0.762 mm (.030 inch) after the initial deflection of the mountings due to the 1g load application.

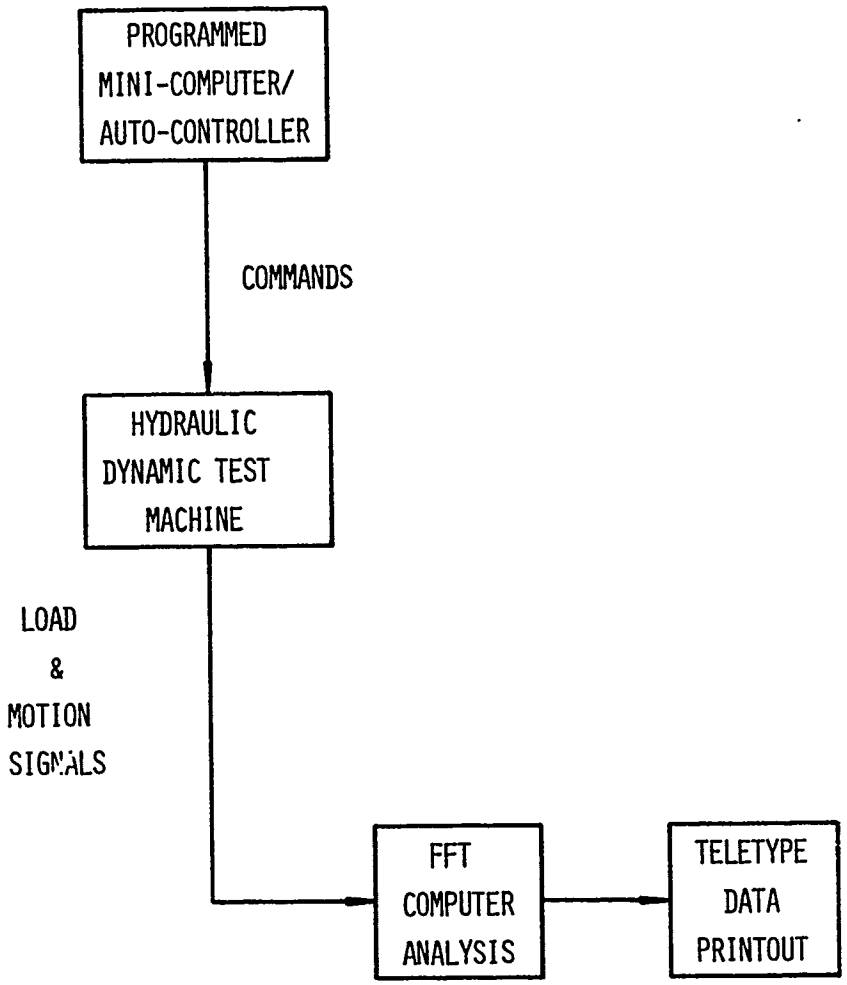

FIGURE 11
SCHEMATIC OF TEST SYSTEM FOR HEAO-B ISOLATORS

SEGMENT #1

	X	VEL	FK	FC	FTOT
MEAN	-.02110		-1012.		-1012.
RMS	.01681	.7624	958.0	148.0	969.4
(1)	.02374	1.044	1355.	206.2	1370.

K'(RMS). = .5698E+05 K''(RMS) = 8802. C(RMS) = 194.1
K'(1) = .5706E+05 K''(1) = 8683. C(1) = 197.4

C(DISS) = 182.0 DELTA = 8.652
U(DISS) = 15.33 TAN DEL = .1522
P(DISS) = 105.8 Q = 6.572
FREQ = 7.000

SEGMENT #3

	X	VEL	FK	FC	FTOT
MEAN	-.02131		-996.3		-996.3
RMS	.01649	2.100	966.2	173.4	981.6
(1)	.02328	2.926	1363.	230.2	1382.

K'(RMS) = .5860E+05 K''(RMS) = .1052E+05 C(RMS) = 82.58
K'(1) = .5854E+05 K''(1) = 9887. C(1) = 78.67

C(DISS) = 74.23 DELTA = 9.586
U(DISS) = 16.72 TAN DEL = .1689
P(DISS) = 327.3 Q = 5.921
FREQ = 20.00

SEGMENT #5

	X	VEL	FK	FC	FTOT
MEAN	.00102		-31.41		-31.41
RMS	.04205	6.680	2208.	285.4	2227.
(1)	.05945	9.338	3114.	401.2	3140.

K'(RMS) = .5252E+05 K''(RMS) = 6787. C(RMS) = 42.72
K'(1) = .5238E+05 K''(1) = 6748. C(1) = 42.96

C(DISS) = 44.15 DELTA = 7.341
U(DISS) = 79.67 TAN DEL = .1288
P(DISS) = 1970. Q = 7.762
FREQ = 25.00

FIGURE 12
TYPICAL DATA

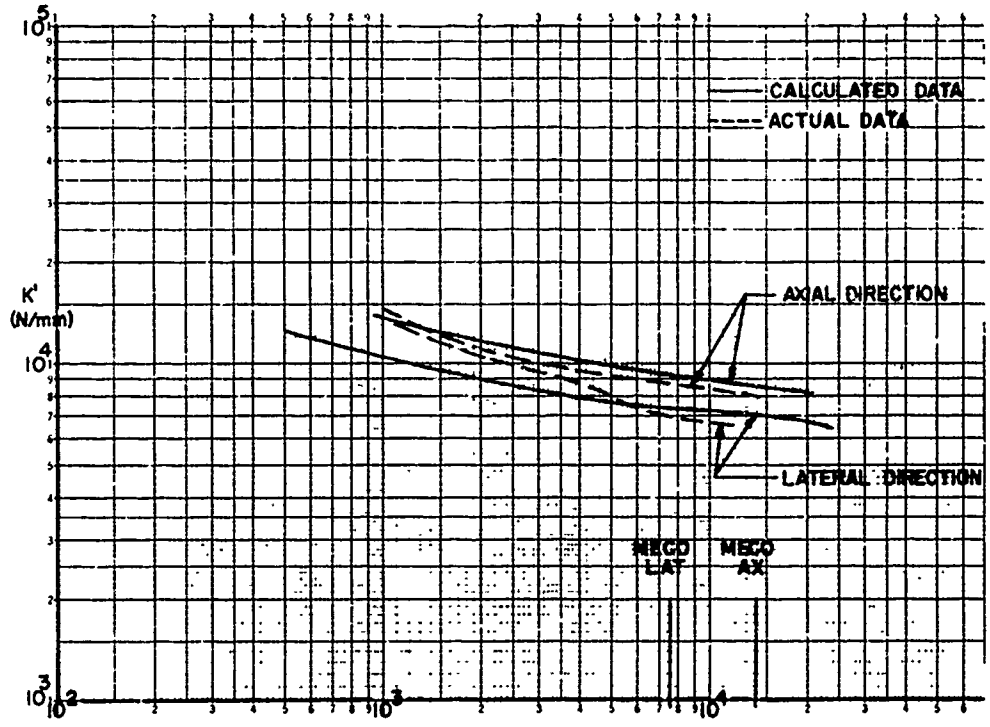

FIGURE 13
DYNAMIC SPRING RATES vs. LOAD (N) ACTUAL VERSUS CALCULATED BTR !!

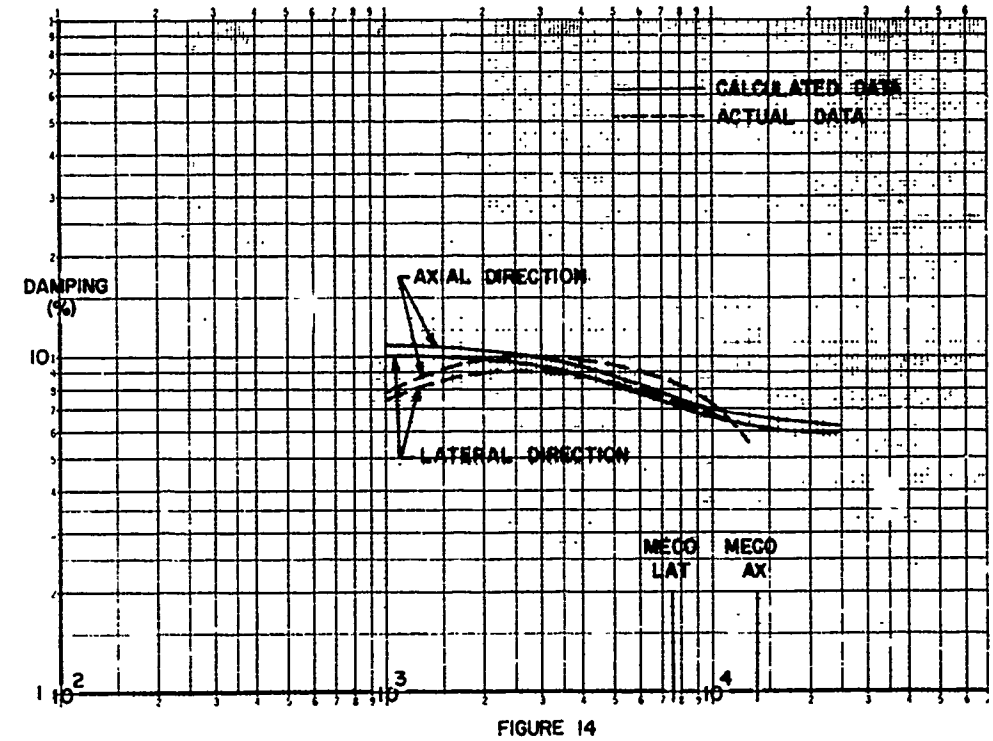

FIGURE 14
PER CENT DAMPING vs. LOAD (N) ACTUAL VERSUS CALCULATED BTR II

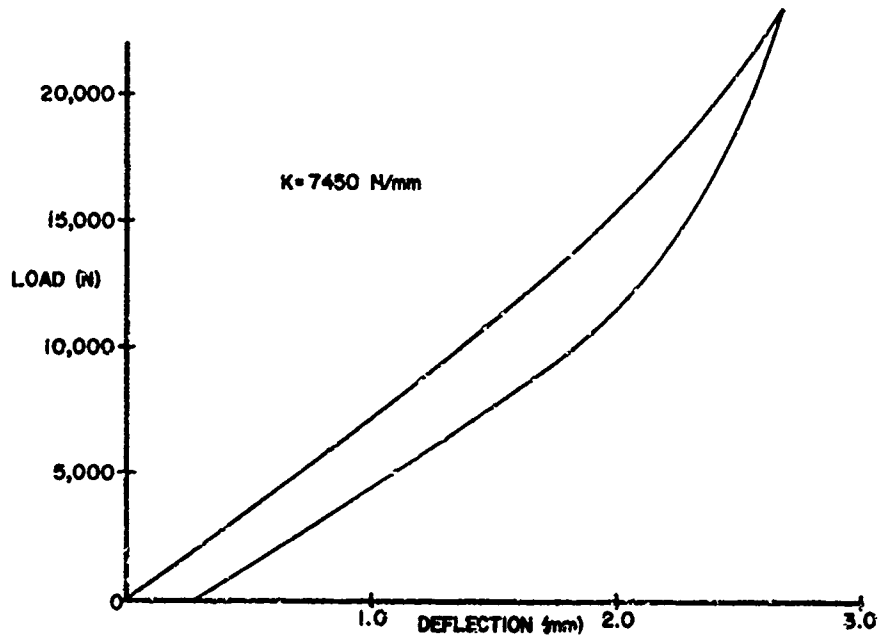

FIGURE 15
AXIAL LOAD-DEFLECTION CURVE HEAO-B ISOLATOR

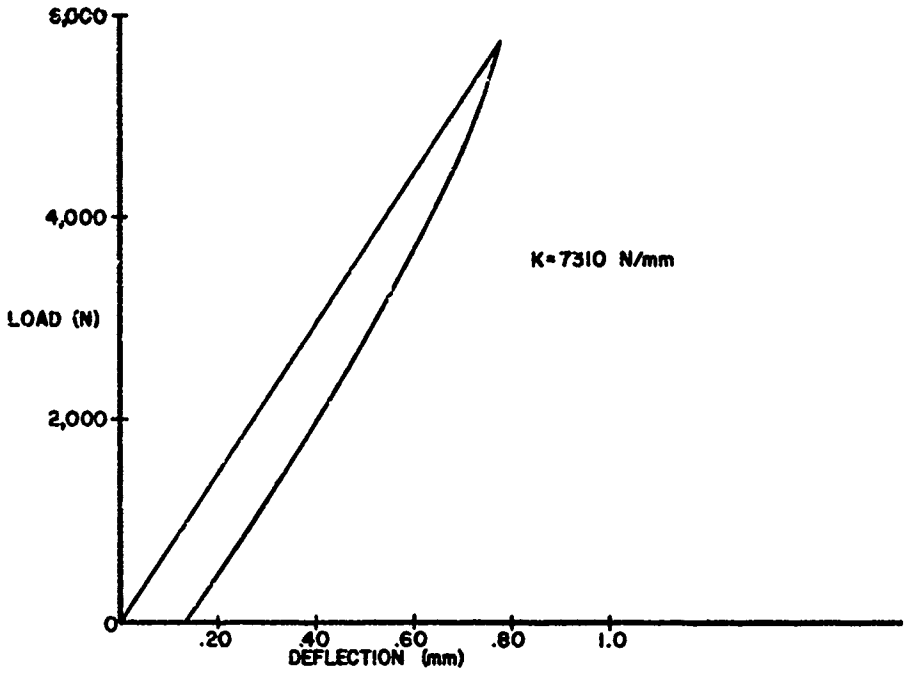

FIGURE 16
LATERAL LOAD-DEFLECTION CURVE HEAO-B ISOLATOR

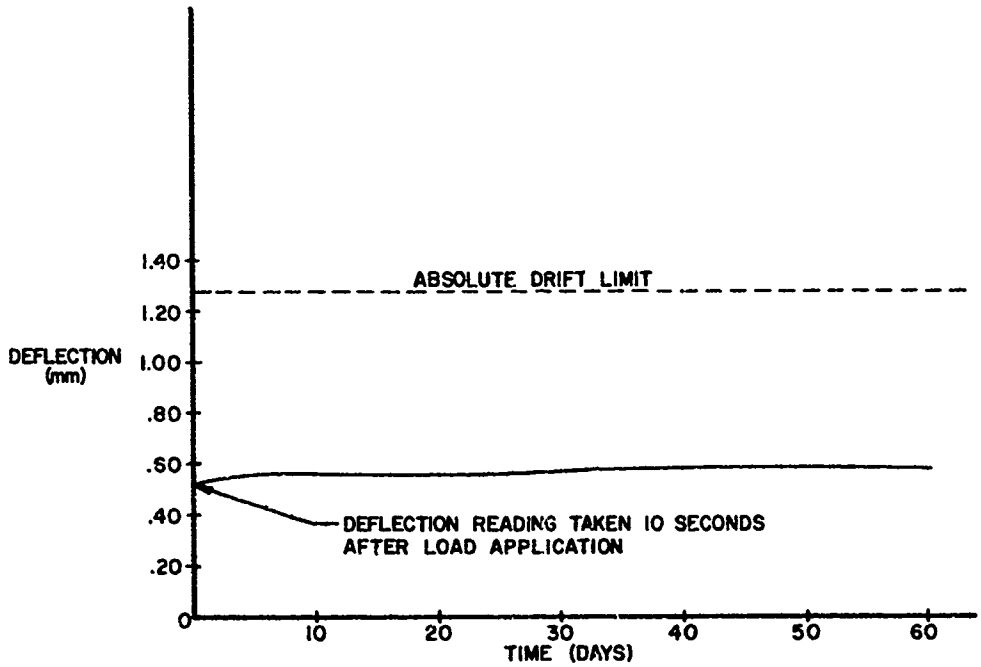

FIGURE 17
DRIFT CURVE AXIAL DIRECTION LOAD OF 3558N (800 LB)

Figure 17 presents the data gathered to date during the drift test. Projections are that the actual drift will be less than half of the maximum allowable by a wide margin. It should be noted that the drift margin was based on available data on the BTR II elastomer as loaded in shear only. The actual mountings are loaded in a combination of shear, tension, and compression. Thus, the actual drift was expected to be well within the maximum limit even prior to the beginning of the drift testing.

Finally, the aft mount mass was measured at 4.54 kg (10.01 lbs) and the front mounts at 4.97 kg (10.96 lbs). These figures were well within the allowable budget of 5.90 kg (13 lbs).

CONCLUSIONS

The completion of the testing of the HEAO-B vibration mounts and the analysis of the data serve to support several conclusions:

1. A body of data comprising the dynamic characteristics of an elastomeric material may confidently be applied to predict the dynamic performance of products in which such an elastomer is used, even though the basic material test sample is quite different in size and configuration from the end product.

2. The HEAO-B isolation mounts will perform as specified. Thus, providing the desired predictability of loading on the X-ray experiment.

3. From the plots of Figure 13, it may be calculated that the natural frequency of the system composed of the X-ray experiment and the four isolation mounts will be between 35 Hz and 21 Hz. This system will very effectively isolate the experiment from any high frequency random vibration generated by the missile engines and from most shock loadings which the experiment may encounter.

4. The HEAO-B isolation mounts exhibit low drift (creep) characteristics which should provide a very stable orientation of the experiment, thus lending to the overall accuracy of the various experiments in the HEAO-B package.

REFERENCES

1. Warnaka, G. E., "Dynamic Strain Effects in Elastomers". Rubber and Chemistry Technology, XXXVI, No. 2 (April-June 1963).

2. Painter, G. W., Dynamic Properties of BTR Elastomer. Presented at the SAE National Aeronautic Meeting, Ambassador Hotel, Los Angeles, CA., September 29 - October 4, 1958.

3. Danko, D. M. and Svarovsky, J. E., An Application of Mini-Computers for the Determination of Elastomeric Damping Coefficients and Other Properties. Reprinted from "The Measurement of the Dynamic Properties of Elastomers", SP-375. SAE. March, 1973.

ACKNOWLEDGEMENTS

The authors would like to acknowledge the support provided by the following individuals during the design-development of the HEAO-B Isolation Mounts:

- Mr. R. Hall of AS&E for definition of the isolator envelope and for specifying the isolator operating environment.

- Mr. V. Trovato of AS&E for materials and process support during the engineering development test phase.

- Mr. G. Turos of Lord Kinematics for co-ordination of the total fabrication and test cycle.

- Mr. G. Sydney of Lord Kinematics for materials and process data support during the design and fabrication phases of the program.

- Mr. R. Wilcox of Lord Kinematics for supervision of the design of test fixtures and the actual conduct of the tests on the isolators.

IMPACT

BIRD IMPACT LOADING

J. S. Wilbeck, Capt. USAF
Air Force Materials Laboratory
Wright-Patterson Air Force Base, Ohio

and

J. P. Barber
University of Dayton Research Institute
Dayton, Ohio

An extensive experimental program was undertaken to investigate the mechanics of bird impact and to define the loads which birds exert at impact. Bird impact pressures were measured by impacting birds against a heavy steel plate in which piezoelectric transducers were flush mounted. Data was collected for bird masses ranging from 60g to 4kg and velocities ranging from 50 to 300 m/s. The experimental data is presented and compared with the predictions of a fluidynamic theory.

INTRODUCTION

Birds and aircraft occupy the same air space and collisions between the two are inevitable. As aircraft speeds have increased, the severity and importance of bird/aircraft impact have also increased. As a result, efforts have been made to reduce the probability of collision by controlling the movement of birds and by changing the flight paths of aircraft. These actions can and have reduced the probability of collision but have not eliminated it.

The design of birdstrike resistant aircraft requires a better and more detailed knowledge of the response of critical aircraft components to bird impact. Programs designed to apply modern structural analysis techniques to the investigation of aircraft windshield and engine blade responses to impact have been initiated. With such tools proven and placed at the designers disposal, the process of obtaining birdstrike resistant transparency and blade designs should become much more efficient.

One of the most important inputs to a structural analysis code is the loading. The loading is particularly important in the analysis of transient response such as occurs in bird impact. For a few of the impact cases of interest, it would seem that the only loading information needed is the initial momentum of the impacting bird. Initial studies by Tsai, et al, [1] demonstrated the ability to predict the maximum deflection of simple beams impacted by soft rubber projectiles. The only information required were beam properties and the momentum of the projectile. Their analytical model gave good results for impacts of short duration (relative to the period of the beam.) However, it became apparent that for impact durations on the order of a quarter-period of the beam or greater, this model was not applicable.

In many of the impact cases of interest, such as the impact of a large bird against a flexible transparency, the duration of impact is not short relative to the period of the structure. Thus a much more detailed description of the impact loading is required. Also, any analysis of damage in the target near the point of impact requires a knowledge of the local impact pressures. The research described in this paper was designed to provide experimentally obtained and quantified loading input data. An experimental program was undertaken to measure the spatial and temporal distribution of the pressures exerted on a rigid target during the normal impact (90°) of a bird.

EXPERIMENTAL PROCEDURE

In order to study the pressures exerted by birds at impact, birds must first be launched to velocities of interest. A suitably instrumented target must then be constructed and measurements of the pressures obtained. A compressed air launching technique was developed and a flat, steel plate was employed to minimize the effect of target response on the measurements.

A compressed air gun located at the Air Force Materials Laboratory (AFML) was used to launch birds ranging in mass from 60 to 600g. A compressed air gun located at Arnold Engineering Development Center (AEDC) was used for launching birds ranging from 1 to 4kg. Both guns were capable of launching birds at velocities up to 300 m/s.

The target used at the AFML facility is shown in Fig. 1. It was a heavy steel plate in which pressure transducers were mounted. The transducers used for these tests were piezoelectric quartz pressure transducers manufactured by PCB Corporation. Four transducers were mounted flush to the surface and located at the center of impact and 1.27 cm, 2.54 cm, and 3.81 cm from the center. The steel plate, 15.25 cm in diameter and 5.08 cm thick, was mounted as shown in the figure. The transducers had a specified frequency band width from 0 to 100 kHz. A steel target of similar design was used at AEDC. Because of the larger birds tested at AEDC, the target was considerably larger, being 76.20 cm in diameter and 10.16 cm thick, and was able to accommodate up to 29 pressure transducers. Both experimental facilities are discussed in greater detail in Refs. [2,3].

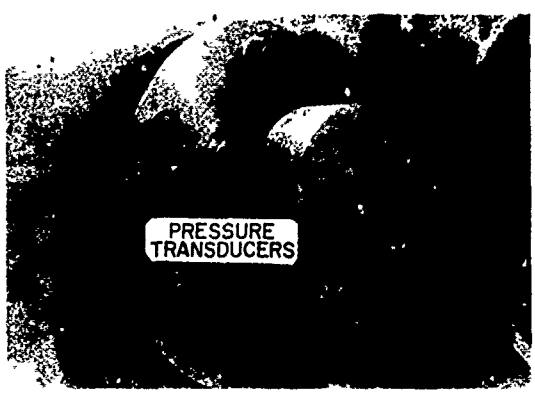

Fig. 1. The target plate at AFML.

THEORETICAL CONSIDERATIONS

In order to facilitate reduction and analysis of the large body of data collected, a theoretical description of bird impact was undertaken. This analysis was not intended to provide a rigorous description of bird impact, but rather to provide theoretical guidance to the experiments and data reduction process.

For the case of impact in which the stresses generated by projectile deceleration greatly exceed the yield strength of the projectile material, the problem can be approached hydrodynamically [4]. It became apparent during initial testing that this was true for the case of birds impacting steel targets at velocities above 50 m/s. An approximate theory was developed in which the bird was represented by a homogeneous right circular cylinder of fluid with a length to diameter ratio of approximately 2. This approximation greatly simplified the theoretical problem. An extensive amount of theoretical and experimental research has been conducted on the impact of fluids on solid targets, in which the target is assumed to have little or no plastic deformation.

The majority of work in this area has been focused on the impact of water jets and water droplets, both in the study of rain and steam erosion, as well as water jet cutting. A detailed description for the normal impact of a right circular cylinder of fluid against a rigid plate has been developed in the literature [5,6,7,8]. The impact may be divided into four phases as illustrated in Fig. 2. The initial impact phase (a) consists of very high shock pressures generated at the projectile-target interface. As the shock propagates into the projectile (b), radial release of the shocked material results in a decaying pressure at the target face. The pressure decay continues until a state of steady flow (c) is reached. At the end of the projectile approaches the target (d), the pressure decays to zero.

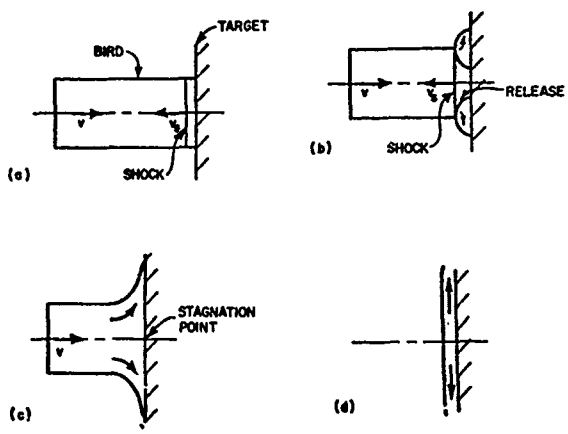

Fig. 2. The phases of bird impact (a) initial impact (b) shock decay (c) steady flow (d) termination.

During the initial impact phase, the particles at the front surface of the projectile are instantaneously brought to rest relative to the target face and a shock propagates into the projectile as shown in Fig. 2. As the shock wave propagates into the projectile it brings the material behind the snock to rest. The pressure in the shock region is initially uniform across the impact surface. For the normal impact of a cylinder on a flat plate, the flow across a shock can be considered one-dimensional, adiabatic, and irreversible. If the target is assumed to behave in an elastic manner, the pressure behind the shock may be derived from the shock relations as

$$P = \rho\, v_s\, v \left\{ \frac{\rho' v_s'}{\rho' v_s' + \rho\, v_s} \right\}, \qquad (1)$$

and ρ and ρ' are the densities of the projectile and target, respectively, v_s and v_s' are the shock velocities of the projectile and target, and v is the impact velocity. For the case of water impacting a steel target, $\rho' v_s' \gg \rho\, v_s$, so that Eq. (1) may be approximated by the relationship for the impact of a rigid target

$$P = \rho\, v_s\, v \qquad (2)$$

From this relationship, it is clear that the shock pressure depends not only on the impact velocity, but also on the shock velocity (which is, in general, a function of the impact velocity) and the bird density.

Although the shock pressure is very high, on the order of hundreds of MN/m^2, it lasts for only a few microseconds. The edge of the projectile is a free surface and the material near the edge is subjected to a very high pressure gradient. This pressure gradient causes the material to accelerate radially outward and a radial release wave forms. As this release wave propagates inward, a decrease in pressure results. The arrival of this release wave at the center of the projectile marks the end of the initial impact phase.

As the radial stresses in the projectile decrease during the pressure decay, shear stresses develop in the projectile material. If the shear strength of the material is sufficient to withstand these shear stresses, the radial motion of the projectile will be restricted. If, however, the shear stresses in the projectile are greater than the shear strength of the material, the material will "flow". The shear strength of birds is so low that the pressures generated are usually sufficient to cause flow. For the impact velocities of interest (above 50 m/s), the bird can be considered to behave as a fluid. After several reflections of the release waves, a condition of steady flow is established and steady pressure and velocity fields are established.

During the release phase, the shock is weakened by the release waves, with an accompanying decrease in shock velocity. For a subsonic impact, the shock wave will be ultimately eliminated by the release waves. In a supersonic impact the shock wave will not disappear.* The shock propagation velocity will decrease until it becomes equal to the impact velocity (a standing shock.) Behind this standing shock, the flow will be subsonic and will follow steady flow streamlines. The velocity and pressure fields in the fluid during steady flow will be different for the two cases.

For the case of a subsonic impact, the pressure at any point in the flow field during steady flow can be related to the velocity at that point by Bernoulli's equation. For the normal impact of a uniform, cylindrical projectile on a rigid plate, axial symmetry dictates that the pressure at the center of the plate is the stagnation pressure, P_s (gage pressure), and the velocity at the center is zero. Therefore, at the center of the plate, Bernoulli's equation takes the form,

$$\int_{P_o}^{(P_s + P_o)} \frac{dP}{\rho} = \frac{v^2}{2} \qquad (3)$$

where P_o and v are the pressure and velocity of the uniform flow field some distance away from the impact surface and are approximated by the atmospheric pressure and the initial impact velocity. If the fluid is assumed incompressible, Eq. (3) gives,

$$P_s = \frac{1}{2} \rho v^2 \qquad (4)$$

For most materials, the density tends to increase with the applied pressure, i.e., they are compressible, and Eq. (3) becomes

$$P_s = \frac{k}{2} \rho v^2 \qquad (5)$$

where $k \geq 1$.

Along the surface away from the center of the plate, the velocity increases and the pressure decreases. The pressure must be zero as the radial distance from the center approaches infinity.

For the case of a supersonic impact a standing shock is set up in the flow. The

* In this context, subsonic and supersonic refer to the comparison between the impact speed and the sound speed in the projectile.

change in particle velocity across the shock may be small. However, the flow behind the shock will be subsonic because of the greatly increased local sound speed. Bernoulli's equation of the form given in Eq. (3) cannot be used since the shock is a discontinuity. Instead, the change in stream properties across the shock must be evaluated using shock relations. In the region just behind the shock, the stream properties may not be constant over the cross-section since the shock will not, in general, be planar. However, at the center of the projectile the shock can be assumed planar. One-dimensional shock equations can be used to determine the pressure P_1, the density ρ_1, and the velocity v_1, at the center behind the shock. Applying Bernoulli's equation along the streamline which passes through the center of the shock wave and intersects the stagnation point, the relation for the stagnation pressure takes the form

$$\int_{(P_1 + P_o)}^{(P_s + P_o)} \frac{dP}{\rho} = \frac{v_1^2}{2} \qquad (6)$$

During impact, bird material is turned near the target surface. As a particle of fluid nears the target surface, its velocity decreases and the local pressure increases. During steady flow a pressure field is set up in the fluid. As the end of the projectile enters this pressure field, the field is disrupted due to the intrusion of a free surface (the end of the bird.) Steady flow no longer exists and the pressures at the impact surface decrease. This pressure decrease continues until the end of the projectile reaches the surface of the plate. At this time the impact event is ended.

The total duration of the impact can be approximated by the time needed for the projectile to "flow through" its length, i.e.,

$$t = \ell/v, \qquad (7)$$

where ℓ is the length of the projectile. Inherent in this relationship is the assumption that the projectile does not decelerate during impact.

EXPERIMENTAL RESULTS

During the course of this program a great many bird impact tests were conducted. The pressure traces obtained from the center transducer on two of these shots are shown in Fig. 3. Here the pressure and the time are presented in non-dimensionalized form, obtained by dividing the pressure by $1/2\ \rho v^2$ (the steady flow stagnation pressure for an incompressible fluid, Eq. (4)), and the time

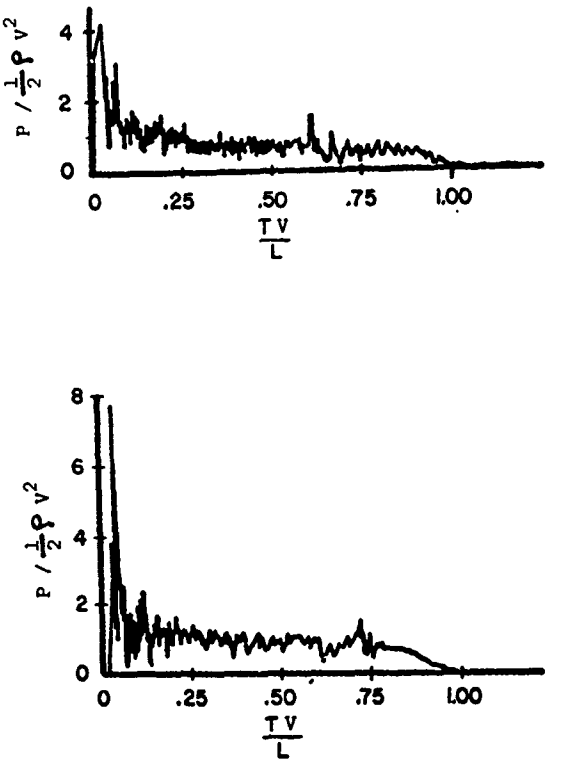

Fig. 3. Center transducer pressure traces.

by ℓ/v (the theoretical duration of impact, Eq. (7)). The bird sizes ranged from 60g to 4kg. All of this data was reduced and analyzed. Measurements of peak (shock) pressure, steady flow pressure, and pressure duration were obtained.

In order to use Eqs. (2) and (3) to predict impact pressures, a constitutive relationship was needed to represent the bird (chicken) material used in these tests. Work by Wilbeck [2] showed that a gelatin mixture with 10 percent porosity (ρ = 0.95 g/cc) was an adequate simulant for a chicken. The constitutive model derived for that mixture was used to represent birds.

Earlier it was pointed out that the highest pressures generated during the impact should occur during the initial stages of the impact. The pressure should rise to the shock (Hugoniot) pressure. The initial impact pressures measured for all the normal impact tests for which the initial impact pressure could be read are presented in Fig. 4. The measured impact pressures agree well with the calculated pressures, Eq. (2), for large birds (i.e., 4kg). However, the results for smaller birds show significant departures from prediction. The discrepancy appears to increase with decreasing bird size.

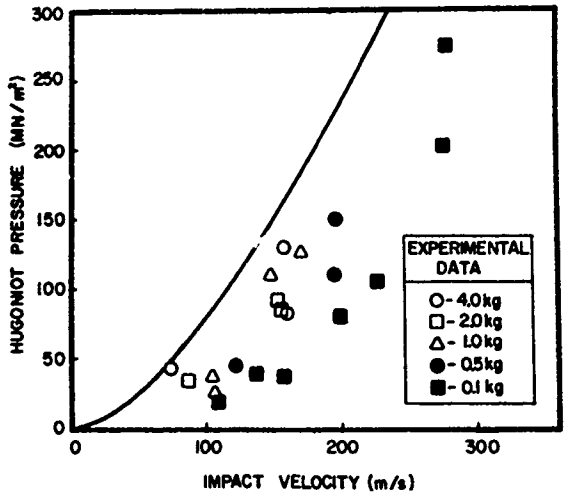

Fig. 4. Initial impact (Hugoniot) pressures versus impact velocity for normal impact.

This may be explained by considering the shock process. The duration of the shock pressure is directly proportional to the bird diameter or radius. Large birds produce the full shock pressure for longer duration than do small birds. The limited band width of the transducers (100 kHz) results in a significant attenuation of the measured signal for the short shock durations (several μs) which might be expected for small birds. Thus, it is not entirely surprising that the full shock pressure is not detected in small bird impacts.

For virtually all the impacts conducted a steady pressure region in the pressure record could be identified, as seen in Fig. 3. The center transducer data for normal impacts was collected and compared to predicted stagnation pressures. For the assumed bird material model, the impacts were supersonic and the predicted stagnation pressures were obtained using Eq. (6). The results are shown in Fig. 5. The pressures measured at the center of the plate correlate well with the predicted difference between experimental results of small birds (60g) and medium size (600g) birds. The limited large bird data also shows good agreement.

The steady flow pressure data obtained from the transducers located off-center is presented in Fig. 6. The experimental results are compared to a theoretical distribution, developed in Ref. [2], which satisfies three conditions; (a) the pressure at the center of impact is the stagnation pressure, (b) the pressure is zero (atmospheric) at large distances from the center, and (c) momentum is conserved. The data is presented in Fig. 6.

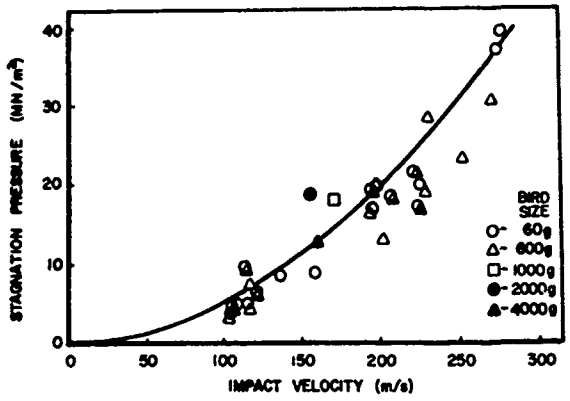

Fig. 5. Steady flow pressure versus impact velocity at center of impact for normal impact.

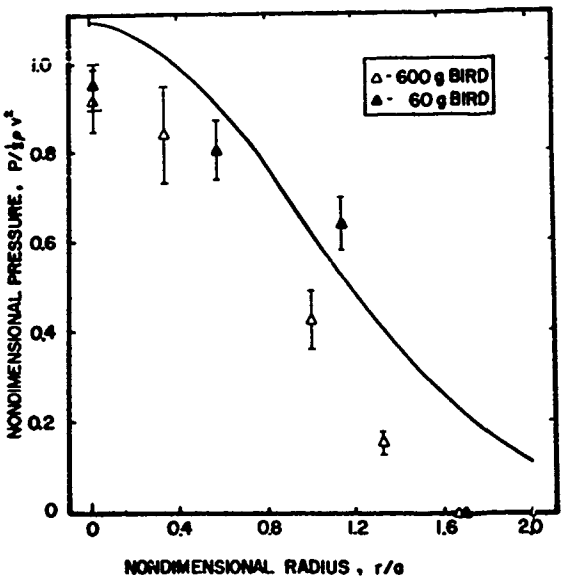

Fig. 6. Steady flow nondimensional pressure distribution for normal impacts.

Because of the large scatter in the data, only average values are presented. The large error bars on the mean values of pressure are indicative of this scatter which was most probably due to lack of cylindrical symmetry in real birds and to real variations in bird properties from bird to bird.

As seen from the two examples in Fig. 3, the duration of the impact was adequately given by the relation $t = \ell/v$, Eq. (7).

SUMMARY AND CONCLUSIONS

In summary, the pressure measurements

indicate that birds behave as a fluid during impact. The pressure records consist of an initial high pressure associated with the one-dimensional impact stress in the bird. This pressure decays by radial release of the high impact pressures. A steady flow regime is then established. The steady pressures finally decay and the pressure drops to zero when the end of the bird reaches the plate.

The important features of bird impact pressures can be analytically described, assuming the bird has material properties similar to gelatin with approximately 10 percent porosity. The initial impact pressures can be calculated using the Hugoniot relation ($P = \rho v_s v$) for a mixture, together with the shock properties of gelatin. Steady flow pressures and pressure distributions can be obtained using Bernoulli's equation and potential flow theory, as described in Ref. [2]. The duration of impact is simply the time required for the bird to travel its own length.

RECOMMENDATIONS

The development of a standard substitute bird for use in development and qualification testing should be pursued. The current investigation has shown wide variation in every parameter of impact loading which was measured. These variations are undoubtedly due to real variations in bird material properties, bird structure, and bird geometry. These variations are beyond the control of the experimenter or test engineer. The demonstrated variations can be very large and represent an unacceptable and uncontrollable test variation. In contrast to real birds, the use of substitute bird materials would provide highly repeatable loading. This repeatability offers very significant advantages in the development and qualification of aircraft components. Further work is required to more carefully investigate and document the properties of candidate substitute bird materials such as gelatin with 10 percent porosity. The effects of substitute bird geometry also require investigation.

ACKNOWLEDGMENTS

This research was jointly supported by the Air Force Materials Laboratory and the Air Force Flight Dynamics Laboratory. Impact testing was conducted at AFML's Impact Mechanics Facility and at Arnold Engineering Development Center. The authors wish to thank Mr. R. Peterson of AFFDL for his assistance and continued support of this program. The efforts of the technical staff of the University of Dayton in conducting the experiments, reducing the data and preparing this report are also gratefully acknowledged.

REFERENCES

[1] S.W. Tsai, C.T. Sun, A.K. Hopkins, H.T. Hahn, and T.W. Lee, "Behavior of Cantilevered Beams Under Impact by a Soft Projectile," AFML-TR-74-94, Nov. 1974.

[2] J.S. Wilbeck, "Impact Behavior of Low Strength Projectiles," PhD Thesis, Texas A&M University, May 1977. (to be published as AFML-TR-77-134.)

[3] J.P. Barber, J.S. Wilbeck, and H.R. Taylor, "Bird Impact Forces and Pressures on Rigid and Compliant Targets," (to be published as AFFDL-TR-77-60.)

[4] H.G. Hopkins and H. Kolsky, "Mechanics of Hypervelocity Impact of Solids," Proceedings of the Fourth Symposium on Hypervelocity Impact, Eglin AFB, Florida, 1960.

[5] S.S. Cook, "Erosion by Water-Hammer," Proc. Roy. Soc. London, Ser. A, Vol. 119, pp. 481-488, 1928.

[6] F.P. Bowden and J.E. Field, "The Brittle Fracture of Solids by Liquid Impact, by Solid Impact, and by Shock," Proc. Roy. Soc. London, Ser. A, Vol. 263, pp. 331-352, 1964.

[7] F.P. Bowden and J.H. Brunton, "The Deformation of Solids by Liquid Impact at Supersonic Speeds," Proc. Roy. Soc. London, Ser. A, Vol. 263, pp. 433-450, 1961.

[8] L.A. Glen, "On the Dynamics of Hypervelocity Liquid Jet Impact on a Flat Rigid Surface," Jour. App. Math. Phys. (ZAMP), Vol. 25, pp. 383-398, 1974.

DISCUSSION

Voice: I would like to ask a question. Where are we in the state of the art? Could you summarize where we are in Foreign Object Damage (FOD) and in blade design in general?

Capt. Wilbeck: In FOD of course there are several areas which we worry about. We have been studying lately such things as sand impact. Sand particles do cause small craters; small craters cause cracks and cracks can ruin titanium. So we are looking at that sort of thing right now to try to understand different types of particle impacts. As far as bird impact, we have a new program out, just won by General Electric to develop design methodology for engine fan blades. It is a very large program which will take data such as was just generated here and develop computer analyses which will aid in designing engine fan blades which will not break the first time around. Building fan blades is like the old pholosophy of building many things; you build one, test it and if it breaks you come back and build another. This is a very expensive process which costs many millions of dollars, on such things as composite fan blades. We feel with this type of program we will learn to design intelligently.

Voice: Is there any merit to the consideration of the design of a frangible composite blade as opposed to a titanium blade?

Capt. Wilbeck: There are two basic approaches to making a blade, one is to make a blade which will survive the bird impact. That is the normal process. In the normal approach you make a titanium blade or a steel blade which will actually eat the bird up and keep going. The other approach is a frangible blade, one that might be made of graphite epoxy which totally shatters in a million pieces when struck. One of the biggest problems with blade breakage is not that you loose one blade, because I could fly with one blade going sometimes. What I can't allow is that the titanium blade goes through the engine, it will churn through the next few stages and you may end up with a titanium fire and everything else. It is a very big problem so you try to keep the blade from breaking in the first place. The other approach is to make the blade frangible so it will break into many pieces, sawdust in essense which the engine can ingest. I think both approaches are being tried right now. Many people feel you can't afford to loose one blade; if that is the case then the frangible blade is not a good approach. If it is a fact that you can afford to loose one or two blades and not get into too much of a vibration problem then the frangible blade concept deserves some consideration.

Gary Fox, (Rohr Marine:) Is there a problem with the bones in the chicken as opposed to modeling with it with just gelatin? It seems to me it would be more difficult.

Capt. Wilbeck: That is a very good question. As I said you have to assume some sort of homogenious material as far as what theory can do. We have seen no effects with bones. The pressures we are talking about is between 30,000 psi on impact so bone probably flows just like the rest of the bird. We have seen no effects due to bones up to four killogram birds. We have never seen bone impact, of course I am not sure you wouldn't know what you were seeing but we have not seen any effect of something like that. We always thought it was possible but we haven't seen the effects.

Dr. D.I.G. Jones, (Air Force Materials Lab.:) What was your rationale for choosing a 10 percent porosity.

Capt. Wilbeck: I was going to get back into that. First of all if you look at a bird you realize it is a porous medium, it has lungs and air sacks and other sorts of things. Historically people who made substitute birds made them with porosity because without porosity the density was too high; gelatin has a density of 1.05 gr/cc and some rubber compounds have a density of 1.5 grams per cc. They would inject porosity to decrease the density. Another reason for putting in the porosity in that porosity does several things. It decreases density, decreases shock velocity and increases compressibility. In order to simulate the sort of shocks we are talking about, if you had no porosity the shocks would be an order of magnitude greater than we are seeing. If you put in the 10 percent porosity the shock velocity drops considerably and the shocks come in line with what we are seeing. Again there is both a physical and theoretical reason for putting porosity in.

Mr. Silver, (Westinghouse Electric): Referring to your data fit to the actual birds where your curves almost match, is that 10 percent porosity curve analytical?

Capt. Wilbeck: Yes, all the data I showed you, the two data traces, were for 10 percent porosity.

Mr. Silver: Would 15 percent or a little higher have fit those heavy birds a little better?

Capt. Wilbeck: Which data are we talking about, the shock pressure or the steady flow pressure?

Mr. Silver: The shock pressure.

Capt. Wilbeck: Sure! If I increase the porosity it would fit the data better. But I will not change the porosity solely because it fits my data better. I have to have a physical reason for doing that. My physical reason for making it 10 percent was first of all gelatin has a density similar to the flesh of a bird, chickens for example have a density of .95 and so physically by best approach is 10 percent porosity. I think my theory would not be significantly different if I changed the porosity by 5 or 10 percent. My accuracy of data measurement is no greater than that, I think.

Mr. Silver: You might get a little surface effect that would increase the porosity.

Capt. Wilbeck: Yes, of course there are feathers, there are all sorts of problems and surface effects is one.

Mr. Silver: Could you actually have a test using a bag of gelatin with inserted porosity?

Capt. Wilbeck: We currently shoot a commercial gelatin. We have shot gelatin with 10 percent porosity and shot rubber with 40 percent porosity. Gelatin with 10 percent porosity gives results which are close to the data I am showing here. It looks better because it is not a cylinder and birds are not cylindrical.

Mr. Wayman, (McDonnel-Douglas): Are you saying there is no justification for using bones? I know in watching our movies of bird impacts we see bits of the bones still intact after the impact.

Capt. Wilbeck: I see no pressures being generated by bones which is significantly different than that being generated by just pure gelatin. There is no pressure data that we see anywhere that shows us getting higher pressures than we expected and I don't think that a bone would give me a higher pressure. A bone being porous might give me a lower pressure than nonporous water. I see no reason from a pressure point of view of putting it in.

Voice: Are you saying that pressure is the only damaging effect?

Capt. Wilbeck: Well again the only thing that makes a hard object worse than a soft object is that the shock pressure is higher and it lasts longer. With a soft object you get roughly the same shock you get with a hard object but slightly different because of the difference impedances. You get the same sort of high pressures; but you get release weights in a soft object. In a steel bullet you don't get release weights. So your shock pressure lasts for a longer period of time. We have never seen any for example in the steady flow region where you would expect to see a high pressure spike from a bone impact coming in later on in time, we haven't seen anything of the sort.

FREQUENCY RESPONSE AND DIFFERENTIATION REQUIREMENTS FOR IMPACT MEASUREMENTS

Anthony S. Hu, Sc.D. and Han-Tau Chen, M.S.
Physical Science Laboratory
New Mexico State University
Las Cruces, New Mexico 88003

Impact response data are often subjected to integration and differentiation procedures. These procedures are low- and high-pass filtering processes. This paper discusses the measurement frequency response requirements using harmonic analysis and shows how these requirements are related to three differentiation procedures. Results indicated that for operations in the frequency domain, the bandwidth used for differentiation must be higher than that used to reconstruct the function itself. For operations in the time domain, the sampling rate must be sufficiently high to avoid frequency cutoff.

INTRODUCTION

In impact experiments, the responses of the test object and other related components are frequently recorded using electronic and photographic methods. A complete set of kinematics consisting of the data of acceleration, velocity, and displacement is often required in biomechanical experiments. Depending upon the type of transducers, various integration and differentiation procedures can be used.

Integration and differentiation, when considered in frequency domain, are low- and high-pass filtering processes where the frequency harmonics (components) are weighted at -6 dB/octave and +6 dB/octave respectively. Therefore, an acceleration measurement requires higher frequency response than a velocity measurement. A velocity measurement in turn, requires higher frequency response than a displacement measurement. Although integrations and differentiations can be applied quite freely to the measurements, they have drawbacks. For example, a single integration accumulates bias error proportional to time and a double integration accumulates bias error proportional to time-squared. On the other hand, a differentiation removes the bias error but amplifies the high frequency noise associated with the measurement.

This paper discusses the frequency response requirements for measurement data which are subjected to the processes of integration and differentiation. This allows compatible kinematic comparisons between the electronic and the photographic data. Furthermore, since the frequency response requirement becomes more stringent only when taking derivatives, this paper discusses only the differentiation requirements.

HARMONIC ANALYSIS

Fourier series, in a least-squares error sense, is a powerful tool involving periodic functions. Since many real-world impact data do not involve periodic functions (aperiodic functions), the more complicated Fourier transform must be used [1]. However, if proper arrangement of a section of the data can be made, Fourier series analysis is still applicable.

Figure 1a illustrates a section of the aperiodic data with initial value b and period T. The slope between the initial and final value is m. When this section of the aperodic data is made to repeat itself as shown in Figure 1b, this function becomes periodic and the Fourier series representation is

This work was supported by the Department of Transportation, National Highway Traffic Safety Administration under Contract DOT-HS-6-01400. The opinions, findings and conclusions stated herin are those of the authors and are not necessarily those of the Department of Transportation.

$$f(t_i) = \frac{1}{2}a_o + \sum_{n=1}^{N} \left(a_n \cos \frac{2n\pi}{T} t_i + b_n \sin \frac{2n\pi}{T} t_i\right) \text{ for } 0 \leq t_i \leq T \qquad (1)$$

and the Fourier coefficients are

$$a_n = \frac{2}{T} \sum_{i=1}^{I} f(t_i) \cos \frac{2n\pi t_i}{T} (\Delta t)$$

$$\text{for } n = 0,1,2,....N \qquad (2)$$

$$b_n = \frac{2}{T} \sum_{i=1}^{I} f(t_i) \sin \frac{2n\pi t_i}{T} (\Delta t)$$

$$\text{for } n = 1,2,....N \qquad (3)$$

where

t_i = sampled time
N = total number of harmonics in frequency domain
n = frequency index, 1,2,....,N
i = time index, 1,2,...,I
I = total number of data points in time domain
Δt = time increment

The value of N is established by checking the diminishing values of a_n and b_n as n increases or by checking the magnitude of the complex Fourier coefficient c_n.

$$c_n = \sqrt{a_n^2 + b_n^2} \text{ for } n = 1,2,....N \qquad (4)$$

Because of the discontinuities between the initial and final data, this series converges slower than those functions with no discontinuities. Figure 1c shows how a continuous function can be created [2] by subtracting the initial value b, removing the slope m, and creating an image for the extended half period. In addition to the fast convergence, this is an odd function thus eliminating the computation of a_n ($a_n = 0$). One disadvantage is that the harmonic component is equivalent to a lower frequency because of the longer period T. It is obvious that the reconstructed function $f(t_i)$ must be corrected by the reverse process, i.e., adding the slope m and the initial value b. Similarly, the calculated first derivative must be corrected by the constant m.

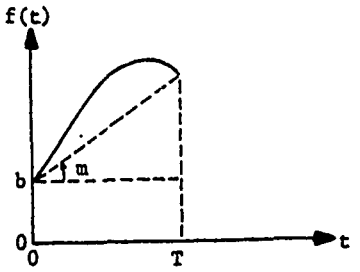

(a) A section of aperiodic data

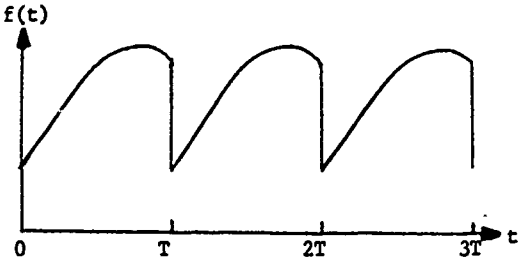

(b) A periodic function

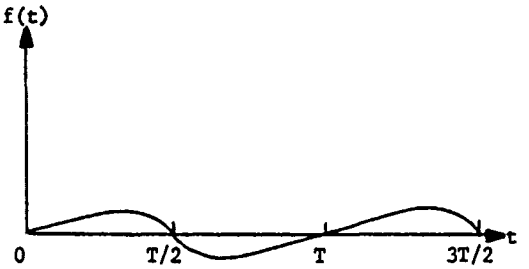

(c) A continuous periodic function

Fig. 1. Fourier series analysis setup.

DIFFERENTIATIONS

Differentiation, when considered in frequency domain, is a high-pass filtering process where the frequency harmonics are weighted at 6 dB/octave or twice heavier for each doubling of the harmonics. For example, if the 50th harmonic is 80 dB down (0.01%) in the fundamental frequency in a function, then it becomes only 46 dB down (0.5%) in the first derivative. When this function is twice differentiated, the harmonic becomes only 12 dB down (24%) in the fundamental frequency.

Three differentiation methods are compared. They are the truncated Fourier series, the Lanczos convergence factors, and the Lagrangian polynomial methods. The Lagrangian polynomial method operates in the time-domain rather than in the frequency-domain as do the first two methods. It uses a polynomial of degree four relevant to five successive points. These three methods are applied to two examples: (1) a human head rotation rate-gyro data under a crash impact condition and (2) a cascaded sinusoidal waves of various frequencies.

Truncated Fourier Series Method

When Figure 1 is differentiated term-by-term, the first two derivatives are

$$f'(t_i) = \sum_{n=1}^{N} \left[\left(\frac{2n\pi}{T}\right) \left(-a_n \sin \frac{2n\pi}{T} t_i + b_n \cos\frac{2n\pi}{T} t_i\right)\right] \text{ for } 0 \leq t_i \leq T \quad (5)$$

$$f''(t_i) = \sum_{n=1}^{N} \left[\left(\frac{2n\pi}{T}\right)^2 \left(-a_n \cos\frac{2n\pi}{T} t_i - b_n \sin\frac{2n\pi}{T} t_i\right)\right] \text{ for } 0 \leq t_i \leq T \quad (6)$$

They are the derivatives of a truncated Fourier series.

On the one hand, the derivative can be accurately calculated if a large number of harmonics is used to cover the significant frequency range of the derivative but not higher than half of the data sampling frequency ($1/\Delta t$) to avoid "aliasing" according to sampling theory. On the other hand, the number of harmonics should be kept small because the effect of the observation (measurement) error increases as the number of harmonics increases. The accuracy also depends upon the rate of change (frequency response) of the function.

It can be shown [2] [3] that the residual of a truncated Fourier series has the characteristics of a modulated carrier wave of high frequency. This modulating effect is not significant in the function itself. However, when this Fourier series is differentiated term-by-term, loss of accuracy is noted in the derivatives. This error is a result of the fact that both the modulation and carrier waves are differentiated rather than the modulation alone without the carrier. These high frequency components cannot be ignored because they are important in the derivatives although they are insignificant in the original function due to the high-pass filtering effect in the differentiation process.

Lanczos Convergence Factor Method

The adverse effect of the high harmonics can be significantly reduced with a modified process given by Lanczos [3] and Haut [2]. Lanczos used a modified operator to replace the formal differentiation. This operator, when applied to a truncated Fourier series, reduces the differentiation process to a term-by-term multiplication by the Lanczos convergence factor in the form of $(\sin nx)/nx$. When this process is repeated again, it reduces the two differentiation processes to a term-by-term multiplication by the same factor squared. The first two derivatives are

$$f'(t_i) = -\frac{2N}{T} \sum_{n=1}^{N} a_n \left(\sin\frac{2n\pi}{T} t_i\right) \left(\sin\frac{n\pi}{T}\right) + \frac{2N}{T} \sum_{n=1}^{N} b_n \left(\cos\frac{2n\pi}{T} t_i\right) \left(\sin\frac{n\pi}{N}\right)$$

$$\text{for } 0 \leq t_i \leq T \quad (7)$$

$$f''(t_i) = -\frac{4N^2}{T^2} \sum_{n=1}^{N} a_n \left(\cos\frac{2n\pi}{T} t_i\right) \left(\sin^2 \frac{n\pi}{N}\right) - \frac{4N^2}{T^2} \sum_{n=1}^{N} b_n \left(\sin\frac{2n\pi}{T} t_i\right) \left(\sin^2 \frac{n\pi}{N}\right)$$

$$\text{for } 0 \leq t_i \leq T \quad (8)$$

The factors $(\sin \frac{n\pi}{N})/(\frac{T}{2N})$ are the Lanczos convergence factors.

Lagrangian Interpolation Polynomial Method

This method fits each data point using a Lagrangian interpolation polynomial of degree four relevant to five successive points [4]. The derivatives are expressed as:

$$f'(t_1) = \frac{1}{12\Delta t}[-25f(t_1)+48f(t_2)-36f(t_3) +16f(t_4)-3f(t_5)] \quad (9a)$$

$$f'(t_2) = \frac{1}{12\Delta t}[-3f(t_1)-10f(t_2)+18f(t_3) -6f(t_4)+f(t_5)] \quad (9b)$$

$$f'(t_i) = \frac{1}{12\Delta t}[f(t_{i-2})-8f(t_{i-1})+8f(t_{i+1}) -f(t_{i+2})]$$

$$\text{for } i = 3,4,\ldots,I-3,I-2 \quad (9c)$$

$$f'(t_{I-1}) = \frac{1}{12\Delta t}[-f(t_{I-4})+6f(t_{I-3})-18f(t_{I-2}) +10f(t_{I-1})+3f(t_I)] \quad (9d)$$

$$f'(t_I) = \frac{1}{12\Delta t}[3f(t_{I-4})-16f(t_{I-3})+36f(t_{I-2}) -48f(t_{I-1})+25f(t_I)] \quad (9d)$$

EXAMPLE 1: BIOMECHANICAL IMPACT DATA

Figure 2 is the head angular velocity of a test subject during a rear sled impact. The original function is identified by the short vertical lines while the reconstructed function $f(t_i)$ using Eq. (1) with 30 harmonic ($N = 30$, or 37.5 Hz), is identified by the crosses. There is essentially no difference between these two curves. In other words, using 30 harmonics with fundamental frequency of 1.25 Hz ($f_o = 1/0.8$), the angular velocity can be

faithfully represen: d by the first 30 coefficients a_n and b_n. The magnitude of the complex Fourier coefficients c_n is shown in Figure 3 which is commonly known as the frequency spectrum. It shows that the sampling rate of 500 Hz is quite sufficient.

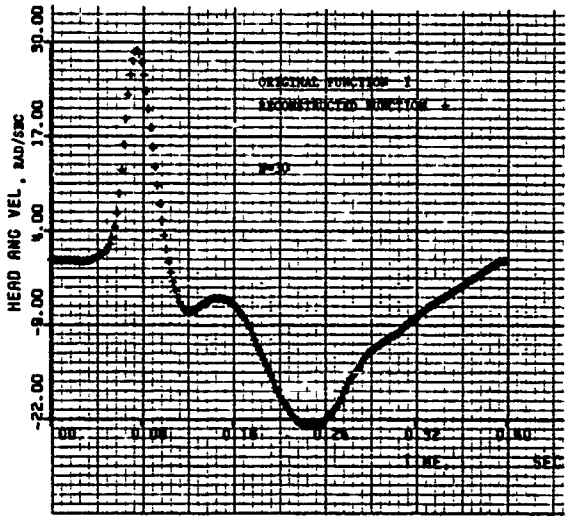

Fig. 2. Original and reconstructed functions, Example 1.

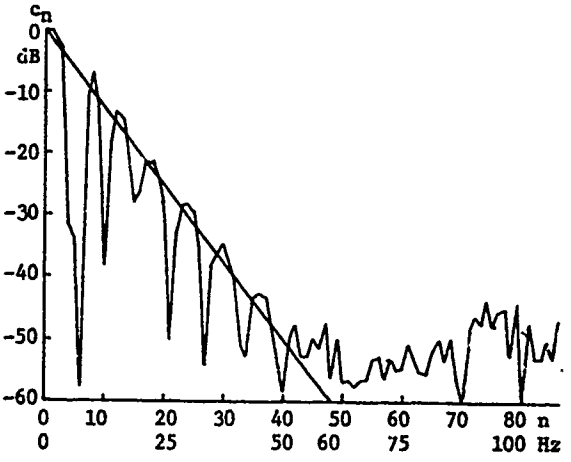

Fig. 3. Frequency spectrum, Example 1.

Figure 4 shows the derivatives f'(t) (angular accelerations) computed according to Eq. (7) using 30, 60 and 90 harmonics as compared with the derivative computed according to Largangian interpolation polynomial of degree 4 relevant to five successive points [4]. The Lanczos factor data are indicated by the short vertical lines while the Lagrangian polynomial data are indicated by the crosses. One point of comparison is the positive peak at 0.064

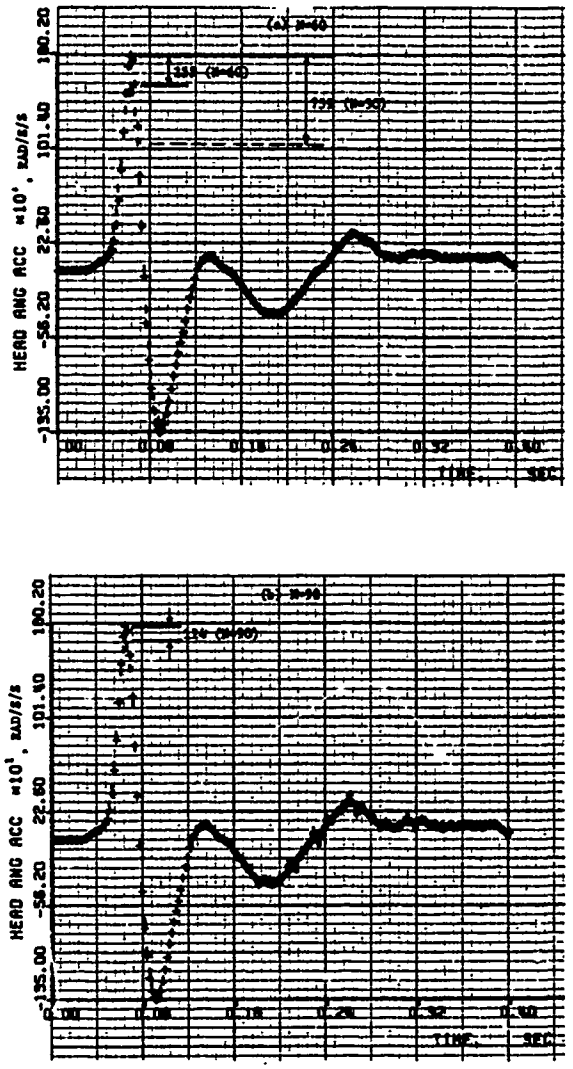

Fig. 4. Comparison of derivatives, Example 1.

seconds. It shows the difference between the two methods is 759, 225 and 114 radians/sec^2 for N = 30, 60 and 90 respectively. This example illustrates that the number of harmonics required to calculate the derivative is much higher than that indicated in the frequency spectrum of the function itself. However, this number should not be so large in order to prevent the high frequency noise from occurring. This noise can be observed in Figure 4b.

EXAMPLE 2: CASCADED SINUSOIDAL WAVES

In order to examine the frequency requirement of a sinusoidal wave for differentiation, a general test function is generated as shown in Figure 5. This function consists of a five-

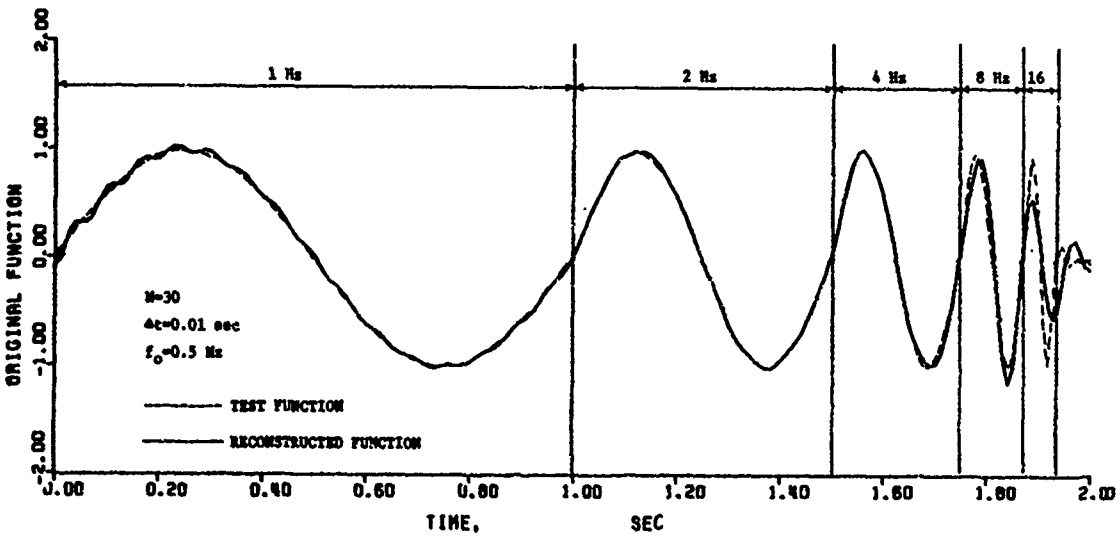

Fig. 5. A cascaded sinusoidal test function.

cycle sinusoidal wave with frequencies of 1, 2, 4, 8 and 16 Hz (f_o = 1/2) by using the set-up of Figure 1b. The time increment is 0.01 second and the total number of harmonics N used throughout this example is 30 (15 Hz). Figure 6 shows the frequency spectrum. Using Eq. (1), the reconstructed function is also shown in Figure 5. The difference between the original and the reconstructed functions is negligible up to 4 Hz input.

Fig. 6. Frequency spectrum, Example 2.

Figure 7 is the normalized derivatives of the test function calculated by three methods, i.e., the truncated Fourier series, the Lanczos convergence factors, and the Lagrangian polynomial. Each calculated derivative is compared with the ideal derivative. Normalization of each cascaded section is required for better curve scaling. Each section is scaled to 1/2mπ for m = 1, 2, 3, 4, or 5, where m is the number of each curve section.

The carrier modulating effect in the truncated Fourier series derivative is clearly noticeable in Figure 7a where the oscillating frequency is 15 Hz for N = 30. Furthermore, the signal attenuation as a function of frequency becomes more severe as compared with Figure 5. The Lanczos convergence factor method (Figure 7b) removes the carrier modulating effect but the frequency attenuation is more severe than that of the truncated Fourier series. Figure 7c seems to indicate that, at least in this example, the Lagrangian polynomial method provides better results than the other two methods. The apparent frequency attenuation is caused by insufficient number of sample points (rate) because Lagrangian polynomial method is independent of the total number of harmonics N. The Lagrangian polynomial is processed in the time-domain while the truncated Fourier series and the Lanczos converge factors are processed in the frequency domain. By using higher sampling rate, the Lagrangian polynomial method error will be reduced.

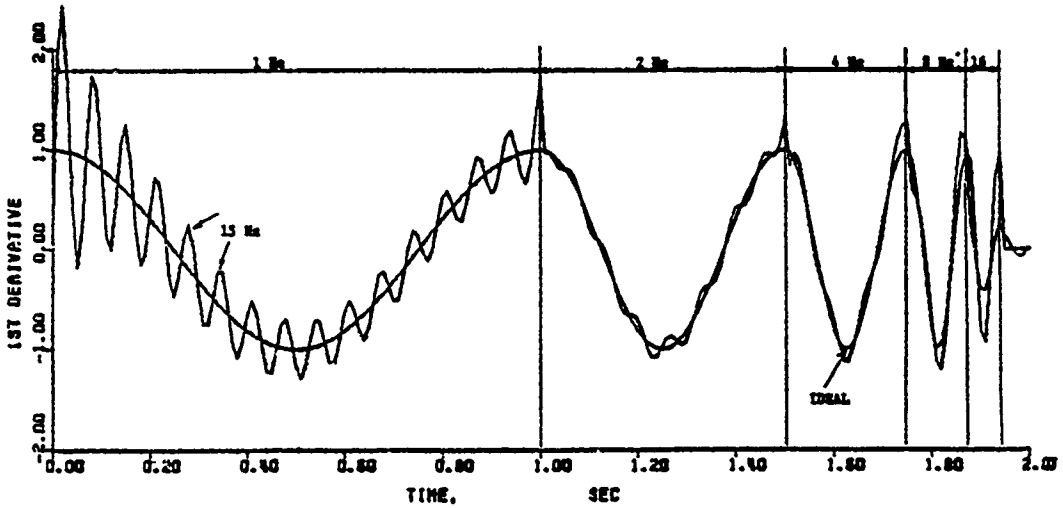

(a) Truncated Fourier series method

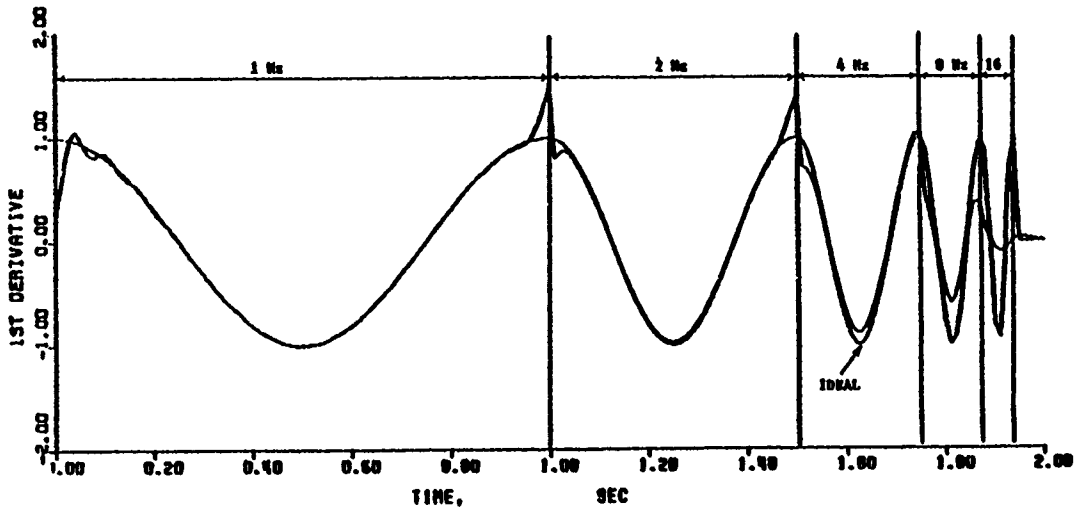

(b) Lanczos convergence factor method

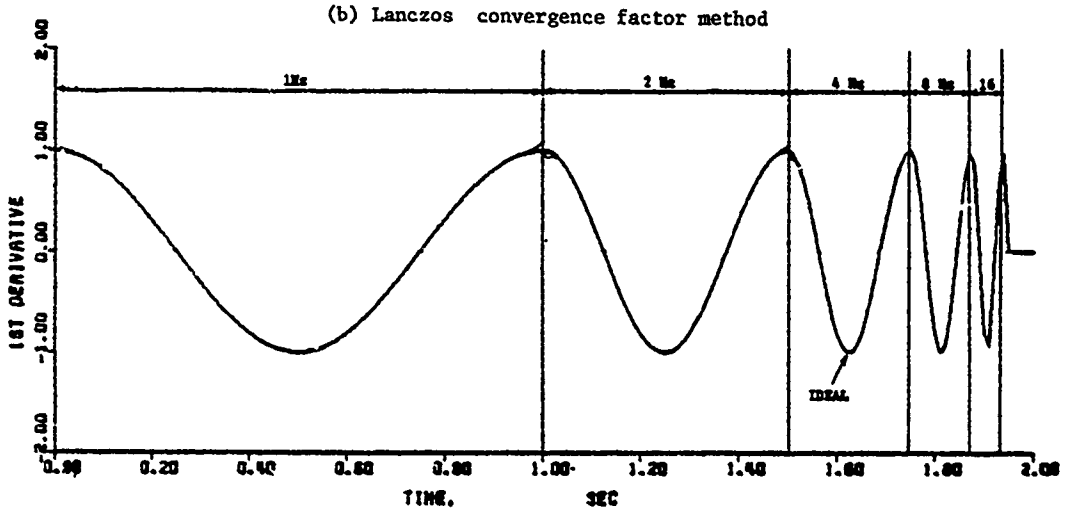

(c) Lagrangian polynomial method

Fig. 7. First derivative of the test function.

Figure 8 is the second derivatives of the test function calculated from the same three methods. The truncated Fourier series result is essentially useless unless data smoothing process is used to remove the carrier modulating effect. The Lanczos convergence factor result is smooth but the frequency attenuation becomes even more severe than that of the first derivative. The error is significant for any frequency component higher than 2 Hz. The Lagrangian polynomial data, again, seems to have better results than those obtained by the other two methods.

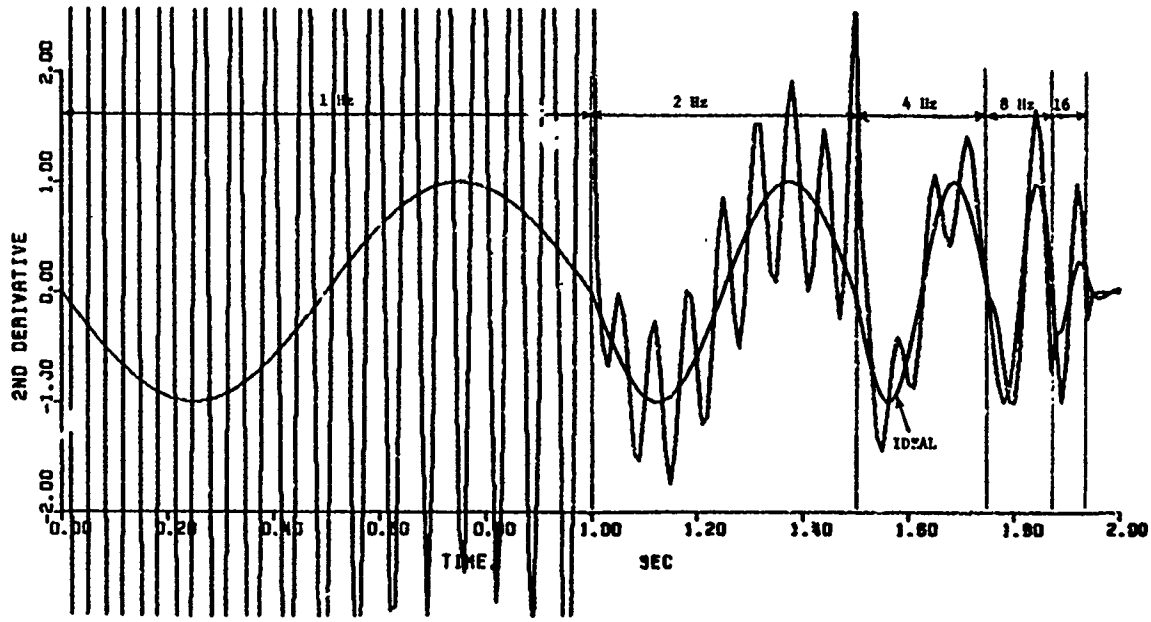

(a) Truncated Fourier series method

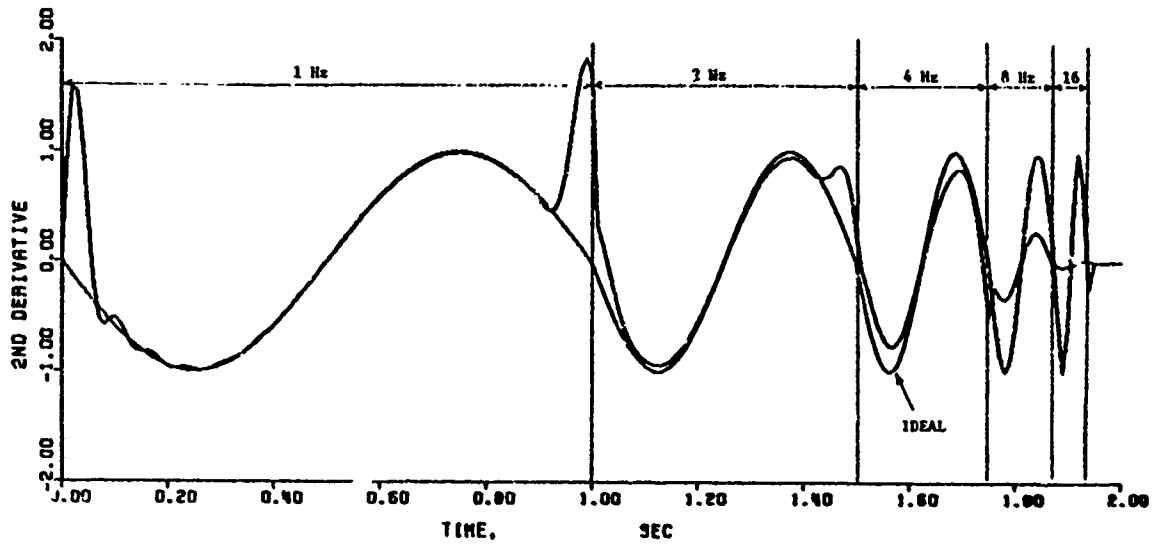

(b) Lanczos convergence factor method

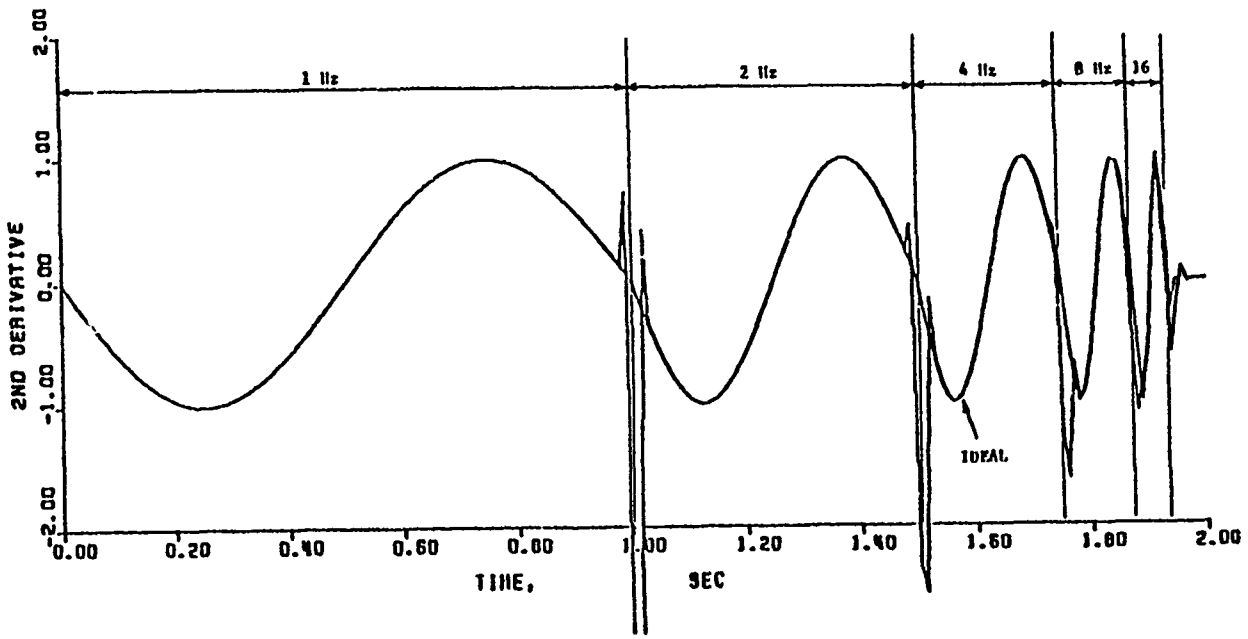

(c) Lagrangian polynomial method

Fig. 8. Second derivative of the test function.

CONCLUSIONS

This paper discussed the importance of the harmonic analysis in establishing a data channel frequency response and sampling rate requirements. Three commonly used differentiation methods, i.e., the truncated Fourier series, the Lanczos convergence factors, and the Lagrangian polynomial were demonstrated in the examples.

For the first two methods, it can be concluded that the selection of the total number of harmonics used for differentiation must be higher than that used to reconstruct the function itself. A 6 dB/octave for the first derivative and a 12 dB/octave for the second derivative high-pass filtering effect must be taken into consideration. The total number of harmonics is limited by the data measurement error and the computational error. One way of increasing the harmonic frequencies without increasing the number of harmonics is to operate the original data in piecemeal sections in time-domain.

The last method is independent of the selection of the harmonics because it operates in time-domain. In general, it is superior to the first two methods as long as the sampling rate is high as compared to the highest frequency component of the function.

REFERENCES

[1] H. P. Hsu, Fourier Analysis, Simon and Schuster, New York, 1970.

[2] R. C. Haut, E. P. Remmers, and W. W. Meyer, "A Numerical Method of Film Analysis with Differentiation with Application in Biomechanics," Proc. Soc. Photo-optical Instrumentation Engineers, Vol. 57, pp. 53-61, 1974.

[3] C. Lanczos, Applied Analysis, Prentice Hall, New Jersey, 1956.

[4] F. B. Hilderbrand, Introduction to Numerical Analysis, McGraw-Hill, New York, 1956.

STRUCTURAL RESPONSE OF EARTH PENETRATORS IN ANGLE-OF-ATTACK IMPACTS

J. D. Colton

SRI International
Menlo Park, California

An analysis based on a one-dimensional beam-mass model was developed to predict the early-time response of penetrator structures in angle-of-attack impacts. It was found that the peak compressive strain, which determines whether or not the penetrator casing fails, depends on the magnitude of the lateral load produced by impacts at an angle of attack, the load rise time (which is inversely proportional to impact velocity), and the relative mass of the nose and aft sections. By relating the loading to the impact conditions through empirical data, a procedure was devised to characterize the strength of penetrator structures in terms of impact velocity and angle of attack. The resulting critical impact curves can be used to make tradeoffs among structural dimensions (e.g., length and wall thickness), to select the best structure for a particular application, and to provide a framework for planning and interpreting experiments and more detailed calculations.

INTRODUCTION

Earth penetrators are designed to impact targets ranging from soil to soft rock and to penetrate up to several hundred feet. This may require high impact velocities, up to several thousand feet per second, and can result in severe loads on the penetrator. Determining the mechanical feasibility of deploying an earth penetrator thus requires study of terradynamics, or the motion of the penetrator through the target material that determines the loads on the penetrator and its trajectory; the early-time impact and structural response of the casing; and the response of the internal components.

This paper describes an analysis for determining the load-response relationship of penetrator structures. It also describes a procedure for combining this relationship with the impact-load relationship to arrive at the impact-response relationship used to develop critical impact curves for penetrator structures. The procedure is illustrated for a simple steel tube and is also applied to more realistic penetrator structures.

BACKGROUND

Most earlier work on earth penetrators focused on terradynamics [1-3]. Of particular interest in that work are the loads produced on the penetrator by the target material. Both calculated impact loads [4] and measured acceleration response [2] show that the resultant force-history for normal impact consists of two distinct parts: an approximately linear rise to a peak force F over the time t_r required for the structure to penetrate to its full diameter, followed by a very gradual decay associated with the rigid body deceleration of the structure. For example, for a nominal full scale structure [6 inches (15.24 cm) in diameter, 60 inches (152.4) long, and weighing 400 pounds (181 kg)] impacting sandstone at 1500 ft/sec (457 m/sec), the loading rise time is about 1 msec and the peak force is about 500,000 pounds (2.24×10^6 N) [4].

Tests on deep-penetrator structures have revealed some of the important features of the structural response. In reverse ballistic tests performed at AVCO [5], relatively low strains were produced in a simple penetrator structure under a normal impact with a rock simulant; however, under an angle-of-attack impact, much larger strains were produced by the bending induced in the penetrator. In ballistic tests performed on scale model penetrators at Martin Marietta Aerospace Company [6], the penetrator structure failed in angle-of-attack impacts; these test results also indicate that large strains and failure were caused by bending. Below, we postulate how these failures occur.

The axial component of the load produces compressive stress along the entire length of the penetrator. The lateral component of the load produces bending stresses whose magnitudes in tension and compression are equal at a given axial location. Thus, the total stress of greatest amplitude is compressive and above a

critical velocity produces local yielding of the penetrator wall. The weakened cross section at this location allows continued deformation which increases the bending load, and ultimately leads to divergent bending and fracture. Since incipient yielding in compression defines the onset of this divergent instability, the elastic response up to yielding determines if failure occurs. Thus, an analysis need predict only the elastic response, and the critical response parameter is the maximum total compressive stress.

Observed maximum compressive strains and failures in penetrator structures occur at several diameters from the penetrator nose [5,6]. The stress distribution in the cross section at these locations therefore depends only on the resultant forces applied to the end of the structure. That is, failure depends only on the resultant axial and lateral loading forces and not on the details of the pressure load distribution on the penetrator nose. This observation allows us to use a relatively simple response analysis.

OBJECTIVES AND APPROACH

Our primary objectives were to develop a simple predictive analytical method that would account for penetrator bending induced by angle-of-attack impacts and that would determine the effect of structural and loading parameters on the survivability of a penetrator casing on impact. These results could then be used first, to identify those parameters to which the damage producing loads are sensitive, such as impact velocity and angle of attack; second, to provide a means of arriving at an optimum structural design within the parameter ranges dictated by system requirements; and third, to select specific configurations and loads for testing and more detailed calculations.

The approach to predicting penetrator response is based on elastic Timoshenko beam theory with axial thrust. This formulation includes the two dominant response mechanisms governing angle-of-attack impacts: axial compression, and bending at any cross section along the structure. The nose, aft mass, and payload are modeled as rigid masses, as indicated in Figure 1. This structure is loaded by a resultant force with a linear rise and then a constant level that approximates the very gradual decay found for actual penetrators. Loading is through a fixed point in the front mass. Thus, the load is specified by the rise rime t_r, the magnitude F of the axial force, and the ratio η of the lateral force to axial force. The resultant load decomposes into its axial and lateral components, and the response in these two directions is determined independently. The loads are related to the impact conditions through available experimental and analytical load data, as discussed later. The method of characteristics is used to solve the governing equations numerically [7].

This analysis is an efficient way to calculate the elastic response of penetrators, allowing a broad range of loading and structural parameters to be examined at a low cost. It does not replace more elaborate finite element and finite difference codes, but rather, it supplements code calculations at the design stage when a number of configurations are being considered and structural details are yet to be determined.

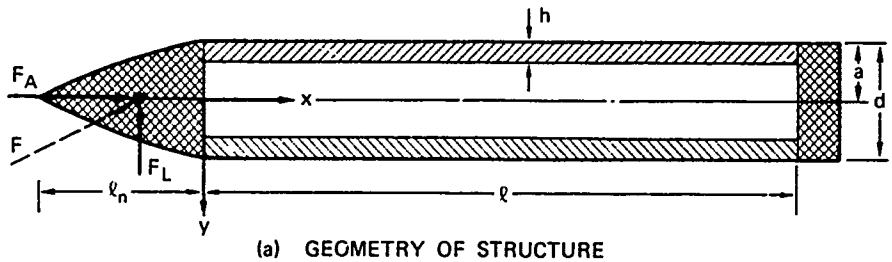

(a) GEOMETRY OF STRUCTURE

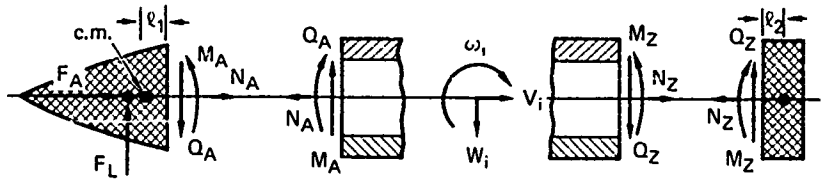

(b) FORCES AND MOMENTS ON THE BEAM AND FRONT AND AFT RIGID MASSES

Fig. 1 - Mathematical Model of an Idealized Penetrator Structure

ILLUSTRATION OF APPROACH FOR A SIMPLE TUBE

The analysis was used to develop, for design purposes, a relationship between the impact parameters and the response parameters. This section discusses the relationship between the dominant impact parameters (impact velocity and angle of attack) and the dominant response parameter (peak compressive stress) for a simple tube. The impact-response relationship, including both terradynamics and structural response, is complex and not understood for many impact conditions. However, some insight can be gained by introducing an appropriate set of parameters describing the loading on the penetrator. The impact-load relationship (determined only from terradynamics) and the load-response relationship (determined entirely by structural response) is then treated separately and combined to produce the impact-response relationship sought.

Load-Response Relationship

We have determined the load-response relationship using the analysis described above, by applying loads with the different rise times shown in Figure 2(a) and with a lateral-to-axial load ratio of 0.2. The structure used in this example was a simple steel tube with a length-to-diameter ratio of $\ell/d = 6$ and a radius-to-thickness ratio of $a/h = 4$. Figure 2(b) shows the bending and axial stress histories at

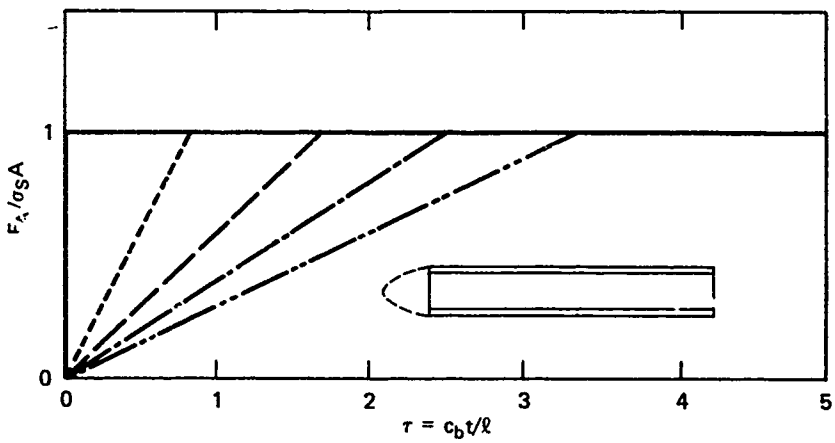

(a) AXIAL LOADING FORCE, F_A VERSUS TIME ($\eta = 0.20$)

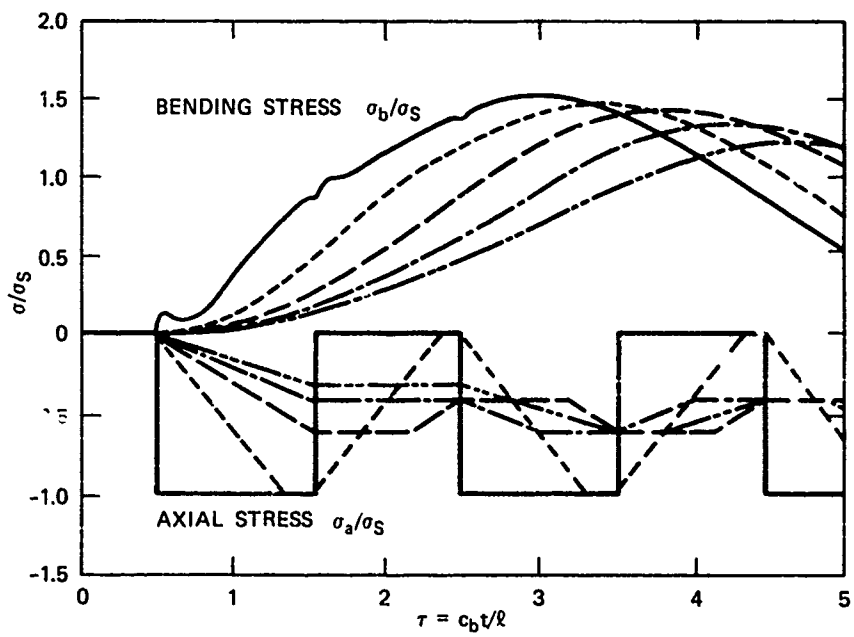

(b) STRESS VERSUS TIME AT $\chi = x/L = 0.4828$

Fig. 2 - Response of a Simple Steel Tube to Loads with Different Rise Times ($\ell/d = 6$, $a/h = 4$)

station $\chi = x/\ell = 0.4828$, normalized with respect to the normal stress σ_s at the loaded end of the tube.

The largest bending stress ($\sigma_b/\sigma_s = \pm 1.51$) is produced by the loading of zero rise time (step input). In order of increasing loading rise times the peak bending stresses σ_b/σ_s produced are 1.48, 1.40, 1.31, and 1.20. As the rise time increases further, the peak stress at this location approaches the steady-state value of $\sigma_b/\sigma_s = 0.793$. Furthermore, the time at which the peak occurs increases with rise time.

For the axial stress, the peak stress at a given location is determined by whether the loading rise time is less than or greater than the time at which a reflected tensile stress wave from the aft free end arrives at the location. For loading curves with rise times of less than one transit time, the maximum axial stress produced is $\sigma_a/\sigma_s = 1.00$. For the loading curves with rise times of more than one transit time, the maximum stress is $\sigma_a/\sigma_s = -0.617$. The steady-state value at this location is $\sigma_a/\sigma_s = -0.517$.

Thus, the largest effects of increasing the loading rise time are the increase in the time at which peak bending occurs and the variation in axial stress for loading rise times near one transit time. The variation in loading rise time has less effect on the peak bending stress and on the peak axial stress for rise times larger than two transit times.

We now determine the dominant response parameter, the normalized peak compressive stress. For each rise time and value of η, we find σ_{max}, the total compressive stress that is maximum in space and time. We normalize it with respect to the amplitude of the normal stress σ_s on the loaded end. We can also use curves similar to those shown in Figure 2 to determine σ_{max}/σ_s for different values of η. Since the axial and bending responses are independent, the total stress for different values of η can be computed by weighting the bending component by the appropriate factor. The load-response relationship is summarized in Figure 3 as curves of the normalized peak response stress as a function of rise time for several values of η.

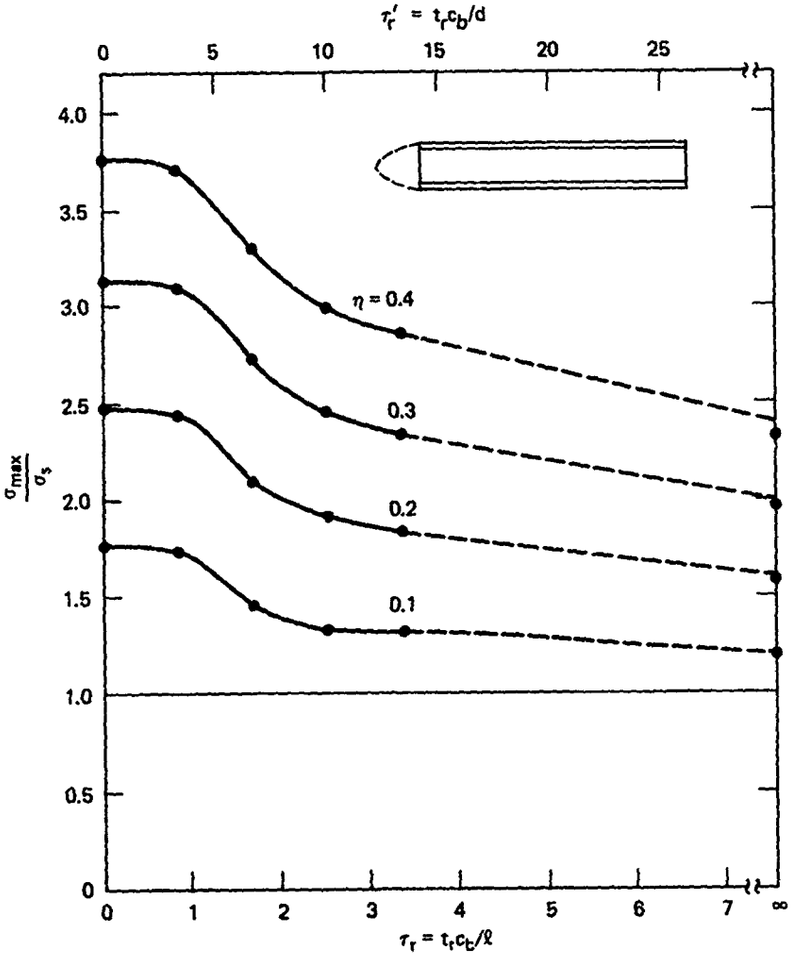

Fig. 3 - Load-Response Relationship for a Simple Steel Tube ($\ell/d = 6$, $a/h = 4$)

Impact-Load Relationship

The dominant impact parameters are the impact velocity V, the angle of attack α, and the target impedance* Z. Thus, the impact-load relationship relates the loading parameters t_r, F, and η to V, α, and Z. The rise time is well approximated by the submersion time of the tapered penetrator nose length ℓ_n:

$$t_r = \ell_n / V \qquad (1)$$

The dependence of the loading force F on the impact parameters is not as well understood. However, a reasonable approximation is that F is proportional to the impact velocity V,

$$F = b(Z)\, V \qquad (2)$$

where the proportionality factor b(Z) depends on the target material. For normal impacts, this relationship has been verified both experimentally and theoretically for soil targets; it also appears to hold for rock targets but fewer experimental data are available.† For angle-of-attack impacts, we assume that the lateral load is proportional to the axial load for the time of interest (slightly longer than the rise time).

The dependence of the load ratio, or eccentricity factor, η on the impact parameters is complex and has not been adequately investigated. However, some information is available. For normal impacts ($\alpha = 0$), we know that $\tan^{-1}\eta = 0$. To estimate η for one nonzero value of α, we used the analysis to interpret a reverse ballistics test (Test D-1) performed at AVCO [5]. Our purpose was not to predict the response, but rather, to determine the eccentricity factor in that test by adjusting the axial and lateral load amplitudes so that the predicted strain response would best match the measured strain response.

AVCO (Test D-1) used a 3-inch-diameter (7.6 cm), 28-inch-long (71.1 cm) steel penetrator structure consisting of a 12-inch-long (30.5 cm) solid nose and a 16-inch-long (40.6 cm) cylindrical cavity. The cavity was 1.8 inches (4.6 cm) in diameter. This structure was impacted by a 15.2-inch-diameter (38.6 cm) mortar projectile at 1500 ft/sec (475 m/sec) at a 5 degree angle of attack. The strains measured at three axial locations were reduced to their axial and bending components at each of three times. The nine axial and nine bending strain data points are shown in Figures 4(b), 4(c), and 4(d).

*The impedance Z here includes any target properties affecting the loading parameters, including moduli, strength, density, and viscosity and frictional coefficients.

†P. F. Hadala, private communication, January 1977.

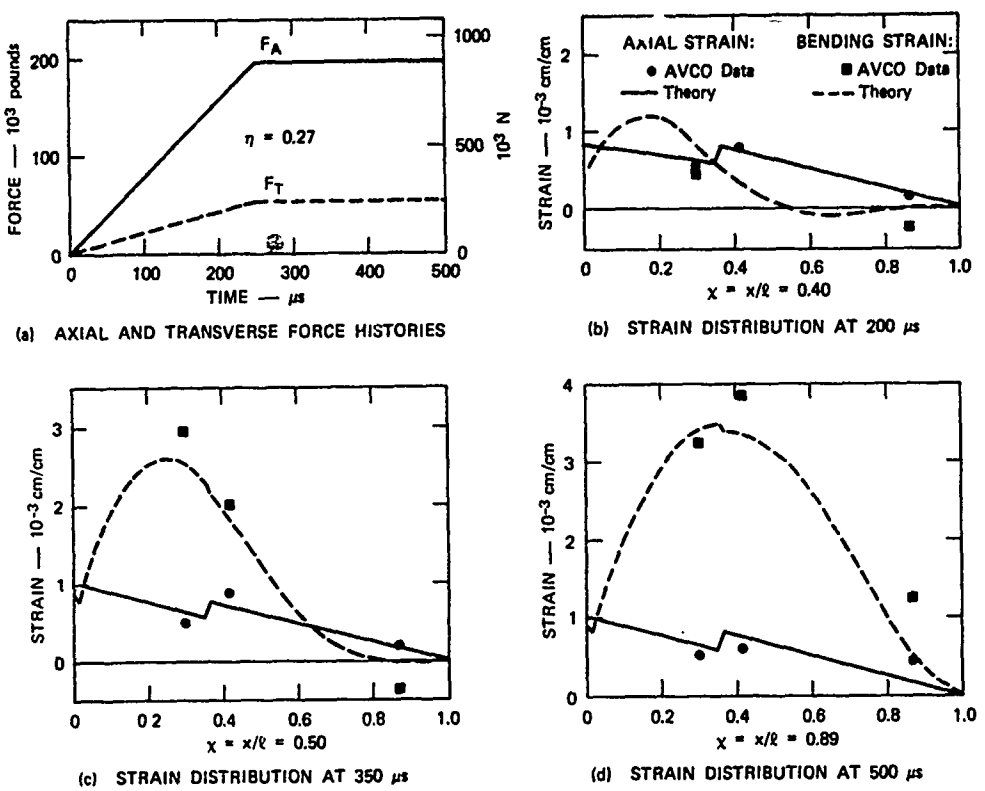

(a) AXIAL AND TRANSVERSE FORCE HISTORIES

(b) STRAIN DISTRIBUTION AT 200 μs

(c) STRAIN DISTRIBUTION AT 350 μs

(d) STRAIN DISTRIBUTION AT 500 μs

Fig. 4 - Comparison of the Predicted Strain with the Measured Strain in AVCO Reverse Ballistics Test D-1

In applying the analysis to this experiment, the shapes of both axial and lateral load-time histories were taken as bilinear, with the rise time of 250 μsec corresponding to a 4.5-inch (11.4 cm) nose length divided by the impact velocity of 1500 ft/sec (475 m/sec). In the analysis, the loads were applied at the center of mass of the rigid nose of the idealized structure.

The axial and lateral load amplitudes that give best agreement between measured and calculated strains were determined independently. For example, the axial response was first calculated for an axial load of unit amplitude. Then, for each axial strain datum point, the unit load was weighted so that the calculated axial strain agreed with the measured strain. The axial load amplitude F that best matched the axial strain data was taken as the average of the nine such weighting factors; thus, F_A = 195,000 pounds (8.67×10^6N). By the same method, we found that a lateral load amplitude of 53,000 pounds (2.36×10^5N) best matched the bending strain data.

These load histories and resulting calculated strain distributions are also shown in Figure 4. In general, good agreement was obtained between the calculated and measured strains. For this 5 degree angle of attack, the eccentricity factor is $\eta = 53{,}000/195{,}000 = 0.27$. Thus, the eccentricity angle, $\tan^{-1}\eta = 15$ degrees, is greater than the angle of attack α by a factor of about 3. We now assume that the eccentricity angle increases linearly with angle of attack:

$$\tan^{-1}\eta = 3\alpha \qquad (3)$$

over the range of α of interest.

Impact-Response Relationship

The impact-response relationship is now found by translating the three parameters t_r, σ_{max}/σ_s, and η in the load-response relationship of Figure 3 into the impact parameters V and α using equations (1), (2), and (3).

First, t_r is related to impact velocity by using equation (1), which requires specifying the nose length ℓ_n. For this example, we have chosen $\ell_n = 1.5d$. Second, σ_{max}/σ_s is related to the impact force F through equation (2). However, so that the results will apply to any targets for which a linear force-velocity relationship is reasonable, we normalize the peak response stress with respect to the average loading pressure $P = F/A'$ at a particular velocity, where A' is the frontal area of the penetrator. For this normalization, we choose P_{1000}, the loading pressure generated at an impact velocity of 1000 ft/sec (305 m/sec). The peak response stress normalized with respect to P_{1000} is related to the normalized stress of Figure 3 through the identity

$$\frac{\sigma_{max}}{P_{1000}} = \frac{\sigma_{max}}{\sigma_s} \frac{F(V)/A}{F(1000)/A'} \qquad (4)$$

Substitution of equation (2) into equation (4) and rearrangement gives

$$\frac{\sigma_{max}}{P_{1000}} = \frac{\sigma_{max}}{\sigma_s} \frac{V}{1000} \frac{A'}{A} \qquad (5)$$

where V is in ft/sec. For the simple steel tube, $A'/A = 2.29$.

Finally, the η = constant curves of Figure 2 are relabeled as α = constant curves according to equation (3). The resulting impact-response relationship is shown in Figure 5. Although this impact-response relationship relies on two assumptions concerning the impact-load relationship, the load-response relationship involves no such assumptions. Thus, when more information about the impact-load relationship is available, the procedure developed here can be repeated with the same load-response relationship.

CRITICAL IMPACT CURVES

A more useful form of the impact-response relationship is found by constructing cross plots from Figure 5 for which the normalized peak response is constant, as shown in Figure 6. These curves are called critical impact curves and give the trade-off between impact velocity and angle of attack at the maximum capability of the penetrator. That is, for a given penetrator (fixed σ_{max}) and target (fixed P_{1000}) determined experimentally or analytically), the curve for the appropriate ratio of σ_{max}/P_{1000} gives the combination of allowable values of V and α. For example, for $\sigma_{max}/P_{1000} = 6$, if the penetrator is to survive at angles of attack as large as 5 degrees, the impact velocity must not exceed 1400 ft/sec.

The critical impact curves can also be used to select the penetrator material, on the basis of yield stress, for a given range of V and α within which the penetrator must function. For example, if for a given system and target the maximum impact velocity is 2000 ft/sec and the maximum angle of attack is 5 degrees, a material with a yield strength of at least 10 P_{1000} is needed. Similarly, the critical impact curves of Figure 6 could be used to select targets for which a given system (that is, specified combinations of σ_y, V, and α) could be used.

Critical impact curves are perhaps most useful for comparing the performance of different penetrator structures, as illustrated below.

Critical impact curves were developed for the the four penetrator structures shown in Figure 7. Structure B is similar to that already used for deep penetration into hard targets. Structure C is similar to that proposed for shallow penetration. A and D were analyzed to determine the effects of changing ℓ/d (along the rows of Figure 6) or a/h (along the columns of Figure 6).

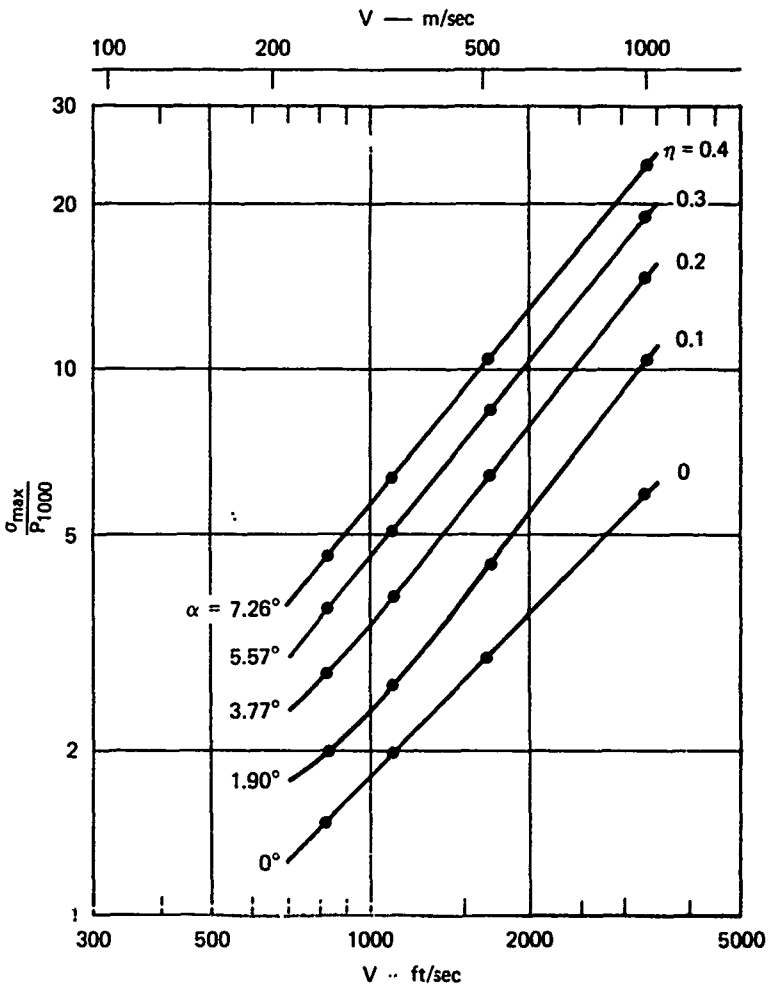

Fig. 5 - Impact-Response Relationship for a Simple Steel Tube ($\ell/d = 6$, $a/h = 4$, $\ell_n = d$)

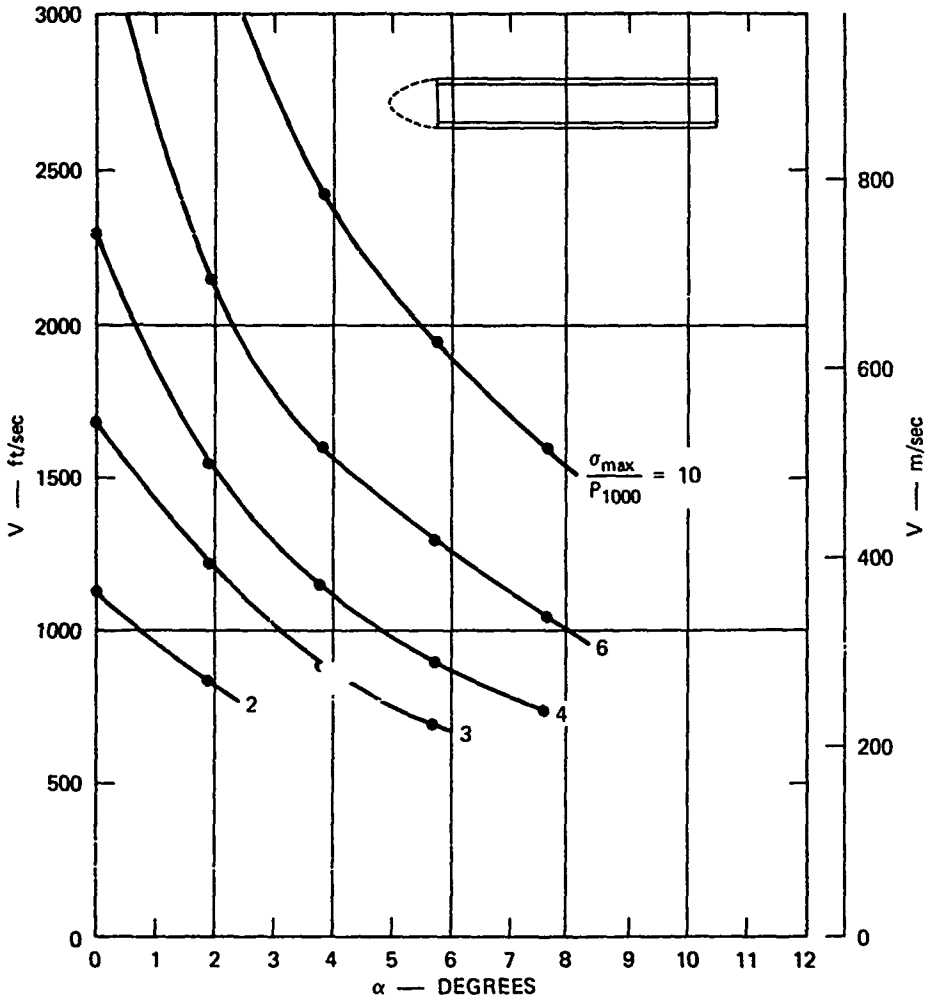

Fig. 6 - Critical Impact Curves for a Simple Steel Tube
($\ell/d = 6$, $a/h = 4$)

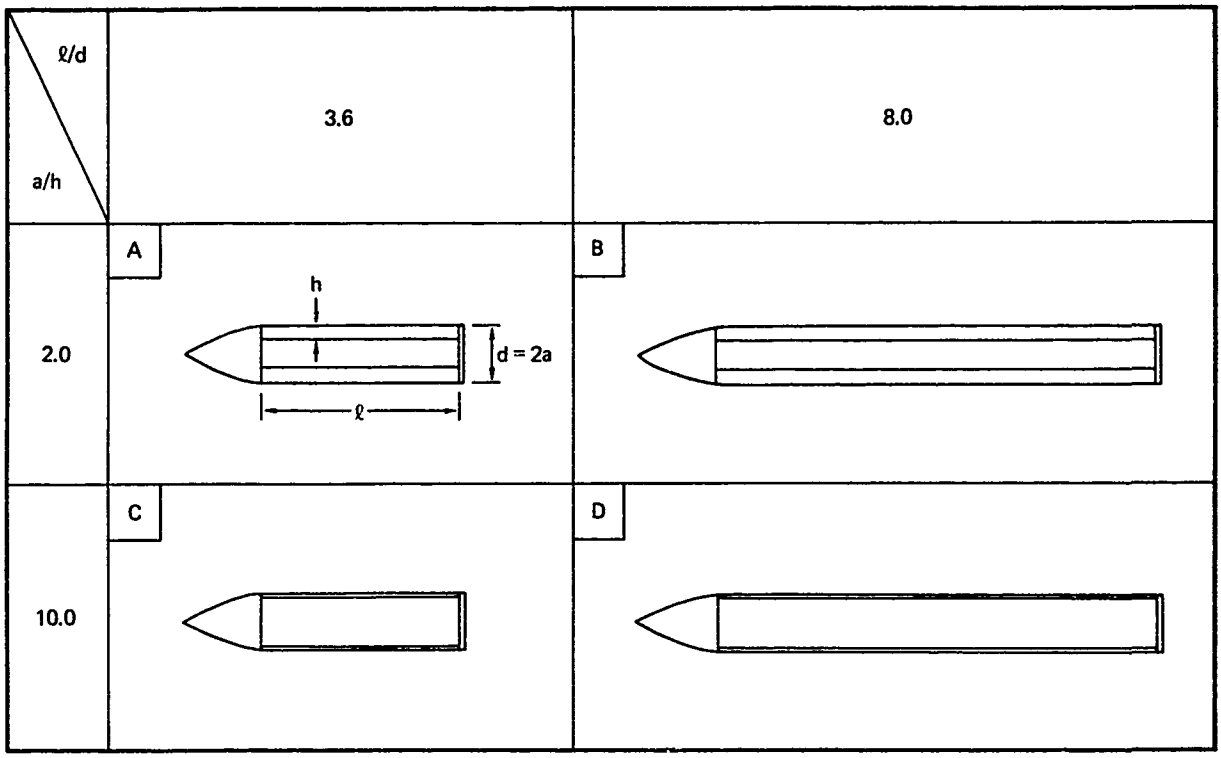

Fig. 7 - Penetrator Structures Analyzed

Figure 8 shows the critical load curves for $\sigma_{max}/P_{1000} = 10$ for these four structures. For two structures of the same thickness, the shorter structure has curves with a steeper slope for $\tau' \leq 20$ (compare curves of structures B and C). For $\tau' > 20$, the response of the shorter structures is quasi-steady; that is, the peak stress depends on the load amplitude but not the rise time. In constrast, for the rise times considered here, the peak stress in the longer structures depends on both rise time and load amplitude.

Such curves can be used to plan experiments. For example, the critical load curve for structure B shows that, for impacts at about 2000 ft/sec and a 3-degree angle of attack, the severity of the response is very sensitive to the angle of attack. Thus, it may be important to be able to control the angle of attack in a test of this structure or, at least, to be able to measure it accurately. In contrast, structure C is more sensitive to impact velocity. Thus, in testing structure C it is more important to control or measure impact velocity than angle of attack.

Critical impact curves can also be used to interpret results of experiments or more detailed load and structural response calculations (for example, a finite element code prediction). A particular experiment or detailed calculation gives a single point on a critical impact curve. Although such a datum point represents a more complete response description than a similar point generated by the beam-mass model used here, many points are needed to determine the shape of the curve. The curves calculated with the beam-mass model can be used to determine this shape. Thus, the appropriate values of V and α can be selected to minimize the data points needed to define the curve. For example, for structure B small increments in α and larger increments in V should be made to efficiently define the $\sigma_{max}/P_{1000} = 10$ curve for small α.

The critical impact curves are perhaps most useful for making design trade-offs among candidate penetrator structures. For example, the curves for structures B (deep penetrator) and C (shallow penetrator) pass through a similar region in the V-α plane and intersect at V = 1500 ft/sec and α = 5.7 degrees. However,

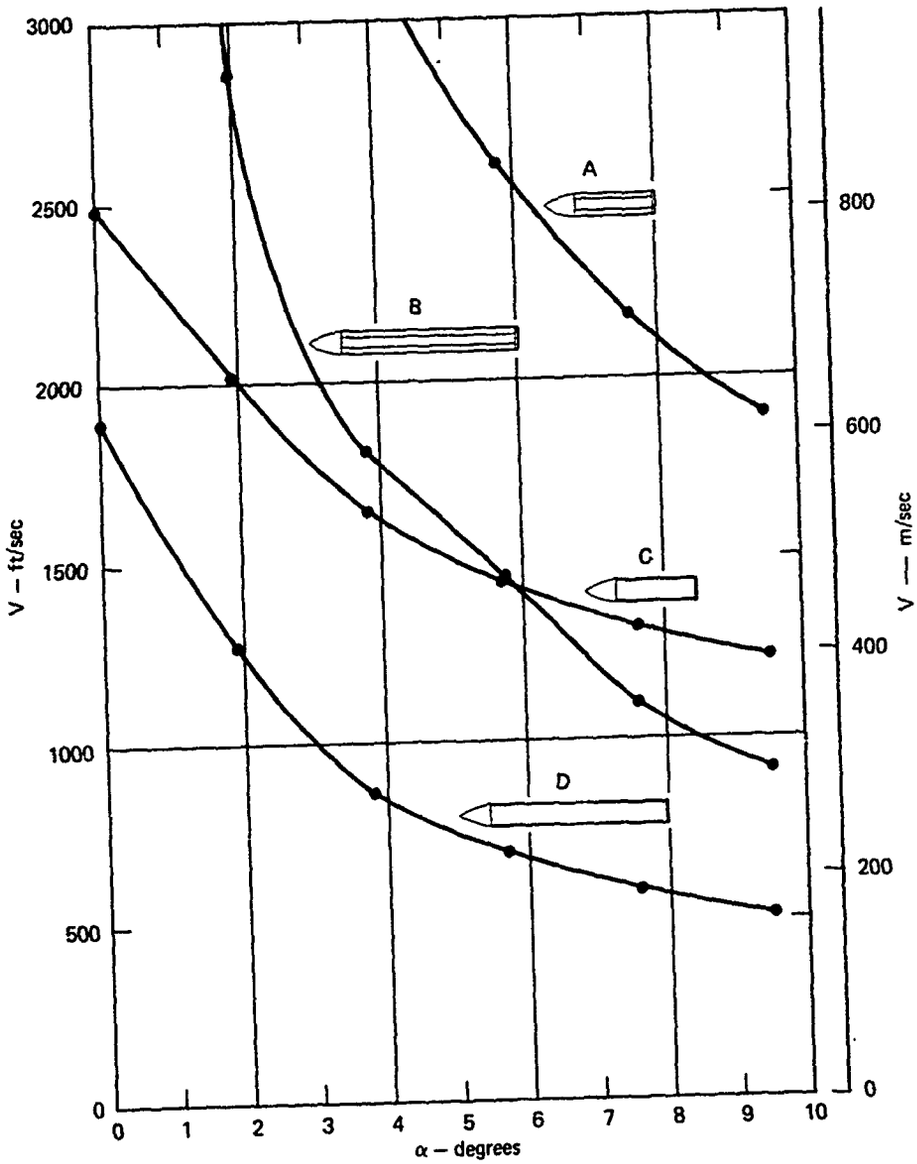

Fig. 8 - Critical Impact Curves for Different Steel Penetrator Structures ($\sigma_{max}/P_{1000} = 10$)

the curve for B (deep penetrator) is steeper and, for small angles of attack, can withstand greater impact velocities. Both these penetrators can be made stronger by increasing only the wall thickness (from that of structure C to that of structure A) or by decreasing the length (from that of structure B to that of structure A). Each such change would reduce the payload volume. Also, for small angles of attack, the velocity range can be extended more by increasing wall thickness than by decreasing length. Similar conclusions can be drawn by comparing curves for structures B and C with that of structure D.

CONCLUSIONS

We have developed a procedure for characterizing, in terms of critical impact curves, the ability of penetrator structures to withstand impacts. This procedure characterizes the response over a range of impact conditions, allowing trade-offs among structural dimensions, yield strength, and target characteristics and selection of the best structure from a group of structures for a particular application. The procedure develops critical impact curves that can be used to plan and interpret experiments and more detailed calculations.

REFERENCES

1. W. J. Patterson, "DNA/Sandia Soil Penetration Experiment at DRES: Results and Analysis," Sandia Laboratories Report SAND-75-0001 (March 1975).

2. P. F. Hadala, "Evaluation of Empirical and Analytical Procedures Used for Predicting the Rigid Body Motion of an Earth Penetrator," Waterways Experiment Station Paper S-75-15 (June 1975).

3. M. H. Wagner, K. N. Kreyenhagen, and W. S. Goerke, "Numerical Analysis of Projectile Impact and Deep Penetration into Earth Media," Waterways Experiment Station Contract Report S-75-4 (August 1975).

4. K. N. Kreyenhagen and Y. M. Ito, "Internal Response in Earth Penetrators," presented at the DNA Earth Penetration Technology Review Meeting (October 1975).

5. D. Henderson et al., "Impact and Penetration Technology," Progress Report No. 2 under Contract DNA-75-C-0181 AVCO Corporation, (June 1975).

6. M. Anthony, Martin Marietta Aerospace Company, "Impact of Earth Penetrator Models into Simulated Rock Targets," presented at the DNA Earth Penetration Technology Review Meeting (October 1975).

7. J. D. Colton, "Multiple Fracture of Beams and Plates Under Localized Impulsive Loading," Poulter Laboratory Technical Report No. 004-75, SRI (November 1973).

SCALING AND PREDICTION OF IMPACT PUNCTURE OF SHIPPING CASKS FOR RADIOACTIVE MATERIALS

W. E. Baker
Southwest Research Institute
San Antonio, Texas

Shipping casks for spent fuels from nuclear reactors must be designed to be proof against several hypothetical accidents, including falling on a sharp object which could puncture the outer casing and penetrate some distance into the radiation shielding material inside the casing. These casks are quite massive, and typically have carbon steel or stainless steel jackets encasing thick lead shielding. To aid in puncture-resistant design, drop tests have been conducted at Oak Ridge National Laboratory on prismatic and cylindrical simulants of shipping casks of various sizes, and several empirical design formulas for incipient casing puncture developed on the basis of the test results, which apply only to full-scale test drops.

The ORNL data base can be used to generate more general relations between energy for incipient puncture, casing thickness for different materials, and diameter of cylindrical casks, if the data are properly scaled by similitude analysis. Also, energy balance methods can be used in conjunction with information on the character of the impact damage to generate approximate theoretical predictions of scaled impact energy for incipient puncture and scaled casing thickness. This paper reports the similitude and energy balance analyses, and gives scaled puncture threshold prediction equations. The equations are valid for any self-consistent set of units. All data from ORNL tests are shown to agree well with the scaled equations, which are independent of scale and apply for similar jacket materials.

The paper also demonstrates that differences in material properties for the cask materials due to strain rate effects have negligible effect on scale modeling of the penetration process, for geometric scale factors up to about twenty.

INTRODUCTION

Shipping casks for spent fuels from nuclear reactors must be proof against several hypothetical accidents, including a free drop of 40 inches onto the end of a 6-inch-diameter steel rod. This test is intended to guarantee that the outer casing of the cask will not be punctured in a shipping accident.

Most shipping casks are quite massive, lead-shielded and steel-jacketed. To determine combinations of jacket materials and total cask weights which would pass the puncture test, Spaller[1] planned and conducted a series of drop tests of prismatic simulants of shipping casks. His tests included full-scale and model simulants with two jacket materials; ASTM A245 Grade A hot-rolled steel and ASTM A240 type 304L stainless steel, backed by thick layers of chemical lead, ASTM B29-55. He was able to establish incipient puncture impact energies quite accurately for a variety of jacket thicknesses and puncture rod diameters. Spaller recommended the following empirical equations for thickness of the two jacket materials to just prevent puncture of a full-scale cask dropped from 40 inches onto a 6-inch rod:

$$h = (1.22 \times 10^{-3})\, W^{0.618} \qquad (1)$$

for A245 Grade A steel and

$$h = (2.07 \times 10^{-5})\, W - (1.306 \times 10^{-10})\, W^{2} \qquad (2)$$

for type 304L stainless steel. In these equations, W is cask weight in pounds and h is jacket thickness in inches. He also recommended that other tests be run to extend these equations to other materials and to include effects of curvature of the outer jacket of casks.

In later work, Nelms[2] conducted a number of additional tests on prismatic casks with a variety of jacket materials, and also conducted tests of cylindrical models of casks with a single jacket material, ASTM A245 steel. To support his data analysis and development of

prediction equations, Nelms tested the jacket materials used in both his tests and Spaller's earlier tests, and reported ultimate tensile strengths σ_u for all of the materials, and failure strain ε_u and yield stress σ_y for some of the materials. Nelms realized that puncture data for different materials might correlate if some measure of material strength were included in the analysis, and used the parameter (E_i/σ_u) for his correlations where E_i is the measured incipient impact energy for jacket puncture. In testing models of cylindrical casks, Nelms found that more energy was needed for puncture of cylindrical models than for prismatic models; and that this energy decreased slightly with increase in cask diameter. Empirical equations obtained by Nelms were:

For prismatic cask simulants impacting rods with diameter of d inches,

$$\left(\frac{E_i}{\sigma_u}\right) = 2.4\ d^{1.6}\ h^{1.4} \qquad (3)$$

For cylindrical casks of diameter D inches with jackets of ASTM A245 steel, with thickness h of 0.075 in.,

$$E_i = 3040\ d - 256 - 16D \qquad (4)$$

For prototype (full-scale) cylindrical casks,

$$\left(\frac{E_i}{\sigma_u}\right)_p = (10.5 - 0.0554D)\ h^2 - 11.8h^3 \qquad (5)$$

The experimental work in refs. 1 and 2 is obviously done with considerable care, and is accurately and fully reported. But, much more general inferences than equations (1) through (5) can be drawn from the test data if the results are properly scaled. Further, approximate analytic expressions can be generated to relate puncture threshold to parameters describing the lead-backed jacket and the impacted rod. These two kinds of generalizations are the topic of this paper.

SCALING OF CASK PENETRATION

Most of the tests reported in refs. 1 and 2 are tests of scale models of full-scale shipping cask simulants, with geometric scale factors as small as 0.052. The tests showed very repeatable scaled deformation patterns of steel jackets and lead shielding, established quite accurately the impact energies for incipient jacket puncture for a range of scale models and several full-scale simulants, and showed that the impact energy governed puncture for these low-velocity impacts with massive items, rather than the impact velocity. One can therefore list the physical parameters entering this problem, preparatory to assembling them in dimensionless groups in a similitude analysis. These are given in Table 1, together with their dimensions in a force, length, time (F, L, T) system.

Some parameters included in Table 1 can be shown to be redundant for this problem by physical evidence, and some which could have been included are not, also because they are shown in ref. 1 to be unimportant. We included impact energy E, cask mass M and impact velocity v. But, impact energy is simply the kinetic energy

$$E = (1/2)\ Mv^2 \qquad (6)$$

Table 1.
List of Physical Parameters

Symbol	Dimensions	Parameters
E	FL	Impact energy
M	FT^2/L	Total mass of cask
v	L/T	Impact velocity
h	L	Thickness of cask sheathing
H	L	Thickness of lead
d	L	Diameter of impacted rod
b	L	Minimum face dimension of impacted cask
D	L	Diameter of cylindrical cask
y(r)	L	Deformation of sheathing and lead
y_m	L	Maximum deformation
r_1	L	Radius of deformed region
V_1	L^3	Volumeof depression in lead
V_2	L^3	Volume of lead with permanent strain
σ_{yi}	F/L^2	Yield stress of i^{th} material
σ_{ui}	F/L^2	Ultimate stress of i^{th} material
S_i	F/L^2	Strain-hardening slope for i^{th} material
ϵ_i	--	Strain in i^{th} material

and results in ref. 1 show quite clearly that M and v themselves are superfluous and E determines impact deformation. Also, from discussion in ref. 1, it is clear that the exact size of the impacting cask is unimportant, provided that the impacting surface is somewhat larger than the radius of the deformed region, and that the lead shielding is much thicker than the steel sheathing. We can therefore eliminate the parameters M, v, b and H from Table 1 as redundant for this problem, subject to the restrictions that

$$h/H \ll 1$$
$$r_1/b < 1 \qquad (7)$$

(There is strong physical evidence that strain rates $\dot{\epsilon}_i$ do not affect the scaling. We will present our arguments for their exclusion later.)

Eliminating four parameters in Table 1 leaves 13 quantities, which can be combined into 13 - 2 = 11 dimensionless groups, using the methods of dimensional analysis.[3] One possible set of these groups (or Pi terms) is given in Table 2. Let us discuss the implications of keeping all of these terms constant as scale is changed, which is the requirement for valid scale modeling.

Terms π_3 through π_7 state that the scaled geometry of the deformed lead-backed sheathing and the lead itself should be identical, if other scaled terms are also held constant, regardless of the complexity of the deformation pattern, for prismatic casks. There is ample

Table 2.
Pi Terms for Cask Impact

No.		
π_1	$(E/\sigma_{ui}d^3)$	An energy ratio
π_2	(h/d)	Geometric similarity
π_3	(y/d)	
π_4	(y_m/d)	
π_5	(r_1/d)	
π_6	(V_1/d^3)	
π_7	(V_2/d^3)	
π_8	(D/d)	
π_9	$(\sigma_{yi}/\sigma_{ui})$	Constitutive similarity
π_{10}	(S_i/σ_{ui})	
π_{11}	ε_i	Response

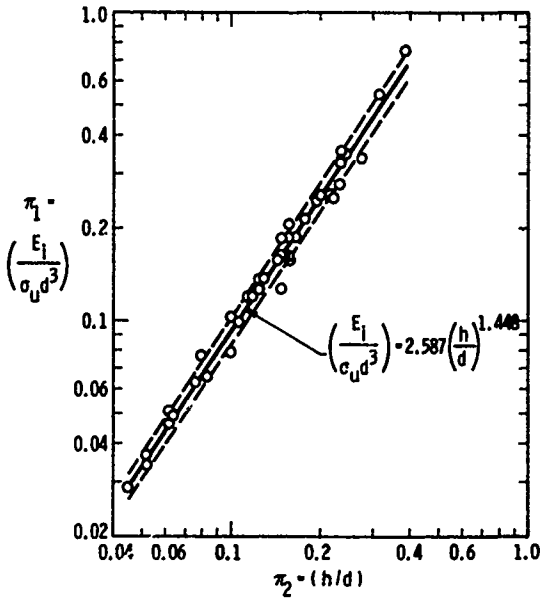

Figure 1. Scaled Penetration Data for Prismatic Casks

evidence in refs. 1 and 2 that this is so, with very repeatable and similar deformation patterns. Terms π_9 and π_{10} simply state that the plastic portions of the stress-strain curves for each material being deformed should be similar. When materials are not changed as model scale is changed, this is obviously true; it is also approximately true when sheathing is changed from hot-rolled steel to stainless steel. For other materials tested by Nelms, such as brass, copper, etc., thess terms are not necessarily invariant. Term π_{11} simply states that strains are unchanged at similar points in the deformed materials. So, for prismatic casks we are left with the term π_1 which one should be able to scale with term π_2, which in turn was deliberately varied over a considerable range in the experiments. For cylindrical casks, the term π_8 can be important, and was varied by Nelms in one set of tests. We can test this scaling law by replotting the data in refs.1 and 2 in scaled form, provided we enter appropriate values for the strength parameter σ_{ui} in term π_1. The original data appear in various tables in refs. 1 and 2. We present the data for prismatic casks in Figure 1* and Table 3. We do not include here the data obtained by Nelms for jacket materials which differed markedly from ductile steel. Use of the term π_1 is shown in Figure 1 to collapse all data onto a single curve, verifying the scaling law over the range of these test data. It is also apparent from Figure 1 that the logarithmic plot is linear, so an equation of the form

$$\left(\frac{E_i}{\sigma_u d^3}\right) = A\left(\frac{h}{d}\right)^n \qquad (8)$$

should fit the scaled data very well. We made a least-squares fit to an equation of this form, using all of the scaled values for π_1 and π_2. This gave

$$\left(\frac{E_i}{\sigma_u d^3}\right) = 2.587\left(\frac{h}{d}\right)^{1.448}, \pm 9.4\% \qquad (9)$$

The fitted curve and the error band are shown in Figure 1. This fit should not be used beyond the limits of the scaled data, which are:

$$0.045 \leq \left(\frac{h}{d}\right) \leq 0.37$$

$$0.037 \leq \left(\frac{E}{\sigma_u d^3}\right) \leq 0.80 \qquad (10)$$

The single equation (9) should replace the pair of empirical fits given by equations (1) and (2) and the dimensional fit of equation (3). The exponent in equation (1), if inverted to give W (or E for constant H) in terms of h, is 1.618, which is not greatly different from our exponent of 1.448. If equation (3) is made dimensionless by dividing through by d^3, the exponent in it is 1.4, which is even closer to our fit. We see no

*In this table, as in Tables 4 and 5 and Figures 4 and 5, the original data are all presented in English units as they appeared in the references. But, the scaled pi terms are all nondimensional and valid for the International System of Units (SI), or any other self-consistent set of units.

Table 3.
Data for Penetration of Prismatic Casks

h, in	d, in	E_i, in-lb	σ_u, ksi	$\pi_1 = \left(\frac{E_i}{\sigma_u d^3}\right)$	$\pi_2 = \left(\frac{h}{d}\right)$	Material
0.0495	0.3115	258	41.9	0.2037	0.159	
0.072	0.3115	471	47.8	0.3260	0.231	
0.117	0.3115	1063	47.1	0.7467	0.376	
0.0495	0.375	332	41.9	0.1503	0.132	
0.072	0.375	619	47.8	0.2456	0.192	
0.117	0.375	1345	47.1	0.5415	0.312	
0.072	0.4365	750	47.8	0.1887	0.165	
0.072	0.450	814	47.8	0.1869	0.160	A245 Grade A Steel
0.051	0.500	522	41.9	0.09967	0.102	
0.0595	0.500	708	47.1	0.1203	0.119	
0.072	0.500	943	47.8	0.1578	0.144	
0.110	0.500	1875	60.1	0.2496	0.220	
0.1183	0.500	2095	47.1	0.3558	0.237	
0.136	0.500	2595	62.0	0.3348	0.272	
0.072	0.552	1107	47.8	0.1377	0.130	
0.0495	0.625	784	41.9	0.07664	0.0792	
0.072	0.625	1409	47.8	0.1207	0.1152	
0.031	0.500	489	84.2	0.04646	0.062	
0.50	0.500	829	84.2	0.07876	0.100	304L Stainless Steel
0.0625	0.500	1328	84.2	0.1262	0.135	
0.074	0.500	1950	84.2	0.1852	0.148	
1.39	6.0	3.611×10^6	60	0.2786	0.232	A245 Grade A Steel
0.883	6.0	1.745×10^6	62.9	0.1284	0.1472	
0.5	6.0	1.150×10^6	81.2	0106557	0.0833	304L Stainless Steel
0.078	0.5	1668	85.1	0.1569	01156	304L Stainless Steel,annealed
0.120	0.5	2011	46.5	0.3459	0.240	ASTM-A366 Carbon Steel
0.038	0.5	337	43.0	0.06270	0.076	
0.076	0.5	1897	93.8	0.1618	0.152	304 Stainless Steel,annealed
0.107	0.5	1743	54.4	0.2563	0.214	ASTM A245 Steel
0.031	0.5	279	43.7	0.05108	0.062	
0.063	0.5	771	45.5	0.1355	0.126	Low Carbon Steel
0.074	0.5	1759	87.3	0.1612	0.148	316 Stainless Steel
0.078	0.5	1807	90.7	0.1593	0.156	321 Stainless Steel
0.078	0.6	2520	85.1	0.1377	0.130	304L Stainless Steel,annealed
01031	0.6	637	86.6	0103404	0.0517	
0.120	0.6	2532	46.5	0.2521	0.200	
0.038	0.6	443	43.0	0.04770	0.0633	ASTM-A366 Carbon Steel
0.027	0.6	591	94.6	0.02892	0.045	304 Stainless Steel,annealed
0.107	0.6	2509	54.4	0.2131	0.1783	ASTM-A245 Carbon Steel
0.031	0.6	347	43.7	0.03671	0.0517	Low Carbon Steel
0.063	0.6	973	45.5	0.09899	0.105	

need to make a fit similar to equation (2) to a higher order functional relationship for stainless steel jackets (nor did Nelms in ref. 2). The scaled data for stainless steel and carbon steel jackets are shown in Figure 1 to agree very well and a single curve fits all data.

Nelms[2] conducted some puncture tests of prismatic cask models with jacket materials quite different from the ductile carbon and stainless steels included in Table 3 and Figure 1. These materials included brass, copper, annealed tool steels, 4130 stainless steel, and

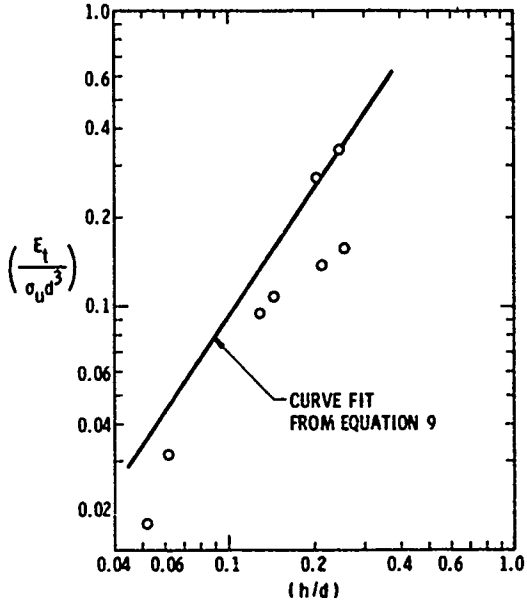

Figure 2. Scaled Penetration Data for Prismatic Casks with Materials other than Ductile Steels

a hardened 301 stainless steel. The high yield strength materials in this group usually had ultimate strains much lower than the ductile materials employed before, as did the brass. The copper had both low yield and high ductility. Both brass and copper have decidedly different elastic material properties from the steels. So, one would not expect as good correlation between scaled incipient puncture energy π_1 and scaled thickness π_2 because the constitutive pi terms π_9 and π_{10} in Table 2 are not invariant. The scaled data for this limited test series are shown in Figure 2, together with the curve fit given by Equation (9). One can see that the data do deviate significantly from the previous curve fit, and that one cannot arbitrarily change jacket materials and expect accurate scaling.

Why do we feel that strain-rate effects are unimportant in the scaling? Stress-strain data taken at very low strain rates in a laboratory test machine may indeed not be representative of the material characteristics at the somewhat higher rates representative of these low-velocity impacts and penetrations. But, the crucial question in estimating the effects of strain rate on the scaling of the penetration process is really, "How much do constitutive properties change between scale model and full-scale?" Mild steel shows as much change in properties with strain rate as any steel, as shown in Figure 3 from ref. 4. Properties of lead are shown in Figure 4, from ref. 5. The maximum difference in strain rates between model scale and prototype is in inverse ratio to the geometric scale (being proportionally higher in the small models); this is about 20 times in the experiments of Spaller[1]. If mean strain rates full-scale are about 1/sec, they will be no greater than 20/sec in the models. From Figures 3 and 4, one can see that ultimate stress

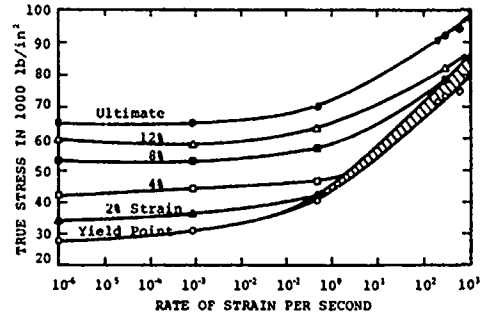

Figure 3. True Yield Stresses at Various Strains vs. Strain Rate for Mild Steel at Room Temperature

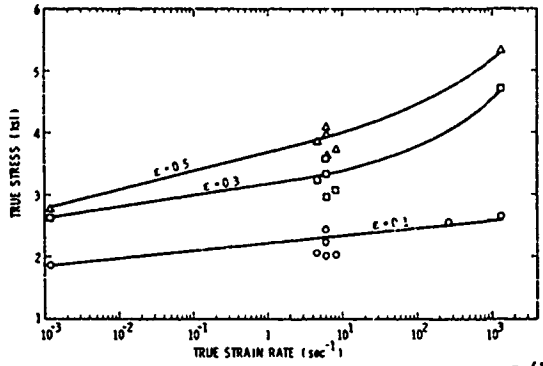

Figure 4. Stress-Strain Data for Lead at 78°F[5]

for mild steel only increases about 10% over this change in strain rate, while for lead the change is about 15%. The standard deviation in the determination of incipient penetration energy is of this same order (9.4%), so differences caused by higher strain rates in the models should be essentially undetectable. This is indeed borne out by the scaled data in Figure 1, which include results over geometric scale factors of about one to twenty. The full-scale data are quite indistinguishable from the small model data. Further, the observation that incipient puncture was dependent only on impact energy and not impact velocity for otherwise identical tests indicates independence from strain rate, because the tests at higher velocity are also tests at higher strain rate.

ENERGY SOLUTIONS FOR DEFORMATION AND PUNCTURE OF PRISMATIC CASKS

Analyzing the dynamic processes occurring during impact of the cask simulants onto the rods, and subsequent puncture, is quite difficult and expensive if one attempts to follow the entire time history of the process. But, by using the observed deformation patterns, one can sometimes obtain approximate analytic predictions by balancing the impact energy against plastic strain energy which is absorbed by the cask in deforming the sheathing and the lead and shearing through the sheathing. Methods of this kind have been quite useful in predicting permanent deformations of blast-loaded structures,[6,7] and in determining the form of penetra-

tion equations for tornado-borne missiles impacting steel reactor containment shells.

The steel sheathing develops plastic strain energy by bending, U_b, by extension or stretching, U_e, and by shearing U_s at the periphery of the sharp-edged rod being impacted. Deformation patterns in ref. 1 are very similar to those for steel panels impacted by long rod missiles. Expressions for U_b and U_e were developed in ref. 8, and are:

$$U_b = \frac{\pi}{2}\sigma_y y_m h^2 \frac{\left(r_1^2 - \frac{d^2}{4}\right)}{\left(r_1^2 - dr_1 + \frac{d^4}{4}\right)} \qquad (11)$$

$$U_e = \pi\sigma_y y_m^2 h \frac{\left(\frac{r_1^4}{3} - \frac{d^2 r_1}{2} + \frac{d^3 r_1}{3} - \frac{d^4}{16}\right)}{\left(-r_1^2 + dr_1 - \frac{d^4}{4}\right)^2} \qquad (12)$$

Review of the damage patterns in ref. 1 show that r_1 is essentially a constant times d, r_1 3d/2. Substituting into equation (11) and (12) gives

$$U_b = \pi\sigma_y y_m h^2 \qquad (13)$$

$$U_e = \pi\sigma_y y_m^2 h \qquad (14)$$

We can estimate U_s by considering the plug sheared out of the sheathing on impact as resisted by ultimate shear stress τ_u, integrated around the periphery of the impacted rod, and displaced the thickness h of the sheathing. We also assume that τ_u is related to σ_u by

$$\tau_u = \sigma_u/2 \qquad (15)$$

which corresponds to the Tresca yield condition for a biaxial stress state. These assumptions yield:

$$U_s = \left(\frac{\pi}{2}\right)\sigma_u d h^2 \qquad (16)$$

The total strain energy for steel sheathing deformation is then

$$U_t = U_b + U_e + U_s$$

$$U_t = \pi\left(\sigma_y y_m h^2 + \sigma_y y_h^2 + \frac{\sigma_u}{2} h^2 d\right) \qquad (17)$$

The contribution of plastic strain energy in the sheathing to absorbing the impact energy is then simply

$$E_s = U_t \qquad (18)$$

We can arrange eqs. (17) and (18) to cast them into the form of the π terms from our model analysis, giving:

$$\left(\frac{E_s}{\sigma_u d^3}\right) = \pi\left\{\left(\frac{h}{d}\right)\left(\frac{y_m}{d}\right)^2\left(\frac{\sigma_y}{\sigma_u}\right) + \left(\frac{h}{d}\right)^2\left[\left(\frac{y_m}{d}\right)\left(\frac{\sigma_y}{\sigma_u}\right) + \left(\frac{1}{2}\right)\right]\right\} \qquad (19)$$

From the ASTM standards, the ratio

$\frac{\sigma_y}{\sigma_u}$ equals 0.625 for ASTM A245 steel and equals 0.357 for 304L stainless steel.

Strain energy absorption in the lead is somewhat more difficult to estimate accurately, because we know only the shape and size of the surface deformation near the impact. This shape, for incipient perforation of the sheathing, is shown schematically in Figure 5. A much larger, and unfortunately unknown, volume V_2 of lead

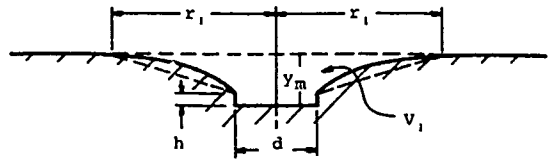

Figure 5. Schematic of Deformation in Lead

than the volume of the surface depression V_1 in Figure 5 has been plastically deformed. To estimate strain energy absorbed in the lead, we make several simplifying assumptions and use information from Figure 4. We first approximate the volume V_1 by the conic frustrum, shown in dashed lines in Figure 5. This gives

$$V_1 = \frac{\pi d^2 h}{4} + \frac{\pi(y_m - h)}{3}\left(r_1^2 - \frac{r_1 d}{2} + \frac{d^2}{4}\right) \qquad (20)$$

Using $r_1 \approx \frac{3d}{2}$, this reduces to

$$V_1^2 = \pi d^2\left(\frac{13 y_m}{12} - \frac{5h}{6}\right) \qquad (21)$$

We then estimate that the lead is being loaded at a mean strain rate of 10/sec, and establish from data in Figure 4 an approximate strain-hardening ratio $S/\sigma_y = 2.267$, to account in an approximate manner for the severe strain-harden-

ing in the lead. We next assume that the volume ratio V_2/V_1 is in proportion to scaled maximum deformation y_m/d. All of these assumptions lead to the approximate relation for strain energy U_L still containing an unknown ratio

$$\frac{V_1}{V_2} < 1;$$

$$U_L = \pi d^3 \sigma_L \left(\frac{V_1}{V_2}\right) \left[1 + 2.267 \left(\frac{y_m}{d}\right)\right] \times \left[\frac{13}{12}\left(\frac{y_m}{d}\right) - \frac{5}{6}\left(\frac{h}{d}\right)\right] \quad (22)$$

Equating this to the portion of impact energy absorbed by the lead and rearranging, we have

$$\left(\frac{E_L}{\sigma_u d^3}\right) = R\pi \left[1 + 2.267 \left(\frac{y_m}{d}\right)\right] \times \left[\frac{13}{12}\left(\frac{y_m}{d}\right) - \frac{5}{6}\left(\frac{h}{d}\right)\right] \quad (23)$$

where R is an undetermined dimensionless ratio given by

$$R = \left(\frac{\sigma_L}{\sigma_u}\right)\left(\frac{V_1}{V_2}\right) \quad (24)$$

Consider now the two prediction equations developed by energy balances, eq. (19) and (23). Data from refs. 1 and 2 allow prediction of the scaled impact energy for incipient puncture, because all quantities on the right hand side are reported in ref. 1, including values of (y_m/d) corresponding to the maximum energy for no penetration. Table 4 includes all of these data, and in the sixth column the values of $(E/\sigma_u d^3)$ computed from eq. (19), using the appropriate values of (σ_y/σ_u) for the two steels. These scaled energies are also plotted in Figure 6, labeled "Steel Deformations." One can see that they lie well below the curve which we previously fitted to the scaled experimental impact energies for incipient puncture, which has been transposed from Figure 1. Also, the dependence of scaled energy on (h/d) is different, having a much steeper slope on this plot.

Because the prediction equation for energy absorbed in deforming lead contains an unknown parameter R, we cannot simply compute scaled energy from eq. (23) and add to values for energy absorbed in steel deformation. Instead, we must use experimental values of scaled energy

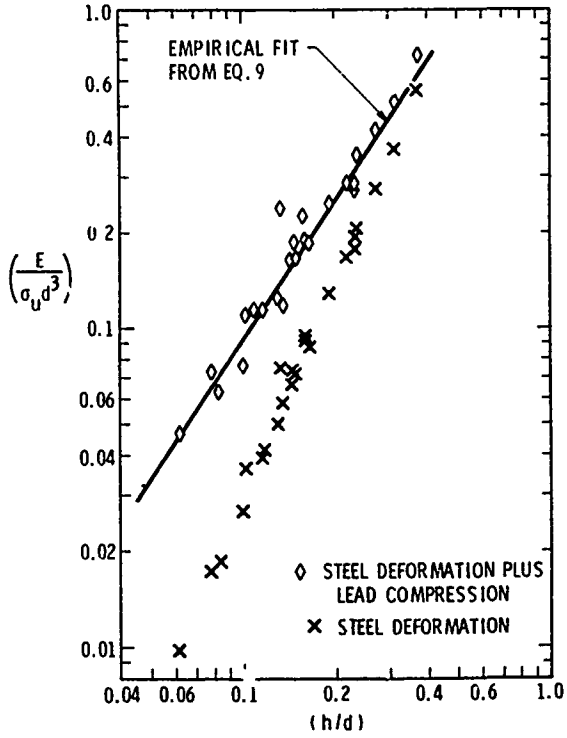

Figure 6. Energy Solutions

to help us estimate R, as follows:

1) Compute measured scaled energy from the definition of term π_1 using data from ref. 1 including experimental values of incipient puncture energy listed in 4th column of Table 4. These values are given in the fifth column of the table.

2) Compute the ratio $(E/\sigma_u d^3)/R$ from eq. (23) divided by R. These values are given in the seventh column of Table 4.

3) Obtain an estimate of R for each test point. This is done by subtracting column six from column five, and dividing the result by column seven. The estimates are listed in column eight.

4) For each jacket material, average the estimates of R. For hot-rolled steel, $R_{avg} = 0.09945$, while for stainless steel, $R_{avg} = 0.04710$. We expect the value for stainless steel to be somewhat lower than for hot-rolled steel, because stainless steel has a higher ultimate stress (see eq. 24).

5) Using the appropriate average value for R, compute an adjusted scaled energy by multiplying R_{avg} by column seven and adding to column six. These values are given in the last column, column nine, and are plotted in Figure 6.

Table 4.
Predictions from Energy Solutions

Col. 1	Co. 2	Col. 3	Col. 4	Col. 5 Measured	Col. 6 Steel	Col. 7 Lead	Col. 8	Col. 9 Adjusted
d,in	$\left(\frac{h}{d}\right)$	$\left(\frac{y_m}{d}\right)$	E_i, in-lb	$\left(\frac{E_i}{\sigma_u d^3}\right)$	$\left(\frac{E_s}{\sigma_u d^3}\right)$	$\left(\frac{E_L}{\sigma_u d^3}\right)/R$	R	$\left(\frac{E_t}{\sigma_u d^3}\right)$
A245 Grade A Steel								
0.3115	0.1589	0.3413	274	0.2164	0.0929	1.3225	0.09339	0.2244
0.3115	0.2311	0.3538	497	0.3440	0.1778	1.0796	0.1539	0.2852
0.3115	0.3756	0.5140	1,092	0.7671	0.5588	1.6586	0.1256	0.7237
0.375	0.132	0.3675	344	0.1557	0.07495	1.6593	0.04867	0.2400
0.375	0.192	0.3467	650	0.2579	0.1283	1.2096	0.1071	0.2486
0.375	0.312	0.4515	1,410	0.5768	0.3641	1.4566	0.1460	0.5090
0.4365	0.1649	0.2978	808	0.2033	0.08732	0.9746	0.1190	0.1842
0.450	0.1600	0.3067	853	0.1958	0.08518	1.0594	0.1044	0.1905
0.500	0.102	0.2304	535	0.1021	0.03168	0.7872	0.08946	0.1100
0.500	0.119	0.2362	780	0.1325	0.04185	0.7559	0.1199	0.1170
0.500	0.144	0.2834	949	0.1588	0.06682	0.9649	0.09532	0.1628
0.500	0.22	0.3622	1,920	0.2556	0.1671	1.1959	0.07400	0.2860
0.500	0.2366	0.402	2,130	0.3618	0.2072	1.4310	0.1080	0.3495
0.500	0.272	0.4252	2,600	0.3355	0.2745	1.4435	0.04275	0.4181
0.552	0.1304	0.2428	1,158	0.1440	0.04991	0.7520	0.1251	0.1247
0.625	0.0792	0.1792	808	0.07899	0.01705	0.5660	0.1094	0.07334
0.625	0.1152	0.2331	1,463	0.1254	0.03921	0.7515	0.1147	0.1139
6.0	0.2317	0.3854	3.611+6	0.2786	0.1925	1.3211	0.06517	0.3239
6.0	0.1472	0.3073	1.745+6	0.1284	0.07440	1.1206	0.04819	0.1858
							(Avg. 0.09945)	
Type 304L Stainless Steel								
0.5	0.062	0.2048	463	0.04399	0.00984	0.7830	0.04361	0.04672
0.5	0.100	0.2678	765	0.07268	0.02675	1.0440	0.04593	0.07592
0.5	0.135	0.3228	1,270	0.1207	0.05811	1.2903	0.04851	0.1189
0.5	0.148	0.410	1,910	0.1815	0.07238	1.9450	0.05610	0.1640
6.0	0.0833	0.2448	1.039+6	0.05713	0.01840	0.9362	0.04137	0.0625
							(Avg. 0.04710)	

The equations for predicting scaled energies for incipient penetration, based on the procedure described, are:

For A245 Grade A steel sheathing,

$$\left(\frac{E_t}{\sigma_u d^3}\right) = \left(\frac{E_s}{\sigma_u d^3}\right) + \left(\frac{E_L}{\sigma_u d^3}\right) = \pi \left\{ 0.625 \left(\frac{h}{d}\right)\left(\frac{y_m}{d}\right)^2 + \left(\frac{h}{d}\right)^2 \left[0.625 \left(\frac{y_m}{y_d}\right) + \frac{1}{2} \right] + 0.09945 \left[1 + 2.267 \left(\frac{y_m}{d}\right) \right] \left[\frac{13}{12} \left(\frac{y_m}{d}\right) - \frac{5}{6} \left(\frac{h}{d}\right) \right] \right\} \quad (25)$$

For 304 L stainless steel sheathing,

$$\left(\frac{E_t}{\sigma_u d^3}\right) = \pi \left\{ 0.357 \left(\frac{h}{d}\right)\left(\frac{y_m}{d}\right)^2 + \left(\frac{h}{d}\right)^2 \left[0.357 \left(\frac{y_m}{d}\right) + \frac{1}{2} \right] + 0.04710 \left[1 + 2.267 \left(\frac{y_m}{d}\right) \right] \times \left[\frac{13}{12} \left(\frac{y_m}{d}\right) - \frac{5}{6} \left(\frac{h}{d}\right) \right] \right\} \quad (26)$$

By inspecting Figure 1 and 6, one can see that predictions from eq. (25) and (26) do describe nearly the same relationship between

scaled impact energy for puncture and scaled sheathing thickness as the purely empirical fit given by eq. (9). The scatter is, however, somewhat greater for the energy method prediction equations. A least-square fit to a logarithmic relation between scaled impact energy and scaled sheathing thickness yields the equation

$$\left(\frac{E_i}{\sigma_u d^3}\right) = 2.920\left(\frac{h}{d}\right)^{1.491} \pm 13.5\% \qquad (27)$$

with limits the same as given in eq. (10). By comparing with eq. (9), we can show that either equation gives predictions which lie within the error band for the other over the entire range of (h/d).

IMPACT PUNCTURE OF CYLINDRICAL CASKS

Spaller[1] conducted a few exploratory tests of cylindrical cask models to supplement his primary data for prismatic casks. Nelms[2] ran a more extensive series of model impact tests of cylindrical casks, obtaining values for incipient puncture energies for several combinations of $\pi_8 = (D/d)$ and $\pi_2 = (h/d)$ and a single jacket material, A245 steel. Nelms' tests covered three values of π_2, with π_8 being systematically varied for each value of π_2. Both investigators found that cylindrical casks were somewhat more resistant to puncture than prismatic casks with equal jackets, and Nelms obtained enough data to generate the empirical equations (4) and (5).

Nelms' data for cylindrical cask puncture thresholds can be generalized somewhat, using the dimensionless pi terms from our model analysis and using eq. (9) to extend the range of one parameter. To do this, we first generate a new pi term from π_8 by inverting,

$$\pi_8' = \frac{1}{\pi_8} = \frac{d}{D} \qquad (28)$$

We then scale Nelms' data, in Table 5, but also include scaled values for $\pi_8' = 0$, from the fit to prismatic cask test data in equation (9). The scaled data are also plotted in Figure 7. The plots show that scaled impact energy π_1 is a weak function of π_8'. The general dependence is

$$\pi_1 = f\ (\pi_2, \pi_8')$$

or

$$\left(\frac{E_i}{\sigma_u d^3}\right) = f\left[\left(\frac{h}{d}\right), \left(\frac{d}{D}\right)\right] \qquad (29)$$

Table 5. Data and Scaled Data for Cylindrical Cask Puncture Tests

d, in	D, in	E_i, in-lb	$\left(\frac{E_i}{\sigma_u d^3}\right)$	$\left(\frac{h}{d}\right)$	$\left(\frac{d}{D}\right)$
0.4	4.19	877	0.2670	0.1875	0.09542
0.4	4.65	868	0.2644	0.1875	0.08598
0.4	5.20	863	0.2629	0.1875	0.07692
0.4	6.16	853	0.2600	0.1875	0.06494
0.5	4.19	1213	0.1892	0.150	0.1193
0.5	4.66	1202	0.1874	0.150	0.1073
0.5	5.15	1198	0.1868	0.150	0.09709
0.5	6.17	1181	0.1843	0.150	0.08103
0.5	6.65	1173	0.1830	0.150	0.07519
0.5	7.18	1166	0.1819	0.150	0.06964
0.6	4.65	1482	0.1338	0.125	0.1290
0.6	5.22	1472	0.1381	0.125	0.1149
0.6	6.65	1451	0.1310	0.125	0.09025
0.6	6.9	1444	0.1304	0.125	0.08696
-	-	-	0.2407	0.1875	0
-	-	-	0.1720	0.150	0
-	-	-	0.1307	0.125	0

Notes:

1) For all tests, h=0.075 in and σ_u=51,300 psi.

2) Last three values are obtained from fit to prismatic cask data.

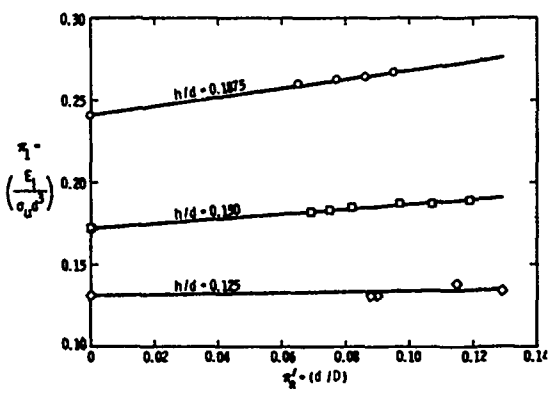

Figure 7. Scaled Puncture Energy for Cylindrical Casks

An excellent empirical fit describing the function f in eq. (29) is

$$\left(\frac{E_i}{\sigma_u d^3}\right) = 2.587\left(\frac{h}{d}\right)^{1.448}\left\{1 + \left(\frac{d}{D}\right)\left[-258.03\left(\frac{h}{d}\right)^2 + 94.873\left(\frac{h}{d}\right) - 7.5723\right]\right\} \qquad (30)$$

which holds for

$$0.125 \leq \left(\frac{h}{d}\right) \leq 0.1875,$$

$$0 \leq \left(\frac{d}{D}\right) \leq 0.129 \qquad (31)$$

The solid lines in Figure 7 represent equation (30) bounded by the expressions (31), and can be seen to pass almost exactly through all data points. Note also that the scaling extends the overall range of the test data and permits correlation with prismatic cask data.

DISCUSSION AND CONCLUSIONS

Based on Staller's[1] and Nelms'[2] experimental data on puncture resistance of prismatic simulants of shipping casks for spent nuclear reactor fuels, the author has conducted a similitude study and developed an empirical relation between scaled energy for incipient cask shell puncture and scaled shell thickness. This relation, eq. (9), fits all model-scale and full-scale data in refs. 1 and 2 quite well.

Both the impact test data and material test data taken at various strain rates for steels and lead indicate that variation in material properties due to different average strain rates in models and prototypes do not measurably affect the validity of the scaling law for scale factors up to twenty.

Approximate analytic formulas for predicting impact energies to puncture can be developed by equating strain energies developed in plastically deforming the sheathing and lead shielding in the cask simulants to the impact energy. The author develops and presents such formulas. They require input from experimental data to determine certain constants, but, once these constants are determined, they give good predictions of puncture energy and essentially the same relationship between scaled energy and scaled sheathing thickness as eq. (9). Furthermore, these relations show that the majority of the impact energy is absorbed by deforming the lead shielding for small values of scaled sheathing (h/d), but that the steel sheathing absorbs much more energy as (h/d) increases.

The model analysis is used as a basis for a two-parameter fit to data for puncture of cylindrical casks, including data for prismatic casks. A single empirical equation fits all of these data very well.

The empirical and energy equations in this paper are limited in their applicability to the specified ranges of scaled parameters, and to other restrictions based on the limitations of the tests in ref. 1 and 2. The other restrictions are normal impacts, room temperature of cask, no gap between sheathing and lead, and the specific geometry of the impacted "piston" (sharp-cornered, right circular cylinder). Limited additional tests are reported in ref. 1 which partially evaluate the effects of temperatures from -80°F to +180°F, and of small gaps between sheathing and lead simulating gaps which could exist in real casks. Spaller[1] concluded that:

1) Casks at temperature significantly below room temperature require increased impact energy to puncture.

2) Casks at elevated temperatures (up to +180°F) show no significant decrease in puncture resistance over casks at room temperature (70°F).

3) Gaps between sheathing and lead shielding had no apparent effect on puncture resistance.

These conclusions all render the prediction of puncture energies from the basic data in ref. 1, and from prediction equations in this paper, somewhat conservative.

REFERENCES

1. A. E. Spaller, "Structural Analysis of Shipping Casks, Vol. 2. Resistance to Puncture," ORNL TM-1312, Vol. 2, Oak Ridge Nat. Lab., Oak Ridge, Tenn., Sept. 1966.

2. H. A. Nelms, "Structural Analysis of Shipping Casks. Vol. 3. Effects of Jacket Physical Properties and Curvature on Puncture Resistance," ORNL TM-1312, Vol. 3, Oak Ridge Nat. Lab., Oak Ridge, Tenn., June 1968.

3. W. E. Baker, P. S. Westine and F. T. Dodge, SIMILARITY METHODS IN ENGINEERING DYNAMICS, Hayden Book Co., Rochell Park, NJ, 1973.

4. N. J. Huffington, Jr. (ed.), BEHAVIOR OF MATERIALS UNDER DYNAMIC LOADING, Am. Soc. of Mech. Eng., N.Y., 1965.

5. U. S. Lindholm and A. Nagy, "Compression Test on Lead Samples," Final Test Report, P. O. RQ/MR 18349 from Knolls Atomic Power Lab., Gen. Elec. Co., Schenectady, N. Y., March 1977.

6. P. S. Westine and W. E. Baker, "Energy Solutions for Predicting Deformations in Blast-loaded Structures," Edgewood Arsenal Contractor Report EM-CR-76027, Report No. 6, Edgewood Arsenal, MD, Nov. 1975.

7. P. S. Westine and P. A. Cox, "Additional Energy Solutions for Predicting Structural Deformations," Edgewood Arsenal Contractor Report EM-CR-76031, Report No. 4, Edgewood Arsenal, MD, Nov. 1975.

8. W. E. Baker, J. C. Hokanson and R. A. Cervantes, "Model Tests of Industrial Missiles," Final Report, SwRI Project 02-9153-001, Southwest Res. Inst., San Antonio, TX, May 1976.

FINITE ELEMENT ANALYSIS OF MULTICOMPONENT STRUCTURES IN RIGID BARRIER IMPACTS

J. K. Gran, L. E. Schwer,
J. D. Colton, and H. E. Lindberg
SRI International
Menlo Park, California

Techniques are presented for the transient analysis of multicomponent structures impacting rigid barriers using the finite element method. The analysis considers distortion and failure of joints, multiple impacts, and elastic-plastic material behavior. The models for each component of an example structure are developed separately, guided by the results of impact experiments. A comparison of the predictions of these finite element models with the results of the experiments demonstrates the applicability and accuracy of the models. The complete structure is then analyzed by combining the component models. The net result is good correlation of experiment and analytical prediction for the acceleration of a mass on a rather complex structure.

INTRODUCTION

The structural analyst working in the fields of crashworthiness, safety analysis, or shock isolation is often asked to analyze the transient response of structures in which several structural components are joined together with bolts or spot welds. The analysis of such multicomponent structures in rigid barrier impacts poses difficult modeling problems, because joints may fail during the time of interest and more than one structural member may strike the barrier. Standard finite element techniques are generally sufficient for modeling the individual structural components, but analysis of joint distortion and failure, and treatment of multiple impacts require innovative techniques.

This paper describes the development and application of two modeling techniques that can be incorporated into most finite element programs for the analysis of multicomponent structures: a simple method by which shearing bolts can be modeled and a straightforward method of treating multiple impacts against a rigid barrier during a single simulation. An example also illustrates the use of experiments to define the requirements of analytical models and guide their development.

First a multicomponent structure and its experimentally determined response in rigid barrier impacts is described. For each component of the structure, a finite element model is developed. The level of refinement necessary to achieve accurate predictions is determined by comparing the models against experiments designed to measure the response of a single component. The shearing bolt model and the multiple impact model are then developed and the predictions of these models are compared with experimental measurements. Finally, the component models are assembled to analyze the complete structure.

STRUCTURAL RESPONSE

Consider the multicomponent structure shown in Figure 1. It consists mainly of a circular plate bolted at 30° intervals to the flange of an L-section circular ring. The web of the ring is attached to a thin cylindrical shell with two rows of rivets. In the figure, the shell edge is shaded for clarity. The gap between the edge of the plate and the inside surface of the shell is about 8/10 of a bolt diameter. A rigid mass, representing electronic and mechanical equipment, is integrally connected to a rectangular mounting pad. The pad is bolted to the plate with four bolts. All structural elements except the high strength steel bolts are 6061-T6 aluminum. The response of this structure, especially the acceleration of the equipment mass, during a lateral impact of the shell against a rigid barrier is to be determined.

An initial set of experiments was conducted to determine the important response features and the sequence of the response [1]. The structure drawn in Figure 1 was launched so that it struck side-on into a rigid barrier. In high speed impacts (>10 m/sec) the shell wall suffers permanent radial deformation locally at the impact point. The ring forms a plastic hinge near the impact point but otherwise remains elastic. In the impact configuration shown, the bolt nearest the impact point shears to failure while plastically deforming the bolt holes in the ring and plate. Most of the early load to the plate comes

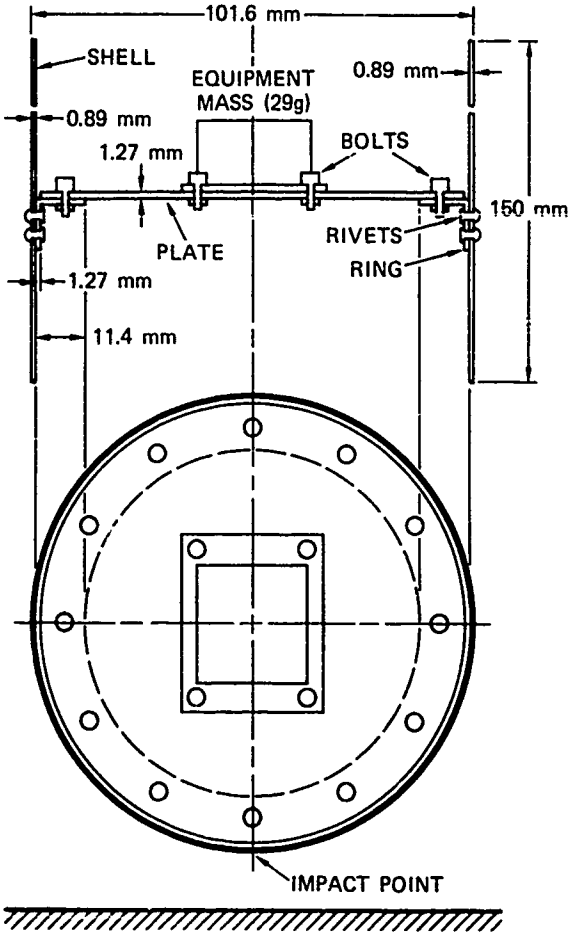

Fig. 1 - Multicomponent Structure in Impact Orientation

from this bolt and the two neighboring bolts. The plate then continues its forward motion until it strikes the inside of the shell. This second impact produces plastic strain in the plate. For about 250 μsec the plate strains are almost entirely membrane, and it is during this interval that the peak in-plane acceleration of the equipment mass occurs. The only forces acting on the equipment mass are the equipment mounting bolt forces. Depending on the mass of the equipment and the impact velocity, these bolts may also break.

The value of these initial experiments is twofold. First, they determined the response features that must be included in an accurate analytical model. These are the plastic hinge in the ring, bolt failure, plate impact, plate plasticity, and equipment acceleration due to bolt forces. Second, the experiments suggested a major simplification in the analysis. That is, even though the structure is three-dimensional the significant response features are all basically planar phenomena. Thus, for this problem, plate bending and out-of-plane ring bending can be neglected. Also, by inspection, the shell stiffness is small compared to that of the ring, so the shell can be treated in a simplified way.

COMPUTATIONAL MODELS

To analyze the structural response and predict the acceleration of the equipment mass, two-dimensional finite element models for the plate, ring, and bolts, and an algorithm for multiple impacts were first developed separately. The shell effects were approximated by including a nominal length of shell in the ring cross section. The bolts were modeled with simple beam elements. For each component an experiment was performed to determine the mesh refinement necessary in the model and to verify the accuracy of the predictions. Then these models were combined to model the complete structure. The computational models were developed using a modified version of SUPER,* a three-dimensional general purpose finite element structural analysis code.

Plate Model

The circular plate was modeled with elastic-plastic constant strain triangular plate elements in plane stress. The element mesh used in the analysis of the complete structure is shown in Figure 2. It contains 37 elements and 28 nodes. Near the impact point the element side lengths are as small as 5 mm so that local plastic response and high strain gradients are calculated accurately. The plasticity model consists of a Von Mises yield criterion with linear strain hardening.

A mesh similar in refinement to the one in Figure 2, but without nodes at the bolt holes, was used to analyze the experiment designed to measure the response of the plate alone. In the experiment, a 5.1-mm-thick, 99.8-mm-diameter plate was press-fit into a 0.9-mm-thick wall shell. A uniaxial strain gage aligned to measure radial strain was mounted on each side of the plate, 25 mm from the impact point. In the analysis, all the plate nodes were given an initial velocity except the node at the impact point, which was held fixed.

---

* The SUPER code was originally written at the University of Illinois at Chicago Circle by Belytschko et al. [2] for the transient analysis of three-dimensional space frames. The governing equations are formulated using a finite element technique that incorporates rigidly convected or corotational coordinates to treat arbitrary large displacements with small strains. Both explicit and implicit solution techniques are included, plus a modal analysis option for determining natural frequencies and corresponding mode shapes. The code has since been modified at SRI to expand its range of applicability in structural analysis. In particular, a three-dimensional triangular plate/shell element as suggested by Marchertas and Belytschko [3] has been incorporated. The code is still under development and no comprehensive documentation is available.

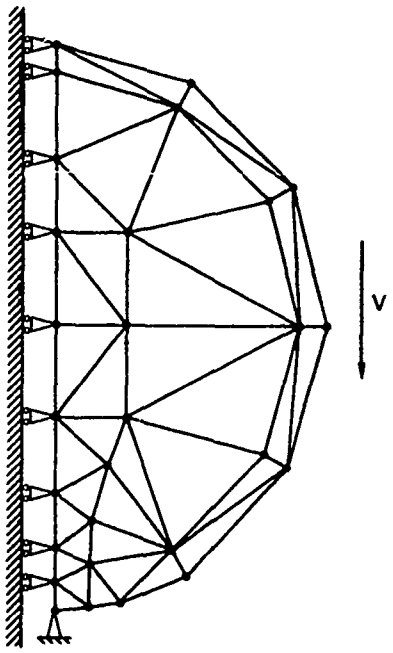

Fig. 2 - Plate Model: constant strain triangle element mesh

Figure 3 compares the radial strain predicted in the SUPER calculation with the radial membrane strain measured in the experiment. The calculated strain is from a 10-mm element at the strain gage location. The measured strain is the average from the gage on each side of the plate. The predicted peak strain is in good agreement with the measurement; the shorter rise time in the calculation is due to the idealization of the impact. In a posttest inspection, the plate showed clear signs of plastic flow within a 4-mm-radius region around the impact point. The calculated plastic zone extended 5 mm from the impact point. The results of an elastic calculation (not shown) indicated that the effect of this plastic flow is to decrease by about 50% the radial strains 25 mm away from the impact point.

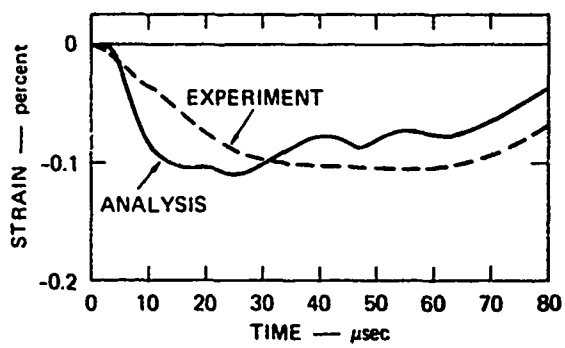

Fig. 3 - Measured and Predicted Plate Strains

Ring Model

The L-section ring was modeled with straight three-dimensional elastic-plastic beam elements, constrained to move only in a plane parallel to the plate. The beam cross-section and the element mesh are shown in Figure 4. The mesh consists of six elements, each approximately 25 mm long. The effects of the shell that surrounds the ring were approximated by including a 33-mm length of shell in the beam cross-section. This length represents twice the decay distance of edge effects in an axisymmetric shell analysis.

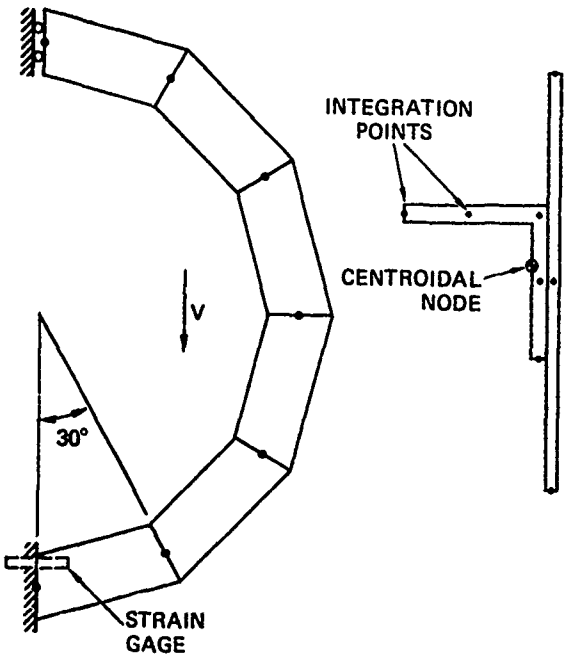

Fig. 4 - Ring Model: beam element mesh and beam cross-section (not to scale)

The integration points shown in Figure are used to numerically evaluate the nodal forces and moments. By using a modified trapezoidal integration scheme, it is possible to preserve the exact elastic bending stiffness of the element. The beam cross section is divided into strips and across each strip the axial stress is allowed to vary linearly. The total nodal forces and moments are then found by adding the contributions of all the strips.

In the experiment used to test the accuracy of the ring model, a ring and shell were riveted together just as in a complete structure, but a plate was not included. One of several strain gages, oriented in the circumferential direction, was mounted on the flange of the ring near the inside rim at 0° (behind the impact point). This gage is drawn in Figure 4. Gages were also located 60°, 90°, 120°, and 180° from the impact point. The assembly was launched into a rigid barrier at 5.2 m/sec.

In Figure 5, the strain measured at 0° is compared with the strain calculated at node 1, integration point 1, in the analysis of the test. The peak strains agree well even though they exceed the elastic limit (0.445%). The rise time in the calculation is considerably lower than measured, but again, this is due to the idealization of the impact in the analysis. Generally, comparisons of calculated and measured strains at the 60°, 90°, 120°, and 180° locations show that the calculated strains rise more quickly and to a greater magnitude than the measured strains. However, in both theory and experiment the peak strain level drops off sharply away from the impact point, and an accurate prediction of these low level strains in the analysis of the complete structure is of secondary importance.

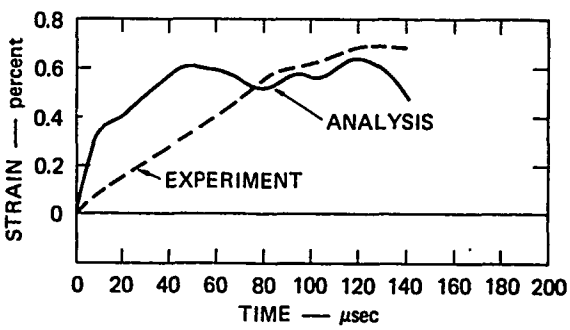

Fig. 5 - Measured and Predicted Ring Strains

Bolt Model

In the development of the bolt model, several quasi-static lap shear tests were performed to determine the combined force-deflection properties of the shearing bolts and the distorting bolt holes. The test configuration is illustrated in Figure 6. In the first set of tests, three 25-mm-wide strips of high alloy steel were bolted together with a single 1.2-mm-diameter high strength steel bolt and nut. The middle strip was 2.5 mm thick; the outer strips were 1.27 mm thick. In an Instron machine, the outer strips were pulled in one direction, the inner strip was pulled in the opposite direction, and the resulting force-deflection curve was recorded. The cross-head speed was 0.5 mm/min. A typical loading force-deflection relation is shown by the dashed curve in Figure 7. Since hole distortion was negligible in these tests, they provided a direct measure of the energy absorbing capacity of the bolts alone.

In the second set of tests, the steel strips were replaced with 6061-T6 aluminum strips. In eight tests the breaking force ranged from 1086 N to 1935 N and averaged 1886 N. The breaking displacement ranged from 0.58 mm to 0.86 mm and averaged 0.76 mm. A typical loading force-deflection relation for these tests is shown by the heavy solid curve in Figure 7. The force measured here is twice as great as that required

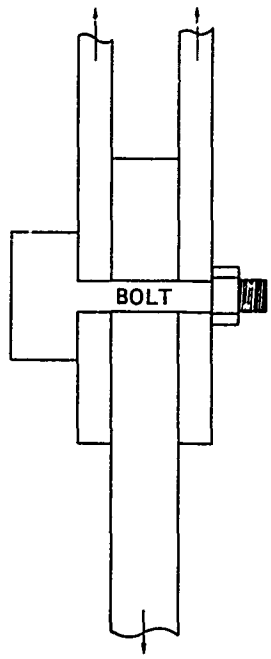

Fig. 6 - Quasi-Static Bolt Test Configuration

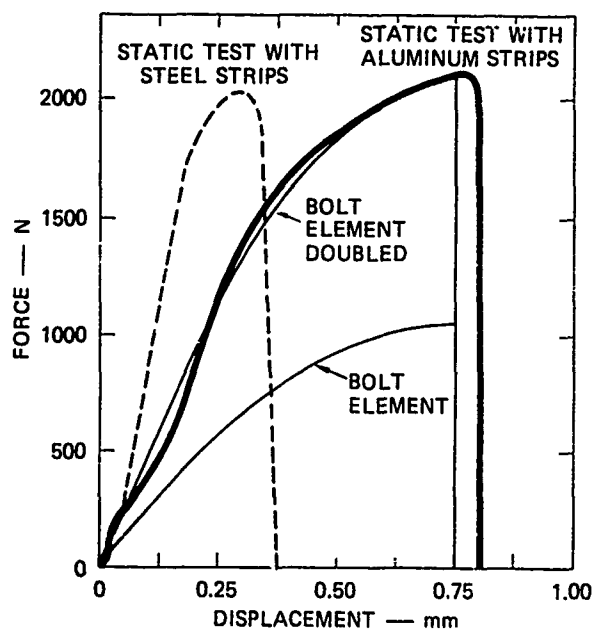

Fig. 7 - Quasi-Static Test Results and Bolt Element Characteristic

to break one bolt since the bolt was sheared in two places (between the outer and inner aluminum strips). In addition, this force-deflection relation represents the combined effects of the bolt shearing and the local plasticity in the aluminum strips. Based on the area under the two experimental force-deflection curves, the energy absorbed through bolt deformation is about equal to the energy absorbed through hole distortion in the aluminum strips.

The technique used to model these characteristics uses a lumped stiffness beam element, with a modification to account for bolt breaking. Consider the shear deformation of the clamped-clamped beam shown in Figure 8. In the absence of axial stiffness, the internal moments M and shear forces V are given by

$$\begin{bmatrix} M_I \\ M_J \end{bmatrix} = K \begin{bmatrix} 4 & 2 \\ 2 & 4 \end{bmatrix} \begin{bmatrix} \theta_I \\ \theta_J \end{bmatrix} \tag{1}$$

and

$$V_I = V_J = \frac{M_I + M_J}{\ell} \tag{2}$$

where K is the bending stiffness and ℓ is the length. For the particular case of a clamped-clamped beam

$$\theta_I = \theta_J = \theta = \tan^{-1} \frac{d}{\ell} \tag{3}$$

where d is the shear deflection. It follows from Eqs. (1) and (2) that

$$M_I = M_J = 6\,K\theta \tag{4}$$

and

$$V_I = V_J = \frac{12K\theta}{\ell} \tag{5}$$

The shear force F, which is work conjugate with the shear displacement d, is

$$F = V \cos\theta \tag{6}$$

Combining Eqs. (5) and (6) gives the force-deformation relation for the bolt element

$$F = \frac{12K\theta}{\ell} \cos\theta \tag{7}$$

Choosing ℓ = 0.76 mm and K = 0.106 N-m gives a good approximation to the typical experimental curve representing the combined effects of bolt shearing and bolt hole distortion. A comparison is shown in Figure 7.

To model breaking of the bolt, additional logic was introduced in the subroutine that calculates the bolt force. If the absolute value of the bolt force exceeds a prescribed value, the internal forces are set equal to zero. For the force-deformation curve shown in Figure 7, the bolt-breaking force was taken as 943 N, which occurs at a shear displacement of 0.76 mm. These values match the mean results of the quasi-static shear tests. For simplicity, since the peak

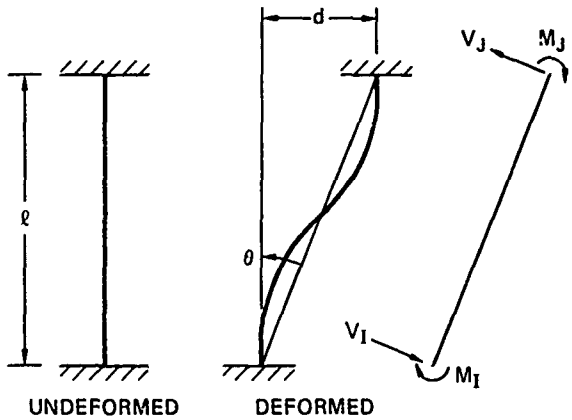

Fig. 8 - Forces and Displacements for the Bolt Element

equipment acceleration occurs while the mounting bolts are being loaded, experimental unloading characteristics were not modeled, and the unloading path for this bolt model is the same as that for loading. Results of impact tests, shown below, indicate that for general use the bolt model should include experimental unloading characteristics.

The principal advantage of this bolt model is that one simple element is used to account for both the shearing of the bolt and the plastic deformation of the bolt holes. The alternative of including a sufficient number of elements around the bolt holes to account for the local plasticity would make the cost of a numerical simulation prohibitive. However, the bolt element formulation also has limitations. For example, in two- or three-dimensional analyses where rotational degrees of freedom are admitted at the bolt element nodes, spurious internal moments generated by the bolt elements would cause additional bending deformation and would alter the force-deformation characteristics of the element.

An experiment was performed to check the predictions of the bolt model (and the multiple impact model discussed below). The structure consisted of the standard plate, ring, and shell. However, to check the bolt model for the simplest feasible configuration, the plate was attached to the ring with a single 1.2-mm-diameter high strength steel bolt at the 0° location (in line with the impact point). To hold the assembly aligned during acceleration, a second bolt was installed in a radial slot at the back edge of the plate, so that it exerted no force in the direction of impact. Strain gages were mounted along the diameter passing through the impact point to measure radial strain on both surfaces of the plate, at 15.7 mm from the leading edge. A contact-sensing gage (thin films of copper that closed a circuit) was mounted on the inside of the shell at the impact point to sense the impact of the plate against the shell. The assembly

was launched into a rigid barrier at 8.6 m/sec.

Figure 9 shows a comparison of the membrane strain measured in the experiment and the strain predicted in the corresponding finite element analysis. Zero time in this plot is the initial barrier contact. The origin in the calculated curve is shifted along the time axis to the point when strains are first measured in the experiment. Up to about 140 μsec, the strains are due to the single bolt force; after that the second impact forces dominate. The measured strain due to the bolt force is matched very well by the calculation. The dip in the calculated strain just before the second impact is caused by the bolt's breaking at a shear displacement of 0.76 mm. There is no corresponding dip in the experimental strain because in this particular test the bolt did not fracture. (In other experiments with different instrumentation the 0° bolt commonly fractured.)

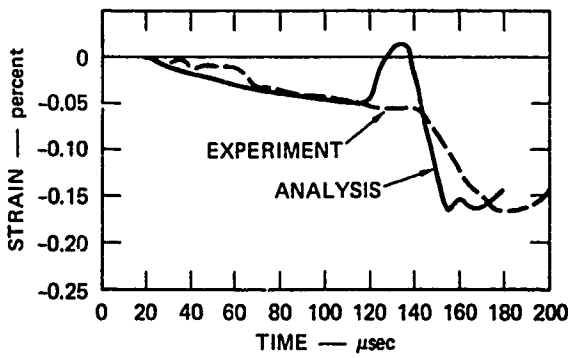

Fig. 9 - Measured and Predicted Plate Strains Due to Single Bolt Force and Second Impact

Multiple Impact Model

A multiple impact algorithm was developed to model the impact of the plate against the shell wall. This was accomplished by modifying the subroutines in which the initial conditions are specified and the equations of motion are integrated. In the modified subroutines the maximum allowable displacement of a given node in a given direction is specified, and the position of the node is monitored at each time step. If the explicit integration of the equations of motion produces a displacement greater than the specified maximum, the displacement is adjusted to equal the specified maximum and the new internal forces are computed with the node in this position. In the example, the leading node in the plate is allowed a displacement of 0.89 mm before it must stop at the shell wall. As long as the calculated force between the plate and shell is compressive, the plate and shell remain in contact. As soon as this force becomes tensile, the contact is broken and the plate is allowed to move away from the shell. This sequence is illustrated in Figure 10

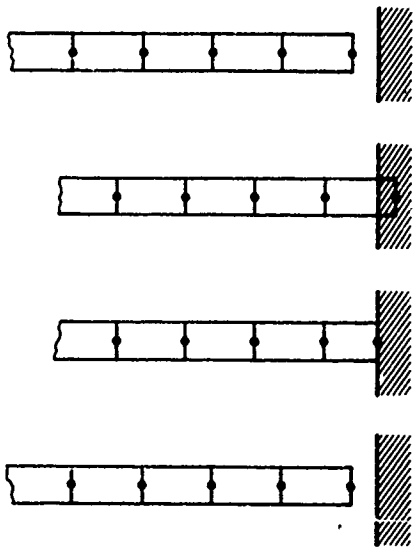

Fig. 10 - Illustration of Multiple-Impact Model

The technique of adjusting the nodal displacements during a time increment could lead to computational instabilities if the increments of displacement are too large. However, no instabilities were detected during the example calculations, and it was not necessary to reduce the time step from that required by the explicit integration in the plate model (0.5 μsec).

The results of the experiment with the plate and single bolt were used to check the performance of the multiple impact model. Figure 9 shows the comparison. The contact gage sensed the impact of the plate against the shell at 126 μsec. However, the gage thickness is about 0.1 mm, and a finite time is required to develop close mechanical contact and for disturbances to propagate to the strain gages. Thus, the measured strains do not show signs of the second impact until about 140 μsec. In the calculation, the second impact occurs at 140 μsec on the scale in Figure 9. The level of strain after the second impact is calculated very accurately, although again, because of the idealization of the impact in the calculation, the predicted rise time is less than the measured time.

ANALYSIS OF COMPLETE STRUCTURE TO PREDICT EQUIPMENT MASS ACCELERATION

The finite element models developed for the plate, ring (and shell), bolts, and multiple impacts were combined to analyze the complete structure drawn in Figure 1 and to predict the acceleration of the equipment mass in a high speed lateral impact. The bolted equipment mass was modeled as a rigid body connected to

nodes at the bolt holes in the plate and to weightless rigid links at the interfaces between beam elements in the ring. This arrangement is shown in Figure 11. (The bolt elements could not extend to the centroidal nodes in the ring because these nodes could not be located at the bolt holes)

To test the model an experiment was performed in which the structure was launched into a rigid barrier at 12.3 m/sec. An accelerometer was mounted on the back side of the equipment mass to measure in-plane acceleration. Radially oriented strain gages were mounted in front of the mass on both sides of the plate.

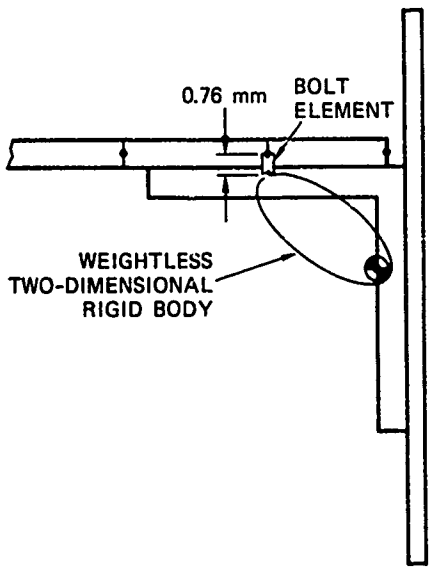

Fig. 11 - Bolt Connection Arrangement

Figure 12 compares the predicted and measured equipment mass accelerations. Both curves begin with a low level plateau corresponding to the period during which the ring deforms locally and the front bolts between the plate and ring begin to shear. This slows the plate slightly and the equipment bolts respond by deforming slightly. Thus, the equipment mass is slightly decelerated. When the second impact occurs, between the plate and shell, the plate slows sharply as its energy is absorbed in plastic deformation at the front edge. The equipment mass continues forward, producing large deformations in the equipment bolts. Thus, its acceleration rises sharply. At the velocity of this impact the equipment bolts are sheared almost to the breaking point, producing an equipment acceleration of approximately -13,000 g. When the equipment mass stops its forward motion, at about 190 μsec, the equipment bolts begin to unload. At this time, since the unloading characteristic of the bolts were not included in the bolt element, the predicted and measured equipment accelerations diverge. This simulation required 54 minutes of central processor time on a Burroughs 6700 computer.

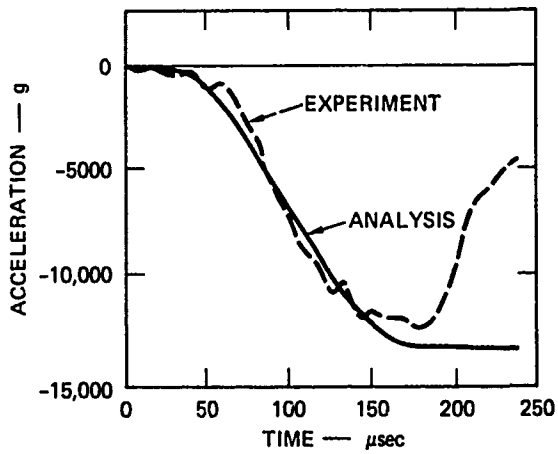

Fig. 12 - Measured and Predicted Equipment Mass Accelerations

SUMMARY AND CONCLUSIONS

A two-dimensional finite element model was used to analyze a multicomponent structure in rigid barrier impacts producing multiple impacts. Experiments showed that the model describes the response of a three-dimensional shell-ring-plate structure and predicts with good accuracy the sequence and details of the structural response and the acceleration of bolted equipment. Furthermore, at each step in the development of the model, confirmation was made with experiments on the components that make up the complete structure. The type of elements and mesh sizes required for good agreement with experiment were determined, and this should be useful information for more general modeling in similar impact problems.

The bolt model and multiple impact model developed in this work were demonstrated to be useful calculational tools that can be incorporated into most finite element programs. An analysis of the local plasticity occurring in bolt hole distortion is avoided with the force-deformation bolt model, and the bolt element does not reduce the allowable time step in the calculation from that required by the smallest plate elements. The multiple impact model allows one to perform a single, continuous analysis of elastic-plastic impact problems, avoiding restarts that require complicated "initial" conditions for multiple impacts.

ACKNOWLEDGMENTS

The authors are grateful to W.J. Coffey and the Department of the Army, under whose sponsorship this work was performed. The authors also thank the referees of the Shock and Vibration Bulletin for their helpful comments.

REFERENCES

1. J. D. Colton and J. K. Gran, "Response of Adaption Kits in Side Impacts," SRI International Interim Report, prepared for U. S. Army Armament Research and Development Command, Contract No. DAAA21-76-C-0076, Sept. 1977.

2. T. Belytschko, L. Schwer, and M. J. Klein, "Large Displacement, Transient Analysis of Space Frames," Int. J. Num. Meth. Eng., Vol. II, No. 1, p. 65, 1977.

3. A. Marchertas and T. Belytschko, "Nonlinear Finite Element Formulation for Transient Analysis of Three-Dimensional Thin Structures," ANL Rept. ANL-8104, prepared for U. S. Atomic Energy Commission, June 1974

DISCUSSION

Voice: We use staybolts to mount guns on gun mount rings, would you mind clarifying or stating something about the clearance between the bolts and the holes.

Mr. Colton: I can't quantify them. All I can say it was a tight fit since you have to press the bolts through the holes. I have also been thinking about the torque on the nuts.

Voice: Yes, Battelle has done quite an extensive study of that and also on the flatness of the surface between the bolt heads and the plates; but they haven't gone into the study that you have. This does enter into it especially on the buckling of the plate. Also was there a radius in your L shaped ring?

Mr. Colton: Yes, but it probably wasn't indicated in the drawing. With regard to the bolts and quasi-static pull test that we performed to determine their strength, we fabricated all of those parts in the same way that we fabricated the shell structure so that the tolerances were accounted for in the force displacement curve that we measured.

Mr. Sierakowski, (University of Florida): I noticed that all your input into the computer program for your bolt shear test and your bolt element characteristics were done statically, did you do any dynamic testing such as drop testing?

Mr. Colton: No, and the main reason was that the strain rates are higher than you can get with any testing machine. The closest thing we did to checking the dynamic deformation of the bolts was that test in which we mounted the plate on the ring with a single bolt. That is essentially a dynamic test, if you look at it it is a little bit indirect, but it is a dynamic test; that is if there were some dynamic effects that were much different than the static test they would show up in that experiment.

"TESTING PIPING CONSTRAINT ENERGY ABSORBERS FOR REACTOR CONTAINMENT APPLICATIONS"

R. C. Yaeger and R. C. Chou*
Franklin Institute Research Laboratories
Philadelphia, Pennsylvania

INTRODUCTION

The Duke Power Co. of Charlotte, North Carolina, has developed a design concept for durable low cost energy absorbers to be used as piping constraints in reactor containment structures. Safe secure constraint for pipe sections which have been damaged in a reactor containment accident must be assured. In the extreme accident case, a free moving pipe section, during a post-accident period, could hit the containment wall and result in containment rupture; the consequences of such a rupture could be catastrophic.

Duke Power Company needed a population of experimental data in order to apply their design concept to real reactor installations. In conjunction with Franklin Institute Research Laboratories (FIRL) and others, a program of controlled experiments was developed for this purpose.

FIRL personnel designed and developed a special drop test machine to perform the many tests in this program. Impact velocities as high as 70 feet per second are routinely available for the lighter drop weights. The machine is easily calibratable and highly reproducible as to its performance. Impact velocities within five percent of required values can be guaranteed. Drop weights are controlled to the nearest 10 pounds routinely; lesser values can be controlled if required. The drop weight can be varied from 70 lbs to 7000 pounds. One of the more valuable features of the machine is the ability to separate part of the tup mass for tests requiring small weights. The principal part of the tup can be stopped by built-in hydraulic snubbers while the separated portion strikes the test specimen. The separation is accomplished with simple foolproof hardware; this system functioned smoothly whenever it was used during the program.

The use of bungee cord assist enabled the designer to obtain the required performance in a machine with reasonable overall dimensions. In order to accommodate the great range of performance which was inherent in the requirements, the machine could be configured to use zero to twenty strands of one inch diamater bungee cord in groups of four strands.

Close attention to the demands of personnel safety made it possible to complete the entire program without injury. This versatile test machine is described in detail in the paper; performance data, photographs, etc., are given.

The instrumentation/data acquisition/data processing systems used during this program were extensive for tests of this type. Force, velocity, deformation, etc., were recorded in analog form as a function of time on tape throughout the energy absorption pulses. Data were digitized and processed in digital form to produce final results in the form of computer-made plots with the following coordinates:

Strain vs. time
Strain vs. deformation
Strain rate vs. deformation
Force transmitted vs. time
Deformation vs. time
Force vs. deformation

Routine checks on the quality of the results were made by comparing the kinetic energy of the impact mass with the energy absorbed ($\int F dy$) and by comparing the mass impact momentum to $\int F dt$. It was also possible to compare $\int v dt$ with measured specimen deformation. This system is described briefly in the paper.

The program of tests is discussed; including some of the problems along with their solutions. Typical analog records are shown; digital plots of the same data are shown.

The original program of simple crush pipe specimens was extended to include honeycomb pad

*Mr. Yaeger was the project manager; Mr. Chou designed the drop test machine.

sections and finally dual pipe sections installed at a 90 degree angle with respect to each other.

The bulk of the program data are not presented herein. Samples are shown in this paper as an aid in describing the test machine and its use.

ACKNOWLEDGEMENT

It is both an obligation and a pleasure to acknowledge the fact that this work was the result of a major team effort at FIRL. Many people worked actively on the program; too many to list them all in this brief review. The principals involved, in addition to the writers, were: Dr. G. P. Wachtell (Project Scientist), Mr. C. T. Davey (Instrumentation) and Mr. E. J. Dougherty (Data Processing). The Duke Power Co. was fortunate in having Mr. A. P. Cobb, Jr., available to manage their part of the program; he always arranged to be on hand when questions arose involving the overall program.

THE PROBLEM

When the program was first presented it was obvious to those involved that no test equipment available at FIRL could perform these tests. A familiarity with other equipment available in the U.S. convinced us that most potential performing laboratories would have to build something for the job. The FIRL proposal included design and fabrication of a new facility.

In brief, it was our task to impact a large family of weights at controlled velocities on a number of special short pipe sections like the one shown in Figure 1, and to measure the energy absorbed by, and the forces transmitted by, those short pipe sections in stopping the weights. The range of weights extended from a minimum of 31.7 Kg (70 lbs) to a maximum of 3324 Kg (7330 lbs). The velocities ranged from 305 cm/sec (10 ft/sec) to 2134 cm/sec (70 ft/sec).

It was further required that it be possible to account for any significant amount of the energy transferred from the impacting weights. A form of energy balance was required so that the dissipative effectiveness of the crushing pipe sections could be determined during the dynamic tests.

The great bulk of data to be expected from a program which involved hundreds of test specimens demanded some form of automatic data processing. This became a program requirement early in the design period.

With hundreds of specimens in the initial program, it was essential that a systematic program be established for their processing, care and handling. This problem was compounded by the later addition of a number of honeycomb pad specimens and some crossed pipe specimens. None were lost and within the limits of the quantities supplied by the client, no program delays were recorded for lack of properly prepared specimens.

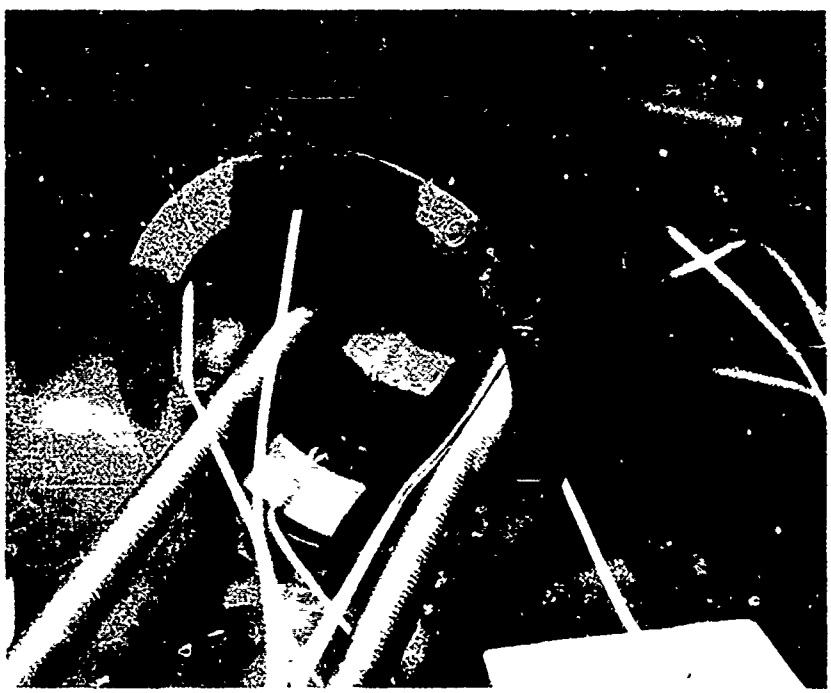

Figure 1. Test Specimen. White leads are from eight strain gauges. Gauge No. 3, inside bottom of pipe, is clearly seen.

Not the least of the problems was the need to keep all proposed costs down on a competitively bid project.

The resulting drop test machine is not like the shock test machines used to test equipment to existing military specifications. Its range of impact velocities and load carrying capability would make it useful for such tests but we would have to shift the measurement emphasis from energy absorption to pulse shapes and peak deceleration values.

THE FOUNDATION

We started at the bottom with the problem of measuring the energy and momentum transmitted by the machine to its mounting base. We liked the idea of having a known, large base mass for this purpose mounted on known springs. We had such an item on hand in a 72562 Kg (160,000 lbs) mass on air springs under the FIRL Seismic Simulator.* The use of this mass required us to idle the simulator for a few months (initial estimates were 2 months -- it eventually stretched to 7 months) but the schedule was not crowded and the mass was used for this program.

It was possible to achieve some economies in the design of the machine by using the existing foundation block. The structure of the seismic simulator was useful as the main support for the drop test towers and its slides. Adequate electrical power was available in that area of the building and a heavy duty bridge crane covered the entire area. This bridge crane saved the cost of a special hoist for the drop weights When the need for bungee cord assistance appeared, the crane became invaluable. Figure 2 is a photograph showing the general area in which the machine was installed. The arches of the seismic simulator, which served as tower supports, and the outline of the foundation block are clearly seen in this view. The proposed use of the machine on this foundation required recording the block motion throughout each test; provision for this was included in the measurement system.

VELOCITY REQUIREMENTS

With the available ceiling height in the selected FIRL high bay testing area and the higher velocities needed, it was tempting to conduct these tests at an outdoor location. As it turned out we would have been outside between November and May in an extremely bad winter. It would certainly have been a problem.

Some form of velocity boost was required; a review of available methods narrowed quickly to the use of bungee cord(s) of suitable length. Some apprehension was felt concerning the number of cords which would be required for the larger masses involved and for the repeatability of the bungee performance. The program required $\pm$ 5% velocity accuracy and only 2 specimens had been planned for a given test condition. We had a small margin for error in the base program, none in the add-ons.

It was planned to use a daily bungee cord exercise routine both when calibrating the machine and at the start of every test day. This exercise routine, combined with equations developed from calibration test data with bungee assist permitted us to obtain the desired repeatability. Appendix A shows these equations, one of which was developed for the bungee assisted drops and the other which was used for the gravity drops at the lower velocities.

The success obtained in using bungee cord in this machine was due, in a large way, to the manner in which it was used. The cords themselves were all made in one special run with special attention paid, by the manufacturer, to uniformity of product. The machine was designed so that no greater than 100% extension was possible. Each 25.4 mm (1 in.) diameter cord was made up double length (2 strands per cord) with cable thimbles in an eye-splice installed by the cord manufacturer. The cords were strung on the machine frame in the manner shown on Figure 3. The original plan was to measure the load on each cord, as stretched, as a method to control performance uniformity. The cord end clevises were strain gaged for that purpose. The exercise routine proved to be adequate however and the cord load measurement system was abandoned.

The moving impact mass picked up each double bungee strand on a shoulder-shaped steel structure as it was lifted above the test anvil. In the maximum stretch condition (see Figure 4) each strand was pulling downward with a force of 454 Kg (1000 lbs). With 20 strands installed at full extension and a moving mass of 680 Kg (1500 lbs) the total lift was over 9070 Kg (10 tons) on the worst-case drops. With forces like this around we had to be very strict about safety procedures and equipment. We were very strict and no technician has been hurt using the test equipment to date.

The general design approach used simplified equations relating the kinetic energy at impact, the potential energy of elevation, the mass of the falling object and the energy which could be stored in the bungee at a given elevation. The kinetic energy term was an input for each test using the known mass and the desired impact velocity. The spring constant of the bungee came from manufacturers data; with K_B known, the energy stored was a second power term in drop height. The potential energy term involved the first power of the drop height. Each case involved solution of a simple quadratic; these were run off on a programmable hand calculator. Preliminary selections of the number of bungee strands (groups of four were used to preserve

*This facility is used normally to qualify Nuclear Power Plant hardware.

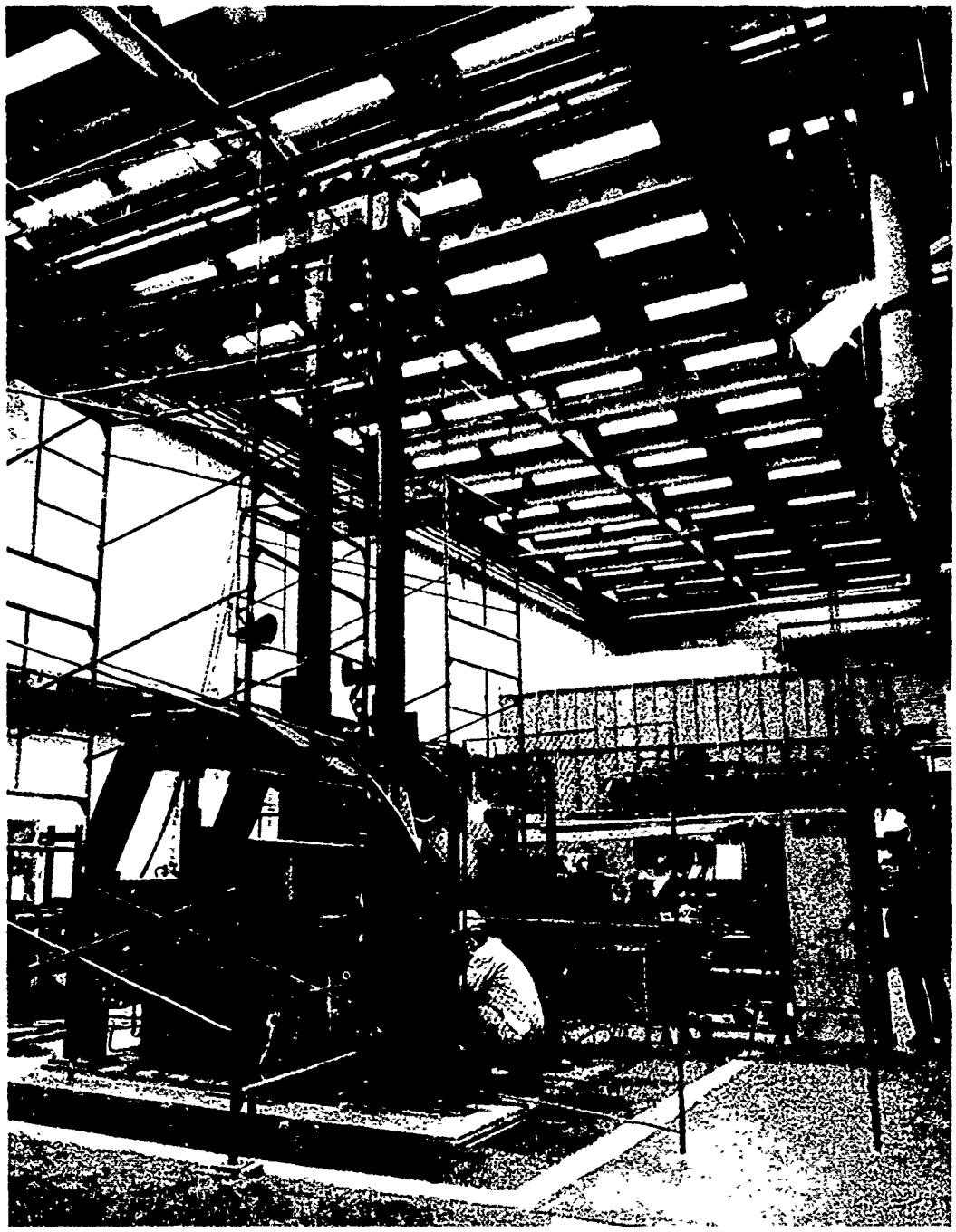

Figure 2. Drop Test Facility - Overall View

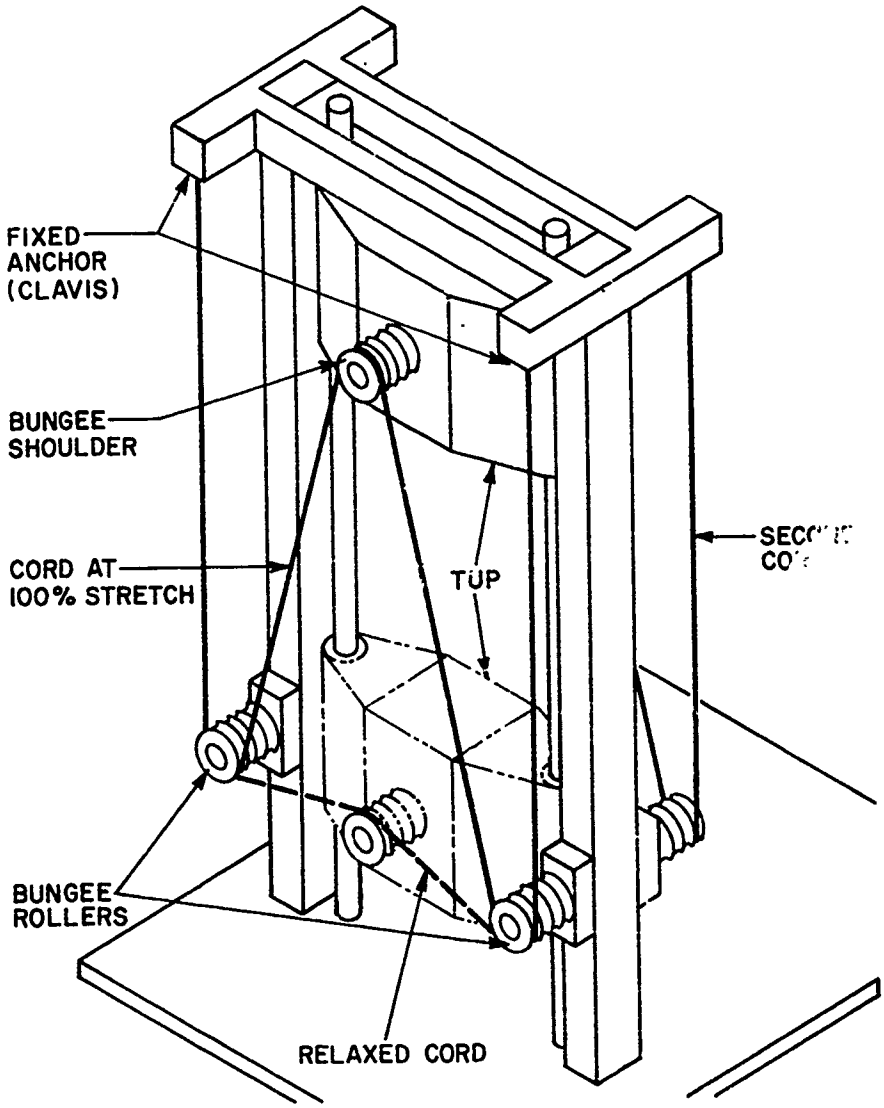

Figure 3. General Arrangement, FIRL Drop Test Facility

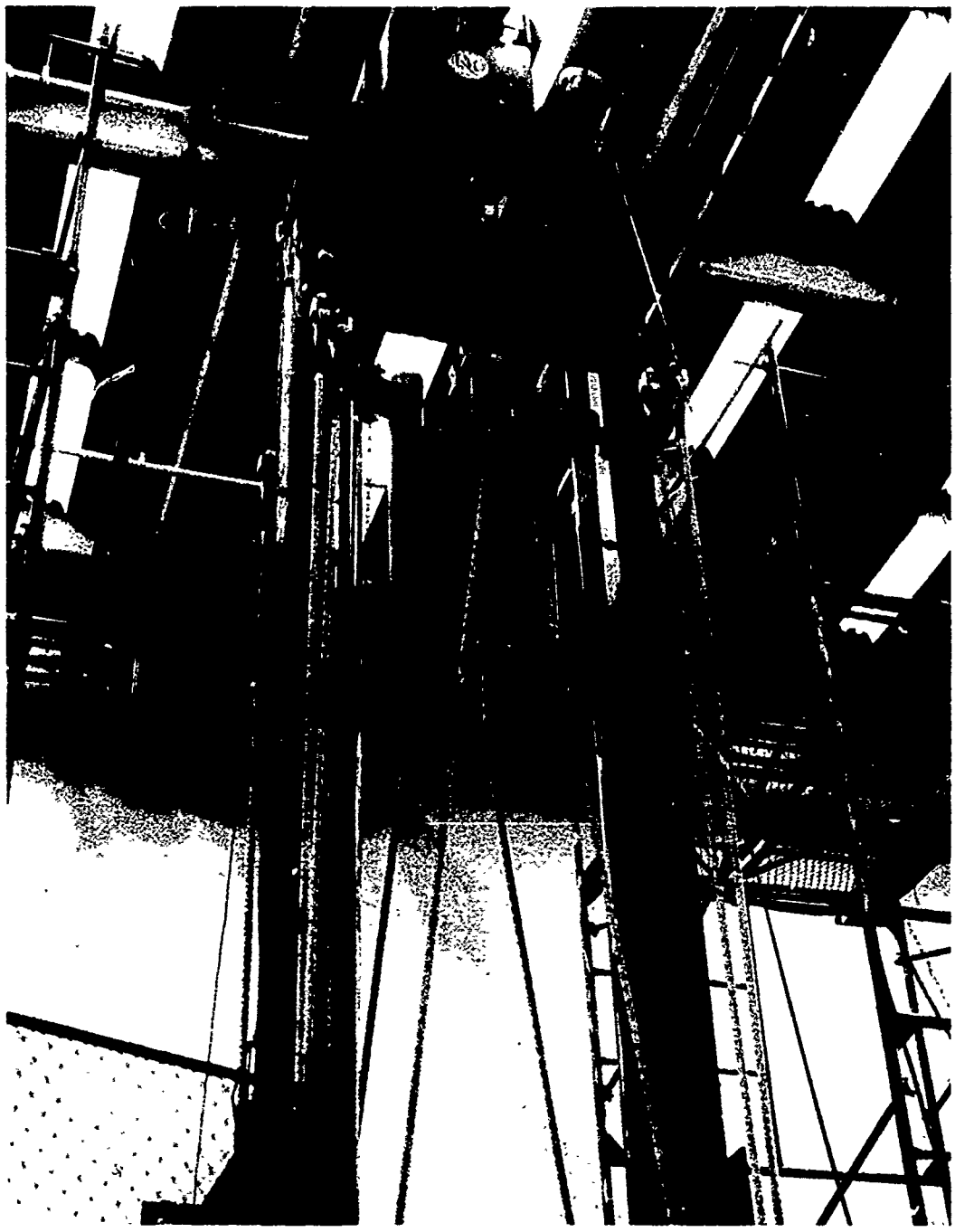

Figure 4. Upper Drop Test Machine Detail

symmetry) were tested on paper for all known cases; nominal drop heights were computed. Tables of such values were used for preliminary test procedures. In some actual cases, the number of strands had to be increased when the available drop height was exhausted without achieving the desired velocity.

MOVING WEIGHTS

It was apparent from the beginning, that no single moving mass structure could satisfy the required 100:1 range of impact weight. We finally settled on a concept of three structures to cover that range; one of them was a part of one of the others. These structures were called "tups" in this program.

We arrived at a heavy structure which weighed approximately 408 Kg (900 lbs); it could be loaded with a family of weights to the maximum required value. The largest weights weighed 227 Kg (500 lbs) which further aggravated the safety situation. All such weights were fitted with threaded lifting eyes to permit safe easy handling. This so-called heavy tup was used only for gravity drops down to its unloaded weight (see Figure 5).

For the medium weights and for all high velocity drops the so-called light tup was used. This had a minimum weight of approximately 245 Kg (540 lbs); it was used with add-on weights to a maximum weight of 1075 Kg (2370 lbs). While the striker face on the heavy tup was integral with the structure, on the light tup it had a variety of forms. In most cases, it consisted of a special structural item bolted to the bottom of the tup core structure. When a large number of weights were required, the striker could be changed to a hardened plate fastened to the lowest weight. The light tup is shown in one of its configurations in Figure 6.

All weights had to be firmly attached to the moving mass structures. Each of the larger weights (see Figure 5) was held in place by 2-1-1/2" d. (3.81 cm) steel studs passing through the weights and the large tup structure. A central network of reinforcing mass transmitted forces from these weights directly to the impact surface. Smaller weights were held in place by 1 inch diam. (2.54 cm) copscrews. No weights depended on bolt tensions for the transmission of direct impact force. All fasteners were torqued in place with oversize adjustable wrenches and extension handles. Technicians were selected for their ability to cope with the physical requirements of the test equipment.

In order to reach the lowest required weight it was necessary to use a carriage which was too small to support the main bearings. In those cases the so-called slider was used. This was a carriage (Figure 7) which was part of the light tup structure at release but which separated from the light tup structure prior to impact on the specimen. The light tup was snubbed to a stop for this condition by means of a pair of hydraulic shock absorbers shown in Figure 7.

MAIN STRUCTURE

In order to perform a controlled series of tests it was necessary to guide the moving weights. It was also necessary to provide support for the bungee cords, the instrumentation, etc. Two square-section hollow steel columns were erected and fastened securely within the seismic simulator framework. The hollow steel tubular guide rods were fastened to these columns in a way which permitted their accurate, parallel alignment. Each tup was used as an alignment key by raising it to a number of levels above the anvil and checking the slope and the bearing clearances. Jackscrews at intervals permitted the technicians to warp the guide rods into precise alignment for minimum friction along their length. Additional comments on the guide rod bearings are given in the next section.

An upper structure was assembled to tie the columns together, support the bungee cords and permit entry of both the crane hook/block and a purchased quick release hook.

Between the columns, at their lower end, was a base (thick steel plate) surmounted by an anvil structure (see section on instrumentation below).

Near the lower ends of the columns, bungee rollers were installed as well as a sturdy safety bar which did not permit either tup to strike the anvil when work was going on at the base of the columns. An overall view of the machine structure is shown as Figure 8. The entire working area was surrounded with a safety cage which had to be closed prior to each test drop.

TUP BEARINGS

Probably more design time was spent on this detail than on any other. We were concerned with friction drag, on the one hand and the prospect of inadequate guidance on the other. Pressure pad bearings were considered but considerations of cost and delivery caused them to be dropped. The eventual selection was four plain sleeve bearings, each one of which covered an arc of 225° around the guide rod perimeter. The 660 bronze bushings had a nominal clearance of 0.0127 cm (0.005 in.) on the 7.62 cm (3 in.) diameter guide rods. Two kinds of alignment shims were used for basic alignment. For the heavy tup, the shims on one guide rod were elastic material set up so that a slight pressure was exerted on the other guide rod at all times. This worked well with the heavy weights; it would not have been acceptable for the lighter tup. For that structure, rigid shims were used; considerable difficulty was experienced in setting up these rigid shims.

The bearings were oil lubricated in the early tests; a light grease was used for the latter tests. Lubricant was renewed on the basis

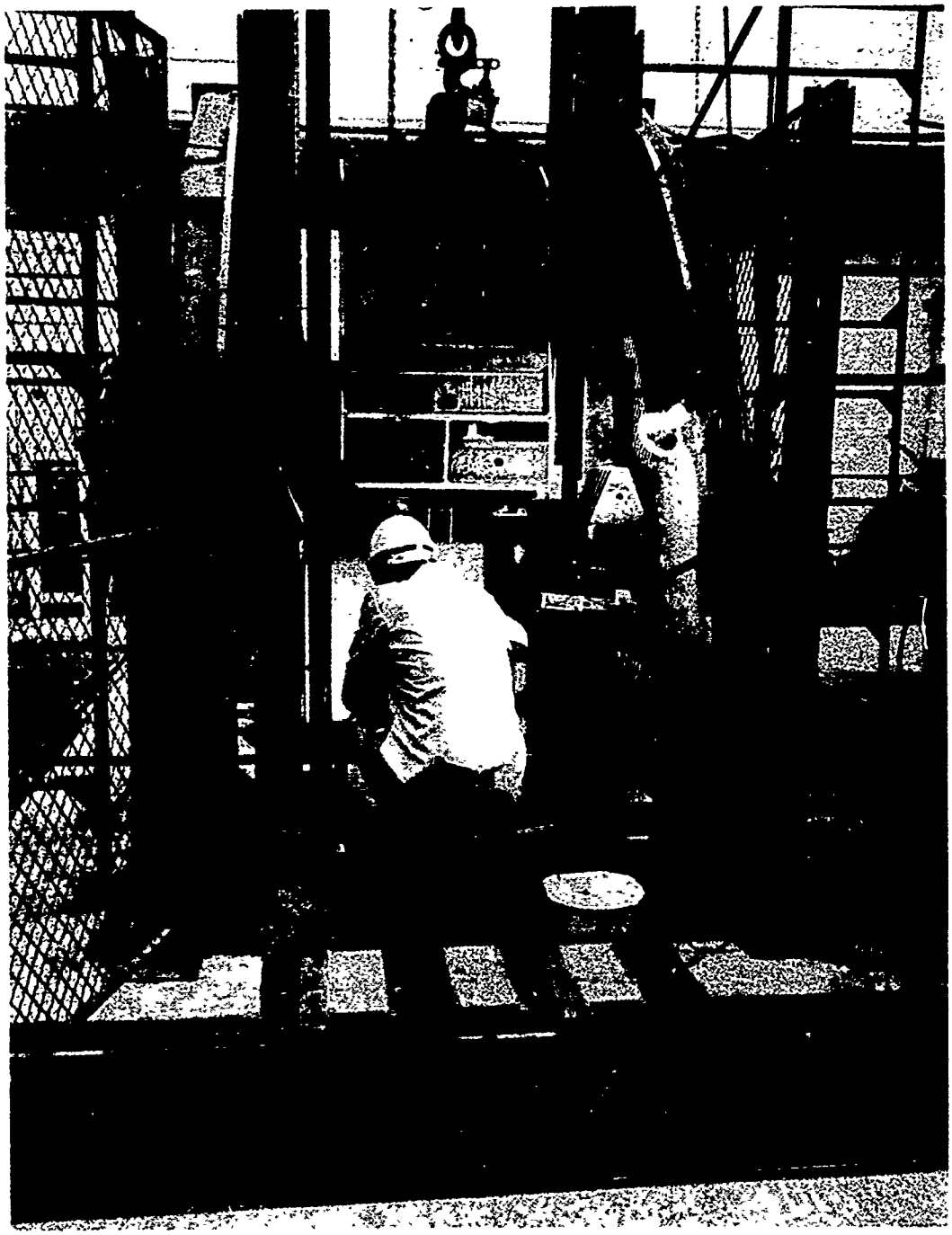

Figure 5. Heavy Tup on Drop Test Machine

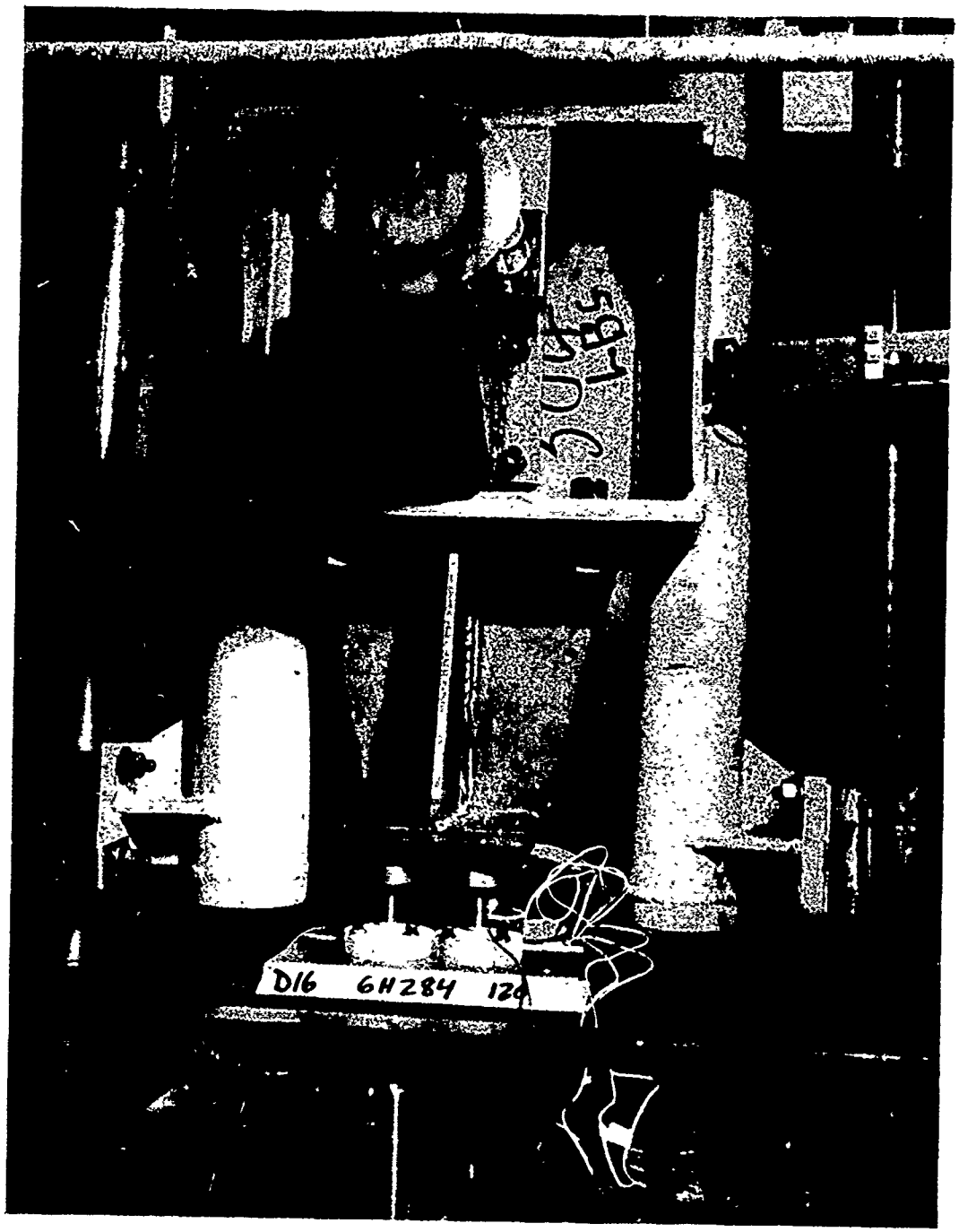

Figure 6. Light Tup Detail

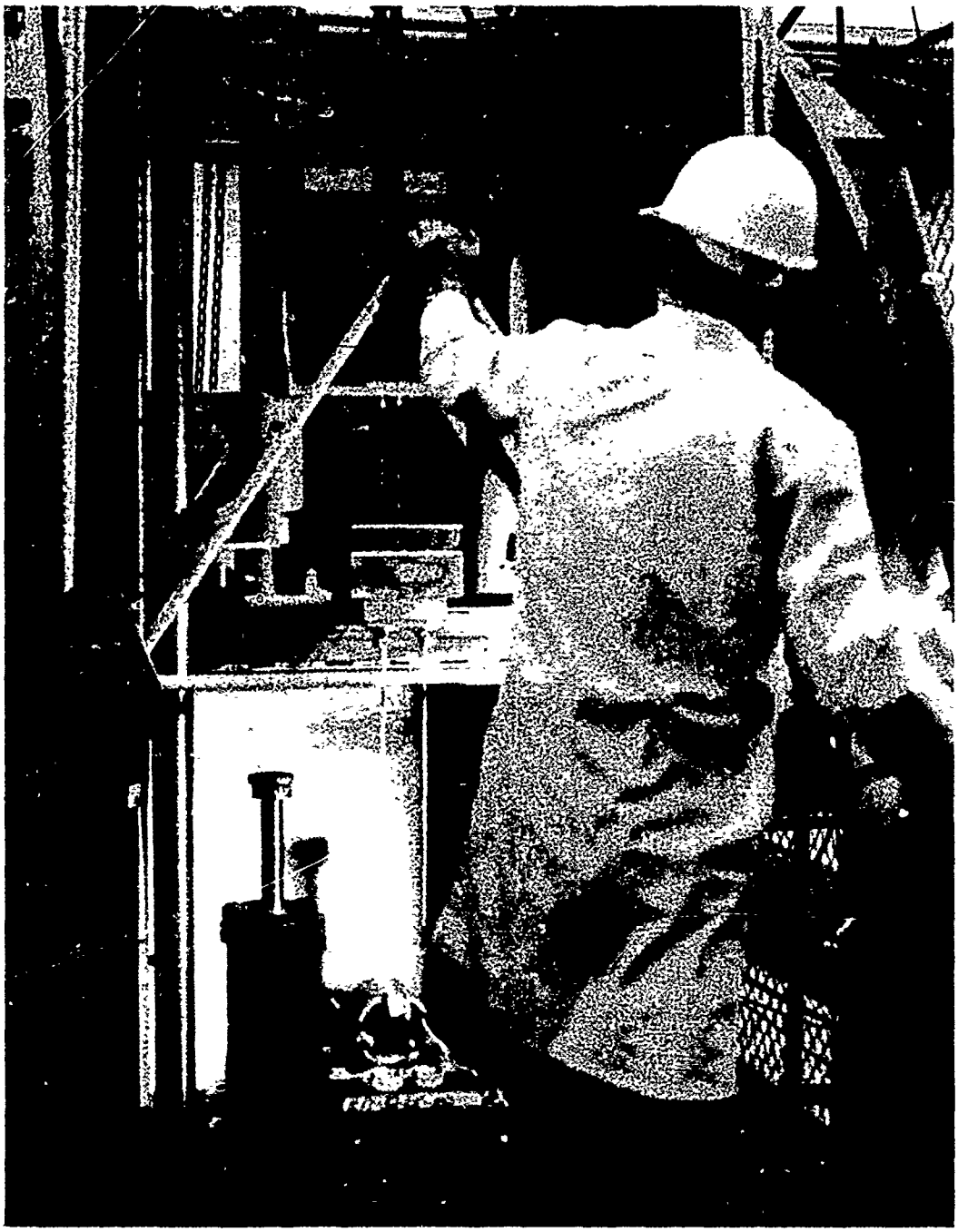

Figure 7. Slider Test

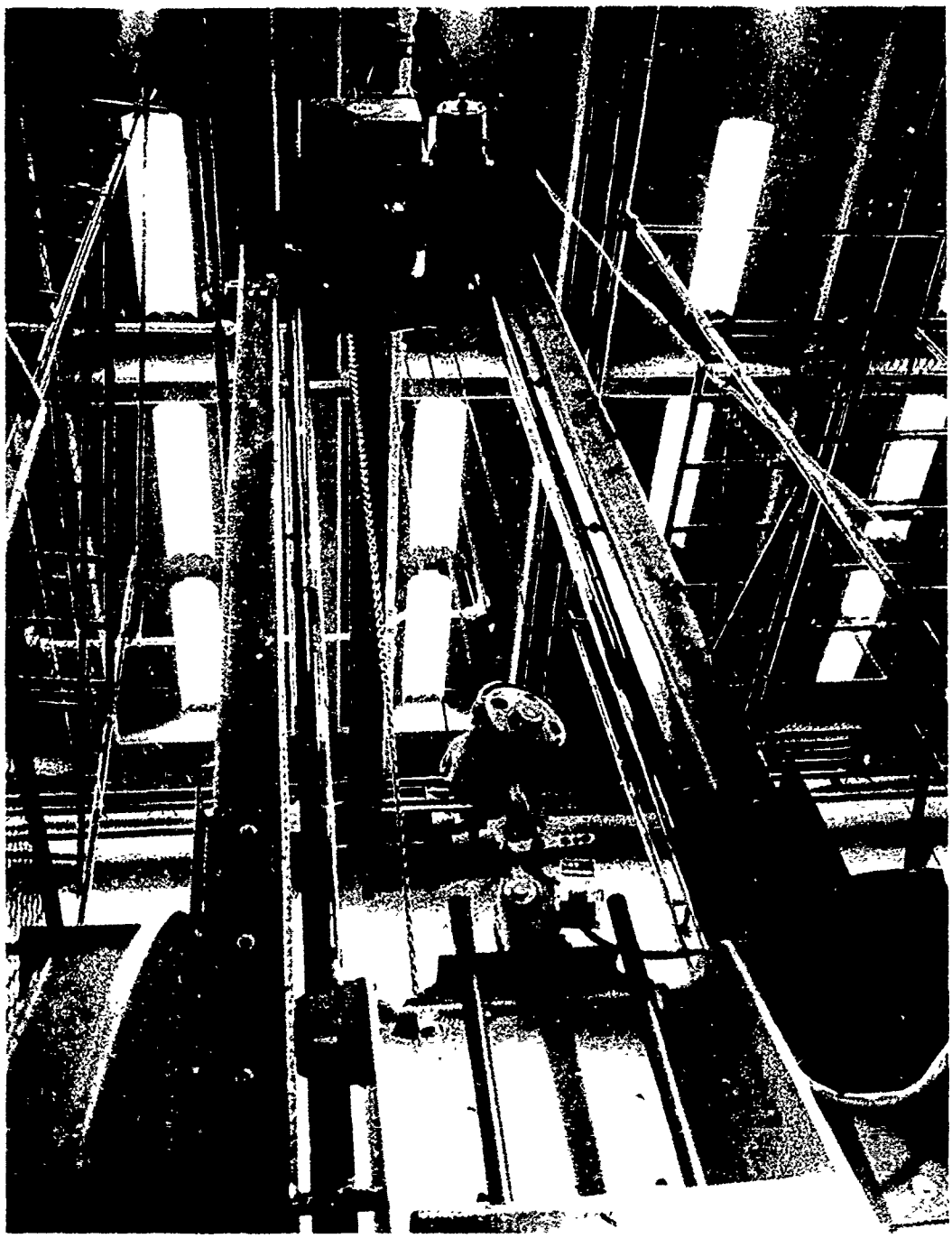

Figure 8. Overall View of Machine Structure

of a visual inspection.

MEASUREMENTS

The following paragraphs describe briefly, each of the parameters which were measured and/or controlled at the test site. Combinations of these data items are discussed in the next section on Data Processing.

The weight of each impact mass was a controlled parameter. Each basic tup structure was weighed prior to assembly on the machine. Each tup was equipped with a family of weighed and marked add-on weights in standardized values (500 lbs, 250 lbs, 100 lbs, etc.); fasteners for these weights were also carefully weighed. It was possible to obtain any required weight in this manner. Changing weights was the slowest step in the testing process, therefore, all tests were arranged in order of increasing weight to minimize time required for this step. The total weights were known to within less than a pound when normal care was used in selection of the add-on weights.

The velocity at impact and for the period of time immediately following the impact was measured directly. Impact velocity was measured directly with a light beam/photocell arrangement interrupted by a carefully machined grid. A secondary measurement of impact velocity was made with a self-generating linear velocity transducer (LVT). This secondary transducer also produced a velocity vs. time record throughout the impact period. The long magnetic transducer core was installed on each of the tups in turn; we experienced difficulty with these LVT cores and with the LVDT core on high velocity tests.

The force exerted by the crushing pipe on its support was measured with quartz thrust washers installed under the anvil block. This provided a continuous force signal throughout the impact period.

The displacement of the tup with respect to the anvil from the moment of initial contact was measured with a linear variable differential transformer(LVDT). The transformer core was installed on each of the tups in turn. The contact signal was provided when the lower tup surface closed the circuit between two parallel aluminum foil strips fastened to the top of each specimen over a layer of double surfaced insulating tape.

The magnetic core for the LVT and the iron core for the LVDT presented problems (see below) because of the size of some of the specimens. We had to allow for measurements on speciments as large as 12 in. diameter. The coils for these transducers had to be installed in deep holes in the cement block; a core drill was used to make these holes at the time of machine assembly. Each coil was suspended from a nylon holder which provided a funnel shaped entry for the core. Alignment of the cores with the coil entry was checked prior to each drop. The foam blocks which were used to decrease lateral vibration had a secondary benefit (see below); they enabled the technician to preposition the core tips over the coils.

Strain gages were attached to each specimen and outputs from these were recorded as a function of time. The number of gages varied with the type of specimens used.

During the early tests, temperature of the specimens at the points of greatest strain was of interest. A number of these were recorded as a function of time for these tests. Interest in temperature as a variable reduced based on the early data.

The motion of the foundation block was recorded as a displacement vs. time signal from an LVDT anchored to a fixed point.

All functions were recorded directly on magnetic tape with an accurate time base signal. Special event signals were added to assist the data processing system in handling the data from a given test. Special data sheets were used to make certain that all keying information was written down by the technicians at the time of each test.

In order to maintain a high level of confidence in the value of the data which was recorded on tape, a quick-lock playback system was included. Key channels (force, time base, velocity and displacement) were played back immediately following each test on a multichannel pen-motor recorder. We were fooled a few times by spurious high frequency noise on some of the traces. In general, however, results accepted on the basis of the quick-lock examination turned out to be usable data. When the quick-lock was bad, in most cases we were able to repeat the test immediately.

SPECIMEN HANDLING

With hundreds of specimens on hand it was essential that care be observed in their handling and processing. These were no ordinary pieces of pipe; they were obtained from identifiable mill runs in the same manner as all nuclear grade pipe. They were most carefully cut to size and cleaned free of scale, etc. FIRL personnel set up a production line for measurement, cleaning, marking, strain gaging, etc., of each specimen prior to the tests. A form of bonded stock was set up and one man had the responsibility to account for each specimen at any time. Photographs were taken before and after each test and a post test examination was mandatory for each specimen.

DATA PROCESSING

The data processing was performed on a small digital computer which had been programmed specifically to do this task. Analog tape records were fed into the computer along with key data peculiar to that test. The computer digitized

the data and operated on it in that form. The final product from each test was in the form of detailed computer-produced listings, a specified number of X-Y plots, a number of key special parameters and digitized data tapes. Filtering of the final data was minimized to avoid any loss of real data. As a result, some of the traces appear to be noisy. Finished 11" x 17" plots were provided of the following types:

Force vs. time
Deformation vs. time
Strain vs. time
Force vs. deformation
Strain vs. deformation
Strain rate vs. deformation

Samples of some of these plots are shown as Figures 9 to 13. Figure 9 is the digitized force vs. time plot produced on the computer. Figure 10 is a similar plot of deformation vs. time for the same test. Figure 11 is the cross plot of force vs. deformation of that data. Figure 12 is a typical analog trace forshortened to include the full record. Figures 9-11 show only the initial pulse. Figure 13 is a digital playback on a strip chart recorder of the key variables.

The computer determined the impact energy from the impact velocity and the tup weight. It compared this figure with the area under the force vs. deformation curve and computed the percent discrepancy. The computer compared the tup impact momentum with the area under the force vs. time curve for the duration of the crush and computed percent discrepancy. The comparison was also made between the maximum deformation given by LVDT data and the final measured specimen height. It was also possible to check displacement against the integral of velocity vs. time. Differences in these parameters were monitored to detect problems with the equipment/instrumentation before they became serious. The digital tapes which were obtained during the processing were supplied to the client for his use in further treatment of the data.

CALIBRATION

Force calibration was accomplished by referencing the quartz washers against a calibrated static test machine.

Displacement calibrations were performed before every test using measured blocks under the tup resting on the anvil.

The light grid velocity sensor was as good as the time base signal. The LVT sensor was calibrated against the grid sensor.

Strain gage bridges were calibrated with shunt resistors on the tape prior to each test.

The basic approach to calibration involved a tri-level schedule. The most complete and accurate calibrations were performed at least every three months (sometimes more often if an item became suspect as a result of key parameter shift). Some items were recalibrated at the start of every test day. The LVDT, for example, was calibrated over its full range daily to make certain that no sublety caused us to lose valuable data. Immediately prior to every test single point calibrations were performed on the tape. These were electrical signals comparable to values of force, velocity, etc. Every test had a mechanical spacer type displacement calibration at 2 points which spanned the expected specimen deformation. Figure 14 shows a summary of all of the test drops plotted in terms of the nominal goal impact velocity and the measured impact velocity error. The overall average velocity error was 4.55%. Points on the figure represents the average error of the tests performed at that nominal velocity value.

PROBLEMS

In spite of all the excellent planning and the built-in checks a minor number of tests had to be rerun. Some of the causes may be of interest as well as the adopted solutions.

Deformation and velocity were recorded as a function of time using sensors of an inductive type. The deformation sensor was a linear variable differential transformer with the coil supported solidly in the anvil plate and the iron core, rod suspended from the moving tup. The velocity sensor was similar except that the core was a permanent magnet. These cores were fastened on the end of 6.35 mm (1/4 in.) diameter aluminum rods; the total length of the rod/core combinations was of the order of 61 cm (24 in.). As the test velocities increased these long thin structures became a cause for concern. The retention system for the LVT magnet had to be revised; the original swaged tube proved itself to be completely unsatisfactory. The slider mode of operation introduced a minor lateral motion of the tup which resulted in appreciable vibration of the free end of the rods. The amplitude of this vibration exceeded the capability of the coil entrance funnels; several tests were lost. The correction proved itself to be simple; two rods were tied together with a foam spacer shaped as shown in Figure 15. The foam disintegrated on impact causing no affect on the test itself. This measure was effective in every case where it was used; it was recommended by one of the FIRL technicians who operated the drop test machine.

The analog quick-look capability, which was used for these tests, was based on a comparatively low frequency response penmeter type stripchart recorder. In nearly all instances this was an acceptable system; i.e., bad tests were detected prior to entering the processing mill and good tests were verified. In a few cases high frequency noise, on the records, was not seen on the stripchart playback. This same noise played havoc with the digital processing system. In future tests of this type we will use the computer for the quick-look and use it on-line full time for the test program.

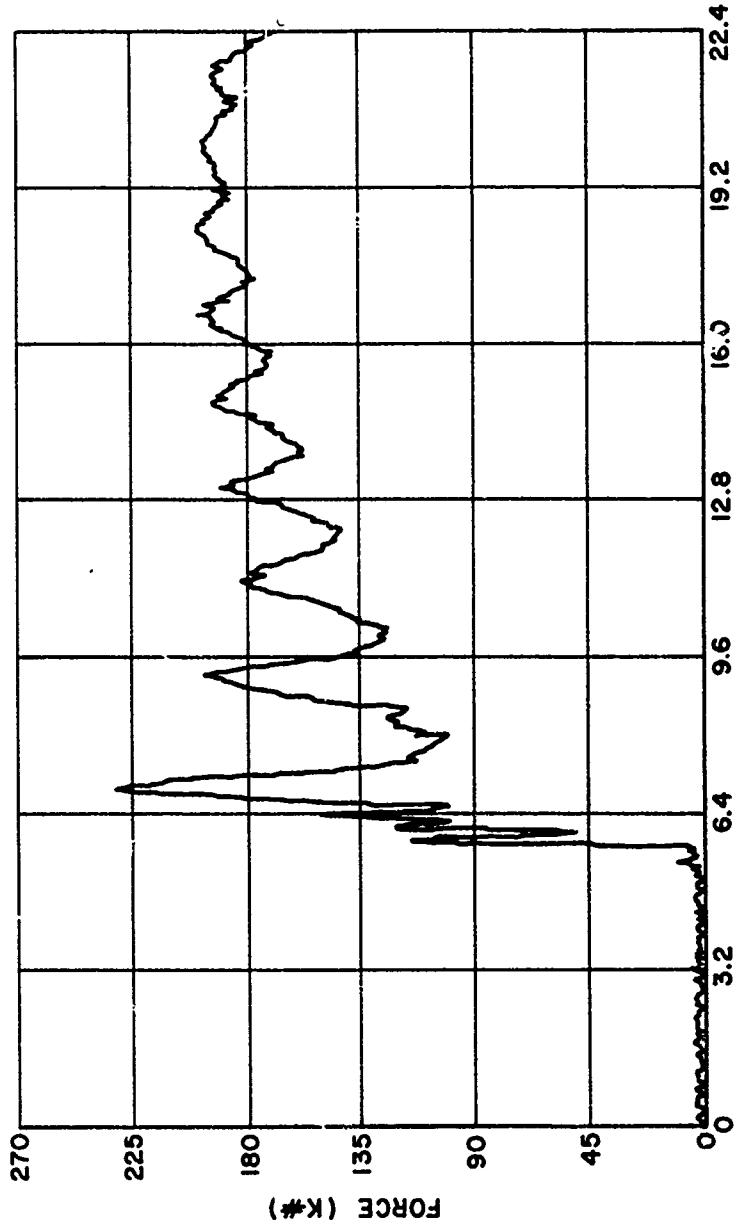

Figure 9. XY Plot - Force vs. Time

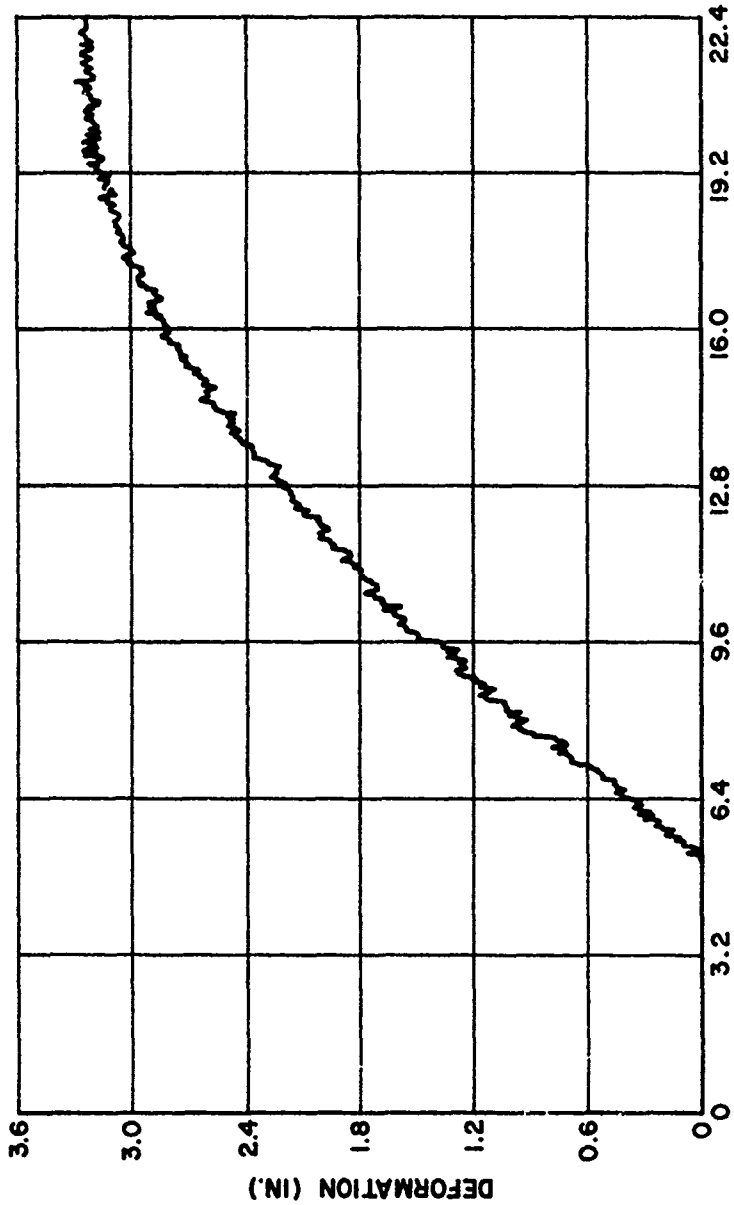

Figure 10. XY Plot - Deformation vs. Time

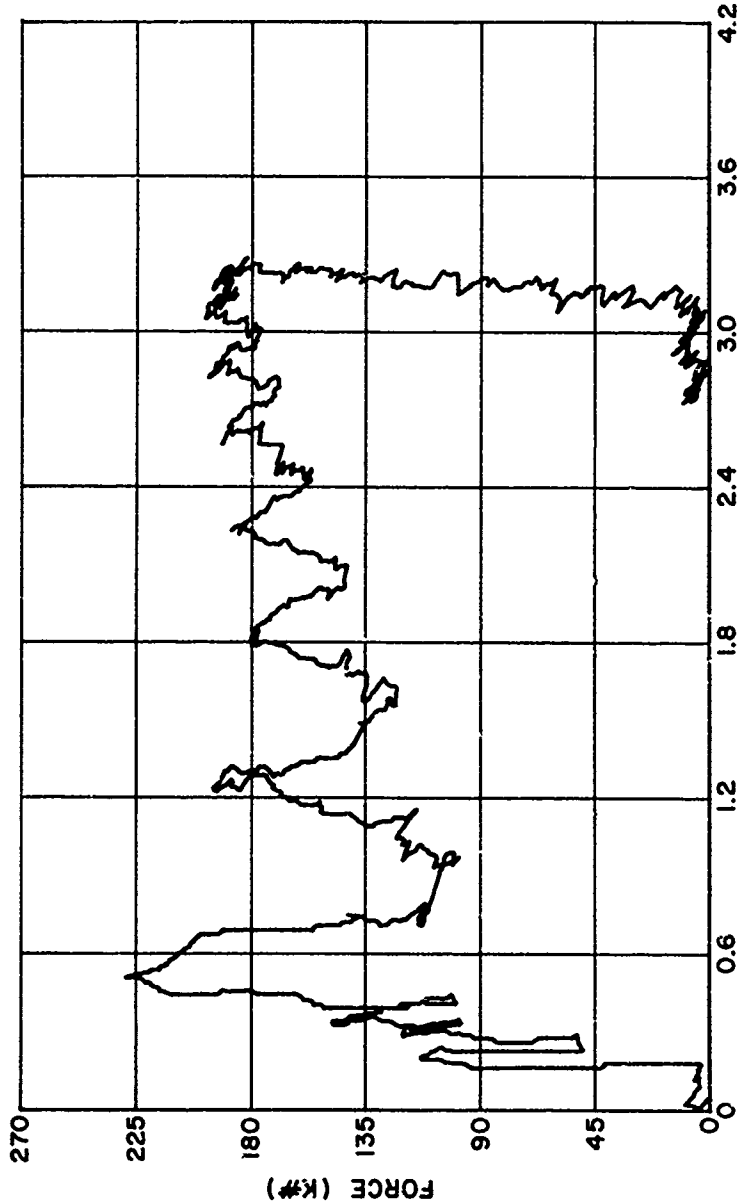

Figure 11. XY Plot - Force vs. Deformation

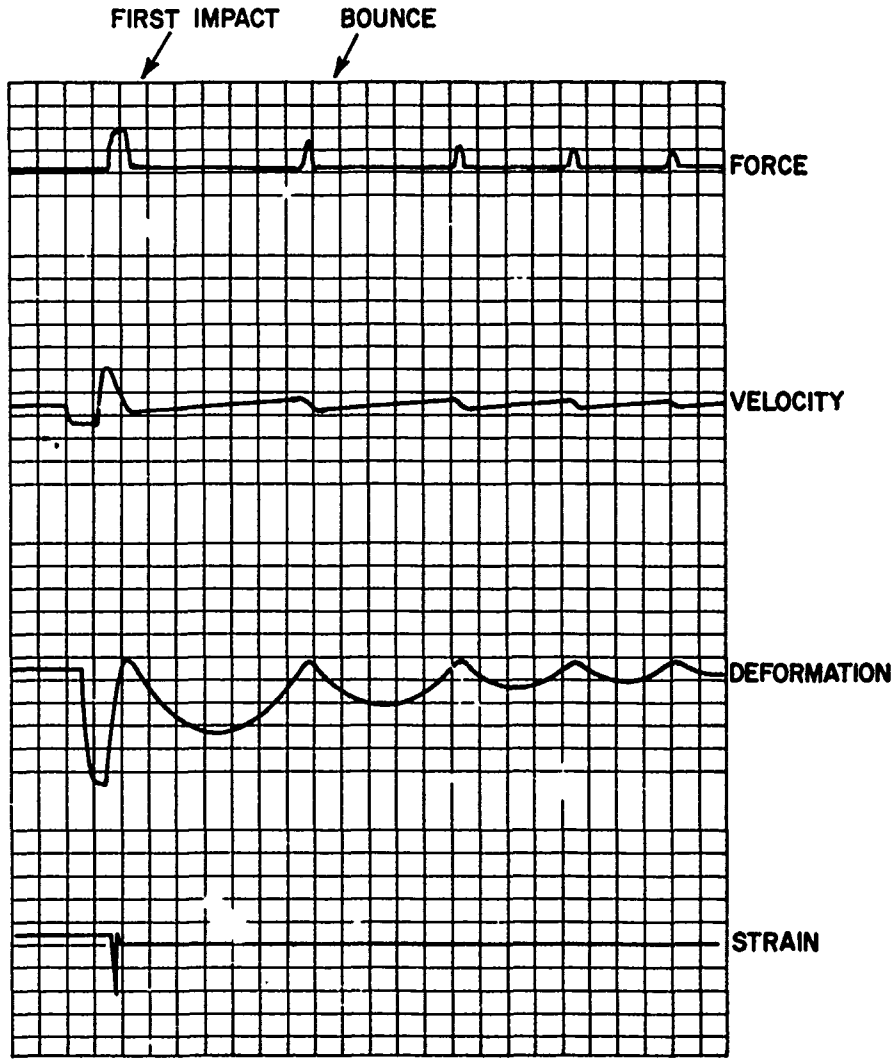

Figure 12. Typical Chart Playback of Force, Velocity, Deformation and Strain

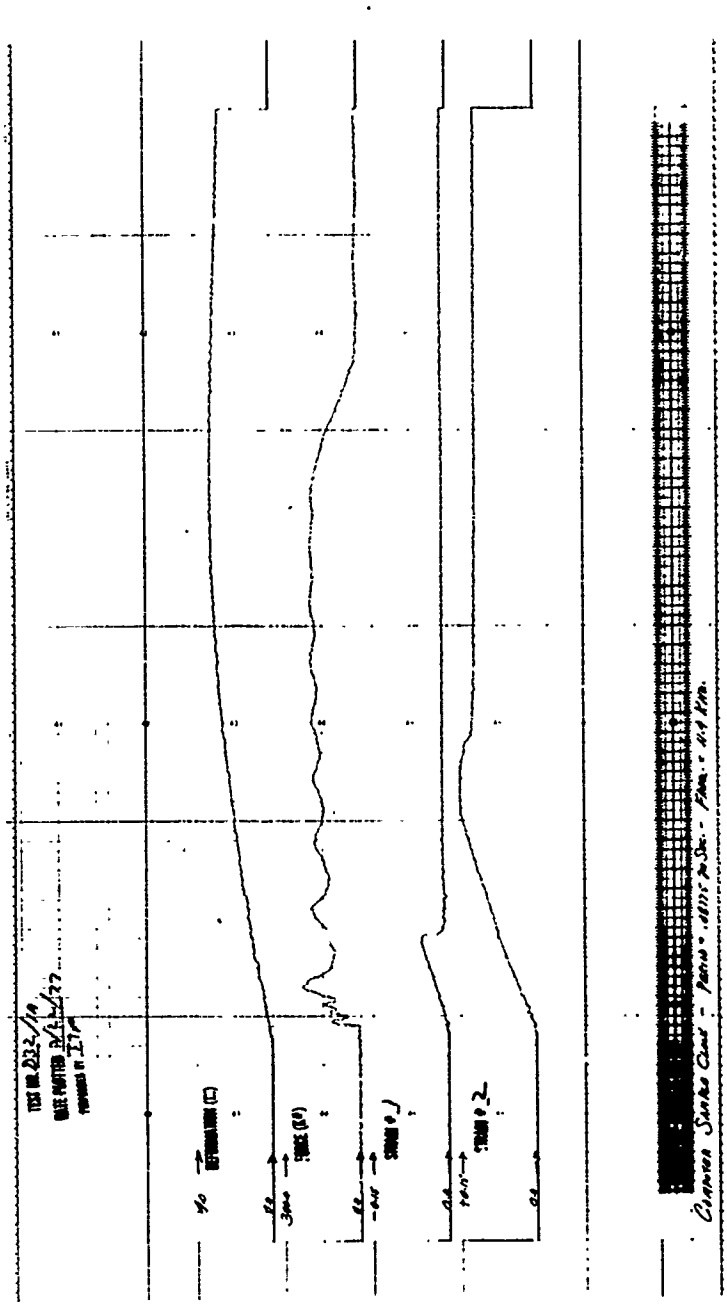

Figure 13. Playback of Digital Strip Charts

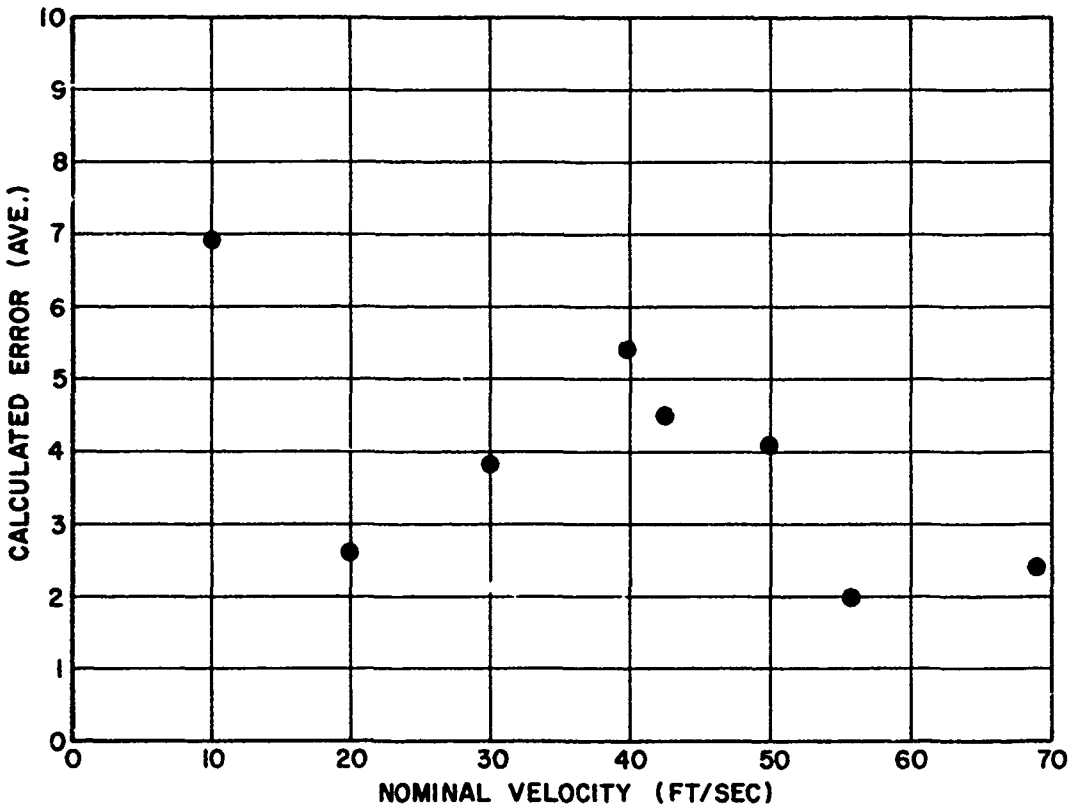

Figure 14. Nominal Impact Velocity Vs. Calculated Error

Figure 15. Bungee-Accelerated Light Tup with Slider Showing Styrofoam X in Place on LVT and LVDT Rods

Original planning for this program assumed same amount of computer time-sharing but that proved itself to be impractical.

We experienced a number of analog tape recorder problems, probably at least one instance of every conceivable type of such a problem. More time was lost because of these problems than any other factor. In the future we plan to process on-line and record only the digital information. The traffic in analog tapes, playbacks, etc., caused more problems than it solved.

APPENDIX A

MACHINE PERFORMANCE EQUATIONS

Section 5.3 of Ref. 1)*

Calibration tests were performed without bungee to determine the additional drop height, δh_f, to be added to the theoretical value to achieve a desired impact velocity, V. An additional drop height, δh_r, was also determined by calculation, to allow for movement of the reaction mass. The travel distance before "contact" for a gravity drop after tup release is h-D, where h is the height of the tup face above the anvil and D is the specimen diameter. If h_t is the theoretical free-fall distance for a frictionless drop with immovable reaction mass

$$h = h_t + D + \delta h_f + \delta h_r$$

where

$$h_t = V^2/2g$$

Calibration tests were also performed with bungee to determine the value of h required to achieve a desired impact velocity (see below).

DETERMINATION OF δh_f

It was assumed that friction was due mainly to viscous drag in the bearing lubricant, so that friction force was proportional to instantaneous velocity. The energy consumed by friction was, therefore:

$$W\, h_f = \text{Const} \times \int_0^{h_t} v\, dy$$

where v(y) is approximated by its value for frictionless fall through distance y:

$$v = \sqrt{2gy}$$

Therefore, h_f is proportional to $1/(wh_t^{3/2})$.

Since $h_t^{1/2}$ is proportional to V,

$$h_f = \text{Const} \times \frac{h_t^2}{W_t V_t}$$

The empirical value of the constant was found to be approximately 900.

*These equations were developed by Dr. G.P. Wachtell.

DETERMINATION OF δh_r

Since $W << W_r$, where W = tup weight and W_r = reaction mass weight (concrete block), the velocity after impact is approximately (by conversation of momentum)

$$V_r = V\, W/W_r$$

where V_r is the velocity common to the tup and reaction mass after impact. The kinetic energy that remains is approximately

$$\frac{W_r V_r^2}{2g} = \frac{W}{W_r} \times \frac{WV^2}{2g}$$

This represents an additional energy with which the tup should impact the specimen in order to deliver the desired energy to the specimen. This leads to

$$\delta h_r = \frac{W}{W_r} h_t$$

This is a minor correction. Consequently, in calculating δh_r, no correction was applied to W_r for the effect of rotation in reducing the effective value of the reaction mass. (Rotation occurs because the dynamic test machine was not located directly over the center of mass of the concrete block). That is, the value used for W_r was the weight of the concrete block 160,000 pounds. Thus, the final height equation was:

$$h = h_t + D + \frac{900\, h_t^2}{W_t V} + \frac{W\, h_t}{160{,}000}$$

where h, h_t and D are in feet, W is in pounds, and V is in fps.

It was possible to keep impact velocities within 5% of the nominal values by means of this equation. It was applied in all gravity drop tests.

CALIBRATION TESTS WITH BUNGEE

These calibration tests were performed with four bungee cords (the minimum number, since the number of cords is a multiple of 4). To simplify the allowance for friction (which was expected to be negligible) it was assumed that friction force was constant (rather than proportional to v). The energy released by the bungee cord was approximated as being proportional to h_d^2, where h_d is the drop height, h-D. This is an approximate assumption rather than a theoretically accurate one for two reasons:

1. h_d depends on D. Furthermore, the bungee cord is completely relaxed when the bungee guide is low enough to be disengaged from the bungee.
2. Although the bungee force is quite accurately proportional to the distance by which the cord is stretched, this stretching is not proportional to h_d as the bungee is stretched from a "U" shape (small h_d) to a "W" shape (large h_d).

The approximation is satisfactory, however, because the number of cords was kept small enough so that h_d was fairly large.

With these assumptions,

$$\frac{W}{2g} V^2 = Wh_d + NC_b h_d^2 - Fh_d$$

where N is an integer equal to one fourth the number of bungee cords and C_b and F are constants.

Empirically, it was found that $C_b = 73.6$ and $F = 0$. Solving for h_d leads to:

$$h - D = h_d = \frac{W}{147.2\, N} \left[1 + 4.57\, NV^2/W - 1 \right]$$

This equation was used to determine where to position the tup for each dynamic test in which bungee cords were used. In using this equation with the slider, W was taken to be the sum of the tup weight and carriage weight, rather than the tup weight alone, and the gravitational effect in further accelerating the tup after the carriage contacted the shock absorbers was neglected. The 5% allowable velocity error (from nominal value) was not exceeded in normal use of this equation.

REFERENCE

1. Messrs. C.T. Davey, E.J. Dougherty, G.P. Wachtell, and R.G. Yaeger, "Crush Pipe-Test Program", Vols. I & II, FIRL Report No. F-C4568, dated July 22, 1971.

PREDICTION OF CONSTRAINED SECONDARY FRAGMENT VELOCITIES

Peter S. Westine
Southwest Research Institute
San Antonio, Texas

and

John H. Kineke , Jr.
Ballistic Research Laboratories
Aberdeen Proving Grounds
Aberdeen, Maryland

Two new solutions are presented. One presents a nondimensionalized solution for estimating the specific impulse imparted to flat surfaces, cylindrically shaped bodies, and spherically shaped objects in the vicinity of cylindrical explosive charges. The second solution shows how to estimate the velocity of fragments which had been constrained cantilever and clamped-clamped beams of any material and cross-sectional area by accounting for the structural strain energy associated with fracturing these structural components at their supports.

The applied specific impulse solution from the detonation of line sources is obtained by performing a model analysis, and curve fitting the resulting pi terms to experimental test data. Forty-eight tests on a variety of spheres and cylinders with different orientations, various amounts of explosive, and numerous standoff distances were subjected to blast waves from line sources and had the impulse imparted to the object determined by measuring velocities.

Fragment velocities for objects which had originally been constrained as cantilever or clamped-clamped beams were obtained by modifying the impulse-momentum relationship used in velocity predictions for unconstrained fragments. Use of approximate analytical energy solutions for various modes of failure in brittle as well as ductile materials indicated that the impulse term could be reduced by the square root of a structural strain energy related to toughness (area under the true stress-strain curve) and fragment volume. Sixty observed velocities on 1020 steel, 1095 steel, and 2024-T3 aluminum beams of different sizes and with various applied specific impulses were used to complete empirically this second solution and demonstrate its validity.

INTRODUCTION

The velocity of an unconstrained secondary fragment is estimated by applying the conservation of linear momentum principle. The impulse imparted to the potential fragment by an explosive detonation is computed, and the velocity is obtained by dividing this impulse by the fragment mass. Such an approach assumes that the object, which is about to become a fragment, is unconstrained or free-standing. In reality, most secondary fragments attain a much lower velocity because of the energy that must be consumed in fracturing the supports.

The purpose of this paper is to present approximate engineering procedures for estimating secondary fragment velocities when constrained objects are exposed to explosive detonations. To do this, the problem is divided into two parts--the first for estimating the specific impulse imparted to flat, cylindrical, or spherical secondary fragments in the vicinity of cylindrical explosive charges; and the second for estimating the velocity of constrained beams of any material and cross-sectional area which could become secondary fragments because of this impulsive load.

A combined theoretical and experimental program was conducted which led to Equation (1) for estimating the specific impulse imparted to a target by the detonation of a line explosive source, and Equation (2) for estimating the velocity of constrained cantilever beam-like fragments loaded by a uniform impulse.

$$\frac{i}{\gamma R_e}\left(\frac{R_e}{\ell_e}\right)^{0.333}\left(\frac{R_e}{R_s}\right)^{0.158} = 1.20 \times 10^{+6}\left(\frac{R_e}{R}\right)$$

(Cont'd)

$$\text{for } \frac{R}{R_e} \leq 5.25 \qquad (1\text{-a})$$

$$\frac{i}{\gamma R_e}\left(\frac{R_e}{\ell_e}\right)^{0.333}\left(\frac{R_e}{R_s}\right)^{0.158} = 4.16 \times 10^{+6}\left(\frac{R_e}{R}\right)^{7/4}$$

$$\text{for } \frac{R}{R_e} \geq 5.25 \qquad (1\text{-b})$$

where

i = specific impulse ($N - S/M^2$)

R_e = radius explosive (M)

ℓ_e = length of explosive (M)

R_s = radius of fragment (M)

R = standoff distance (M)

γ = target shape factor (1.0 for flat surfaces, $\pi/4$ for cylinders, and 2/3 for spheres)

$$\frac{\sqrt{\rho_s}V}{\sqrt{T}} = -0.2369 + 0.3931\left(\frac{ib}{\sqrt{\rho_s TA}}\right)\left(\frac{\ell}{b/_2}\right)^{0.3}$$

$$\text{for } \frac{ib}{\sqrt{\rho_s TA}}\left(\frac{\ell}{b/_2}\right)^{0.3} > 0.603 \qquad (2\text{-a})$$

$$V = 0$$

$$\text{for } \frac{ib}{\sqrt{\rho_s TA}}\left(\frac{\ell}{b/_2}\right)^{0.3} \leq 0.603 \qquad (2\text{-b})$$

---

where

V = fragment velocity (M/S)

ρ_s = fragment mass density (kG/M^3)

T = toughness of fragment material (Pa)

b = loaded width of beam (M)

ℓ = length of beam (M)

A = cross sectional area of beam (M^2)

i = specific impulse ($N - S/M^2$)

These equations work for cantilever beams of any material and any cross-sectional area. To estimate the velocity, the specific impulse i imparted to the beam is estimated from the standoff distance and line charge geometry using Equation (1). Substituting this impulse, beam properties, and beam geometry into Equation (2) gives the fragment velocity. If the quantity $(ib/\sqrt{\rho_s TA})(\ell/b/_2)^{0.3}$ is less than 0.603, the fragment will not break free; hence, its velocity is zero.

An equation similar in format to Equation (2), but with different coefficients for slope and intercept, can also be used for beams with other boundary or support conditions. Although a large quantity of data is not yet available to demonstrate this observation, enough data exist on clamped-clamped beams to show that the coefficients -0.6498 instead of -0.2369 and 0.4358 instead of 0.3931 work better for this boundary condition.

This paper proceeds by describing Equations (1) and (2) in greater detail, showing how these equations compare with test results, and presenting derivations.

Cantilever Beam Fragment Velocities

Constrained secondary fragments will have some velocity less than unconstrained ones when loaded by a close-in explosive detonation. To measure velocities experimentally for a variety of cantilever beam fragments, technicians placed various size fragments near line explosive charges. All fragments were aligned parallel to the explosive source, and the majority of the fragments were cylinders with a diameter of 3.17 mm. Most of these cylindrical beams were made of either 1020 or 1095 steel. Their length to radius ratios varied from 6 to 12 to 18. The explosive charges were usually 0.1016 m in diameter although some were 0.0508 and others 0.0762 m in diameter so a variation would occur in size of charge relative to size of specimen. Standoff distance from the center of the charge to the target varied from 0.086 to 0.350 meters so a variety of fragment velocities would be obtained. A limited number of additional tests were also conducted using cylindrical beams of 2024-T3 aluminum and 1095 steel beams with square 2.5 by 2.5 mm cross-sections.

The important conclusion to be drawn from this test data is that the quantity $\sqrt{\rho_s}V/\sqrt{T}$ can be plotted as a function of $(ib/\sqrt{\rho_s TA})(\ell/b/_2)^{0.3}$. Figure 1 is this plot for 53 cantilever beam data points. For convenience, all 1095 steel beams are plotted as triangles, all 1020 beams are plotted as squares, and all 2024-T3 beams are plotted with an X. If the symbol is not shaded in, the $\ell/b/_2$ ratio equaled 6; if partially shaded, the $\ell/b/_2$ ratio equaled 12; and if completely colored in, the $\ell/b/_2$ ratio equaled 18. All tests have a shape factor for a cylinder of $\pi/4$; except for the 1095 square cross-section beams which have a shape factor of 1.0, and a triangular symbol pointing to the right.

Although scatter occurs, the experimental data appears to follow a straight line on this plot of scaled velocity $\sqrt{\rho_s}V/\sqrt{T}$ versus scaled applied impulse $(ib/\sqrt{\rho_s T}A)(\ell/b_{/2})^{0.3}$. The implications of this observation are that a conservation of linear momentum law is being followed by these test results.

Many data points are presented with a scaled velocity $\sqrt{\rho_s}V/\sqrt{T}$ of either 0 to 0.1. The velocities of these fragments were not measured in experiments; this data comes from threshold experiments to determine what impulse will just cause fracture of the support. If the support does not break, these fragments are plotted as having a velocity of 0, and if the support breaks, it is plotted as a small unmeasured finite scaled velocity $\sqrt{\rho_s}V/\sqrt{T}$ of 0.1.

The nondimensional ratios, or pi terms, in Figure 1 have physical significance. This significance is better understood if we ignore the modification made by the geometric ratio $(\ell/b_{/2})^{0.3}$ in the abscissa to Figure 1. This term only makes small changes which we believe are caused by biaxial states of stress in short specimens. If the abscissa is squared and multiplied plus divided by ℓ^2, a quantity can be obtained which is given by $(i^2b^2\ell^2/\rho_s A\ell)/(TA\ell)$. The numerator of this quantity is the time equals "zero plus" kinetic energy attained by the beam from the explosive source. This kinetic energy goes into strain energy at rupture, and kinetic energy of the resulting fragment. The denominator of the abscissa $(TA\ell)$ is related to the structural strain energy at fracture. Hence the ratio $(i^2b^2\ell^2/\rho_s A\ell)/(TA\ell)$ represents the initial kinetic energy imparted to the structure by the blast source divided by the strain energy in the structure at fracture.

If the ordinate to Figure 1 is squared and multiplied plus divided by $A\ell$, a ratio is obtained that is given by $\rho_s A\ell V^2/TA\ell$. The numerator of this second ratio is the kinetic energy in the resulting fragment, and the denominator is once again the strain energy in the beam at fracture. These observations show that the solution which has been developed represents energy ratios relating: (1) the energy imparted to the beam to strain energy, and (2) the kinetic energy of the fragment to strain energy.

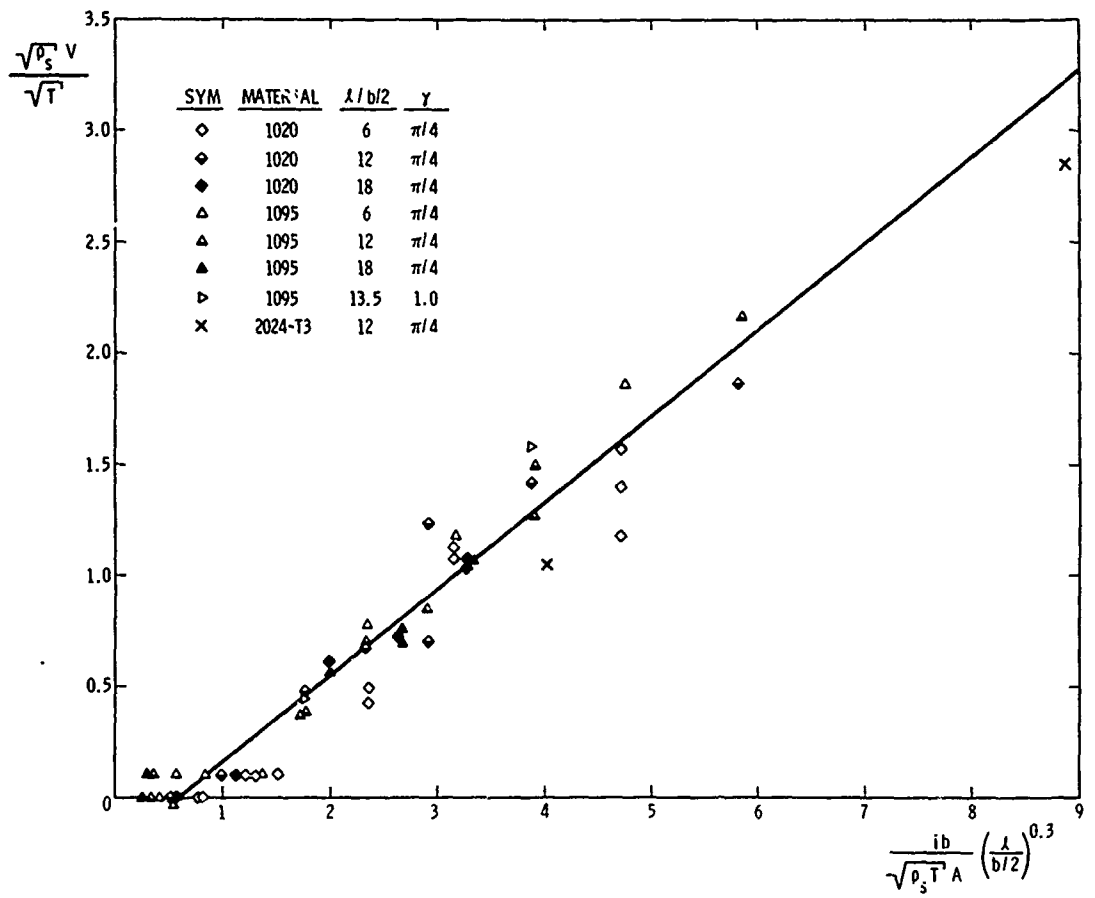

Fig. 1 - Scaled fragment velocities for constrained cantilever beams

It is interesting to study the limits given by equation for the line in Figure 1. This equation was presented in the introduction as Equation(2). Very small yet finite values of scaled velocity, setting $\sqrt{\rho_s}V/\sqrt{T}$ equal to zero, yield the nondimensionalized impulse for just fracturing the specimen.

$$\frac{ib}{\sqrt{\rho_s TA}}\left(\frac{\ell}{b/2}\right)^{0.3} = 0.603 \qquad (3)$$

(scaled impulse to just fracture)

This ratio relates the energy imparted to the beam to the strain energy to fracture, and is independent of fragment kinetic energy as it should be.

The other limit to Equation (2) is for very large values of scaled impulse. Under these conditions the coefficient 0.2369 becomes insignificant and we obtain

$$\frac{\rho_s VA}{ib}\left(\frac{b/2}{\ell}\right)^{0.3} = 0.3931 \qquad (4)$$

(scaled velocity for very large impulses)

This asymptote, if we ignore the geometric ratio $(b/2\ell)^{0.3}$, is a statement of impulse-momentum. The limit is independent of structural strain energy as it should be with most of the applied energy going into the kinetic energy of the fragment.

Because both asymptotes approach reasonable values, this graphical solution increases in credibility. The major difficulty that will be encountered in using this solution is specifying the toughness of the beam material. Toughness as used in this paper is the classical definition of area under the true stress versus the true strain curve for tensile specimens taken to fracture. Toughness measurements made in this manner only crudely correlate with Izod or Charpy measurements or engineering stress-strain curves. The one helpful fact is that fragment velocity is not a very sensitive function of material toughness. At very low velocities, the velocity is proportional to the square root of toughness and at high velocities the velocity is independent of toughness. These observations show that some error in knowing toughness can be tolerated and reasonable answers will still follow.

Constrained Beam With Other Boundary Conditions

Not all potential secondary fragments have cantilever supports. Other "beam-like" fragments can have simple supports or clamped-clamped supports as possible boundary conditions. Little data are available on either of these two conditions; however, the data which do exist on clamped-clamped beams suggest the use of the same analysis when the coefficients are changed.

Figure 2 is the plot of scaled fragment velocity $\sqrt{\rho_s}V/\sqrt{T}$ versus scaled applied specific impulse $(ib/\sqrt{\rho_s TA})(\ell/b/2)^{0.3}$ for clamped-clamped beams. The number of data points is not as numerous; however, the functional format of the solution is precisely the same as for cantilever beams. Test conditions are similar to those in the cantilever beam experiments except for the additional support and closer standoff distances needed to fracture specimens. All tests were on cylindrical specimens of either 1020 or 1095 steel, and of a length to radius ratio of either 6 or 18.

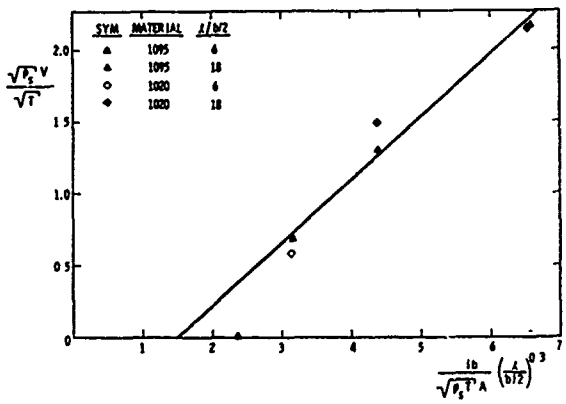

Fig. 2 - Scaled fragment velocities for constrained clamped-clamped fragments

A straight line curve-fitted to these fragment velocities from clamped-clamped beams is given by:

$$\frac{\sqrt{\rho_s}V}{\sqrt{T}} = -0.6498 + 0.4358\left(\frac{ib}{\sqrt{\rho_s TA}}\right)\left(\frac{\ell}{b/2}\right)^{0.3} \qquad (5)$$

The same qualitative observations made about the limits for this clamped-clamped beam solution apply as in the case of cantilever beams.

No solution is presented for simply-supported beams or beams with other support conditions because the data are not available. We believe that the same format could be used, and that a solution is possible when the data become available.

Specific Acquired Impulse

A generalized solution for determining the impulse per unit projected target area imparted to spheres, right circular cylinders, and flat

objects exposed to a detonating line explosive sources was developed using similitude theory, experimental test data, and empirical observations. The solution considers a long cylindrical line explosive source of length ℓ_e, radius R_e, and energy per unit volume e. If this charge is detonated instantaneously, a shock wave must be propagated through an atmosphere defined by its mass density ρ_o, sonic velocity c_o, and ambient atmospheric pressure p_o. Because secondary fragment velocities depend upon the specific impulse imparted to the fragments per unit projected area, we determine the specific impulse i that would be imparted to an infinitely large flat plate struck head-on. This impulse, termed specific acquired impulse, can depend upon fragment geometry and orientation. To make a complete definition, we assumed that the fragment geometry could be defined by two parameters, such as the radius R_s and length ℓ_s in the case of a cylinder. In addition, the impulse imparted to the fragment depends on a nondimensional shape factor γ which accounts for its orientation as well as geometry.

Eleven different parameters have been used to determine specific acquired impulse. In functional format these parameters are given by Equation (6).

$$i = \Psi_i \left[e, \ell_e, R_e, \rho_o, c_o, p_o, R, R_s, \ell_s, \gamma \right] \quad (6)$$

This eleven parameter space of dimensional parameters can be reduced to an eight parameter space of nondimensional numbers by conducting a model analysis. Results from this analysis are given by:

$$\frac{i}{\rho_o p_o R_e} = \Psi \left[\frac{e}{p_o}, \frac{\ell_e}{R_e}, \frac{\rho_o c_o}{p_o}, \frac{R}{R_e}, \frac{R_s}{R_e}, \frac{\ell_s}{R_e}, \gamma \right] \quad (7)$$

To simplify this solution further, we wrote a dimensional version of the dimensionless Equation (7). This can be accomplished by recognizing that many parameters are essentially invariant and can be treated as constants. The atmospheric conditions p_o, c_o, and ρ_o, for example, are under ambient sea level conditions with sufficient small variation to treat each as a constant. In addition, all chemical explosives have an energy per unit volume e which is almost a constant, $8 \times 10^{+9} n/m^2$. Treating these four parameters as constant reduces the eight parameter space given in Equation (7) to a six parameter space of dimensional numbers.

$$\frac{i}{R_e} = \Psi \left[\frac{R}{R_e}, \frac{\ell_e}{R_e}, \frac{R_s}{R_e}, \frac{\ell_s}{R_e}, \gamma \right] \quad (8)$$

Further reduction of Equation (8) was obtained by applying empirical observations. Two of the parameters in Equation (8), i/R_e and γ, can be combined to form $i/\gamma R_e$ from our definition of the shape factor. The shape factor γ is that numerical constant which is needed to relate impulse imparted to a cylinder, impulse imparted to a sphere, or impulse imparted to any shape fragment to that impulse which would be imparted to a flat surface, $\gamma = 1$. Thus by definition, Equation (9) can be written from Equation (8).

$$\frac{i}{\gamma R_e} = \frac{\Psi_i}{\gamma} \left[\frac{R}{R_e}, \frac{R_s}{R_e}, \frac{\ell_e}{R_e}, \frac{\ell_s}{R_e} \right] \quad (9)$$

Of the parameters in Equation (9), the main two are the scaled impulse $i/\gamma R_e$ and the scaled standoff distance R/R_e. The other three parameters (R_s/R_e, ℓ_e/R_e, and ℓ_s/R_e) are geometric aspect ratios which usually are secondary effects. If the fragment is always aligned parallel to the line charge and the line charge is larger than the fragment, the scaled length of fragment ℓ_s/R_e should not enter the problem. Experimental test results on spheres and cylinders substantiated this observation. The functional relationship which was curve-fitted to test results is given by Equation (10) which assumes that ℓ_s/R_e is insignificant.

$$\frac{i}{\gamma R_e} = \Psi \left[\frac{R}{R_e}, \frac{R_s}{R_e}, \frac{\ell_e}{R_e} \right] \quad (10)$$

Experimental model tests were conducted in which small spheres and cylinders were placed at various standoff distances from the center line of various size cylindrical explosive Comp B charges. All cylinders and spheres in these tests were unconstrained. Basically, the test procedure was to detonate a cylindrical explosive charge and measure the resulting velocity imparted to these unconstrained fragments. Cylinders were oriented with this axis parallel to a line radiating from the explosive as in Figure 3-a, in which case a flat target surface was exposed and the shape factor γ equals 1.0. In addition, other cylinders were oriented with their axis perpendicular to line radiating from the charge as in Figure 3-b, in which case the shape factor γ equals $\pi/4$. The other unconstrained targets were spheres as in Figure 3-c which have a shape factor γ of 2/3. These shape factors can all be calculated analytically, although this calculation will not be made in this paper. The velocities of the fragments were all measured using sequential flash x-rays. By using conservation of momentum, the average

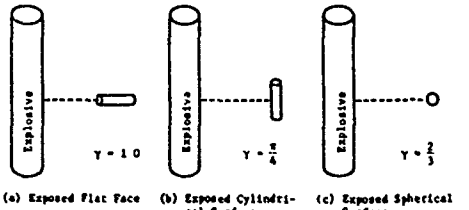

Fig. 3 - Target orientation for unconstrained tests

applied specific impulse is obtained from the fragment mass M, projected area A_s, and measured velocity V. This applied specific impulse i equals $MV/A_s\gamma$.

The solution was completed empirically by first plotting the two principle terms, $i/\gamma R_e$ and R/R_e, versus each other while different symbols were used for various quantities R_e/R_s and ℓ_e/R_e. Such a plot indicated the existence of two different regions to the solution for values of R/R_e either greater or less than 5.25. A systematic trend also indicated that although R_e/R_s and ℓ_e/R_e had a weak influence on scaled impulse $i/\gamma R_e$, large values of R_e/R_s and smaller values of ℓ_e/R_e had smaller scaled impulses $i/\gamma R_e$ for almost constant values of scaled standoff distance R/R_e. These observations suggested that for each of the two R/R_e domains, the scaled standoff distance could be related to the scaled impulse $i/\gamma R_e$, scaled charge aspect ratio ℓ_e/R_e, and scaled radii ratio R_e/R_s through a log linear approximation. After performing a least squares analysis to obtain the coefficients and exponents in each of the R/R_e realms, we found that in both domains the terms $i/\gamma R_e$, ℓ_e/R_e, and R_e/R_s could be combined to approximately form the quantity $(i/\gamma R_e)\,(R_e/R_s)^{0.158}(R_e/\ell_e)^{0.333}$. The two equations for the two R/R_e domains which resulted from these efforts were already presented as Equations (1) in the introduction to this paper. The units on i must be $N - S/m^2$ and on R_e must be m, for Equations (1a) and (1b) to be correct. The other ratios in Equation (1a) and (1b) are nondimensional. Figure 4 is a plot showing the functional relationships given by Equations (1a) and (1b) and all the test data obtained in this program. Different shaped symbols denote whether tests were on a sphere (a circle), a cylinder with a cylindrical surface (a three sided triangle), as in Figure 3-b, or a cylinder with an exposed flat face (a four sided square), as in Figure 3-c. If the symbol is not darkened, the ℓ_e/R_e ratio equaled 4.0; otherwise, the darkened symbols indicate ℓ_e/R_e ratios of 2.0 in flat faced encounters or 9.33 in cylindrical encounters. The direction in which the symbol points indicates the R_e/R_s ratio (either 4, 12, or 16) in Figure 4. The test data appear to collapse into a single function in Figure 4, and Equations (1a) and (1b) are excellent approximations to these test results.

The ordinate in Figure 4 has a quantity called R_{eff} in it instead of $R_e(\ell_e/R_e)^{0.333}$. This quantity R_{eff} stands for the effective radius of the equivalent sphere of explosive which could be formed from a cylinder of radius R_e and length ℓ_e. Because R_{eff} is related to R_e and ℓ_e through Equation (11), either the dependent terms in Equations (1a) and (1b), or the ordinate to Figure 4 may be used.

$$R_{eff} = 0.9086\left(\frac{\ell_e}{R_e}\right)^{0.333} R_e \qquad (11)$$

The existence of two straight line regions for values of R/R_e less than and greater than 5.25 is apparent in Figure 4. In the near field where R/R_e is less than 5.25, the slope of the line in Figure 4 is minus 1.0 which means that $(i/\gamma R_{eff})$ times (R/R_e) equals a constant for invariant R_e/R_s. This observation means that the normally reflected specific impulse close to the cylindrical charge is caused primarily by momentum of the explosive products. In other words, the impulse close to the charge is caused by adding up the mass times the velocity products of all the particles from the explosive, casing, and engulfed air. Because the specific impulse i is caused by momentum in explosive products, it dissipates with standoff distance inversely as the surface area of a cylinder which encloses the cylindrical source. The surface area equals $2\pi R\ell_e$; hence, the appearance of an "iR" product close to an explosive line source. Only as standoff distances grow larger do the effects of momentum loss through air drag and gravitational effects reduce this phenomena sufficiently for shock wave phenomena to become more important and the slope of the line to change in Figure 4.

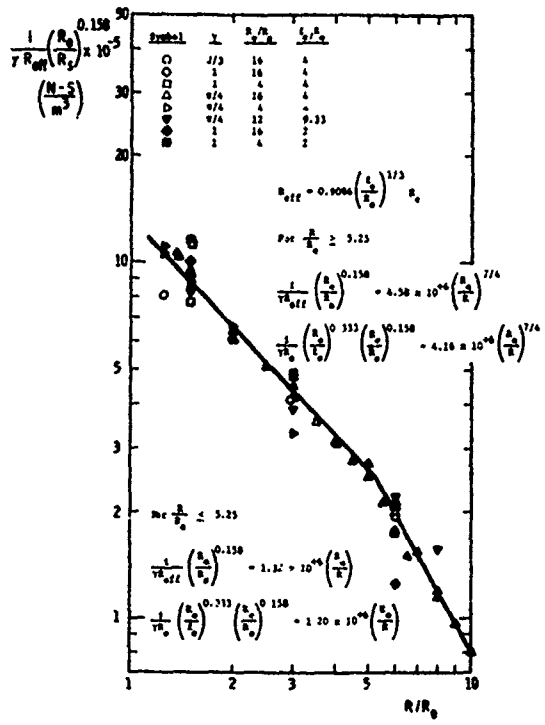

Fig. 4 - Specific Acquired Impulse

Analytical Development of Constrained Fragment Equations

Whenever a secondary fragment is unconstrained, its velocity is estimated by applying the conservation of impulse-momentum. On the other hand, should a structural constraint

resist the motion, the imparted impulse is reduced by an amount I_{st} and conservation of impulse momentum must be rewritten as:

$$I - I_{st} = mV \tag{12}$$

where I is the total acquired impulse and m is the total mass of the fragment. The impulse I_{st} to just break the fragment free of its supports equals $\sqrt{2mU}$ as a limiting value, with U the strain energy stored in the fragment at fracture of the supports. The relationship of I_{st} to U is obtained by equating the kinetic energy imparted to the structure when the supports fail to the ultimate structural strain energy U as in the following derivation.

$$U = \frac{1}{2}mV_o^2 = \frac{m}{2}\left(\frac{I_{st}}{m}\right)^2 = \frac{I_{st}^2}{2m} \tag{13}$$

Substituting the square root of Equation (13) in Equation (12) and rearranging algebraically gives:

$$\frac{I}{\sqrt{mU}} = \sqrt{2} + \frac{mV}{\sqrt{U}} \tag{14}$$

The total impulse imparted to a structural element is easily obtained by using Equation (1), and multiplying the specific impulse i by the projected area to obtain the total impulse. The total m is the mass density times the volume of the fragment. This solution is completed when procedures are developed for estimating the strain energy U, and all quantities are substituted in Equation (14).

The strain energy U consumed in fracturing a cantilever beam was estimated by assuming a deformed shape and substituting into the appropriate mechanics relationships for different modes of response in both ductile and brittle beams. A number of different solutions resulted; however, enough similarities were noted in all solutions to permit important generalizations to be made after these strain energies had been determined.

We began by assuming that the deformed shape at fracture for a cantilever beam is given by:

$$y = w_o\left(1 - \cos\frac{\pi x}{2\ell}\right) \tag{15}$$

where w_o is the tip deflection. ℓ is the total length of the beam, x is position along the beam, and y is the deformation at any position x. Notice that this deformed shape has no deformation at the root of the beam, a maximum deformation at the tip of the beam, no slope at the root of the beam, a maximum slope at the tip of the beam, a maximum elastic moment or curvature at the root of the beam, and no elastic moment or curvature at the tip of the beam. Because these boundary conditions are the appropriate ones, this assumed deformed shape is reasonable. If we perform a bending analysis for a rigid, perfectly-plastic beam, the strain energy stored in the beam is given by the moment-curvature relationship.

$$U = \int_o^{\ell} M_y \frac{d^2y}{dx^2}\,dx \tag{16}$$

Substituting the yield stress times the plastic section modulus $\sigma_y Z$ for the yield moment M_y, and differentiating Equation (15) twice before substituting gives:

$$U = \frac{\pi^2 w_o \sigma_y Z}{4\ell^2}\int_o^{\ell} \cos\frac{\pi x}{2\ell}\,dx \tag{17}$$

Completing the integration gives:

$$U = \frac{\pi\sigma_y Z w_o}{2\ell} \tag{18}$$

But the maximum stress ε_{max} equals the half thickness h/2 times the small deformation approximation to the curvature:

$$\varepsilon_{max} = \frac{h}{2}\left(\frac{d^2y}{dx^2}\right)_{max} \tag{19}$$

which becomes a maximum at the root of the cantilever where d^2y/dx^2 equals $\pi^2 w_o/4\ell^2$, and:

$$\varepsilon_{max} = \frac{\pi^2 h w_o}{8\ell^2} \tag{20}$$

Substituting Equation (20) for w_o in Equation (18) and rearranging terms gives:

$$U = \frac{4Z\ell\sigma_y\varepsilon_{max}}{\pi h} \tag{21}$$

But the quantity $\sigma_y\varepsilon_{max}$ in a rigid, perfectly-plastic ductile material as in this analysis is the area under the stress-strain curve which is called toughness T. Expressing U in terms of toughness and dividing by toughness times beam volume $A\ell$ gives the desired result.

$$\frac{U}{TA\ell} = \frac{4Z}{\pi Ah} \tag{22}$$

(bending solution ductile material)

Next we developed an elastic bending solution for the strain energy in brittle beams. The strain energy in an elastic beam is given by:

$$U = \frac{EI}{2}\int_o^{\ell}\left(\frac{d^2y}{dx^2}\right)^2 dx \tag{23}$$

Assuming the same deformed shape as in Equation (15) and differentiating twice to substitute gives:

$$U = \frac{\pi^4 EIw_o^2}{32\ell^4} \int_0^{\ell} \cos^2\left(\frac{\pi x}{2\ell}\right) dx \qquad (24)$$

Or after integrating:

$$U = \frac{\pi^4 EIw_o^2}{64\ell^3} \qquad (25)$$

Because we have used the same deformed shape in this elastic analysis as in the plastic analysis, the maximum strain is still related to the peak deformation w_o through Equation (20). Substituting w_o from Equation (20) into Equation (25) and gathering terms gives:

$$U = \frac{E\varepsilon_{max}^2}{2}\left(\frac{I}{\frac{h}{2}}\right)\left(\frac{\ell}{h}\right) \qquad (26)$$

But $E\varepsilon_{max}^2/2$ is the area under an elastic, brittle, stress-strain curve which is toughness T. Expressing U in terms of toughness, recognizing that $I/(h/2)$ is the elastic section modulus S, and dividing by $TA\ell$ gives the desired result for a bending solution in a brittle material.

$$\frac{U}{TA\ell} = \frac{S}{Ah} \qquad (27)$$

(bending solution brittle material)

The strain energy can also be estimated for other modes of failure such as brittle shear and ductile shear. Although we omit the details of these calculations from this paper, the results for ductile shear are given by Equation (28) and for brittle shear by Equation (29) where μ is Poisson's ratio.

$$\frac{U}{TA\ell} = \frac{1}{2} \qquad (28)$$

(shear solution ductile material)

$$\frac{U}{TA\ell} = \frac{1}{2(1+\mu)} \qquad (29)$$

(shear solution brittle material)

Equations (22, 27, 28, and 29) should be inspected to note the similarities which exist in them. The major observation is that no matter what mode of failure is hypothesized, the strain energy at failure equals $(TA\ell)$ times a constant. For some modes of failure, the constant may be a weak function of the cross-sectional shape of the fragment (a function of S/Ah or Z/Ah), but this constant varies very little. Table A is included to emphasize the limited variation in these constants.

TABLE A
Variations In Strain Energy Coefficients $U/TA\ell$

Type of Failure / Shape of Beam Cross Section	Ductile Bending	Brittle Bending	Ductile Shear	Brittle Shear
General Solution	$\frac{4}{\pi}\left(\frac{z}{Ah}\right)$	$\left(\frac{S}{Ah}\right)$	$\frac{1}{2}$	$\frac{1}{2(1+\mu)}$
Circular Solid	0.270	0.125	0.500	0.385
Rectangular Solid	0.318	0.167	0.500	0.385
I-Beam	≈0.637	≈0.500	0.500	0.385

The second major observation is that only toughness T appears to be the one mechanical property of importance. All four solutions conclude that this area under the stress-strain curve times the volume of the specimen times a constant, equals the strain energy U expended in fracturing the specimen.

For analytical purposes, these conclusions indicate that the mode of failure does not have to be determined. The solution can proceed by assuming that strain energy is given by

Equation (30), and that the constant C will be obtained from experimental test results.

$$U = C(TA\ell) \qquad (30)$$

The influence of assuming other deformed shapes has not been discussed. A different deformed shape will not change our conclusions that U is directly proportional to $(TA\ell)$; however, a different shape will result in a slightly different numerical proportionality constant C. Because we are willing to allow C to be determined experimentally, the qualitative conclusions still can be applied in our development of a solution.

All four modes of failure were developed for failure in a cantilever beam. Other boundary conditions such as clamped-clamped, simply-supported, etc., will give similar qualitative results; however, the proportionality coefficient C is a function of support conditions.

The solution for predicting the velocity of constrained secondary fragments can now be completed by substituting into Equation (14). If we let the total impulse I equal $ib\ell$ where b is the loaded width, the total mass m of the fragment equals $\rho_s A\ell$, and the strain energy U be given by Equation (30), then:

$$\frac{ib\ell}{\sqrt{(\rho_s A\ell)(CTA\ell)}} = \sqrt{2} + \frac{\sqrt{\rho_s A\ell}V}{\sqrt{CTA\ell}} \qquad (31)$$

Or after reduction:

$$\frac{ib}{\sqrt{\rho_s TA}} = \sqrt{2C} + \frac{\sqrt{\rho_s}V}{\sqrt{T}} \qquad (32)$$

Equation (32) is a two parameter space of nondimensional energy ratios. If the term

$\sqrt{\rho_s}V/\sqrt{T}$ is squared, this group is the ratio of fragment kinetic energy per unit volume to strain energy expended per unit volume. The square of the term $ib/A\sqrt{\rho_s T}$ represents the energy per unit length of fragment. This solution infers that the constrained secondary fragment velocity is independent of beam length ℓ. Experimental test results show that this conclusion is not quite accurate.

The final equation which was developed had a format given by:

$$\frac{\sqrt{\rho_s}V}{\sqrt{T}} = C_0 + C_1\left(\frac{ib}{\sqrt{\rho_s TA}}\right)\left(\frac{\ell}{b/2}\right)^N \qquad (33)$$

Probably the most confusing point is why test results appear to be a function of $\ell/b_{/2}$ when the theoretical energy solution infers that velocity should be independent of $\ell/b_{/2}$. Obviously this empirical observation means we are excluding some process from calculations which should be considered. Although we can only conjecture about what effects are entering the fragment fracturing process, our opinion is that a biaxial rather than uniaxial state of stress is occurring because of the short stubby nature of most constrained specimens. The parameters ℓ/b only ranges from 3 to 9. For very long specimens which have not been tested, measured velocities might become independent of the length to width ratio. Equation (33) only combined $ib/\sqrt{\rho_s TA}$ and $\ell/b_{/2}$ because of empirical observation on tests of fairly short cantilever beams.

A second concern might arise from our exclusion of rotational kinetic energy in this analysis for fragment velocity in constrained cantilever beams. In spite of the fact that symmetry is destroyed in a cantilever beam, the rotational kinetic energy of a fragment can be ignored because it is small relative to the translational kinetic energy of a fragment. For example, in various tests, double flash x-rays measured rotational velocity as well as translational velocity. These rotational velocities were all less than 251 rad/sec for all of these experiments. If one computes $1/2I\omega^2$ for comparison with $1/2MV^2$ in these tests, the rotational kinetic energy will be found to be less than 1% of the translational kinetic energy.

Other boundary conditions such as clamped-clamped beams will also yield a solution with a format as in Equation (33). The major difference is that the coefficients C_0 and C_1 can be different even though strain energy coefficients as in Table A may be identical for the same mode of response. For cantilever beams and clamped-clamped beams, the theoretical strain energy coefficients both equal $4/\pi(2/Ah)$ for ductile bending, (S/Ah) for brittle bending, 0.500 for ductile shear, and $1/2(1 + \mu)$ for brittle shear. This observation does not mean that cantilever and clamped-clamped beams have the same C_0 and C_1 coefficients in Equation (33), because clamped-clamped beams can develop extensional modes of response which cantilever beams cannot do. In clamped-clamped beams, the theoretical scaled strain energy coefficient $(U/A\ell T)$ for ductile extension is 0.500 and for brittle extension is 0.375. The limited amount of test data on clamped-clamped beams which has already been discussed suggests that these differences do exist.

Summary

Two solutions have been presented--the first for predicting the specific impulse imparted to fragments from cylindrical explosive sources, and the second for predicting the velocity of constrained fragments. Both analyses are combined theoretical and empirical solutions. Sufficient quantities of experimental data exist to establish the validity of both the loading solution and the velocity solution for fragmenting cantilever beams. A limited amount of clamped-clamped beam data infers that the solution can be extended to beams with other boundary conditions. A Ballistic Research Laboratory contractor's report, with the same authors and title as this paper, will describe this effort in greater detail and present all test data for those who are interested.

Acknowledgements

This study was funded by PA, A4932MM&T Project No. 5751264 on Advanced Technology for Suppressive Shielding of Hazardous Production and Supply Operations for the Production Base Modernization and Expansion Programs, under the direction of Dr. D. Katsanis and Mr. B. Jezek. The authors are indebted to them and many others for their assistance. Mr. Walter G. Smothers of Ballistic Research Laboratories painstakingly performed all constrained and unconstrained fragmentation experiments; Mrs. Elva Hernandez of Southwest Research Institute typed this paper; and Mr. Victor Hernandez of Southwest Research Institute drew all figures. The cooperation of these individuals and others is appreciated.

DISCUSSION

Mr. Sierakowski, (University of Florida:) On one of the slides you show specific acquired impulse yet in your discussion you mentioned specific impulse and total specific impulse several times. Are there any differences in all this terminology?

Mr. Westine: Yes. Total impulse is specific impulse times some area. It would have units of force times time. A specific impulse is total impulse divided by an area; in other words it is an impulse per unit area and it has units of force times time divided by length squared. I tried to be careful with those two. As far as using the phrase specific impulse where I meant to say specific acquired impulse, that was just sloppiness in stringing too many words together.

IMPEDANCE TECHNIQUES FOR SCALING AND FOR PREDICTING STRUCTURE RESPONSE TO AIR BLAST

F.B. Safford
Agbabian Associates, El Segundo, California

R.E. Walker
U.S. Army Waterways Experiment Station
Vicksburg, Mississippi

T.E. Kennedy
Defense Nuclear Agency, Washington, D.C.

Transfer impedances were measured on a 1/12-scale model and on its prototype structure. The structure was the Perimeter Acquisition Radar Building (PARB) of the SAFEGUARD ABM System, which measures 125 ft (38 m) in height, 194 ft (59 m) on its front, and 210 ft (64 m) on its side, with exterior walls 3 to 6 ft (0.9 to 1.8 m) thick. The impedance measurements for both structures were then used with air-blast loads to predict internal acceleration responses. Predictions for the model were compared to test acceleration records taken when the model was excited by an air blast generated from a 500-ton (453,550 kg) TNT explosion. The data were scaled for comparison with prototype responses.

1. INTRODUCTION

Equipment survival is of paramount importance in the design of ground-based strategic and tactical systems against nuclear-weapon effects, and frequently becomes a driving consideration when the overall cost of such a system is considered. As is to be expected, every effort is made during the conceptual and design phases to minimize system equipment costs while trying to assure a high probability of survival. Historically, this has entailed a tradeoff between the cost of designing special shock-resistant equipment, and the cost of using unhardened commercial equipment with shock-isolation techniques. However, the expected levels of shock and vibration must be established before techniques to protect the equipment can be decided upon. Current computer technology includes long run times, modeling assumptions, and somewhat awkward structural and air-blast loading approximations. Therefore, reliable predictions of the shock and vibration environment inside protective structures are generally limited to about 50 Hz. This is not a serious problem for the structural designer, since the structural frame generally is loaded by the lower frequencies; however, the internal equipment is generally sensitive to the frequencies above 50 Hz. The equipment must be assessed for survivability by determining failure, malfunction, and degradation levels (often referred to as "fragility") in terms of threat motions, i.e., characteristic acceleration time histories expected, rather than simple sine waves, saw-tooth shock pulses, or presently used approximations [1,2,3,4].*

An alternative procedure to determine the internal response motions of a protective structure, particularly in the higher frequencies, is to measure the impedances of the structure from exterior loading surfaces to internal points of interest. With this method, selected points on the structure are vibrated with a fixed-force vibrator as the frequency of vibration is smoothly changed over the frequency range of interest. By measuring the structural response at selected points inside and on the structure, a quantitative measure is obtained of the structure response to the vibratory force. The complex ratio of the output acceleration to the input force (magnitude and phase) obtained can be multiplied by an arbitrary input force to predict structural motions. The main limitation on the use and application of this technique is that the structural system must be

*Numbers in brackets indicate references listed at the end of the paper.

linear or nearly linear so that the principles of superposition apply. The impedances obtained are nonparametric functions and samples of the distributed system. Bandwidth of the measurements is limited by the vibrators used, which for this study ranged from 30 Hz to 3000 Hz for a model structure and 7 Hz to 300 Hz for a prototype structure.

This technique was applied to the evaluation of the interior shock and vibration environment of the Perimeter Acquisition Radar Building (PARB) of the SAFEGUARD ABM System [5,6]. The prototype building is a reinforced-concrete protective structure that measures 125 ft (38 m) in height, 194 ft (59 m) on its front, and 210 ft (64 m) on its side, with exterior walls 3 to 6 ft (0.9 to 1.8 m) thick. In this case, a 500-ton (453,550 kg) TNT high-explosive blast load on a 1/12-scale model of the building* had produced a set of acceleration time-history data that could be used for comparisons. Impedance testing was conducted on both the model and the prototype structures (see Fig. 1). These data were convolved with air-blast loads to obtain response predictions. The predictions for the model were compared to the acceleration records from the high-explosive test to assess the accuracy of the method. Subsequently, test data and acceleration predictions for the model were scaled both geometrically and by impedance methods, for comparison with the acceleration predictions for the prototype structure.

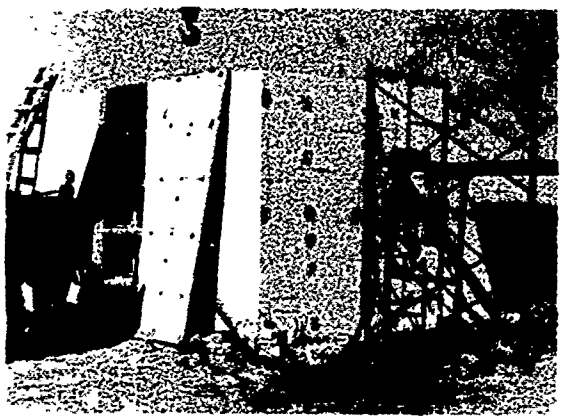

(a) 1/12-scale model, Defence Research Establishment, Suffield, Canada

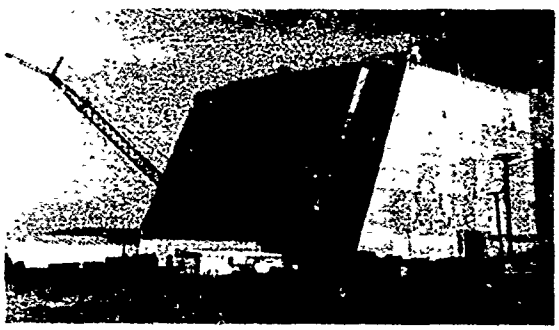

(b) Prototype, North Dakota

Fig. 1 - Perimeter Acquisition Radar Building (PARB)

*DIAL PACK Event [7,8]

2. SYSTEM FUNCTIONS

2.1 General

Dynamic properties of passive systems may be represented by a complex ratio of the input loading to the output response of a system. This complex ratio may be presented in the form of magnitude and phase, real and imaginary, and real vs. imaginary, all as a function of frequency. Inverse transformation provides yet another form of this ratio in the time domain: the impulse function. The complex ratios obtained may be viewed as samples from a continuum both in space and bandwidth, and are nonparametric. These functions can be determined analytically from a mathematical model or can be physically measured. Fig. 2 illustrates the concept.

- IMPEDANCE AS FUNCTION OF FREQUENCY

$$Z(\omega) = \frac{\text{INPUT FORCE}}{\text{OUTPUT VELOCITY}}$$

- TRANSFER FUNCTION AS FUNCTION OF FREQUENCY

$$\tau(\omega) = \frac{\text{OUTPUT MOTION}}{\text{INPUT MOTION}} = \frac{\text{OUTPUT FORCE}}{\text{INPUT FORCE}}$$

Fig. 2 - Impedance and transfer functions conceptualized

The response of a vibrated point on a structure is inversely proportional to the impedance, which will be defined herein for a given frequency as the driving force on the structure divided by the velocity at a point on the structure. The motion of the structure may be recorded as displacement, velocity, or acceleration, and, when ratioed with input force, is defined by the following terms.

$$\frac{\text{Force}}{\text{Displacement}} = \text{Dynamic Stiffness}$$

$$\frac{\text{Displacement}}{\text{Force}} = \text{Compliance}$$

$$\frac{\text{Force}}{\text{Velocity}} = \text{Impedance}$$

$$\frac{\text{Velocity}}{\text{Force}} = \text{Mobility}$$

$$\frac{\text{Force}}{\text{Acceleration}} = \text{Dynamic Mass}$$

$$\frac{\text{Acceleration}}{\text{Force}} = \text{Inertance}$$

Another important function is the ratio of input motion to output motion or of input force to output force. This is defined as a transfer function. Thus, if the base of a structure is put into motion by a blast or earthquake, multiplying this base motion by the transfer function produces the motion at another part of the structure. The terms "impedance" and "transfer function" have been used to simplify the presentation of this report; and where specific functions are displayed, as in data plots, these terms are defined.

2.2 Measurements

In the past, the frequency response characteristics of structures have been measured by quasi-steady-state methods. One method, referred to as the slow sine-sweep method, involves varying an input sinusoidal forcing function over the frequency region of interest and measuring the output responses. It has been used extensively in impedance and transfer function testing. Considerable error may occur if steady-state response is arbitrarily assumed. To minimize such error, convergence techniques are used in the testing procedures. This involves progressively slower sweep rates (or time-of-frequency variation) until essentially asymptotic response amplitudes are obtained. For the projects reported in this paper, the slow sine-sweep method was used. On subsequent projects, random, rapid sine-sweep (chirp), impulse, and pulse-train methods have been used. Some of these latter excitation methods are very beneficial in the reduction of data processing costs and the minimization of noise [9].

Input-force signal levels were set at the highest level compatible with test objectives and the linearity of the test article, to obtain favorable signal-to-noise ratios. This objective is more often limited to the force-generating equipment available. Impedance tests performed on a 1/12-scale model of a protective structure at the Defence Research Establishment, Suffield, Canada, ranged from 15 to 45 lb (67 to 200 N). An electromagnetic vibrator (MB model PM50) was used as an excitation source. Identical impedance measurements on the prototype structure in North Dakota ranged from 1000 to 5000 lb (4,500 to 22,000 N). For the prototype an electrohydraulic exciter was used (CGS). Nominally, this change in force level between the two structures corresponded to the scaled impedance difference of 144. The shaker used for the prototype building is pictured in Fig. 3.

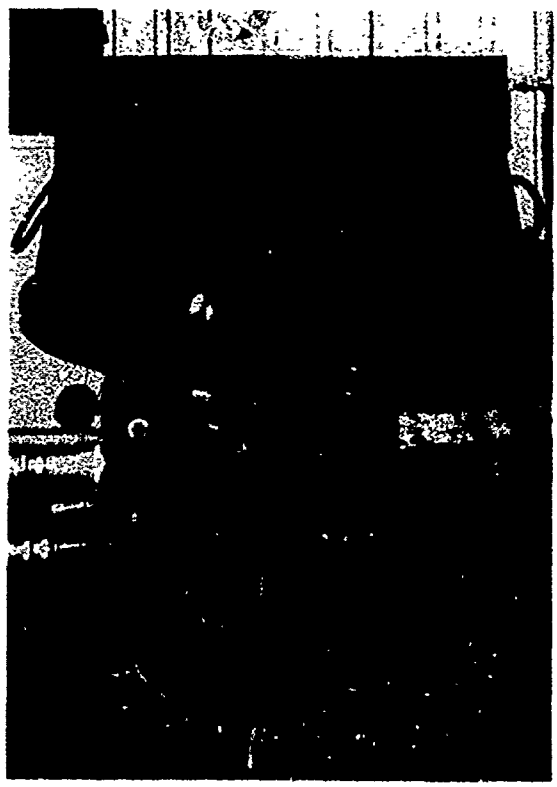

Fig. 3 - Electrohydraulic shaker used for measurements of the prototype PARB (Waterways Experiment Station)

2.3 Linearity

At the onset of testing, a survey was made to ascertain the linearity of the system by multilevel tests and by reciprocity, and to determine system symmetry and cross-axis coupling. Quantitative information gained at an early stage allows for reductions in test efforts or provides information for alternative procedures. Linear systems will provide system functions that are virtual overlays of each other, although made at several different

input-force levels. For the Perimeter Acquisition Radar Building (PARB) of the SAFEGUARD system, force input of 1000 lb to 7000 lb (4,500 to 31,000 N) demonstrated for this range that essential linearity of the building existed. Reciprocity measurements were made on the PARB model in Canada and the prototype PARB in North Dakota in accordance with the diagrams in Fig. 4. Reciprocal impedance measurements for both buildings are given in Figs. 5 and 6. Extensive use of reciprocity was made in the prototype building, since it was much easier to move accelerometers around the exterior surfaces than to move the large and heavy vibrator.

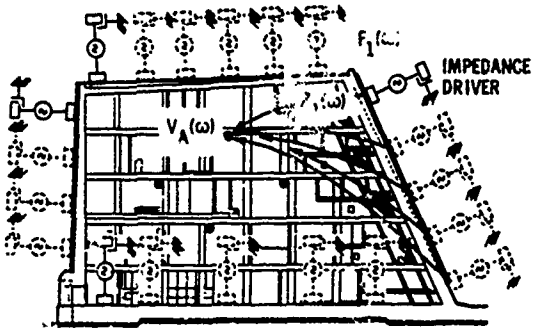

(a) Model PARB: Direct measurements (from surface to response point)

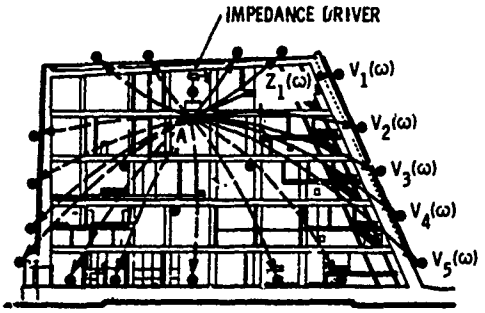

(b) Prototype PARB: Reciprocity measurements (from response point to surface)

Fig. 4 - Measurement methods used on PARB model and prototype

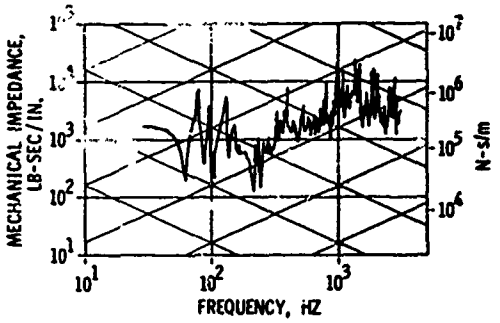

(a) Drive point, roof center (T-7); measurement point, 5th floor center (1-VT)

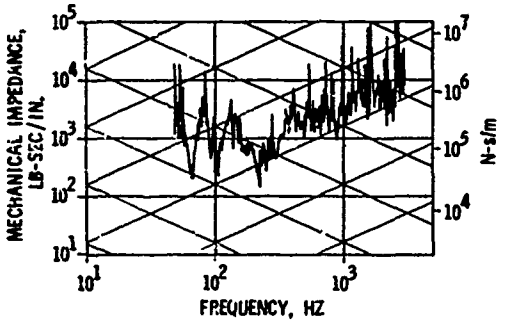

(b) Drive point, roof center (T-7); measurement point, 5th floor center (1-VT)

Fig. 5 - Model PARB data for determining reciprocity

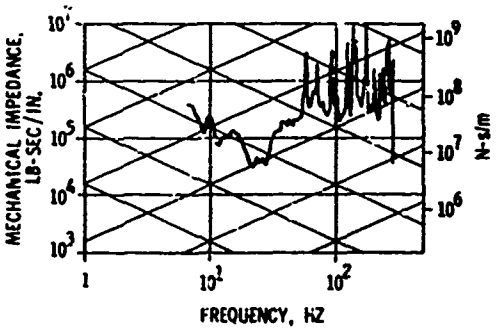

(a) Drive point, 5th floor center (1-VT); measurement point roof center (T-7)

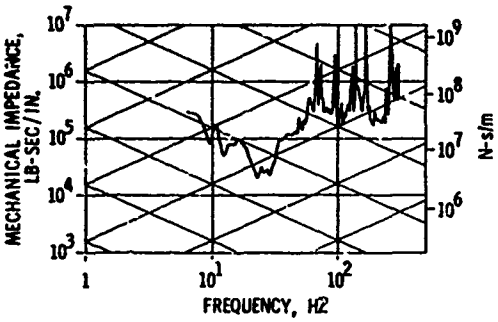

(b) Drive point, 5th floor center (1-VT); measurement point roof center (T-7)

Fig. 6 - Prototype PARB data for determining reciprocity

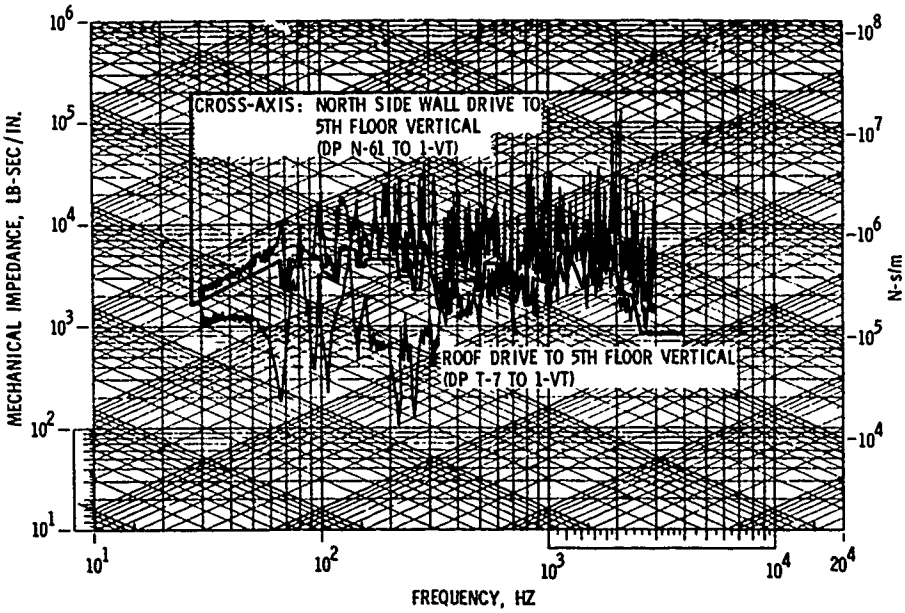

Fig. 7 - Model PARB cross-axis transfer impedances to 5th floor vertical response point: North wall hroizontal drive point compared with roof vertical drive point

2.4 Cross-Axis Coupling

Cross-axis coupling is the motion induced in a test article orthogonal to the direction of input force or motion. Fig. 7 overlays cross-axis coupling impedance on an axially aligned impedance measurement for the same accelerometer location. Accounting for cross-axis coupling was not required for response predictions on this building. The frequency magnitudes of the external blast loads were very small in the frequency range where cross coupling was a significant proportion of the regular impedance measurements. The root sum square for all four walls contributed less than 5% to vertical motion.

2.5 Symmetry

Where a test article or structure possesses geometric symmetry, or at least appears reasonably symmetric, only one-half or one-quarter of the structure (as the case may be) need be measured, thus shortening the testing. Decisions to use symmetric measurements should be made by impedance surveys. Where unsymmetric elements or components exist, either local measurements, substitution, or a strategy of redistribution of the measurement matrix can often be judiciously used. For both the model and prototype buildings, symmetry was employed about the longitudinal axis.

2.6 System Functions

Typical system functions of inertance magnitude ($\ddot{X}/F[\omega]$), phase, and impulse functions are given in Fig. 8 for the scale model and in Fig. 9 for the prototype. These nonparametric functions have been digitally processed into final form for use in response predictions of the structures.

For a few locations, response predictions require a large number of measurements taken over the structure's external surfaces. These predictions can also be used to predict responses at additional internal locations of the building by using transfer functions. The response prediction at the first location is multiplied by a transfer function to another location to obtain the response at the second location. Transfer functions are obtained by the complex ratio of the motion at a remote location to the motion at the drive-point location, as illustrated in Fig. 10. Transfer functions are represented as

$$\tau(\omega) = \left| \frac{\ddot{X}_{out}}{\ddot{X}_{in}} (\omega) \right| \exp(-j\phi\omega) \qquad (1)$$

Responses at other locations in the structure were calculated in accordance with the following equations:

$$\ddot{X}_i(\omega) = \ddot{X}_5(\omega)\, \tau_{i/5}(\omega) \qquad (2)$$

where

$\ddot{X}_i(\omega)$ = frequency response at location i

$\ddot{X}_5(\omega)$ = frequency response calculated for center of the 5th floor

$\tau_{i/5}(\omega)$ = transfer function location i to 5th floor

$$\ddot{x}_i(t) = \mathcal{F}^{-1}\left[\ddot{X}_i(\omega)\right] \qquad (3)$$

Measured transfer functions to the 4th, 3rd, and 2nd floors of both the model and prototype structures are presented in Figs. 11 and 12.

2.7 Scaling

Geometric scaling of the 1/12-scale model to the prototype is given by the following table.

TABLE 1
Geometric Scaling

Function	Prototype (p)		Model (m)
Stiffness	$\left(\frac{F}{\ddot{X}}\right)_p$	=	$12\left(\frac{F}{\ddot{X}}\right)_m$
Impedance	$\left(\frac{F}{\dot{X}}\right)_p$	=	$144\left(\frac{F}{\dot{X}}\right)_m$
Mass	$\left(\frac{F}{\ddot{X}}\right)_p$	=	$1728\left(\frac{F}{\ddot{X}}\right)_m$
Frequency	f_p	=	$\frac{1}{12} f_m$

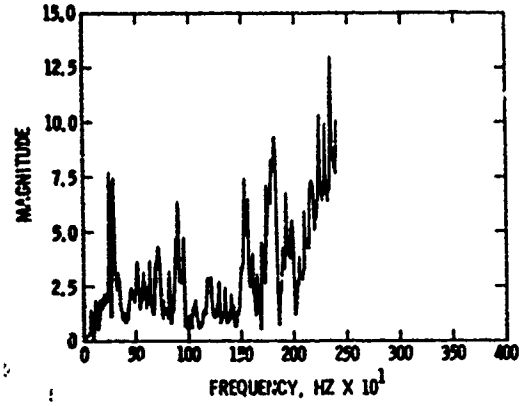

(a) Fourier magnitude: inertance

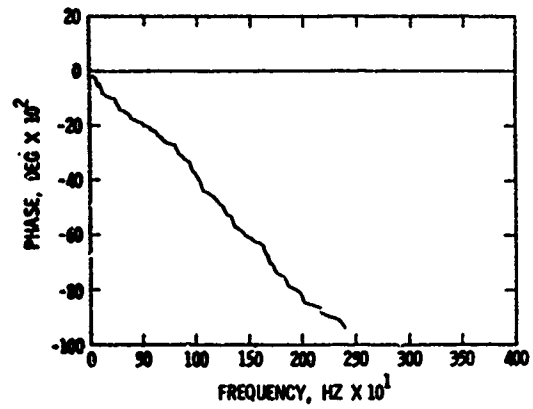

(b) Fourier phase: inertance

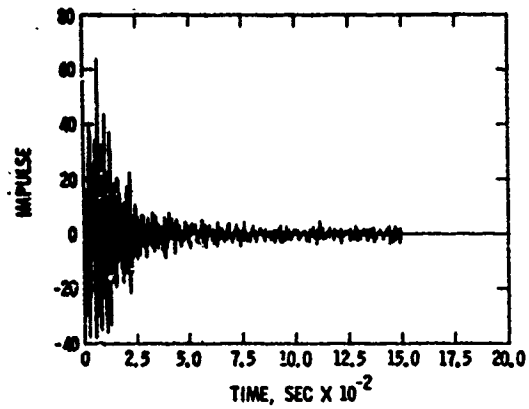

(c) Impulse: inertance

Fig. 8 - Typical model digitized measurement in final form for computations

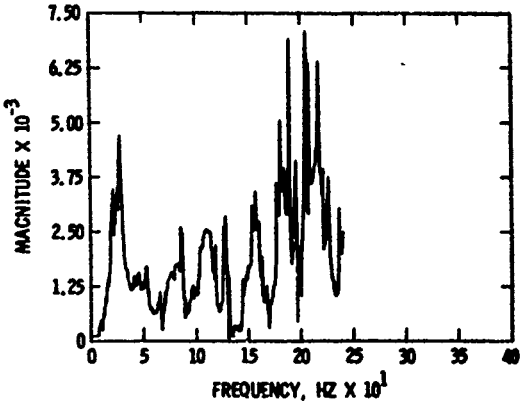

(a) Fourier magnitude

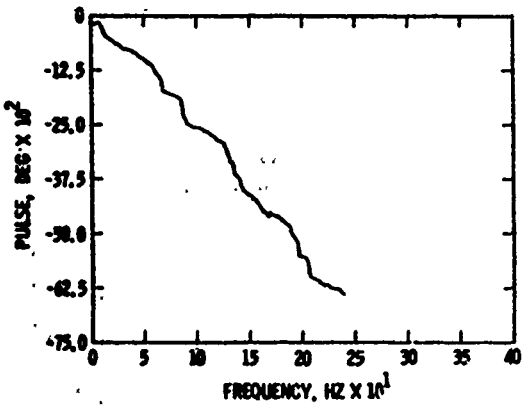

(b) Fourier phase

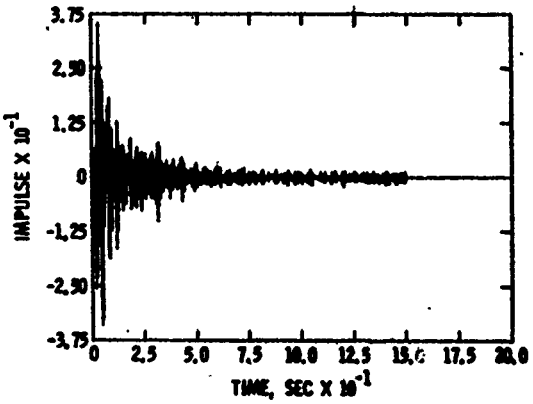

(c) Impulse

Fig. 9 - Typical prototype digitized measurement in final form for computations

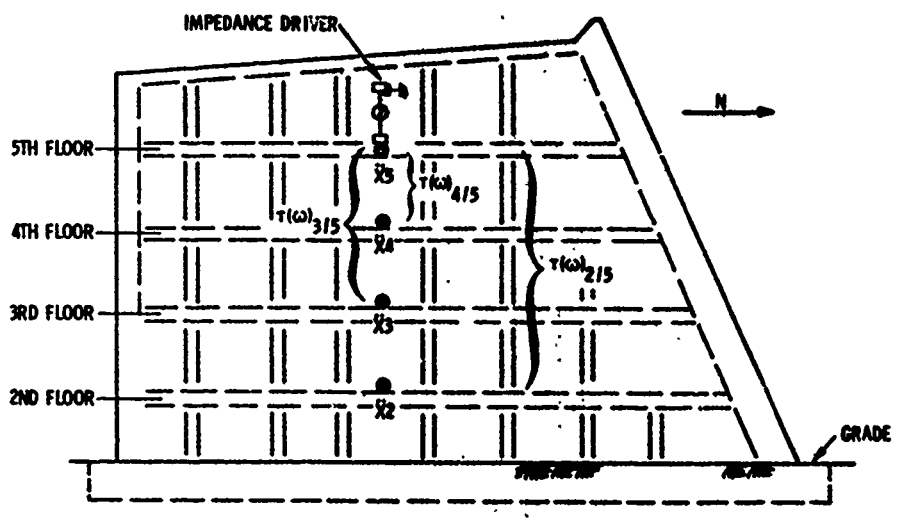

Fig. 10 - Method of measurement of transfer functions

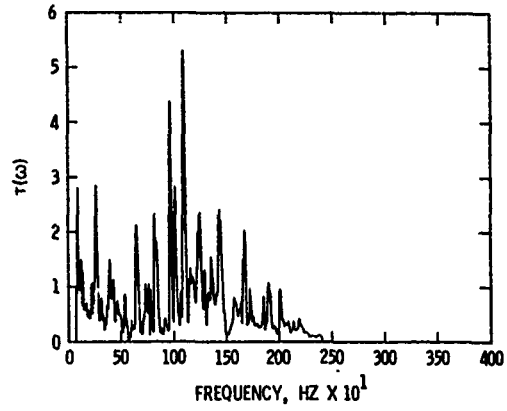

(a) 5th floor to 4th floor

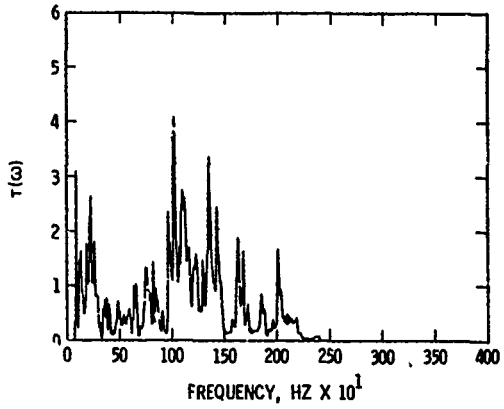

(b) 5th floor to 3rd floor

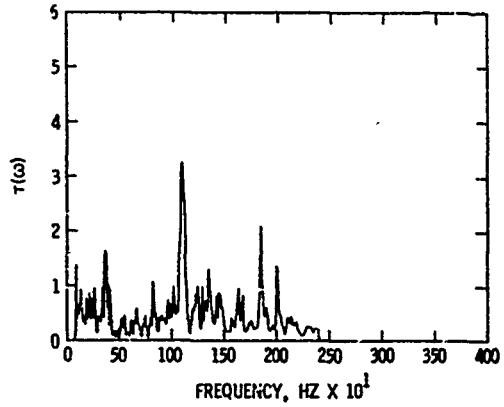

(c) 5th floor to 2nd floor

Fig. 11 - Model PARB: Transfer function magnitudes (acceleration ratio) for calculation of response prediction

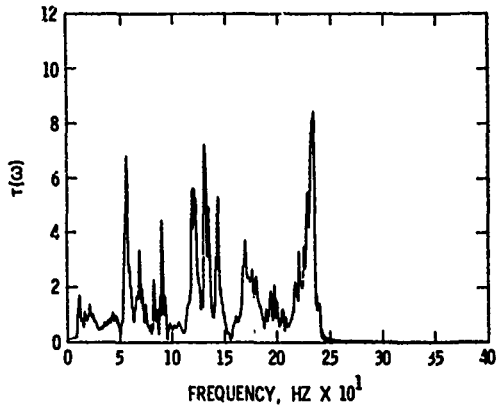

(a) 5th floor to 4th floor

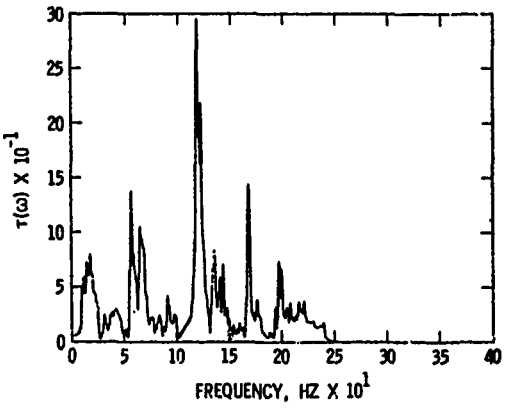

(b) 5th floor to 3rd floor

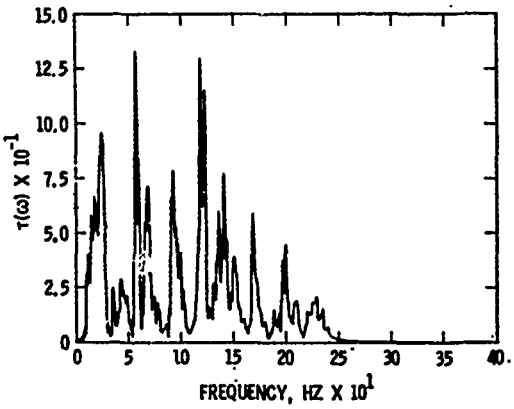

(c) 5th floor to 2nd floor

Fig. 12 - Prototype PARB: Transfer function magnitudes (acceleration ratio) for calculation of response prediction

A scaling comparison of both magnitude and frequency was made between representative and paired inertance measurements of the model and prototype buildings. These functions, such as those shown in Figs. 8 and 9, are compared for the 5th floor and similarly for each floor. Scaling parameters were determined by keying corresponding model and prototype functions at their peak amplitudes and then iteratively determining amplitude and frequency scale factors

TABLE 2
Scaling Factors, Model to Prototype, for Geometric and Inertance Measurement Scaling

Floor	Scale Factors				Difference (Reference Geometric)	
	Inertance		Geometric			
	Displacement Factor (a)	Frequency Factor (b)	Displacement Factor (λ)	Frequency Factor (λ)	Displacement (%)	Frequency (%)
5th	18.4	10.2	12	12	+53	-15
4th	10.5	12.7	12	12	-12	+6
3rd	25.3	14.0	12	12	+111	+17
2nd	34.5	9.7	12	12	+188	-19

for a minimum error difference. The scale factors determined by this procedure are given in Table 2 for each location.

3. PREDICTION OF STRUCTURE RESPONSE TO AIR BLAST

The method used to calculate the response accelerations of the 1/12-scale model and of the prototype Perimeter Acquisition Radar Building (PARB) is similar for both. Verification or checks on the accuracy of the response predictions is made by comparing the predictions with response records of the scale model taken during the DIAL PACK Event [7,8]. The DIAL PACK Event was a 500-ton (453,550 kg) TNT explosion that subjected air-blast and ground-shock loads to several targets. Calculations for both structures were made for the vertical direction only; and as such, the traveling air-blast pressure loading over the roof surface comprises the external forcing function. Exclusion of the cross-coupling contributions to structural motions from pressure loads on the external four walls is considered to have minimal effect on the calculated responses. As discussed in Section 2.4, the rapid roll-off of pressure amplitudes with frequency allowed for this reduction in computational effort.

All data and calculations are internally consistent and show comparable amplitudes for pressures, motions, yield, time, and frequency. However, the absolute values have been normalized so that this report could be declassified.

3.1 1/12-Scale Model

Response predictions use inertance functions, a pressure zone for each inertance function, air-blast pressure functions, pressure-area zone engulfment, traveling pressure-wave function, and transfer functions.

3.1.1 Inertance Functions and Associated Pressure-Area Zoning

The use of inertance measurements to predict the response of a structural system to blast loading is basically a special application of the impedance technique. An inertance test measures the point acceleration response of a structure due to a point force load. Blasts such as the air-pressure loads acting on the model PARB structure in the DIAL PACK Event are a continuous forcing function acting on a continuous structure. Thus, the sampled impedance information must be summed over the structure to obtain the internal point responses of the structure due to loads acting everywhere on the external surfaces of the structure.

Each inertance function must be associated with a specific area of the structure upon which the air-blast pressure acts. This assumes that the inertance function is essentially constant for this area. Finite-element plate models were initially used to map the model and to provide, thereby, preliminary measurement and drive-point locations. Additional refinement of drive-point locations was done during field testing, where quick-look analog impedance measurements verified that a reasonable density of measurement would be acquired for the model structure. The smooth change in functions obtained when moving from one area to the next indicated that a reasonable number of measurements had indeed been obtained. Potentially, interpolation of the measurements could have been made during computation, should the need have arisen. Additional measurements showed that the structure had a

high degree of symmetry (see Sec. 2.5), which therefore allowed for a higher density of measurement per surface area.

Boundaries for local areas of each acceptance measurement were drawn by observation and evaluation of the data. The impedance zone and input pressure zone associated with each of the 29 measurements are shown in Fig. 13.

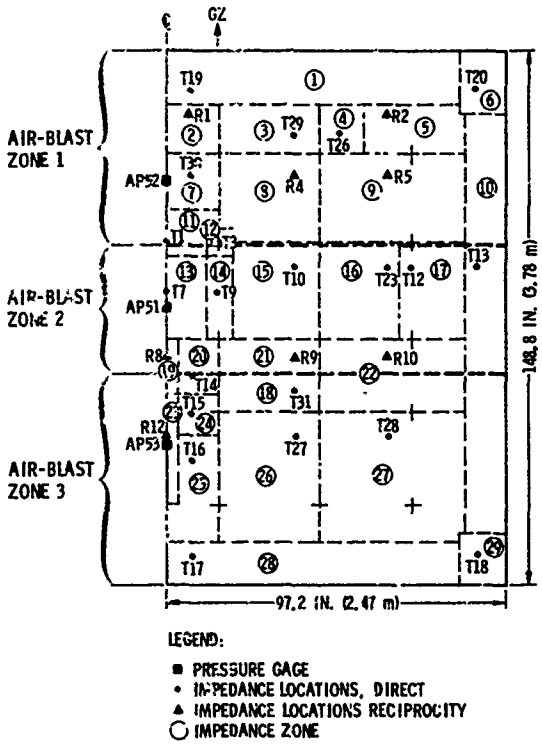

Fig. 13 - Zoned roof on PARB model showing impedance zones, air-blast zones, and impedance measurement drive locations

3.1.2 Pressure-Input Development

Only three air-blast measurements [7,8] on the roof were obtained from the DIAL PACK Event (Figs. 14,15). The aboveground structure perturbs the air-blast loading by overexpanding the transient air flow, which is particularly observable as the pressure notch in the time history of Fig. 14b and as the perturbation in the frequency spectrum of Fig. 15b. Hence, test data rather than conventional blast curves (Figs. 14d, 15d) were used as forcing functions.

The air-blast zones shown in Fig. 13 were configured on a simple geometric basis. The air-blast functions were considered to be constant within each air-blast zone. The potential for extrapolation and interpolation exists for this type of data.

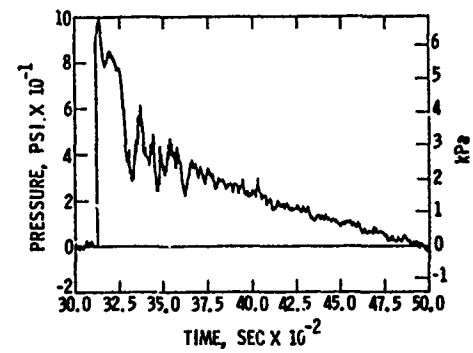

(a) Air-pressure gage AP51

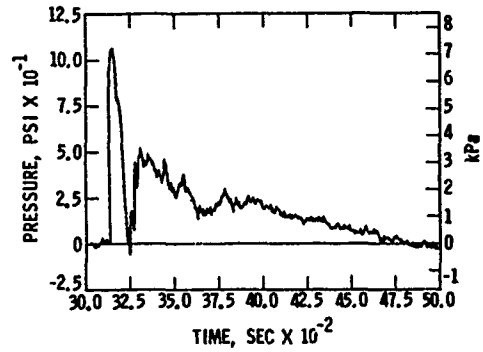

(b) Air-pressure gage AP52

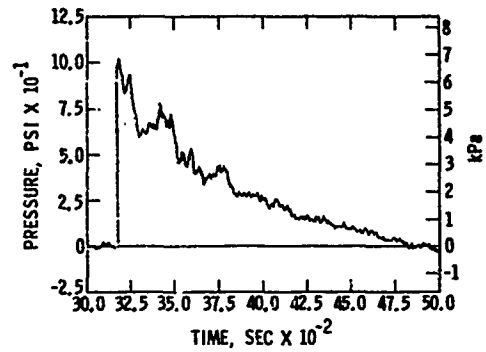

(c) Air-pressure gage AP53

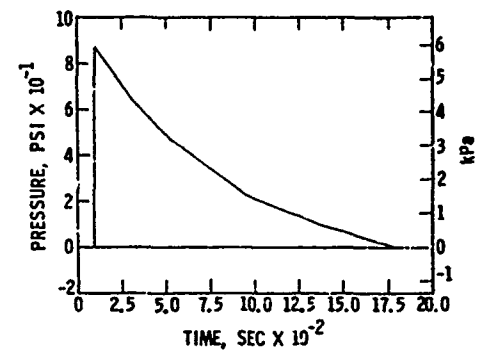

(d) Analytic (Brode)

Fig. 14 - Air-blast measurements on model PARB roof and conventional air-blast representation of pressure-time histories

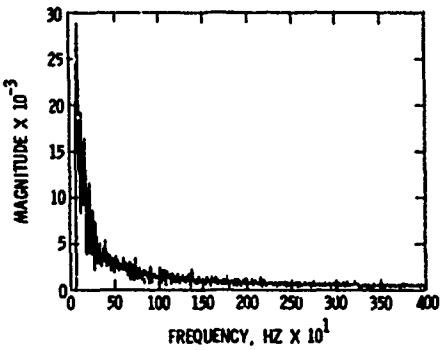

(a) Air-pressure gage AP51

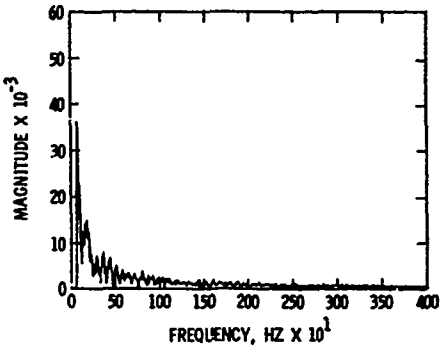

(b) Air-pressure gage AP52

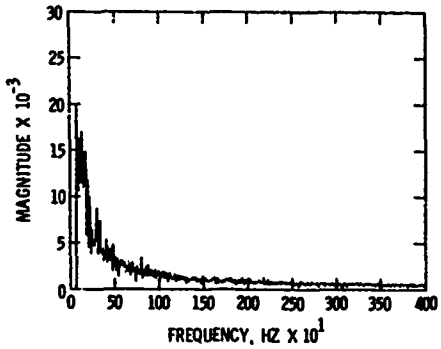

(c) Air-pressure gage AP53

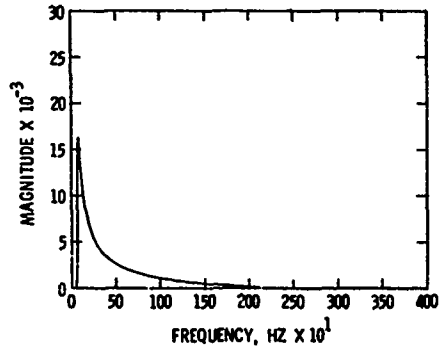

(d) Analytic (Brode)

Fig. 15 - Air-blast measurements on model PARB roof and conventional representation of Fourier magnitude pressure spectra

a. *Pressure Area Zones.* For a local surface area, A_{ik}, which is associated with one transfer inertance function, it is necessary to account for the velocity of the air load as it traverses the surface. This accounting, as illustrated in Fig. 16, is required to assure a proper surface loading.

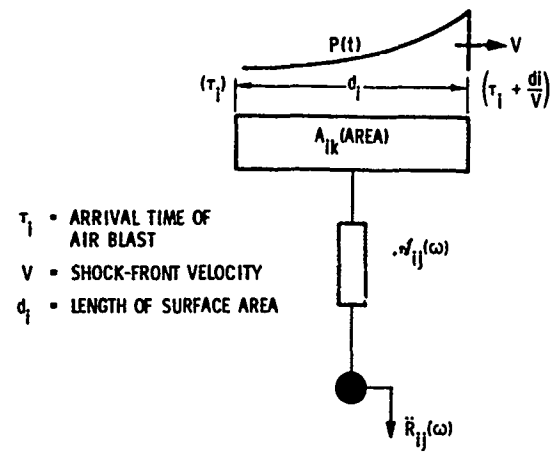

Fig. 16 - Moving air load over a local surface area associated with a transfer inertance function to an internal point in structure

Upon arrival of the air blast at time τ_i, the air blast successively loads the surface in increments ΔX where $n\Delta X = d_i$, the length. The incremental loading time is given by $\Delta t = \Delta X/V$. This incremental loading subdivides the local surface into segments $A_{ik}(\Delta X/d_i)$. The fineness of ΔX is obtained from the Δt selected and can be as small as the digitizing rate. Depiction of air-blast engulfment and the development of an effective pressure as seen by a local area is shown in Fig. 17.

A pressure-time history of frontal velocity V, which is successively translated and sectioned over the surface A_{ik} of length d_i equal to $n\Delta X$ increments is given by an effective pressure (P_{eff}):

$$P_{eff}(t) = \frac{1}{n}\left[P(t) + P\left(t - \frac{\Delta X}{V}\right)u\left(t - \frac{\Delta X}{V}\right) + P\left(t - \frac{2\Delta X}{V}\right)u\left(t - \frac{2\Delta X}{V}\right) \ldots P\left(t - \frac{(n-1)\Delta X}{V}\right)u\left(t - \frac{(n-1)\Delta X}{V}\right)\right] \quad (4)$$

and transformation in the frequency domain gives:

$$P_{eff}(\omega) = \frac{P(\omega)}{n}\left[1 + \exp\left(-j\frac{\Delta X}{V}\omega\right) + \exp\left(-j\frac{2\Delta X}{V}\omega\right) + \exp\left(-j\frac{3\Delta X}{V}\omega\right)\ldots + \exp\left(-j\frac{(n-1)\Delta X}{V}\omega\right)\right] \quad (5)$$

and the expression of Eq. 5 converges to:

$$P_{eff}(\omega) = P(\omega)\left[\frac{\sin\left(\frac{n\Delta X}{2V}\right)\omega}{n\sin\left(\frac{\Delta X}{2V}\right)\omega}\right]\exp\left(-j\frac{(n-1)\Delta X}{2V}\omega\right) \quad (6)$$

For small angles ($\theta \approx \sin\theta$) the engulfing function of Eq. 6 may be represented by:

$$\frac{\sin\left(\frac{n\Delta X}{2V}\right)\omega}{n\sin\left(\frac{\Delta X}{2V}\right)\omega} \approx \frac{\sin\left(\frac{n\Delta X}{2V}\right)\omega}{n\left(\frac{\Delta X}{2V}\right)\omega} \quad (7)$$

which is the $S_i(X)$ function in the frequency domain, such as represented in Fig. 18a, and an approximate boxcar function in the time domain. The cyclic nature of the actual engulfing function (Eq. 6) is illustrated in Fig. 18b and implies a critical selection of a time step Δt (dependent on mesh length/wave velocity) for the frequency limit involved. Somewhat akin to the Nyquist folding frequency, the engulfing function as shown in Fig. 18a has a time step Δt (dependent on mesh length/velocity) and a frequency cutoff $1/2\ \Delta t$ (0.1 msec) for 5 kHz. These values are more than sufficient for the model inertance function, where measurements were made to 3 kHz. Obviously, serious effects are encountered when too large a time step (mesh length/velocity) is taken in using a traveling wave, since the results will ultimately include the effects of the function as shown in Fig. 18b, where frequency amplitudes above cutoff are contained in the data or computations. Not too obvious in the engulfing functions is the maximum amplitude in the frequency function of unity and the area of the approximate boxcar function in the time domain of unity. Fig. 19 provides, for a traveling load over a surface, the maximum mesh length at the folding frequency for a range of traversing velocities.

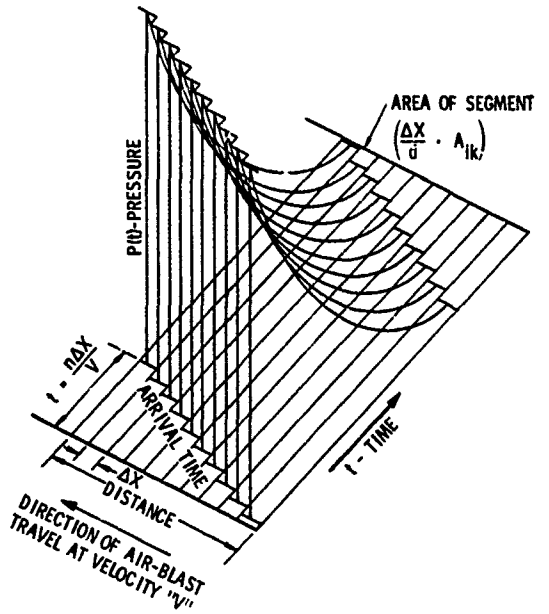

(a) Three-dimensional view of air-blast engulfment

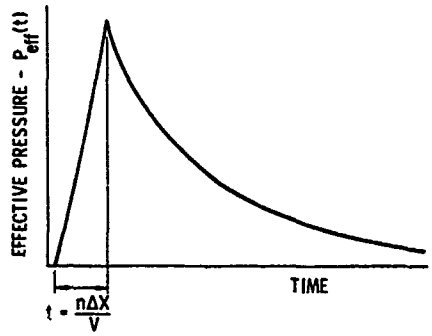

(b) Profile of effective pressure over a local area

Fig. 17 - Depiction of air-blast engulfment and development of effective pressure over a local area (exaggerated scale)

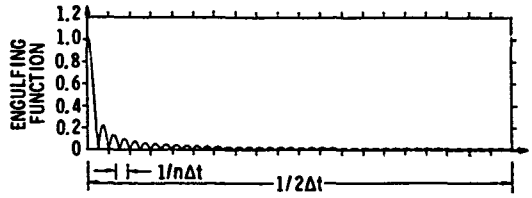

(a) Properly selected time step

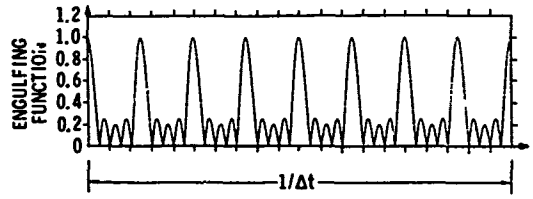

(b) Improperly selected time step

Fig. 18 - Plot of magnitude of engulfing function for two different time steps
Δt = (mesh length/blast velocity)

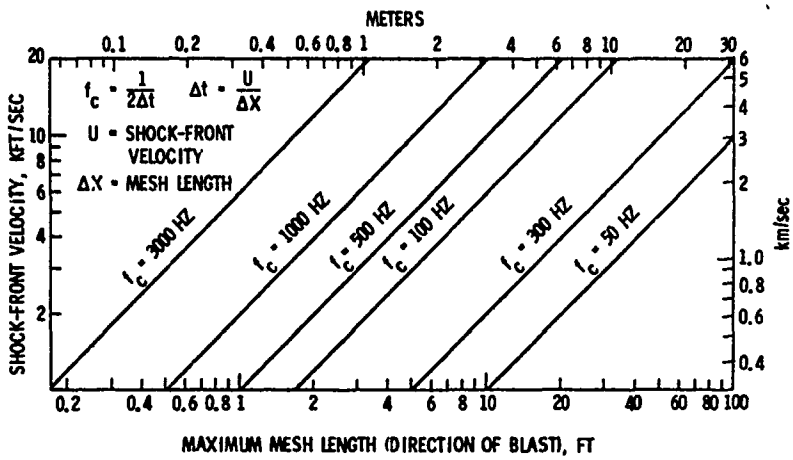

Fig. 19 - Traveling air-blast loading on surface; maximum mesh length in blast direction at folding frequency (f_c) for range of shock-front velocities

b. *Traveling Wave over a Surface.* Somewhat similar to the engulfing function for local areas (mesh size) is the wave travel over the entire structure. In this case, the travel distance or time increment is from the boundary of one local area to the next. Where the boundary distances are equal and the blast velocity constant, the traveling wave function would be:

$$\left[\frac{\sin\left(\frac{N\Delta t}{2}\right)\omega}{\sin\left(\frac{\Delta t}{2}\right)\omega}\right] \exp\left(-j\frac{(N-1)\Delta t}{2}\omega\right) \qquad (8)$$

where

N = number of equal local areas on roof

Δt = traverse time across local area

As before, for small angles $\theta \approx \sin\theta$, and the function of Eq. 5 becomes:

$$\left[\frac{\sin\left(\frac{N\Delta t}{2}\right)\omega}{\left(\frac{\Delta t}{2}\right)\omega}\right] \exp\left(-j\frac{(N-1)\Delta t}{2}\omega\right) \qquad (9)$$

The traveling wave for the roof is a summation having a maximum amplitude in the frequency domain of $N\Delta t$ (the total traverse time of the wave over the roof). The amplitude of the approximate boxcar function is unity and has an area of $N\Delta t$ in the time domain.

The local areas of the roof are not equal, and the foregoing discussion is useful only in understanding the characteristics of the function. The unequalness of the local roof areas requires that the function of Eq. 5 be placed in the form

$$\left[1 + \exp(-j\tau_1\omega) + \exp(-j\tau_2\omega) + \exp(-j\tau_3\omega) + \ldots \exp(-j\tau_{N-1}\omega)\right] \qquad (10)$$

where τ_i = time of arrival at each local area boundary.

3.1.3 Response Prediction at First Location

Response calculations were made in the vertical direction from roof loads of a traveling air blast for the center of the 5th floor of the, 1/12-scale model. The method of calculation is given as:

$$\text{Response} = \begin{pmatrix}\text{Local}\\ \text{Inertance}\end{pmatrix} \begin{pmatrix}\text{Local}\\ \text{Area}\end{pmatrix} \times \begin{pmatrix}\text{Local}\\ \text{Pressure}\end{pmatrix} \times \begin{pmatrix}\text{Local}\\ \text{Engulfment}\\ \text{Function}\end{pmatrix} \begin{pmatrix}\text{Traveling}\\ \text{Wave}\\ \text{Function}\end{pmatrix}$$

Computations were performed in the frequency domain as represented by Eq. 11 and transformed to the time domain by Eq. 12.

$$\ddot{X}(\omega) = \sum_{i=0}^{N} \mathcal{A}_i(\omega) \left[A_i \cdot P_i(\omega) \cdot Si_i(\omega) \right] \exp(-j\tau_i\omega) \tag{11}$$

where

$\mathcal{A}_i(\omega)$ = i-th inertance function $[\ddot{X}/F_i(\omega)]$

A_i = i-th local area (mesh) of external load

$P_i(\omega)$ = i-th external pressure load

$Si_i(\omega)$ = i-th local engulfment function

$$\left[\frac{\sin\left(\frac{n\Delta t\omega}{2}\right)}{n \sin\left(\frac{\Delta t\omega}{2}\right)} \right]$$

$\exp(-j\tau_i\omega)$ = traveling wave function

$$\left[1 + \exp(-j\tau_1\omega) + \exp(-j\tau_2\omega) \ldots \right]$$

τ_i = arrival time of blast wave at local area boundary

Then

$$\ddot{x}(t) = \mathcal{F}^{-1}\left[\ddot{X}(\omega)\right] \tag{12}$$

3.1.4 Response Predictions at Other Locations

Response predictions at additional internal locations (i.e., locations in addition to the "first") of the building are facilitated by use of transfer functions. The response prediction at the first location on the 5th floor is multiplied by a transfer function to another location to obtain the response at the second location, as discussed in Section 2.6.

3.2 Prototype PARB

Predicting the response of the prototype PARB follows the same procedure as that used for the model. Each variable will be discussed, and differences in procedure will be emphasized.

Selection of local impedance zones and pressure areas for each inertance function followed the methods used for the model. The zones for the 36 impedance measurements selected are shown in Fig. 20. Impedance measurements A-1 and A-29 were used on the basis of symmetry in two other locations (Fig. 20), since poor data records were obtained in Zones 34 and 36.

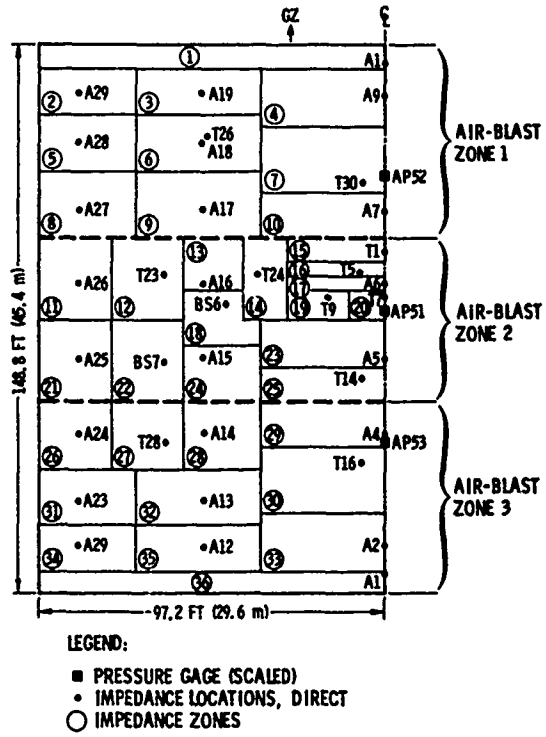

Fig. 20 - Zoned roof of PARB prototype showing impedance zones, air-blast zones, and impedance measurement drive points (direct and reciprocity)

3.2.1 Pressure Input Development

Pressure-time histories from the DIAL PACK Event were scaled geometrically for computations on the prototype PARB. Pressures for both model and prototype are identical but scaling of characteristic time is required.

$$P_p(t) = P_m\left(\frac{t}{\lambda}\right)$$

$$P_p(\omega) = \lambda P_m(\lambda\omega) \tag{13}$$

Effects on waveforms of the DIAL PACK pressure records by scaling (Reynolds number, $\rho VL/\mu$) to the prototype were evaluated to determine whether serious errors would result. Information on transient blast waves interacting with structures is quite limited. Some information having applicability to the PARB configuration has been found and evaluated for scale-factor effects. These data are from shock tubes, water tables, and nose cones.

3.2.2 Air-Blast-Wave Engulfment

a. *Pressure Area Zones.* The engulfing function developed for the model (Eq. 7) was applied also for the local pressure areas (impedance zones) of the prototype. The only change required was a coarser mesh, owing to the lower cutoff frequency of 300 Hz (Fig. 19).

b. *Traveling Wave over a Surface.* The traveling wave function, Eq. 10, used for the model was applied to the prototype.

3.2.3 Response Predictions at First Location

Response predictions for the prototype were made with Eqs. 11 and 12 in a manner similar to that used for the model.

3.2.4 Response Predictions for Other Locations

Response predictions for the prototype at other locations were made in a manner similar to that used for the model.

3.3 Development of Scaling Relationships

Scaling relationships for the 1/12-scale model calculations and DIAL PACK Event records of the model PARB are developed in this section. These scaling relationships provide for both geometric scaling and scaling based on comparison of inertance functions from the model and the prototype from Table 2.

3.3.1 Geometric Scaling

a. *Areas.* Surface area of the air blast for the model scaled to the prototype is

$$A_p = \lambda^2 A_m \tag{14}$$

where

A = area (sq ft)

p = prototype

m = model

λ = scale factor (12)

b. *Air Blast.* The air-blast pressures from DIAL PACK are scaled for the prototype where pressure amplitudes for model and prototype are equivalent, but the time duration is scaled by $\lambda = 12$.

$$P_p(t) = P_m\left(\frac{t}{\lambda}\right)$$

$$P_p(\omega) = \lambda\, P_m(\lambda\omega) \tag{15}$$

c. *Inertance Functions.* Inertance functions are scaled as given in Table 1.

$$\mathcal{A}_p(\omega) = \frac{1}{\lambda^3}\,\mathcal{A}_m(\lambda\omega) \tag{16}$$

d. *Geometrically Scaled Response.*

$$\ddot{X}_p(\omega) = \sum_{i=0}^{N}\left\{\frac{1}{\lambda^3}\,\mathcal{A}_i(\lambda\omega)\left[\lambda^2 A_i \cdot \lambda P_i(\lambda\omega) \cdot Si_i(\lambda\omega)\right]\exp(-j\tau_i\lambda\omega)\right\}_m \tag{17}$$

$$\ddot{X}_p(\omega) = \ddot{X}_m(\lambda\omega) \tag{18}$$

$$\ddot{x}_p(t) = \frac{1}{\lambda}\,\ddot{x}_m\left(\frac{t}{\lambda}\right) \tag{19}$$

where

p = prototype

m = model

λ = scale factor

$\mathscr{A}_i(\lambda\omega)$ = i-th impedance function $[\ddot{X}/F_i(\omega)]$

A_i = i-th local area of external load

$P_i(\lambda\omega)$ = i-th static external pressure load

$Si_i(\lambda\omega)$ = i-th local engulfment function

$$\left[\frac{\sin\left(\frac{n\Delta t\lambda\omega}{2}\right)}{n\sin\left(\frac{\Delta t\lambda\omega}{2}\right)}\right]$$

$\exp(-j\tau_i\lambda\omega)$ = traveling wave function $[1 + \exp(-j\Delta t\lambda\omega) + \exp(-2j\Delta t\omega)\ldots]$

τ_i = arrival time of blast wave at local area boundary

3.3.2 Scaling by Use of Measured Inertance Functions

a. *Scaling of Areas, Pressures, and Wave Engulfment.* Scaling of areas, pressures, and wave engulfment are geometric, as presented in Section 3.1.

b. *Inertance Function Scaling.* Several not-to-scale conditions existed between the prototype and model PARBs. These conditions cannot really be quantitatively established, although discussion and identification of each is given in Section 4. A scaling comparison in both magnitude and frequency was made as discussed in Section 2.7. The scale factors determined by this procedure are presented in Tables 2 and 3 for each location.

c. *Measured Impedance Scaling (not-to-scale effects).*

$$\ddot{X}_p(\omega) = \sum_{i=0}^{N}\left\{\frac{1}{ab^2}\mathscr{A}_i(b\omega)\left[\lambda^2 A_i \cdot \lambda P_i(\lambda\omega) \cdot Si_i(\lambda\omega)\right]\exp(-j\tau_i\lambda\omega)\right\}_m \quad (20)$$

$$\ddot{X}_p(\omega) = \frac{\lambda^3}{ab^2}\ddot{X}_m(b\omega) \quad (21)$$

$$\ddot{x}_p(t) = \frac{\lambda^3}{ab^3}\ddot{x}_m\left(\frac{t}{b}\right) \quad (22)$$

3.4 Prototype Responses Compared with Responses Scaled from Model

Acceleration response motions from DIAL PACK records and model calculations are scaled to the prototype calculations and presented in Figs. 21 through 28. Scaling was made by inertance function ratios.

TABLE 3
Acceleration Response Scaling, Model to Prototype, of Geometric and Inertance Measurement Scale Factors

Floor	Acceleration Response Scaling				Difference (Reference Geometric)	
	Inertance		Geometric			
	Fourier Magnitude (λ^3/ab^2)	Time History and Shock Spectra (λ^3/ab^2)	Fourier Magnitude	Time History and Shock Spectra ($1/\lambda$)	Fourier Magnitude (%)	Time History and Shock Spectra (%)
5th	$\frac{1}{1.11}$	$\frac{1}{11.3}$	1	$\frac{1}{12}$	+10	-6
4th	$\frac{1}{0.98}$	$\frac{1}{12.4}$	1	$\frac{1}{12}$	-2	+3.3
3rd	$\frac{1}{2.87}$	$\frac{1}{40}$	1	$\frac{1}{12}$	+65	+70
2nd	$\frac{1}{1.88}$	$\frac{1}{18.2}$	1	$\frac{1}{12}$	+47	+34

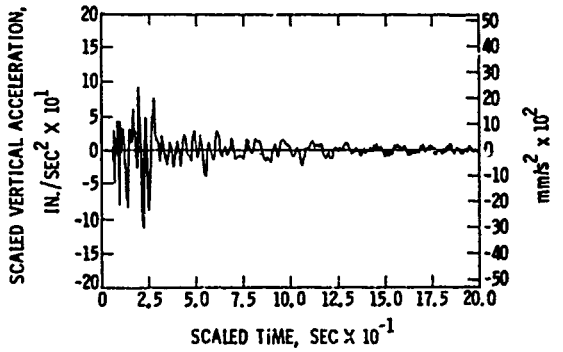

(a) DIAL PACK model response

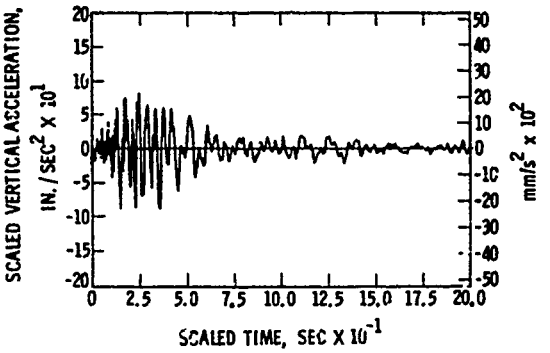

(b) Predicted model response

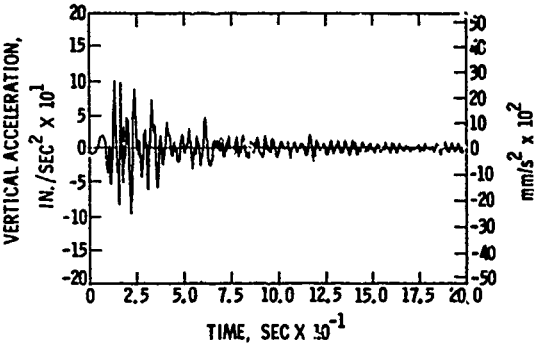

(c) Predicted prototype response

Fig. 21 - Comparison of prototype and scaled model PARB acceleration-time histories: 5th floor center

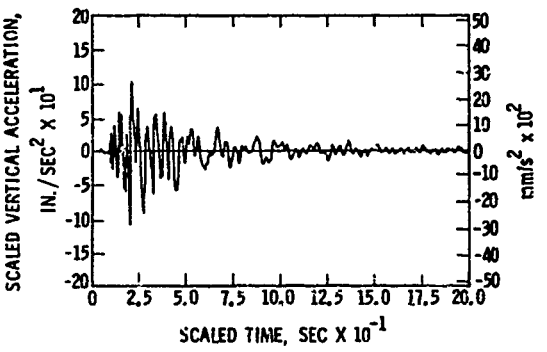

(a) DIAL PACK model response

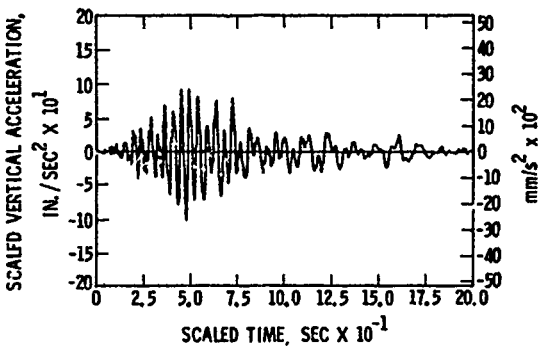

(b) Predicted model response

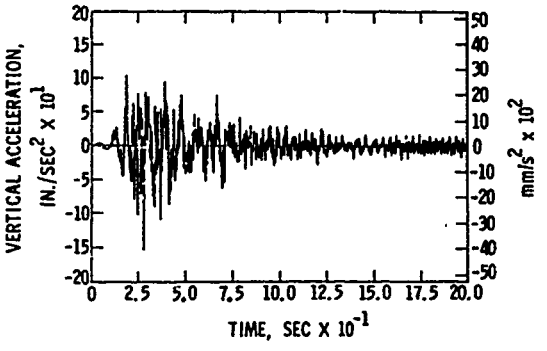

(c) Predicted prototype response

Fig. 22 - Comparison of prototype and scaled model PARB acceleration-time histories: 4th floor center

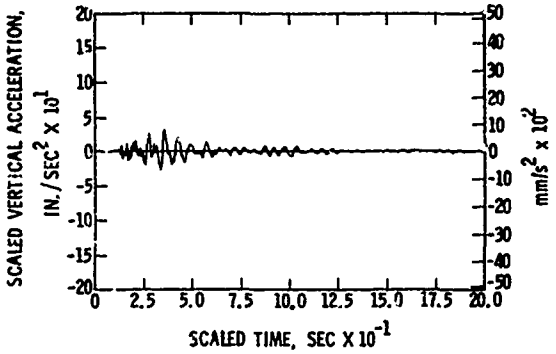

(a) DIAL PACK model response

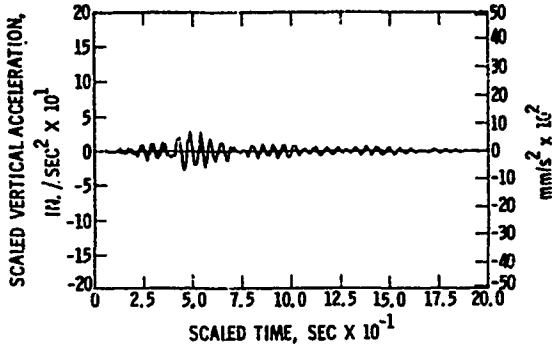

(b) Predicted model response

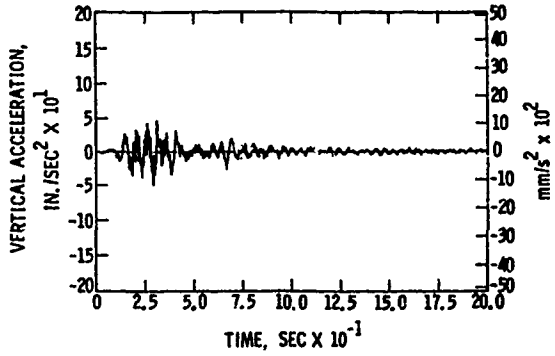

(c) Predicted prototype response

Fig. 23 - Comparison of prototype and scaled model PARB acceleration-time histories: 3rd floor center

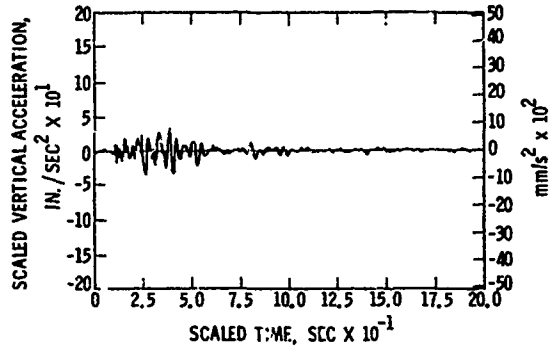

(a) DIAL PACK model response

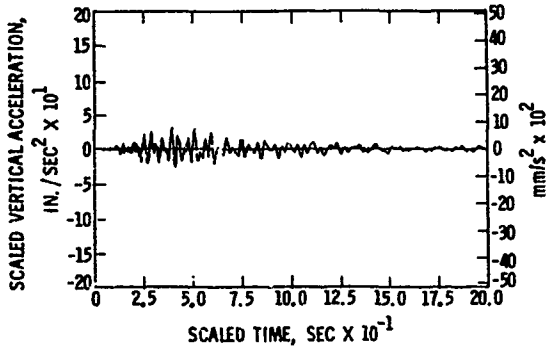

(b) Predicted model response

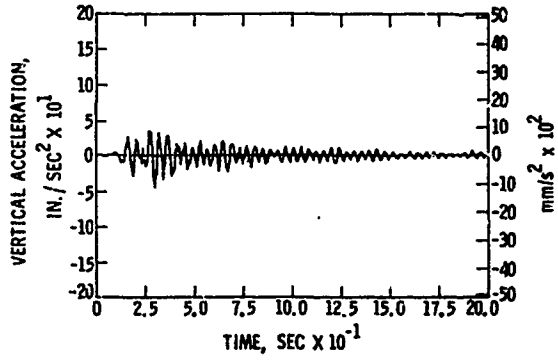

(c) Predicted prototype response

Fig. 24 - Comparison of prototype and scaled model PARB acceleration-time histories: 2nd floor center

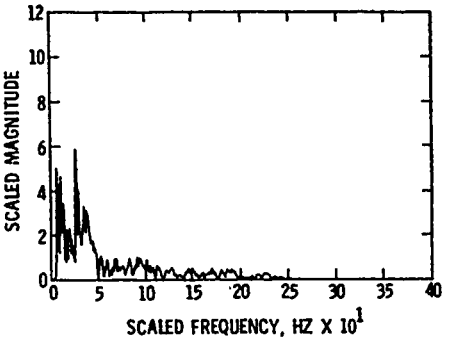

(a) Scaled DIAL PACK model response

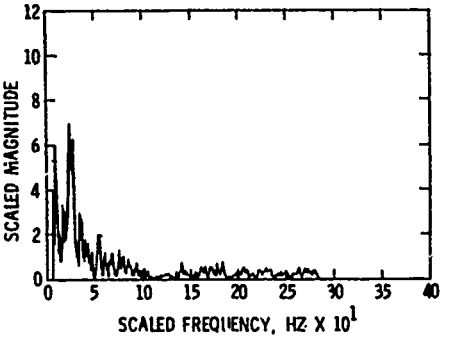

(b) Scaled predicted model response

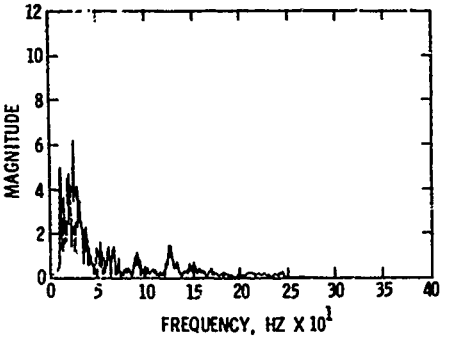

(c) Predicted prototype response

Fig. 25 - Comparison of prototype and scaled model Fourier magnitudes of acceleration: 5th floor center

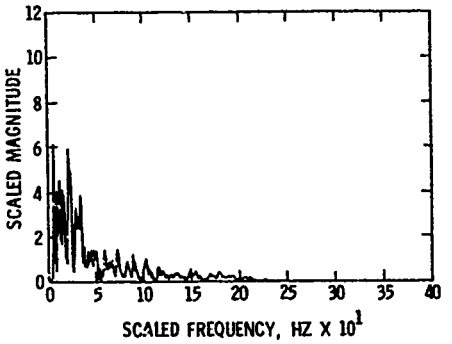

(a) Scaled DIAL PACK model response

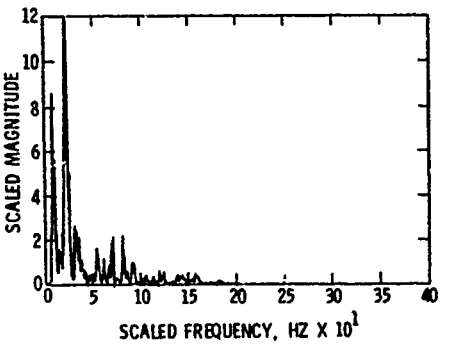

(b) Scaled predicted model response

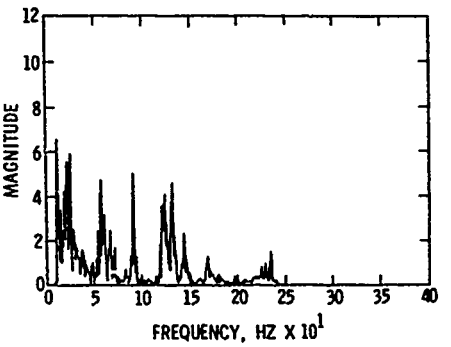

(c) Predicted prototype response

Fig. 26 - Comparison of prototype and scaled model Fourier magnitudes of acceleration: 4th floor center

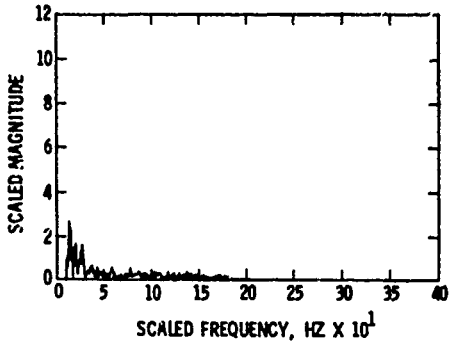

(a) Scaled DIAL PACK model response

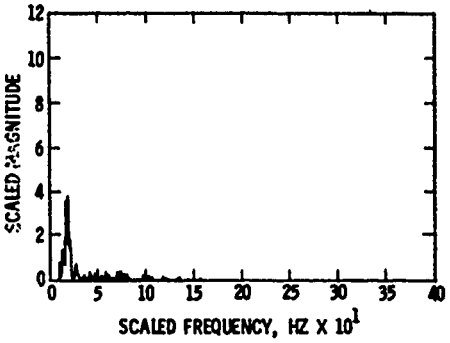

(b) Scaled predicted model response

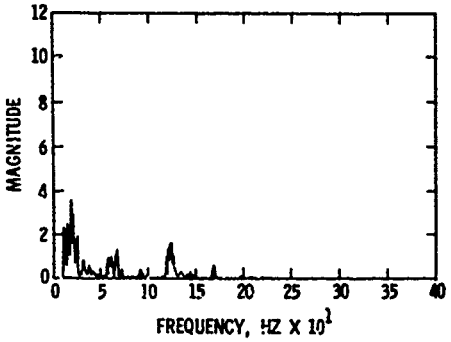

(c) Predicted prototype response

Fig. 27 - Comparison of prototype and scaled model Fourier magnitudes of acceleration: 3rd floor center

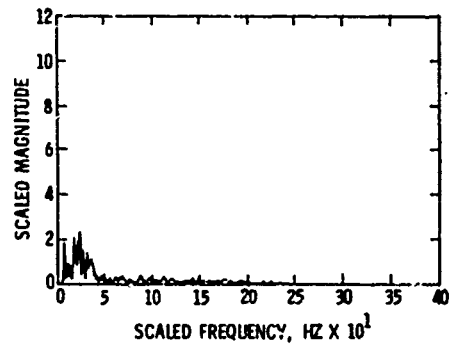

(a) Scaled DIAL PACK model response

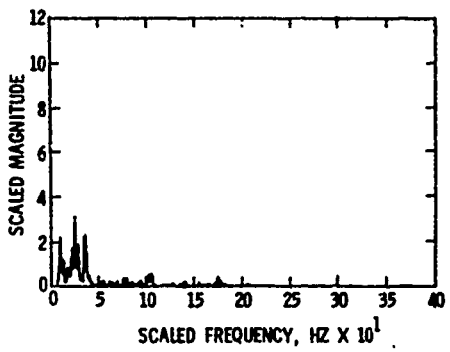

(b) Scaled predictod model response

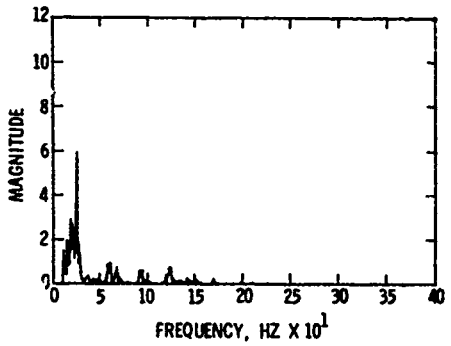

(c) Predicted prototype response

Fig. 28 - Comparison of prototype and scaled model Fourier magnitudes of acceleration: 2nd floor center

4. RESULTS AND CONCLUSIONS

Overall similarity of scaled DIAL PACK test records and model calculations to prototype calculations is quite good for acceleration-time histories and Fourier magnitude frequency spectra.

Deviations noted in the calculated rise and fall times for time histories involve both data measurements and subsequent processing. Some improvements in technique were applied to the prototype calculations. Differences observable in the Fourier transforms, particularly in the 4th and 3rd floors, are attributable to not-to-scale effects in the prototype and to measurement processing techniques for floor-to-floor transfer functions.

Scaling the model data geometrically did not provide a good fit. Several not-to-scale effects existed in the prototype that had not been or could not be accounted for in the model. These effects included the following:

a. *Structure.*

Prototype roof--radar base slab

Prototype--2nd floor mezzanine

Prototype--utility tunnel

Model--excessively large base slab

b. *Equipment in Prototype Structure.*

Tactical support equipment on shock-isolated platforms, 2nd floor 365,000-lb (165,000 kg) sprung weight of 22 platforms, and 3rd floor 203,000-lb (92,000 kg) sprung weight of 4 platforms

SAFCA communication equipment on shock-isolated platforms, 3rd floor 86,126-lb (39,100 kg) sprung weight of 3 platforms

Weapons systems equipment hard mounted on 3rd floor

The radar base slab on the prototype roof stiffens the area covered and adds weight. The 2nd floor mezzanine, the utility tunnel of the prototype, and the extra large base slab in the model contribute to the scaling problem. Equipment installed in the prototype, particularly on the 2nd and 3rd floors, has a decided effect in altering the floor frequency responses. The weapon system equipment hard mounted to the 3rd floor is massive and, in the case of the precise power units, acts as a stiffener. (These power units cover approximately one-third of the 3rd floor area.) The numerous shock-isolated platforms are dynamically responsive over a wide frequency band and dynamically interact with the floors to alter floor responses substantially.

Scaling of damping as viscous equivalent did not appear to be the most appropriate form. Further work and investigation need to be undertaken to scale for material damping.

The following conclusions are drawn from the work discussed in this paper:

- The use of impedance testing is a useful technique for predicting structural response and to verify finite element model calculations.
- Existing vibration and measurement equipment is capable of vibrating and measuring the response of the largest structures, e.g., dams and massive protective structures.
- Computer technology has advanced to such a level that it is possible to process impedance measurement data and associated input loads in large quantities.
- The test technique and experimental application briefly outlined in this paper provide a basis for the continued improvement of impedance technology. Several improvements have been identified to reduce test time, to increase accuracy, to reduce noise, and to simplify data processing.
- Scaled impedance measurements from a model structure may be used in response predictions over a wide frequency range and for a range of input loads. From these response predictions, shock and vibration criteria scaled up from the model may be established for internally mounted equipment prior to construction of prototype structures.
- Air-blast loads should be determined for each structure by analytic/computer methods or experimentally from scaled models in blast simulation. Air-blast sensitivity studies strongly suggest that simplistic air loads on protective structures are insufficient to provide threat criteria for weapons systems equipment.
- Mesh dimensions (loaded surfaces) of protective structures must be carefully sized with respect to air-blast front velocity.
- Mode shapes, resonant frequencies, and damping may be extracted from impedance

measurements. Significantly higher damping values have been extracted from the PARB structure than are normally used in finite element models.

5. ACKNOWLEDGMENTS

Prediction projects based on impedance measurements for large aboveground structures were initiated by Mr. John Lewis, Chief, Strategic Structures Division (SPSS), Defense Nuclear Agency, and continued by his successor, Dr. Eugene Sevin.

Professor Robert Plunkett, University of Minnesota, served as consultant during the development and evaluation of techniques for this study. Optimization investigations were made in consultation with Professors George A. Beckey and S.F. Masri, University of Southern California. Transient air-blast scaling analysis was provided by Dr. Arthur R. Maddox, Naval Weapons Center, China Lake, California.

REFERENCES

1. R.C. Rountree and F.B. Safford, "Methodology and Standardization for Fragility Evaluation," *Shock and Vibration Bulletin No. 41.* Washington, DC: Naval Research Lab. Dec 1970.

2. F.B. Safford and R.J. Tuttle, "Transient Shock Fragility and Hardness Assessment of Commercial Communications Equipment," Paper No. 740801. *Nat'l Aerospace Eng. and Manufacturing Meeting, Soc. of Automotive Engineers, San Diego, CA, Sep 30, 1974.*

3. J.C. Calkins and A.G. Piersol, "Simulation of the Sparrow Flight Vibration Environment," Paper No. 730939, *Nat'l Aerospace Eng. and Manufacturing Meeting, Soc. of Automotive Engineers, Los Angeles, CA, Oct 16, 1973.*

4. D.B. Meeker and A.G. Piersol, "Accelerated Reliability Testing Under Vibroacoustic Environments," Paper presented at the Annual Meeting, Amer. Soc. of Mech. Engineers, New York City, NY, Dec 1974.

5. T.E. Kennedy and F.B. Safford, "The Use of Vibration/Impedance Measurements to Predict Blast-Induced Structural Vibrations," *Proc. 4th Int. Symp. on Military Applications of Blast Simulation, Atomic Weapons Res. Estb. Foulness, Southend-on-Sea, England, Sep 1974.*

6. F.B. Safford and R.E. Walker, *Prediction of Model and Prototype PARB Structure Responses Using Impedance Analysis Techniques,* R-7240-4036. El Segundo, CA: Agbabian Assoc. and Vicksburg, MS: Army Eng. Waterways Exp. Station, Dec 1975.

7. T.E. Kennedy, *Dynamic Response of Small Shear Wall Structures, Project LN316 Event DIAL PACK,* (U), TR-N-72-8. Vicksburg, MS: Army Eng. Waterways Exp. Station, Jan 1972. (AD 528 460L) (SECRET)

8. J.A. Malthan, *Safeguard Ground Facilities Special Engineering Studies: Task 4--Data and Correlation Analysis for Structural Response Measurements, Event DIAL PACK,* R-7124-4-2484. El Segundo, CA: Agbabian Assoc., Jan 1973. (AD 910 209L)

9. F.B. Safford, "Response Predictions and Induced Motion Simulation from Measured and Scaled System Functions," Short Course on Impedance and Dynamic Analysis of Structures, the Pennsylvania State University, Univ. Park, PA, Aug 15-19, 1977.

PROBABILISTIC FAILURE ANALYSIS OF LINED TUNNELS IN ROCK

David A. Evensen, Jon D. Collins
J. H. Wiggins Company
Redondo Beach, California

A study was performed to develop a methodology for planning of nuclear underground tests such that the negative impact of the uncertainty in the free-field weapons effects and the structure capabilities would be minimized. A probabilistic procedure was developed using a deterministic structural model as a basis to obtain the fragility curves of the structures. The paper discusses how to guide the design of the structures to maximize the acquisition of good data, and the methodology could be directly applicable to future nuclear tests.

INTRODUCTION

Two serious problems with any single shot nuclear test are (1) that of scaling the predicted environment incorrectly or (2) improperly estimating the capability of the structure that is to be tested. It is not unusual to have situations where no useful data were obtained because the environment was too high. Therefore, it is desirable to design tests such that the probability of obtaining useful data is maximized. In the case of many such tests, survival of the structure through the tests is not necessarily the objective, but rather the determination of the environmental level that causes the structure to fail. Therefore, it is advantageous for tests to be designed such that the structure will have approximately a 50% chance of failing at the design range from the explosion source.

There are some significant uncertainties involved in the test design. The blast source will have an uncertainty in its yield. The shock wave from the blast through the surrounding media also will have considerable uncertainty. Data presented in the Air Force Manual for Design and Analysis of Hardened Structures (Reference 5) indicate that with a known yield there will be an uncertainty factor of ✕ 2.5 for the particle velocity in hard rock. If the media is soft rock or dry soil, the uncertainty is even greater.

The other significant uncertainty is the capability of the test structure to withstand the load. Prediction of the precise failure level is not possible because of the difficulty in predicting the post-yield behavior and the structure-media interaction. Consequently, it would not be unusual to predict an uncertainty factor in the structural capability as large as 1.5. A structural capability uncertainty model can be developed using the basic mathematical model utilized to predict the nominal failure level. A factor should probably also be added to the model to account for systematic error rising from inadequacy of the mathematical model itself.

Failure of the structure will occur as shown in Figure 1, when the load exceeds the capability (resistance of the structure). Load and capability are shown by two probability density functions and the illustration indicates that for some of the time, the load will exceed the resistance and thus produce failure. It is significant in the present problem that both distributions will be very broad due to their large uncertainties.

Note, that in Figure 1 the mean structural capability is 1.5 times the most probable free-field stress, and yet, there is a significant probability

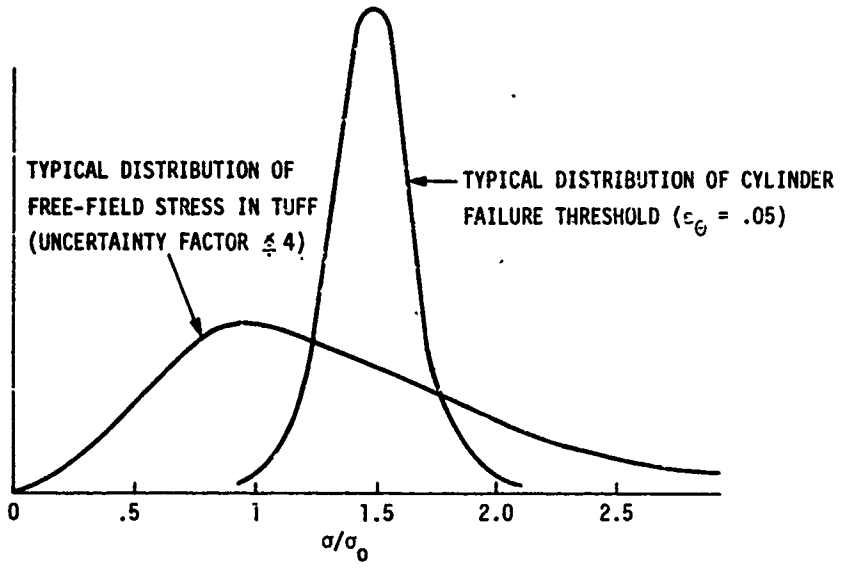

Figure 1. Distributions of Uncertainty in Free-Field Stress and Structural Capability

of failure (in this case $P_f \approx .3$).

It is possible from the information described above to get an idea of the possible range of failure thresholds which could occur in a test. If there has been one or more previous tests that contribute data of limited value, it is possible to improve the test design using a system identification procedure. If the previous test(s) were in similar media or if the structures were similar, then it could be assumed that the knowledge from these tests would permit revision of some of the mean values and reduce the uncertainties in the test plan.

In the remaining sections of this paper, procedures are developed and demonstrated which consider these problems and provide a methodology for optimum test planning with full consideration of uncertainty.

GENERAL METHODOLOGY

The objective of this study was to identify and quantify all of the sources of uncertainty associated with the testing of buried cylinders in a shock environment created by a nuclear weapon. A flow diagram for the procedure of the study is given in Figure 2.

Basic to the work is the identification and utilization of a valid deterministic structural model. If a good deterministic model cannot be found, the statistical analysis will suffer accordingly. A statistical procedure is not a remedy for poor modeling. Once the model has been identified, then it is possible to determine the characteristic uncertainties of the parameters of the model. Then, since failure is what is being sought in this study, a failure criteria must be established (i.e., at what level of strain does the structure fail?).

The model, the data uncertainty, and the criteria constitute the basic elements of the problem. From these, one can develop a statistical model which will indicate the probabilistic variation in failure occurrence. In this study, a Monte Carlo approach is used which results in the development of fragility curves for structural failure as a function of free-field stress.

The fragility curve completes the single structure analysis. However, in a test, many structures are involved, and it is the desire of the test designer to have the results of the tests straddle the failure thresholds. Failure

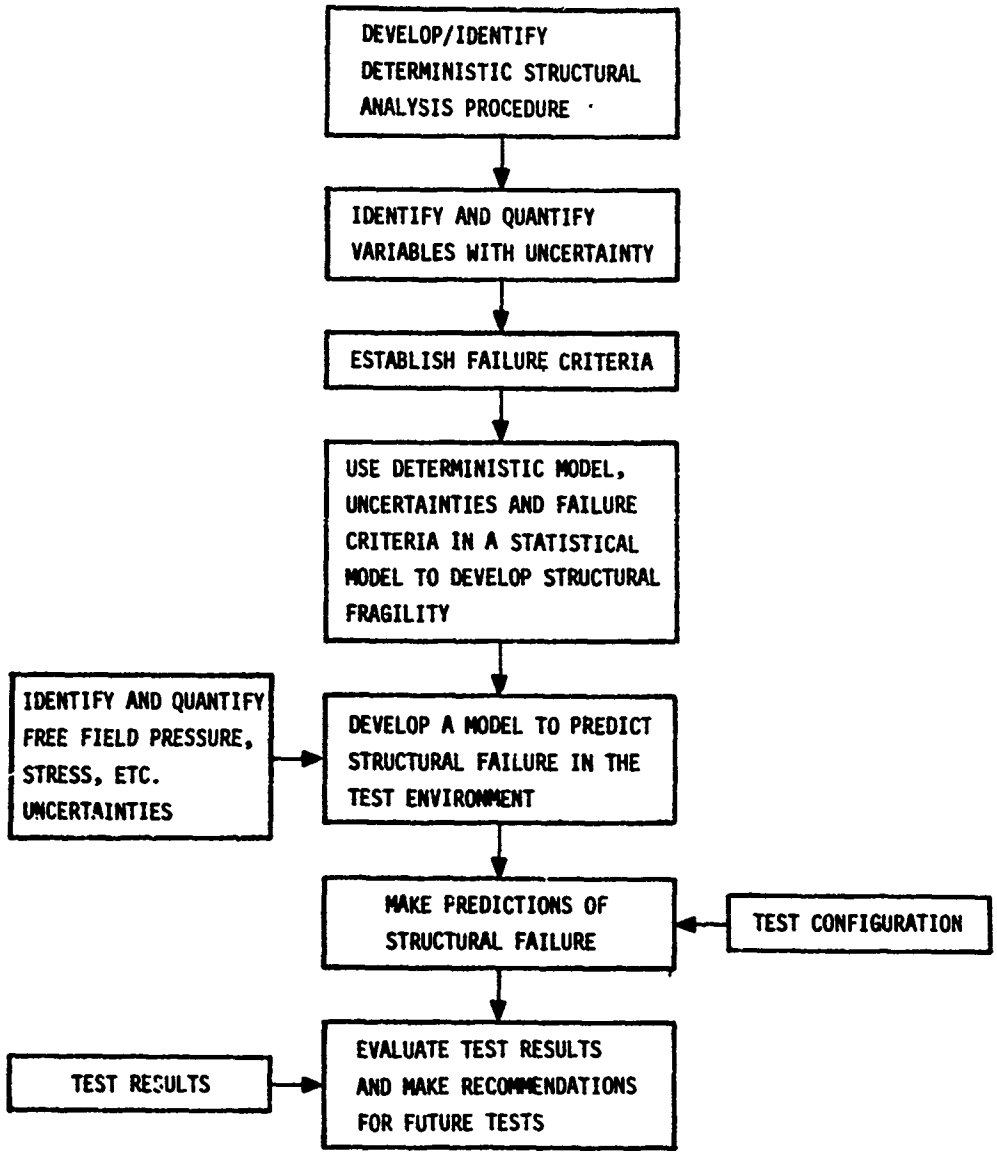

Figure 2. Methodology

of 50% of the structures could be assumed to indicate a successful test.

Prediction of the number of structures failing in an actual test requires an additional model, which is presented subsequently. This model, using the structure configuration, the structure location, the structure uncertainty, the weapon yield, and the uncertainty in free-field stress must predict the most probable range of number of structures which will fail. The procedure produces a probability density function of the number of structures failing, the expected number of failures, and the 90% confidence limits. Then, with the prediction and the test results, it is possible to evaluate the success of the test design and to make recommendations on future tests of similar design.

DEVELOPMENT OF A PROBABILISTIC STRUCTURAL FAILURE MODEL

Background - The development of a probabilistic structural failure model is straightforward and is basically composed of two distinct parts. First, one begins with a deterministic model for the failure of the structure. In the present case, the design procedure outlined (for lined tunnels in rock) in AFWL-TF-74-102 (Ref. 5) and developed by Newmark (Ref. 9) was used. This deterministic model satisfied a fundamental requirement that the design procedure be describable by mathematics, i.e., that it can be described by flow charts and computer operations. The computer model has certain input parameters (i.e., design parameters) and one or more output parameters (e.g., a design pressure, a design thickness, etc.).

The second step in the development of the probabilistic failure model is to treat the input parameters as random variables. This procedure is accomplished by establishing a mean value (of each input parameter), a standard deviation, and a distribution function for the random variable. The result of this approach is that the output (design) variable is also random, and consequently one is able to obtain a probability of failure (vs. free-field pressure, say) as opposed to discrete (one-valued) design pressure which would be obtained from the deterministic procedure.

Deterministic Model of Tunnel Failure - The basic design procedures, assumptions, and approximations used are outlined in Ref. 5, the Air Force Manual for Design and Analysis of Hardened Structures. In particular, the design approach outlined therein was developed for lined tunnels in rock by Newmark (Ref. 9), who has since published related studies (Ref. 10 and 11). Newmark's basic assumptions and approximations are listed below and are discussed in Ref. 6.

The assumptions and approximations include

- Quasi-Static Design, Inertia Neglected
- An Axi-Symmetric, Plane-Strain Assumption
- Continuity of Stresses and Strains Assumed
- Elasto-Plastic Behavior of the Materials

A typical (idealized) lined tunnel in rock is shown in Figure 3.

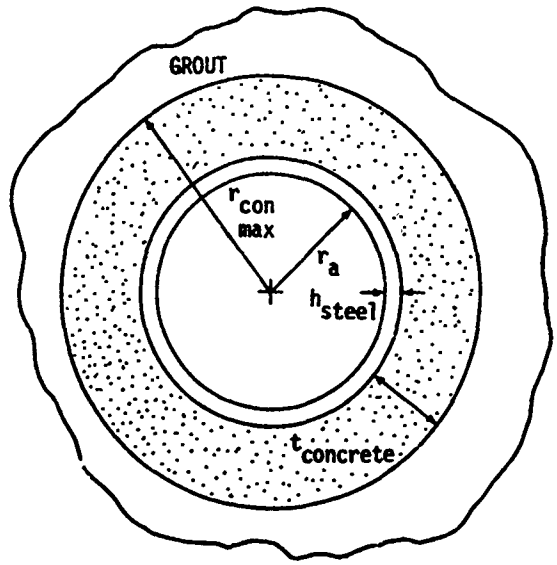

Figure 3. Typical (Idealized) Lined Tunnel in Rock

Non-Symmetric Behavior and Collapse - The assumptions of axi-symmetric response of the tunnel and liner say nothing about the behavior of the tunnel near collapse. In fact, the loading is not perfectly axi-symmetric, and the cavity does deform as an oval, causing bending of the walls. To resist such bending, the concrete liner is reinforced with steel bars (i.e., re-bar).

The design of the cavity walls to resist bending is somewhat imprecise, since the non-symmetry of the loads (which produces the bending) is not well known. It is understood, however, that these non-symmetric effects become increasingly important as the axi-symmetric response increases. For example, consider a circular ring loaded by an axi-symmetric pressure, p_o, and a non-symmetric pressure $p_2 \cos 2\theta$. Thus, the total pressure load is

$$p(\theta) = p_o + p_2 \cos 2\theta$$

The corresponding radial deflection is given by

$$w(\theta) = w_o + w_2 \cos 2\theta$$

where w_o is the axi-symmetric response, and w_2 is the buckling mode.

From the theory of buckling (see Ref. 13, for example) it can be shown that w_2 has the form

$$w_2 = \frac{\alpha\, p_2}{\left(1 - \frac{p_o}{p_{cr}}\right)} \qquad (1)$$

In other words, as the axi-symmetric pressure p_o approaches the critical (i.e., buckling) pressure p_{cr}, the non-symmetric response w_2 becomes unbounded. (In equation 1, the factor α is just a constant of proportionality.

It is anticipated that a relation similar to equation (1) will hold for the lined tunnels considered herein. That is, above a critical axi-symmetric pressure, p_{cr}, it is expected that the steel liner will buckle and the tunnel walls will collapse.

Specifying Failure in Terms of the Steel Liner Strain, ε - In most analytical design procedures, it is customary to specify the load (in this case the free-field pressure, p_o, say) and then compute the response (the strain ε_θ in the concrete or in the steel liner, say). However, because of the rigid-plastic assumption for the steel, Newmark (Ref. 9) found it simplest to specify a certain liner strain (ε) and to then compute the corresponding pressure in the free-field, p_o. Galbraith (Ref. 7) indicated that recent test cylinders were designed for circumferential strains, ε, ranging from

$$.005 \leq \varepsilon \leq .08 \qquad (2)$$

and that the strain gage reading showed strains on the same order as the design values. In general

$$\varepsilon_{test} \leq \varepsilon_{design} \qquad (3)$$

for the strains recorded on the test cylinders.

The question naturally arises, "What is a reasonable value of the circumferential strain at failure, ε_{fail}?" According to Galbraith (Ref. 7) the cylinders designed for

$$.005 \leq \varepsilon \leq .02 \qquad (4a)$$

were not expected to fail, and those designed for

$$.06 \leq \varepsilon \leq .08 \qquad (4b)$$

were expected to fail, and those for which

$$.02 \leq \varepsilon \leq .06 \qquad (4c)$$

were expected to be in a transition region. The strain gage readings (from individual locations on the steel liner) indicated that the strains measured in the test were somewhat less than the designed - for values (see equation 3, above).

Until a better value becomes available, a (somewhat arbitrary) failure strain of

$$\varepsilon_{fail} = .05 \qquad (5)$$

will be chosen for the steel liner.

As long as

$$\varepsilon < \varepsilon_{fail} \qquad (6a)$$

then the cylinder will be said to "have not failed," and when

$$\varepsilon \geq \varepsilon_{fail} \qquad (6b)$$

the cylinder is presumed to have failed.

Development of Tunnel Fragility Curves - Newmark's design procedure is deterministic. That is, a circumferential strain, ε, is assumed, the properties of the steel, the concrete, the grout and the rock, etc., are all taken to be known, and a corresponding free-field pressure, p_o, is computed. The value of p_o determined in this fashion corresponds in a one-to-one fashion with the assumed strain, ε. This deterministic design procedure is outlined in Ref. 6, and is discussed therein.

In the probabilistic approach, however, Young's modulus for the rock E_r, is assumed to be normally distributed with a mean, $\bar{E}_r$, and a standard deviation, σ_{E_r}. In a similar fashion, other input quantities, like the ultimate compressive strength of the rock (σ_{ult}), the unconfined compressive strength of the concrete (f_c'), etc. are taken to be statistically distributed.

When a relationship is known between input quantities, the statistical variables are correlated, and only one quantity is allowed to be independent. For example, in the case of concrete, the empirical relation

$$E_{concrete} = 57{,}000\ \sqrt{f_c'}$$

(where f_c' is the unconfined compressive strength in lb/in^2) is known to fit the data fairly well (Ref. 12). Thus, in the probabilistic study, f_c' is taken to be independent (with a mean and standard deviation of its own) and the modulus E_{con} is taken to be dependent (by virtue of equation 7).

The purpose of the probabilistic approach is to compute a probability of failure, i.e., the probability that the tunnel collapses. Since we have previously defined failure by $\varepsilon > \varepsilon_{fail}$ in Equation (6b), the probability of failure becomes

$$P(\text{failure}) = P(\varepsilon > \varepsilon_{fail}) \qquad (8)$$

that is, the probability that the failure strain (ε_{fail}) is exceeded. Details of the probabilistic calculations are discussed in the paragraphs which follow.

Recall from the Introduction that the objective is to generate a "fragility curve" of failure probability (P_f) vs. the free-field over-pressure in the rock, p_o. To generate probability data for the fragility curves, a computational technique known as a "Monte Carlo" procedure was used. This technique has been made practical with the advent of the high-speed computer and it can be briefly described with the aid of Figure 4.

Beginning on the left of Figure 4, note the block labeled "parameter uncertainties," which represents the fact that the input design parameters (E_{rock}, ν_{rock}, etc.) are known just statistically. For example, Young's modulus for the rock (E_{rock}) has a mean value ($\bar{E}_r$) and a standard deviation (σ_{E_r}). Based upon experimental data for rock and from knowledge of similar material property data, the assumption is made that E_r is normally distributed. The mean value ($E_r = 0.87 \times 10^6$ lb/in^2), 6.0×10^9 N/m^2 and the standard deviation ($\sigma_{E_r} = .07 \times 10^6$ lb/in^2), $.48 \times 10^9$ N/m^2 were estimated (Ref. 2 and 7). In a similar fashion, statistical properties were estimated for all eleven of the input design parameters. (These results are presented in Table I).

Returning now to Figure 4, the parameter uncertainties are defined (on the left of the Figure) using Table I. The next step in the Monte Carlo procedure is to extract a random sample (a set of eleven input design parameters) from our statistically distributed input variables. This sampling is achieved computationally by means of a subroutine which serves as a random number generator. The subroutine generates eleven (11) statistically independent random variables (one for E_r, one for ν_{rock}, etc.), and these variables thus define the input design variables for (one cycle of) the Monte Carlo procedure.

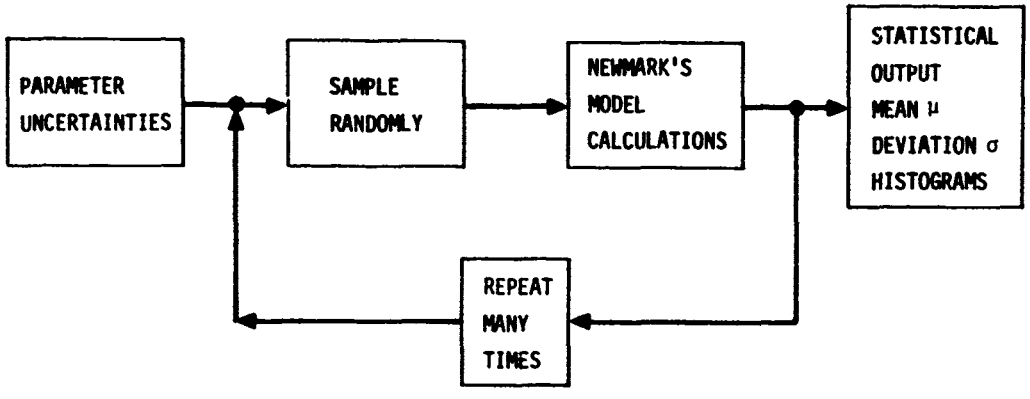

Figure 4. Monte Carlo Computational Procedure

The eleven (random) input variables are then used in Newmark's model

PARAMETER	MEAN, μ	DISTRIBUTION	STANDARD DEVIATION, σ	JUSTIFICATION FOR VALUES AND DISTRIBUTION
CRØCK E_r, Young's Modulus for rock and grout	$.87 \times 10^6$ lb/in^2 (6.0×10^9 N/m^2)	Assumed Normal	$.07 \times 10^6$ lb/in^2 ($.48 \times 10^9$ N/m^2)	Estimated Ref. [2] and [7]
GNURØK ν_r, Poisson's Ratio for rock and grout	.2	Assumed Normal	.05	Reference [2]. Design used $\nu_r = .33$, according to Ref. [7].
GNUCØN ν_c, Poisson's Ratio for concrete	.14	Assumed Normal	.02	Best Guess. Design Used $\nu_c = .167 = \frac{\nu_r}{2}$
FYIELD f_y, Yield Stress for the steel liner	38 kips/in^2 ($.26 \times 10^9$ N/m^2)	Normal	2.3 ksi ($.016 \times 10^9$ N/m^2)	Test data from Steel Coupons Reference [7] and Ref. 12, p. 5, 4000 tests.
FCPRIM f'_c, Unconfined compressive strength of concrete	5500 lb/in^2 (static) (3.8×10^7 N/m^2) 8000 lb/in^2 (dynamic) (5.5×10^7 N/m^2)	Normal	500 lb/in^2 (3.45×10^6 N/m^2)	Includes dynamic strength increase, $K_{dyn} = 1.45$. See Ref. [6] and specifications on tests
XKCON k_{sc}, Friction-Dependent Constant, for concrete	$\mu_k = 3$ $\mu_\phi = 30°$	Assumed log-normal for ϕ	F = 1.5 $20° \leq \phi \leq 45°$	$k = \frac{1 + \sin\phi}{1 - \sin\phi}$ with k = 3 used in design
XKROK k_{sr}, Friction-Dependent Constant for Rock	$\mu_k = 1.19$ $\mu_\phi = 5°$	Assumed log-normal for ϕ	F = 3 $5/3° \leq \phi \leq 15°$	$k = \frac{1 + \sin\phi}{1 - \sin\phi}$, and $\phi \geq 0$ varies greatly. $\phi = 5°$ used in design.
SIGULT σ_{ult}, Ultimate (unconfined) Compressive Strength for Rock	2900 lb/in^2 (2.0×10^7 N/m^2)	Assumed Normal	725 lb/in^2 (5.0×10^6 N/m^2)	Reference [2]. Design value used by Merritt was 1500 lb/in^2 = σ_{ult}
HSTEEL h_s, Thickness of the Steel Liner	.746 in (1.89 cm)	Assumed Normal	.002 in. (.05 mm)	Estimated, See Ref. [6]
RSUBA r_a, Inside Radius of the steel liner	24 in. (61 cm)	Assumed Normal	.125 in. (.3175 cm.)	Reference [7] and Specification from drawings
RCNMAX $r_{con_{max}}$, Outside radius of the concrete	29.75 in (75.56 cm)	Assumed Normal	.375 in. (.95 cm.)	Reference [7] Specification from drawings

Table I. Table of Uncertainties

calculations (for lined tunnels in rock) to compute a corresponding free-field pressure. This procedure of random sampling and design calculation is repeated many times, and it constitutes what is referred to as a "Monte Carlo" approach.

Table I, referred to in the previous paragraphs, contains estimates of the mean, standard deviation, and type of probability distribution used in the calculations. A detailed discussion of the entries in this Table is given in Ref. 6.

As was indicated previously, Newmark's design procedure involves choosing a liner strain (ε) and then computing a corresponding free-field pressure (P). With no uncertainties in the problem, a curve of free-field pressure vs. liner strain is obtained such as the line labeled "nominal design values" in Figure 5.

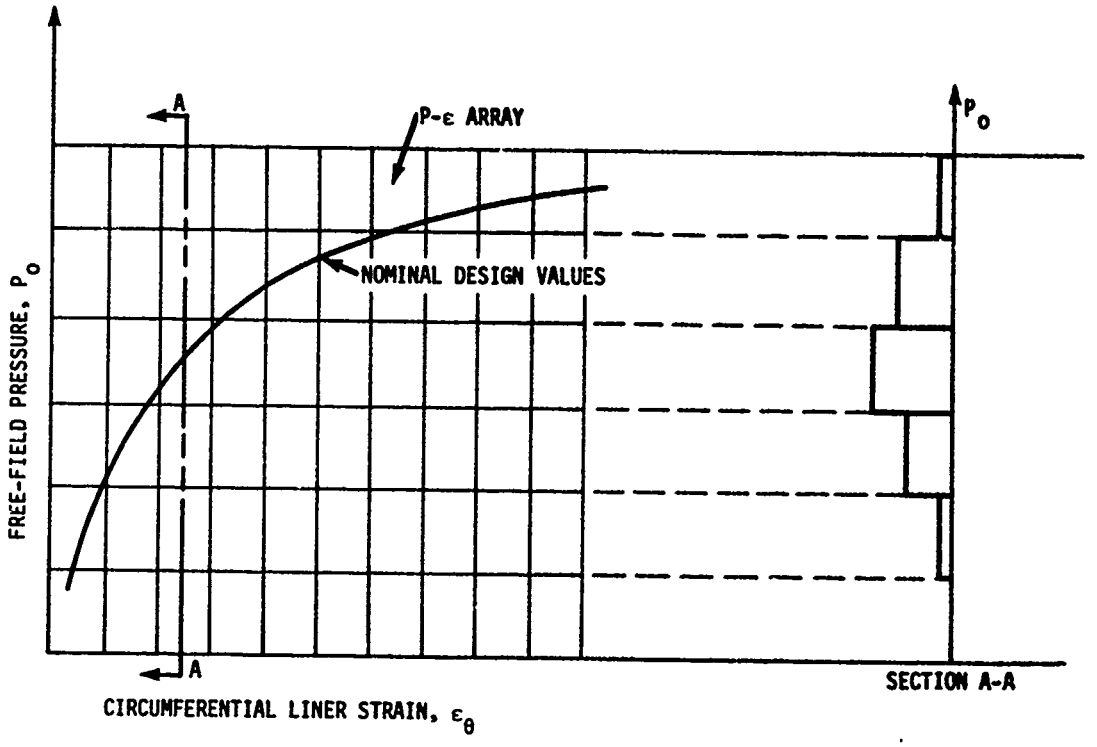

Figure 5. Frequency Distribution (for a given strain, ε) for Probabilistic Analysis

In the Monte Carlo procedure, it is still necessary to choose a liner strain (ε), but now for any particular ε one finds a distribution of pressures (such as shown in Section A-A of Figure 5). Thus, for each (fixed) value of ε, the procedure is to sample randomly from the eleven input design variables, and then repeat the sampling (Monte Carlo) many times (enough to reasonably populate the distribution in Section A-A). Thus, one can consider a rectangular array in the P vs. ε plane, as shown in Figure 5.

Now, to compute a probability of failure, first take a horizontal cut through the P-ε array as shown in Figure 6, Section B-B. For a cut (section) at constant pressure P in Figure 6, one has a frequency distribution of the number of occurrences vs. liner strain, ε. For the calculations discussed herein, a total of 20 divisions in ε (ranging from $.01 \leq \varepsilon \leq .20$) was used. These frequency distributions were each normalized to unity, such that the probability satisfied the relationship

$$P(.01 \leq \varepsilon \leq .2) = 1 \qquad (9)$$

There is a different frequency distribution (number of occurrences vs. ε) for each horizontal cut (e.g., Section B-B) through the P vs. ε array. For any one cut, the pressure P is constant, and the probability of failure (at that pressure) is given by

$$P(\varepsilon > \varepsilon_{fail}) = \int_{\varepsilon=\varepsilon_{fail}}^{\varepsilon=.2} f(\varepsilon)d\varepsilon \qquad (10)$$

where $f(\varepsilon)$ is the frequency distribution involved. In this paper the failure strain ε_{fail} was set at 0.05 [cf. equation (5)].

$$P(\varepsilon > .05) = \int_{\varepsilon=.05}^{\varepsilon=.2} f(\varepsilon)d\varepsilon \qquad (11)$$

or

$$P(\varepsilon > .05) = F(.2)-F(.05)$$

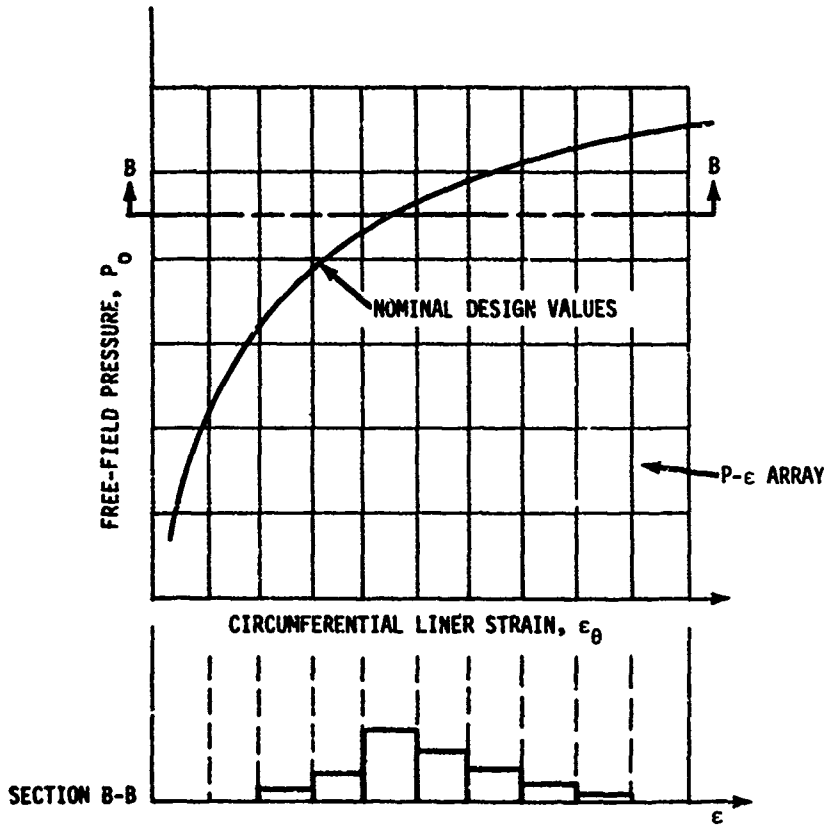

Figure 6. Frequency Distribution for a Cut at Constant Pressure (Probabilistic Analysis)

where $F(\varepsilon)$ is the cumulative distribution function defined by

$$F(y) = P(\varepsilon \leq y) = \int_{-\infty}^{y} f(\varepsilon)d\varepsilon \quad (12)$$

Equations (10) and (11) represent the probabilities in terms of area under the frequency distribution curve (See Figure 7).

In actual calculations on the computer, one encounters histograms* since the procedure is to discretize the P vs. ε plane, and it is simplest to work with the cumulative distribution (cf. equation (12)). Thus, for each cut at constant pressure (Figure 6) one has a histogram from which a probability of failure can be determined using

$$P_{fail} = P(\varepsilon > \varepsilon_{fail}) \quad (13)$$

This procedure established a one-to-one relationship between the probability of failure P_f and the free-field pressure, P. The one-to-one relationship (between P_f and P, for a given failure strain ε_{fail}) is shown plotted in Figure 8, for a particular concrete thickness, t_c.* Figure 8 represents what is commonly called a "fragility curve." Previous state-of-the-art has been to determine such fragility curves <u>experimentally</u>, whereas

*A histogram is a frequency distribution for a discrete variable (as opposed to a continuous variable). See Ref. 1.

*Note that Figure 8 has been nondimensionalized by dividing the free-field stress (P or σ) by the design stress, σ_o.

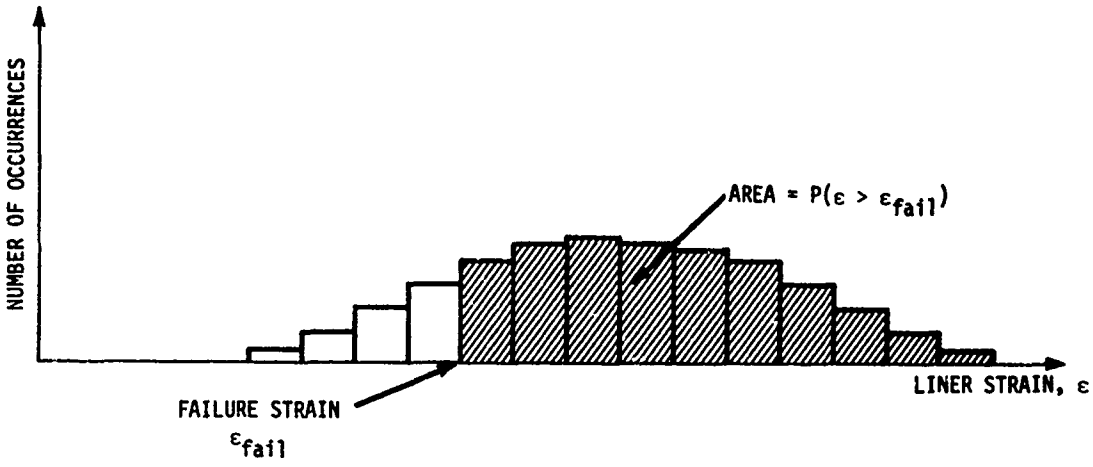

Figure 7. Probability of Failure Illustrated as an Area

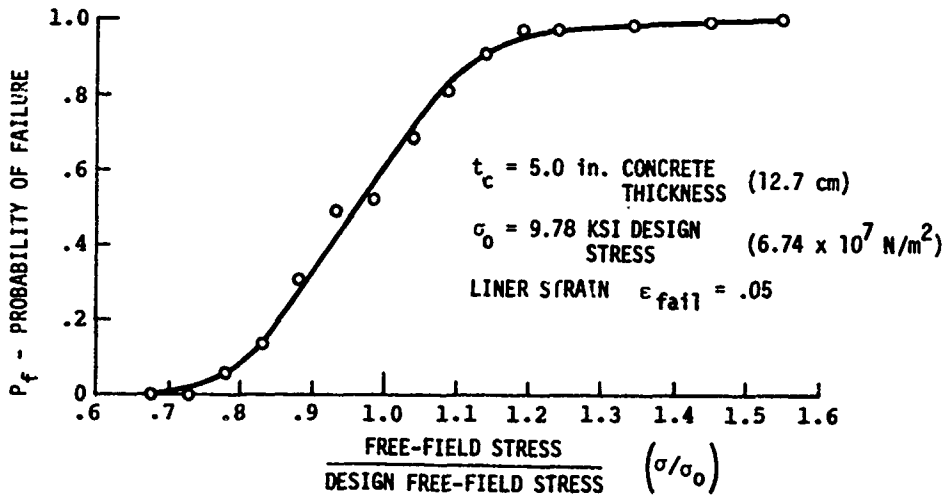

Figure 8. Dimensionless Fragility Curve for 5.0 in. Concrete Thickness

Figure 8 has been analytically derived, as was just discussed.

Note that the failure criterion ($\varepsilon > .05$) appears explicitly on the fragility curve. The specification of a failure strain ($\varepsilon = \varepsilon_{fail}$) is an involved subject which has been touched on only briefly herein.

It is clear that the selection of a failure strain is by no means a closed topic, and it is also clear that the probabilistic design approach outlined herein can treat whatever failure strain that the analyst chooses. It is also possible to give probabilistic values to a range of failure strains (ε) and integrate over the corresponding fragility curves. This procedure would be more accurate and realistic than specifying a discrete failure strain (like $\bar{\varepsilon} = .05$) but was not within the scope of this study.

COMPUTATION OF FAILURE PROBABILITY

The question now arises, "How does one use the fragility curve?" (See Figure 8.) Experimental data (from several tests) has shown the

dependence of free-field pressure P_o on the range, R, and it is now desired to convert the fragility curves from P_f vs. P_o to P_f vs. R. Such a conversion will provide the desired "P_f - maps" similar to those sketched in Figure 9.

given approximately by

$$F(P_o) = \frac{1}{P_o\sqrt{2\pi}\,\sigma_{\ln P}} \exp\left(-\frac{1}{2}\left\{\frac{\ln P_o - \overline{\ln P_o}}{\sigma_{\ln P}}\right\}^2\right) \tag{15}$$

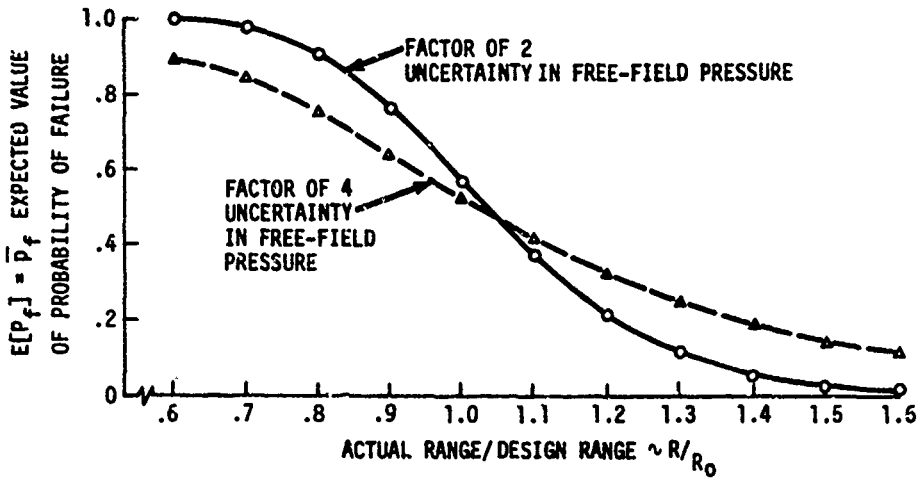

Figure 9. P_f - Maps Using Two Different Uncertainty Factors

Regarding the dependence of free-field stress on the range, R, it is customary to present instead the "particle velocity" V as a function of R. For example, Reference 8 shows that particle velocity V varies inversely as the square of the range R. Free-field pressure is related to particle velocity by

$$P_o = \rho C_L V \tag{14}$$

where ρ is the mass density of the medium (i.e., the tuff), C_L is the corresponding longitudinal wave speed, and V the particle velocity. Uncertainties in ρ and C_L cause the scatter in the data for P_o to be greater than the scatter for V. The inverse dependence upon R^2 also holds for P_o, and Reference 8 states that the data have an "uncertainty factor" of 4, as opposed to a factor of 3.5 for velocity V alone.

It is customary to plot P_o (or V) against R on log-log paper, and if the fact that P_o is statistically distributed (with a mean and standard deviation) is taken into account, then the probability density function for P_o is which is a so-called "log-normal" distribution (Ref. 1). In equation (15) $\overline{\ln P_o}$ is the mean value (of the logarithm $\ln P_o$) and varies inversely with the square of the range R. Thus, the R-dependence in equation (15) is contained in $\overline{\ln P_o}$.

From the theory of probability (Ref. 1) the expected value of any continuous variable x is given by

$$E[x] = \bar{x} = \int_{\text{all } x} x\, f(x)\,dx \tag{16}$$

where f(x) is the probability density function. Similarly, if a variable g depends upon x, one has

$$E[g(x)] = \bar{g} = \int_{\text{all } x} g(x)\, f(x)\,dx \tag{17}$$

where $\bar{g}$ is the expected value of g(x). Accordingly, for the problem at hand, the above results give

$$E[P_f] = \bar{P}_f = \int_{\text{all } P_o} P_f(P_o) f(P_o) dP_o^* \quad (18)$$

where

$\bar{P}_f$ is the expected value of the probability of failure,

$P_f(P_o)$ is the fragility curve(s) developed previously, and

$f(P_o)$ is the probability density function given by equation (15).

Note the $\bar{P}_f$ depends upon the range R (parametrically) by virtue of the fact the $\overline{\ln P_o}$ is a function of R.

In principle, the integration described by equation (18) can be done numerically, using the density function (16) and a piece-wise linear approximation to the appropriate fragility curve, i.e., $P_f(P_o)$. In practice, however, it was simplest to non-dimensionalize the problem and then perform the numerical integration.

For example, let σ be the free-field stress in rock (i.e., the over-pressure) and σ_o be the design value of over-pressure. Similarly, let R be the range from the point of detonation, and R_o the design range. Then a plot of (σ/σ_o) vs. (R/R_o) appears as shown in Figure 10. Note that

$$\overline{\ln(\sigma/\sigma_o)} = -2 \ln(R/R_o) \quad (19)$$

from Figure 10, and the bounds on the data in the figure relate to the fact that (σ/σ_o) is statistically distributed. When expressed in non-dimensional form, equation (15) gives

$$f(\sigma/\sigma_o) = \frac{1}{(\sigma/\sigma_o)\, k\sqrt{2\pi}} \times \exp\left(-\frac{1}{2}\left\{\frac{\ln(\sigma/\sigma_o) + 2 \ln(R/R_o)}{k}\right\}^2\right) \quad (20)$$

where k is a measure of the breadth of the distribution, and where equation (19) has been used for $\overline{\ln(\sigma/\sigma_o)}$.

*See Reference 3 for the derivation equating the result in equation (18) with the (related) procedure using the difference or two probability density functions.

The remaining problem is to calculate $E[P_f]$ which is given by

$$E[P_f] = \bar{P}_f = \int_{\text{all } (\sigma/\sigma_o)} P_f(\sigma/\sigma_o) f(\sigma/\sigma_o) d(\sigma/\sigma_o) \quad (21)$$

Equation (21) is the non-dimensional analog of equation (18) and the dependence of $\bar{P}_f$ on the range (R/R_o) shows up in equation (20).

The integration described by equation (21) was performed numerically using a straightforward FØRTRAN IV computer program. A piecewise-linear approximation to each fragility curve was used, and the computer program was verified by performing one integration on a programmable calculator. The procedure used was to select a (non-dimensional) range (R/R_o), calculate the corresponding value $E[P_f]$, and then repeat the integration for as many values of (R/R_o) as desired. This integration procedure was performed for each of four fragility curves, corresponding to four concrete thicknesses: 2.5, 5.0, 10, and 15 inches thick.

The resulting P_f - map is shown in Figure 9, which applies for all four thicknesses. What has happened is that by non-dimensionalizing the fragility curves and then performing the smoothing process of integration, the differences between 2.5, 5.0, 10, and 15 inch thicknesses are removed. Note that if the data had not been non-dimensionalized, one would have obtained a separate curve (P_f - map) for each concrete thickness. Since the non-dimensional fragility curves have some slight differences, the four integrations (for t_c = 2.5, 5.0, etc.) were slightly different when plotted on Figure 9, but the differences were on the order of 0.02 (in $\bar{P}_f$) which is approximately the size of the circle around each data point.

The dashed line in Figure 9 was determined using

$$k = \frac{\ln 4}{1.96} = 0.7073 \quad (22)$$

in equation (20), which corresponds to an uncertainty factor of 4 in the pressure vs. range relationship. If the uncertainty were somehow reduced to a factor of 2 (instead of 4) then the corresponding constant becomes

$$k = \frac{\ln 2}{1.96} = .3536 \quad (23)$$

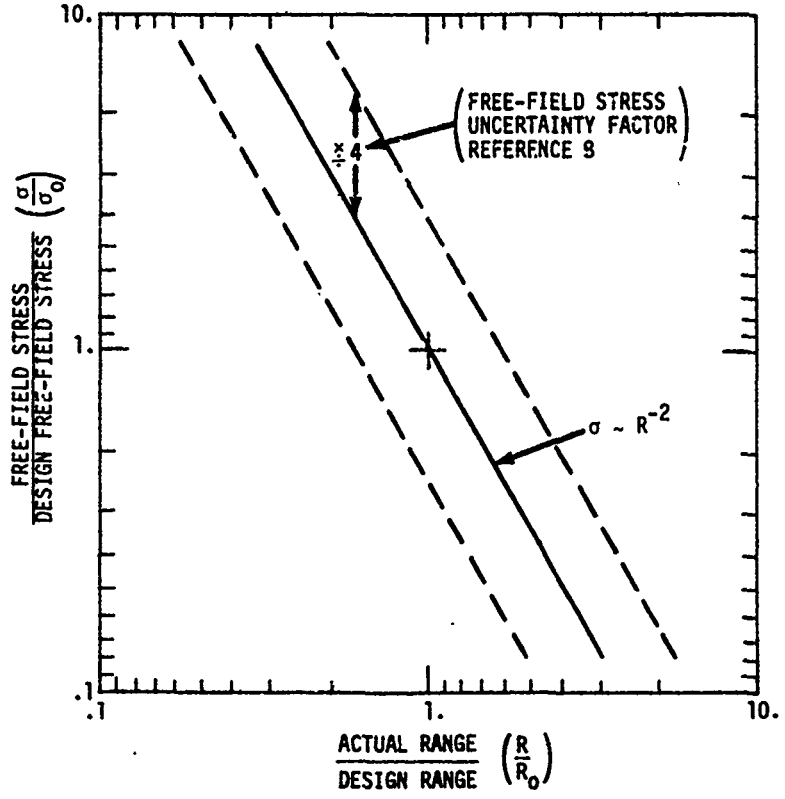

Figure 10. Dimensionless Plot of Free-Field Stress Variation with Range

in equation (20), and the resulting P_f - map is shown as a solid line in Figure 9.

TEST PREDICTIONS AND EVALUATION

Once the structural details are known, it is a fairly straight-forward procedure to calculate the corresponding expected value of failure probability, $\bar{P}_f$. For example, knowing the tunnel dimensions, steel thickness, concrete thickness, etc., one can compute a free-field design stress, σ_o, for the structure, using a design liner strain.* Having the free-field stress σ_o, one then uses a predicted curve of stress vs. range (for the test event) to read off a design range, R_o. The location of the particular tunnel determines the actual range, R. Then, one simply computes the ratio (R/R_o) and reads off the corresponding value of $\bar{P}_f$ using Figure 9.

The results of this procedure are given in Table II, Column (A), which shows the expected value of probability of failure ($\bar{P}_f$) vs. structure number.* Note that the failure probabilities $\bar{P}_f$ in Column (A) were computed assuming a factor of four uncertainty in the free-field pressure vs. range characteristics.

When the uncertainty factor is reduced to 1.1, the results are shown in Column (B) on Table II. The data of Column (B) were determined by essentially performing the numerically integration (described previously, equation 21) using a factor

$$k = \frac{\ln 1.1}{1.96} = 0.0485 \qquad (24)$$

*ε_θ = .05 was used herein.

*The structures are simply arranged in the order of increasing $\bar{P}_f$.

STRUCTURE NUMBER	FAILURE PROBABILITIES	
	(A) FACTOR OF 4 UNCERTAINTY	(B) FACTOR OF 1.1 UNCERTAINTY
1	.1	.005
2	.12	.005
3	.26	.005
4	.40	.005
5	.44	.03
6	.44	.03
7	.45	.10
8	.47	.12
9	.49	.28
10	.56	.75
11	.63	.86
12	.63	.86
13	.70	.99
14	.74	.99

Table II. Failure Probabilities

in the log-normal distribution (20). For such a relatively small uncertainty, $f(\sigma/\sigma_c)$ in equation (20) behaves much like a Dirac delta-function* and this fact enabled the integration to be done by hand.

Table II describes 14 independent tests (i.e., "events" in the terminology of probability theory) each with a corresponding probability. (That is, the i^{th} structure has a probability of failure P_{f_i}, etc.) Given M independent events each with a different probability P_i, Collins (Ref. 4) has computed the probability of exactly one failure, exactly two failures, etc. The results are a series of summations and products described mathematically by

$$P(0) = \prod_{i=1}^{M} (1-p_i) \tag{12a}$$

$$P(1) = \sum_{j=1}^{M} p_j \prod_{i=1}^{M} (1-p_i) \quad \text{for all } i \neq j \tag{12b}$$

$$P(2) = \sum_{j=1}^{M} \sum_{k=1}^{M} p_j p_k \prod_{i=1}^{M} (1-p_i) \quad \text{for all } i \neq j \neq k \tag{12c}$$

$$P(3) = \sum_{j=1}^{M} \sum_{k=1}^{M} \sum_{\ell=1}^{M} p_j p_k p_\ell \prod_{i=1}^{M} (1-p_i) \quad \text{for all } i \neq j \neq k \neq \ell \tag{12d}$$

$$P(M) = \prod_{i=1}^{M} p_i \tag{12e}$$

$$P(N \text{ of } M \text{ in } A) = \sum_{s=N}^{M} P(s) \tag{12f}$$

where P(0) is the probability of exactly 0 failures, P(1) the probability of exactly 1 failure, etc.

These summations involve a very large number of terms (e.g., like 14 - factorial) and reduce to the binomial theorem when all events have identical probabilities. The large number of terms precluded the possibility of evaluating the summations algebraically, but they were amenable to evaluation by a computer simulation technique. The results of the calculations are shown in Figure 11, for a factor of 1.1

*A narrow, highly peaked function with an area of unity.

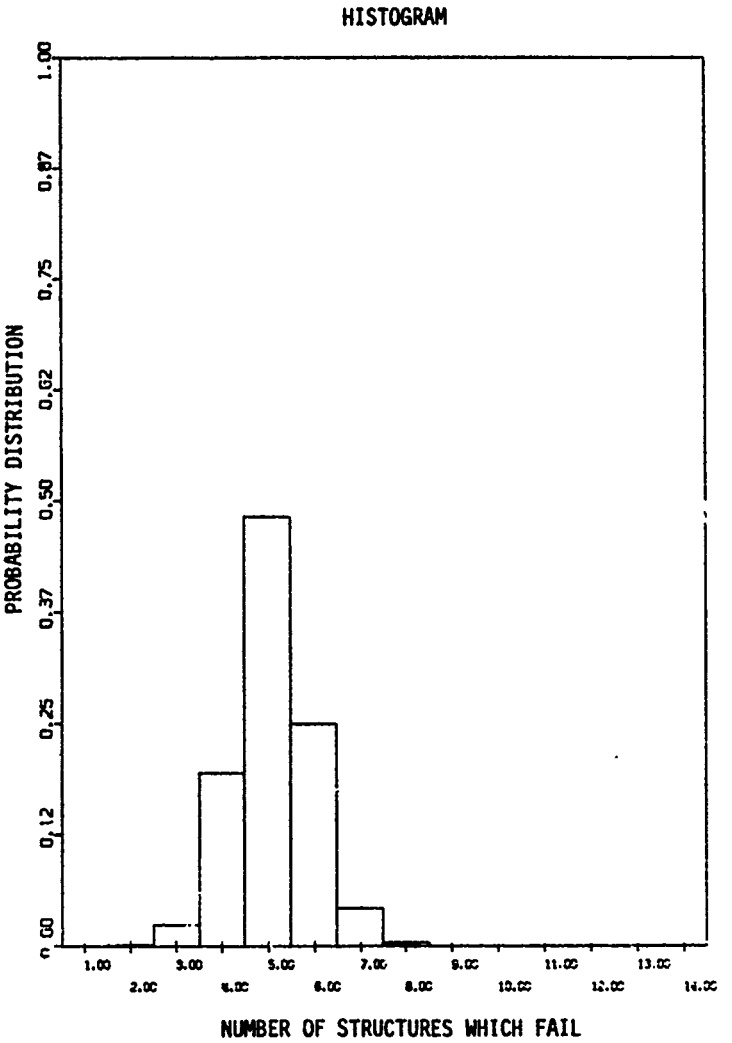

Figure 11. Frequency Distribution (Histogram) for Actual Test (Factor of 1.1 Uncertainty)

uncertainty in the free-field pressure.

Figure 11 shows the probability distribution (histogram) for the actual test, assuming a factor of 1.1 uncertainty as just discussed.

In this instance, the probability of having exactly 5 failures is quite large, about 0.45. Similarly, the probability of exactly 4 or exactly 6 failures is about 0.2 and 0.25, respectively. From the corresponding cumulative distribution, one can readily determine that the number of expected failures lies between 4 and 6, within 90 per-cent confidence limits. This analytical result is in agreement with the actual test, in which four* (4) cylinders failed.

CONCLUSIONS

The major conclusions drawn from the results of this study are:

- The work developed analytical fragility curves, whereas they are customerily determined experimentally.

*The four failures do not include one shearing failure which coincided with a geological fault.

- The analysis successfully predicted the number of failures in an actual test, within statistical bounds.

In addition, the study demonstrated a general methodology which can be applied to other tests and other structures. Furthermore, it appears that Newmark's design procedure, when coupled with statistical modeling, is adequate for the design of lined tunnels in rock, despite the simplifications and assumptions inherent in the procedure.

Regarding the limitations of the present study, recall that it is based on a failure strain which was assumed as $\varepsilon_{fail} = 0.05$. Perhaps a better procedure would have been to allow ε_{fail} to be randomly distributed as well (with a mean of .05, say) but this refinement was beyond the scope of the present study. If ε_{fail} had been treated randomly, the limits on the number of expected failures would have been widened somewhat.

Another limitation of this study is that the 14 structures were all treated independently, with no correlation among them. Future studies should include the effects of correlation, as discussed in Ref. 6. Finally, recall that the analysis is dependent on Newmark's design procedure, which assumes axi-symmetry. A further refinement would be to include nonsymmetric behavior in the design equations.

ACKNOWLEDGMENTS

This study was sponsored by the Strategic Structures Division of DNA with Dr. Kent Goering as Technical Monitor; his support, comments, and constructive criticism are gratefully acknowledged. Bruce Kennedy of the J.H. Wiggins Company was responsible for much of the computer implementation and Monte Carlo procedures.

Engineers at several other DNA contractors were responsive to our requests for test details and design uncertainties. The late Frank Galbraith of Meritt CASES was particularly helpful in this regard. Others who contributed necessary information include:

Scott Butters of Terra Tek,
Dr. Peter Dai and Norman Lipner of TRW
Harvey Haynes of NCEL, Port Hueneme and
Coy Vincent of Physics International

Helpful discussions with these colleagues are gratefully acknowledged.

REFERENCES

1. Benjamin, J.R. and Cornell, C.A., Probability, Statistics and Decisions for Civil Engineers, McGraw-Hill, New York, 1970.

2. Butters, Scott, Terra Tek, Salt Lake City, Utah (private communication).

3. Collins, Jon D., "Structural System Failure Analysis in a High Load Environment," ASCE Structural Division Conference, University of Wisconsin, Madison, Wisconsin, August 23-26, 1976.

4. Collins, Jon D., and Kennedy, B., "MX-Fast Computer Program Description," Technical Report No. 75-3031-1, J.H. Wiggins Company, under Contract F04701-72-C0147 to Air Force Weapons Laboratory, Kirtland AFB, July 3, 1975.

5. Crawford, R.E., Higgins, C.J., and Bultmann, E.H., The Air Force Manual for Design and Analysis of Hardened Structures, Report AFWL-TR-74-102, Air Force Weapons Lab., Kirtland AFB, N.M., October 1974.

6. Evensen, D.A., and Collins, J.D., "Test Planning with Uncertainty," Report No. 76-1270, J.H. Wiggins Company, on Contract No. DNA 001-76-C-0282, for Defense Nuclear Agency, Washington, D.C., August 20, 1976 (also available as DNA Report No. 4099F).

7. Galbraith, F., and Merritt CASES, Redlands, California (private communication).

8. Lipner, N., Anderson, D.C., and Dai, P.K., "Ground Motion Environments for Generic Site Conditions," Final Report on Contract DNA 001-74-C-0249, TRW Systems Group, December 31, 1975.

9. Newmark, N.M., "Design of Rock Silo and Rock Cavity Linings," Report for Space and Missile Systems Organization, Norton AFB, California, August, 1969.

10. Newmark, N.M., "Design Studies of Tunrel and Pipe Seals (TAPS)," Final Report to Test Command DASA, October 5, 1970. (For Official Use Only)

11. Newmark, N.M., "Design Studies for Lined Tunnels and Capsules," Final Report to Test Command, DASA, April 19, 1971. (For Official Use Only)

12. Norris, C.H., et al, Structural Design for Dynamic Loads, McGraw-Hill, New York, 1959.

13. Timoshenko, S.P., and Gere, J.M., Theory of Elastic Stability, 2nd Edition, McGraw-Hill, New York, 1961.

NOTATION

C_L	Logitudinal wave speed (e.g., in rock)
E_r, E_{con}	Young's modulus for rock and concrete, respectively
$\bar{E}_r$	Mean value of E_r
E[ ]	Expected value of [ ]
$E[P_f]$	Expected value of the probability of failure; mean value
EI	Bending stiffness (of the tunnel wall)
f_c'	Unconfined compressive strength of the concrete
f(x)	Probability density function, of a continuous variable, x
$f(\varepsilon)$	Probability density function, expressed in terms of strain, ε
$F(\varepsilon)$	Cumulative distribution function
g(x)	An (arbitrary) function of x
$\bar{g}$	Mean value of g(x)
k	A constant
$\ln P_o$	Natural logarithm of the free-field pressure, P_o.
$\overline{\ln P_o}$	Mean value of the logarithm, $\ln P_o$
P_{cr}	Critical pressure; buckling pressure
P_f	Probability of failure
$\bar{P}_f$	Mean value of probability of failure
P_o	Free-field pressure, stress
p_o, p_2	Applied (radial) pressure acting on a ring in the zeroth and second harmonics, respectively
t_c	Concrete thickness
R	Range (from point of detonation)
R_o	Design range, range at which the structure is designed to fail
V	Particle velocity
w_o, w_2	Radial response of the ring, in the zeroth and second harmonic, respectively
ε_{fail}	The circumferential strain at failure
ε, ε_θ	Circumferential strain
σ_{E_r}	Standard deviation for Young's modulus of rock
σ_{ult}	Ultimate compressive strength of the rock
(σ/σ_o)	Free-field stress in rock, non-dimensionalized on the design stress, σ_o
σ_{lnp}	Standard deviation of the logarithm of the free-field pressure
θ	Circumferential coordinate (radians)
ν_{rock}	Poisson's ratio for rock

*U.S. GOVERNMENT PRINTING OFFICE: 1978 361-250/078 1-3